INIS-DE--0012

DE98F8424

Nuclear Astrophysics

Proceedings of the International Workshop XXVI
on Gross Properties of Nuclei and Nuclear Excitations
Hirschegg, Austria, January 11 − 17, 1998

Edited by

M. Buballa   W. Nörenberg
J. Wambach   A. Wirzba

29 - 26

GSI

HIRSCHEGG '98:

NUCLEAR ASTROPHYSICS

Proceedings of the International Workshop XXVI
on Gross Properties of Nuclei and Nuclear Excitations
Hirschegg, Austria, January 11 − 17, 1998

Edited by

M. Buballa
W. Nörenberg
J. Wambach
A. Wirzba

Gesellschaft für Schwerionenforschung (GSI)
Darmstadt
1998

δ ... ...

To be ordered from

PREFACE

The International Workshop XXVI on Gross Properties of Nuclei and Nuclear Excitations was devoted to the topic of Nuclear Astrophysics. The aim was to bring together experimentalists and theorists from astrophysics and nuclear physics to broadly discuss issues of mutual interest.

In setting up the program we enjoyed – and hereby acknowledge – the help from the advisors Gottfried Münzenberg (GSI), Vijay R. Pandharipande (University of Illinois at Urbana-Champaign), Claus Rolfs (Ruhr-Universität Bochum) and Friedrich-K. Thielemann (Universität Basel). At the workshop the status of current research was reviewed and extensively discussed. The present volume summarizes the scientific content of the meeting by including most of the talks and contributions. We thank the authors for submitting their manuscripts in time, enabling us to stay within a rapid publication schedule.

We acknowledge financial support from the DFG and GSI, which made it possible to invite leading experts in the field to contribute to the workshop. Special thanks go to Jörn Knoll for developing an efficient administrative network tool from which we benefited greatly.

Last but not least, we thank Sonja Sisak for her kind, patient and efficient help in organizing the meeting and preparing the proceedings for publication.

Darmstadt, March 1998

The Organizers

M. Buballa
W. Nörenberg
J. Wambach
A. Wirzba

Contents

Supernova physics

Cosmic rays

Stellar evolution and key reactions in nucleosynthesis

- 9 -

MANY-BODY THEORY OF NUCLEAR AND NEUTRON STAR MATTER

V. R. PANDHARIPANDE, A. AKMAL and D. G. RAVENHALL

Department of Physics, University of Illinois at Urbana-Champaign
1110 W. Green St., Urbana, Illinois 61801, USA

Abstract

We present results obtained for nuclei, nuclear and neutron star matter, and neutron star structure obtained with the recent Argonne v_{18} two-nucleon and Urbana IX three-nucleon interactions including relativistic boost corrections. These interactions predict that matter will undergo a transition to a spin layered phase with neutral pion condensation. We also consider the possibility of a transition to quark matter.

1 Introduction

Properties of matter having densities up to ~ 1 nucleon/fm^3 are important in determining the structure and maximum mass of neutron stars. At such densities the average interparticle spacing is ~ 1 fm. It is well known that the rms charge radius of proton is ~ 0.8 fm, thus one may be concerned that nucleons 1 fm apart have too large a structural overlap, and may even cease to be nucleons. However, the large charge radius of protons is due to a diffuse cloud attributed to mesons. The charge form factor of the proton, as well as the magnetic form factors of the proton and the neutron are well approximated by the dipole form:

$$F(q) = (1 + q^2/q_0^2)^{-2}; \quad q_0 = 0.84 \; \frac{GeV}{c}. \tag{1}$$

The charge density obtained by inverting this form factor is:

$$\rho_{ch}(r) = 3.3 \; e^{-r/0.23} \; \text{fm}^{-3}, \quad r \text{ in fm}. \tag{2}$$

The charge densities of two protons placed at ± 0.5 fm on the z-axis are shown in fig.1. We see that there is not too much structural overlap of protons 1 fm apart. We may therefore assume that they still are protons, and absorb the effects of the overlap into the two nucleon interaction. This assumption is supported by studies of the deuteron. The deuteron wave function peaks at
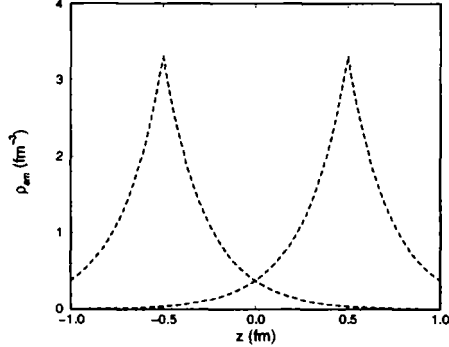
Figure 1: Charge density of two nucleons at $z = \pm 0.5$ fm, along the z-axis

~ 1 fm separation between the neutron and the proton in agreement with the observed deuteron form factors [1].

In nuclear many-body theory, nuclei and nuclear matter are described by the Hamiltonian:

$$H = \sum_i \frac{-\nabla^2}{2m} + \sum_{i<j}(v_{ij} + \delta v(\mathbf{P}_{ij})) + \sum_{i<j<k} V_{ijk}, \qquad (3)$$

in which $i, j, k, \ldots$ denote nucleons. The first term is the nonrelativistic kinetic energy, and the second contains the two nucleon interaction v_{ij} in the center of mass frame of the interacting pair. The relativistic boost interaction $\delta v(\mathbf{P}_{ij})$ describes the dependence of two-nucleon interaction on their total center of mass momentum $\mathbf{P}_{ij}$, and the last term contains the three nucleon interaction. In principle the H can have additional terms, such as the boost correction for three-nucleon interaction, four nucleon interaction, *etc.*; however these terms are believed to have a negligible effect on neutron star structure. The above H describes only the hadronic part of neutron star matter which also contains electrons and, at high densities, muons to preserve charge neutrality and beta equilibrium. The relativistic kinetic energies of the leptons and the Coulomb interaction energies are to be added to the above hadronic H.

Recent developments in various terms of the nuclear Hamiltonian are discussed in the next section, while progress in the variational calculations of the properties of matter from this H is reviewed in sect. 3. The results for neutron

stars are given in sect. 4, while the possibility of a phase transition to quark matter is considered in sect. 5. A more detailed description of this work will be published elsewhere.

2   Modern Models of Nuclear Forces

In the early 1990's the Nijmegen group [2] carefully examined all the data on NN scattering at energies below 350 MeV published between 1955 and 1992. They extracted 1787 proton-proton and 2514 proton-neutron "reliable" data, and showed that these could determine all NN scattering phase shifts and mixing parameters quite accurately. NN interaction models which fit this Nijmegen data base with a $\chi^2/N_{data} \sim 1$ are termed "modern". These include the Nijmegen models [3] called Nijmegen I, II and Reid 93, the Argonne v_{18} [4] (A18) and CD-Bonn [5]. In order to fit both the proton-proton and neutron-proton scattering data simultaneously and accurately, these models include a detailed description of the electromagnetic interactions and terms that violate the isospin symmetry of the strong interaction via the differences in the masses of the charged and neutral pions, etc.
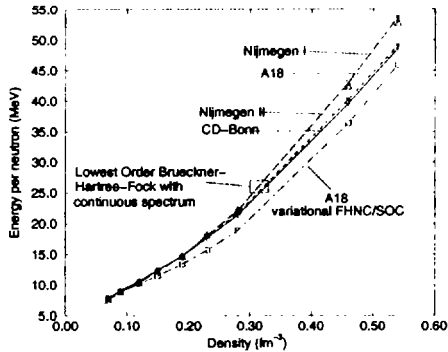
Figure 2: The $E(\rho)$ of neutron matter calculated from modern potential models. The upper four curves show results obtained with Brueckner-Hartree-Fock calculations, while the lower curve is with variational calculations.

In these five models the two nucleon interaction v_{ij} is expressed as a sum of the one-pion exchange potential v_{ij}^{π} and the rest of the interaction v_{ij}^{R}. They use different parameterizations of the v_{ij}^{R}, and the Nijmegen-I and CD-Bonn

also include nonlocalities suggested by boson-exchange representations. Thus, like the older models, they make different predictions for many-body systems. However, the differences in their predictions are much smaller than those between older models, presumably because they exactly fit the same large data set. For example, the triton ground state energies predicted by the modern Nijmegen and Argonne models, without the $\delta v(\mathbf{P}_{ij})$ and V_{ijk} terms in the Hamiltonian, are between -7.62 and -7.72 MeV [6], while that of CD-Bonn is -8.00 MeV [5]. This should be compared with the spread from -7.35 MeV (original Reid) to -8.35 MeV (Bonn-A) in the predictions of the older models. The predictions for the energies of dense neutron matter obtained from the modern potentials using lowest order Brueckner-Hartree-Fock (LOB) method [7] are also quite close together as shown in fig. 2. This figure also shows the energies of neutron matter calculated from the A18 potential by the variational method using chain summation techniques [8]. The difference between the results obtained for this modern potential using LOB and variational methods is larger than that in the results of all the modern potentials with the LOB method.

The modern potentials, like their predecessors, do not explain all of the observed nuclear properties. They all underbind the triton, and overpredict the density of nuclear matter. It is necessary to add three-nucleon (NNN) interactions to the Hamiltonian to reproduce these observables. The Urbana models of NNN interaction have only two terms:

$$V_{ijk} = V_{ijk}^{2\pi} + V_{ijk}^R, \qquad (4)$$

the first gives the two-pion exchange NNN interaction via the pion-nucleon delta resonance [9], and its strength is denoted by the parameter $A_{2\pi}$; the second is a phenomenological spin-isospin independent, shorter range term with strength denoted by U_0. The values of the parameters $A_{2\pi}$ and U_0 of the Urbana-IX (UIX) NNN potential are chosen such that in combination with A18 NN potential triton energy is reproduced via exact calculations and the equilibrium density of nuclear matter is reproduced via variational calculations [10]. The boost interaction $\delta v(\mathbf{P}_{ij})$ was negelected in these calculations to determine $A_{2\pi}$ and U_0. Its effect is discussed later. It is unlikely that a combination of CD-Bonn and UIX potentials will reproduce the triton energy. Parameters of the NNN interaction have to refitted for each model of the NN interaction, as in the recent work of the Bochum group [11] using the Tucson-Melbourne [12] model of $V_{ijk}^{2\pi}$. The fitted V_{ijk} then partly corrects for the deviation of the model v_{ij} from its exact representation. We hope that predictions of the modern combinations of v_{ij} and V_{ijk} will be significantly less

Table 1: Results of Quantum Monte Carlo Calculations in MeV

^AZ	$(J^\pi; T)$	v_{ij}^π	$V_{ijk}^{2\pi}$	v_{ij}^R	V_{ijk}^R	E_{GFMC}	$\Delta E_{expt.}$	ΔE_{VMC}
^{2}H	$(1^+; 0)$	-21.3	0	-0.8	0	-2.22	0	0
^{3}H	$(\frac{1}{2}^+; \frac{1}{2})$	-43.8	-2.2	-14.6	1.0	-8.47	-0.01(1)	0.15
^{4}He	$(0^+; 0)$	-99.4	-11.7	-36.0	5.3	-28.30	0.00(2)	0.52
^{6}He	$(0^+; 1)$	-109	-13.6	-56	6.4	-27.64	-1.63(14)	2.8
^{6}Li	$(1^+; 0)$	-129	-13.5	-50	6.3	-31.25	-0.74(11)	3.2
^{7}He	$(\frac{3}{2}^-; \frac{3}{2})$	-110	-14.1	-61	6.7	-25.2	-3.7(2)	4.7
^{7}Li	$(\frac{3}{2}^-; \frac{1}{2})$	-153	-17.1	-68	8.2	-37.4	-1.8(3)	4.7
^{8}He	$(0^+; 2)$	-121	-15.8	-74	7.5	-25.8	-5.6(6)	6.1
^{8}Li	$(2^+; 1)$	-157	-22.2	-104	11.0	-38.3	-3.0(6)	8.6
^{8}Be	$(0^+; 0)$	-224	-28.1	-72	13.3	-54.7	-1.8(6)	6.6

model dependent than those of the v_{ij} alone.

It has recently become possible to calculate all the bound states of up to eight nucleons from realistic nuclear forces with the Greens Function Monte Carlo (GFMC) method. Since solar and primodial fusion reactions primarily involve nuclei having $A \leq 8$, they have a special role in the universe. Here we use the results obtained with A18, without $\delta v(\mathbf{P}_{ij})$, and UIX interactions to test the accuracy of variational wave functions and the interaction models. The calculated energies from [10] and [13] are listed in Table I. Its first two columns specify the nuclear state and the next four give the calculated expectation values of the interaction components. The last three columns list the energy calculated with GFMC, the difference between the experimental and GFMC energies, and that between our optimum variational and GFMC energies. The v_{ij}^π seems to give the dominant contribution to nuclear binding, while v_{ij}^R is also essential for all but the deuteron. There is a large cancellation between the kinetic and two-nucleon interaction contributions, causing the total nuclear energy to be much smaller than the $\langle v_{ij} \rangle$. The $\langle V_{ijk}^{2\pi} \rangle$ is much smaller than $\langle v_{ij}^\pi \rangle$; however, it is a significant fraction of the nuclear binding energy. The $\langle V_{ijk}^R \rangle$ is the smallest, and $\Delta E_{expt.}$, the difference between experiment and theory is even smaller. In the neutron rich nuclei ^{7}He and ^{8}He, the $\Delta E_{expt.}$ is comparable to the $\langle V_{ijk}^R \rangle$, indicating that the UIX model may not be describing the interaction between three neutrons very well. All the p-shell nuclei having $A > 5$ are underbound, and the problem increases with the magnitude of nuclear isospin T. New models of V_{ijk} are being studied to reduce the $\Delta E_{expt.}$.

Table 1 also reveals another problem; the difference ΔE_{VMC} between GFMC

and variational Monte Carlo (VMC) energies is surprisingly large in the p-shell nuclei. Earlier successes in variational calculations of the $A \leq 4$ s-shell nuclei led to hopes that the variational calculations of larger nuclei and uniform nucleon matter, using cluster expansions [14], and chain summation methods [8] may have less than 10 % errors. The present VMC for ^{8}Be, which includes many three-body correlations omitted in variational calculations of larger nuclei and uniform matter, has a 12 % error. It appears that important aspects of the wavefunctions of p-shell nuclei are still not understood.

All NN interaction models are obtained by fitting NN scattering data in the center of mass frame. The model v_{ij} denotes the interaction between two nucleons in the frame in which their total momentum $\mathbf{P}_{ij} = \mathbf{p}_i + \mathbf{p}_j$, is zero. In the rest frame of all nuclei other than the deuteron, the $\mathbf{P}_{ij}$ of a pair of nucleons is non-zero. One then has to use the correct NN interaction:

$$v(\mathbf{P}_{ij}) = v_{ij} + \delta v(\mathbf{P}_{ij}), \tag{5}$$

between particles with total momentum $\mathbf{P}_{ij}$. The correction $\delta v(\mathbf{P}_{ij})$ is called the boost interaction [15]; it is zero when $\mathbf{P}_{ij} = 0$.

It is useful to consider a familiar example. The Breit interaction [16] between two particles of mass m and charge Q is, ignoring spin dependent terms for brevity, given by:

$$\frac{Q^2}{r_{ij}} \left(1 - \frac{\mathbf{p}_i \cdot \mathbf{p}_j}{2m^2} - \frac{\mathbf{p}_i \cdot \mathbf{r}_{ij}\mathbf{p}_j \cdot \mathbf{r}_{ij}}{2m^2 r_{ij}^2} \right), \tag{6}$$

which depends upon both $\mathbf{p}_i$ and $\mathbf{p}_j$. We can express it in our notation as a sum of v_{ij} and $\delta v(\mathbf{P}_{ij})$:

$$v_{ij} = \frac{Q^2}{r_{ij}} \left(1 + \frac{p_{ij}^2}{2m^2} + \frac{(\mathbf{p}_{ij} \cdot \mathbf{r}_{ij})^2}{2m^2 r_{ij}^2} \right), \tag{7}$$

$$\delta v(\mathbf{P}_{ij}) = -\frac{Q^2}{r_{ij}} \left(\frac{P_{ij}^2}{8m^2} + \frac{(\mathbf{P}_{ij} \cdot \mathbf{r}_{ij})^2}{8m^2 r_{ij}^2} \right), \tag{8}$$

where $\mathbf{p}_{ij} = (\mathbf{p}_i - \mathbf{p}_j)/2$, is the relative momentum. The dependence of v_{ij} on $\mathbf{p}_{ij}$ is included in all modern models, however, the $\delta v(\mathbf{P}_{ij})$ has been neglected in the majority of nuclear and neutron star calculations.

Following the work of Krajcik and Foldy [17], Friar [18] obtained the following equation relating the boost interaction of order P^2 to the interaction in the center of mass frame:

$$\delta v(\mathbf{P}) = -\frac{P^2}{8m^2}v + \frac{1}{8m^2}[\mathbf{P} \cdot \mathbf{r}\mathbf{P} \cdot \nabla, v] + \frac{1}{8m^2}[(\sigma_i - \sigma_j) \times \mathbf{P} \cdot \nabla, v]. \tag{9}$$

The general validity of this equation in relativistic mechanics and field theory was recently discussed [15]. Nonrelativistic Hamiltonians containing boost interactions include all terms quadratic in the particle velocities. The contribution of the two-body boost interaction to the energy of light nuclei has been evaluated with VMC method [19, 20, 21]; it is repulsive and equals ~ 37 % of that of V_{ijk}^R listed in Table 1. Therefore about 37 % of the V_{ijk}^R in UIX simulates the contribution of the neglected δv. The three-nucleon interaction to be used in Hamiltonians containing δv is denoted by V_{ijk}^*; the strength of V_{ijk}^{*R} is 0.63 times that of V_{ijk}^R in UIX, while $V_{ijk}^{*2\pi} = V_{ijk}^{2\pi}$. In nuclei and in nuclear matter at densities up to ~ 0.2 nucleons/fm^3 Hamiltonians containing $V^* + \delta v$ and V alone give rather similar results, but at higher densities they differ substantially. Naturally the results of the Hamiltonian with $V^* + \delta v$ are more reliable.

One can also consider relativistic nuclear Hamiltonians of the type:

$$H_R = \sum \sqrt{p_i^2 + m^2} + \sum (\tilde{v}_{ij} + \delta v(\mathbf{P}_{ij})) + \sum \tilde{V}_{ijk} + ..., \qquad (10)$$

where $\tilde{v}, \tilde{V}, ...$ include relativistic nonlocalities [21], and the boost interactions include terms of higher order in $\mathbf{P}_{ij}$. We must refit the two-nucleon scattering data to determine the $\tilde{v}$ in H_R, using relativistic kinetic energies [19, 21]. Uncorrelated nucleons in nuclei have small momenta of order $m/4$, thus the correction to their nonrelativistic kinetic energy is negligible. However, due to correlations induced by the strong $\tilde{v}$, a pair of nucleons acquire large relative momenta at small r_{ij}. The results obtained for light nuclei with H_R and the H given by eq.(3) are very similar [21], indicating that substantial improvements are obtained by including the relativistic boost interactions in the nonrelativistic Hamiltonian, as is well known for electromagnetic interactions.

3   Dense Nucleon Matter

The equation of state (EOS) of cold symmetric nuclear matter (SNM) and pure neutron matter (PNM) has been recently calculated with the variational method using chain summation techniques [8, 22]. Calculations have been done with the Hamiltonians with and without boost interactions.

We will first discuss the results presented in ref. [8] for the Hamiltonian without boost interactions. The calculated SNM and PNM energies are shown in figs.3 and 4 along with the results of earlier calculations [23, 24]. The density dependence of the U-DDI interaction was choosen to obtain the empirical saturation properties of SNM, so the minimum of that curve may be regarded
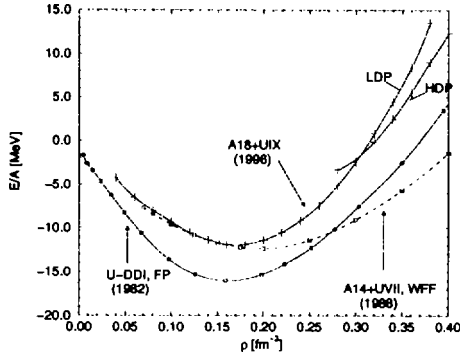
Figure 3: $E(\rho)$ of SNM calculated from A18 and UIX interactions compared with the results of earlier calculations. The two sets of variational minima obtained at $\rho > 0.28/fm^3$ are labeled LDP and HDP for low and high density phases.

as experimental data. The calculated energy of -12 MeV/A is higher than the observed -16 MeV/A. However we now believe that much of this difference is due to the simplicity of the variational wave functions used in nucleon matter calculations. Use of improved variational wave functions should lower the SNM energy by more that two MeV/A. Comparison of VMC and GFMC results for energies of eight neutrons bound in a weak potential well [25] indicate that the present variational wave functions are more accurate for PNM than for SNM.

The calculated energies indicate a phase transition in SNM at a density of $\sim 0.3/fm^3$ (fig.3) and in PNM at $\sim 0.2/fm^3$ (fig.4). Detailed analysis of the pair distribution functions and sums of response functions [8] indicate that the phase at higher densities has spin-isospin order expected from neutral pion condensation, first considered by Migdal [26]. The variational wave functions used in this study are appropriate for isotropic matter. The phase transition is signaled by a change in the range and strength of tensor correlations. It is likely that the phase at higher density will be better described with a liquid crystal wave function with alternating spin layers [27] used in many studies with effective interaction models.

As realized long ago by Migdal, this transition is very sensitive to the short range behavior of the $\sigma_i \cdot \sigma_j$ and $\sigma_i \cdot \sigma_j \tau_i \cdot \tau_j$ interactions between nucleons. It did not occur in either SNM or PNM with the Urbana v_{14} model of 1981,
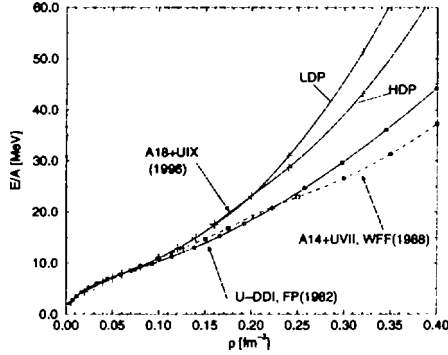
Figure 4: $E(\rho)$ of PNM. See fig.3 caption for details.

while it occured only in PNM with the later Argonne v_{14} model of 1984. The Urbana-Argonne potentials have similar forms, but are fit to different data sets. The 1981 (1984) Urbana (Argonne) v_{14} models were fit to the n-p phase shifts available in the late 1970's (early 1980's), while the A18 is fit directly to the Nijmegen 1994 p-p and n-p scattering data base. The quality of the fit obtained by the A18 potential is much higher, and thus it is likely that it provides a more accurate representation of the nuclear force. The pion exchange part, $V_{ijk}^{2\pi}$, of the three-nucleon interaction is essential for the transition to occur in SNM, while in PNM it occurs at a much higher density in the absence of V_{ijk}.

The composition of nucleon matter energy calculated from A18 and UIX interactions is listed at selected densities in table 2, in which T-1B denotes the Fermi gas kinetic energy. The v-2B-S and T-2B-S list the two-body (2B) cluster contributions to the potential and kinetic energy from the static parts of the pair interaction and correlation operators. The v-2B-MD and T-2B-MD show 2B contributions having one or more momentum dependent (MD) interaction or correlations. These are conveniently regarded as the difference between the total 2B energies and their static parts. The static many-body (MB) contributions, MB-S, as well as the expectation values of the three-nucleon interactions are calculated with the Fermi hypernetted and single operator chain summation methods, presumably quite accurately. However, the MB contributions containing MD interaction or correlations, as well as the boost interaction $\delta v(\mathbf{P}_{ij})$, are evaluated from dressed three-body clusters. The δE-2B lists an estimate of the change in energy that may be obtained by allowing additional

Table 2: Composition of nucleon matter energy in MeV.

Type	SNM	SNM	SNM	SNM	PNM	PNM	PNM	PNM
$\rho(fm^{-3})$	0.08	0.16	0.32	0.64	0.08	0.16	0.32	0.64
T-1B	13.9	22.1	35.1	55.7	22.1	35.1	55.7	88.4
v-2B-S	-36.5	-66.7	-117.9	-227.2	-26.7	-49.4	-93.0	-185.7
T-2B-S	10.0	20.3	37.5	74.1	7.4	13.1	24.9	44.8
v-2B-MD	0.4	2.1	9.4	28.6	1.3	3.9	18.0	53.3
T-2B-MD	0.2	0.6	1.9	5.4	1.1	2.8	10.9	35.6
MB-S	3.4	5.5	9.2	25.6	3.2	6.4	1.8	-9.0
MB-MD	0.7	3.2	13.4	61.7	0.1	1.1	14.2	60.1
$V_{ijk}^{2\pi}$	-0.8	-3.6	-13.3	-82.0	0.3	1.2	-17.4	-76.9
V_{ijk}^{*R}	0.9	4.0	19.4	98.2	0.5	2.8	19.3	101.0
$\delta v(\mathbf{P}_{ij})$	0.6	2.1	6.4	21.0	0.7	2.2	6.9	21.5
δE-2B	-0.6	-1.8	-5.2	-9.2	-0.8	-1.3	-2.5	-5.5
Total E	-8.0	-12.2	-4.2	58.4	9.7	17.9	38.8	127.6

flexibility in the two-body correlations. We note that at high densities the MD parts, the V_{ijk}^{*} and $\delta v(\mathbf{P}_{ij})$ give significant contributions.

4 Neutron Star Matter

The matter at subnuclear densities in the outer and inner crusts of neutron stars has interesting structures as discussed at this meeting by Pethick and Ravenhall [28, 29]. Here we focus on the matter below the crust assuming that it is a uniform mixture of neutrons, protons, electrons and muons in beta equilibrium. The calculated energies of SNM and PNM are fitted by generalized Skyrme type effective interactions [30] having different parameters below and above the pion condensation phase transition. The beta equilibrium conditions are calculated from these effective interactions.

Ignoring mixed phase regions the normal matter at density and proton fraction of 0.204 fm^{-3} and 0.073 is found to be in equilibrium with pion condensed matter at 0.237 fm^{-3} and 0.057 for our most reliable model with boost and three-nucleon interactions. Obviously the matter in the phase with pion condensation has a lower charge density than the matter without condensation. Therefore, in reality the transition will proceed through mixed phase regions of the type discussed by Glendenning [31] and Heiselberg et. al. [32] in the context of the transition from hadronic to quark matter. The mixed phase regions in the pion condensation transition do not seem to have a large effect on

the structure of neutron stars because the discontinuity in the charge density is rather small. For example, the predicted thickness of the mixed phase regions varies from $\sim$ 40 to 14 m in stars with 1.41 to 2.1 $M_\odot$; however these predictions are quite crude because our calculations of the pion condensed phase are still incomplete.

The calculated density dependence of the proton fraction in neutron star matter is shown in fig.5 for the Hamiltonians containing only A18, A18+ δv, A18+δv+UIX*, and A18+UIX interactions. The earlier results obtained with the U-DDI interaction (FPS) are shown for comparison. Both the boost and the three nucleon interactions increase the proton fraction in matter, but it remains below the critical value of 0.148 needed for direct Urca cooling, in the range of neutron star densities. The plus signs in fig.5 show the proton fractions calculated with the A18 interaction alone with the LOB method [7]. These are in reasonable agreement with the results of our calculations up to a density of 0.6 fm^{-3}. The density dependence of the electron chemical potential in matter is shown in fig.6.
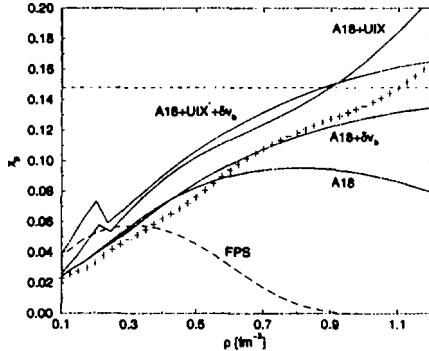
Figure 5: The proton fraction in matter in beta equilibrium for various model Hamiltonians. The plus signs show the results obtained for the A18 Hamiltonian with LOB method.

The predicted neutron star properties appear in figures 7 and 8. The dotted lines in these figures show results obtained using the PNM EOS. They are not very different from those obtained with matter in beta equilibrium. Due to the presence of momentum dependent and three-nucleon interactions in the present nuclear Hamiltonians, the predicted sound velocity in matter
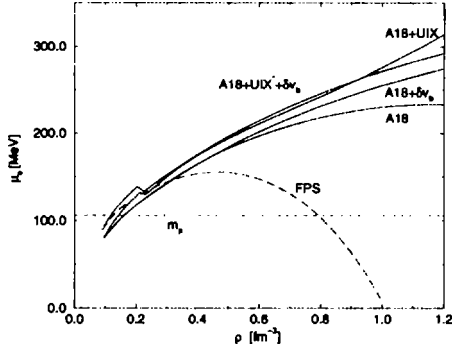
Figure 6: The electron chemical potential in neutron star matter for various model Hamiltonians. Matter contains muons when μ_e exceeds the muon mass m_μ.

can exceed the velocity of light. The densities at which superluminal sound occurs in each model are marked by vertical bars in fig.7. These densities are very close to the maximum densities that can occur in neutron stars, therefore limiting the the velocity of sound to be $\leq c$ does not have a significant effect on the predicted maximum masses.

Observations of binary neutron stars have confirmed the existence of 1.4 $M_\odot$ neutron stars allowed by all models. Recently several authors [33, 34, 35] have argued that there are indications of the existence of neutron stars with $M \sim 2M_\odot$, which would rule out models without three-body forces, but see ref. [36] and Lamb's contribution [37].

5   Transition to Quark Matter

It is expected that at some large density there will be a transition from nucleon matter to quark matter (QM). Several authors [38] have studied the energy of cold QM using the Bag-model, in which the total energy density contains a "Bag-constant" B, that takes into account the difference between the energies of the physical and QM vacua, and the energy of quarks interacting via one gluon exchange interaction calculated in first order of α_s. The u and d quarks are assumed to be massless, and mass of s quarks is taken as 150 MeV. The energy density of QM obtained with B = 122 and 200 MeV/fm^3 is compared
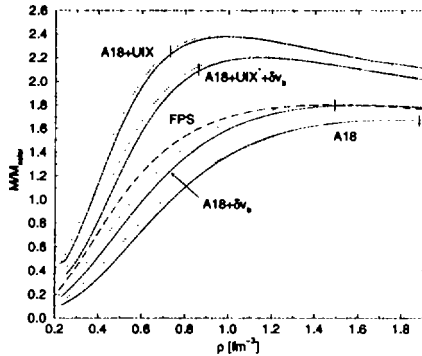
Figure 7: The dependence of neutron star mass on its central density for various model Hamiltonians. The full (dotted) lines show results obtained with the EOS of matter in beta equilibrium (PNM), and the vertical bars show where matter becomes superluminal in these models.
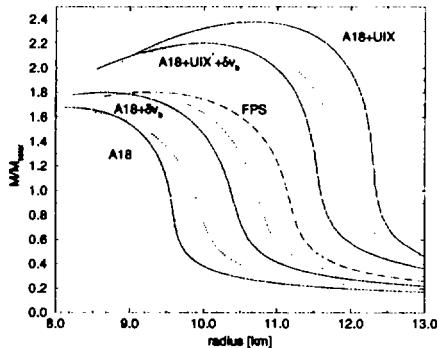
Figure 8: Neutron star mass-radius relation obtained from various model Hamiltonians. See caption of fig.7 for notation.

with that of nucleon matter (NM) in beta equilibrium for the more realistic models containing boost interaction, in fig. 9. The value B = 122 MeV/fm^3 is supported by an analysis using the average of nucleon and delta-resonance masses [39]. In the absence of three-body interactions NM is found to have lower energy than QM up to a large density of ~ 1.6 fm^{-3}. However, the transition density is lowered to ~ 1 fm^{-3} after including the contributions of the three nucleon interaction.
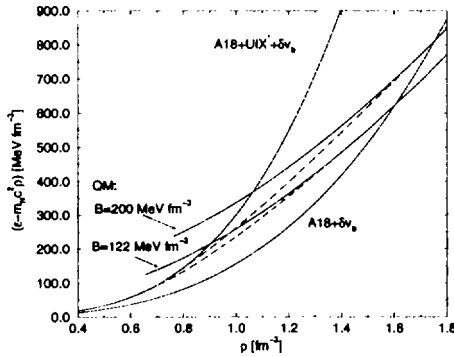
Figure 9: The energy densites of electrically neutral QM and NM are shown by full lines, while the dashed lines show those for matter with mixed QM and NM phases.

Glendenning [31] realized that it is not necessary to require the QM and NM phases to be separately charge neutral; a mixture of NM and QM can exist in a uniform lepton gas. Neglecting the energy of the interface between the QM and NM, and using the A18 + δv + UIX* model of NM, the transition occurs over the density range $\rho = 0.74$ to 1.80 fm^{-3} for B = 200, and 0.58 to 1.46 fm^{-3} for B = 122 MeV/fm^3. At the lower end of this density range we have mostly NM with drops of QM, while at the higher end we will have mostly QM with drops of NM [32].

The dependence of the mass of neutron stars on their central density, obtained after incuding the effects of the transition to quark matter on the EOS are shown in fig.10. For B = 122 Mev/fm^3 and the A18 + δv + UIX* NM Hamiltonian stars with masses above 1.5 $M_\odot$ seem to have drops of quark matter in their cores. The maximum mass is reduced to $\sim 1.9 M_\odot$ corresponding to a central density of ~ 1.1 fm^{-3}. In this model pure quark matter appears at

- 25 -
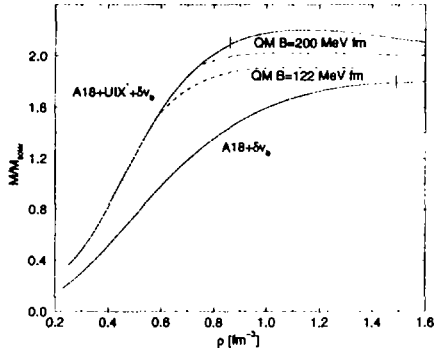
Figure 10: Dependence of neutron star mass on its central density. Full lines show results obtained with NM EOS, while dashed lines show results obtained after including the effect of the transition to QM on the EOS.

$\rho = 1.46$ fm^{-3}; therefore even the most massive stars have mixed QM and NM phases in their interior. On the other hand, if B = 200 Mev/fm^3 the maximum mass becomes $\sim 2M_\odot$, and stars with masses from 1.93 to 2.01 $M_\odot$ have quark drops in their interior.

Acknowledgments

We would like to thank A. Arriaga, G. Baym, J. Carlson, J. Forest, H. Heiselberg, C. J. Pethick, S. C. Pieper, R. Schiavilla, E. F. Staubo and R. B. Wiringa for many of the results discussed here, and M. Hjorth-Jensen for communicating the results of neutron matter calculations. This work has been partly supported by the US National Science Foundation under Grant PHY94-21309.

References

[1] J. L. Forest, V. R. Pandharipande, S. C. Pieper, R. B. Wiringa, R. Schiavilla and A. Arriaga, Phys. Rev. C **54**, 646 (1996).

[2] V. G. J. Stoks, R. A. M. Klomp, M. C. M. Rentmeester and J. J. de Swart, Phys. Rev. C **48**, 792 (1993).

[3] V. G. J. Stoks, R. A. M. Klomp, C. P. F. Terheggen and J. J. de Swart, Phys. Rev. C **49**, 2950 (1994).

[4] R. B. Wiringa, V. G. J. Stoks and R. Schiavilla, Phys. Rev. C **51**, 38 (1995).

[5] R. Machleidt, F. Sammarruca and Y. Song, Phys. Rev. C **53**, R1483 (1996).

[6] J. L. Friar, G. L. Payne, V. G. J. Stoks and J. J. de Swart, Phys. Lett. B **311**, 4 (1993).

[7] L. Engvik, M. Hjorth-Jensen, R. Machleidt, H. Muther and A. Polls, Nucl. Phys. (1997) to be published.

[8] A. Akmal and V. R. Pandharipande, Phys. Rev. C **56**, 2261 (1997).

[9] J. Fujita and H. Miyazawa, Prog. Theo. Phys. **17**, 360 (1957).

[10] B. S. Pudliner, V. R. Pandharipande, J. Carlson, S. C. Pieper and R. B. Wiringa, Phys. Rev. C **56**, 1720 (1997).

[11] W. Glockle, private communication (1997).

[12] S. A. Coon, M. D. Scadron, P. C. McNamee, B. R. Barrett, D. W. E. Blatt and B. H. J. McKellar, Nucl. Phys. A **317**, 242 (1979).

[13] R. B. Wiringa, Proc. of XV th Int. Conf. on Few Body Problems, (1997) to be published

[14] S. C. Pieper, R. B. Wiringa and V. R. Pandharipande, Phys. Rev. C **46**, 1741 (1992).

[15] J. L. Forest, V. R. Pandharipande and J. L. Friar, Phys. Rev. C **52**, 568 (1995).

[16] H. A. Bethe and E. E. Salpeter, *Quantum mechanics of one and two electron atoms*, page 170, Academic Press (1957).

[17] R. A. Krajcik and L. L. Foldy, Phys. Rev. D **10**, 1777 (1974).

[18] J. L. Friar, Phys. Rev. C **12**, 695 (1975).

[19] J. Carlson, V. R. Pandharipande and R. Schiavilla, Phys. Rev. C **47**, 484 (1993).

[20] J. L. Forest, V. R. Pandharipande, J. Carlson and R. Schiavilla, Phys. Rev. C **52**, 576 (1995).

[21] J. L. Forest, University of Illinois Ph. D. Thesis (1997).

[22] A. Akmal, V. R. Pandharipande and D. G. Ravenhall, Phys. Rev. C, to be published (1998).

[23] B. Friedman and V. R. Pandharipande, Nucl. Phys. A **361**, 501 (1981).

[24] R. B. Wiringa, V. Fiks and A. Fabrocini, Phys. Rev. C **38**, 1010 (1988).

[25] B. S. Pudliner, A. Smerzi, J. Carlson, V. R. Pandharipande, S. C. Pieper and D. G. Ravenhall, Phys. Rev. Lett. **76**, 2416 (1996).

[26] A. B. Migdal, Rev. Mod. Phys. **50**, 107 (1978).

[27] T. Kunihiro, T. Muto, T. Takatsuka, R. Tamagaki and T. Tatsumi, Prog. Theor. Phys. Suppl. **112** (1993).

[28] C. J. Pethick and D. G. Ravenhall, in these proceedings.

[29] C. J. Pethick and D. G. Ravenhall, Ann. Rev. Nuc. Par. Sci. **45**, 429 (1995).

[30] V. R. Pandharipande and D. G. Ravenhall, Proc. NATO Adv. Res. Workshop on Nuclear Matter and Heavy Ion Collisions, Les Houches, ed. M. Soyeur et. al., Plenum, New York, 103 (1989).

[31] N. K. Glendening, Phys. Rev. D **46**, 1274 (1992).

[32] H. Heiselberg, C. J. Pethick and E. F. Staubo, Phys. Rev. Lett. **70**, 379 (1993).

[33] M. H. van Kerkwijk, P. Bergeron and S. R. Kulkarni, Ap. J. **467**, L89 (1996).

[34] P. Kaaret, E. C. Ford and K. Chen, Ap. J. **480**, L27 (1997).

[35] W. Zhang, T. E. Strohmayer and J. H. Swank, Ap. J. **482**, L167 (1997).

[36] M. C. Miller, F. K. Lamb and D. Psaltis, Ap. J. in press

[37] F. K. Lamb, in these proceedings.

[38] B. Freedman and L. McLerran, Phys. Rev. D **17**, 1107 (1978).

[39] J. Cleymans, R. V. Gavai and E. Suhonen, Phys. Rept. **130**, 217 (1986).

NEUTRON STAR PROPERTIES WITH NUCLEAR BHF EQUATIONS OF STATE

M. Baldo[a], G. F. Burgio[a], H. Q. Song[b] and F. Weber[c]

[a] *I.N.F.N. Sezione di Catania, c.so Italia 57, I-95129 Catania, Italy*

[b] *Institute of Nuclear Research, Academia Sinica, Shangai 201800, China*

[c] *Sektion Physik, Universität München, Am Coulombwall 1, D-85748 Garching, Germany*

Abstract

We study the properties of static and rotating neutron stars adopting non-relativistic equations of state (EOS) for asymmetric nuclear matter based on the Brueckner-Hartree-Fock (BHF) scheme. The BHF calculation, with the continuous choice for the single particle potential, appears to be very close to the full EOS, which includes the three-hole line contribution calculated by solving the Bethe-Fadeev equations within the gap choice for the single particle potential. Three-body forces are included in order to reproduce the correct saturation point for nuclear matter. A comparison with fully relativistic many-body calculations of nuclear matter EOS is made.

1 Introduction

The properties of neutron stars such as masses and radii depend on the equation of state (EOS) at densities up to an order of magnitude higher than those observed in ordinary nuclei. Therefore the knowledge of the EOS in the superdense regime is fundamental for the study of astrophysical compact objects [1]. For this purpose we derive an equation of state for asymmetric nuclear matter, using a non-relativistic many-body theory within the framework of the Brueckner-Hartree-Fock (BHF) scheme [2, 3]. In this approach, the basic input is the two-body nucleon-nucleon (NN) interaction. The BHF approximation, with the continuous choice for the single particle potential, reproduces closely the many-body calculations up to three hole-line level [4]. However, as it is well known, the empirical saturation point is not reproduced. Therefore we have included a contribution coming from three-body forces to reproduce the correct saturation point [5]. Those EOS's are the fundamental input for constructing models of static and rotating neutron stars in the framework of

Einstein's theory of general relativity by applying a refined version of Hartle's stellar structure equations [6, 7]. We calculate properties of neutron stars like gravitational mass, equatorial and polar radius, for sequences of star models either static or rotating at their respective general relativistic Kepler frequencies. We compare with predictions from fully relativistic microscopic EOS.

2 Equation of state

Microscopic calculations of nuclear matter EOS have been performed in the framework of the Brueckner–Hartree–Fock (BHF) scheme [2]. The energy per particle E/A within the BHF scheme is given in terms of the so-called reaction matrix G. The latter is obtained by solving the Brueckner–Bethe–Goldstone (BBG) equation

$$G(\omega) = V + V \frac{Q}{\omega - H_0} G(\omega), \qquad (1)$$

where ω is the unperturbed energy of the interacting nucleons, V is the free nucleon-nucleon (NN) interaction, H_0 is the unperturbed energy of the intermediate scattering states and Q is the Pauli operator which prevents scattering into occupied states. With the G-matrix we can calculate the total energy per nucleon

$$\frac{E}{A} = \frac{3}{5} \frac{\hbar^2 k_F^2}{2m} + U(n), \qquad (2)$$

being $U(n)$ the contribution of the potential energy to the total energy per particle

$$U(n) = \frac{1}{2A} \sum_{k,k' \leq k_F} \langle kk'|G(\omega = \epsilon(k) + \epsilon(k'))|kk'\rangle_a \qquad (3)$$

where the subscript a indicates antisymmetrization of the matrix element. The single-particle energies are denoted by ϵ. In this scheme, the only input quantity we need is the bare NN interaction V in the Bethe-Goldstone equation (1).

The Brueckner-Hartree-Fock (BHF) approximation for the EOS in symmetric nuclear matter, within the continuous choice [3], reproduces closely results which include up to three hole-line diagram contributions to the BBG expansion of the energy, calculated within the so called *gap choice* for the single particle potential [4]. In Fig.1 we show the energy per nucleon calculated within this scheme in the case of symmetric and neutron matter using

the Argonne v_{14} model [8] for the two-body nuclear force. The open squares represent the solution of the Bethe-Fadeev equations for the three hole-line in the gap choice. These results extend to higher densities the calculations published in ref.[4] for symmetric nuclear matter. Recently it has been shown that the results up to three hole-lines are independent from the choice of the single particle potential [9], which gives evidence of convergence of the BBG expansion.

For neutron matter the results are preliminary. In any case we found a negligible difference between the BHF results in the continuous and in the gap choice. Correspondingly the three hole-line contribution in neutron matter turns out to be much smaller than in symmetric nuclear matter. All these results together give support to the use of the BHF approximation in the continuous choice in the study of neutron stars.
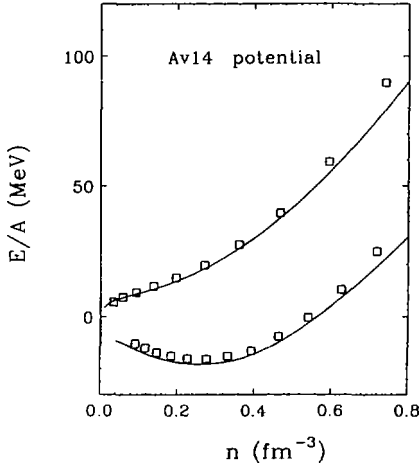
Figure 1: The energy per baryon E/A is plotted vs. the number density n for symmetric matter (lower curve) and for neutron matter (upper curve). The solid line represents a Brueckner calculation with Av14 potential with the continuous choice. The squares are the solutions of the Bethe-Fadeev equations with the gap choice.

We notice that the BHF fails to reproduce the empirical saturation point of nuclear matter. This well known deficiency, which does not depend on the choice of the two-body force, is commonly corrected introducing three-
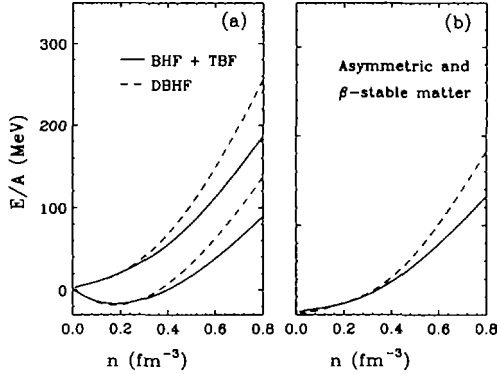
Figure 2: The energy per baryon E/A is plotted vs. the number density n in panel (a) for symmetric matter (lower curves) and for neutron matter (upper curves). The solid line represents non-relativistic BHF calculations with three-body forces and the dashed line a relativistic Dirac-Brueckner one. Panel (b): as in panel (a) but for β-stable nuclear matter.

body forces (TBF). We adopted the Urbana three-nucleon model [10], which consists of an attractive term due to two-pion exchange with excitation of an intermediate Δ-resonance, and a repulsive phenomenological central term. Several details are given in ref.[5].

The corresponding EOS obtained using the v_{14} potential is depicted in Fig.2a) for symmetric and neutron matter (solid line). This EOS saturates at $n_o = 0.178 \; fm^{-3}$, $E_o/A = -16.46 \; MeV$ and it is characterized by an incompressibility $K_\infty = 253 \; MeV$. In Fig.2a) we plot also the EOS from a recent Dirac-Brueckner calculation (DBHF) [11] with the Bonn-A two-body force (dashed line). In the low density region the BHF equation of state with TBF and DBHF equation of state are very similar, whereas at higher density the DBHF is stiffer. The discrepancy between the non-relativistic and relativistic calculation of the EOS can be easily understood by noticing that the DBHF treatment is equivalent [12] to introduce in the non-relativistic BHF the three-body force corresponding to the excitation of a nucleon-antinucleon pair, the so-called Z-diagram which is repulsive at all densities. In BHF treatment, on the contrary, both attractive and repulsive three-body forces are introduced, and therefore a softer EOS is expected.

The properties of neutron stars (NS) depend on the knowledge of the EOS

over a wide range of densities, *i.e.* from the density of iron at the star's surface up to several times the density of normal nuclear matter encountered in the core [1]. It is commonly accepted that the interior part of a neutron star is made mainly by nuclear matter (eventually superfluid) with a certain lepton fraction, although the high-density core might suffer a transition to other hadronic components. Here we assume that a neutron star is composed only by nucleons and leptons, *i.e.* an uncharged mixture of neutrons, protons, electrons and muons in β-equilibrium. The presence of leptons softens the EOS with respect to the pure neutron matter case. In Fig.2b) the EOS for β-stable matter is shown for the cases previously discussed. It has to be stressed that in β-stable matter the density dependence of the nuclear symmetry energy affects the proton concentration [13]. As it has been recently pointed out by Lattimer et al. [14], the value of the proton fraction in the core of NS is crucial for the onset of direct Urca processes, whose occurrence enhances neutron star cooling rates.

From the energy per baryon of asymmetric nuclear matter in β-equilibrium, we calculate the nuclear contribution P_{nucl} to the total pressure of stellar matter as well as the mass density ρ_{nucl}. Then the total pressure and total mass density can be easily calculated by adding the leptonic contributions. For more details, see ref.[5].

3 Neutron star structure

Neutron stars are objects of highly compressed matter so that the geometry of space-time is changed considerably from flat space. Thus Einstein's general theory of relativity must be applied. Therein the Einstein curvature tensor $\mathcal{G}_{\mu\nu}$ is coupled to the energy-momentum density tensor $\mathcal{T}_{\mu\nu}$ of matter (G denotes the gravitational constant):

$$\mathcal{G}_{\mu\nu} = 8\,\pi\,G\,\mathcal{T}_{\mu\nu}(\rho, P(\rho)) \tag{4}$$

The knowledge of the EOS, *i.e.* pressure P as function of the energy density ρ is therefore required in order to solve eq.(4). For a spherically symmetric and static star, Einstein's equations reduce to the familiar Tolman–Oppenheimer–Volkoff (TOV)[15] equations

$$\frac{dP(r)}{dr} = -\frac{Gm(r)\rho(r)}{r^2}\frac{(1 + \frac{P(r)}{c^2\rho(r)})(1 + \frac{4\pi r^3 P(r)}{c^2 m(r)})}{(1 - \frac{2Gm(r)}{rc^2})} \tag{5}$$
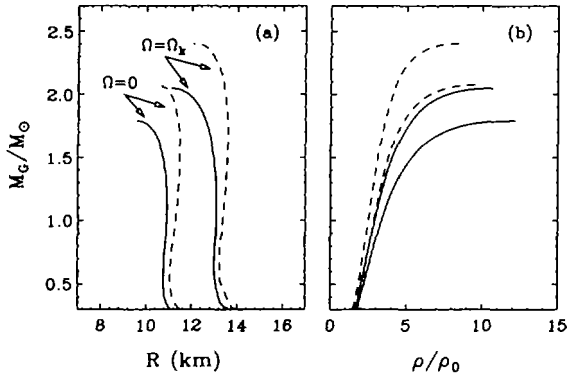
Figure 3: The gravitational mass M_G, expressed in units of the solar mass $M_\odot$, is displayed vs. radius R (panel (a)) and the central energy density ρ (in units of $\rho_0 = 140 MeV/fm^3$) (panel (b)) for sequences of star models constructed for BHF+TBF (solid line) and DBHF (dashed line) equations of state. The two (lower) upper lying curves refer to (non-) rotating star models.

$$\frac{dm(r)}{dr} = 4\pi r^2 \rho(r) \tag{6}$$

For a given EOS *i.e.* $P(\rho)$, one can solve the TOV equations by integrating them for a given central energy density ρ, from the star's center to the star's radius defined by $P(R_s) = 0$. This gives the stellar radius R and the gravitational mass is then

$$M_G \equiv m(R) = 4\pi \int_0^R dr\ r^2 \rho(r). \tag{7}$$

The case of rotating stars is more complicated, since changes occur in the pressure, energy density and baryon number density because of the rotation. In this work we adopt the method developed in ref.[6], which is a redefined version of Hartle's perturbative method [7] for the investigation of the general relativistic Kepler frequency of a rotating neutron star. We recall that for rotation at frequencies beyond the Kepler value Ω_K, mass shedding at the

equator sets in which makes the star unstable. Therefore Ω_K sets an absolute upper bound on the rotational frequency. For every nuclear EOS there are uniquely determined values of Ω_K for each star in the sequence up to the limiting mass value. In Fig.3 we show the results obtained with our BHF plus TBF equation of state for asymmetric nuclear matter and with the Dirac-Brueckner one. We display the gravitational mass M_G, in units of the solar mass $M_\odot$ ($M_\odot = 1.99\ 10^{33}$ g), as a function of the radius R and the central energy density ρ (in units of $\rho_0 = 140\ MeV/fm^3$). The upper lying curves show the increase of mass due to rotation at the (absolute limiting) Kepler frequency, i.e. $\Omega = \Omega_K$. The solid (dashed) line indicates a sequence of star models obtained with the BHF+TBF (DBHF) equation of state. We observe larger gravitational masses, i.e. up to 14% mass increase for BHF+TBF and 15% for DBHF, relative to the spherical (non-rotating) Oppenheimer-Volkoff star model of the same ρ value. The large mass increase obtained is accompanied by relatively large (equatorial) radius value. Moreover one sees that, for a fixed value of the gravitational mass, the central star density ρ decreases for increasing values of the rotational frequency. This is because of the centrifugal force acting on the star's matter together with the nuclear force. Their intensity must be counterbalanced by the attractive gravitational forces. More details on rotating stars will be given in a forthcoming paper[16].

4   Conclusions

In conclusion, we computed some properties of NS's on the basis of a microscopic EOS obtained in the framework of BHF many–body theory with two plus three–body nuclear interactions. Our EOS with three-body forces is able to reproduce the correct saturation point of nuclear matter. The comparison with the DBHF method shows that the relativistic effects represent a particular repulsive three-body force and gives rise to a stiffer EOS. Therefore the predicted values for the limiting mass and radius of neutron stars are higher in the DBHF case than in the non-relativistic BHF calculation. The inclusion of rotation substantially changes the limiting values of the gravitational mass by about 14-15 % for configurations rotating at their respective general relativistic Kepler frequency. A more detailed comparison between the predictions of non-relativistic BHF microscopic EOS and observational data on pulsars, i.e. fast rotation and large enough neutron star masses, is currently in progress.

References

[1] S. Shapiro and S. Teukolsky, "Black Holes, White Dwarfs and Neutron Stars", (John Wiley & Sons 1983) USA

[2] H. A. Bethe, Ann. Rev. Nucl. Sci. **21** (1971) 93.

[3] M. Baldo, I. Bombaci, L.S. Ferreira, G. Giansiracusa and U. Lombardo, Phys. Rev. **C43** (1991) 2605 and references therein.

[4] H.Q. Song, M. Baldo, G. Giansiracusa and U. Lombardo, Phys. Lett.**B411** (1997) 237; B.D. Day and R.B. Wiringa, Phys. Rev. **C32** (1985) 1057.

[5] M. Baldo, I. Bombaci, and G.F. Burgio, Astron. and Astrophys. **328** (1997) 274.

[6] F. Weber and N.K. Glendenning, Phys. Lett. **B265** (1991) 1; F. Weber and N.K. Glendenning, Astrophys. Journ. **390** (1992) 541.

[7] J.B. Hartle, Astrophys. Journ. **150** (1967) 1005; J.B. Hartle and K.S. Thorne, Astrophys. Journ. **153** (1968) 807.

[8] R.B. Wiringa, R.A. Smith and T.L. Ainsworth, Phys. Rev. **C29** (1984) 1207.

[9] H.Q. Song, M. Baldo, G. Giansiracusa and U. Lombardo, Phys. Rev. Lett. (1998) submitted.

[10] J. Carlson, V.R. Pandharipande and R.B. Wiringa, Nucl. Phys. **A401** (1983) 59.

[11] G.Q. Li, R. Machleidt and R. Brockmann, Phys. Rev. **C45** (1992) 2782.

[12] M. Baldo, G. Giansiracusa, U. Lombardo, I. Bombaci and L.S. Ferreira, Nucl. Phys. **A583** (1995) 599.

[13] I. Bombaci and U. Lombardo, Phys. Rev. **C44** (1991) 1892.

[14] J. Lattimer, C. Pethick, M. Prakash and P. Haensel, Phys. Rev. Lett. **66** (1991) 2701.

[15] R.C. Tolman, 1934, Proc. Nat. Acad. Sci. USA **20** (1934) 3; J. Oppenheimer and G. Volkoff, Phys. Rev. **55** (1939) 374.

[16] M.Baldo et al., in preparation.

NUCLEAR MATTER AND ELECTRON SCATTERING

INGO SICK

Dept. für Physik und Astronomie, Universität Basel
CH 4056 Basel, Schweiz

Abstract

We show that inclusive electron scattering at large momentum transfer allows a measurement of *short-range* properties of nuclear matter. This provides a very valuable constraint in selecting the calculations appropriate for predicting nuclear matter properties at the densities of astrophysical interest.

Introduction

Infinite nuclear matter is of great interest for a number of reasons. In terms of nuclear structure, nuclear matter represents a particularly simple "nucleus" for which calculations have achieved a much higher quality standard than for finite nuclei with A>4; accordingly, a much sharper comparison between experiment and theory can be performed. In terms of astrophysics, nuclear matter is the basic starting point for the understanding of objects such as neutron stars.

Modern calculations of nuclear matter properties start from parametrisations of the nucleon-nucleon-interaction known from nucleon-nucleon-scattering. For this interaction, the Schrödinger equation can be solved using approaches such as Bruckner theory or Correlated Basic Function theory (CBF).

These calculations give results for the binding energy and density of nuclear matter which lie within the Koester band. This band misses the experimental point (16 MeV/nucleon, $0.162 fm^{-3}$) known from the Weizäcker mass formula and the interior density of nuclei as measured via electron scattering. Relativistic calculations appear to get closer to experiment, but the low order of the Bruckner calculations performed casts doubts upon the results.

In order to reproduce the binding energies of both light nuclei and nuclear matter the nucleon-nucleon force is supplemented by a three-body force. This three-body force essentially accounts for the non-nucleonic degrees of freedom (presence of pions, deltas, ...) neglected. While the longest range piece of the 3-body force can be calculated from the diagram involving the exchange of

two pions between the 3 nucleons, with excitation to the Δ in the intermediary state, the shorter range parts are purely phenomenological.
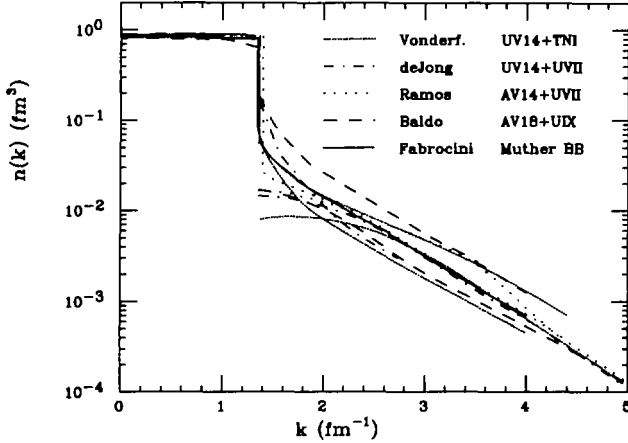
Figure 1: Momentum space densities at the experimental nuclear matter density for a number of modern calculations, identified by the authors or the N-N force employed [1].

The choice of the three-body force unfortunately leaves considerable freedom. The basic difficulty is due to the fact that for nuclear matter we really up to now have only $2\frac{1}{2}$ observables, the $\frac{1}{2}$ standing for the poorly known incompressibility modulus. In addition, the observables available all concern *average* properties dominated by *long range*. Given this experimental input, extrapolation to the *large* densities of interest for e.g. neutron stars is particularly difficult.

In this paper, we show that modern electron scattering data allow to gain additional information on the properties of nuclear matter. These concern properties at *short range* which are of particular relevance when aiming at the prediction of nuclear matter properties at the higher nucleon densities. These shorter range properties, measured by determining the nuclear matter momentum distribution at *large* nucleon momenta, provide an additional observable.

In figure 1 we show the momentum distributions $n(k)$ obtained by a number of modern calculations of nuclear matter properties. A variation of $n(k)$ by up to a factor of two is observed for momenta above the Fermi momentum. Fixing

$n(k)$ at momenta $k \gg k_F$ provides a much-needed additional observable, and constrains the behaviour of nuclear matter properties when using these N-N forces to calculate nuclear matter properties at the larger densities.

Quasielastic electron scattering

The experimental observable we exploit concerns inclusive electron-nucleon scattering. Figure 2 shows a schematic representation of the scattered electron energy loss spectrum, displaying coherent scattering, the quasielastic peak corresponding to elastic electron-nucleon scattering with knockout of the nucleon, and contributions at higher energy loss ω accounting for excitation and break-up of the nucleon.
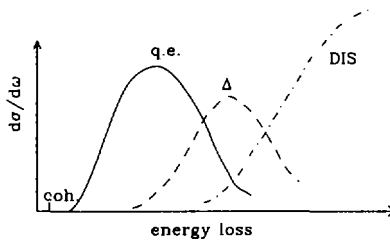
Figure 2: Schematical energy loss spectrum for inclusive electron-nucleus scattering.

Here, we concentrate on the low-ω tail of the quasi-elastic peak. It is straightforward to understand that large momentum transfer $\vec{q}$ (of order GeV/c) and low ω (of order several hundred MeV) corresponds to scattering from nucleons of high initial momentum $\vec{k}$. The kinetic energy of the knocked-out nucleon is given, approximately, by $((\vec{k} + \vec{q})^2 + m^2)^{1/2} - m$, and this energy amounts approximately to the electron energy loss ω. Large q and small ω implies $\vec{k} \sim -\vec{q}$, with q and k both being large.

The inclusive cross sections for many nuclei have been measured in ref. [2] for the kinematics of interest here. These data have been used in ref. [3] to determine the cross section for infinite nuclear matter. This can be done in a straightforward way when recognizing that the spatial resolution of the electromagnetic probe is of order $1/q$, which is small. For a *local* property one can use LDA and split up the cross section into a part coming from the

constant-density nuclear interior ($\sim A$) and a part coming from the nuclear surface ($\sim A^{2/3}$). Extrapolation the cross section, divided by A, as a linear function of $A^{-1/3}$ to $A^{-1/3} = 0$ ($A = \infty$) yields the nuclear matter cross section.

In order to quantitatively exploit the inclusive electron-scattering cross sections, we need the nuclear matter spectral function $S(k, E)$, the quantity which gives the probability to find in nuclear matter nucleons of given momentum k and removal energy E. This quantity has been calculated using the CBF approach and the Urbana $V_{14}+$TNI nucleon-nucleon interaction [4]. It displays, at large k, the property expected for correlated nucleons, a ridge of the strength $S(k, E)$ at $E \sim k^2/2m$. This ridge corresponds to pairs of nucleons of high momenta $\vec{k}, -\vec{k}$ in the nuclear matter ground state. Figure 3 gives a contour plot of $ln(S(k, E) \cdot k^2)$ exhibiting this ridge, which is responsible for the tail of $n(k)$ shown in figure 1.
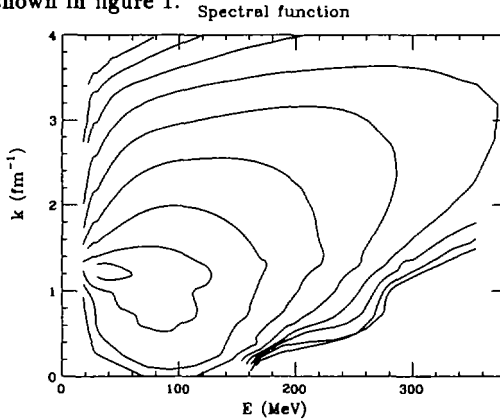
Spectral function

Figure 3: Contour plot of the spectral function S(k,E) ($\cdot k^2$), displaying the ridge at $E \sim k^2/2m$ due to correlated nucleons of high momentum.

For a quantitative interpretation of the inclusive cross sections one has to go beyond PWIA. The final state interaction (FSI) of the knocked-out nucleon has to be accounted for. The approach of Benhar et al [5], which treats this FSI in terms of Correlated Glauber Theory (CGT), allows to achieve this. Essential inputs to CGT are the small-angle N-N scattering amplitudes (taken from N-N scattering data) and the two-nucleon pair correlation function (taken from the CBF calculation).

Results

In order to best display the results, we will consider the ratio of nuclear matter and deuteron cross sections for the same q, ω. At momenta significantly above the Fermi momentum k_F the ratio of nuclear matter and deuteron momentum space densities is essentially constant. When considering the cross section ratio, much of the "trivial" q, ω-dependence drops out and the main information on nuclear matter then is contained in the largely k-independent ratio which, at least qualitatively, reflects the nuclear matter/d ratio at large k. The deuteron cross section for the kinematics of interest and the exact value of q, ω needed can be obtained by interpolating the deuteron data using the y-scaling approach [6].

NM, E=3.6GeV, θ=30°
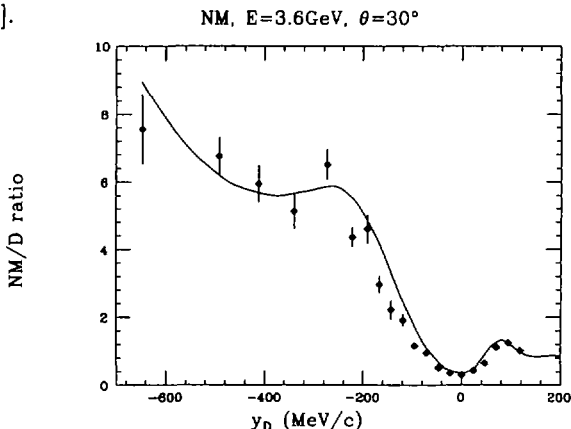
Figure 4: Cross section ratio of nuclear matter and the deuteron, as a function of the scaling variable y. The result of the CBF calculation is shown as a solid line.

Figure 4 shows the ratio for one of the kinematics at large q, small ω where data are available. Data and theory are plotted as a function of the variable y_D, which is basically the component of the nucleon momentum k parallel to $\vec{q}$. The dip at $y = 0$ corresponds to the maximum of the quasielastic peak dominated by nucleons of low momentum k, the region of $y < -300 MeV/c$, corresponds to the high-momentum tail of $n(k)$ of interest here.

Figure 4 shows that the particular nuclear matter spectral function used here agrees well with the data. The comparison between calculation and experiment is very sensitive to the $n(k)$ at large k. Tests carried out by renor-

malizing the spectral function at $k > k_F$ have shown that the cross section ratio at $y < -300 MeV/c$ is essentially proportional to $S(k, E)$ at $k > k_F$. We conclude that the experimental ratio nuclear matter-to-deuteron for $k > k_F$ is 5.5 ± 0.8, as compared to the value of 6.0 as given by the CBF theory.

Together with similar data taken at other kinematics, the electron-scattering data fix the nuclear matter-to-deuteron ratio with $10\div15\%$ accuracy. This uncertainty in the ratio is much smaller than the spread between modern calculations for $n(k)$, which, according to fig. 1, amounts to about a factor of two. This shows that quasielastic electron scattering does provide additional experimental input concerning nuclear matter properties. It measures an observable that, due to its short-range nature, is particularly valuable in constraining the theories when aiming at the nuclear matter-properties at the higher densities relevant for astrophysical applications.

References

[1] R.B. Wiringa, V. Fiks, and A.Fabrocini. *Phys. Rev. C*, 38:1010, 1988.

[2] D. Day, J.S. McCarthy, Z.E. Meziani, R. Minehart, R. Sealock, S.T. Thornton, J. Jourdan, I. Sick, B.W. Filippone, R.D. McKeown, R.G. Milner, D.H. Potterveld, and Z. Szalata. *Phys. Rev.*, C48:1849, 1993.

[3] D. Day, J.S. McCarthy, Z.E. Meziani, R. Minehart, R.M. Sealock, S. Thornton, J. Jourdan, I. Sick, B.W. Filippone, R.D. McKeown, R.G. Milner, D. Potterveld, and Z. Szalata. *Phys.Rev.C*, 40:1011, 1989.

[4] O. Benhar, A. Fabrocini, and S. Fantoni. *Nucl. Phys.*, A505:267, 1989.

[5] O. Benhar, A.Fabrocini, S. Fantoni, G.A. Miller, V.R. Pandharipande, and I. Sick. *Phys. Rev.*, C44:2328, 1991.

[6] D. Day, J.S. McCarthy, Z.E. Meziani, R. Minehart, R. Sealock, S.T. Thornton, J. Jourdan, I. Sick, B.W. Filippone, R.D. McKeown, R.G.Milner, D.H. Potterveld, and Z. Szalata. *Phys. Rev. Lett.*, 59:427, 1987.
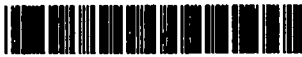
DE98F8408

DE011451289

NUCLEON SELF-ENERGY IN THE RELATIVISTIC BRUECKNER THEORY

T. WAINDZOCH, C. FUCHS and A. FAESSLER

Institut für Theoretische Physik, Universität Tübingen
Auf der Morgenstelle 14, D-72076 Tübingen, Germany

Abstract

The self-energy of the nucleon in nuclear matter is calculated in the relativistic Brueckner theory. We solve the Thompson equation for the two nucleon scattering in the medium using different Bonn potentials. The self-energy has a rather strong momentum dependence while the equation of state compares well with previous calculations.

1   Introduction

The relativistic Dirac-Brueckner-Hartree-Fock (DBHF) approach has been remarkably successful in describing the nuclear matter saturation mechanism [1]. The major improvement with respect to non-relativistic treatments is based on an additional density dependence of the formalism introduced by the self-consistent spinor basis. To solve the Bethe-Salpeter equation, respectively its three-dimensional reduction, a variety of approaches based on different techniques and various bare nucleon-nucleon interactions have been developed over the last decades. All the calculations are able to describe nuclear matter properties quite reasonable. Meanwhile two main results can be regarded as settled: firstly the nuclear single particle potential originates from the cancelation of large repulsive vector and attractive scalar fields, respectively self-energy components, and secondly the magnitude of the effective mass M^* is reduced to values around $\sim 0.6M$ at saturation density. The determination of the momentum dependence of the nuclear self-energy is a subtle problem which has not yet led to settled results. Its detail understanding is, however, of importance for a description of heavy ion collisions, where nuclei might overlap and where particles with large relative momenta are positioned closely in configuration space.

Generally, the techniques applied in the standard relativistic Brueckner approach assumes a weak momentum dependence of the self-energy inside the Fermi sea. This assumption was supported by various calculations in the past

[1, 2, 3]. Using the method proposed by Horowitz and Serot [2] one projects onto the Lorentz-invariants of the T-matrix (or in-medium G-matrix). A simpler, however less accurate method is to determine the self-energy components by a fit to the single particle potential [3].

In the present work we discuss the approach of Horowitz and Serot using different Bonn potential versions for the bare nucleon-nucleon potential [4].

2 The self-energy in nuclear matter

In the relativistic Brueckner approach the nucleon inside the nuclear medium may be viewed as a dressed particle in consequence of its two-body interaction with the surrounding nucleons. This problem is stated as a coupled set of three non-linear integral equations

$$T = V + i \int VQGGT \tag{1}$$

$$G = G^0 + G^0 \Sigma G \tag{2}$$

$$\Sigma = -i \int_F (Tr[GT] - GT) \tag{3}$$

The T-matrix is calculated in the ladder approximation of the Bethe-Salpeter equation (1) while the bare nucleon-nucleon interaction is described by a one-boson exchange potential V. The two-nucleon propagator iGG is generally replaced by an effective propagator, the Thompson propagator. The Pauli operator Q accounts for the influence of the medium by the Pauli principle and projects the intermediate scattering states outside the Fermi sea. The dressed one-body propagator G is calculated via the Dyson equation (2) from the free propagator and the self-energy. The latter is determined by summing up the direct and the exchange interactions with all the nucleons inside the Fermi sea F, see Eq. (3). On general physical grounds [5], the self-energy can be expressed in the nuclear matter rest frame as

$$\Sigma(k) = \Sigma_s(k) - \Sigma^\mu(k)\gamma_\mu = \Sigma_s(k) - \gamma_0\Sigma_0(k) + \vec{\gamma}\vec{k}\Sigma_v(k). \tag{4}$$

In order to project out the self-energy components, the T-matrix has to be decomposed into its Lorentz invariants (scalar, vector, tensor, pseudo-vector and axial-vector)

$$T = T^S 1\otimes 1 + T^V \gamma^\mu \otimes \gamma_\mu + T^T \sigma^{\mu\nu} \otimes \sigma_{\mu\nu} + T^P \left(\frac{\not{k}\gamma_5}{2M^*}\right)\otimes\left(\frac{\not{k}\gamma_5}{2M^*}\right) + T^A(\gamma_5\gamma^\mu)\otimes(\gamma_5\gamma_\mu) \tag{5}$$

which is usually done in the two-particle center-of-mass frame. K is the momentum transfer. The projection method is in detail described in Ref. [2].

The structure of the self-energy, i.e. its density and momentum dependence has been discussed in detail in Ref. [6] where different Bonn potentials have been applied as the bare NN-interaction. As the most prominent result we observe a remarkably strong momentum dependence of the scalar and time-like vector self-energy components around the Fermi momentum. Fig.1 shows the momentum dependence of the three self-energy components $\Sigma_s, \Sigma_0, k_F\Sigma_v$ at nuclear matter density $\rho = 0.166 fm^{-3}$ using the Bonn A potential.
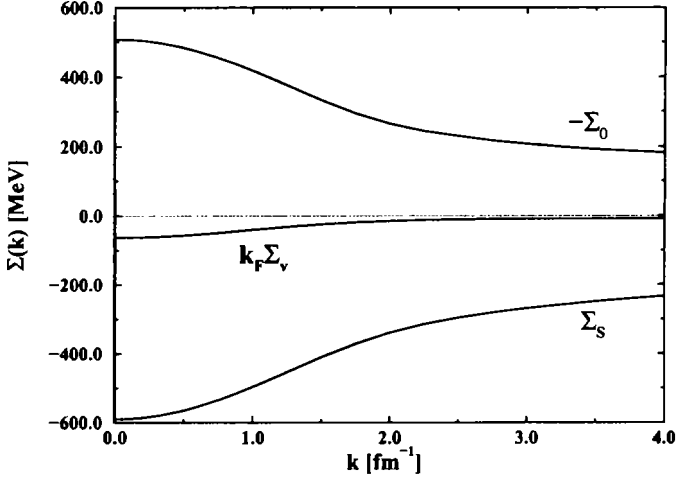
Fig. 1. Self-energy components for nuclear matter density $\rho = 0.166 fm^{-3}$ in the relativistic Brueckner approach using the Bonn A potential.

These findings are contrary to results obtained in the previous approximation scheme, where one usually assumes a rather weak momentum dependence of the self-energy from the beginning [3].

The equation of state, however, is rather insensitive to the detailed structure of the self-energy. In the relativistic Brueckner approach the energy per particle is defined in analogy to the non-relativistic Hartree-Fock method as the kinetic plus half the potential energy [6]. The resulting equations of state

for the three different versions of the Bonn potential are shown in Fig.2. As a matter of fact, the results are almost identical to the results obtained in Ref. [3] where a weak momentum dependence of the self-energy was assumed from the beginning. Notice that the calculated saturation points are close to the empirical saturation point.
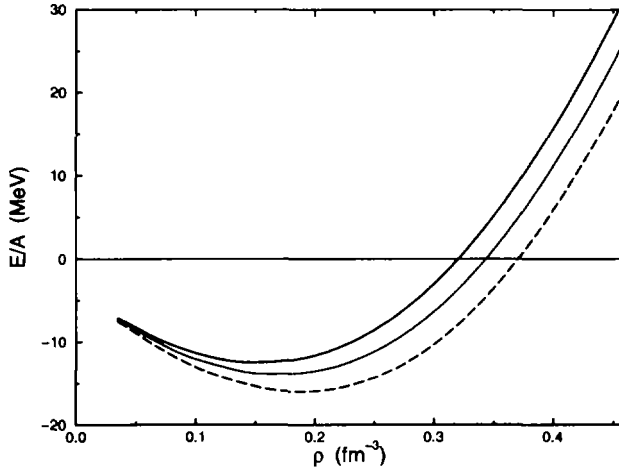
Fig. 2. The equation of state for the A (dashed), B (dot) and C (solid) versions of the Bonn potential.

3 Summary and outlook

We investigated the momentum dependence of the nuclear self-energy in the relativistic Brueckner approach. Contrary to the usual assumption of a weak momentum dependence we found a rather strong dependence of the self-energy on the nucleon momentum. Although the result for the equation of state is rather unaffected, this might still be of great importance for the simulations of heavy ion collisions where the detailed form of the effective mass for the nucleons plays an enormous role. Therefore we are planning to investigate the momentum dependence of the self-energy in more detail in the future. Especially the self-consistency scheme applied so far, the so called reference spectrum approximation [5], needs to be improved. Within this approximation

scheme, the effective mass of the nucleon

$$M^*(k) = M - \Sigma_s(k) \tag{6}$$

is generally fixed to its value at the Fermi surface $M^*(k) = M^*(k_F)$, assuming a weak momentum dependence of the self-energy $\Sigma_s(k)$. However, our findings show that this assumption is no longer justified. Therefore we should consistently take into account the full momentum dependent effective mass of the nucleon in the relativistic Brueckner theory. Work in this direction is in progress and will be presented elsewhere [7].

References

[1] B. ter Haar, R. Malfliet, Phys. Rep. **149**, 207 (1987).

[2] C.J. Horowitz, B.D. Serot, Nucl. Phys. **A464**, 613 (1987).

[3] R. Brockmann, R. Machleidt, Phys. Rev. C **42**, 1965 (1990).

[4] R. Machleidt, Advances in Nuclear Physics, **19**, 189, eds. J.W. Negele, E. Vogt, (Plenum, N.Y., 1989).

[5] B.D. Serot, J.D. Walecka, Advances in Nuclear Physics, **16**, 1, eds. J.W. Negele, E. Vogt, (Plenum, N.Y., 1986)

[6] L. Sehn, C. Fuchs, Amand Faessler, Phys. Rev. C **56**, 216 (1997).

[7] T.Waindzoch, C. Fuchs, and A. Faessler, in preperation

PHASES OF DENSE MATTER WITH
NON-SPHERICAL NUCLEI

C. J. PETHICK[a,b] and D.G. RAVENHALL[b]

[a]*NORDITA, Blegdamsvej 17, DK-2100 Copenhagen Ø, Denmark*
[b]*Department of Physics, University of Illinois at Urbana-Champaign,
1110 West Green Street, Urbana, Illinois 61801-3080, USA*

Abstract

A brief review is given of some of the important physics related to
phases with non-spherical nuclei that can exist in neutron stars and in
matter in stellar collapse at densities just below the saturation density
of nuclear matter. Comparisons are made with other systems that ex-
hibit similar liquid-crystal-like phases, both in nuclear physics and in
condensed matter physics. A short account is given of recent work on
the elastic properties of these phases, and their vibration spectrum, as
well as on neutron superfluid gaps.

Many different physical systems exhibit modulated phases, in which the
density of particles or some related variable varies periodically in space in one
or more dimensions. Liquid crystals provide one such example: in smectic A
liquid crystals the density varies periodically in one spatial direction, thereby
giving rise to a layered structure, while in columnar phases the density corre-
sponds to that for an array of infinitely long rods located on a triangular lattice
in the plane perpendicular to the rods [1]. For a general account of modulated
phases the reader is referred to Ref.[2]. In nuclear physics modulated phases
occur in the obvious example of crystal lattices of nuclei in matter at terrestrial
densities, and phases having the symmetries of smectic A and columnar phases
are expected to occur in matter at sub-nuclear densities [3]. Pion condensed
phases are also modulated structures, the simplest ones resembling smectic A
liquid crystals [4], in the sense that the pion field is periodic in only one direc-
tion, while more complicated phases can be favored when higher-order effects
are taken into account [5]. The transition from hadronic matter to quark mat-
ter may also occur via a series of modulated phases[6, 7], but whether or not
this is the case depends on properties of finite size droplets of quark matter
which are at present poorly understood.

In this paper we shall give a qualitative, descriptive account of the mod-
ulated phases that occur in matter at densities just below that of nuclear

matter. References will be given to more detailed works with explicit calculations. Rather generally, modulated phases occur when there are competing interactions. In the case of the liquid-crystal-like phases of hadrons at subnuclear densities, the two interactions are the Coulomb and surface energies. Consider matter made up of nuclei with a proton fraction close enough to 1/2 that neutron drip does not occur, immersed in a background of electrons. The optimal size of a nucleus may be determined from the liquid drop model. The bulk and symmetry contributions to the nuclear energy are independent of the nuclear size, and the optimal size is determined by a competition between the nuclear surface erergy, which favors large nuclei, and the Coulomb energy, which favors small nuclei. The configuration having minimum energy is determined from the virial-like condition that the surface energy is twice the Coulomb energy, and for proton fractions close to 1/2, this leads to the result that the optimal nuclear mass number, A, is given by $A \approx 12.5/x^2$, where $x = Z/A$, Z being the atomic number of the nucleus. This is consistent with the fact that for roughly symmetric nuclei, the optimal nuclei are those around iron.

Next we discuss the basic physics which makes roughly round nuclei unfavorable at high densities. The temperature will be assumed to be zero, and often we shall not mention the possible presence of neutrons outside nuclei, which has little effect on the nature of the arguments about equilibrium shapes, but which must be included in quantitative calculations of physical properties of neutron-rich matter such as is encountered in neutron stars. When the nuclear size becomes comparable with the spacing between nuclei, the contributions to the Coulomb energy due to interactions between different nuclei, of nuclei with the electron background, and of the electron background with itself become important. One physically obvious limiting case that one can consider is that when nuclei fill all of space. Matter is then electrically neutral locally, since the proton and electron densities are the same everywhere, and consequently the Coulomb energy vanishes. In the condition for the equilibrium nuclear size it is the *total* Coulomb energy that occurs, not just the Coulomb energy of the protons of a nucleus interacting with themselves via the electrostatic interaction. Thus the reduced Coulomb energy at high density results is a reduced tendency of the Coulomb energy to favor small nuclei, and thus the equilibrium nuclear size increases. The formation of the liquid crystal phases may be understood as being due to the instability of round nuclei to fission: because of the reduced Coulomb energy, nuclei become so large that they are unstable to fission according to the condition first discussed by Bohr and Wheeler [8]. This is that a spherical nucleus will become unstable to small quadrupolar

distortions if the the Coulomb energy exceeds twice the surface energy, or for roughly symmetric nuclei, $Z^2/A \geq 50$. A detailed study shows that the fission condition is relatively unaffected in dense matter, and consequently in dense matter, nuclei eventually become so large that they will undergo fission. It is therefore physically reasonable that the equilibrium configuration is an array of long rods, which may be viewed as elongated nuclei joined together. Nuclei become unstable to fission when the radius of a nucleus is roughly one half of the radius of a sphere whose volume is the average volume per nucleus, that is when nuclei fill roughly 1/8 of space.

The fact that non-spherical nuclei are the equilibrium configuration may be understood in terms of the way in which the Coulomb energy depends on the nuclear shape. At low densities spherical nuclei are favored because the electric field of a charged sphere falls off inversely as the square of the distance from the center of the nucleus. Most of the Coulomb energy is associated with the electric field in the immediate vicinity of the nucleus, out to a distance of order the nuclear radius outside the nucleus. On the other hand, for charged rods and plates the electric field falls off more slowly, and there is a significant contribution to the Coulomb energy from distances from the nucleus much larger that the radius of the rod or the thickness of the plate. For a charged plate the electric field is constant, and thus it is obvious that nuclei having the form of plates will be prohibitively expensive energetically at low densities. Detailed calculations show that the sequence of phases expected with increasing density is spherical nuclei, rod-like ones, then plate-like ones. After this one finds bubble phases, where the nuclear matter and the separating space undergo an inversion, and the sequence of shapes is gone through in reverse order.

The next topic we consider is the question of whether the phases with non-spherical nuclei are energetically favorable. The virial-like condition enables one to determine which nuclear shapes are favorable, but it does not answer the question of whether or not a phase with uniform nuclear matter, and an accompanying uniform background of electrons, could be preferable. The difference between the energy of a uniform phase and one with nuclei may be regarded as being made up of two contributions: the first due to bulk energies, including symmetry energies, and others due to surface and Coulomb effects. For symmetric nuclear matter the bulk energy difference is large, since it corresponds to the energy required to stretch nuclear matter from the saturation density to the actual density, and this overwhelms the surface and Coulomb contributions. Consequently, for roughly symmetrical nuclear matter non-spherical phases are energetically favorable over a density range of almost a factor 10.

The story is quite different for matter in neutron stars, where nuclear matter is surrounded by neutrons. The bulk energy change in going from the uniform state to the one with nuclei gives a rather small energy gain, since only minor readjustments of the proton and neutron distributions are required, and the gains are comparable with the total surface and Coulomb energies. Results do depend on the equation of state of nuclear matter, and for what one presently regards as the most reliable equation of state, one finds that the phases with non-spherical nuclei are indeed the equilibrium ones in a certain density range. The relevant density range for the case of neutron stars is much less than for nearly symmetrical nuclear matter since because the density of neutrons outside nuclei is rather close to that of the nuclear matter inside nuclei, a change in nuclear filling factor from 10% to roughly unity gives rise to only a relatively small density change. An important problem for future work is to pin down better the equation of state of uniform matter consisting of neutrons with a small concentration of protons.

Despite the rather small density range over which non-spherical nuclei are expected to be stable in neutrons stars, these phases are estimated to make up roughly half of the matter by mass in the crust of a neutron star[9]. Thus their properties will be important for any sorts of physics that involve the crust of the star. One class of properties are elastic ones. Clearly in the case of plate-like nuclei, there is no restoring force for displacements that lie in the plane of the plates, and similarly for the case of rods. This will be important for plate tectonics, that has been invoked in theories of magnetic field evolution. Detailed calculations of elastic properties have been performed in Ref. [10]. The possible vibrations of these phases are different from those of an ordinary solid, and in phases with plate-like nuclei one expects there to be oscillations corresponding to the coupled density and isospin density waves that occur in uniform matter, and in addition, modes in which the restoring force is provided by the buckling of the plates. These modes have a dispersion relation that is linear in the wave number, but which is proportional to $\sin\theta \, \cos\theta$, where θ is the angle between the wave vector and the normal to the plates [11, 12]. Further work is needed to investigate how these phases affect other properties, such as neutrino emission, which is an important cooling mechanism for neutron stars.

Another set of problems that arise in connection with the phases with non-spherical nuclei concern superfluid gaps, which are of interest for models of glitches, the sudden speed-ups observed in the frequencies of a number of pulsars. In such models pinning of vortices in the neutron superfluid to nuclei is invoked, and this is sensitive to superfluid gaps [13]. A neutron outside nuclei

can rather easily move into the nuclear matter, where the pairing interaction is expected to be weaker than in the neutron liquid outside. As a consequence, the pairing gap for neutrons is reduced, because it depends on some average of the pairing interactions in the nuclear matter and in the neutron liquid. Since the pairing gap depends exponentially on the pairing interaction, this indicates that there can be significant changes in the gap due to this effect[14]. In this connection it is important to note that the superfluid coherence length, which determines the size of a Cooper pair in the medium, is much larger than the spatial scale of structures, and consequently the gap at any point does not depend only on the pairing interaction at that point, but also at other points out to a distance of order the coherence length.

In conclusion, it is clear that there are many problems remaining in understanding phases with non-spherical nuclei. There is a continuing need to make more precise our understanding of neutron-rich matter, and the knowledge gained is of use not only in the context of neutron stars, but also for the less neutron rich nuclei that are presently studied so extensively in the laboratory. The essential point to bear in mind is that the situations of interest in neutron stars are so neutron rich that even approximate information about such matter can provide rather tight constraints on properties of matter with a neutron excess of 1/3 or less typical of laboratory situations.

References

[1] For an excellent account of liquid crystals that includes recent work on the smectic A and columnar phases, see P. G. de Gennes and J. Prost, *The Physics of Liquid Crystals*, 2nd ed. (Clarendon, Oxford, 1993).

[2] M. Seul and D. Andelman, Science **267** (1995) 476.

[3] For a review of modulated phases in nuclear matter at subnuclear densities, see C. J. Pethick and D. G. Ravenhall, Ann. Rev. Nucl. Part. Sci. **45** (1995) 429, where a comprehensive bibliography may be found.

[4] G. Baym and D. K. Campbell, in *Mesons in Nuclei*, ed. M. Rho and D. H. Wilkinson (North Holland, Amsterdam, 1979), Vol. III, p.1033.

[5] T. Takatsuka, R. Tamagaki, and T. Tatsumi, Prog Theor. Phys. Suppl. **112** (1993) 67

[6] H. Heiselberg, C. J. Pethick and E. F. Staubo, Phys. Rev. Letts. **70** (1993) 1355.

[7] N. K. Glendenning, these proceedings.

[8] N. Bohr and J. A. Wheeler, Phys. Rev. **56** (1939) 426.

[9] For a schematic picture of a neutron star which indicates where these phases lie in a neutron star, see the contribution of H. Heiselberg and M. Hjorth-Jensen to these proceedings.

[10] C. J. Pethick and A. Y. Potekhin, Nordita preprint 96/80, to appear in Phys. Lett.B.

[11] L. D. Landau and E. M. Lifshitz, *Theory of Elasticity*, 3rd edition, (Pergamon, Oxford, 1986), p. 182.

[12] E. Olsson and C. J. Pethick, unpublished work.

[13] M. A. Alpar, in *The Lives of the Neutron Stars* ed. M.A. Alpar, Ü. Kiziloğlu, and J. van Paradijs (Kluwer, Dordrecht, 1995) p. 185.

[14] Detailed calculations of this effect has been made by F. De Blasio, G. Lazzari, C. J. Pethick, and J. Sauls, unpublished work.

NEUTRON-PHONON INTERACTION IN NEUTRON STAR CRUSTS

A. SEDRAKIAN

Center for Radiophysics and Space Research,
Cornell University, Ithaca 14853, NY

Abstract

The phonon spectrum of Coulomb lattice in neutron star crusts above the neutron drip density is affected by the interaction with the ambient neutron Fermi-liquid. For the values of the neutron-phonon coupling constant in the range $0.1 \leq \lambda \leq 1$ an appreciable renormalization of the phonon spectrum occurs which can lead to a lattice instability manifested in an exponential growth of the density fluctuations. The BCS phonon exchange mechanism of superconductivity leads to neutron pairing with a gap in the neutron excitation spectrum comparable to that due to direct nuclear interaction.

1 Introduction

Below the melting temperature $T_m \simeq Z^2 e^2 / 100 \, r_i \sim 10^9 - 10^{10}$ K, where r_i is the average interion spacing, Z is the ion charge, the ionic component of plasma in neutron star crusts is arranged in a Coulomb lattice. The screening of the electrostatic potential of the lattice by electrons is ineffective since the ratio $\lambda_D/r_i < 1$, where λ_D is the Debye screening radius, and, therefore, electrons are distributed almost uniformly. Above the neutron drip density 4×10^{13} g cm^{-3} the intervening space between the clusters is filled by a neutron fluid which goes over to a superfluid state below the critical temperature of the order $T_c \sim 10^9$ K; (for a review of the early work see, e.g., ref. [1]; recent progress is summarized in ref. [2]). Although initial studies of the collective effects in the crusts were focused either on the properties of the highly compressed solid matter or the unbound neutron fluid at subnuclear densities (with an exception of the equation of state where phase equilibrium conditions are imposed) this separation is justified only when the interaction between these components of the crusts is weak; this is not, however, always the case. The purpose of this work is to continue the discussion of the interaction between the neutrons in the continuum and the excitations of the crustal lattice, i.e. phonons, set up in an earlier work [3].

Figure 1: The phonon Dyson equation and the vertex equation for coupled system of fermions (solid lines) and phonon (wavy lines). The fermion Dyson equation is given by the block in Fig. 3. The thick lines correspond to the full propagators, while the thin lines to the free ones.

2 The Phonon Spectrum

The self-consistent coupled fermion-phonon problem is shown in terms of Feynman diagrams in Fig. 1 and 3. In this section we shall give the finite temperature solution of the Dyson equation for phonons which are coupled to fermions of arbitrary relativism; in the present case the neutrons are only mildly relativistic (if at all) while the electrons are ultrarelativistic. The problem can be solved for an arbitrary coupling strength since the perturbation series converge rapidly with respect to another parameter - ratio of the phonon to the fermion energies: as a result one may restrict to the lowest order term in the integral equation for the vertex (Migdal theorem). The sequence in which the Dyson equations for the fermions and phonons should be solved is fixed by the fact that the phonons affect only a narrow range of energies in the fermion propagator (of the order the Debye frequency ω_D), which implies that the polarization function can be evaluated with free fermion propagators:

$$\gamma^0 G^0(\vec{p}, i\omega_\nu) = \frac{\Lambda_+(\vec{p})}{i\omega_\nu - (\epsilon_p - \mu)}; \quad \Lambda_+(\vec{p}) = \frac{1}{2}\left\{1 - \frac{\vec{\alpha}\cdot\vec{p}}{\epsilon_p} + \frac{\gamma_0 m}{\epsilon_p}\right\}, \quad (1)$$

where $\epsilon(p) = \sqrt{p^2 + m^2}$, $\vec{\alpha} = \gamma_0\vec{\gamma}$ and we have kept only the positive energy states from the outset; (to excite an excitation at the top of the Fermi sea and an anti-particle at rest one needs to overcome an energy barrier of the order of the Fermi energy ϵ_F, however $\omega \leq \omega_D \ll \epsilon_F$). The Matsubara frequencies assume discrete odd integer values $\omega_\nu = (2\nu+1)/\beta$ where $\nu = 0, \pm1, \pm2, \ldots$ and β is the inverse temperature and the other notations have their usual meaning. We find the retarded polarization function depicted in Fig. 1 by performing the frequency summation over the product of the fermion propagators and an analytical continuation to the real axis:

$$\Pi^{(R)}(\vec{k}, \omega) = \mathcal{M}_k^2 \int \frac{d^3p}{(2\pi)^3} \frac{f(\epsilon_{p+k} - \mu) - f(\epsilon_p - \mu)}{\omega - \epsilon_{p+k} + \epsilon_p + i\delta} \left\{1 - \frac{\vec{p}\cdot(\vec{p}+\vec{k})}{\epsilon_p \epsilon_{p+k}} + \frac{m^2}{\epsilon_p \epsilon_{p+k}}\right\},$$
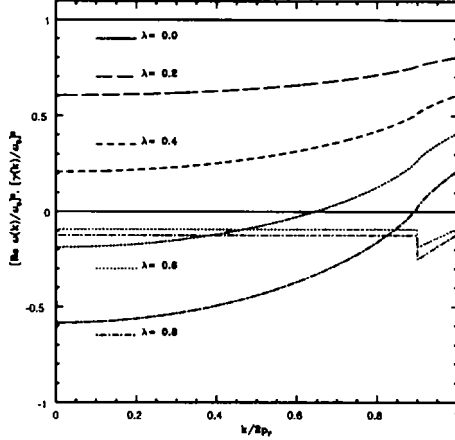
Figure 2: The renormalization of the phonon spectrum $\omega(k)$ and the damping $\gamma(k)$ of the modes (light lines) as a function of the momentum transfer for several values of the neutron-phonon coupling constant.

where $\mathcal{M}_k$ is the fermion-phonon coupling matrix element and $f(x) = [1 + \exp(\beta x)]^{-1}$ is the Fermi distribution function. The scalar polarization function above corresponds to particle–hole excitation for arbitrary degree of relativism of the system and finite-temperatures; for applications to the neutron subsystem one may take the non-relativistic limit. Fig. 2 shows the real part (more precisely $1 + \mathrm{Re}\Pi(\mathbf{k},\omega)$) and the imaginary part of the polarization function as a function of the momentum transfer for $\beta^{-1} = 0$ and a typical ratio $c_s/v_F = 0.1$, where c_s and v_F are the sound and Fermi velocities, respectively. The first quantity is just the renormalization of the phonon frequencies $[\omega(k)/\omega_0]^2$, where ω_0 is the unperturbed phonon frequency which are treated in the Debye model. The eigen modes of the system vanish first in the long-wave limit where, with increasing coupling constant, the curves cross zero. The disappearance of the real solutions to the dispersion relation indicates instability of the system with respect to the density fluctuations, as can be seen by inspecting the proper solutions which exhibit exponentially growing amplitude of phonon mode.
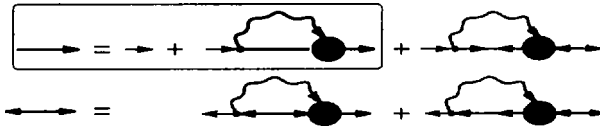
Figure 3: The Dyson equations for the normal and anomalous fermion propagators. The contributions from the anomalous sector are shown by the light lines.

If this is the case, one may conclude that the starting lattice structure does not correspond to the true minimum of the energy of the system (in other words is not the 'true vacuum'). Available estimates of the neutron-phonon coupling constants are, however, unreliable for two reasons: first, preliminary considerations [3], based on a fit to the elastic neutron-nucleus scattering cross-sections, does not include the medium effects (which most likely will reduce the effective cross-section) and, in addition, the substantial imaginary part of the optical potential responsible for the absorptive processes should be included in the estimates. Second, the compositions of the crustal matter due to different authors (see refs. in [2, 3]) imply coupling constants from marginal up to of the order unity at $n_0/3$, where n_0 is the nuclear saturation density, and consequently, very different assessments about the role of the neutron-phonon interaction.

3   Phonon Exchange Interaction and Neutron Pairing

The net two-body interaction between neutrons in the continuum comprises the nuclear component (which is dominated by the attractive $^1S_0$ channel at densities of interest) and the component due to the phonon exchange. Since the latter interaction is attractive as well, the BCS pairing for some values of neutron-phonon coupling constant might be influenced by the phonon-exchange mechanism. The respective gap equations, which include the retardation of the effective interaction, emerge as a solution to the set of diagrams in Fig. 3. We find (for simplicity the $\beta^{-1} = 0$ limit is given below)

$$
\begin{aligned}
\Delta(\omega)z(\omega) &= \int_0^\infty d\xi \, [\mathcal{K}_+(\omega,\xi) + \mathcal{W}] \operatorname{Re} \frac{\Delta(\xi)}{\sqrt{\xi^2 - \Delta(\xi)^2}} \\
\omega \left[1 - z(\omega)\right] &= \int_0^\infty d\xi \, \mathcal{K}_-(\omega,\xi) \operatorname{Re} \frac{\xi}{\sqrt{\xi^2 - \Delta(\xi)^2}}
\end{aligned}
\tag{2}
$$

where $z(\omega)$ is the wave function renormalization and the effective interactions via phonon exchange and direct nuclear force are defined respectively

$$
\begin{aligned}
\mathcal{K}_\pm(\omega,\xi) &= \frac{1}{(2\pi)^2 v_F} \int_0^{2p_F} \mathcal{M}_k^2 \left[\frac{1}{\xi + \omega + \omega(k) + i\delta} \pm \frac{1}{\xi - \omega + \omega(k) - i\delta} \right] k\ dk \\
\mathcal{W} &= \frac{1}{(2\pi)^2 v_F} \int_0^{2p_F} |V(k)| k dk.
\end{aligned}
\tag{3}
$$

Here the nuclear interaction is given by the time-local interaction $V(k)$; note that a pairing description based on the pion exchange model would allow for the effects of retardation, pion mode softening, condensation etc. The formal structure of equations (2) coincides with the Eliashberg equations for metallic superconductor in the presence of the repulsive Coulomb force between the electrons. For the values $\omega_D = 0.7$ MeV and $\lambda = 0.45$ (which correspond to the density $0.3n_0$, for the composition of Arponen, see [3]) and $\mathcal{W} = 0$, eqs. (2) predict a value $\Delta = 0.03$ MeV, which is basically less, but comparable to the gap found neglecting the neutron-phonon coupling.

To conclude, if in a certain region of neutron star crusts the neutron-phonon coupling is not negligible (i.e. $\lambda \leq 1$), a number of novel effects emerge, which are potentially important for the correct description of phenomena in neutron star crusts. The crucial problem is whether the calculations of the coupling constants beyond the simple estimates would lead to significant values of the neutron-phonon coupling constant. In addition one may need a better understanding of the sources of the discrepancies between different models of neutron star crust composition and a reassessment based on the progress achieved in the many-body theory of nuclear matter in recent years.

Acknowledgment

References

[1] S. L. Shapiro, and S. A. Teukolsky, *Black Holes, White Dwarfs, and Neutron Stars: The Physics of Compact Objects*, Wiley, NY, (1983) p. 188.

[2] C. J. Pethick and D. G. Ravenhall, Annual Rev. Nucl. Part. Phys. **45** (1995) 429.

[3] A. Sedrakian, Astrophys. & Space Sci. **236** (1996) 267.

Mean–field models and exotic nuclei

M. Bender[a], T. Bürvenich[a], K. Rutz[a,b], J. A. Maruhn[a], W. Greiner[a],
and P.-G. Reinhard[c]

[a] Institut für Theoretische Physik, Universität Frankfurt, Germany

[b] Gesellschaft f"ur Schwerionenforschung mbH, Darmstadt, Germany

[c] Institut für Theoretische Physik, Universität Erlangen, Germany

Abstract

We discuss two widely used nuclear mean–field models, the relativistic mean–field model and the (nonrelativistic) Skyrme–Hartree–Fock model, and their capability to describe exotic nuclei. Test cases are superheavy nuclei and neutron-rich Sn isotopes. New information in this regime helps to fix hitherto loosely determined aspects of the models.

1 Introduction

This contribution discusses nuclear mean–field models and their capabilities to describe exotic nuclei. The two most widely used mean–field models are considered, the relativistic mean–field model (RMF) and its nonrelativistic cousin, the Skyrme–Hartree–Fock model (SHF). For both variants, there exists a widespread literature which we cannot report here in depth. Reviews for the RMF may be found, e.g., in [1, 2]. No recent reviews are available for the SHF. But a useful recent reference may be [3] where limitations of older forms and appropriate extensions of SHF are discussed. We ought to mention that there is a third model in the competition which we omit here to keep the presentation short. It is the Gogny force [4] which has much similarities with SHF.

All these models aim at a fully selfconsistent description of nuclei employing effective interactions developed for the purpose of effective Hartree calculations. The model thus stays in between the more elaborate many-body theories which try a description in terms of a basic nucleon-nucleon interaction (see the contribution from V.R. Pandharipande in these proceedings) and the more phenomenological approach on the basis of the liquid drop model plus shell corrections [5]. The actual effective interactions of RMF and SHF can be restricted by very general arguments to a form with only few free (6-10) parameters which are to be adjusted phenomenologically. Fitting to a few key data of nuclear structure allows to obtain a very good description of almost all stable nuclei from ^{16}O on up to the heaviest elements [2, 3]. Stable nuclei, however, represent a very narrow valley in the $N-Z$-plane and thus there remain several loosely fixed aspects in the models, particularly concerning isovector properties. Exotic nuclei which are now becoming more and more accesible are a challenge for mean field models and will provide at the same time useful key data for further development. It is the aim of this contribution to explore the predictions of SHF and RMF when proceeding into the exotic regions of the nuclear chart, here in
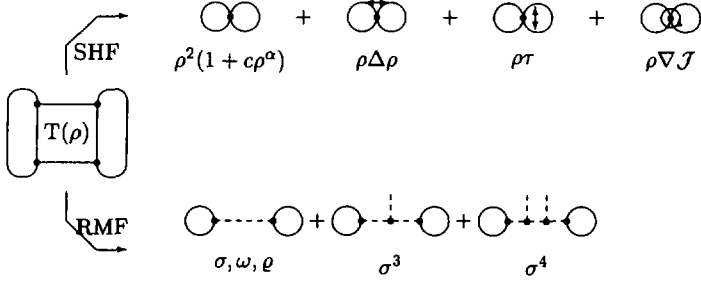
Figure 1: Illustration of the T–matrix expansion towards the Skyrme–Hartree–Fock or relativistic mean–field approach.

particular to neutron rich isotopes and to superheavy elements. We will first try in section 2 to explain quickly the formal structure of SHF and RMF, and then discuss a few key results in section 3.

2 RMF and SHF functionals in comparison

The RMF and SHF can be formulated in terms of effective energy density functional somehow similar as it is widely used in electronic systems [6]. We cannot provide the corresponding functionals in all details here (for this purpose see e.g. [2, 3]). Instead we try to present and discuss the essential features grafically in fig. 1. Starting point is the T matrix which is assumed to be given from some microscopic calculations in nuclear matter at density ρ. This serves as effective interaction for nuclear mean field calculations. Both, SHF as well as RMF, can be thought as being derived from a local expansion of the underlying T matrix. The nonrelativistic SHF (upper branch in fig. 1) expands in terms of a zero-range effective force with gradient corrections ($\propto \Delta\rho$) to account for small effects from the spatial extension of the T–matrix and kinetic currents τ to account for its temporal extension. The very involved density dependence of the T-matrix is parametrised in an ad hoc fashion in terms of a power–law density–dependence on the two-body interaction. The spin–orbit force $\propto \nabla\mathcal{J}$ is to be added explicitly in a separate step. The RMF (lower branch in fig. 1), on the other hand, parametrises the T-matrix in terms of nucleons and meson fields which is the natural approach in the relativistic domain. A reasonable description requires just three effective mesons fields (σ = scalar–isoscalar, ω=vector–isoscalar, ρ= vector–isovector) with point coupling to the nucleons. The density dependence is here described indirectly through a nonlinear selfcoupling of the σ field (terms indicated with σ^3 and σ^4 in fig. 1). The spin–orbit is automatically implied in the

relativistic formulation.

At first glance, the two expansions, SHF and RMF, look very different. The differences are, however, not so large as one would suspect. It is, in fact, possible to map the RMF model to a large extend into the SHF model by using standard techniques of a nonrelativistic expansion, see e.g. [2]. The crucial point is that the scalar density can be expanded as $\rho_s \sim \rho_0 - (\tau - \nabla \cdot \mathcal{J})/2m^*$. The ρ_0 is the zeroth component of the vector density which becomes the normal density in the nonrelativistic limit. The scalar density is thus expressed in terms of the of the vector density and subsequent kinetic as well as spin-orbit terms. The meson propagators still produce a finite-range interaction. It can be expanded into zero-range plus gradient correction as $[-\Delta + m^2]^{-1} \sim m^{-2} + m^{-4}\Delta$. We thus perform a double expansion which finally yields the SHF–terms as sketched in fig. 1. It is thus found that the zero-range two-body force in SHF emerges from a combination of the (attractive) scalar interaction and the (repulsive) vector interaction of the RMF, the gradient terms stem from the expansion of the meson folding, and effective mass term as well as spin-orbit term emerge simultaneously from the v/c expansion of ρ_s. At this place, one advantage of the RMF becomes obvious, namely that it incorporates the spin-orbit force without separate adjustment.

Thus far the mapping is obvious and it shows the intimate relation between RMF and SHF. There are, however, serious problems if we want to compare the density dependence. This feature is modelled in a somewhat ad hoc fashion in both approaches and the indirect parametrisation in the RMF via a nonlinear selfcoupling of the scalar field is hard to map into the ρ^α dependence of the two-body interaction in SHF. One can establish a relation in the near vicinity of the bulk equilibrium density ρ_0 by means of a Taylor expansion in orders of $\rho - \rho_0$ for both models. But a quantitative comparison in the low-density and high-density regime shows that SHF and RMF behave basically different in these extremes. These difference are not explored in stable nuclei because these concentrate predominantly around the bulk equilibrium density. But they can grow important when stepping deeply into the realm of exotic nuclei.

Starting from the given energy functionals, one derives variationally the selfconsistent equations in straightforward manner [2, 3]. The equations are solved on grids in coordinate space using standard numerical techniques of gridding and iterations, see e.g. [7]. We are actually using codes in radially symmetric representation as well as in axially symmetric representation for deformed nuclei.

3   Results and discussion

3.1   Quality of the parametrisations

As pointed out above, nowadays mean field models provide a very good description of the gross properties of stable nuclei. We will demonstrate that here, pars pro
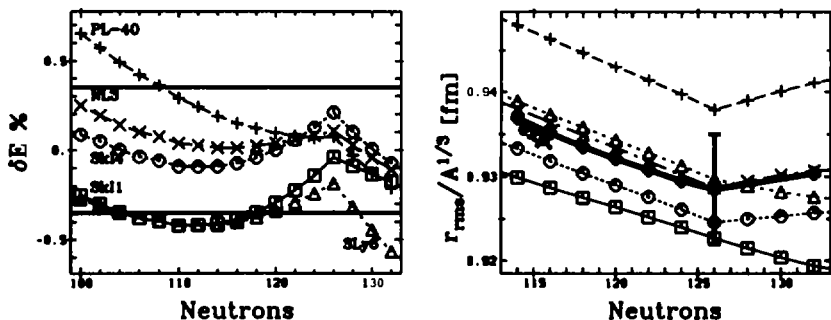
Figure 2: *Left panel: Relative error (in %) of binding energies, $\delta E = (E_{\text{theor}} - E_{\text{exp}})/E_{\text{exp}}$, for Pb isotopes and a selection of typical mean-field parametrisations as indicated. Right panel: rescaled charge r.m.s. radii for Pb isotopes. The thick line with rhombes represents the experimental values. The error bar which is shown for the case of $N = 126$ serves to indicate the average error of the mean-field description for the r.m.s. radii.*

toto, for the example of Pb isotopes. The left panel in fig. 2 shows the relative error in binding energies. The two horizontal lines at 0.35% indicate the average error in binding energies for good fits [2, 3]. One sees that all results remain essentially within these bounds (note that extreme isotopes represent already an extrapolation of the model). At second glance, however, one realizes unresolved trends, particularly this pronounced kink at the magic neutron number $N = 82$. It indicates that the mean-field models produce a too large two-neutron shell gap (see caption of fig. 4). But it is not hopeless to overcome this problem. Research in that direction is underway.

The right panel in fig. 2 shows rescaled charge r.m.s. radii in comparison with available experimental data (heavy line and rhombs). The error bar is to indicate the average error of good fits which amounts to about 0.7% deviation. Again, all forces remain within these bounds (except perhaps for PL–40 which experiences an unlucky fluctuation just in the Pb region), and again, we see deviations in trends. The data have a pronounced kink at the magic $N = 82$. This kink is not reproduced by all SHF forces in conventional parametrisation but emerges correctly in the RMF. The problem in the SHF comes from a too restricted form of the spin–orbit force. An appropriate generalisation (inspired be the RMF) solves the problem and yields SHF forces which follow the given trend [3], see SkI4 in the figure. Note that the kink became apparent only after data for [214]Pb were available. This can already be considered as an exotic nucleus, and the example demonstrates how new data deepen our understanding of mean-field models.

Neutrons
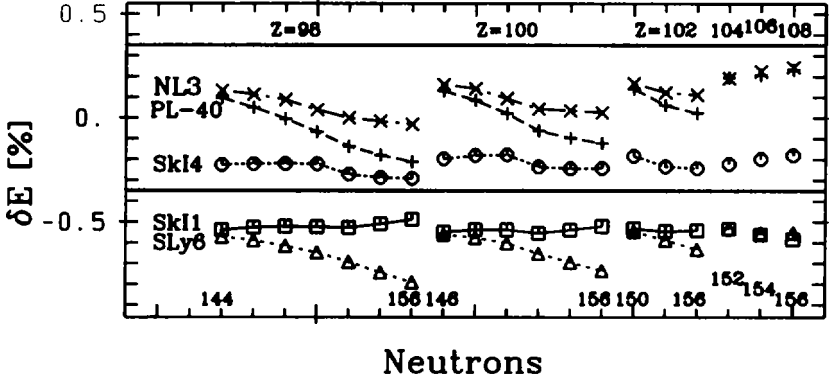
Figure 3: *Relative error (in %) of binding energies, $\delta E = (E_{\text{theor}} - E_{\text{exp}})/E_{\text{exp}}$, for a variety of superheavy elements and a selection of typical mean-field parametrisations as indicated.*

3.2 Extrapolation to superheavy nuclei

The search for new elements was a strong motivation for heavy-ion physics, and with great experimental effort a large amount of new superheavy isotopes has been accessed. They constitute a critical probe for theories because the high level density in this region makes the results very sensitive to details of a model. Binding energies are usually the first available information an we concentrate the discussion on them. Fig. 3 shows the relative error in binding energies. It is obvious that in this extrapolation the errors of the various forces spread more than in the case of the Pb isotopes shown before (note that we have already preselected well performing forces and that the spread would look even larger when showing a larger selection). It is gratifying, however, to see that there remain three forces which stay well within the bounds of 0.35% error. It is noteworthy that from the SHF models only SkI4 succeeds which employs the extended form of spin-orbit coupling [3]. As in the case of Pb isotopes, there remain nonetheless unresolved trends, here mainly in the form of non-zero slopes. A slope in δE means that the two-neutron separation energies S_{2n} deviate from the experimental values. From the three well performing forces, we will have the best S_{2n} for SkI4. This case, however, has a faint kink at $N = 150$ which means that SkI4 predicts a weak shell closure where there is none in the data. After all, the slopes as well as the kink are very small effects (smaller e.g. than in the case of Pb) such that we can be very satisfied with the performance of all three forces which fit into the desired error band, SkI4, NL3, and PL–40.

Having preselected three successful forces in the regime of existing superheavy
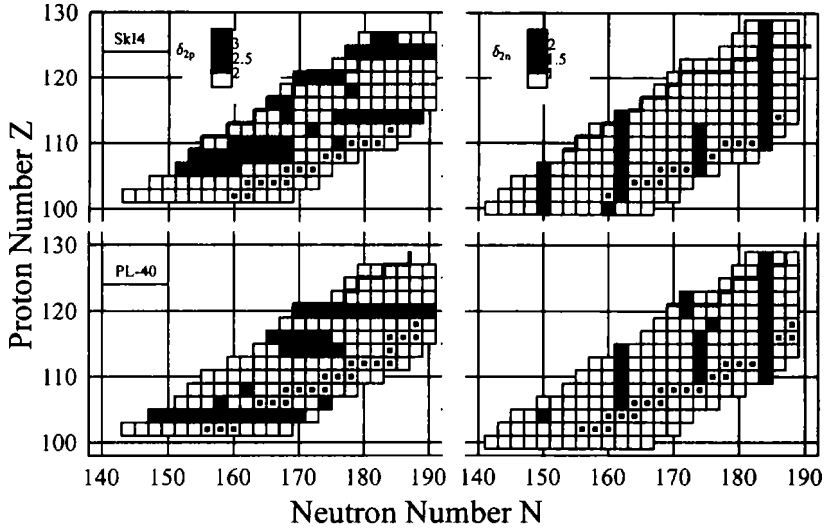
Figure 4: *Grey scale plots of the shell gaps in the region of superheavy nuclei for the nonrelativistic Skyrme parametrisation SkI4 (upper panels) and the relativistic mean field model with parametrisation PL–40 (lower panels). Dark spots represent large shell gaps and white spots small ones. The left panels show the two-neutron shell gaps, $\delta_{2n} = E(N+2, Z) - 2E(N, Z) + E(N-2, Z)$, and the right panel the corresponding two proton shell gaps.*

nuclei, we can now try to extrapolate further to even heavier systems. A most interesting question there is the appearance of doubly magic systems. These can be found by scanning the two-neutron and two-proton shell gaps. Large values indicate a shell closure. Fig. 4 shows these shell gaps for the RMF force PL–40 (lower panels) and the SHF force SkI4 (upper panel). The dark sports indicate large shell gaps, and double magic nuclei are to be expected where large neutron and proton shell gaps coincide. For the lower Z and N we have the regime of deformed ground state, and there we find that SkI4 predicts a doubly magic (deformed) $^{270}\text{Hs}^{162}_{108}$ whereas PL–40 has a magic $Z = 104$ proton shell but no convincing accompagning neutron shell. The two forces thus differ significantly in their predictions. This feature persists into the regime of the spherical doubly magic systems where SkI4 points at $Z = 114, N = 184$ but PL-40 at $Z = 120, N = 172$. this shows that faint differences in the spectral distribution carry forth to substantially different extrapolations for superheavy nuclei. These are thus a most critical probe for nuclear structure models.

3.3 Neutron rich Sn isotopes

Another direction is the extrapolation towards neutron rich isotopes which is particularly important for astrophysical purposes. Fig. 5 contains relevant results. The left upper panel shows the binding energy of pure neutron matter at low densities for various parametrisations. We see a large variation of the results. The SHF models show the larger variance which is no surprise because there are much more (and less well determined) isovector degrees of freedom in the parametrisations. The RMF models are more similar to each other but have a distinctively different low density asymptotics which is due to the fact that the density dependence is differently parametrised in SHF and RMF. The plot contains also the results from a microscopic calculation (rhombs connected by heavy lines) which should be very reliable at those low densities [8]. The comparison clearly prefers the SHF trends (except the somewhat strange SkI1). Low densities are explored in the tail of neutron rich nuclei, and thus we expect to see similarly deviating extrapolations in that regime.

The lower left panel of fig. 5 shows the S_{2n} for the neutron rich Sn isotopes. The large step comes at the magic $N = 82$ as expected. Left to that we have the regime of stable nuclei where all forces differ very little. For larger neutron numbers, on the other hand, we see substantial differences in the predictions, and one can note that many differences become manifest right after the shell gap. That means that we will have useful key data soon when the next exotic Sn isotopes are measured.

One may ask whether the isotope shifts in the charge r.m.s. radii could become an equally useful probe as it was the case for Pb. The right lower panel of fig. 5 shows these isotopic shifts for a variety of SHF and RMF forces. There is indeed a large spread in the predictions which makes this a useful observable to look at. But the mechanism producing these variations is different from the case of Pb. This has yet to be further explored.

The differences in the neutron binding energies (see upper left panel) will influence most the neutron properties. The neutron skin is an observable which is most sensitive to those. We define it here as the difference $R_n - R_p$ of the diffraction radii (for a discussion of their definition see e.g. [2] and references therein). The neutron skins are shown in the upper right panel of fig. 5. The differences are dramatic, as expected, and it is interesting to see that those forces which have low binding at low density produce particularly large skins (and vice versa). It is thus worthwhile to get many reliable data points for neutron skins, or neutron radii respectively.

3.4 Puzzles

Thus far we have seen how nicely mean–field models work for known data and how yet uncertain aspects may be fixed in future by adding information from newly discovered nuclei. There are, however, already a few new data which do not fit in any of the present parametrisations. Two major obstacles are demonstrated in
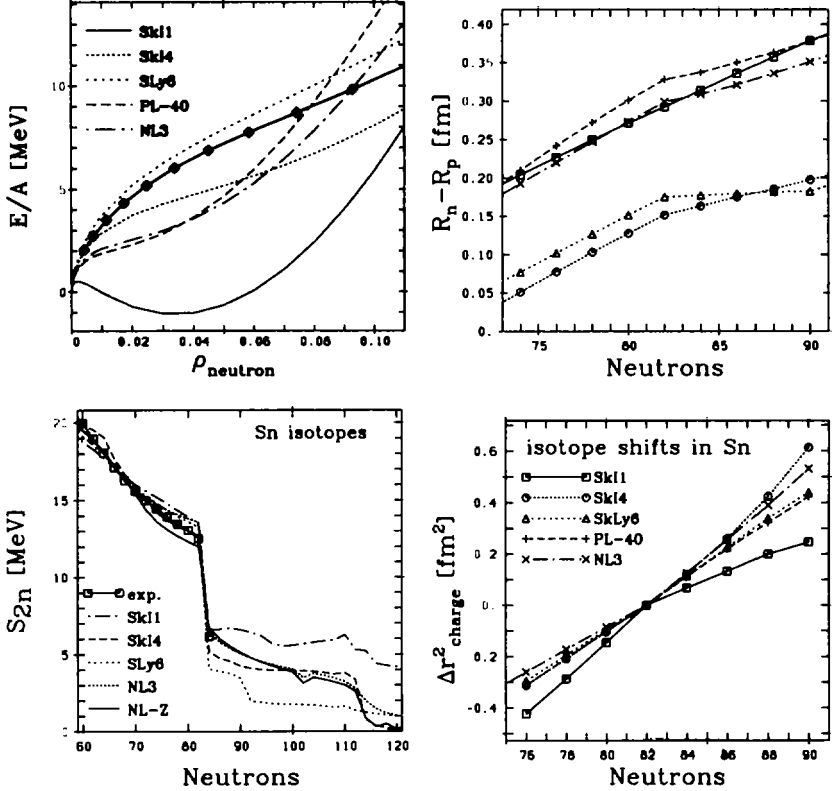
Figure 5: *Trends in neutron rich tin isotopes for a selection of parametrisations as indicated and compared with experimental values where available. Upper left panel: binding energy of pure neutron matter at low densities. Lower left panel: Two neutron separation energies $S_{2n} = E(N-2, Z) - E(N, Z)$. Lower right panel: isotope shifts of charge r.m.s. radii $r^2(N) - r^2(N=82)$. Upper right panel: neutron skin $R_n - R_p$ where R stands for the diffraction radius.*

fig. 6. The left panel compares the single neutron spectra in ^{132}Sn for a variety of forces with experimental information. The critical detail is the sequence of hole
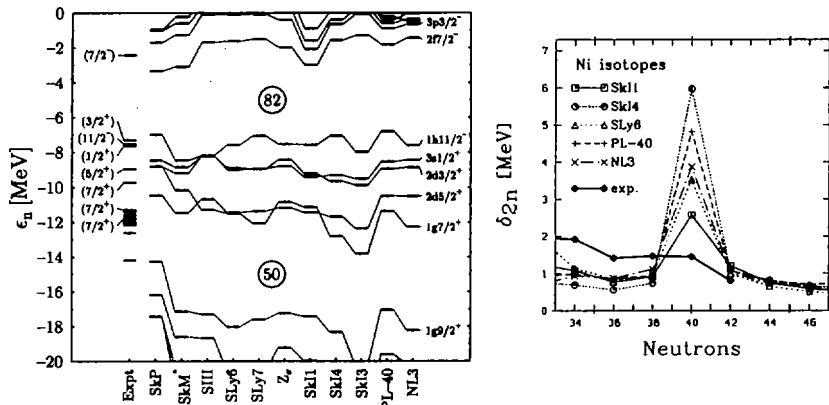
Figure 6: *Left panel: Single neutron spectra in* ^{132}Sn *for a variety of parametrisations as indicated. Right panel:Two neutron shell gap* δ_{2n} *for Ni isotopes in the vicinity of* $N = 40$.

states next to the Fermi surface at $N = 82$. All mean–field models place the $1h_{11/2}$ as first hole state (often with large distance to the next) whereas data show it only as second state. We have tried to refit parametrisations which maintain the same overall quality and fix that problem, but did not succeed. There are indications that this hints to a deeper defect in the energy functional concerning the density dependence of the effective nucleon mass m^*/m.

The right panel of fig. 6 shows the two–neutron shell gap for neutron rich Ni isotopes. All mean–field forces predict a shell closure at $N = 40$ much at variance with the data which have no hint at all for this. We made this observation very recently. Thus we do not yet know whether this defect can be removed with a better refit, or whether it is a resistant feature similar the the wrong neutron level sequence in ^{132}Sn.

4 Conclusions

To conclude: SHF and RMF are found to be formally very similar what two-body interaction, surface terms and kinetic terms is concerned. RMF is superior in that respect that it provide automatic all correct spin-orbit terms which, however, can also be added with comparable performance in SHF models. The major difference lies in the way the density dependence is modelled, and in both case one employs

rather ad hoc ansatzes.

There is a large selection of SHF and RMF forces which perform very well for the bulk properties of stable nuclei with, e.g., an average error in the energy of 0.35%. There are, however, unresolved isotopic and isotonic trends which can be used for further test and improvement of the models, as demonstrated on the connection between isotopic shifts in Pb isotopes and spin-orbit force.

Existing data on superheavy nuclei confine the selection of forces. But there remain some which carry forth the good performance to that regime. Taking these preselected forces and extrapolating further to even heavier nuclei yields dramatically different predictions for superheavy doubly-magic systems. Superheavy nuclei are thus a very demanding probe for mean–field models.

There are huge differences between the forces concerning isovector properties which become manifest for very neutron–rich nuclei. Results on energies, charge and neutron radii of neutron–rich Sn isotopes demonstrate that these data are indeed sensitive probes to distinguish forces.

We have finally sketched two yet unresolved puzzles, the neutron level sequence in ^{132}Sn and the neutron shell closure in ^{68}Ni, where no existing high–quality mean–field parametrisation is able to reproduce the experimental findings.

References

[1] B. D. Serot, J. D. Walecka, Adv. Nucl. Phys. **16**, 1 (1986).

[2] P.-G. Reinhard, Rep. Prog. Phys. **52**, 439 (1989).

[3] P.-G. Reinhard, H. Flocard, Nucl. Phys. **A584**, 467 (1995).

[4] J. Dechargé, D. Gogny, Phys. Rev. C **21**, 1568 (1980).

[5] P. Möller, J. R. Nix, W. D. Myers, W. R. Światecki, At. Data and Nucl. Data Tables **59**, 185 (1995).

[6] E. K. U. Gross, R. M. Dreizler, *Density functional theory*, Springer, 1990.

[7] V. Blum, G. Lauritsch, J. A. Maruhn, P.-G. Reinhard, J. Comp. Phys. **100**, 364 (1992).

[8] B. Friedmann, V. R. Pandharipande, Nucl. Phys. **A361**, 502 (1981).

RELATIVISTIC MEAN FIELD THEORY WITH DENSITY DEPENDENT COUPLING CONSTANTS FOR NUCLEAR MATTER AND FINITE NUCLEI WITH LARGE CHARGE ASYMMETRY*

S. TYPEL and H. H. WOLTER

Sektion Physik, Universität München
Am Coulombwall 1, D-85748 Garching, Germany

Abstract

Nuclear matter and ground state properties for (proton and neutron) semi-closed shell nuclei are described in relativistic mean field theory with coupling constants which depend on the vector density. The parametrization of the density dependence for σ-, ω- and ϱ-mesons is obtained by fitting to properties of nuclear matter and some finite nuclei. The equation of state for symmetric and asymmetric nuclear matter is discussed. Finite nuclei are described in Hartree approximation, including a charge and an improved center-of-mass correction. Pairing is considered in the BCS approximation. Special attention is directed to the predictions for properties at the neutron and proton driplines, e.g. for separation energies, spin-orbit splittings and density distributions.

1 Introduction

Relativistic mean field theory (RMFT) is an elegant and consistent framework with remarkable success in describing nuclear matter and finite nuclei near the valley of stability. The extrapolation of nuclear properties to large charge asymmetry is of considerable interest in nuclear astrophysics, where many reactions occur under extreme conditions of isospin involving exotic nuclides which in most cases cannot be studied directly in the laboratory. RMFT seems to be very well suited for an investigation of nuclei near the neutron and proton driplines. These nuclei display interesting new phenomena like halos due to the weak binding of the outermost nucleons and provide a test of the isovector part of nuclear interaction.

Starting from hadronic field theory with a Lagrangian containing baryon and meson degrees of freedom, RMFT is derived with the classical meson field and the no-sea approximations. [1, 2]. The coupled field equations are

solved self-consistently. In order to obtain a quantitative agreement between theory and experiment one has to go beyond the simple assumption of linear Klein-Gordon or Proca equations for the free meson fields. One possibility is to consider nonlinear self-couplings of the meson fields. This approach was succesfully applied in nonlinear parametrizations, e.g. NL3 [3], with cubic and quartic contributions for the σ-meson in the Lagrangian. But there are problems of stability at high densities and, moreover, the question of the physical foundation arises. A more natural alternative is the introduction of a density dependence in the couplings, which is suggested from Dirac-Brueckner theory of nuclear matter, where the scalar and vector self-energies are density dependent. This can be represented as a density dependence of the couplings in the mean field approximation, which simulates the effective in-medium interaction. The assumption of a density dependence of the couplings in the Lagrangian automatically leads to additional "rearrangement" contributions in the self-energies in the Dirac equation. This mechanism also guarantees thermodynamical consistency of the theory [4].

2 Parametrization

Our Lagrangian includes, besides the fermion fields, isoscalar (σ- and ω-) and isovector (ϱ-) meson fields as well as the electromagnetic field. We omit an isovector scalar (δ-) meson field since its inclusion does not improve our results. In our parametrization the nuclear mass and meson masses are fixed to the usual values of $m_N = 939$ MeV, $m_\sigma = 550$ MeV, $m_\omega = 783$ MeV and $m_\varrho = 763$ MeV. For symmetric nuclear matter we assume a saturation density of 0.153 fm^{-3} and a binding energy per nucleon of -16.247 MeV; additionally, we use a value of 240 MeV for the compressibility [5]. Only the density dependence of the coupling constants was taken to be variable in the fit. For the σ- and ω-meson we choose a restricted Padé-approximation of the density dependence whereas for the ϱ-meson we take an exponential dependence. With the values for nuclear matter given above and the restrictions the actual number of fitting parameters is 4, as compared to 7 for the nonlinear parametrization NL3. The calculated binding energies of the nuclei ^{24}O, ^{40}Ca, ^{48}Ca, ^{56}Ni and ^{208}Pb are fitted to their experimental values.

In Fig. 1 we give the results for the density dependence of the couplings in our parametrization. They show a decrease with increasing baryon density in accordance with the results from Dirac Brueckner theory [6, 7]. The asymmetry energy of nuclear matter results to be 33.39 MeV, very similar to 32.73 MeV in the Finite Range Droplet Model of Ref. [5].
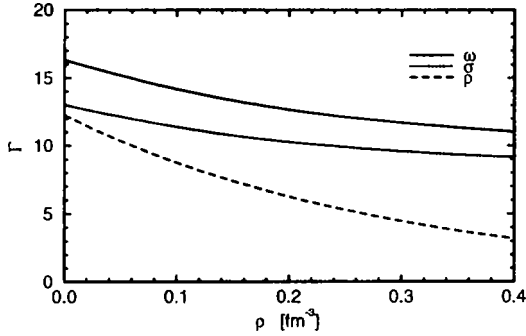
Fig. 1. Density dependence of the baryon-meson couplings.

3 Nuclear Matter

In Fig. 2 we compare the equation of state (EOS) of nuclear matter of our parametrization with the NL3 parametrization of Ref. [3]. For densities below the saturation density for symmetric nuclear matter the EOS in our parametrization looks very similar to the NL3 parametrization. At higher densities, however, the NL3 parametrization shows a much stronger increase, which is a typical effect of constant ω-meson coupling. A larger difference appears in the EOS for neutron matter which is of importance for the description of neutron
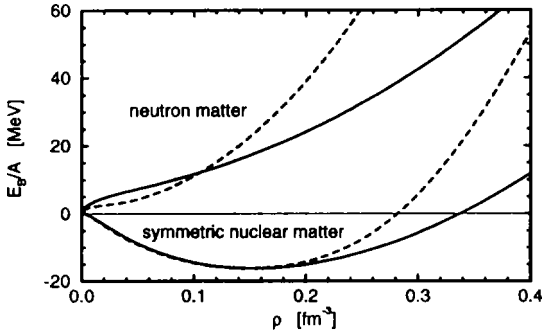
Fig. 2. Equation of state for symmetric nuclear matter and neutron matter with the parametrization NL3 (dashed lines) and the density dependent parametrization (solid lines).

stars and neutron halos in nuclei. The differences in the EOS will also have significant consequences in calculations of heavy ion collisions at high energies with relativistic transport equations, like BUU etc., [8].

4 Finite Nuclei

We describe semi-closed shell nuclei in Hartree approximation assuming spherical symmetry. The center-of-mass correction is calculated nonrelativistically from the ground state wave function and not, as usual, in the harmonic oscillator approximation. We include a charge correction in the vector self energy for the protons by reducing the strength of the electric field by one charge number. Pairing effects in neutron or proton open shells are considered in the BCS approximation with adjusted constants for the pairing gap [3].

The variation of binding energies and of one- and two-nucleon separation energies with the number of nucleons is very well described in our parametrization, even for very light systems (Fig. 3). Charge and neutron radii turn out to be slightly smaller (≈ 0.05 fm) than in the NL3 parametrization, but exhibit the same systematic trends. In a similar way, the spin-orbit splitting decreases with increasing neutron number. They show, like the density distributions, effects of shell structure.
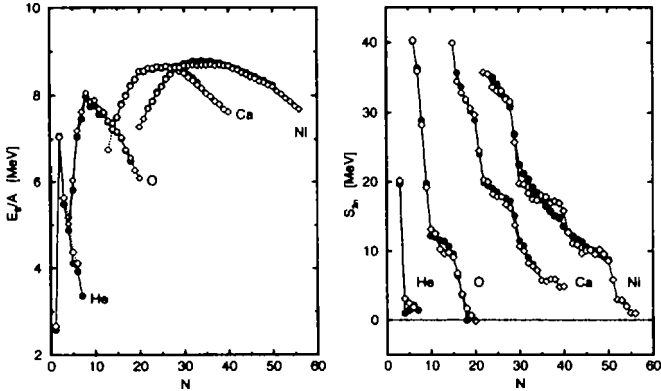
Fig. 3. Binding energies per nucleon (left) and two-neutron separation energies (right) for proton closed shell nuclei with the density dependent parametrization (diamonds) in comparison with data from the 1993 atomic mass evaluation [9] (solid points) as a function of the neutron number.

5 Conclusions and Outlook

Relativistic mean field theory with density dependent couplings is very successful in describing various properties of nuclear matter and finite nuclei, not only for stable nuclei but also for nuclei near neutron and proton driplines. In the latter region a density dependence of the couplings seems to be the preferential approach to a realistic description. Only a small number of parameters is needed.

For an even better fit to experimental data and a more reliable extrapolation to charge asymmetric cases, one can think about various improvements of our calculation. The meson masses can also be varied (useful for a fit to nuclear radii), the functional form of density dependence of the couplings can be changed and the number of nuclei in the fit can be increased. The BCS approximation for the pairing can be replaced by relativistic Hartree-Bogoliubov theory [10], a more appropriate approach for dripline nuclei.

It will be interesting to apply our parametrization also to other cases. Deformed nuclei will be studied in the future [11]. There are already first results on proton scattering on nuclei. Here, a momentum dependence of the couplings has to be introduced in addition.

References

[1] B. D. Serot and J. D. Walecka, Adv. Nucl. Phys. **16** (1986) 1;

[2] Y. K. Gambhir et al., Ann. Phys. (N. Y.) **198** (1990) 132;

[3] G. A. Lalazissis, J. König and P. Ring, Phys. Rev. **C55** (1997) 540;

[4] C. Fuchs, H. Lenske and H. H. Wolter, Phys. Rev. **C52** (1995) 3043;

[5] P. Möller, J. R. Nix, W. D. Myers and W. J. Swiatecki, At. Data Nucl. Data Tables **59** (1995) 185;

[6] B. ter Haar and R. Malfliet, Rhys. Rep. **149** (1987) 207;

[7] R. Brockmann and R. Machleidt, Phys. Rev. **C42** (1990) 1965;

[8] C. Fuchs, T. Gaitanos and H. H. Wolter, Phys. Lett. **B381** (1996) 23;

[9] G. Audi and A. H. Wapstra, Nucl. Phys. **A565** (1993) 1;

[10] W. Pöschl et al., Phys. Rev. Lett. **79** (1997) 3841;

[11] M. L. Cescato, private communication

NEUTRON STARS IN RELATIVISTIC MEAN FIELD THEORY WITH ISOVECTOR SCALAR MESON

S. Kubis, M. Kutschera and S. Stachniewicz
H.Niewodniczański Institute of Nuclear Physics
ul. Radzikowskiego 152, 31-342 Kraków, Poland

Abstract

The equation of state (EOS) of neutron star matter is studied in the relativistic mean field (RMF) theory with the isovector scalar mean field corresponding to the δ-meson [$a_0(980)$]. A range of values of the δ-meson coupling compatible with the Bonn potentials is explored. Parameters of the model in the isovector sector are constrained to fit the nuclear symmetry energy, $E_s \approx 30 MeV$. The quantity most sensitive to the δ-meson cupling is the proton fraction of neutron star matter which increases significantly. The β-stable energy per baryon decreases but the effect is small. The EOS becomes slightly stiffer and the maximum mass of the neutron star increases with increasing δ-meson coupling. The effect is stronger for soft EOS.
PACS: 21.65.+f, 97.60.Jd

1   Nucleon matter in RMF model with the δ-meson

The RMF model [1] of nuclear matter does not include the contribution due to δ-meson although generally the density to which this field can couple does not vanish, $< \bar{\psi}\tau_3\psi > \neq 0$. Contribution of the δ-meson field is not expected to be important for finite nuclei, whose isospin asymmetry is small, as the δ-meson mean field vanishes in symmetric nuclear matter. However, for strongly isospin-asymmetric matter in neutron stars presence of the δ-field can influence properties of dense matter. In Ref.[2] the RMF model was generalized to include the contribution due to δ-meson. Here we investigate consequences of such a generalized RMF theory for neutron stars.

We assume that all the meson fields have Yukawa couplings to nucleons. The interaction lagrangian reads

$$L_{int} = g_\sigma \sigma \bar{\psi}\psi - g_\omega \omega_\mu \bar{\psi}\gamma^\mu\psi - \frac{1}{2}g_\rho \vec{\rho}_\mu \bar{\psi}\gamma^\mu\vec{\tau}\psi + g_\delta \vec{\delta}\bar{\psi}\vec{\tau}\psi. \tag{1}$$

Here $\vec{\delta}$ is the isovector scalar field of the δ-meson. The free-field lagrangians for ψ, σ, ω, and ρ fields are the same as in Ref.[1]. For the δ-field we use the lagrangian

$$L_\delta = \frac{1}{2}\partial_\mu\vec{\delta}\partial^\mu\vec{\delta} - \frac{1}{2}m_\delta^2\vec{\delta}^2. \tag{2}$$

For the σ-field we adopt the potential energy term of Boguta and Bodmer [3],

$$U(\sigma) = \frac{1}{3}bm\sigma^3 + \frac{1}{4}c\sigma^4, \tag{3}$$

where m is the bare nucleon mass.

The ground state values of meson fields are determined by proton and neutron densities. The presence of δ-field splits effective masses of proton and neutron , $m_P = m - g_\sigma\bar{\sigma} - g_\delta\bar{\delta}^{(3)}$, and $m_N = m - g_\sigma\bar{\sigma} + g_\delta\bar{\delta}^{(3)}$.

The energy density of a uniform nucleon matter reads

$$\epsilon = \frac{2}{(2\pi)^3}(\int^{k_P} d^3k\sqrt{k^2+m_P^2} + \int^{k_N} d^3k\sqrt{k^2+m_N^2}) + \frac{1}{2}C_\omega^2 n_B^2 +$$

$$+\frac{1}{2}\frac{1}{C_\sigma^2}[m - \frac{m_P+m_N}{2}]^2 + U(\bar{\sigma}) + \frac{1}{8}C_\rho^2(2x-1)^2 n_B^2 + \frac{1}{8}\frac{1}{C_\delta^2}(m_N-m_P)^2. \tag{9}$$

In the spirit of the RMF theory [1] parameters of the model are fit to reproduce empirical parameters of nuclear matter. In the isoscalar sector, $C_\sigma^2 \equiv g_\sigma^2/m_\sigma^2, C_\omega^2 \equiv g_\omega^2/m_\omega^2, \bar{b} \equiv b/g_\sigma^3$, and $\bar{c} \equiv c/g_\sigma^3$, are adjusted to fit the saturation properties of symmetric nuclear matter, the saturation density $n_0 = 0.145 fm^{-3}$, the binding energy $w_0 = -16 MeV$ per nucleon, and the compressibility modulus $K_V \approx 280 MeV$. The fourth parameter, e.g. $\bar{c}$, can be used to measure stiffness of the equation of state of symmetric nuclear matter.

The coupling parameters, $C_\rho^2 \equiv g_\rho^2/m_\rho^2$, and $C_\delta^2 \equiv g_\delta^2/m_\delta^2$, of the isovector sector determine nuclear symmetry energy,

$$E_s = \frac{1}{8}C_\rho^2 n_0 + \frac{k_0^2}{6\sqrt{k_0^2+m_0^2}} - C_\delta^2\frac{m_0^2 n_0}{2(k_0^2+m_0^2)(1+C_\delta^2 A(k_0,m_0))}, \tag{5}$$

where

$$A(k_0,m_0) = \frac{4}{(2\pi)^3}\int_0^{k_0}\frac{d^3p p^2}{(p^2+m_0^2)^{3/2}} \tag{6}$$

and then these couplings are constrained to obtain $E_s = 31 \pm 4 MeV$ [4]. This requirement is very important as the δ-field contribution is strongly attractive. As shown in Ref.[2] the δ-meson coupling provides a negative contribution to the symmetry energy.

2   EOS of neutron star matter

In the following we shall mainly use two sets of coupling parameters which reproduce the saturation properties but differ at higher densities. Corresponding EOS's are referred to as soft and stiff. The soft EOS is specified by the parameters $C_\sigma^2 = 1.582 fm^2, C_\omega^2 = 1.019 fm^2, \bar{b} = -0.7188$, and $\bar{c} = 6.563$. For the stiff EOS the parameters are $C_\sigma^2 = 11.25 fm^2, C_\omega^2 = 4.395 fm^2, \bar{b} = 0.003825$, and $\bar{c} = 3.5 \times 10^{-6}$.

The parameter $\bar{c}$ for the soft EOS has the highest allowed value, $\bar{c} = 6.563$. The maximum neutron star mass corresponding to this EOS is about $1.44 M_\odot$. This is the mass of the heavier neutron star in the binary pulsar PSR B1913+16 [7], which has the largest precisely measured value of a neutron star mass. Hence this EOS is the softest one still compatible with measured neutron star masses.

The coupling constant g_δ of δ-nucleon interaction is a parameter in OBE fits of nucleon scattering data. Its value is not, however, strongly constrained. Here we adopt a range of δ-meson coupling compatible with the Bonn potentials [5], $C_\delta^2 \leq 4.4 fm^2$. The maximum value of C_δ^2 we use exceeds the one corresponding to the Bonn potential C [5] which is $C_\delta^2 = 2.6 fm^2$. For a given value of C_δ^2 we obtain the ρ-meson coupling C_ρ^2 from Eq.(5).

To obtain the EOS of neutron star matter we first calculate the proton fraction x of β-stable neutron star matter shown in Fig.1 One can notice that for both EOS's the proton fraction is substantially larger for indicated values of the δ-meson coupling, C_δ^2, than for vanishing coupling, $C_\delta^2 = 0$. It exceeds the critical value for the direct URCA $x_{URCA} \approx 0.11$, already at densities less than twice the nuclear saturation density.

The energy density of the β-stable neutron star matter is obtained as a sum of nucleon and lepton contributions and is shown in Fig.2 for soft and stiff EOS. As one can see in Fig.2 the energy per particle increases with δ-coupling C_δ^2. The effect is stronger for the stiff EOS.

It is interesting to note that actually the nucleon contribution to the energy per baryon at a given n_B decreases with increasing C_δ^2 for both EOS's. The reason is the high proton fraction. It is the lepton contribution which makes the total energy per particle higher.
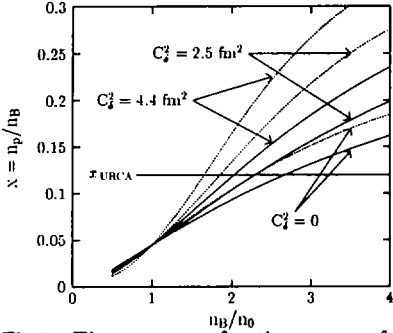
Fig.1 The proton fraction, x, of the neutron star matter for the soft EOS (solid curves) and the stiff EOS (dashed curves), for indicated values of the δ-meson coupling, C_δ^2.
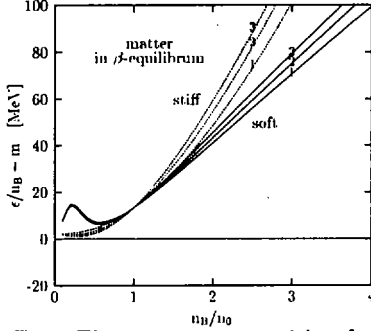
Fig.2 The energy per particle of the neutron star matter for the soft EOS and the stiff EOS. Curves labeled 1, 2, and 3 correspond, respectively, to $C_\delta^2 = 0$, $C_\delta^2 = 2.5fm^2$, and $C_\delta^2 = 4.4fm^2$.

To gauge the influence of the δ-meson coupling on the EOS we have calculated models of neutron stars. The high density EOS calculated in the previous section was matched with the low density EOS due to Baym, Bethe, and Pethick [8] by constructing a proper phase transition. By making this construction we have found interface between crust matter, described by the EOS of Ref.[8], and liquid core matter, described by our RMF theory.

In Fig.3 density profiles are shown for the canonical neutron star mass $1.4M_\odot$. For the soft EOS generally the radii are smaller than for the stiff EOS. The effect of the δ-meson contribution is more profound in case of the soft EOS. The radius increases from $R \approx 10.6km$, for $C_\delta^2 = 0$, to $R \approx 11.9km$, for $C_\delta^2 = 2.5fm^2$, and to $R \approx 12.5km$, for $C_\delta^2 = 4.4fm^2$. For the stiff EOS the radius is $R \approx 13.8km$ for $C_\delta^2 = 0$, $R \approx 14.2km$ for $C_\delta^2 = 2.5fm^2$, and $R \approx 14.6km$, for $C_\delta^2 = 4.4fm^2$. The central density decreases with increasing δ-coupling. In case of the soft EOS, the central density is $n_c \approx 8.5n_0$, $n_c \approx 5.4n_0$ and $n_c \approx 4.4n_0$ for, respectively, $C_\delta^2 = 0$, $C_\delta^2 = 2.5fm^2$ and $C_\delta^2 = 4.4fm^2$. For the stiff EOS corresponding central densities are $n_c \approx 2.3n_0$, $n_c \approx 2.1n_0$ and $n_c \approx 1.9n_0$, respectively.

The neutron star mass as a function of central density is displayed in Fig.4 for the soft and the stiff EOS. We also show results for the intermediate EOS, with parameters given in Sect.2. Maximum mass increases slightly with C_δ^2. The δ-field plays a more important role for the soft EOS. The maximum neutron star mass is $M_{max} = 1.403M_\odot$ for $C_\delta^2 = 0$. Since this value is less than the mass of the neutron star in the binary pulsar PSR B1913+16, which is $1.44M_\odot$,

this EOS is too soft to be realistic. However, with inclusion of the δ-field contribution the maximum neutron star mass increases to $M_{max} = 1.452 M_\odot$, for $C_\delta^2 = 2.5 fm^2$, and to $M_{max} = 1.48 M_\odot$, for $C_\delta^2 = 4.4 fm^2$. Inclusion of the δ-meson with $C_\delta^2 = 2.5 fm^2$ results in about 4% increase of M_{max} that makes the soft EOS astrophysically acceptable.
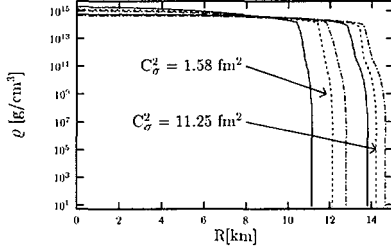
Fig.3 The density profile of $1.4M_\odot$ neutron star for soft and stiff EOS. Solid, dashed and dotted-dashed lines correspond, respectively, to $C_\delta^2 = 0$, $C_\delta^2 = 2.5 fm^2$, and $C_\delta^2 = 4.4 fm^2$.
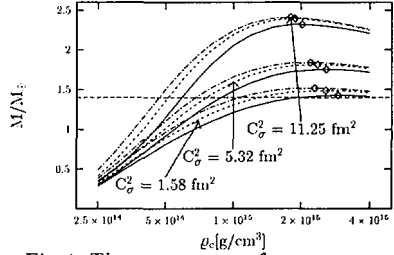
Fig.4 The spectrum of neutron star masses for the soft EOS and the stiff EOS. Also, results for the intermediate EOS are shown. Solid, dashed and dotted-dashed lines correspond, respectively, to $C_\delta^2 = 0$, $C_\delta^2 = 2.5 fm^2$, and $C_\delta^2 = 4.4 fm^2$.

For the stiff EOS the maximum neutron star mass is $M_{max} = 2.275 M_\odot$, $M_{max} = 2.309 M_\odot$ and $M_{max} = 2.313 M_\odot$ for, respectively, $C_\delta^2 = 0$, $C_\delta^2 = 2.5 fm^2$ and $C_\delta^2 = 4.4 fm^2$. In this case M_{max} increases by $\sim 1.5\%$ for $C_\delta^2 = 2.5 fm^2$. Central densities of the above maximum mass neutron stars are, respectively, $n_c \approx 6.2 n_0$, $n_c \approx 5.9 n_0$ and $n_c \approx 5.7 n0$.

References

[1] B. D. Serot and J. D. Walecka, Adv. Nucl. Phys. **16** (1986) 1.

[2] S. Kubis and M. Kutschera, Phys.Lett.B **399** (1997) 191.

[3] J. Boguta and A. Bodmer, Nucl. Phys. **A292** (1977) 413.

[4] W. D. Myers and W. D. Swiatecki, Ann. Phys. **84** (1973) 186;

J. M. Pearson, Y. Aboussir, A. K. Dutta, R. C. Nayak, M. Farine, and F. Tondeur,

Nucl. Phys. **A528** (1991) 1;

P. Möller and J. R. Nix, At. Data and Nucl. Data Tables **39** (1988) 219;

P. Möller, W. D. Myers, W. J. Swiatecki, and J. Treiner, At. Data and Nucl. Data

Tables **39** (1988) 225;

W. D. Myers, W. J. Swiatecki, T. Kodama, L. J. El-Jaick, and E. R. Hilf, Phys. Rev. **C15** (1977) 2032.

[5] R. Machleidt, Adv. Nucl. **Phys. 19** (1989) 189.

[6] M. Kutschera, astro-ph/9612143, in "Solar Astrophysics, Structure of Neutron Stars,

Gamma Flashes. Meeting of the Commission for Astrophysics of the Polish Academy

of Arts and Sciences", ed. K. Grotowski, Cracow, 1997.

[7] J. H. Taylor and J. M. Weisberg, Astrophys. J. **345** (1989) 434.

[8] G. Baym, H. A. Bethe and C. J. Pethick, Nucl. Phys. **A175** (1971) 225.

MATTER COMPOSITION AT HIGH DENSITY BY EFFECTIVE SCALED LAGRANGIAN

CHANG HO HYUN and DONG-PIL MIN

Department of Physics
Seoul National University, Seoul 151-742, Korea

Abstract

We investigate the matter composition at around the neutron star densities with a model lagrangian satisfying Brown-Rho scaling law. We calculate the neutron star properties such as maximum mass, radius, hyperon compositions and central density. We compare our results with those of Walecka model [1].

1   The model

Brown-Rho (BR in short) scaled lagrangian [2] with the inclusion of the scalar field ϕ and the vector mesons ω and ρ reads

$$
\begin{aligned}
\mathcal{L}_{BR} &= \sum_B \bar{\psi}_B [\gamma_\mu (i\partial^\mu - g^*_{\omega B}(n)\omega^\mu - g^*_{\rho B}(n)\vec{\rho}^\mu \cdot \vec{\tau}) - M^*_B(n) + g_{\sigma B}\phi]\psi_B \\
&+ \frac{1}{2}[(\partial\phi)^2 - m^{*2}_s(n)\phi^2] - \frac{1}{4}(F^2_\omega + F^2_\rho) + \frac{1}{2}m^{*2}_\omega(n)\omega^2 + \frac{1}{2}m^{*2}_\rho(n)\rho^2 (1)
\end{aligned}
$$

with those marked with asterisks assumed to follow BR scaling and n respresents density. B represents all the baryon species. BR scaling implies that in the dense matter such physical constants as masses of baryon and meson as well as the pion decay contant subdue the density-dependent scaling, the characteristic function of which scaling can simply be represented by the "universal" function $\Phi(n, x)$ as

$$
\Phi(n, x) \equiv \frac{1}{1 + n/n_0 x} \qquad (2)
$$

where n_0 represents nuclear matter density. The scaling parameter "x" in the above equation is 0.28 for m^*_s, m^*_ω, m^*_ρ, M^*_N and 0.31 for $g^*_{\omega N}$ and $g^*_{\rho N}$ where N represents nucleons. Note that although the functional shapes for all scaling are taken to be of identical form with different scaling parameter, the scaling of the coupling constants is simply taken to follow the same form of Eq.(2). And we do not scale the scalar field coupling $g_{\sigma B}$ [2].

The energy density is the same with the Walecka model and the pressure is

$$
\begin{aligned}
P =\ & \frac{1}{2}m_\omega^{*2}\omega_0^2 + \frac{1}{2}m_\rho^{*2}b_0^2 - \frac{1}{2}m_s^{*2}\phi^2 - u\,y\,m_s^{*2}\phi^2\Phi(n,y) - u\,y\,\Phi(n,y)\sum_B n_B^s M_B^* \\
& +u\,\omega_0^2\left(y\Phi(n,y) - z\Phi(n,z)\right)m_\omega^{*2} + u\,b_0^2\left(y\Phi(n,y) - z\Phi(n,z)\right)m_\rho^{*2} \\
& +E_F^* - \frac{1}{\pi^2}\sum_B \int_0^{k_{FB}} dk k^2 E_B^*
\end{aligned}
\tag{3}
$$

where $u \equiv n/n_0$, $E_F^* = \sum_B E_{FB}^*$, $E_{FB}^* = \sqrt{k_{FB}^2 + m_B^{*2}}$ and $E_B^* = \sqrt{k_B^2 + m_B^{*2}}$.

2 Results for SU(2)

Fig.1 shows matter compositions resulting from the two models. Compared to a type Walecka model (W model) [1], muon appears at slightly higher density and fractions of proton and electron are almost the same with the BR model. Fig.2 compares energy density between two models. Up to $1.5\rho_0$, pressure is not so much different but as density goes high, the difference becomes drastic. At high density, major contributor to pressure is omega meson. In the BR model, $g_{\omega N}$ is about 1.8 times of that of W model. Highly stiff equation of state (EOS) in BR model stems from this large value of $g_{\omega N}$. Two model are compared in the Table 1.

model	$g_{\sigma N}$	$g_{\omega N}$	$g_{\rho N}$	m_s(MeV)	Scaled objects	σ^3 term	σ^4 term
W	7.56	8.59	8.43	500	Nothing	Yes	Yes
BR	5.3	15.2	5.1	700	$m_s, m_\omega, m_\rho, M_N$ $g_{\omega N}, g_{\rho N}$	No	No

Table 1: Differences between W and BR.

We solved Tolman-Oppenheimer-Volkov(TOV) equtions to obtain the maximum mass of a neutron star as a function of central density (Fig. 5). In the BR model maximum mass of a star increases monotonically up to $u_c = 3.8$. At $u_c = 3.8$ it reaches to 2.7 $M_\odot$. On the contrary, there is a maximum mass configuration in the W model at $u_c = 7.8$ with the mass 1.979 $M_\odot$ and radius 8.74 km. To satisfy the observation, the BR model should incorporate the mechanism to constrain the increase of the central density of neutron star by, for instance, the transition to the quark-gluon plasma.
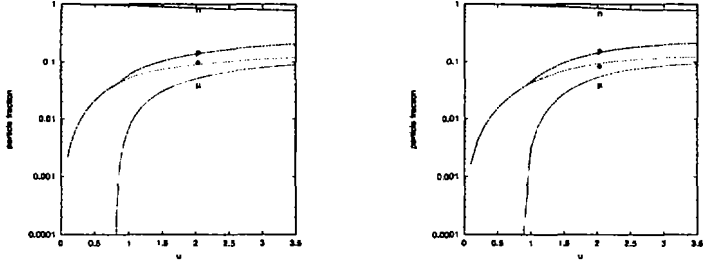
Figure 1: Left panel shows the matter composition of W model prediction and right that of BR model.
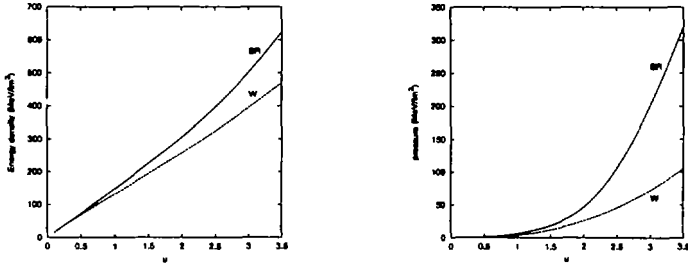
Figure 2: Left for energy density and right for pressure. BR model shows very stiff EOS compared to W model.

3 Extension to SU(3)

Here we make a trial to extend the BR model to baryon octet. (hereafter we call it BR-H model.)

For BR-H model we impose the following assumptions. First, we assume quark scaling such that only u and d quarks undergo the scaling and s quark is blind to it. Second, as for coupling constants of hyperons, we use the same ratios given in Ref. [1]. Summary of coupling constants is given in the Table 2 and scaling law in the Table 3.

Fig. 3 shows matter composition in each model. In the W model, the first hyperon Σ^- appears at around $u \sim 2$. Depending on the adopted coupling constants, this density varies $2 \sim 2.5$. In the BR-H model, Σ^- starts to exist already at $u \sim 1.1$. We can understand this early appearance of hyperons as

follows. Onset of hyperon appearance is governed by the chemical equilibrium,

$$\mu_{\Sigma^-} = \mu_n + \mu_e. \tag{4}$$

At the birth of Σ^-, its Fermi momentum is zero, and the above equation becomes

$$M_{\Sigma^-} = E_{Fn} + (g_{\omega N} - g_{\omega \Sigma^-})\omega_0 - (g_{\rho N} - 2g_{\rho \Sigma^-})\, b_0 + k_{Fe} + g_{\sigma \Sigma^-}\phi. \tag{5}$$

Let us focus on the role of omega meson term and fix the contributions from all other terms for simplicity. We assume that the ratio $g_{\omega \Sigma^-}$ to $g_{\omega N}$ is fixed to 0.659. Since $g_{\omega N}$ in the BR model is larger than that of W model, the above equality is met for smaller value of ω_0 in the BR model than the W model. ω_0 value is increasing function of density. Therefore the above equality is satisfied at lower density in the BR model than the W model and Σ^- appears ealier in the BR model than the W model.
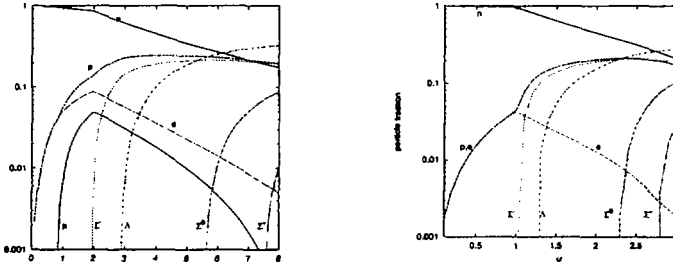
Figure 3: Left for SU(3) W model prediction of matter composition and right for BR-H model prediction.

Energy density and pressure are compared in Fig. 4. TOV equations are solved. For SU(3) W model the result is $M_{max} \sim 1.560 M_\odot$ at $\rho_c \sim 8.8\rho_0$ with the radius 8.59 km which is 0.15 km smaller than the SU(2) W model neutron star. Since the difference is very small, we may not discern the inner composition of matter by measuring the radii of neutron stars. However

model	$g_{\sigma N}$	$g_{\omega N}$	$g_{\rho N}$	$x_{\sigma H}, x_{\rho H}$	$x_{\omega H}$
W	7.56	8.59	8.43	0.6	0.659
BR-H	5.3	15.2	5.1	0.6	0.659

Table 2: Coupling constants. $x_{\alpha H} \equiv g_{\alpha H}/g_{\alpha N}$.

Mass	M_N	m_Λ	m_{Σ^+}	m_{Σ^0}	m_{Σ^-}	m_{Ξ^0}	m_{Ξ^-}
scaling parameter	0.28	0.19	0.19	0.19	0.19	0.09	0.09
Coupling	$g_{\omega N}$	$g_{\omega\Lambda}$	$g_{\omega\Sigma^+}$	$g_{\omega\Sigma^0}$	$g_{\omega\Sigma^-}$	$g_{\omega\Xi^0}$	$g_{\omega\Xi^-}$
constants	$g_{\rho N}$	$g_{\rho\Lambda}$	$g_{\rho\Sigma^+}$	$g_{\rho\Sigma^0}$	$g_{\rho\Sigma^-}$	$g_{\rho\Xi^0}$	$g_{\rho\Xi^-}$
scaling parameter	0.31	0.20	0.20	0.20	0.20	0.10	0.10

Table 3: Scaling laws in the BR-H model. Numbers in the table are scaling parameter "x" in the definition of $\Phi(n,x)$. In the BR-H model, for $S=1$ hyperons we use two thirds of nucleon scaling parameters and one third of nucleon scaling parameters for $S=2$ hyperons.
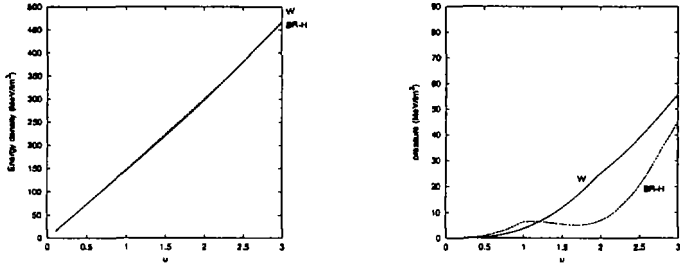
Figure 4: Comparisons of energy density(left) and pressure(right).

since the existence of hyperons affects the cooling mechanism of neutron star, observation of surface temperature of neutron stars may give some light on the matter composition at high density. For BR-H model, maximum mass increases monotonically up to $u = 3.5$ (Fig. 5).

4   Discussion

We investigate high density matter properties with an effective lagrangian satisfying BR scaling law. BR model produces nulcear properties very well at saturation density with a few parameters. However the model predicts a stiffer EOS than the W model result. The origin of this stiffness is that $g_{\omega N}$ value adopted in the BR model is 1.8 times larger than W model. Even though $g_{\omega N}^*$ decreases as density increases and it becomes the same value as the W model at density $u \sim 2.5$, the ratio

$$\frac{g_{\omega N}}{m_\omega} \simeq \frac{g_{\omega N}^*}{m_\omega^*}, \tag{6}$$
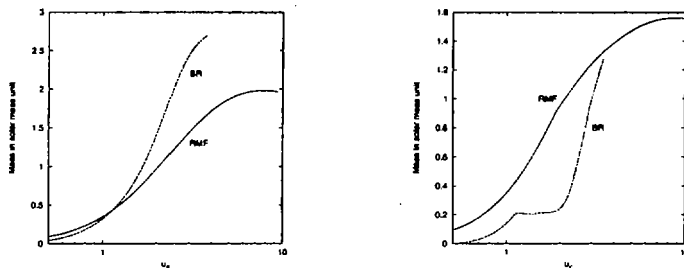
Figure 5: Maximum mass of a neutron star as a function of central density. Left panel is SU(2) prediction and right SU(3).

which is presumed in the BR model up to the density we consider. Hence, although $g_{\omega N}^*$ itself decreases with respect to increasing density, the effect of decreasing $g_{\omega N}^*$ is not manifested in the EOS since the ω_0 contribution to pressure enters in the form

$$\frac{1}{2}m_\omega^{*2}\omega_0^2 = \frac{1}{2}\left(\frac{g_{\omega N}^*}{m^*}\right)^2 n^2. \tag{7}$$

Secondly, $g_{\omega N}$ is not so much high compared to the values in the model suggested by Furnstal et al. (FTS) [3] where $g_{\omega N} = 12 \sim 13$. In the FTS model, however there are higher order terms of ω_0 which play the role of decreasing ω_0 contribution at high density. In order to have a softer EOS in the BR model with large $g_{\omega N}$, $g_{\omega N}^*$ should decrease faster than the present BR model. Investigation of density dependence of $g_{\omega N}^*$ should be done from a systematic theory, e.g. chiral perturbation theory in the future.

References

[1] N. K. Glendenning and S. A. Moszkowski, Phys. Rev. Lett. **67**, 2414 (1991)

[2] C. Song, G. E. Brown, D.-P. Min and M. Rho, preprint, hep-ph/9705255

[3] R. J. Furnstal, H.-B. Tang and B. D. Serot, Phys. Rev. **C 52**, 1368 (1995)
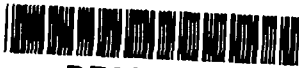
NUCLEON EFFECTIVE MASSES IN
FIELD THEORIES OF DENSE MATTER

C.-H. LEE, S. REDDY and M. PRAKASH

Department of Physics & Astronomy
SUNY at Stony Brook, Stony Brook, NY 11794-3800, USA

Abstract
We point out some generic trends of effective masses in commonly used
field-theoretical descriptions of stellar matter in which several species of
strongly interacting particles of dissimilar masses may be present.

In Refs. [1, 2], it was noted that, in matter containing hyperons, the nucleon
effective mass turned *negative* at a finite baryon density in the field-theoretical
models explored there. This occured for all but a special choice of the strong
interaction couplings [1]. Here, we identify some models in which the above
feature persists at the mean field level and those in which it is absent.

The most commonly used Lagrangians [3-6] fall into three basic categories:

$$
\begin{aligned}
\mathcal{L}_{\mathrm{I}} &= \mathcal{L}_{kin}^{B} - \left(1 - \frac{g_{\sigma B}\sigma}{m_B}\right)m_B\bar{\Psi}_B\Psi_B + \mathcal{L}(\sigma,\omega,\rho) \\
\mathcal{L}_{\mathrm{II}} &= \left(1 + \frac{g_{\sigma B}\sigma}{m_B}\right)\mathcal{L}_{kin}^{B} - m_B\bar{\Psi}_B\Psi_B + \mathcal{L}(\sigma,\omega,\rho) \\
\mathcal{L}_{\mathrm{III}} &= \left(1 + \frac{g_{\sigma B}\sigma}{2m_B}\right)\mathcal{L}_{kin}^{B} - \left(1 - \frac{g_{\sigma B}\sigma}{2m_B}\right)m_B\bar{\Psi}_B\Psi_B + \mathcal{L}(\sigma,\omega,\rho).
\end{aligned}
\tag{1}
$$

Here, m_B is the vacuum baryon mass and $g_{\sigma B}$ is the scalar σ-meson coupling
to the baryon B. The baryon kinetic and the meson Lagrangians are

$$
\begin{aligned}
\mathcal{L}_{kin}^{B} &= \bar{\Psi}_B(i\gamma_\mu\partial^\mu - g_{\omega B}\gamma_\mu\omega^\mu - g_{\rho B}\gamma_\mu\mathbf{t}\cdot\rho^\mu)\Psi_B \\
\mathcal{L}(\sigma,\omega,\rho) &= \frac{1}{2}\partial_\mu\sigma\partial^\mu\sigma - \frac{1}{4}\omega_{\mu\nu}\omega^{\mu\nu} - \frac{1}{4}\rho_{\mu\nu}\cdot\rho^{\mu\nu} \\
&\quad - \frac{1}{2}m_\sigma^2\sigma^2 + \frac{1}{2}m_\omega^2\omega_\mu\omega^\mu + \frac{1}{2}m_\rho^2\rho_\mu\cdot\rho^\mu + U(\sigma,\omega,\rho).
\end{aligned}
\tag{2}
$$

The ω and ρ meson fields are denoted by ω_μ and ρ_μ, and $\mathbf{t}$ denotes the isospin
operator which acts on the baryons. The meson self-interactions are in

$$
\begin{aligned}
U(\sigma,\omega,\rho) &= \frac{\bar{\kappa}}{6}(g_{\sigma N}\sigma)^3 + \frac{\bar{\lambda}}{24}(g_{\sigma N}\sigma)^4 + \bar{\alpha}m(g_{\sigma N}\sigma)\omega_\mu\omega^\mu \\
&\quad - \frac{\zeta}{24}g_{\omega N}^4(\omega_\mu\omega^\mu)^2 - \frac{\xi}{24}g_{\rho N}^4(\rho_\mu\cdot\rho^\mu)^2 + \cdots.
\end{aligned}
\tag{3}
$$

Note that additional nonlinear terms may be introduced in $U(\sigma, \omega, \rho)$, but we concentrate on terms up to quartic order, since even at this level, the number of independent well determined bulk matter properties available to fix the various couplings are limited. After redefining the baryon fields [5], $(1 + g_{\sigma B}/cm)^{1/2}\Psi_B \longrightarrow \Psi_B$ ($c = 1$ for $\mathcal{L}_{II}$ and $c = 2$ for $\mathcal{L}_{III}$), the Dirac baryon effective masses become

$$\frac{m_B^*}{m_B} = \begin{cases} (1 - g_{\sigma B}\sigma/m_B) & \text{for I} \\ (1 + g_{\sigma B}\sigma/m_B)^{-1} & \text{for II} \\ (1 - g_{\sigma B}\sigma/2m_B)(1 + g_{\sigma B}\sigma/2m_B)^{-1} & \text{for III}, \end{cases} \tag{4}$$

which highlights the differences arising from the different σ-couplings. At the mean field level, the corresponding σ-field equations are

$$\frac{\Phi}{C_s^2} + \frac{\partial U}{\partial \Phi} = \begin{cases} \sum_B x_{\sigma B} n_B^s & \text{for I} \\ \sum_B x_{\sigma B} n_B^s (m_B^*/m_B)^2 & \text{for II} \\ \sum_B x_{\sigma B} n_B^s (1 + g_{\sigma B}\sigma/2m_B)^{-2} & \text{for III}, \end{cases} \tag{5}$$

where $\Phi = g_{\sigma N}\langle\sigma\rangle$, $C_s^2 = g_{\sigma N}^2/m_\sigma^2$, and $x_{\sigma B} = g_{\sigma B}/g_{\sigma N}$. The baryon scalar density is

$$n_B^s = \frac{1}{\pi^2} \int_0^{k_{F_B}} dk\ k^2 \left(m_B^*/\sqrt{k^2 + m_B^{*\,2}} \right). \tag{6}$$

The vector fields satisfy

$$W/C_\omega^2 + \zeta W^3/6 - 2\bar{a}M\Phi W = n \sum_B x_{\omega B} Y_B$$
$$R/C_\rho^2 + \xi R^3/6 = n \sum_B x_{\rho B} t_{3B} Y_B, \tag{7}$$

where $W = g_{\omega N}\langle\omega^0\rangle$, $R = g_{\rho N}\langle\rho^0\rangle$, $C_\omega^2 = g_{\omega N}^2/m_\omega^2$, $C_\rho^2 = g_{\rho N}^2/m_\rho^2$, $x_{\omega B} = g_{\omega B}/g_{\omega N}$, $x_{\rho B} = g_{\rho B}/g_{\rho N}$, $Y_B = n_B/n$, and $n = \sum_B n_B$.

At the mean-field level, the thermodynamic potentials corresponding to $\mathcal{L}_I$ through $\mathcal{L}_{III}$ are straightforward to obtain [3-6]. In stellar matter, the conditions of charge neutrality and beta-equilibrium must also be met. The nucleon couplings are usually chosen to reproduce the binding energy (~ 16 MeV), the equilibrium density ($n_0 = 0.16 \pm 0.1$ fm^{-3}), compression modulus (200 MeV $< K_0 <$ 300 MeV), $m_n^*(n_0)/m_n = (0.6 - 0.7)$ of infinite nuclear matter, and the symmetry energy ($\sim 30 - 35$ MeV). In the simplest version, the spin-orbit splitting in nuclei favors $m_n^*(n_0)/m_n \sim 0.6$.
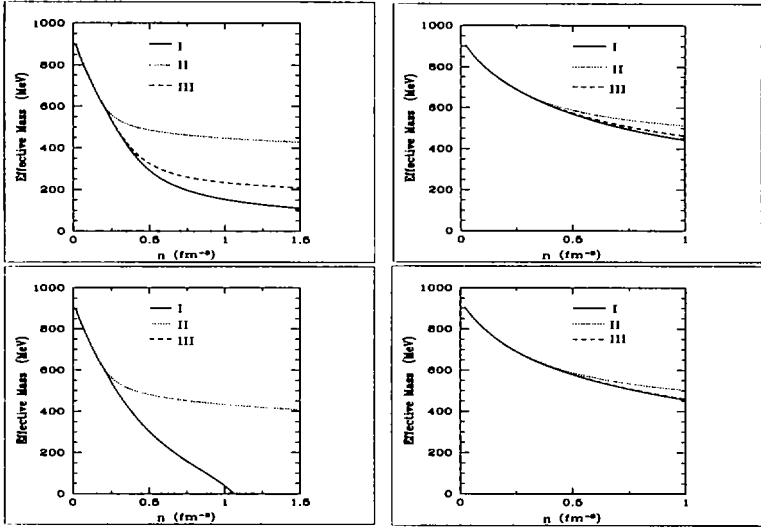
Figure 1: Nucleon effective masses with (lower panels) and without (upper panels) hyperons. For the lower (upper) panels, $m_n^\star(n_0/n)/m = 0.7(0.8)$. Results in the left panels are with $\zeta = \xi = \bar{\alpha} = 0$, and those in the right panels are with $\zeta = 0.06$, $\xi = 1.5$, and $\bar{\alpha} = 0$.

When the set of baryons B is extended to include the Λ, Σ, and Ξ hyperons, hyperon-meson couplings are needed for which some guidance from hypernuclear data exists. In nuclear matter at saturation, the lowest Λ level is bound by 18 MeV. This establishes a correlation between the σ and ω couplings [7]. Fits to Λ-hypernuclear levels constrain the range over which these couplings may be varied to obtain satisfactory neutron star properties. The ρ-coupling is also of similar magnitude. The Σ^- atom analysis sheds light on the Σ^- couplings, which are of similar magnitude to those of the Λ. Very little is known about the Ξ couplings from data; hence, these couplings are usually taken to be of similar magnitude to those of the Λ and Σ^-.

In Fig. 1, we show the nucleon effective masses with (lower panels) and without hyperons (upper panels). Note that for models I and III with $U(\sigma, \omega, \rho) = 0$, small differences in $m_n^\star(n_0)$ are sufficient to drive $m_n^\star$ negative at high density. A similar behavior is observed for small changes in the poorly known hyperon couplings (see Ref. [1]). Non-linear scalar couplings ($U(\sigma, \omega, \rho) \neq 0$))

Model	$U(\sigma,\omega,\rho)$	n_0	$n/n_0 \gg 1$
I	0	×	×
II	0	×	OK
III	0	OK	×
I	$\neq 0$	OK	×
II	$\neq 0$	OK	OK
III	$\neq 0$	OK	×

Table 1: Status of effective field-theoretical models. The fourth column reflects whether or not the nucleon effective mass turns negative at high density.

tend to reduce the differences in $m_n^\star$ among the models (right panels). Models I and III, however, lead to negative $m_n^\star$ albeit at unphysically large densities.

Eq. (4) cleary shows that $m_B^\star/m_B$ will turn negative if, at any density, $g_{\sigma B}\sigma/m_B \geq 1$ for models I and III, *but not for model II.* For models I and III, atleast one of the effective masses, usually that of the lightest baryon, turns negative at high densities unless the couplings are chosen to fulfill $g_{\sigma B}/g_{\sigma N} = M_B/M$. This choice turns out to be unphysical [1]. In contrast, model II offers more protection against small changes both in the physical inputs at n_0 as well as in the hyperon couplings. These features are not affected by non-linear scalar self-interactions. Table 1 assesses the status of these commonly used models.

The interpretation that $m_n^\star \rightarrow 0$ at a finite density may signal a phase transition depends on whether $m_n^\star$ in these effective field-theoretical models can be viewed as an order parameter. Note also that a transition to quark matter may occur at a density smaller than that at which $m_n^\star$ turns negative. Should the propensity of $m_n^\star$ to drastically fall off with density indeed turn out to be realistic, it is worthwhile to examine its physical consequences.

During the early evolution of a protoneutron star, neutrino transport depends sensitively on the specific heat of matter and the neutrino mean free paths, both of which depend on $m_B^\star$. At low temperatures and high densities, effects induced by differences in $m_B^\star$ are the largest and hence easily discernable. Thus, establishing whether or not the deleptonization and cooling time scales provide a discriminatory ground may prove useful.

In Fig. 2, we examine if neutron star masses and radii are possible discriminants. The results shown are for model II for various $\sigma - \Sigma$ couplings with (left panel) and without (right panel) quartic terms in the vector channels. For
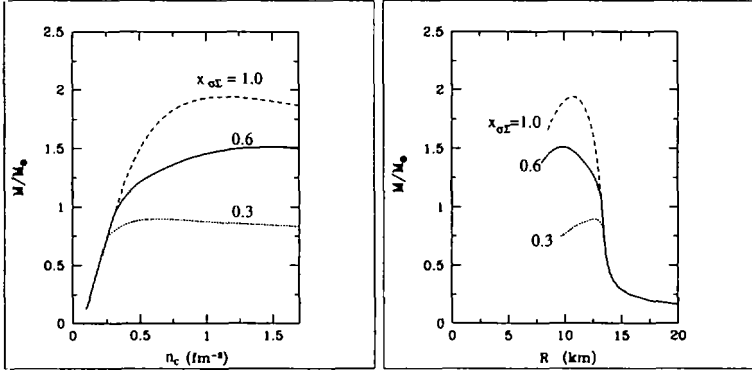
Figure 2: Neutron star properties in model II for different $x_{\sigma\Sigma} = g_{\sigma\Sigma}/g_{\sigma N}$. For the left panel, $\zeta = \xi = \bar{\alpha} = 0$. For the right panel, $\zeta = 0.06$, $\xi = 1.5$, and $\bar{\alpha} = 0$.

$M_{max}/M_\odot > 1.44$, the neutron star masses exhibit more sensitivity than do their radii. It is clear that both mass and radius determinations of the same star are necessary to pin down the supra-nuclear equation of state.

References

[1] R. Knorren, M. Prakash and P.J. Ellis, Phys. Rev. C **52** (1995) 3470.

[2] J. Schaffner and I.N. Mishustin, Phys. Rev. C **53** (1996) 1416.

[3] J.D. Walecka, Ann. of Phys. 83 (1974) 491.

[4] H. Müller and B.D. Serot, Nucl. Phys. A **606** (1996) 508.

[5] J. Zimanyi and S.A. Moszkowski, Phys. Rev. C **42** (1990) 1416; Phys. Rev. C **45** (1992) 844.

[6] N.K. Glendenning, F. Weber and S.A. Moszkowski, Phys. Rev. C **45** (1992) 844.

[7] N.K. Glendenning and S.A. Moszkowski, Phys. Rev. Lett. **67** (1991) 2414.

Probing the nuclear equation of state by heavy-ion reactions and neutron star properties*

P. K. Sahu, W. Cassing and M. H. Thoma

Institut für Theoretische Physik

Universität Giessen

D-35392 Giessen

GERMANY

Abstract

We discuss the nuclear equation of state (EOS) using a non-linear relativistic transport model. From the baryon flow for $Ni+Ni$ as well as $Au+Au$ systems we find that the strength of the vector potential has to be reduced at high density or at high relative momenta to describe the experimental flow data at 1-2 A GeV. We use the same dynamical model to calculate the nuclear EOS and then employ this EOS to neutron star structure calculations. We consider the core of the neutron star to be composed of neutrons with an admixture of protons, electrons, muons, sigmas and lambdas at zero temperature. We find that the nuclear equation of state is softer at high densities and hence the maximum mass and the radius of the neutron star are in the observable range of $M \sim 1.7 M_\odot$ and $R = 8 km$, respectively.

From the astrophysical as well as the experimental points of view the nuclear EOS is a challenging topic. Recent heavy-ion data [1] indicate that the nuclear EOS is rather soft at high density because the strength of the repulsive vector

---

1

potential must be low to explain the flow data in heavy-ion collisions. In the present contribution, we use an extended version of the Walecka relativistic mean-field model[2], which includes the interaction of Dirac nucleons with scalar and vector mesons as well as non-linear self-interactions of the scalar field. The physics behind this phenomenological successful model is that the nucleon- nucleon interaction in mean-field theory contains strong attractive Lorentz scalar and repulsive Lorentz vector components, which almost cancel for low momenta, but produce a strong spin- orbit force consistent with the observed single- particle spectra. In the original Walecka model [3], the vector potential increases linearly with density, whereas the scalar potential changes with density non-linearly. From the heavy-ion flow data we found that the vector potential also should depend non-linearly on the baryon density, i.e., the strength of the vector potential should be reduced at high densities [4] compared to the standard models [2, 3]. We recall that the mean-field energy density for nuclear matter in the relativistic mean-field model can be written as [2]

$$
\begin{aligned}
\varepsilon(m^*, n_b) &= g_v V_0 n_b - \frac{1}{2} m_v^2 V_0^2 + \frac{m_\sigma^2}{2 g_s^2}(m - m^*)^2 + \frac{B}{3 g_s^3}(m - m^*)^3 \\
&+ \frac{C}{4 g_s^4}(m - m^*)^4 + \gamma \int_0^{k_f} \frac{d^3 p}{(2\pi)^3} \sqrt{(p^2 + m^*)},
\end{aligned} \tag{1}
$$

where $m^* = m - g_s \sigma$ is the effective nucleon mass, n_b is the baryon density and the spin and isospin degeneracy is $\gamma = 4$. σ and V_0 are the scalar and vector fields with mass m_σ and m_v, which couple to nucleons with coupling constants g_s and g_v, respectively. B and C are constant parameters describing the scalar field self-interactions and p is the nucleon momentum integrated up to the Fermi momentum k_f. In (1), the vector and scalar potentials depend on density, however, the vector potential increases linearly with density (n_b).

In our present calculation, we have extended (1) to include a non-linear dependence of the vector potential on the baryon density.
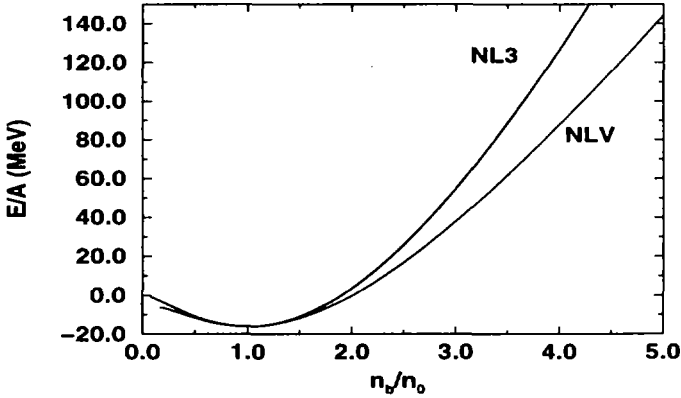
Fig.1 Energy per nucleon vs baryon density in units of $n_0 = 0.145 \, \hat{} \, m^{-3}$.

In Fig. 1 we show the energy per nucleon for our extended model (NLV) in comparison to the standard linear model (NL3), which corresponds to the parameter sets NL3 in ref. [2]. As can be seen from Fig. 2, the thermodynamic pressure

$$P_T = n_b^2 \frac{\partial}{\partial n_b}\left(\frac{E}{A}\right) \qquad (2)$$

is much lower in the extended model NLV for high baryon density as compared to the standard model NL3.
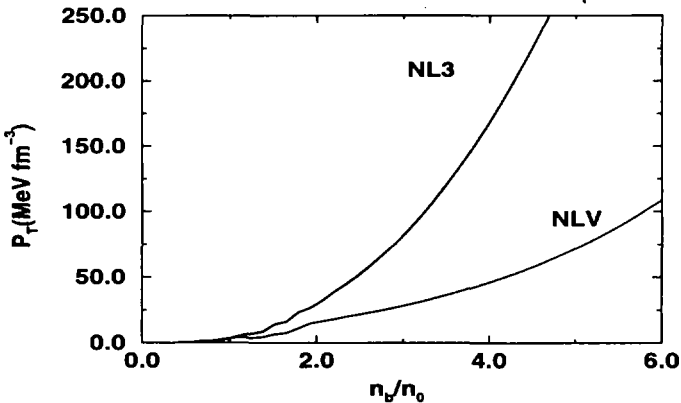
Fig.2 Thermodynamic pressure versus the baryon density

In our neutron star matter calculation we assume that the core of the neutron star matter is composed of neutrons with an admixture of protons, electrons, muons and hyperons [5]. The neutron star structure parameters are calculated by imposing the neutron star matter EOS in the hydrostatic equilibrium of degenerate stars without rotation. The composite EOS for the entire neutron star density was constructed by joining the EOS of high density neutron matter (the present NLV) to that with the known EOS at low density. The details about the hydrostatic equilibrium equations as well as the low density EOS have been discussed in ref. [6]. The resulting maximum mass of neutron stars are $2.2M_\odot$ and $1.65M_\odot$ for the linear (NL3) and non-linear model (NLV), respectively. We observe that the maximum mass of the neutron star for NLV is lower than that for NL3 due to a reduction of the vector field at higher densities. The corresponding neutron star radii are 11.98 km for NL3 and 7.7 km for NLV, whereas the corresponding central densities are $2.0 \times 10^{15} g\ cm^{-3}$ for NL3 and $4.5 \times 10^{15} g\ cm^{-3}$ for NLV at the maximum neutron star mass. In Fig. 3. we show the gravitational neutron star masses versus the central densities. We find that the maximum mass for NLV is in the observable region [7], $1.4M_\odot < M_{max} < 1.7M_\odot$. The corresponding radius is in between 6-8 km.
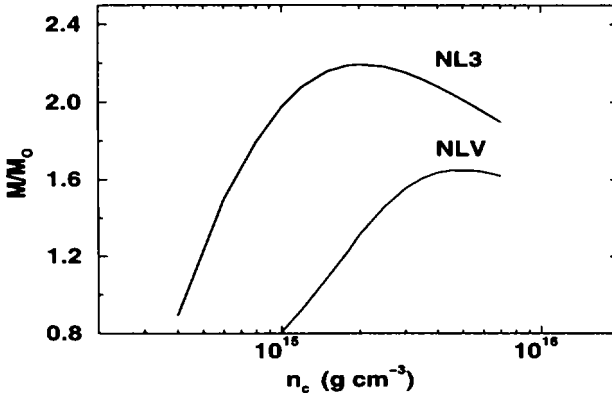
Fig.3 Neutron star mass vs central density

References

[1] N. Herrmann, Nucl. Phys. **A610** (1996) 49c;

[2] A. Lang, B. Blättel, W. Cassing, V. Koch, U. Mosel and K. Weber, Z. Phys. **A340** (1991) 207;

[3] B. D. Serot and J. D. Walecka, Adv. Nucl. Phys. **16** (1986) 1;

[4] P. K. Sahu et al., in preparation;

[5] S. K. Ghosh, S. C. Phatak and P. K. Sahu, Z. Phys. **A352** (1995) 457;

[6] P. K. Sahu, R. Basu and B. Datta, Astrophys. J. **416** (1993) 267;

[7] J. H. Taylor and J. M. Weisberg, Astrophys. J. **345** (1989) 434; A. Wolszczan, Nature, **350** (1991) 688; W. T. S. Deich and S. R. Kulkarni, in Compact Stars in Binaries, J. van Paradijs, et al., eds., Dordrecht, Kluwer (1996).

Kaons in Nuclear Matter

Henning Heiselberg

NORDITA
Blegdamsvej 17, DK-2100 Copenhagen Ø, Denmark

Abstract

The kaon energy in a nuclear medium and its dependence on kaon-nucleon and nucleon-nucleon correlations is discussed. The transition from the Lenz potential at low densities to the Hartree potential at high densities can be calculated analytically by making a Wigner-Seitz cell approximation and employing a square well potential. As the Hartree potential is less attractive than the Lenz one, kaon condensation inside cores of neutron stars appears to be less likely than previously estimated.

1 Introduction

Kaon condensation in dense matter was suggested by Kaplan and Nelson [1], and has been discussed in many recent publications [2, 3]. Due to the attraction between K^- and nucleons its energy decreases with increasing density, and eventually if it drops below the electron chemical potential in neutron star matter in β-equilibrium, a Bose condensate of K^- will appear. It is found that K^-'s condense at densities above $\sim 3 - 4\rho_0$, where $\rho_0 = 0.16$ fm^{-3} is normal nuclear matter density. This is to be compared to the central density of $\sim 4\rho_0$ for a neutron star of mass $1.4 M_\odot$ according to the estimates of Wiringa, Fiks and Fabrocini [4] using realistic models of nuclear forces. The condensate could change the structure and affect maximum masses and cooling rates of neutron stars significantly.

Recently, [5, 7] we have found that the kaon-nucleon and nucleon-nucleon correlations conspire to reduce the K^-N attraction significantly already at rather low densities when the interparticle distance is comparable to the range of the KN interaction. We have calculated the kaon energy as function of density in a simple model where also the low and high density limits and the dependence on the range of the interaction can be extracted.

2 Low Density Limit: Lenz Potential

In neutron matter at low densities when the interparticle spacing is much larger than the range of the interaction, $r_0 \gg R$, the kaon interacts strongly many times with the same nucleon before it encounters and interacts with another nucleon. Thus one can use the scattering length as the "effective" kaon-nucleon interaction, $a_{K-n} \simeq -0.41$fm. The kaon energy deviates from its rest mass by the Lenz potential

$$\omega_{Lenz} = m_K + \frac{2\pi}{m_R} a_{K-n}\, \rho\,. \tag{1}$$

which is the optical potential obtained in the impulse approximation.

3 High Density Limit: Hartree Potential

At high densities when the interparticle spacing is much less than the range of the interaction, $r_0 \ll R$, the kaon will interact with many nucleons on a distance scale much less the range of the interaction. The kaon thus experiences the field from many nucleons and the kaon energy deviates from its rest mass by the Hartree potential:

$$\omega_{Hartree} = m_K + \rho \int V_{K-n}(r)d^3r\,, \tag{2}$$

As shown in [5], the Hartree potential is considerably less attractive than the Lenz potential. This is also evident from Fig. (1).

4 General Case

To demonstrate this transition from the low density Lenz potential to the high density Hartree potential we solve the Klein-Gordon equation for kaons in neutron matter in the Wigner-Seitz cell approximation. With the simplified square well potential this can in fact be done analytically.

4.1 The Recoil Corrected Klein-Gordon Equation

We choose to describe the kaon-nucleon interaction by a vector potential V dominated by the Weinberg-Tomozawa term. In the analysis of Ref. [6] the K^+N interaction was also found to be dominated by ω and ρ vector mesons.

The energy of the kaon-nucleon center-of-mass system with respect to the nucleon mass is then

$$\omega = \sqrt{k^2 + m_K^2} + V + \frac{k^2}{2m_N}\,, \tag{3}$$

where k is the kaon momentum (we use units such that $\hbar = c = 1$), in c.m. frame. We have included the recoil kinetic energy of the nucleon assuming that terms of order $k^4/8m_N^3$ and higher can be neglected. For a relativistic description of the kaon in a vector potential we employ the following recoil corrected Klein-Gordon equation (RCKG) obtained by quantizing Eq. (3) $(k = -i\nabla)$

$$\left\{(\omega - V)^2 + \frac{m_N + \omega - V}{m_N}\nabla^2 - m_K^2\right\}\phi = 0\,. \tag{4}$$

4.2   The Wigner-Seitz Cell Approximation

The Wigner-Seitz cell approximation simplifies band structure calculations enormously. Though it is a poor approximation for solids it is better for liquids. As we only consider qualitative effects we shall assume the Wigner-Seitz cell approximation for the strongly correlated nuclear liquid because the periodic boundary condition is a computational convenience. It contains the important scale for nucleon-nucleon correlations given by the interparticle spacing and, as we shall see, it naturally gives the correct low density (Lenz) and high density (Hartree) limits. We only consider neutrons since the $\sim 10\%$ protons expected in neutron stars do not change results by much.

4.3   Square Well Potential

Since the kaon-nucleon potential is not known in detail and we are only interested in qualitative effects, we will for simplicity approximate it by a simple square well potential

$$V(r) = -V_0\Theta(R - r)\,. \tag{5}$$

The range of the interaction R and the potential depth V_0 are related through the s-wave scattering length $a = R - \tan(\kappa_0 R)/\kappa_0$, where $\kappa_0^2 = (2m_K V_0 + V_0^2)\cdot m_N/(m_N + m_K + V_0)$. If $V_0 \ll m_K$ this reduces to the standard result $\kappa_0^2 = 2m_R V_0$, where $m_R = m_K m_N/(m_K + m_N)$ is the kaon-nucleon reduced mass. However, for small ranges of interaction the potential becomes significant as

compared to the kaon mass which necessitates a relativistic treatment with the Klein-Gordon equation instead of the Schrödinger equation.

The above arguments suggest that the range $R = 0.4 - 1.0$fm covers most realistic possibilities above. For a kaon-neutron scattering length of $a_{K^-n} = -0.41$ fm we find for typical ranges $R = 0.4 - 1.0$ fm kaon-neutron potentials ranging from $V_0 = 463$MeV down to $V_0 = 49$ MeV.
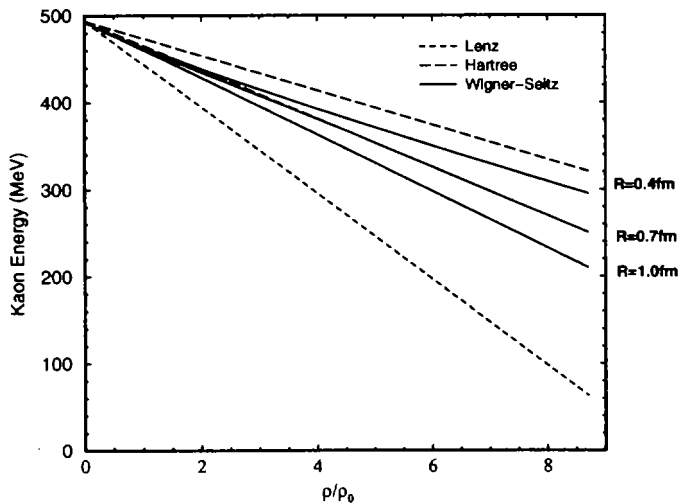
Fig. 1. Kaon energy as function of neutron density. Our calculation (Eq. (6), full curves) are shown for $R = 0.4$ fm, $R = 0.7$ fm and $R = 1.0$ fm. At low densities they approach the Lenz result (Eq. (1), dotted curve) and at high densities they approach the Hartree result (Eq.(2), dashed curves).

5   Results

As shown in [7] the RCKG equation can now be solved for s-waves and the kaon wave-function found. Applying the periodic boundary condition, $\phi'(r_0) = 0$, as required by the Wigner-Seitz cell approximation we arrive at the closed equation

$$\frac{k}{\kappa} \tan(\kappa R) = \frac{e^{2k(R-r_0)} - (1 - kr_0)/(1 + kr_0)}{e^{2k(R-r_0)} + (1 - kr_0)/(1 + kr_0)} , \qquad (6)$$

which determines k and thus the kaon energy. Here, $k^2 = (m_K^2 - \omega^2) m_N / (m_N + \omega)$ and $\kappa^2 = ((\omega + V_0)^2 - m_K^2) m_N / (m_N + \omega + V_0)$. The resulting kaon energy is shown in Fig. (1). By expanding (6) at low densities the kaon energy becomes the Lenz potential whereas at high densities it becomes the Hartree potential.

6 Summary

Kaon-nucleon correlations reduce the $K^- N$ interaction significantly when its range is comparable to or larger than the nucleon-nucleon interparticle spacing. The transition from the Lenz potential at low densities to the Hartree potential at high densities begins to occur already well below nuclear matter densities. For the measured $K^- n$ scattering lengths and reasonable ranges of interactions the attraction is reduced by about a factor of 2-3 in cores of neutron stars. Relativistic effects further reduce the attraction at high densities. Consequently, a kaon condensate is less likely in neutron stars.

Coulomb energies have not been included in the above analysis. They may, as discussed in [8, 9], lead to a mixed phase of nuclear matter with and without a kaon condensate. However, the Coulomb energies are small as compared to kaon masses and therefore the reduction in the kaon energy will also be minor.

My collaborators J.Carlson, V.Pandharipande and C.J.Pethick are gratefully acknowledged.

References

[1] D. B. Kaplan and A. E. Nelson, *Phys. Lett.* **B291** (1986) 57.

[2] G. Brown, C. Lee, M. Rho and V. Thorsson, *Nucl. Phys.* **A 572** (1994) 693

[3] T. Waas, M. Rho and W. Weise, *Nucl.Phys.* **A617** (1997) 449-463.

[4] R. B. Wiringa, V. Fiks and A. Fabrocini, *Phys. Rev.* **C38** (1988) 1010.

[5] V.R. Pandharipande, C.J. Pethick and V. Thorsson, *Phys. Rev. Lett.* **75** (1995) 4567.

[6] R. Büttgen, K. Holinde, A. Müller-Groeling, J. Speth and P. Wyborny, *Nucl. Phys.* **A506** (1990) 586.

[7] J. Carlson, H. Heiselberg, V.R. Pandharipande and C.J. Pethick, to be published.

[8] J. Schaffner, these proceedings.

[9] H. Heiselberg and M. Hjorth-Jensen, these proceedings.

Onset of hyperon formation in neutron star matter

H.-J. Schulze, M. Baldo, and G. F. Burgio

Sezione INFN, Università di Catania, Corso Italia 57, I-95129 Catania, Italy

Abstract

We determine fully self-consistent single-particle potentials and chemical po-
tentials of nucleons and hyperons in asymmetric nuclear matter, using an
extended Brueckner-Hartree-Fock formalism. The results indicate that for-
mation of Σ^- hyperons in β stable nuclear matter sets in at about 3 times
normal density.

The quantitative modelling of neutron stars [1] requires the knowledge of the equation
of state for extremely dense and charge-neutral nuclear matter (up to about ten times
normal density, $\rho_0 \approx 0.17$ fm^{-3}). While at "low" densities the matter consists exclusively of
neutrons and a small fraction of protons and electrons, it is clear that the fast rise of their
chemical potentials with density favors the appearance of different species of particles. Due
to its negative charge, the Σ^- hyperon is the first heavier baryon expected to appear with
increasing density in the reaction $n + e \rightarrow \Sigma^-$ (or $n + n \rightarrow p + \Sigma^-$) in spite of its substantially
larger mass compared to the neutral Λ hyperon ($M_{\Sigma^-} = 1197$ MeV, $M_\Lambda = 1116$ MeV). We
disregard in this work the possible appearance of other species like pions [2] and kaons [3]
as well as the possible formation of quark matter at high density [4]. These phenomena lie
outside the scope of Brueckner theory that is applied here.

Quantitatively the concentrations of the various species in the dense matter are deter-
mined by the equality of chemical potentials (including rest masses) on both sides of the
possible weak interaction reaction equations. In particular we have ($\mu_l = \mu_e = \mu_\mu$ is the
lepton chemical potential)

$$\mu_n = \mu_p + \mu_l , \tag{1}$$

$$2\mu_n = \mu_p + \mu_{\Sigma^-} , \tag{2}$$

$$\mu_n = \mu_\Lambda , \tag{3}$$

that are specific cases of the general formula

$$\mu = b\mu_n - q\mu_l , \tag{4}$$

valid for any particle with baryon number b and charge q. (The chemical potential is uniquely
determined by the baryon number and charge of a particle).

While the chemical potential of the electron is simply given by the free non-interacting
one $[\mu_e \approx k_F^{(p)} = (3\pi^2\rho_p)^{1/3}$ in relativistic approximation], the chemical potentials of the

baryons as functions of total density and concentrations need to be determined by a micro-scopic calculation due to their strong interaction with the baryonic environment.

In this article we present such a microscopic investigation within an extended Brueckner-Hartree-Fock (BHF) scheme that allows to determine the chemical potentials of the different species $(n, p, \Lambda, \Sigma^-, \Sigma^0, \Sigma^+)$ in a fully self-consistent manner. This requires in general the knowledge of the nucleon-nucleon, nucleon-hyperon, and hyperon-hyperon strong interaction potentials in the various channels. While we use in our calculation the Paris nucleon-nucleon [5] and the Nijmegen soft-core nucleon-hyperon [6] potentials, there are currently no realistic hyperon-hyperon potentials available, due to the complete lack of experimental constraints. Fortunately, for small hyperon fractions that are expected in β stable matter, and in particular for the purpose of determining the *onset* of hyperon formation that will be discussed here, the knowledge of the hyperon-hyperon interaction is not required. The extension to finite hyperon densities and towards a realistic microscopic equation of state including large fractions of hyperons is a formidable task for the future that requires novel experimental input in order to constrain the modelling of the hyperon-hyperon interaction.

We briefly outline our formalism in the following and refer to Ref. [7] for a detailed presentation. The problem is complicated by a coupled-channel structure: Whereas for the nucleon-nucleon interaction there are only two separate channels nn, np, or, equivalently, $T = 0, 1$, strong interaction transitions link the different nucleon-hyperon channels with given total charge, namely $(n\Lambda, n\Sigma^0, p\Sigma^-)$ and $(p\Lambda, p\Sigma^0, n\Sigma^+)$. There are in general $2 \times 6 + 2$ different potentials

$$
\begin{pmatrix}
V_{(n\Lambda)(n\Lambda)} & V_{(n\Lambda)(n\Sigma^0)} & V_{(n\Lambda)(p\Sigma^-)} \\
V_{(n\Sigma^0)(n\Lambda)} & V_{(n\Sigma^0)(n\Sigma^0)} & V_{(n\Sigma^0)(p\Sigma^-)} \\
V_{(p\Sigma^-)(n\Lambda)} & V_{(p\Sigma^-)(n\Sigma^0)} & V_{(p\Sigma^-)(p\Sigma^-)}
\end{pmatrix} ,
\begin{pmatrix}
V_{(p\Lambda)(p\Lambda)} & V_{(p\Lambda)(p\Sigma^0)} & V_{(p\Lambda)(n\Sigma^+)} \\
V_{(p\Sigma^0)(p\Lambda)} & V_{(p\Sigma^0)(p\Sigma^0)} & V_{(p\Sigma^0)(n\Sigma^+)} \\
V_{(n\Sigma^+)(p\Lambda)} & V_{(n\Sigma^+)(p\Sigma^0)} & V_{(n\Sigma^+)(n\Sigma^+)}
\end{pmatrix} ,
$$
$$
V_{(n\Sigma^-)(n\Sigma^-)} , \ V_{(p\Sigma^+)(p\Sigma^+)} .
\tag{5}
$$

Based on these potentials, the various G matrices are evaluated by solving numerically the Bethe-Goldstone equation [8], written schematically [The indices a, b, c indicate nucleon-hyperon pairs (NY) as above]

$$
G_{ab}[W] = V_{ab} + \sum_c \sum_{p,p'} V_{ac} |pp'\rangle \frac{Q_c}{W - E_c + i\epsilon} \langle pp' | G_{cb}[W] ,
\tag{6}
$$

with the angle-averaged Pauli operator Q and energy E of a nucleon-hyperon pair:

$$
E_{(NY)} = \frac{k_N^2}{2m_N} + \frac{k_Y^2}{2m_Y} + \mathrm{Re}\, U_N(k_N) + \mathrm{Re}\, U_Y(k_Y) + m_N + m_Y .
\tag{7}
$$

The hyperon single-particle potentials within the continuous choice are given by

$$
U_Y(k) = \sum_{N=n,p} U_Y^{(N)}(k) = \sum_{N=n,p} \sum_{k' < k_F^{(N)}} \langle kk' | G_{(NY)(NY)}[E_{(NY)}(k, k')] | kk' \rangle
\tag{8}
$$

and have separate contributions due to the neutrons and protons in the environment. The total binding energy per baryon, B/A, can be evaluated from the nucleon single-particle potentials:

$$\frac{B}{A} = \left[3 \sum_{N=n,p} \int_0^{k_F^{(N)}} dk \, k^2 \left(\frac{k^2}{2m_N} + \frac{1}{2} U_N(k) \right) \right] \Big/ \left[k_F^{(n)3} + k_F^{(p)3} \right] . \qquad (9)$$

These equations define the BHF scheme with the continuous choice of the single-particle energies. Due to the occurrence of U_N and U_Y in Eq. (7), the set of equations (6-8), together with the appropriate ones for the nucleons, constitutes a coupled system that has to be solved in a self-consistent manner.

We come now to the presentation of our results: We begin in Fig. 1 with the display
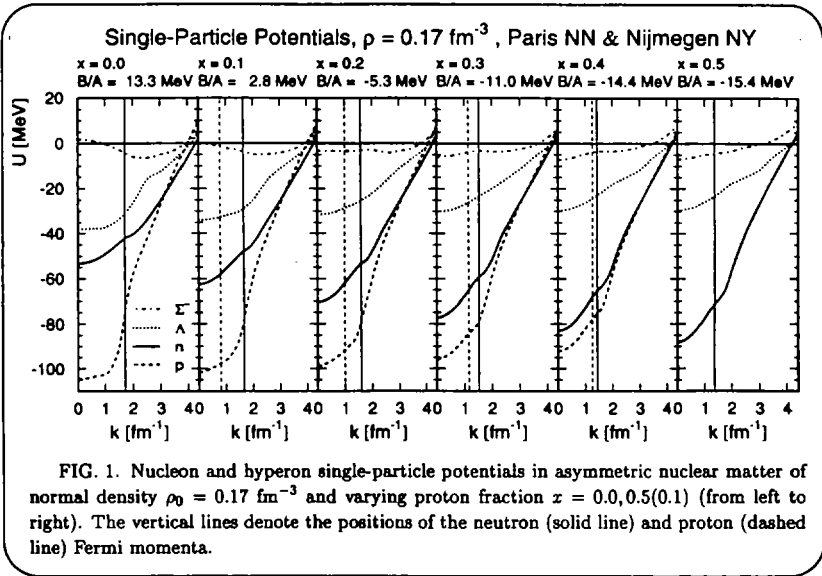
FIG. 1. Nucleon and hyperon single-particle potentials in asymmetric nuclear matter of normal density $\rho_0 = 0.17$ fm^{-3} and varying proton fraction $x = 0.0, 0.5 (0.1)$ (from left to right). The vertical lines denote the positions of the neutron (solid line) and proton (dashed line) Fermi momenta.

of the single-particle potentials of neutrons, protons, Λ, and Σ^- baryons in asymmetric nuclear matter of normal nuclear density ρ_0 and varying proton fraction $x = \rho_p/\rho$. For pure neutron matter ($x = 0$) the proton mean field is much deeper (≈ -105 MeV) than the one of the neutron (≈ -55 MeV), due to the strong attraction in the $^3S_1$ channel of the proton-neutron interaction. With increasing proton fraction the two curves approach each other until they coincide for the case of symmetric nuclear matter ($x = 0.5$). The binding energy per nucleon decreases monotonically with the proton fraction. In general, the hyperon single-particle potentials are weaker than those of the nucleons due to the weaker nucleon-hyperon interaction. The lambda mean field varies from about -40 MeV in pure neutron matter to about -30 MeV in symmetric matter. (Since the lambda is an isoscalar particle, this variation is exclusively due to the different intermediate states in the Bethe-Goldstone equation; it does not occur in a simple mean-field treatment). The Σ^- is

FIG. 2. Left: Chemical potentials of various baryons in pure neutron matter as a function of density. Right: Combinations of chemical potentials determining the hyperon formation threshold in neutron matter.
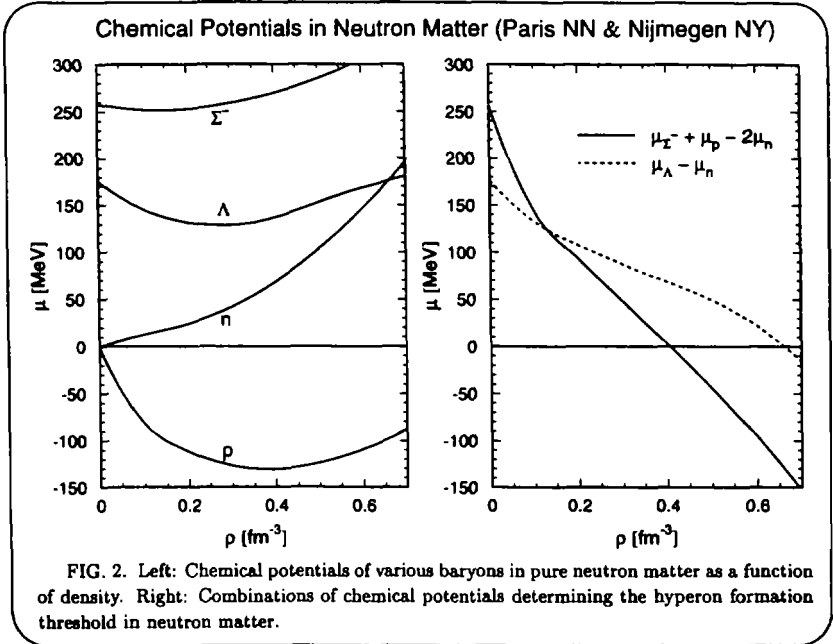
rather weakly bound with a depth of the mean field at zero momentum varying between +2 MeV (neutron matter) and −7 MeV (symmetric matter). There is also a substantial variation of the shape of the Σ^- single-particle potential with proton fraction.

The ordering of the strengths of the different mean fields is also seen in the next Fig. 2, where the chemical potentials $\mu = m - m_n + e_F$ of the different species are shown for pure neutron matter as a function of neutron density. From this plot one can obtain a first estimate of the onset of hyperon formation by solving Eqs. (2,3). This is shown graphically in the figure and leads to the estimates of the hyperon threshold densities in neutron matter $\rho_{\Sigma^-} \approx 0.4$ fm^{-3} and $\rho_\Lambda \approx 0.65$ fm^{-3}.

Continuing our investigation to β stable nuclear matter, we show in Fig. 3 the binding energy per nucleon, B/A, as a function of density and proton fraction. The nucleonic symmetry energy $E_{sym}(\rho) = -[\partial(B/A)/4\partial x](\rho, x = 0)$ is also displayed in the figure. With these results, Eq. (1) can be solved to determine the proton fraction in β stable nuclear matter. The resulting line of β stability, $[\rho, x(\rho)]$, is displayed in the plot. Our results are close to those obtained in previous investigations within nonrelativistic Brueckner theory [9] and confirm the validity of the quadratic dependence of the binding energy on the asymmetry parameter $\beta = 1 - 2x$.

We proceed finally to the determination of the hyperon threshold density ρ_{Σ^-} in the β

FIG. 3. Left: Binding energy per nucleon of asymmetric nuclear matter as a function of baryon density $\rho = \rho_n + \rho_p$ and proton fraction $x = \rho_p/\rho$. The projected curve in the plot is the line of β stability as determined from Eq. (1). Right: Nuclear symmetry energy determined by different methods.
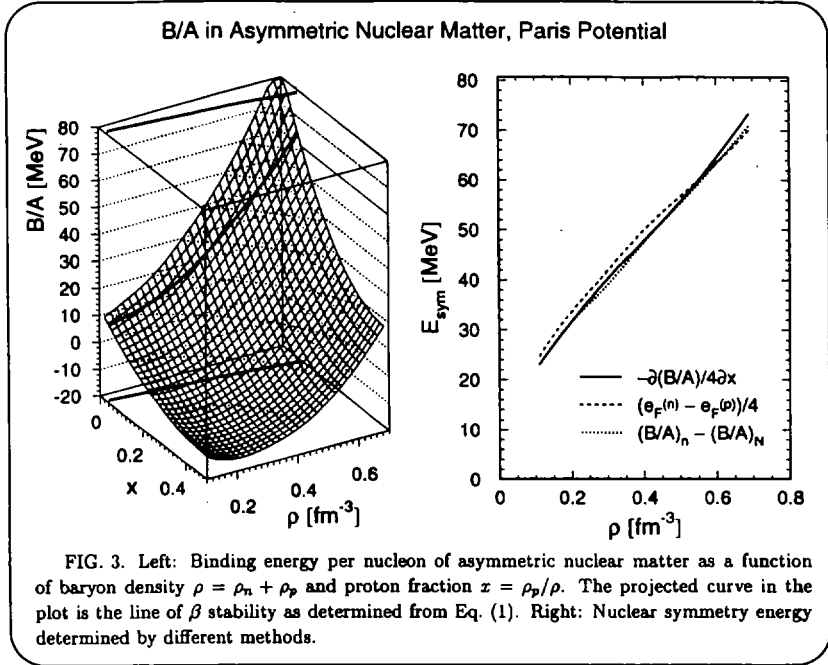
stable matter: This is signalled by the vanishing of the expression $(\mu_{\Sigma^-} + \mu_p - 2\mu_n)$ along the line of β stability. This quantity is displayed in Fig. 4 as a function of density and proton fraction. Clearly, the hyperon threshold density increases fast with the proton fraction. We observe an about 20 percent increase from $\rho_{\Sigma^-} \approx 0.4$ fm^{-3} in pure neutron matter to $\rho_{\Sigma^-} \approx 0.5$ fm^{-3} in β stable matter.

In conclusion, the knowledge of realistic nucleon-nucleon and nucleon-hyperon potentials allows the determination of a microscopic equation of state for asymmetric nuclear matter including small hyperon fractions in a self-consistent Brueckner-Hartree-Fock scheme. We found that with the Nijmegen soft-core nucleon-hyperon potentials, the binding of lambda hyperons in pure nuclear matter is in good agreement with experimental data on Λ hyper-nuclei [10]. The theoretical as well as experimental situation regarding the sigma hyperons is more uncertain [11]. The predicted fairly small attraction of the sigma in nuclear matter seems at least not in contradiction with recent experimental data. It appears appropriate to treat the Σ^- as a non-interacting particle in a first approximation. Consequently, we find rather large threshold densities for the hyperon formation compared to more phenomenological studies [1,12] that usually assume a stronger binding of the Σ.

We have assumed in this work that the neutron star matter is composed exclusively of

FIG. 4. Left side: Combination of chemical potentials for the reaction $n + n \leftrightarrow p + \Sigma^-$ as a function of total density and proton fraction in asymmetric nuclear matter. The projected curves denote the occurrence of chemical equilibrium (solid line), and the line of β stability (dashed line). They are also shown in the plot on the right hand side.
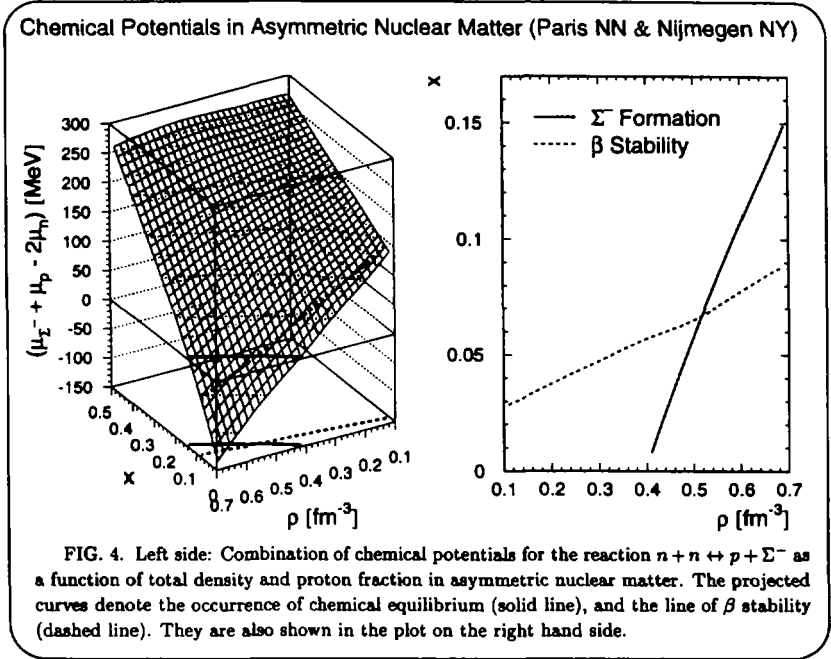
neutrons, protons, and leptons, and have neglected any other components (pions, kaons, quarks) that might as well appear with rising density, but do not fit into the framework of Brueckner theory. Concerning the calculation itself, the biggest problem for the moment is the lack of quantitative knowledge regarding the hyperon-hyperon interactions, that might hopefully be remedied by the proposed new experiments on hypernuclear physics [13]. In that case we will be able to extract a fully microscopic equation of state for hypernuclear matter with arbitrary strangeness fraction. A principle problem concerns the use of a lowest-order Brueckner scheme. Apart from the failure to predict the correct saturation point of nuclear matter, terms of higher order in the hole-line expansion [14] become increasingly important with rising density. This could be addressed partly by use of a relativistic Dirac-BHF method [15], by including three-body forces [16], and by considering higher orders in the hole line expansion, which is however very involved, even for pure nuclear matter.

REFERENCES

[1] A. G. W. Cameron, Astrophys. J. **130**, 884 (1959); V. R. Pandharipande, Nucl. Phys. **A178**, 123 (1971); H. A. Bethe and M. B. Johnson, Nucl. Phys. **A230**, 1 (1974); N. K. Glendenning, Nucl. Phys. **A493**, 521 (1989); G. Baym, Nucl. Phys. **A590**, 233c (1995); M. Prakash, I. Bombaci, M. Prakash, P. J. Ellis, J.M. Lattimer, and R. Knorren, Phys. Rep. **280**, 1 (1997); N. K. Glendenning, Z. Physik **A326**, 57 (1987).

[2] G. E. Brown and W. Weise, Phys. Rep. **27**, 1 (1976); A. Akmal and V. R. Pandhari-pande, Phys. Rev. **C56**, 2261 (1997).

[3] V. R. Pandharipande, C. J. Pethick, and V. Thorsson, Phys. Rev. Lett. **75**, 4567 (1995); G. Q. Li, C.-H. Lee, and G. E. Brown, Nucl. Phys. **A625**, 372 (1997).

[4] E. Witten, Phys. Rev. **D30**, 272 (1984); G. Baym, E. W. Kolb, L. McLerran, T. P. Walker, and R. L. Jaffe, Phys. Lett. **B160**, 181 (1985); N. K. Glendenning, Mod. Phys. Lett. **A5**, 2197 (1990).

[5] M. Lacombe, B. Loiseau, J. M. Richard, R. Vinh Mau, J. Côté, P. Pirès, and R. de Tourreil, Phys. Rev. **C21**, 861 (1980).

[6] P. Maessen, Th. Rijken, and J. de Swart, Phys. Rev. **C40**, 2226 (1989).

[7] H.-J. Schulze, A. Lejeune, J. Cugnon, M. Baldo, and U. Lombardo, Phys. Lett. **B355**, 21 (1995); Phys. Rev. **C46**, (Feb. 1998).

[8] K. A. Brueckner and J. L. Gammel, Phys. Rev. **109**, 1023 (1958); J.-P. Jeukenne, A. Lejeune, and C. Mahaux, Phys. Rep. **25C**, 83 (1976).

[9] A. Lejeune, P. Grangé, M. Martzolff, and J. Cugnon, Nucl. Phys. **A453**, 189 (1986); I. Bombaci and U. Lombardo, Phys. Rev. **C44**, 1892 (1991).

[10] C. B. Dover and A. Gal, Prog. Part. Nucl. Phys. **12**, 171 (1984); D. J. Millener, C. B. Dover, and A. Gal, Phys. Rev. **C38**, 2700 (1988); R. E. Chrien and C. B. Dover, Ann. Rev. Nucl. Part. Sci. **39**, 113 (1989); H. Feshbach, Nucl. Phys. **A507**, 219c (1990); Y. Yamamoto and H. Bando, Prog. Theor. Phys. **83**, 254 (1990).

[11] C. B. Dover, D. J. Millener, and A. Gal, Phys. Rep. **184**, 1 (1989); C. J. Batty, E. Friedman, and A. Gal, Prog. Theor. Phys. Suppl. **117**, 227 (1994); Y. Yamamoto, T. Motoba, H. Himeno, K. Ikeda, and S. Nagata, *ibid.*, 361; R. Sawafta, Nucl. Phys. **A585**, 103c (1995).

[12] S. Balberg and A. Gal, Nucl. Phys. **A625**, 435 (1997).

[13] J. K. Ahn et al., Nucl. Phys. **A585**, 165c (1995); M. Agnello et al., Nucl. Phys. **A623**, 279c (1997); R. Sawafta, *ibid.*, 289c; R. Bertini, *ibid.*, 294c.

[14] B. D. Day, Phys. Rev. **C24**, 1203 (1981); B. D. Day and R. B. Wiringa, Phys. Rev. **C32**, 1057 (1985); H. Q. Song, M. Baldo, G. Giansiracusa, and U. Lombardo, Phys. Lett. **B411**, 237 (1997).

[15] G. Q. Li, R. Machleidt, and R. Brockmann, Phys. Rev. **C45**, 2782 (1992).

[16] M. Baldo, I. Bombaci, and G. F. Burgio, Astron. Astrophys. **328**, 274 (1997).

STRANGE PHASES IN NEUTRON STARS

J. SCHAFFNER-BIELICH and N. K. GLENDENNING

Nuclear Science Division, Lawrence Berkeley National Laboratory
University of California, Berkeley 94720, USA

Abstract

The equation of state and the properties of neutron stars are studied for a phase transition to a charged kaon condensate. We study the mixed phase by using Gibbs condition with comparison to the hitherto applied Maxwell construction. Implications for kaon condensation and for the mass-radius relation of condensed neutron stars are examined.

The high density behavior of the equation of state of nuclear matter is still quite unknown and has led to speculations about the appearance of new phases. At sufficiently high density, there should be a phase transition to a quark plasma. In the following, we will discuss the onset of kaon condensation in neutron matter which might happen at lower density. Kaon condensation in connection with β-stable matter has already been studied in [1]. It received considerable attention after the work of [2] which included strong in-medium effects for the kaons. Once the effective kaon energy hits the electrochemical potential, neutrons can convert to protons and K^-. Using chiral perturbation theory, this happens at $(3-4)\rho_0$ [3]. As the kaon is a boson and condenses, the equation of state is considerably softened and the maximum mass of a neutron star is lowered to $1.5M_\odot$ [4]. This is turn provides a scenario for low mass black holes as proposed by Bethe and Brown [5]. As a side remark, it was found before the kaon condensation scenario was introduced that the less spectacular appearance of hyperons results also in a lower maximum mass of neutron stars [1].

The essential ingredient for kaon condensation is the lowering of the effective mass of the kaon in the medium. One knows from kaon-nucleon scattering that the s-wave K^+N scattering is repulsive. The low density theorem then states that the optical potential in the nuclear medium is then also repulsive and about +30 MeV at normal nuclear density. Surprisingly, also the scattering for the antiparticle, the K^-, shows repulsion which is due to the appearance of the $\Lambda(1405)$ resonance just below threshold [6]. A recent analysis of K^- atoms suggest that the optical potential of the K^- can be as deeply attractive as -200 MeV at normal nuclear density [7]. A coupled channel calculation by

Koch [8] including in-medium effects actually resolved this: as the repulsive
$\Lambda(1405)$ mode is shifted up in the medium due to Pauli-blocking effects, it
leaves only an attractive mode with an optical potential of about -100 MeV
at ρ_0.

Hence, the K^- feels attraction in dense nuclear matter and might con-
dense. Using a Maxwell construction for the phase transition, it was found
that the mass-radius relation changes considerably for a kaon condensed star
[4]. Nevertheless, there are two chemical potentials for neutron star matter, the
baryochemical potential and the electrochemical potential, as baryon number
and charge are conserved quantities. If the phases are in chemical and mechan-
ical equilibrium then the pressure and all chemical potentials involved should
be the same in the two phases:

$$p^{\rm I} = p^{\rm II} \qquad \mu_B^{\rm I} = \mu_B^{\rm II} \qquad \mu_e^{\rm I} = \mu_e^{\rm II} \quad . \tag{1}$$

This is just Gibbs general condition for two phases in equilibrium. A Maxwell
construction can assure that only one chemical potential is common to the
two phases and is therefore not applicable to neutron star matter [9]. One
has an additional degree of freedom to maximize the pressure of the system:
charge. According to Gibbs, there exist now three possible solutions: the
pure nucleon phase with zero charge, the pure kaon condensed phase with zero
charge, and the mixed phase where the two phases have finite charge densities
but neutralize each other. Geometric structures will appear with different local
charges.

We model the onset to kaon condensation by using the relativistic mean-
field model and the following Lagrangian for the kaon-nucleon interaction

$$\mathcal{L}_K = D_\mu^* \bar{K} D^\mu K - m_K^{*\,2} \bar{K} K \tag{2}$$

with a minimal coupling to scalar and vector fields

$$\begin{aligned}
D_\mu &= \partial_\mu + i g_{\omega K} V_\mu + i g_{\rho K} \tau R_\mu \\
m_K^* &= m_K + g_{\sigma K} \sigma \quad .
\end{aligned} \tag{3}$$

The vector coupling constants are fixed by simple quark counting rules, $g_{\omega K} =
g_{\omega N}/3$ and $g_{\rho K} = g_{\rho N}$. The scalar coupling constant is fixed to the optical
potential of the K^- at ρ_0.

Figure 1 shows the equation of state of neutron matter with a kaon con-
densed phase. All three solutions are plotted for an optical potential of the K^-
of $U_K = -140$ MeV. For comparison, the horizontal line shows the case when
using an unphysical Maxwell construction that assumes equality of μ_B in both
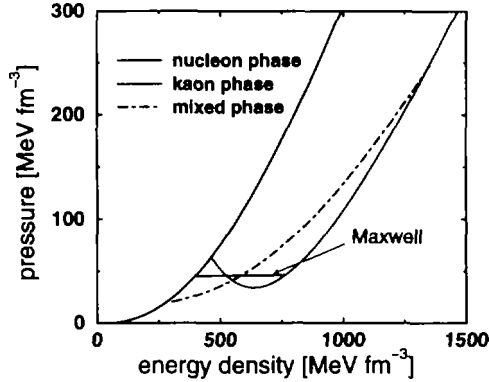
Figure 1: The equation of state for neutron matter with a kaon condensed phase using a Maxwell construction compared to using Gibbs conditions.

phases but not of μ_e resulting in a constant pressure. The kaon condensed phase shows some instability, i.e. a negative curvature, close to the onset of the phase transition point. The mixed phase spans over a wide range of density and starts at much lower density than the pure kaon condensed phase. This solution gives then a continuously growing equation of state without any instability. The equation of state is considerably smoothened compared to the case of a Maxwell construction. It appears much like the equation of state of a second order phase transition with the important difference, however, that there is a density range for which a mixture of two distinct phases occurs.

The charge is distributed between the two phases in the mixed phase. At the beginning of the mixed phase, the bubbles of the new phase are highly negatively charge while occupying only a small amount of the total volume. At higher density, the two phases have just the opposite charge and share equally the available volume. At the end of the phase transition, the situation is reversed and the nucleon phase is highly positively charged while being only in a small fraction of the total volume. Note, that the asymmetry energy of nuclear matter is the driving force so that there is a positive charge in the nucleon phase while the negatively charged kaon in the second phase allows also for a more isospin symmetric system.

There are nucleons in both phases. But they do not mix with each other,
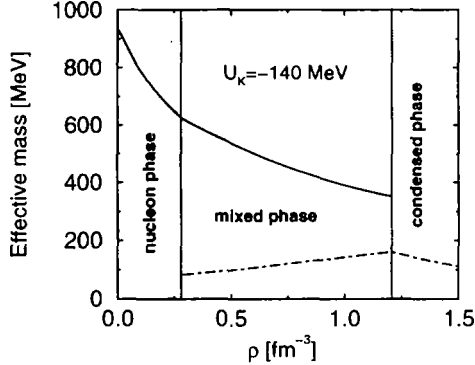
Figure 2: The effective mass of the nucleon in the various phases of neutron star matter.

because they have different in-medium properties. The presence of the kaon shifts the effective mass of the nucleon to lower values as there are different field configurations in this phase. This is visualized in Figure 2. The effective mass of the nucleon is lowered at higher density. In the mixed phase starting at $3\rho_0$, the effective masses of the nucleons on the two phases are different from each other. In the case shown, the effective mass in the kaon condensed phase is about 300 MeV lower than in the nucleon phase. At the end of the mixed phase at $6.5\rho_0$, the solution for the kaon condensed phase remains and the effective mass of the nucleon stays around 200 MeV.

Finally, we discuss the mass-radius relation for a kaon condensed neutron star in Figure 3 for two choices of the optical potential of the K^- at ρ_0. The maximum mass is between $(1.6 - 1.4)M_\odot$ and does not change very much for an optical potential between $U_K = -120$ and -140 MeV. The main difference is the minimum radius reached in the two cases: for the stronger potential the minimum radius is $R = 8$ km while it is still above $R = 12$ km for the weaker potential. The dotted lines are the case when using a Maxwell construction. For some intermediate range, this curve shows a mechanical instability due to the constant pressure. For very high density, the dotted line is then close to the Gibbs construction as the pure kaon condensed phase is reached in the interior of the neutron star where the two constructions coincide. According
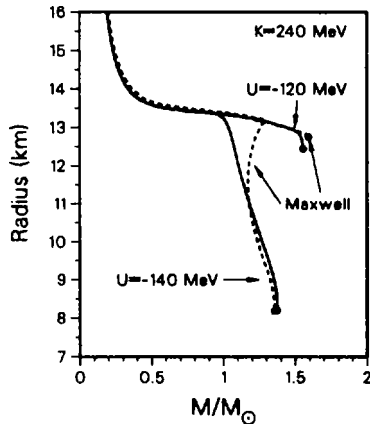
Figure 3: The mass-radius relation of a neutron star with a kaon condensed phase.

to [8], the weaker potential is the more plausible.

In summary, kaon condensation results in an equation of state without a constant pressure zone when applying Gibbs criteria. A mixed phase can exist with a rigid structure with different local charges. The mass-radius relation is considerably smoothened compared to a Maxwell construction.

The present calculation ignores two major points. Finite size effects of the structures in the mixed phase as surface tension and Coulomb energy will change the appearance and disappearance of the mixed phase. The surface tension can be calculated within the model in semi-infinite matter in a selfconsistent manner which we will pursue in the future. Secondly, the appearance of hyperons will shift the onset of kaon condensation to a higher density [10, 11] or can even lead to their disappearance [1, 12]. The inclusion of hyperons will be studied in forthcoming work.

Acknowledgments

References

[1] N. K. Glendenning, Astrophys. J. **293**, 470 (1985).

[2] D. B. Kaplan and A. E. Nelson, Phys. Lett. B **175**, 57 (1986), ibid B 179, 409 (E).

[3] G. E. Brown, K. Kubodera, M. Rho, and V. Thorsson, Phys. Lett. B **291**, 355 (1992).

[4] V. Thorsson, M. Prakash, and J. M. Lattimer, Nucl. Phys. A **572**, 693 (1994).

[5] G. E. Brown and H. A. Bethe, Astrophys. J. **423**, 659 (1994).

[6] P. B. Siegel and W. Weise, Phys. Rev. C **38**, 2221 (1988).

[7] E. Friedmann, A. Gal, and C. J. Batty, Phys. Lett. B **308**, 6 (1993).

[8] V. Koch, Phys. Lett. B **337**, 7 (1994).

[9] N. K. Glendenning, Phys. Rev. D **46**, 1274 (1992).

[10] P. J. Ellis, R. Knorren, and M. Prakash, Phys. Lett. B **349**, 11 (1995).

[11] R. Knorren, M. Prakash, and P. J. Ellis, Phys. Rev. C **52**, 3470 (1995).

[12] J. Schaffner and I. N. Mishustin, Phys. Rev. C **53**, 1416 (1996).

CONSTRAINTS ON NEUTRON STAR MATTER
FROM KILOHERTZ QPOs

F. K. LAMB[1], M. C. MILLER[2], and D. PSALTIS[3]

[1] *University of Illinois at Urbana-Champaign*
Department of Physics and Department of Astronomy
1110 W. Green St., Urbana, IL 61801, USA

[2] *University of Chicago, Department of Astronomy and Astrophysics*
5640 S. Ellis Avenue, Chicago, IL 60637, USA

[3] *Harvard-Smithsonian Center for Astrophysics*
60 Garden St., Cambridge, MA 02138, USA

Abstract

One of the most dramatic discoveries made so far with the *Rossi X-Ray Timing Explorer* is that many accreting neutron stars with weak magnetic fields generate strong, remarkably coherent, high-frequency X-ray brightness oscillations. The ~325–1200 Hz quasi-periodic oscillations (QPOs) observed in the accretion-powered emission are almost certainly produced by gas orbiting very close to the stellar surface and have frequencies related to the orbital frequencies of the gas. The ~360–600 Hz brightness oscillations seen during thermonuclear X-ray bursts are produced by one or two hotter regions on the stellar surface and have frequencies equal to the stellar spin frequency or its first overtone. Measurements of these oscillations are providing tight upper bounds on the masses and radii of neutron stars, and important new constraints on the equation of state of neutron star matter.

1 Introduction

Since the birth of X-ray astronomy 35 years ago, scientists have sought to use the X-radiation that comes from near the event horizons of black holes and the surfaces of neutron stars to probe quantitatively the strong gravitational fields near these objects and to determine the fundamental properties of dense matter (see, e.g., [2, 6]). The *Rossi X-Ray Timing Explorer* (*RXTE*), which was launched on December 30, 1995, was specially designed to have the large area, microsecond time resolution, high telemetry bandwidth, and pointing flexibility needed to address these questions (see [21]). With *RXTE*, strong, high-frequency X-ray brightness oscillations have been discovered from at least

two black holes (see [7]) and sixteen neutron stars (see [13, 23]). As a result, we appear to be on the threshold of achieving this decades-old goal of X-ray astronomy. Here we focus on the oscillations discovered in neutron stars and their implications for the properties of these stars and for neutron star matter.

2 High-Frequency Brightness Oscillations

2.1 Observed Properties

High-frequency X-ray brightness oscillations are observed both in the transient X-ray emission produced during type I (thermonuclear) X-ray bursts (see [18]) and in the persistent, accretion-powered X-ray emission (see [23]).

The high-frequency oscillations observed during X-ray bursts have frequencies in the range 360–600 Hz and rms amplitudes at least as high as ∼35% [19]. Only a single oscillation is observed during a burst, the oscillation appears to be highly coherent during the burst decay (see, e.g., [16]), and the frequency of the oscillations produced by a given star is always the same (measurements of the burst oscillations in 4U 1728−34 over about a year show that the timescale of any variation in the oscillation frequency is ≳ 3000 yr [17]). The evidence is compelling that the oscillations seen during X-ray bursts are produced by regions of brighter X-ray emission that rotate with the star, and that the frequency of the burst oscillations is the stellar spin frequency or its first overtone (see [13, 19]). The spin frequencies of these neutron stars appear to be in the range 250–350 Hz [13].

The kilohertz quasi-periodic oscillations (QPOs) observed in the persistent X-ray emission have frequencies in the range 325–1200 Hz, rms amplitudes as high as ∼15%, and quality factors $\nu/\delta\nu$ as high as ∼200 [23]. Two kilohertz QPOs are commonly observed simultaneously in a given source (see Fig. 1). Although the frequencies of the two QPOs vary by hundreds of Hertz, the frequency separation $\Delta\nu$ between them appears to be nearly constant in almost all cases (see [23]). The frequency separation of the two kilohertz QPOs observed in a given star is closely equal to the spin frequency of the star inferred from its burst oscillations (see [13, 20]).

2.2 Origin of Kilohertz QPOs

Although other types of models have been suggested [4, 22], the fact that the separation $\Delta\nu$ between the frequencies of the two kilohertz QPOs observed from a given star is closely equal to the spin frequency of the star inferred from its burst oscillations is very strong evidence in favor of beat-frequency models
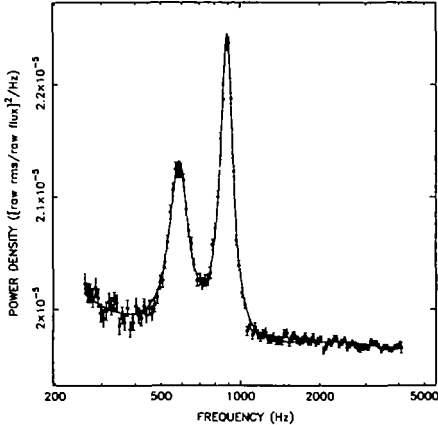
Fig. 1. Power spectrum of Sco X-1 X-ray brightness variations, showing the two simultaneous kilohertz QPOs that are characteristic of the kilohertz QPO sources. The QPOs observed in Sco X-1 are two of the weakest kilohertz QPOs detected, with rms amplitudes ~1%. The continuum power density is consistent with that expected from photon counting noise alone. From [24].

[23]. In these models, the frequency of the higher-frequency QPO is the Keplerian frequency at a special radius and the frequency of the lower-frequency QPO is the difference between the higher frequency and the spin frequency ν_{spin} of the neutron star. The magnetospheric beat-frequency model, which was developed to explain the single, ~15–60 Hz X-ray brightness oscillations discovered in the Z sources a decade ago (see [5]), has been discussed [20] as a possible explanation for the kilohertz QPOs. However, it is difficult to explain many basic features of the kilohertz QPOs using this model, including why there are *two* such QPOs (see [13]).

The most fully developed and successful model of the kilohertz QPOs is the so-called sonic-point beat-frequency model [13]. This model is based on previous work [9, 10] which showed that the drag force produced by radiation from a central star can terminate a Keplerian disk flow near the star. In the sonic-point model, some accreting gas spirals inward in nearly circular orbits until it is close to the neutron star, where radiation forces or general relativistic effects cause a sudden increase in the inward radial velocity. The radius at which this occurs is conveniently referred to as the sonic radius, even though the transition to supersonic flow is not directly relevant in this model.

The sharp increase in the inward velocity is usually caused by the drag exerted on the orbiting gas by radiation from the star, but may instead be caused by general relativistic corrections to Newtonian gravity, if the gas in the Keplerian flow reaches the innermost stable circular orbit without being
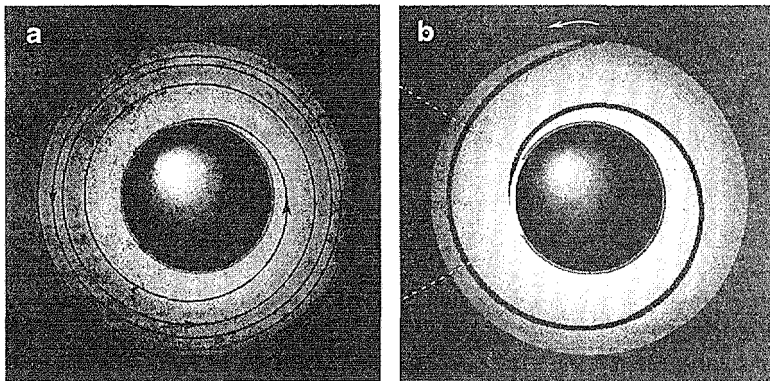
Fig. 2. View of the neutron star and accretion disk along the rotation axis of the disk, which is rotating counterclockwise in this view. (a) Spiral trajectory followed by a single element of gas as it falls supersonically from the sonic radius to the stellar surface. (b) Spiral pattern of higher gas density formed by gas streaming inward along spiral trajectories with the shape shown in (a), from a clump orbiting near the sonic radius. The trajectory and density pattern are from general relativistic gas dynamical calculations [13].

significantly affected by radiation. Gas streams inward from density fluctuations (clumps) orbiting near the sonic radius along tightly spiraling trajectories like that shown in Figure 2a, generating a more open spiral density pattern like that shown in Figure 2b. This pattern rotates around the star with the Keplerian orbital frequency at the sonic point, ν_{Ks}. Collision of the denser gas from the clumps with the stellar surface creates beams of brighter X-ray emission, like that indicated by the white dashed lines in Figure 2b. These beams move around the star's equator, generating a quasi-periodic brightness oscillation with frequency ν_{Ks}. Accreting gas is funneled to certain parts of the stellar surface by the star's weak magnetic field, producing weak X-ray beams that rotate *with the star*. These beams are overtaken by a given orbiting clump once each beat period, so the inward mass flux from the clumps, and hence the accretion luminosity, varies at the sonic-point beat frequency $\nu_{Ks} - \nu_{spin}$.

The sonic-point model explains naturally why the separation between the frequencies of the two kilohertz QPOs is nearly constant and equal to the burst oscillation frequency or half this frequency. It is also consistent with the accretion rates and stellar magnetic fields inferred previously and accounts

for the main features of the kilohertz QPOs, including their high and variable frequencies, their high amplitudes and coherences, and the common occurrence of two simultaneous kilohertz QPOs [13].

3 Constraints from Kilohertz QPOs

3.1 Nonrotating Stars

In order to see how constraints on the equation of state of neutron star matter can be derived, suppose first that the star is not rotating and assume that, for the star in question, ν_{QPO2}^*—the highest observed value of the frequency of the higher-frequency (Keplerian-frequency) QPO in the kilohertz QPO pair—is 1220 Hz (this is the highest QPO frequency detected so far from any neutron star; see [13]). Obviously, the orbital radius R_{orb} of the clumps producing the QPO must be greater than the stellar radius; R_{orb} must also be greater than the radius R_{ms} of the innermost stable circular orbit in order for the clumps to produce a wave train that lasts tens of oscillation periods, as observed. These requirements constrain the representative point of the star to lie in a pie-slice shaped region of the radius-mass plane (see Fig. 3a). This bounds the mass and radius of the star from above. In terms of ν_{QPO2}^*, these bounds are [13]

$$M_{\text{max}}^0 = 2.2\,(1000\,\text{Hz}/\nu_{\text{QPO2}}^*)\,M_\odot \quad \text{and} \quad R_{\text{max}}^0 = 19.5\,(1000\,\text{Hz}/\nu_{\text{QPO2}}^*)\,\text{km.} \quad (1)$$

Figure 3b compares the regions of the radius-mass plane allowed for three values of ν_{QPO2}^* with the mass-radius relations for nonrotating stars given by five representative equations of state.

3.2 Rotating Stars

Rotation affects the structure of the star and the spacetime, altering the region of the radius-mass plane allowed by a given value of ν_{QPO2}^*. Slow rotation expands the allowed region whereas rapid rotation shrinks it greatly. The parameter that characterizes the importance of rotational effects is the dimensionless quantity $j \equiv cJ/GM^2$, where J and M are the angular momentum and gravitational mass of the star. For the spin frequencies ~300 Hz inferred for the neutron stars in the kilohertz QPO sources, j is ~ 0.1–0.3, depending on the mass of the star and the equation of state. For such small values of j, the structure of the star is almost unaffected and a treatment that is first-order in j is adequate. To this order, the existence of upper bounds on the mass and radius can be proved analytically [13]. The bounds for prograde orbits are

$$M_{\text{max}} \approx [1 + 0.75j(\nu_{\text{spin}})]M_{\text{max}}^0 \quad \text{and} \quad R_{\text{max}} \approx [1 + 0.20j(\nu_{\text{spin}})]R_{\text{max}}^0 , \quad (2)$$
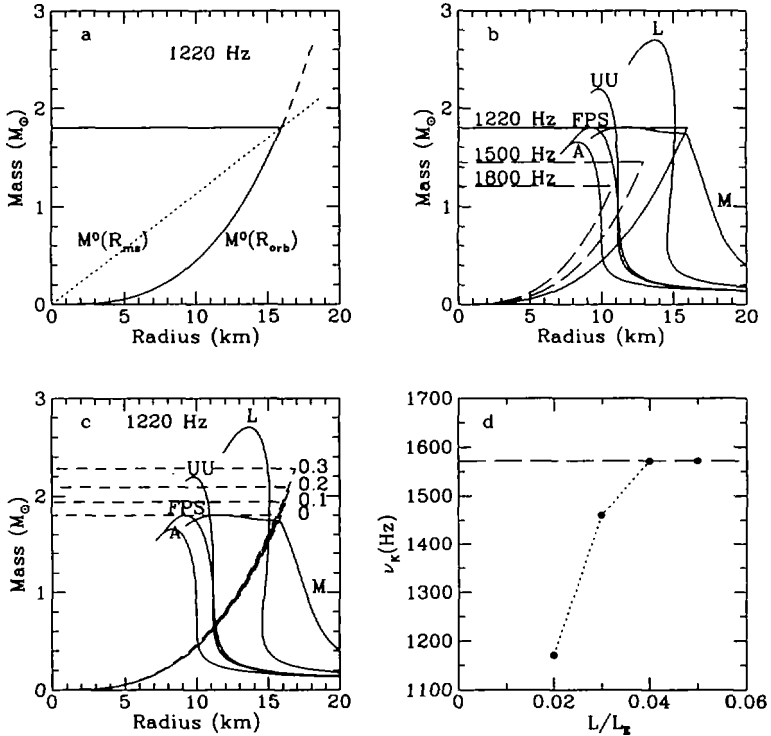
Fig. 3. (a) Radius-mass plane, showing how to construct the region allowed for a nonrotating neutron star with $\nu^*_{\rm QPO2} = 1220$ Hz. $R_{\rm orb}$ must be greater than the stellar radius, so the star's representative point must lie to the left of the (dashed) cubic curve $M^0(R_{\rm orb})$ that relates the star's mass to the radius of orbits with frequency 1220 Hz. The high coherence of the oscillations constrains $R_{\rm orb}$ to be greater than $R_{\rm ms}$, the radius of the innermost stable orbit, which means that the radius of the actual orbit must lie on the $M^0(R_{\rm orb})$ curve below its intersection with the (dotted) straight line $M^0(R_{\rm ms})$ that relates the star's mass to $R_{\rm ms}$. These requirements constrain the star's representative point to lie in the pie-slice shaped region enclosed by the solid line. (b) Comparison of the regions allowed for nonrotating stars with three different QPO frequencies with the mass-radius relations for nonrotating neutron stars given by five representative equations of state. (c) Regions allowed for rotating neutron stars with four values of j and $\nu^*_{\rm QPO2} = 1220$ Hz, when effects of the stellar spin are included to first-order (see text). (d) Illustrative Keplerian QPO frequency vs. accretion luminosity curve predicted by the sonic-point model.
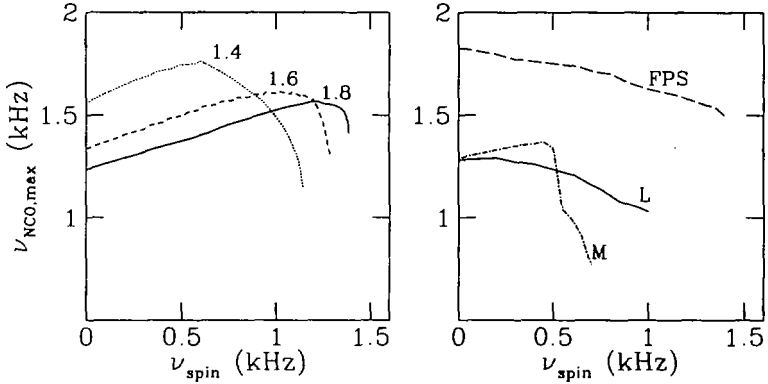
Fig. 4. (a) Maximum frequency of a nearly circular orbit as a function of stellar spin frequency for equation of state FPS and stars with $1.4\,M_\odot$ (dotted line), $1.6\,M_\odot$ (dashed line), and $1.8\,M_\odot$ (solid line) gravitational masses. (b) Maximum frequency of a nearly circular orbit for a star of *any* mass, for the three equations of state indicated. See [12] for details and further discussion.

where $j(\nu_{\rm spin})$ is the value of j for the observed stellar spin rate *at the maximum allowed mass for the equation of state being considered* and $M_{\rm max}^0$ and $R_{\rm max}^0$ are the bounds on the mass and radius for a nonrotating star (see eqs. [1]). Equations (2) show that the region allowed for a slowly rotating star is always larger than the region allowed for a nonrotating star, regardless of the equation of state. Figure 1c illustrates the effects of slow stellar rotation on the allowed region of the radius-mass plane. Detailed calculations show that the mass of the neutron star in 4U 1636−536 must be less than $2.2\,M_\odot$ and its radius must be less than 17 km. The upper bounds may be smaller, depending on the equation of state assumed [13, 14].

For spin frequencies $\gtrsim 400$ Hz, the structure of the star can be significantly affected, as well as the exterior spacetime. In this case both the structure of the star and the spacetime must be computed numerically for each assumed equation of state. Determination of the bounds on the mass and radius of a star for a given QPO frequency and equation of state therefore requires construction of a sequence of stellar models and spacetimes for different masses using the equation of state, with $\nu_{\rm spin}$ as measured at infinity held fixed [13]. Such sequences have been constructed [12] and show that if the neutron star is spinning rapidly, the constraints on the equation of state are tightened dra-

matically. For example, if the ~580 Hz burst oscillation frequency observed in 4U 1636−536 is its spin frequency (rather than twice its spin frequency as indicated by the frequency separation of its two kilohertz QPOs), then very stiff equations of state like the tensor-interaction equation of state [15] are excluded by the 1220 Hz QPO already observed from this star. Regardless of the star's spin rate, a 1500 Hz QPO frequency would constrain the mass and radius of the neutron star to be less than ~$1.7\,M_\odot$ and ~13 km, ruling out several equations of state that are currently astrophysically viable [12].

Figure 4a shows why slow rotation typically loosens the constraints on mass and radius implied by a given QPO frequency, whereas rapid rotation tightens them. At low spin rates the equatorial radius of the star is smaller than the radius of the innermost stable orbit and hence the maximum orbital frequency increases linearly with the star's spin rate (see eqs. [2]). In contrast, at high spin rates the equatorial radius becomes larger than the radius of the circular orbit that would be marginally stable, so no marginally stable orbit exists. The highest frequency orbit for a star of given mass is then the one just above the stellar surface, which increases in radius as the star spins faster, causing the highest possible orbital frequency to decrease with increasing spin rate. Figure 4b displays the maximum frequency of a nearly circular orbit for a star of *any* mass, for three different equations of state. Hence, if *any* neutron star is found to have spin and QPO frequencies that place its representative point above one of these curves, that equation of state is excluded.

3.3   Innermost Stable Circular Orbit

Establishing that an observed QPO frequency is the orbital frequency of the innermost stable circular orbit in an X-ray source would be an important step forward in our understanding of strong-field gravity and the properties of dense matter, because it would be the first confirmation of a prediction of general relativity in the strong-field regime and would also fix (for each equation of state) the mass of the neutron star involved.

Given the fundamental significance of the detection of an innermost stable orbit, it is very important to establish what would constitute strong, rather than merely suggestive, evidence that the innermost stable orbit has been detected. Probably the most convincing signature would be a kilohertz QPO with a frequency that reproducibly increases steeply with increasing accretion rate but then becomes constant and remains nearly constant as the accretion rate increases further. This behavior emerges naturally from general relativistic calculations of the gas dynamics and radiation transport in the sonic-point

model (see Fig. 3d). The constant frequency should always be the same in a given source. Two other possible signatures of the innermost stable orbit are discussed in [13].

Several authors have recently suggested that innermost stable orbits have already been observed. Zhang et al. [27] suggested that the similarity of the highest QPO frequencies seen so far indicates that innermost stable orbits are being detected and that, based on the equations (1) for nonrotating stars, the neutron stars in *all* the kilohertz QPO sources therefore have masses close to $2.0\,M_\odot$. Kaaret, Ford, & Chen [3] suggested that the ~800–900 Hz QPOs discovered in 4U 1608−52 [1] and 4U 1636−536 [26], which were initially observed to have roughly constant frequencies, are generated by the beat of the spin frequency against the frequency of innermost stable orbits in these sources. However, *no clear signature of an innermost stable circular orbit has so far been seen in any source.*

Indeed, subsequent observations of both 4U 1608−52 [8] and 4U 1636−536 [25] are inconsistent with the interpretation that the frequencies of the QPOs seen initially are related to the frequencies of innermost stable orbits around these stars. The 1171 Hz QPO seen by Zhang et al. [26], which was assumed by Kaaret et al. [3] to be at the frequency of the innermost stable orbit in 4U 1636−536 in order to estimate the mass of the star, was later seen at 1193 Hz [25] and still later at 1220 Hz (W. Zhang, personal communication). Hence, there is as yet no evidence for a maximum QPO frequency in 4U 1636−536 and hence there is no basis for the suggestion that an innermost stable orbit has been seen in this source. A recent analysis of 4U 1608−52 data by Méndez et al. [8] shows that this source has two kilohertz QPOs that vary with countrate just like the other sources. There is as yet no evidence for a maximum QPO frequency in 4U 1608−52 and hence there is no basis for the suggestion that an innermost stable orbit has been seen in this source, either.

4   Constraints from Burst Oscillations

As noted in §2, the strong (rms amplitudes up to at least 35%), high-frequency oscillations seen during X-ray bursts are thought to be caused by emission from a single or two nearly antipodal bright regions on the stellar surface, which produce large amplitude brightness oscillations at the stellar spin frequency or its first overtone as the star turns. The anisotropy at infinity of the radiation emitted from such regions, and hence the amplitude of the burst oscillation, typically decreases with increasing gravitational light deflection by the star. Hence, in addition to any constraints on the radius of the star that may be
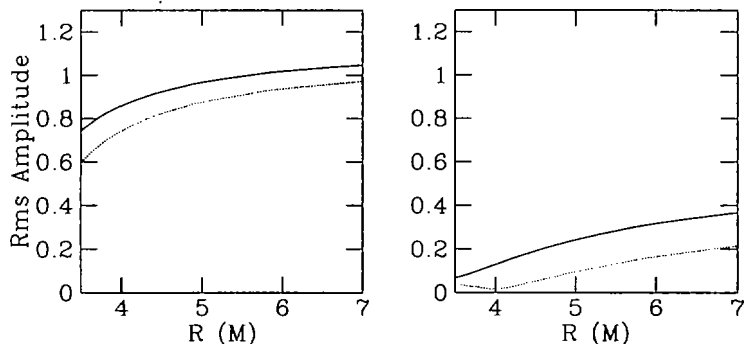
Fig. 5. Upper bounds on the observed fractional rms amplitude of oscillations in the photon number flux during bursts, as a function of neutron star radius. The observer's line of sight is assumed to be in the rotational equator and the aberration and Doppler shifts caused by rotation are neglected. (a) Amplitude as a function of neutron star radius for isotropic emission (dotted line) or the peaked emission expected for a scattering atmosphere (solid line) from a single point. (b) Amplitude as a function of radius for the same intensity distributions as in (a), but for emission from two identical, antipodal emitting points. See [11] for details of the computational method and further discussion.

derived from the X-ray spectra of the bursts, constraints on the compactness of the star (and hence the softness of neutron star matter) can be derived from the observed amplitudes of the burst oscillations [11, 17]. Such constraints are particularly useful because they complement the constraints derived from the kilohertz QPOs, which constrain the stiffness of neutron star matter.

Figure 5 shows results typical of general relativistic calculations of the maximum amplitudes of burst oscillations from one or two bright regions, as a function of stellar radius. *Photon counting rate* oscillations with 2–60 keV rms amplitudes as high as $\sim$35% have been reported in 4U 1636$-$536 with a frequency equal to twice the apparent spin frequency of this neutron star. Figure 5b shows that an oscillation this large in the *photon number flux* would constrain the radius of this star to be greater than 5.5 M. However, the amplitude of the countrate oscillation measured at infinity can be larger or smaller than the amplitude of the oscillation in the photon flux at the star, depending on the detector response as well as the angular dependence and spectrum of the emission from the stellar surface, the stellar spin rate, and whether there is any scattering material surrounding the star, so more detailed modeling will be required to extract the actual constraints on the compactness (see [11]).

5   Concluding Remarks

The discovery using the *Rossi X-Ray Timing Explorer* that many neutron stars with weak magnetic fields produce strong ~300–1200 Hz X-ray brightness oscillations is a spectacular achievement that validates both the scientific expectations that led to the mission and the long years of hard work that were needed to bring it to fruition. The kilohertz QPOs discovered in the accretion-powered emission are already providing interesting new upper bounds on the masses and radii of neutron stars, and on the stiffness of neutron star matter. The high-frequency oscillations discovered in the emission during thermonuclear X-ray bursts are likely to provide interesting new bounds on the compactness of neutron stars and hence on the softness of neutron star matter. Observation of a QPO with a frequency just 100 Hz higher than the highest frequency so far seen would exclude the stiffest proposed neutron star matter equations of state.

Observation of innermost stable circular orbits would be the first confirmation of a strong-field prediction of general relativity and would fix the mass of the star involved, for each equation of state considered. Although there is currently no strong evidence that an innermost stable circular orbit has been discovered around any of these neutron stars, there is reason to hope that such evidence may be forthcoming. Given the rapid pace of discoveries with *RXTE*, the prospects for obtaining compelling evidence of an innermost stable circular orbit appear good.

References

[1] Berger, M., et al. 1996, ApJ, 469, L13

[2] Epstein, R., Lamb, F. K., & Priedhorsky, W. 1986, Astrophysics of Time Variability in X-Ray and Gamma-Ray Sources, Los Alamos Science, No. 13

[3] Kaaret, P., Ford, E. C., & Chen, K. 1997, ApJ, 480, L27

[4] Klein, R. I., Jernigan, J. G., Arons, J., Morgan, E. H., & Zhang, W. 1996, ApJ, 469, L119

[5] Lamb, F. K. 1991, in Neutron Stars: Theory and Observation, ed. J. Ventura & D. Pines (Dordrecht: Kluwer), 445

[6] Lamb, F. K., & Pines, D. 1979, Compact Galactic X-Ray Sources (Urbana: Univ. of Illinois Physics Dept.)

[7] McClintock, J. E. 1998, in Accretion Processes in Astrophysical Systems, ed. S. Holt & T. Kallman (AIP Conf. Proc.), in press (astro-ph/9802080)

[8] Méndez, M., et al. 1998, ApJ, 494, L65

[9] Miller, M. C., & Lamb, F. K. 1993, ApJ, 413, L43

[10] ———. 1996, ApJ, 470, 1033

[11] ———. 1998, ApJ, in press (astro-ph/9711325)

[12] Miller, M. C., Lamb, F. K., & Cook, G. 1998, ApJ, submitted

[13] Miller, M. C., Lamb, F. K., & Psaltis, D. 1998, ApJ, in press (astro-ph/9609157)

[14] ———. 1998, ApJ, in preparation

[15] Pandharipande, V. R., & Smith, R. A. 1975, Nucl. Phys., A237, 507

[16] Smith, D. A., Morgan, E., H., & Bradt, H. 1997, ApJ, 479, L137

[17] Strohmayer, T. E., talk presented at the 1997 November meeting of the High Energy Astrophysics Division of the American Astronomical Society

[18] Strohmayer, T. E., Swank, J. H., & Zhang, W. 1998, in The Active X-Ray Sky, eds. L. Scarsi, H. Bradt, P. Giommi, and F. Fiore, Nucl. Phys. B Proc. Suppl., in press (astro-ph/9801219)

[19] Strohmayer, T. E., Zhang, W., & Swank, J. H. 1997, ApJ, 487, L77

[20] Strohmayer, T., Zhang, W., Swank, J. H., Smale, A., Titarchuk, L., & Day, C. 1996, ApJ, 469, L9

[21] Swank, J., et al. 1995, in The Lives of Neutron Stars, ed. M. A. Alpar, Ü. Kızıloğlu, & J. van Paradijs (Dordrecht: Kluwer), 525

[22] Titarchuk, L., & Muslimov, A. 1997, A&A, 323, L5

[23] van der Klis, M. 1998, in The Many Faces of Neutron Stars, Proc. NATO ASI, Lipari, Italy (Dordrecht: Kluwer), in press (astro-ph/9710016)

[24] van der Klis, M., Wijnands, R., Horne, K., & Chen, W. 1997, ApJ, 481, L97

[25] Wijnands, R.A.D., et al. 1997, ApJ, 479, L141

[26] Zhang, W., Lapidus, I., White, N. E., & Titarchuk, L. 1996, ApJ, 469, L17

[27] Zhang, W., Strohmayer, T., & Swank, J. H. 1997, ApJ, 482, L167

PHASE TRANSITION SIGNAL IN PULSAR TIMING

Norman K. GLENDENNING

Nuclear Science Division & Institute for Nuclear and Particle Astrophysics,
Lawrence Berkeley National Laboratory,
MS: 70A-3307, Berkeley, California 94720

Abstract

A phase transition in the nature of matter in the core of a neutron star, such as quark deconfinement or Bose condensation, can cause the spontaneous spin-up of a solitary millisecond pulsar. The spin-up epoch for our model lasts for 2×10^7 years or 1/50 of the spin-down time (Glendenning, Pei and Weber in Ref. [1]). The possibility exists also for future measurements on X-ray neutron stars with low-mass companions for mapping out the tell-tale "backbending" behavior of the moment of inertia. Properties of phase transitions in substances such as neutron star matter, which have more than one conserved charge, are reviewed.

1 Introduction

Neutron stars have a high enough interior density as to make phase transitions in the nature of nuclear matter a distinct possibility. Examples are hyperonization, negative Bose condensation (like π^- and K^-) and quark deconfinement. According to the QCD property of asymptotic freedom, the most plausible is the quark deconfinement transition. From lattice QCD simulations, this phase transition is expected to occur in very hot ($T \sim 200$ MeV) or cold but dense matter. In this work we will use the deconfinement transition as an example, but in principle, any transition that is accompanied by a sufficient softening of the equation of state and occurs at or near the limiting mass star, can produce a similar signal.

The paper is organized as follows. We discuss first the physical reason why a rapidly rotating pulsar, as it slows down over millions of years because of angular momentum loss through the weak electromagnetic process of magnetic dipole radiation, will change in density due to weakening centrifugal forces and possibly encounter, first at its center, and then in a slowly expanding region, the conditions for a phase transition. Conversely, an accreting star will be spun up from low to high frequency by accretion from a low-mass companion.

This too will have a very long time-scale because accretion is regulated by the radiation pressure of the star's surface, heated by infalling matter.

After having discussed the reasons why we might see signals of phase changes, both in rapidly rotating stars that are spinning down because of angular momentum loss to radiation and stars that are spinning up due to the input of angular momentum by accretion, we discuss some aspects of phase transitions that are common to all first order transitions in neutron star matter, or more generally in isospin asymmetric matter.

2 Effects of Phase Transitions on Rotating Stars

2.1 Evolutionary Path of Neutron Stars

Since neutron stars are born with almost the highest density that they will have in their lifetime, being very little deformed by centrifugal forces, they will possess cores of the high density phase essentially from birth if the critical density falls in the range of neutron stars. However the global properties, such as mass or size, of a slowly rotating neutron star are little effected by whether or not it has a more compressible phase in the core. In principle, cooling rates should depend on interior composition, but cooling calculations are beset by many uncertainties and competing assumptions about composition can yield similar cooling rates depending on other assumptions about superconductivity and the cooling processes. Moreover, for those stars for which a rate has been measured, not a single mass is known. It is unlikely that these measurements will yield conclusive evidence in the present state of uncertainty [2, 3].

Nevertheless, it may be possible to observe the phase transition in millisecond pulsars by the easiest of measurements—the sign of $\dot{\Omega}$. Normally the sign should be negative corresponding to loss of angular momentum by radiation. However a phase transition that occurs near or at the limiting mass star, can cause spin-up during a substantial era compared to the spin-down time · of millisecond pulsars. The transition may be of either first or second order provided that it is to an appreciable more compressible phase. We sketch the conventional evolutionary history [4] of pulsars with the addition of the supposition that the critical density for quark deconfinement falls in the density range spanned by neutron stars.

As already remarked, with the supposition above, the star has a quark core from birth but its properties are so little effected that this fact cannot be discerned in members of the canonical pulsar population. It is born with moderate rotation period, acquired by the conservation of angular momentum during core collapse and with high magnetic field by flux conservation. In
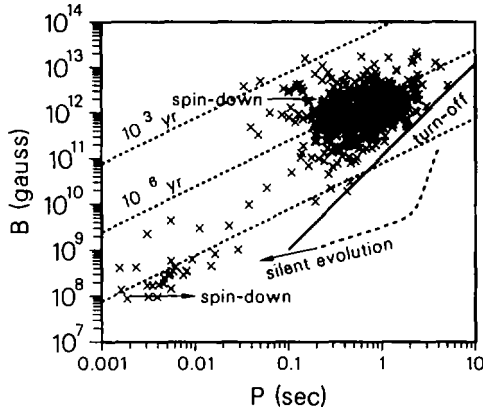
Figure 1: The evolutionary track of pulsars are from high mag-
netic field and moderate rotation period to long period in about
10^7 to 10^8 years, to accreting X-ray neutron stars, to millisecond
pulsars with low magnetic fields.

a diagram of magnetic field strength B and rotation period P (Fig. 1), it is
injected near the line marked 10^3 years (since birth) and with $B \sim 10^{13}$ gauss.
It evolves quickly at constant B toward longer period for $\sim 10^6$ to 10^8 years.
There it lingers with the bulk of the pulsar population at long periods (because
$\dot{P} \sim 1/P$) before the combination of field strength and rotation period are
insufficient to accelerate charged particles that produce the radiation. At that
time the star has entered the radio silent epoch. Some pulsars will have had
a less dense companion or will acquire one from which they accrete matter
and angular momentum. Some will be seen as X-ray emitters during the radio
silent phase. During spin-up to frequencies much higher than those with which
pulsars are born, the neutron star becomes increasingly centrifugally deformed
and its interior density falls. Consequently, the radius at which the critical
phase transition density occurs moves toward the center of the star—quarks
that were deconfined at the birth of the star, recombine to form hadrons. (This
era may also be detectable as discussed in section 2.4.) When accretion ceases,
and if the neutron star has been spun up to a state in which the combination of
reduced field strength (perhaps to ohmic decay) and increased frequency turn

the dipole radiation on again, the pulsar recommences spin-down as a radio visible millisecond pulsar.

During spin-down as a millisecond pulsar, the central density increases with decreasing centrifugal force. First at the center of the star, and then in an expanding region, the highly compressible quark matter will replace the less compressible nuclear matter. The quark core, weighed down by the overlaying layers of nuclear matter is compressed to high density, and the increased central concentration of mass acts on the overlaying nuclear matter, compressing it further (see Figs. 2 and 3). The resulting decrease in the moment of inertia causes the star to spin up to conserve angular momentum not carried off by radiation. The phenomenon is analogous to that of "backbending" predicted for rotating nuclei by Mottelson and Valatin [5] and discovered in the 1970's [6, 7] (see Fig. 4). In nuclei, it was established that the change in phase is from a particle spin-aligned state at high nuclear angular momentum to a superfluid state at low angular momentum. The phenomenon is also analogous to an ice skater who commences a spin with arms outstretched. Initially spin decreases because of friction and air resistance, but a period of spin-up is achieved by pulling the arms in. Friction then reestablishes spin-down. In all three examples, spin up is a consequence of a decrease in moment of inertia beyond what would occur in response to decreasing angular velocity.

2.2 Calculation

In our calculation, nuclear matter was described in a relativistically covariant theory [8, 9, 10] and quark matter in the MIT bag model [11]. The phase transition occurs in a substance of two conserved quantities, electric charge and baryon number, and must be found in the way described in Ref. [12] and in Section 3. The moment of inertia must incorporate all effects described above—changes in composition of matter, centrifugal stretching—and frame dragging, all within the framework of General Relativity. The expression derived by Hartle is inadequate because it neglects these effects [13, 14]. Rather we must use the expression derived by us [15, 16].

For fixed baryon number we solve General Relativity for a star rotating at a sequence of angular velocities corresponding to an equation of state that describes the deconfinement phase transition from charge neutral nuclear matter to quark matter. The equation of state is shown in Fig. 5. The moment of inertia as a function of angular velocity does not decrease monotonically as it would for a gravitating fluid of constant composition. Rather, as described above, the epoch over which an enlarging central region of the star enters the
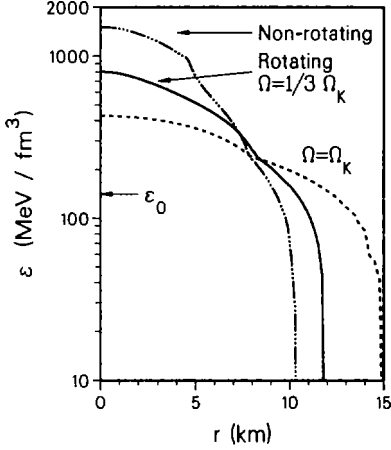
Figure 2: Energy density profiles star at three rotation rates. Notice the 5 km radius quark matter core when the star is not rotating (or only slowly as a canonical pulsar). Mixed phase extends to 8 km.
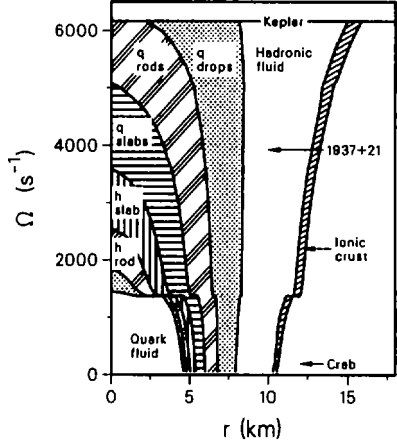
Figure 3: Radial boundaries between different phases for stars of mass indicated on the y axis. Composition consists of quarks, the baryon octet and leptons. The geometric phases will be discussed in Section 3.

more compressible phase is marked by spin-up (Fig. 6). Does the spin-up epoch endure long enough to provide a reasonable chance of observing it some members of the pulsar population? This question we turn to now.

2.3 Spin-up Era

To estimate the duration of the spin-up, we solve the deceleration equation for the star with moment of inertia having the behavior shown in Fig. 6. From the energy loss equation

$$\frac{dE}{dt} = \frac{d}{dt}\Big(\frac{1}{2}I\Omega^2\Big) = -C\Omega^4 \tag{1}$$
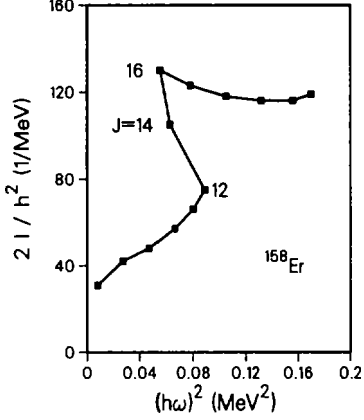
Figure 4: Nuclear moment of inertia as a function of squared frequency for ^{158}Er, showing backbending in the nuclear case.
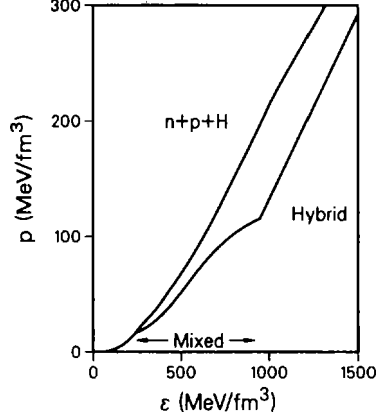
Figure 5: Equation of state for the fist order deconfinement phase transition described in the text.

for magnetic dipole radiation we find

$$\dot{\Omega} = -\frac{C}{I(\Omega)}\left[1 + \frac{I'(\Omega)\,\Omega}{2I(\Omega)}\right]^{-1}\Omega^3\,. \tag{2}$$

This expression reduces to the usual braking equation when the moment of inertia is held fixed. The braking index is a dimensionless combination of three quantities that are observable in principle, namely the angular velocity and its first two time derivatives. It is generally thought to have a constant value, namely 3, for magnetic dipole radiation. However constancy would follow only if the star rotated rigidly. Instead it varies with angular velocity and therefore time according to

$$n(\Omega) \equiv \frac{\Omega\ddot{\Omega}}{\dot{\Omega}^2} = 3 - \frac{3I'\Omega + I''\Omega^2}{2I + I'\Omega} \tag{3}$$

where $I' \equiv dI/d\Omega$ and $I'' \equiv dI^2/d\Omega^2$. This holds in general even for a star whose internal composition does not change with angular velocity (inconceivable). In particular one can see that for very high frequency, the derivatives

will be largest and the braking index for any millisecond pulsar near the Kepler frequency will be less than the dipole value of $n = 3$.
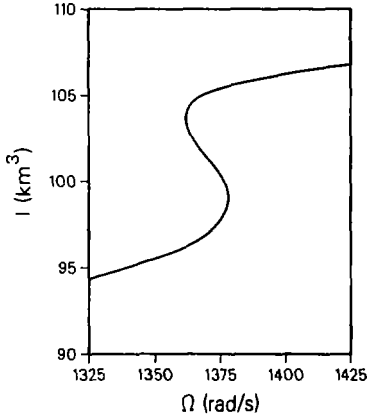
Figure 6: Moment of inertia of corresponding to a change of phase. Time flows from large to small I.
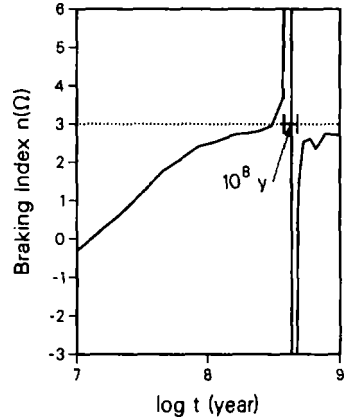
Figure 7: The time evolution of the braking index plotted over two decades that include the epoch of the phase transition.

The braking index is shown as a function of time in Fig. 7. An anomalous value endures for 10^8 years corresponding to the slow spin down of the pulsar and the corresponding slow envelopment of a growing central region by the new phase. The two points that go to infinity correspond to the infinite derivatives of I at which according to (2), the deceleration vanishes. They mark the boundaries of the spin-up era. The actual spin-up lasts for 2×10^7 years or $1/50$ of the spin-down time for this pulsar. This could be easily observed in a solitary pulsar and would likely signal a phase transition.

2.4   X-Ray Pulsars in Low Mass Binaries

As Lamb has discussed in this volume, neutron stars that are accreting mass that is channeled to their surface from a low-mass companion have been observed to rotate in the millisecond range. One of the goals in those studies is to observe phenomena associated with the last stable orbit. Mass, radius, pulsar

frequency and the frame dragging frequency can be determined in principle, and it is the goal of the experiments to do so. From the combination of the frame dragging frequency and radius, the moment of inertia can be obtained as

$$I = \frac{1}{2}\frac{\omega}{\Omega}R^3 \qquad \text{(gravitational units)} \qquad (4)$$

where the frame dragging angular velocity $\omega(R)$ corresponds to R, and Ω is the rotational angular velocity of the pulsar. A few such sets of data corresponding to stars of the same mass would represent points on a plot of moment of inertia vs. angular velocity, as in Fig. 6. If indeed quark matter cores exist in slower pulsars, then the possibility exists that some of the X-ray emitters will lie on the upper branch and others on the lower branch. Even if one did not have observations that lay on the backbend, observations that established the existence of two assymptotes would be quite convincing evidence of a different phase on the two branches.

3   Properties of Phase Transitions

We discuss briefly phase transitions of interest in nuclear and nuclear astro physics. These include pion condensation [17], hyperonization [18], kaon condensation [19], quark deconfinement in stars [20] and recently, H-dibaryon Bose condensation [21].

3.1   Maxwell Construction

Depending on the model or strength of coupling, the above transitions may be first or second order. Until recently [22] first order phase transitions in nuclear matter or neutron star matter (nuclear matter in equilibrium under the constraint of charge neutrality), where implemented with some variant of the Maxwell construction (eg. tangent slope ($\mu = d\epsilon/d\rho$)). Obviously the Maxwell construction can make only one chemical potential common to phases in equilibrium, and is a valid construction for simple substances with one independent component, such as water. However, nuclear systems have two or more conserved charges (baryon and electric charge in the case of neutron star matter or low density nuclear matter, and strangeness in addition on the time-scale of high-energy reactions). For such substances, a little reflection reveals that the chemical potential that is rendered common in the Maxwell construction is neither the baryon nor charge chemical potential but a varying

combination according to the varying composition of matter as a function of baryon density.

The Maxwell construction causes the pressure to be constant in the mixed phase. (This is obvious from the tangent construction in which the energy is a linear function of volume, $E = -pV + \mu N$ (with p and μ constants of the construction) and hence the pressure, $-dE/dV$, is constant.) The consequence for stellar structure is striking: the mixed phase is absent in the monotonic pressure environment of a star and there is a large density discontinuity at the radial point corresponding to the constant pressure of the mixed phase. Inside this radial point the dense quark matter resides; outside is the less dense nuclear matter.

In some work, phase transitions were implemented in a different but equivalent fashion. Charge neutrality was enforced by requiring the charge density to vanish identically. This is valid in either pure uniform phase. However when applied to the mixed phase it is too stringent a way of enforcing charge neutrality. All that is required by the balance of Coulomb and gravitational forces is that the star be charge neutral to a high degree ($Z_{net}/A \leq (m/e)^2 \approx 10^{-36}$); not that the charge density vanishes identically. *Global* neutrality ($\int q(r)dV = 0$) is all that is required. Indeed, when the details are examined, it will be seen that *local* neutrality is incompatible with Gibbs criteria for phase equilibrium. Gibbs conditions and the conservation laws can be satisfied simultaneously only when the conservation laws are imposed in a global sense.

3.2 Gibbs Equilibrium

We briefly review how to find the conditions for phase equilibrium in substances of more than one conserved charge that are in accord with Gibbs criteria for chemical, mechanical and thermal equilibrium [22]. For definiteness we consider a system with two conserved charges (or independent components), namely, baryon number and electric charge number and refer to the phases as 1 and 2. Gibbs conditions are summarized in

$$p_1(\mu_n, \mu_e) = p_2(\mu_n, \mu_e) \tag{5}$$

where μ_n and μ_e are the chemical potentials corresponding to baryon number and electric charge. We understand that temperature T is held fixed. (It is small on the nuclear scale within several seconds of birth of a neutron star, and can set it to zero.) The above equation must hold in conjunction with expressions for the conservation of baryon and charge number, B and Q. The unknowns are the two chemical potentials and the volume V of the sample

containing the charges. (V is not the volume of the star but any *locally inertial* volume in the star, one in which the laws of special relativity hold to high precision [23].) For a volume fraction $\chi = V_2/V$ of phase 2, the conditions of global conservation can be expressed (for a uniform region) as

$$\frac{1}{V} \int_V \rho(r) dr = (1 - \chi)\rho_1(\mu_n, \mu_e) + \chi\rho_2(\mu_n, \mu_e) \equiv \frac{B_1 + B_2}{V} = \frac{B}{V} \quad (6)$$

$$\frac{1}{V} \int_V q(r) dr = (1 - \chi)q_1(\mu_n, \mu_e) + \chi q_2(\mu_n, \mu_e) \equiv \frac{Q_1 + Q_2}{V} = \frac{Q}{V} \quad (7)$$

where $B_{1,2}$ and $Q_{1,2}$ are the baryon and charge numbers, $\rho_{1,2}$ and $q_{1,2}$ are the baryon and charge densities in the volumes V_1 and V_2 occupied respectively by the two phases. The above three equations (5-7) serve to determine the two independent chemical potentials μ_n, μ_e and volume V for a *specified* volume fraction χ of phase '2' in equilibrium with phase '1'. Thus the solutions are of the form

$$\mu_n = \mu_n(\chi), \quad \mu_e = \mu_e(\chi), \quad V = V(\chi) . \quad (8)$$

The equilibrium condition (5) therefore can be rewritten as

$$p_1(\chi) = p_2(\chi) . \quad (9)$$

This shows, as concerns the bulk properties, that the common pressure and all properties of the phases in equilibrium vary as the proportion χ and that the pressure of a multi-component system in the mixed phase is not in general constant. These are fundamentally different properties for phase equilibrium of multi-component substances; they contrast with the properties of single-component substances such as water, in which the properties are independent of the proportion of the phases. For nuclear systems, the only exception to the above conclusion is for symmetric nuclear matter. In that case the system, by preparation, is optimum, and no rearrangement of conserved charges will take place.

3.3   Internal Driving Forces

We discuss now the microphysics responsible for variation of all properties of the phases in equilibrium as their proportion varies. It is clear from the above discussion that there is a degree (or degrees) of freedom in a multi-component substance that can be exploited by the internal forces to lower the energy. To

see this, consider the concentration of the conserved quantities in both of the pure phases. It is some definite number

$$c = Q/B \tag{10}$$

according to the way the system was prepared whether in a test tube by a chemist, or in a neutron star by nature through the partially chaotic processes of a supernova. The degree(s) of freedom that the system can exploit to find the energy minimum in the mixed phase is that of rearranging the concentration of the conserved charges in each phase in equilibrium

$$c_1 = Q_1/B_1 , \qquad c_2 = Q_2/B_2 \tag{11}$$

subject to the overall conservation laws (6,7). More generally, if the system is composed of n conserved charges, there are $n - 1$ such degrees of freedom. In particular, a single component substance does not possess any freedom which is why the pressure and all properties of the two phases remain the same for all proportions of the phases in equilibrium (like water and ice).

In nuclear matter the internal force that drives the redistribution of charge allowed by the conservation laws is the isospin symmetry force that is responsible for the valley of beta stability. About half the symmetry energy arises from the Fermi energy and (in our model) the other half to the coupling of isospin to the ρ meson. Neutron star matter is highly isospin asymmetric. When conditions (say of increasing pressure toward the center of the star) cause a small amount of nuclear matter to transform to the other phase, the isospin driving force will exchange charge between regions of the two phases so as to make the neutron star matter more symmetric (positively charged) to the extent permitted by the conservation laws. The other phase will have a corresponding negative charge. The scope for exchanging charge, changes with the fraction of new phase (hence the non-linearity of energy with volume and the variation of pressure with volume). We show in Fig. 8 how the charge density in each phase varies as their proportion while the total charge is zero. (In the special case of isospin symmetric matter, the concentration is already optimum and the pressure will not vary in the mixed phase.)

The case in which electric charge is one of the conserved quantities is special. Because Coulomb is a long-range force, charges will arrange themselves so as not to create large volumes of like charge. Regions of the two oppositely charged phases will tend to shield each other. The surface interface energy resists breakup into small regions. The competition will define the dimensions of charged regions and their spacing as described next.
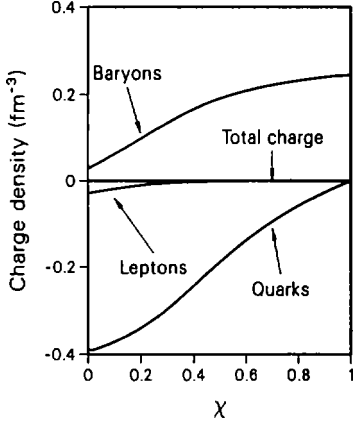
Figure 8: The charge density carried by regions of confined and deconfined phases, and on leptons, assumed to be uniformly distributed. Densities times the respective volume fraction add to zero.
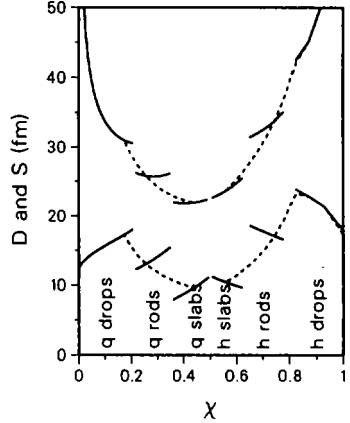
Figure 9: Size $(S = 2r)$ and spacing $(D = 2R)$ of geometrical structures. Notation 'q rods' means quark rods of negative charge immersed in nuclear matter of positive charge. Charge densities of each phase as a function of proportion χ of quark phase are shown in Fig. 8.

3.4 Spatial Structure

To calculate the spatial order we use the Wigner-Seitz *approximation* by choosing a volume v which is the cell size and contains the rare phase of dimension r and the dominant phase in such amount as makes the cell neutral. Therefore cells do not interact. The Coulomb and surface energies per unit volume can be written in the schematic form that shows their dependence on dimension r of the "geometry" and on the proportion χ.

$$E_C/v = C(\chi)r^2, \qquad E_S/v = S(\chi)/r . \tag{12}$$

(The dependence on r can be obtained by dimensional analysis [22, See end of Section V]. Minimizing their sum as a function of r at fixed χ yields

$$E_S = 2E_C \tag{13}$$

as always happens in the minimization of a sum of two quantities that vary as r^2 and $1/r$ respectively. In the above, C and S are specific functions of proportion χ whose form is dictated by the geometry of the cells (eg. sphere, rods and slabs) but for brevity we do not write them down. The above equations serve to define the droplet radius and cell size for each proportion of the phases,

$$r = \Big(\frac{S(\chi)}{2C(\chi)}\Big)^{1/3}, \qquad R = \frac{r}{\chi^{1/3}}, \tag{14}$$

where for spherical geometry, $\chi = (r/R)^3$. As remarked in the introduction, the internal force that drives the charge redistribution between phases in equilibrium is the isospin restoring force. As one can see, the size and spacing of the droplets of rare phase immersed in the dominant will vary as proportion χ. Other geometries besides spheres may minimize the energy according to the proportion. The functional form of S and C is distinct in each case, as is the relation of the dimensions of r and R to χ.

$$C_d(\chi) = 2\pi\{[q_1(\chi) - q_2(\chi)]e\}^2 \chi f_d(x) \tag{15}$$
$$S_d(\chi) = \chi\sigma d \tag{16}$$

where $d = 1, 2, 3$ for the idealized geometries of slabs, rods and drops respectively, σ is the surface tension and

$$x \equiv (r/R)^d, \qquad d = 1, 2, 3 \tag{17}$$

where x is related to the proportion χ by

$$x = \left\{ \begin{array}{ll} \chi & \text{,background phase is 1} \\ 1 - \chi & \text{,background phase is 2} \end{array} \right. \tag{18}$$

and

$$f_d(x) = \frac{1}{d+2}\Big[\frac{1}{(d-2)}(2 - dx^{1-2/d}) + x\Big]. \tag{19}$$

The above considerations are identical to those encountered in a description of nuclei embedded in an electron gas. At higher relative concentration of nuclear matter to electron gas, the spheres will merge to form rods and so on [24]. What is remarkable in the present context is that two phases of one and the same substance, under the action of the isospin symmetry restoring force, are endowed with opposite charge and form a Coulomb lattice. The size and spacing and the geometric form that minimizes the sum of surface and Coulomb energies are shown in Fig. 9.

3.5 Three Theorems

We have thus three theorems concerning the equilibrium configuration of the mixed phase of a first order phase transition of a substance with more than one conserved charge (or independent component in the language of chemistry):

1. All properties of the phases in equilibrium, including common pressure vary as the proportion of phases.

2. If electric charge is one of the conserved charges, the mixed phase will be in the form of a crystalline lattice.

3. Because of theorem 1, the geometry of the crystal and the size and the spacing of the lattice will vary with proportion.

These remarkable properties of first order phase transitions and the role played by the microphysics or internal forces is discussed in detail elsewhere [22, 23, 25]. It will be observed that the above discussion is completely general, and must apply to many systems in physical chemistry, nuclear physics, astrophysics and cosmology. In particular, in nuclear systems it applies to the confined-deconfined phase transition at high density, to the so-called liquid-vapor transition at sub-saturation density as well as to Pion and Kaon condensation if they are first order transitions, and if they occur. (It is understood that if a phase transition is induced by a nuclear collision, complete equilibrium will not be achieved, and in particular, there is insufficient time for formation of spatial structure.)

One step in the calculation remains to be described. The sum of surface and Coulomb energies, requires a knowledge of certain bulk properties like the charge density of each phase in equilibrium. The bulk energy and pressure can be computed according to ones favorite theory, and phase equilibrium finally has to be computed self-consistently, by minimizing the sum of all three energies, which can conveniently be done by iteration. The surface tension is generally not known and needs to be computed self-consistently for the phases in equilibrium. It will be a function of proportion, just as all other properties are.

Of course we have properly referred to the calculation as approximate: the division of total energy into bulk, surface and Coulomb is approximate. If one has reason to question the range of densities spanned by the structured mixed phase, then the alternative is to compute the energy on a lattice.

There is another important consequence of the existence of degree(s) of freedom for rearranging concentrations of conserved quantities in multi-component

substances according to the energy minimization principle. Whereas in one-component substances the properties of each phase in equilibrium are very unlike (as for example the density of ice and water), in a multi-component substances the rearrangement of charges so as to optimize the energy at each proportion of the phases relaxes their differences. This can be seen in Fig. 7 of Ref. [22]. As a consequence, the transition density from the pure low-density phase to the mixed phase is lower than would be expected were the degree(s) of freedom frozen out (as in the pre-1990 studies of deconfinement in neutron stars) [22, 26, 27, 28].

3.6 Summary

A change in phase during the course of spin-down of a millisecond pulsar occasioned by rising internal density due to weakening centrifugal forces will be reflected in a change in moment of inertia. The moment of inertia will follow different laws as a function of rotational frequency before and after the transition as in Fig. 6. The transition from one law to the other can (and is in our example) pass through an era of spin-up. This era lasts for about 1/50 of the spin-down time of millisecond pulsars, which represents an event rate. Spin up is trivial to detect and would be spectacular in a solitary pulsar which ought to be spinning down because of angular momentum loss to radiation.

For a weaker transition than experienced in our model the spin-up region need not occur: the moment of inertia may simply change smoothly from one trajectory to the other. In that case a sufficient number of observations of X-ray emitters in low-mass binaries could still identify a transition, even though the transition era were not actually observed, provided the observed neutron stars lay some on one branch, some on the other.

For distinct branches to exist, it appears to be necessary that the phase transition occurs near the maximum mass. The transition can be first or second order as long as it is accompanied by a sufficient softening of the equation of state.

References

[1] N. K. Glendenning, S. Pei and F. Weber, Phys. Rev. Lett. **79** (1997) 1603.

[2] D. Page, *Thermal Evolution of Isolated Neutron Stars*, To be published in the proceedings of the NATO ASI 'The Many Faces of Neutron Stars' (Kluwer), Eds A. Alpar, R. Buccheri & J. van Paradijs.

[3] C. Schaab, B. Hermann, F. Weber and M. K. Weigel, Astrophys. J. Lett. **480** (1997) L111.

[4] D. Bhattacharya and E. P. J. van den Heuvel, Physics Reports, **203** (1991) 1 .

[5] B. R. Mottelson and J. G. Valatin, Phys. Rev. Lett. **5** (1960) 511.

[6] A. Johnson, H. Ryde and S. A. Hjorth, Nucl. Phys. **A179** (1972) 753.

[7] F. S. Stephens and R. S. Simon, Nucl. Phys. **A183** (1972) 257.

[8] S. I. A. Garpman, N. K. Glendenning and Y. J. Karant, Nuc. Phys. **A322** (1979) 382.

[9] N. K. Glendenning, Astrophys. J. **293** (1985) 470.

[10] N. K. Glendenning and S. A. Moszkowski, Phys. Rev. Lett. **67** (1991) 2414.

[11] A. Chodos, R. L. Jaffe, K. Johnson, C. B. Thorne and V. F. Weisskopf, Phys. Rev. D **9** (1974) 3471.

[12] N. K. Glendenning, Nuclear Physics B (Proc. Suppl.) **24B** (1991) 110; Phys. Rev. D, **46** (1992) 1274.

[13] J. B. Hartle, Astrophys. J. **150** (1967) 1005.

[14] J. B. Hartle and D. Sharp, Astrophys. J. **147** (1967) 317.

[15] N. K. Glendenning and F. Weber, Astrophys. J. **400** (1992) 647.

[16] N. K. Glendenning and F. Weber, Phys. Rev. D **50** (1994) 3836.

[17] A. B. Migdal, Rev. Mod. Phys. **50** (1978) 107.

[18] N. K. Glendenning, Phys. Lett. **114B** (1982) 392;
N. K. Glendenning, Astrophys. J. **293** (1985) 470;
N. K. Glendenning, Z. Phys. A **326** (1987) 57;
N. K. Glendenning, Z. Phys. A **327** (1987) 295.

[19] V. A. Ambartsumyan and G. S. Saakyan, Astron. Zh. **37** (1963) 193 [Soviet Ast. – AJ,4 (1960) 187];
Ya. B. Zel'dovich and I. D. Novikov, *Relativistic Astrophysics, Vol. 1,*

Stars and Relativity (University of Chicago Press, 1971);

N. K. Glendenning, Astrophys. J. **293** (1985) 470;

D. B. Kaplan and A. Nelson, Phys. Lett. **175 B** (1986) 57;

H. D. Politzer and M. B. Weise, Phys. Lett. B **273** (1991) 156;

G. E. Brown, H. Lee, M. Rho, and V. Thorsson, Nucl. Phys. A **567** (1994) 937;

V. Thorsson, M. Prakash and J. M. Lattimer, Nucl. Phys. A **572** (1994) 693;

V. Koch, Phys. Lett. B **337** (1994) 7;

E. E. Kolomeitsev, D. N. Voskresensky and B. Kampfer, Nucl. Phys. A **588** (1995) 889;

N. Kaiser. P. B. Siegel and W. Weise, Nucl. Phys. A **594** (1995) 325;

T. Wass, N. Kaiser and W. Weise, Phys. Lett. B **379** (1996) 34;

J. Schaffner and I. N. Mishustin, Phys. Rev. C **53** (1996) 1416 .

[20] G. Baym and S. A. Chin, Phys. Lett. **62B** (1976) 241;
G. Chapline and M. Nauenberg, Nature **264** (1976) 235; Phys. Rev. D **16** (1977) 456.
B. D. Keister and L. S. Kisslinger, Phys. Lett. **64B** (1976) 117.

[21] N. K. Glendenning and J. Schaffner, H-Dibaryon Bose Condensate in Compact Stars (in preparation) 1997.

[22] N. K. Glendenning, Phys. Rev. D, **46** (1992) 1274.

[23] N. K. Glendenning, *COMPACT STARS, Nuclear Physics, Particle Physics, and General Relativity* (Springer–Verlag New York, 1997).

[24] D. G. Ravenhall, C. J. Pethick and J. R. Wilson, Phys. Rev. Lett. **50** (1983) 2066.

[25] N. K. Glendenning, *A Crystalline Quark-Hadron Mixed Phase in Neutron Stars*, Physics Reports, **264** (1995) 143.

[26] N. K. Glendenning and S. Pei, Phys. Rev. C **52** (1995) 2250.

[27] H. Heiselberg, C. J. Pethick, and E. F. Staubo, Phys. Rev. Lett. **70** (1993) 1355.

[28] V. R. Pandharipande and E. F. Staubo, in *Proc. 2'nd International Conf. of Physics and Astrophysics of Quark-Gluon Plasma*, Calcutta, 1993, Eds. B. Sinha, Y. P. Viyogi and S. Raha, (World Scientific, 1994).

Phase Transitions in Neutron Stars

Henning Heiselberg and Morten Hjorth-Jensen

NORDITA
Blegdamsvej 17, DK-2100 Copenhagen Ø, Denmark

Abstract

Phase transitions in neutron stars due to formation of quark matter, kaon condensates, etc. are discussed with particular attention to the order of these transitions. Observational consequences of phase transitions in pulsar angular velocities are examined.

1 Introduction

The physical state of matter in the interiors of neutron stars at densities above a few times normal nuclear matter densities is essentially unknown. Interesting phase transitions in nuclear matter to quark matter [1, 2], kaon [3, 4] or pion condensates [5, 6], neutron and proton superfluidity [7], hyperonic matter, crystalline nuclear matter [5], magnetized matter, etc., have been considered. We discuss how these phase transitions may exist in a mixed phase, the structures formed and in particular the order of the transition. Observational consequences are discussed.

2 Mixed Phases and Order of Transitions

The mixed phase in the inner crust of neutron stars consists of nuclear matter and a neutron gas in β-equilibrium with a background of electrons such that the matter is overall electrically neutral [8]. Likewise, quark and nuclear matter can have a mixed phase [1] and possible also nuclear matter with and without condensate of any negatively charged particles such as K^- [9], π^-, Σ^-, etc. The quarks are confined in droplet, rod- and plate-like structures [2] analogous to the nuclear matter and neutron gas structures in the inner crust of neutron stars [8]. Depending on the equation of state, normal nuclear matter exists only at moderate densities, $\rho \sim 1 - 2\rho_0$. With increasing density, droplets of quark matter form in nuclear matter and may merge into rod- and later plate-like structures. At even higher densities the structures invert forming plates, rods and droplets of nuclear matter in quark matter. Finally pure quark matter is

formed at very high densities unless the star already has exceeded its maximum mass.

A necessary condition for forming these structures and the mixed phase is that the additional surface and Coulomb energies of these structures are sufficiently small. Excluding them makea the mixed phase energetically favored [1]. That is also the case when surface energies are small (see [2] for a quantitative condition). If they are too large the neutron star will have a core of pure quark matter with a mantle of nuclear matter surrounding and the two phases are coexisting by an ordinary first order phase transition.

The quark and nuclear matter mixed phase has continuous pressures and densities [1] when surface and Coulomb energies are excluded. There are at most two second order phase transitions. Namely, at a lower density, where quark matter first appears in nuclear matter, and at a very high density, where all nucleons are finally dissolved into quark matter, if the star is gravitationally stable at such high central densities. However, due to the finite Coulomb and surface energies associated with forming these structures, the transitions change from second to first order at each topological change in structure [2]. If the surface and Coulomb energies are very small the transitions will be only weakly first order but there may be several of them.
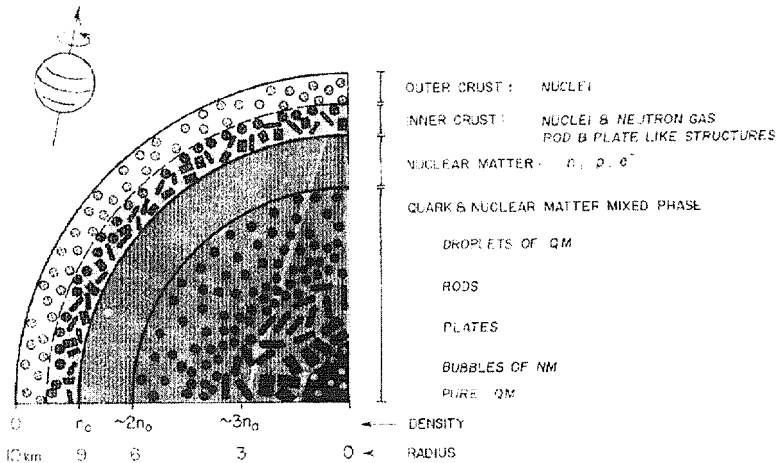
Fig. 1. Nuclear and quark matter tructures in a $\sim 1.4 M_\odot$ neutron star. Typical sizes of structures are $\sim 10^{-14} m$ but have been scaled up to be seen.

3   Rotation

As rotating neutron stars slow down, the pressure and the density in the core region increase due to the decreasing centrifugal forces and phase transitions may occur in the center. At the critical angular velocity Ω_0, where the phase transitions occur in the center of a neutron star, we find that the moment of inertia, angular velocity, braking index etc. change in a characteristic way.

The general relativistic equations for slowly rotating stars were described by Hartle [10]. Hartle's equations are quite elaborate to solve as they consist of six coupled differential equations as compared to the single TOV equation in the non-rotating case. However, Hartle's equations cannot be used in our case because the first order phase transition causes discontinuities in densities so that changes are not small locally. This shows up, for example, in the divergent thermodynamic derivate $d\rho/dP$. From Einstein's field equations for the metric we obtain from the $l = 0$ part the generalized rotating version of the TOV equation [11]

$$\frac{1}{\rho + P}\frac{dP}{da} = -G\frac{m + 4\pi a^3 P}{a^2(1 - 2Gm/a)} + \frac{2}{3}\Omega^2 a, \tag{1}$$

where $m(a) = 4\pi \int_0^a \rho(a')a'^2 da'$. In the centrifugal force term we have ignored frame dragging and other corrections of order $\Omega^2 GM/R \sim 0.1\Omega^2$ for simplicity and since they have only minor effects in our case.

The rotating version of the TOV equation (1) can now be solved for rotating neutron stars of a given mass and equation of state with a phase transition. If a first order phase transition occur in the center at Ω_0 the moment of inertia is generally [11]

$$I(\Omega) = I_0 \left(1 + \frac{1}{2}c_1\frac{\Omega^2}{\Omega_0^2} - \frac{2}{3}c_2(1 - \frac{\Omega^2}{\Omega_0^2})^{3/2} + ... \right), \tag{2}$$

for $\Omega \leq \Omega_0$. Here, $c_2 \sim \Delta\rho\Omega_0^3$ is a small number proportional to the density difference between the two phases and to the critical angular velocity to 3rd power. For $\Omega > \Omega_0$ the c_2 term vanishes.

The pulsars slow down at a rate given by the loss of rotational energy which commonly is assumed proportional to the rotational angular velocity to some power (for dipole radiation $n = 3$)

$$\frac{d}{dt}\left(\frac{1}{2}I(\Omega)\,\Omega^2\right) = -C\Omega^{n+1}. \tag{3}$$

Consequently, as the braking index depends on the second derivative $I'' = dI/d^2\Omega$ of the moment of inertia and thus diverges as Ω approaches Ω_0 from below

$$n(\Omega) \equiv \frac{\ddot{\Omega}\Omega}{\dot{\Omega}^2} = n - \frac{3I'\Omega + I''\Omega^2}{2I + I'\Omega} \simeq n - 2c_1\frac{\Omega^2}{\Omega_0^2} + c_2\frac{\Omega^4/\Omega_0^4}{\sqrt{1 - \Omega^2/\Omega_0^2}}. \quad (4)$$

For $\Omega \geq \Omega_0$ the term with c_2 is absent.

4 Cooling

If the matter undergoes a phase transition at a critical temperature but is supercooled as the star cools down by neutrino emission, a large glitch will occur when the matter transforms to its equilibrium state. If the cooling is continuous the temperature will decrease with star radius and time and the phase transition boundary will move inwards. The two phases could, e.g., be quark-gluon/nuclear matter or a melted/solid phase. In the latter case the size of the hot (melted) matter in the core is slowly reduced as the temperature drops freezing the fluid. Melting temperatures have been estimated in [8] for the crust and in [2] for the quark matter mixed phase. Depending on whether the matter contracts as it freezes as most terrestrial metals or expands as ice, the cooling will separate the matter in a liquid core of lower or higher density respectively and a solid mantle around. When the very core freezes we have a similar situation as when the star slows down to the critical angular velocity, i.e., a first order phase transition occurs right at the center. Consequently, a similar behavior for the moment of inertia, angular velocities, braking index may occur by replacing $\Omega(t)$ with $T(t)$ in Eqs. (2-4).

5 Glitches

The glitches observed in the Crab, Vela, and a few other pulsars are probably due to quakes occurring in solid structures such as the crust, superfluid vortices or possibly the quark matter lattice in the core [2]. These glitches are very small $\Delta\Omega/\Omega \sim 10^{-8}$ and have a characteristic healing time.

In [12] a drastic softening of the equation of state by a phase transition to quark matter leads to a sudden contraction of the neutron star at a critical angular velocity and shows up in a backbending moment of inertia as function of frequency. As a result, the star will become unstable as it slows down, will suddenly decrease its moment of inertia and create a large glitch. If the matter supercools and makes a sudden transition to its stable phase the densities may

- 147 -

also change and the star will have to contract or expand. Consequently, a large glitch will be observed.

6   Summary

We have discussed various possible phase transitions in neutron stars and have argued that we expect several first order order phase transitions to occur when the topological structure of the mixed phase change in the inner crust, nuclear and quark matter mixed phase or Kaon condensates. If a first order phase transitions is present at central densities of neutron stars, it will show up in moment of inertia and consequently also in angular velocities in a characteristic way. For example, the braking index diverges as $n(\Omega) \sim c_2/\sqrt{1 - \Omega^2/\Omega_0^2}$.

References

[1] N.K. Glendenning, *Phys. Rev.* **D46**, 1274 (1992).

[2] H. Heiselberg, C. J. Pethick, and E. F. Staubo, *Phys. Rev. Lett.* **70**, 1355 (1993); *Nucl. Phys.* **A566**, 577c (1994). H. Heiselberg, Proc. of "Strangeness and Quark Matter" (World Scientific, 1995), p. 298.

[3] D. B. Kaplan and A. E. Nelson, *Phys. Lett.* **B291** (1986) 57.

[4] V.R. Pandharipande, C.J. Pethick and V. Thorsson, *Phys. Rev. Lett.* **75** (1995) 4567. J. Carlson, H. Heiselberg, V.R. Pandharipande and C.J. Pethick, these proceedings.

[5] G. Baym and C. J. Pethick, *Ann. Rev. Nucl. Sci.* **25**, 27 (1975); *Ann. Rev. Astron. Astrophys.* **17**, 415 (1979).

[6] A. Akmal and V. R. Pandharipande, *Phys. Rev.* **C56**, 2261 (1997).

[7] Ø. Elgarøy, L. Engvik, M. Hjorth-Jensen, and E. Osnes, *Phys. Rev. Lett.* **76**, 1428 (1996).

[8] D. G. Ravenhall, C. J. Pethick, J. R. Wilson, *Phys. Rev. Lett.* **50** (1983) 2066; C. P. Lorenz, D. G. Ravenhall, C. J. Pethick, *Phys. Rev. Lett.* **70** (1993) 379.

[9] J. Schaffner, these proceedings.

[10] J. B. Hartle, Astrophys. J. **150**, 1005 (1967).

[11] H. Heiselberg and M. Hjorth-Jensen, astro-ph/9801187.

[12] N.K. Glendenning, S. Pei and F. Weber, *Phys. Rev. Lett.* **79**, 1603 (1997).

Medium Effects and the Structure of
Neutron Stars in the Effective Mass Bag Model [1]

K. SCHERTLER[2], C. GREINER, and M. H. THOMA [3]

Institut für Theoretische Physik, Universität Giessen
35392 Giessen, Germany

Abstract

One of the most intriguing consequence of the extreme conditions inside neutron stars is the possibility of the natural existence of a deconfined strange quark matter phase in the high density interior of the star. The equation of state (EOS) of strange quark matter (SQM) was recently improved in the framework of the MIT bag model by including medium effects. It was found that medium effects increase the energy per baryon of SQM and therefore lower the stability of this phase. In this work we investigate the influence of medium effects on the structure of hybrid stars within this model. We found that the medium effects reduce the extent of a pure SQM phase in the interior of an hybrid star significantly in favor of a mixed phase of quark and hadronic matter.

1   Introduction

The possibility of a deconfined phase of strange quark matter (SQM) in the interior of neutron stars is still stimulating the work of many authors [1, 2]. The gross structure of a neutron star like its mass and radius (MR) is influenced by the composition of its stellar material. This holds especially in the case of the existence of strangeness bearing "exotic" components like hyperons, kaons or SQM which may significant change the characteristic MR relation of the star.

The scope of this work is to study the influence of medium effects in the SQM phase on the gross structure of hybrid stars, i.e. neutron stars which are made of hadronic matter in the outer region, but with a SQM core in the interior. The deconfinement phase transition from hadronic matter to the SQM phase is constructed according to Glendenning [1]. We only require the weaker condition of global charge neutrality instead of assuming charge neutrality in either phase. The latter assumption would have the drastic consequence of

---

[2]E-mail: klaus.schertler@theo.physik.uni-giessen.de
[3]Heisenberg Fellow

strictly excluding a possible mixed phase of quark matter and hadronic matter. Such mixed phase is supposed to form a crystalline lattice of various geometries of the rarer phase immersed in the dominant one and probably exists over a wide range of densities inside the star [1, 2].

2 SQM and the effective mass bag model

SQM has been suggested as a possible stable or metastable phase of nuclear matter [3]. The equation of state of this system is commonly described as a non-interacting Fermi gas of quarks at zero temperature, taking into account the bag constant [3, 4]. Also quark interactions within lowest order perturbative QCD have been considered.

In condensed matter as well as in nuclear physics medium effects play an important role. One of the most important medium effects are effective masses generated by the interaction of the particles with the system. The EOS of SQM was recently improved in the framework of the MIT bag model by including these medium effects [5]. The quarks are considered there as quasi-particles which acquire an effective mass by the interaction with the other quarks of the dense system. The effective masses following from the hard dense loop quark self energy are given in [5, 6]. They are used in the ideal Fermi gas EOS at temperature $T = 0$ with respect to thermodynamic self-consistency in the sense of [7]. It was found [5], that the energy per baryon of SQM increases with increasing coupling constant g which enters into the effective masses. This makes the SQM phase energetically less favorable. We will refer to this model [5] as the "effective mass bag model".

3 The gross structure of neutron stars

Now we want to use the EOS in the effective mass bag model to calculate the MR relation of pure SQM stars and hybrid stars by solving the Tolman-Oppenheimer-Volkoff equations [8]. For the SQM EOS we assume a bag constant of $B^{1/4} = 165$ MeV ($B \approx 96$ MeV/fm^3) and current quark masses of $m_u = m_d = 0$, $m_s = 150$ MeV [9]. For the hadronic phase of the hybrid star we use an EOS calculated in the framework of the nonlinear Walecka model including nucleons, hyperons (Λ and Σ^-), electrons, muons and σ, ω and ρ mesons [9, 10]. We choose a compression modulus of $K = 300$ MeV. For subnuclear densities we use the Baym-Pethick-Sutherland EOS [11]. Fig. 1 shows the resulting MR relations for various values of the coupling constant g [9]. To investigate the influence of medium effects on the MR relation, we consider g
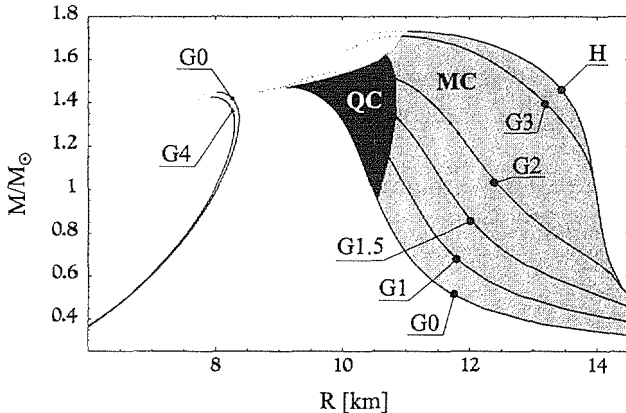
Figure 1: Mass radius relation for pure SQM stars ($R < 9$ km) and hybrid stars ($R > 9$ km), G0 = (g=0), ..., H = pure hadron , QC = star has a quark core, MC = star has a mixed core, $B^{1/4} = 165$ MeV, $K = 300$ MeV.

as an parameter ranging from $g = 0$ (no medium effects) to $g = 4$ [9, 12]. The left hand side ($R < 9$ km) shows the pure SQM star results. As already found in [5], we see that medium effects have only an slight influence on the MR relation of a pure SQM star. This situation changes if we look at the hybrid star results on the right hand side of fig. 1 ($R > 9$ km). With increasing g, the MR relation approaches the curve of the pure hadron star (denoted by H). There are two different shaded regions denoted by QC (quark core) and MC (mixed core). Every star located inside the QC region possess a pure SQM core while the MC region denotes stars with a mixed phase core.

To discuss the radii of the quark and mixed cores, we assume an canonical mass of $M = 1.4 M_\odot$. Fig. 2 shows the schematic view of the canonical star for different increasing g [9]. We find that a small coupling constant of $g = 1.5$ ($\alpha_s \approx 0.18$) is able to shrink the radius of the pure quark phase (QP) from $R \approx 6$ km (with neglected medium effects, fig. 2a) to $R \approx 3$ km (fig. 2c). Already at $g = 2$ ($\alpha_s \approx 0.32$) the pure SQM core is vanished completely (fig. 2d). Note that in spite of a completely vanishing quark core, the pure hadron phase (HP) has grown only moderately. One could say that in a wide range of g ($g \lesssim 3$) medium effects are not able to displace the quark phase in favor of a pure hadronic phase. The essential effect is the transformation of the pure SQM phase into a SQM phase immersed into the mixed phase (MP)

which therefore dominates the star. Only for $g \gtrsim 3.5$ a phase transition to SQM is completely suppressed (fig. 2f).
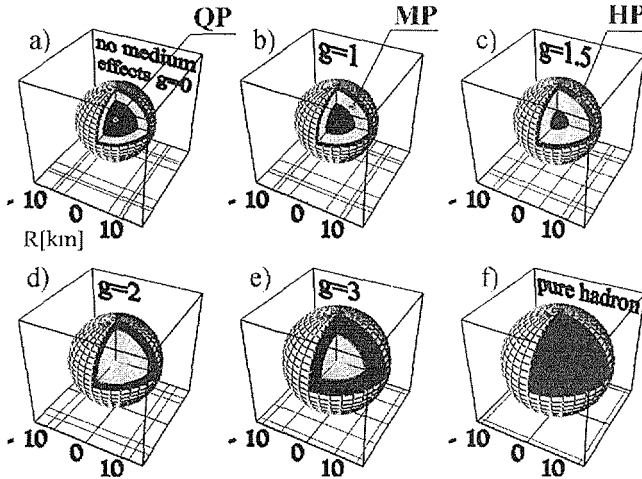
Figure 2: Schematic gross structure of an $M = 1.4 M_\odot$ star.

4 Conclusion

We have investigated the gross structure of non-rotating pure strange quark matter and hybrid stars using the effective mass bag model [5, 9] for the description of the quark matter EOS. This model is based on the quasi-particle picture where the quarks of a Fermi-gas acquire medium-dependent effective quark masses generated by the interaction of the quarks with the other quarks of the system. We found that the basic influence of medium effects described by this model and parameterized by the strong coupling constant g is to reduce the extent of a pure quark matter phase in the interior of an hybrid star significantly in favor of a mixed phase. For a wide range of the coupling constant ($g \lesssim 3$, $\alpha_s \lesssim 0.72$) SQM is therefore present in the dense interior of the star at least as a mixed phase of quark and hadronic matter.

References

[1] N.K. Glendenning, Phys. Rev. **D46**, 1274 (1992),

[2] H. Heiselberg, C.J. Pethick, E.F. Staubo, Phys. Rev. Lett. **70** (1993) 1355; E.F. Staubo, H. Heiselberg, C.J. Pethick, Nucl. Phys. **A566** (1994) 577; N.K. Glendenning, S. Pei, Phys. Rev. **C52** (1995) 2250; M. Prakash, J.R. Cooke, J.M. Lattimer, Phys. Rev. **D52** (1995) 661; M. Prakash, I. Bombaci, M. Prakash, P.J. Ellis, J.M. Lattimer, R. Knorren, Phys.Rept. **280** (1997) 1; D. Bandyopadhyay, S. Chakrabarty, S. Pal, Phys. Rev. Lett. **79** (1997) 2176; A. Drago, U. Tambini, astro-ph/9703138.

[3] A.R. Bodmer, Phys. Rev. **D4** (1971) 1601; E. Witten, Phys. Rev. **D30** (1984) 272.

[4] E. Fahri and R.L. Jaffe, Phys. Rev. **D30** (1984) 2379; B.A. Freedman and L.D. McLerran, Phys. Rev. **D16** (1978) 1169.

[5] K. Schertler, C. Greiner, M.H. Thoma, Nucl. Phys. **A616** (1997) 659.

[6] V.V. Klimov, Sov. Phys. JETP **55** (1982) 199; H.A. Weldon Phys. Rev. **D26** (1982) 1394 and 2789; H. Vija and M.H. Thoma, Phys. Lett. **B342** (1995) 212; J.-P. Blaizot and J.-Y. Ollitrault, Phys. Rev. **D48** (1993) 1390.

[7] M.I. Gorenstein, S.H. Yang, Phys. Rev. **D52** (1995) 5206.

[8] J.R. Oppenheimer, G.M. Volkoff, Phys. Rev. **55** (1939) 347.

[9] K. Schertler, C. Greiner, P.K. Sahu, M.H. Thoma, astro-ph/9712165.

[10] N.K. Glendenning, F. Weber, S.A. Moszkowski, Nucl. Phys. **A572** (1994) 693; J.I. Kapusta, K.A. Olive, Phys. Rev. Lett. **64** (1990) 13; J. Ellis, J.I. Kapusta, K.A. Olive, Nucl. Phys. **B348** (1991) 345; S.K. Gosh, S.C. Phatak, P.K. Sahu, Z. Phys. **A352** (1995) 457.

[11] G. Baym, C.J. Pethick, P. Sutherland, Astrophys. J. **170** (1971) 299; G. Baym, H.A. Bethe, C.J. Pethick, Nucl. Phys. **A175** (1971) 225.

[12] A. Peshier, K. Schertler, M. H. Thoma, to be published in Annals of Physics, hep-ph/9708434.

Core Collapse Supernova

E. MÜLLER

Max-Planck-Institut für Astrophysik
Karl-Schwarzschild-Str. 1
D-85748 Garching, Germany

Abstract

Theoretical and numerical models of core collapse supernovae are discussed including the prompt and the delayed explosion mechanism.

1   Introduction

Supernova explosions are either powered by the gravitational binding energy released during the collapse of a stellar core to a neutron star [2] or a black hole, or as first suggested by Hoyle & Fowler (1960) by the energy released during the explosive burning of degenerate thermonuclear fuel (helium and/or carbon and oxygen).

Observationally, supernovae are divided into two distinct spectral types, which are distinguished by the *absence (Type I)* or *presence (Type II)* of hydrogen lines in their spectra [36]. During the last decade astronomers have accumulated increasing evidence that both types do not form a homogeneous set, but should be divided into distinct subtypes (see, e.g., [22]). Accordingly, SNe are nowadays classified as Type Ia, Ib and Ic and as Type II-L and II-P, where L and P denote a light curve of linear type and plateau type, respectively. This classification scheme, which was initially suggested by observational data only, reflects differences in the explosion mechanism (core collapse or thermonuclear) and the progenitor star.

Type Ia supernovae are almost definitely thermonuclear explosions of degenerate white dwarfs. Type II supernovae are definitely the result of the core collapse of a massive ($M \gtrsim 9\,M_{\odot}$) evolved star, as proven by observations (in particular of neutrinos) of SN1987A [1]. Type Ib/Ic supernovae are most likely driven by the collapse of the evolved core of massive stars, which have lost their hydrogen or even part of their helium envelope by either a stellar wind (Wolf-Rayet progenitors with $M \gtrsim 30\,M_{\odot}$) or, if being a member of a close binary, by mass transfer (helium star progenitors with $3\,M_{\odot} \lesssim M \lesssim 5\,M_{\odot}$ and initial masses $12\,M_{\odot} \lesssim M_i \lesssim 18\,M_{\odot}$) [45, 22].

2   The energy source of core collapse supernovae

Theoretical and numerical models of core collapse SNe are based on the idea, that the implosion of the iron core of a massive main sequence star ($M \gtrsim 9 \ M_\odot$) at the end of its thermonuclear evolution causes a supernova explosion with violent mass ejection ($v_{eject} \approx 10^4$ km/sec) and the formation of a compact remnant, i.e., a neutron star or a black hole. The energy source for the explosion is the gravitational binding energy of the forming neutron star, which is of the order

$$E_b \approx 3 \ 10^{53} \left(\frac{M}{M_\odot} \right)^2 \left(\frac{R}{10 \text{ km}} \right)^{-1} \text{ erg }, \tag{1}$$

where M and R are the mass and the radius of the neutron star, and $M_\odot$ is the solar mass. As predicted by theoretical models and as proven through observations of SN1987A, the overwhelming fraction of the binding energy (about 99%) is carried away by neutrinos. Roughly 1% of the binding energy is transfered into kinetic energy ($\approx 10^{51}$ erg) of the ejecta, and only about 10^{-4} of the liberated energy is emitted in form of electromagnetic radiation ($\approx 10^{49}$ erg).

3   Collapse and bounce

According to Chandrasekhar (1939) a star, which is supported against gravity by the (zero temperature) pressure of its relativistic electrons, can only be stabilized, if its mass is less than a critical mass

$$M_{Ch} = 1.457 \, (2Y_e)^2 \ M_\odot , \tag{2}$$

which is the famous Chandrasekhar mass. At finite temperature the critical mass of a stable iron core should increase, but this increase is almost perfectly canceled by a decrease of the critical core mass due to Coulomb lattice correlations [3].

At the end of Si-core burning the electron fraction in the iron core of a massive star has a value $0.42 \lesssim Y_e \lesssim 0.44$, because of electron captures which occurred during oxygen and (core) silicon burning. The central entropy of the core is of the order 1 k_B/nucleon [42, 49, 50]. The mass of the iron core eventually exceeds the Chandrasekhar mass, because (i) the mass of the core grows as a result of Si-shell burning, (ii) electron captures further reduce the lepton number in the core as neutrinos are lost from the star, and (iii) the pressure in the core is reduced due to (endothermic) photo-disintegration of

nuclei by energetic photons. The relative importance of the last two processes depends on the stellar mass. For very massive stars ($M \gtrsim 20 \ M_\odot$) photo-disintegrations are more important than EC's, but the opposite is true for less massive stars, because of their lower central entropies

The initial entropy of the core is small ($S \approx 1 \ k_B$/nucleon) and remains small during collapse ($\Delta S \lesssim 0.5$), because neutrinos are trapped at densities $\rho \gtrsim 3 \, 10^{11} \mathrm{gcm}^{-3}$ [8]. This near adiabaticity of the collapse has important consequences. Firstly most of the nucleons remain bound in nuclei, because the entropy of a nucleus of mass number A is much less (about a factor A) than the entropy of A free nucleons. Therefore, the pressure is dominated by relativistic electrons (and neutrinos after trapping) until nuclear matter density is reached. This in turn implies that the collapse of (non-rotating) iron cores cannot be stopped at densities less than nuclear matter density.

When the central density of the core exceeds nuclear matter density the EOS stiffens, i.e., the adiabatic index γ increases from a value somewhat below $4/3$ to a value $2.5 - 3.0$. Starting at the center of the core successive mass shells are stopped. Pressure waves move outwards in radius and accumulate within a millisecond near the sonic point, where they steepen into a shock wave. Due to its inertia the homologous core overshoots its equilibrium position and rebounds behind the shock wave, which has already started propagating outward. The shock detaches from the rebounding core close to the sonic point, which roughly coincides with the outer edge of the *inner core.*

This *bounce* of the inner core occurs on the time scale of a radial pulsation, which is of the order 1 millisecond. For a stiff nuclear EOS the maximum density reached during bounce is less than two times nuclear saturation density, whereas for a soft nuclear EOS the collapse can continue up to $3 - 4$ times, and for a very soft nuclear EOS (with $\gamma = 2$) even up to 10 times nuclear saturation density, if effects of general relativity are included in the calculation [4, 5].

4   Prompt explosions and shock propagation

The initial energy of the shock wave is approximately equal to the kinetic energy of the inner core at the moment of *last good homology*, which is defined as the time, when the center of the core begins to be decelerated by the stiffening nuclear EOS [9].

During bounce the kinetic energy of the inner core is quickly transferred to the shock wave, which is an efficient absorber of sound waves. Numerical simulations and analytical estimates [37] show that the initial energy of the

shock wave is of the order of

$$E_{shock}^{(i)} \approx (4 - 10) \cdot 10^{51} \text{ erg} , \qquad (3)$$

much more than is required to explain the observed (kinetic and electromagnetic) energy output of a supernova. However, while propagating outward the shock wave is severely damped by photo-disintegration of heavy nuclei into free nucleons (if $S \gtrsim 5$ k$_B$/nucleon) or alpha particles (if 3 k$_B$/nucleon $\lesssim S \lesssim$ 5 k$_B$/nucleon), the energy loss being of the order [26, 34]

$$E_{loss} = (1.6 - 1.8) \cdot 10^{51} \text{ erg} / 0.1 \, M_\odot \qquad (4)$$

After the shock wave has crossed the neutrino sphere, it is further weakened by neutrino losses.

When most of the initial shock energy is lost due to photo-disintegration, the shock is no longer strong enough to lead to complete disintegration of the nuclei in the post–shock region and turns into an accretion shock, if no further energy source is available. Such an additional source of energy is the heating of the shocked matter immediately behind the shock by energetic neutrinos diffusing out of the opaque central regions of the collapsed core (see below).

Numerical simulations had to be performed to clarify, whether the energy losses of the shock are so severe that it stalls and turns into an accretion shock, or whether the shock wave is able to reach the outer layers of the star and cause a supernova explosion. As the (crucial) energy loss due to photo-disintegration is proportional to the difference between the mass of the iron core and that of the inner core (at bounce), it is obvious that the best candidates for Type II SNe are stars with small iron cores ($M \lesssim 1.2 \ M_\odot$) and low initial entropy, the latter resulting in a large mass of the inner core [25]. In particular, the energy loss given in Eq. 4 implies a limiting mass, which can be photo-disintegrated by the shock, of the order

$$M_{core} - M_{IC} \lesssim 0.45 \ M_\odot . \qquad (5)$$

For an inner core with a mass in the range $0.8 \ M_\odot \lesssim M_{IC} \lesssim 0.9 \ M_\odot$ as found in numerical simulations a so-called *prompt explosion* can only occur, if $M_{core} < 1.35 \ M_\odot$.

Among researchers in the field there is now general agreement that when the detailed effects of neutrino transport are taken into account currently available initial models and in particular models with iron cores more massive than about $1.35 \ M_\odot$ cannot explode by the prompt mechanism, no matter what the right equation of state is (for more details, see e.g., [38]).

shock front: $R_s \approx$ 200-300 km

$R_{gain} \approx$ 100-150 km

heating region

$\nu_e, \bar{\nu}_e$

p,n

n,p

e^-, e^+

ν-diffusion

proto-neutron star

ν - sphere (energy dependent!)

R $\approx$ 80-100 km
M $\approx$ 1.2 $M_\odot$
T $\gtrsim$ 10 MeV

$R_\nu \approx$ 50-70 km
$L_{\nu_i} \approx 2 \times 10^{52}$ erg/s $\times$ exp [-t/t$_L$]
$t_L \approx$ 0.5-0.7s
$<\varepsilon_{\nu_e}> \approx$ 15 MeV
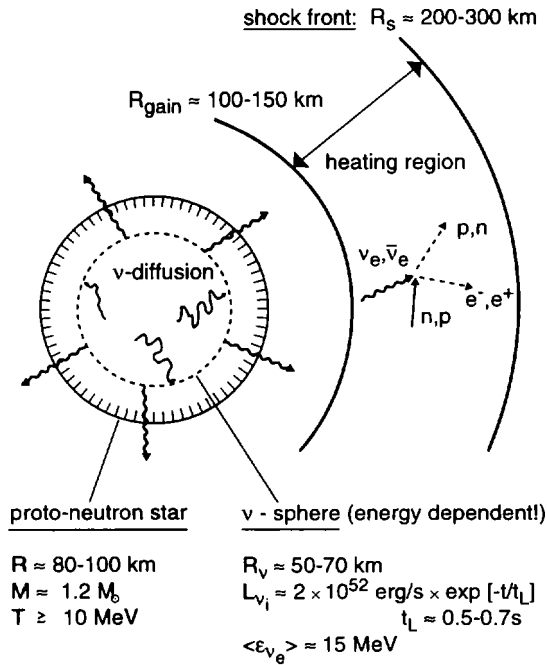
Figure 1: Sketch of the proto-neutron star and the "hot bubble" region.

5 Delayed explosions

A more viable Type II supernova explosion mechanism which relies on neutrino heating was found by Wilson (1985) [7, 48, 18, 28]. In this so–called *delayed explosion mechanism* energy is deposited in the layers between the nascent neutron star and the stalled prompt supernova shock during a period of a few 100 ms by absorption of a small fraction (between 1% and 10%) of the neutrinos emitted from the collapsed core (see Fig. 1). The neutrino energy deposition increases the pressure behind the shock front and the respective layers of the star begin to expand. Because of this expansion an extended region of low density, but quite high temperature is created above the surface of the proto-neutron star. The persistent energy input by neutrinos maintains high pressure in the radiation dominated "hot bubble" region, thus driving the shock outward, which eventually causes the supernova explosion.

During the phase of matter accretion, lasting for up to more than hundred milliseconds after core bounce, material is falling through the standing accretion shock. Initially cooling processes dominate in this material, which radiates away its gravitational binding energy by neutrinos, and settles onto the proto-neutron star. As the neutron star becomes more and more compact and the accretion rate shrinks with the decreasing density of the infalling layers of the progenitor star, there is a moment, when net heating by neutrino energy deposition *must* win against neutrino cooling.

Simulations showed that neutrino heating indeed works as predicted by the analytical considerations discussed above [46, 7, 48, 47, 18, 10, 28].

6 Convection

The criterion for the occurrence of convection in matter with density ρ, entropy per baryon S and electron number fraction Y_e is given by [21]

$$-\frac{\partial \ln \rho}{\partial \ln P}\bigg|_{S,Y_e} \left[\frac{\partial \ln P}{\partial S}\bigg|_{\rho,Y_e} \frac{dS}{dr} + \frac{\partial \ln P}{\partial Y_e}\bigg|_{\rho,S} \frac{dY_e}{dr} \right] > 0 \qquad (6)$$

where r is the radial coordinate. Hence, a sufficient condition for convective motion is given, when both the gradients of entropy and electron number fraction are negative, i.e., $dS/dr < 0$ and $dY_e/dr < 0$.

6.1 Convection inside the proto–neutron star

After the shock wave stalls ($\approx$ 10 ms after bounce) and before the delayed neutrino heating mechanism begins to become effective ($\approx$ 100 ms after bounce) the outer parts of the proto-neutron star are convectively unstable because of two reasons. Firstly, the deleptonization occurring in the shocked matter outside the neutrino-sphere produces a negative lepton gradient. Secondly, the weakening (and the eventual stalling) of the prompt shock wave gives rise to a negative entropy gradient in the same region. According to Eq. 6 this is a sufficient condition for convective motion to occur. This situation is commonly encountered in supernova simulations [11, 15, 10].

The existence of convective instabilities inside the proto-neutron star has been demonstrated in two-dimensional [12, 13, 29, 30] and three-dimensional hydrodynamic simulations [39, 40, 41], which covered the onset and growth of the convective instability until $\approx$ 50 ms after core bounce. The size of the convective cells depends on whether the flow is simulated in two or three space dimensions [41]. In 2D the convective structures are roughly a factor of two

larger than in 3D, where the dominant modes have (angular) wavelengths of about $20^o - 30^o$.

As the convective velocities reach and even partially exceed the local sound speed ($v_{conv} \approx 10^9$ cm/s) strong pressure waves and even weak shock waves are generated by the convective flow. This convective activity inside the proto-neutron star causes significant inhomogeneities in the temperature and density stratifications. The inhomogeneities vary in time and space implying non-radial mass motions and a time-dependent mass quadrupole moment associated with the outer layers of the proto-neutron star. Both effects generate gravitational radiation with typical frequencies in the range of several hundred Hz to about one kHz. An additional gravitational wave signal can be expected from the anisotropic neutrino emission found in the multi-dimensional models [20, 14, 41].

The convective mixing found in the multi–dimensional simulations around and below the neutrino-spheric region near the proto-neutron star surface is accompanied by an increase of the neutrino luminosities during the early phase of the supernova explosion. Since the convection is dynamical and violent and the gas velocities are close to the local speed of sound, neutrinos are transported out of the dense interior of the newly-formed neutron star much faster than by diffusion. The corresponding increase of the neutrino emission may provide an important aid to the neutrino-powered explosion mechanism.

6.2   Convection in the "hot bubble" region

Noting that the hot bubble is convectively unstable Colgate [18, 19] and Bethe (1990) pointed out that this situation may give rise to a dynamical overturn of hot, neutrino-heated, rising material and cold post-shock matter, and can lead to large-scale deviations from spherically symmetric supernova explosions. This instability was indeed found in numerical simulations [16, 23, 24, 30, 31, 32, 33, 35, 40, 43, 44, 51].

In order to describe the formation of the convective instability and to simulate the convective motion in the "hot bubble" region an adequate treatment of neutrino–matter interaction is necessary and the generation and transport of neutrinos must be modeled. This can only be done in some approximate manner, because a multi-dimensional, multi-flavor and energy-dependent treatment of neutrino transport is presently not feasible. Moreover, the neutrino luminosities from the collapsed stellar core are dependent on convective processes below and around the "neutrino sphere" (see previous subsection) and cannot be accurately determined without an elaborate treatment of neutrino transfer

in this turbulent region. Possibly even methods to simulate neutrino transport in more than one dimension have to be applied. Finally, the neutrino emission depends on the uncertain nuclear equation of state and on the neutrino interaction rates in the high–density material, which are only known with an accuracy of, may be, a factor of two.

Because of this lack of knowledge, Janka & Müller (1996) have performed a sensitivity study instead of calculating a consistent but specific model. Certainly, consistency of the modeling is preferable. However, selecting a specific physical input, like EOS and neutrino opacities, as it was done by other workers in the field, provides only little insight into the physical conditions required for a successful explosion. Instead, Janka & Müller (1996) took a published model of a stellar core shortly after core bounce and replaced the inner high–density region somewhat inside the neutrino-sphere by an inner boundary condition, which was allowed to contract in a controlled way and where the neutrino fluxes (and spectra) were set to chosen values. This allowed them to study the impact of the neutrino energy deposition and convection in the outer part of the collapsed core on the mechanism of the explosion.

Janka & Müller (1996) obtained powerful explosions and cases of failure or very weak explosions in *both* one-dimensional and two–dimensional simulations. The crucial parameter turned out to be the neutrino luminosities of ν_e and $\bar{\nu}_e$ after bounce and their decrease with time. Strong explosions require sufficiently high neutrino fluxes for a sufficiently long period. The turbulent overturn of cold post-shock material and high-entropy, neutrino-heated gas provides an efficient mechanism to transport energy from the neutrino-heated region to the shock front and clearly aids the re-expansion of the stalled shock front. However, turbulence in the neutrino-heated layer is a crucial help for the explosion only in a narrow range of neutrino luminosities. For lower neutrino fluxes the neutrino-heating is too weak and powerful explosions cannot be obtained even with convection. For higher neutrino fluxes convection reduces the neutrino luminosity that is necessary to end up with a certain explosion energy.

The non-spherical stratification and mass flow resulting from the convective instabilities in the neutrino heated region are, like the ones occurring inside the proto-neutron star, a source of gravitational radiation. Because of the longer time scales (up to a few 100 ms) and the larger radii (up to several 1000 km) involved in the "hot bubble" convection, the typical frequencies of the emitted gravitational radiation are expected to be significantly lower and the corresponding amplitudes to be smaller [41].

References

[1] Arnett, W.D., Bahcall, J.N., Kirshner, R.P. & Woosley, S.E., 1989, Ann. Rev. Astron. Astrophys. **27**, 629;

[2] Baade, W. & Zwicky, F., 1934, Phys. Rev. **45**, 138;

[3] Baron, E. & Cooperstein, J., 1990, Astrophys. J. **353**, 597;

[4] Baron, E., Cooperstein, J. & Kahana, S., 1985a, Phys. Rev. Lett. **155**, 126;

[5] Baron, E., Cooperstein, J. & Kahana, S., 1985b, Nucl. Phys. **A440**, 744;

[6] Bethe, H.A., 1990, Rev. Mod. Phys. **62**, 801;

[7] Bethe, H.A. & Wilson, J.R., 1985, Astrophys. J. **295**, 14;

[8] Bethe, H.A., Brown, G.E., Applegate, J.H. & Lattimer, J., 1979, Nucl. Phys. **A324**, 487;

[9] Brown, G.E., Bethe, H.A. & Baym, G., 1982, Nucl. Phys. **A375**, 481;

[10] Bruenn, S.W., 1993, in: Nuclear Physics in the Universe, eds. M.W. Guidry and M.R. Strayer, IOP, Bristol, 31;

[11] Burrows, A., 1987, Astrophys. J. **318**, L57;

[12] Burrows, A. & Fryxell, B.A., 1992, Science **258**, 430;

[13] Burrows, A. & Fryxell, B.A., 1993, Astrophys. J. **418**, L33;

[14] Burrows, A. & Hayes, J., 1996, Phys. Rev. Let. **76**, 352;

[15] Burrows, A. & Lattimer, J.M., 1988, Phys. Rep. **163**, 51;

[16] Burrows A., Hayes J. & Fryxell B.A., 1995, Astrophys.J. **450**, 830;

[17] Chandrasekhar, S., 1939, An Introduction to the Study of Stellar Structure (Dover Publisher, New York), Chapter XI;

[18] Colgate, S.A., 1989, Nature **341**, 489;

[19] Colgate, S.A., Herant, M. & Benz, W., 1993, Phys. Rep. **227**, 157;

[20] Epstein, R., 1978, Astrophys. J. **223**, 1037;

[21] Epstein, R.I., 1979, Mon. Not. Roy. Astron. Soc. **188**, 305;

[22] Filippenko, A. V., 1997, in: Thermonuclear Supernovae (eds. P. Ruiz-Lapuente, R. Canal and J. Isern, Kluwer, Dordrecht, 1;

[23] Herant, M., Benz, W. & Colgate, S.A., 1992, Astrophys. J. **395**, 642;

[24] Herant, M., Benz, W., Hix, W.R., Fryer, C.L. & Colgate, S.A., 1994, Astrophys. J. **435**, 339;

[25] Hillebrandt, W., 1987, in: High Energy Phenomena Around Collapsed Stars, ed. F. Pacini, Reidel, Dordrecht, 73;

[26] Hillebrandt, W. & Müller, E., 1981, Astron. Astrophys. **103**, 147;

[27] Hoyle, F. & Fowler, W.A., 1960, Astrophys. J. **132**, 565;

[28] Janka, H.-Th., 1993, in: Frontier Objects in Astrophysics and Particle Physics, eds. F. Giovannelli and G. Mannocchi, Società Italiana di Fisica, Bologna, 345;

[29] Janka, H.-Th. & Müller, E., 1993, in: Frontiers of Neutrino Astrophysics, eds. Y. Suzuki and K. Nakamura, Universal Academy Press, Tokyo, 203;

[30] Janka, H.-Th. & Müller, E., 1996, in Supernovae and Supernovae Remnanst (IAU Coll. 145, Xian, China, 1993), eds. R. McCray and Z. Wang, Cambridge Univ. Press, Cambridge, 109;

[31] Janka, H.-Th. & Müller, E., 1995, Phys. Rep. **256**, 135;

[32] Janka, H.-Th. & Müller, E., 1995, Astrophys. J. **448**, L109;

[33] Janka, H.-Th. & Müller, E., 1996, Astron. Astrophys. **306**, 167;

[34] Mazurek, T.J., 1982, in: Supernovae: A Survey of Current Research, eds. M.J. Rees and R.J. Stoneham, Reidel, Dordrecht, 371;

[35] Miller, D.S., Wilson, J.R. & Mayle, R.W., 1993, Astrophys. J. **415**, 278;

[36] Minkowski, A.M., 1941, Publ. Astron. Soc. Pac. **53** 224;

[37] Mönchmeyer, R., 1993, Ph.D. thesis, Technical University München, unpublished;

[38] Müller, E., 1990, J. Phys. G **16**, 1571;

[39] Müller E., 1993, in: Proc. of the 7th Workshop on Nuclear Astrophysics (Ringberg Castle, March 1993), eds. W. Hillebrandt and E. Müller,Report MPA/P7, Max-Planck-Institut für Astrophysik, Garching, 27;

[40] Müller, E. & Janka, H.-Th., 1994, Reviews in Modern Astronomy 7, ed. G.Klare, Astronomische Gesellschaft, Hamburg, 103;

[41] Müller, E. & Janka, H.-Th., 1997, Astron. Astrophys. **317**, 140;

[42] Nomoto, K. & Hashimoto, M., 1988, Phys. Rep. **163**, 13;

[43] Shimizu, T., Yamada, S. & Sato, K., 1993, Publ. Astron. Soc. Japan **45**, L53;

[44] Shimizu, T., Yamada, S. & Sato, K., 1994,Astrophys. J. **432**, L119;

[45] Wheeler, J.C. & Harkness, R.P., 1990, Rep. Prog. Phys. **53**, 1467;

[46] Wilson, J.R., 1985, in: Numerical Astrophysics, eds. J.M. Centrella, J.M. LeBlanc and R.L. Bowers, Jones and Bartlett, Boston, 422;

[47] Wilson, J.R. & Mayle, R., 1988, Physics Reports, **163**, 63;

[48] Wilson, J.R., Mayle, R., Woosley, S.E. & Weaver, T.A., 1986, Ann. N.Y. Acad. **479**, 267;

[49] Woosley, S.E. & Weaver, T.A., 1986, Ann. Rev. Astron. Astrophys. **24**, 205;

[50] Woosley, S.E. & Weaver, T.A., 1988, Phys. Rep. **163**, 79;

[51] Yamada, S., Shimizu, T. & Sato, K., 1993, Prog. Theor. Phys. **89**, 1175.

SUPERNOVA NUCLEOSYNTHESIS AS A TOOL TO ANALYZE THE EXPLOSION MECHANISM

F.-K. Thielemann[1,4], F. Brachwitz[1], C. Freiburghaus[1], T. Rauscher[1]

K. Iwamoto[2], K. Nomoto[2], M. Hashimoto[3], W.R. Hix[4]

[1] *Departement für Physik und Astronomie, Universität Basel,*
CH-4056 Basel, Switzerland

[2] *Department of Astronomy and Research Center for the Early Universe,*
University of Tokyo, Tokyo 113, Japan

[3] *Department of Physics, Faculty of Science, Kyushu University,*
Fukuoka 810, Japan

[4] *Oak Ridge National Laboratory, Oak Ridge, TN 37831-4576, USA*

Abstract

Type II supernovae (SNe II) are linked to the gravitational collapse of massive stars ($M > 8 M_\odot$) at the end of their hydrostatic evolution. The resulting central hot proto-neutron star cools via neutrino emission. Neutrino opacities and transport determine the neutrino emission luminosity, which, together with the neutrino heating effiency in adjacent layers, is responsible for the explosion and ejection of matter. This affects the nucleosynthesis products via two main uncertainties, (i) the locations of the mass cut between the ejecta and the remaining neutron star and (ii) the total explosion energy responsible for explosive nucleosynthesis. Thus, observations can constrain these quantities.

Type Ia supernovae (SNe Ia) are explained by exploding white dwarfs in binary stellar systems. The favored systems are accreting white dwarfs, approaching the (maximum stable) Chandrasekhar mass before contraction and central ignition. Their major uncertainties are related (i) to the the accretion rate in the binary system which determines the carbon ignition density and (ii) the flame speed after central ignition. We provide several new constraints to the "average" SNe Ia systems, representing the major source of Fe-group nuclei in the Galaxy.

1 Introduction

Many contributions to this conference were devoted to the essential nuclear input for astrophysical calculations, i.e. experimental cross sections in hy-

drostatic burning stages of stellar evolution, electron captures in late burning stages and in stellar collapse, the nuclear equation of state and its influence on the supernova core collapse, neutrino transport and opacities in dense nuclear matter, the precision of cross section predictions for explosive burning, the properties (e.g. masses and half-lives) of nuclei far from beta-stability and resulting effects on abundance features of heavy nuclei. These topics are also covered in the NuPECC report on nuclear and particle astrophysics [3] and a recent review concentrating on experimental approaches [18]. In this contribution we present applications of such nuclear properties to specific astrophysical sites and test how resulting abundance compositions from explosive burning can give clues to the detailed working of supernovae.

Nuclear burning can in general be classified into two categories: (1) hydrostatic burning stages on timescales dictated by stellar energy loss and (2) explosive burning due to hydrodynamics of the specific event. Both are of importance for supernovae. In SNe II the outer ejected layers are unprocessed and contain results of prior H-, He-, C-, and Ne-burning in stellar evolution. In general, the initial hydrostatic composition also influences the ejected yields of explosively processing layers. Hydrostatic burning stages are characterized by temperature thresholds, permitting Maxwell-Boltzmann distributions of (charged) particles (nuclei) to penetrate increasing Coulomb barriers: H-burning [conversion of ^{1}H into ^{4}He via pp-chains, initiated by ^{1}H$(p,e^+)^2$H, or the CNO cycle with the slowest reaction ^{14}N$(p,\gamma)^{15}$O] He-burning [^{4}He$(2\alpha,\gamma)^{12}$C (triple-alpha) and ^{12}C$(\alpha,\gamma)^{16}$O], C-burning [^{12}C$(^{12}$C, $\alpha)^{20}$Ne], and O-burning [^{16}O$(^{16}$O$,\alpha)^{28}$Si]. The alternative is that photodisintegrations start to play a role when $30kT \approx Q$ (the Q-value of the inverse capture reaction). This ensures sufficient photons with energies $>Q$ in the Planck distribution and leads to Ne-Burning [^{20}Ne$(\gamma,\alpha)^{16}$O, ^{20}Ne$(\alpha,\gamma)^{24}$Mg] at $T>1.5 \times 10^9$K (preceding O-burning) due to a small Q-value of ≈ 4 MeV and Si-burning at temperatures in excess of 3×10^9K [initiated like Ne-burning by photodisintegrations]. The latter ends in a thermodynamic equilibrium with an abundance distribution around Fe (nuclear statistical equilibrium, NSE), as Q-values of 8-10 MeV along the valley of stability permit photodisintegrations at these temperatures as well the penetration of the corresponding Coulomb barriers.

In such an NSE the abundance of each nucleus $Y_{(Z,A)}$ with atomic weight A and charge Z, measured in mole per gram of matter, is only governed by chemical potentials and thus only dependent on temperature T, density ρ, its nuclear binding energy B, and partition function G(T), while fulfilling mass conservation $\sum_i A_i Y_i = 1$ and charge conservation $\sum_i Z_i Y_i = Y_e$ (the total

number of protons equals the net number of electrons). Y_e is changed by weak interactions (beta-decays and electron captures) on longer timescales. While still approaching NSE, different nuclear mass regions, usually separated by closed shells and small Q-values, can already be in equlibrium with the background of free neutrons, protons and alphas, but such quasi-equilibrium (QSE) clusters have total abundances which are offset from their NSE values [39, 46, 41].

2 Explosive Burning

Many of the hydrostatic burning processes occur also under explosive conditions at higher temperatures and on shorter timescales, cases, but often the beta-decay half-lives of unstable products are longer than the timescales of the explosive processes under investigation. This requires in general the additional knowledge of nuclear cross sections for unstable nuclei [35, 41]. A recent reaction rate sensitivity analysis of explosive burning products [44], however, also noticed that due to equilibrium effects (NSE and QSE) the dependence on cross section uncertainties (in explosive burning) is strongly reduced. Extensive calculations of explosive C, Ne, O, and Si burning have been performed for many years [1]. The fuels for explosive nucleosynthesis consist mainly of N=Z nuclei like ^{12}C, ^{16}O, ^{20}Ne, ^{24}Mg, or ^{28}Si, resulting in intermediate to heavy nuclei, again with N≈Z, unless densities are high enough to ensure substantial electron captures due to energetic, degenerate electrons.

We will concentrate here only on explosive Si-burning which differs strongly from its hydrostatic counterpart. Explosive Si-burning can be devided into three different regimes: (i) incomplete Si-burning and complete Si-burning with either (ii) a normal (high density, low entropy) or (iii) an alpha-rich (low density, high entropy) freeze-out of charged-particle reactions. At high temperatures or during a "normal" freeze-out, the abundances are in a full NSE. An alpha-rich freeze-out is caused by the inability of the triple-alpha reaction ^{4}He$(2\alpha, \gamma)^{12}$C, transforming ^{4}He into ^{12}C, and the ^{4}He$(\alpha n, \gamma)^9$Be reaction, to keep light nuclei like n, p, and ^{4}He, and intermediate mass nuclei beyond A=12 in an NSE during declining temperatures, when the densities are small. This causes a large alpha abundance after freeze-out, which shifts abundances in QSE groups to heavier nuclei, transforming e.g. ^{56}Ni, ^{57}Ni, and ^{58}Ni into ^{60}Zn, ^{61}Zn, and ^{62}Zn. It leads also to a slow supply of ^{12}C still during freeze-out, leaving traces of alpha nuclei, ^{32}S, ^{36}Ar, ^{40}Ca, ^{44}Ti, ^{48}Cr, and ^{52}Fe, which did not fully make their way up to ^{56}Ni. This effect, typical for SNe II, is a function of remaining alpha-particle mass fraction (or entropy).

We will omit here the discussion of r-process nucleosynthesis (rapid neutron capture) and just point out that it relates to subsets of explosive Si-burning, either with low or high entropies and thus experiencing a normal or alpha-rich freeze-out. The requirement of a neutron/seed ratio of 10 to 150 after charged particle freeze-out translates in a normal freeze-out into a $Y_e = <Z/A>$ as low as 0.12-0.3, as found in neutron star matter. Another option is an extremely alpha-rich freeze-out with a moderate $Y_e > 0.40$ [38, 47, 10].

3   Type II Supernova Explosions

All stars with main sequence masses $M > 8M_\odot$ [11, 42] produce a collapsing core after the end of their hydrostatic evolution, which proceeds to nuclear densities. The total energy released, $2-3 \times 10^{53}$erg, equals the gravitational binding energy of a neutron star. Because neutrinos are the particles with the longest mean free path, they are able to carry away that energy in the fastest fashion as seen for SN1987A in the Kamiokande, IMB and Baksan experiments [5]. The most promising mechanism for supernova explosions is based on neutrino heating beyond the hot proto-neutron star via the dominant processes $\nu_e + n \rightarrow p + e^-$ and $\bar{\nu}_e + p \rightarrow n + e^+$ with a (hopefully) about 1% efficiency in energy deposition. The neutrino heating efficiency depends on the neutrino luminosity, which in turn is affected by neutrino opacities [37, 25, 19, 36, 8]. The explosion via neutrino heating is delayed after core collapse for a timescale of seconds or less. The exact delay time t_{de} depends on the neutrinos transport and convection entropy gradients [12, 17, 6, 26].

3.1   Induced Nucleosynthesis Calculations

The uncertainties of self-consistent models, suggests instead to make use of the fact that typical kinetic energies of 10^{51} erg are observed and light curve as well as explosive nucleosynthesis calculations can be performed by introducing a shock of appropriate energy in the pre-collapse stellar model [42, 46, 40, 29]. Present explosive nucleosynthesis calculations for SNe II are still based on such induced supernova explosions by either depositing thermal energy or invoking a piston with a given kinetik energy of the order 10^{51} erg. Induced calculations (lacking self-consistency) utilize the constraint of requiring ejected ^{56}Ni-masses from the innermost explosive Si-burning layers in agreement with supernova light curves, being powered by the decay chain ^{56}Ni-^{56}Co-^{56}Fe. This can also serve as guidance to the supernova mechanism with mass cuts, based on ^{56}Ni in the ejecta [40, 29].
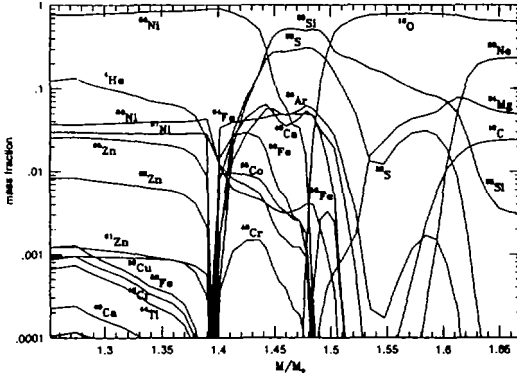
Figure 1: Isotopic composition of the ejecta for a core collapse supernova from a $13 M_\odot$ star ($3.3 M_\odot$ He-core). The exact mass cut in $M(r)$ between neutron star and ejecta depends on the details of the delayed explosion mechanism.

Fig. 1 shows the composition after explosive processing for a constant $Y_e=0.4989$ in the inner ejcta, which experience incomplete and complete Si-burning. Huge changes in the Fe-group composition occur when this is changed to 0.4915 for mass zones below $M(r)=1.5 M_\odot$. Then the abundances of ^{58}Ni and ^{56}Ni become comparable. All neutron-rich isotopes increase (^{57}Ni, ^{58}Ni, ^{59}Cu, ^{61}Zn, and ^{62}Zn), the even-mass isotopes (^{58}Ni and ^{62}Zn) show the strongest effect. One can also recognize the increase of ^{40}Ca, ^{44}Ti, ^{48}Cr, and ^{52}Fe with an increasing alpha-rich freeze-out.

In Fig. 2 we display the Y_e-distributions of a $20 M_\odot$ star and the position of the outer boundary of explosive Si-burning with complete Si exhaustion, where predominantly ^{56}Ni is produced. This changes as a function of the delay time t_{de} (here 0, 0.3, 0.5, 1, and 2s) between core bounce and explosion because matter is accreted onto the proto-neutron star. Observed ^{56}Ni ejecta indicate the corresponding neutron star masses. The upper mass limit of neutron stars, due to the nuclear equation of state [34], causes therefore also the upper mass limit of stars which undergo successful supernova explosions before the formation of central black holes set in. Different maximum stable masses between the initially hot and a cold neutron star, possibly related to kaon condensates [4, 34], could result in a supernova explosion *and* afterwards the formations of a central black hole.

Observational constraints for individual supernovae (e.g. SN1987A, SN1993J)
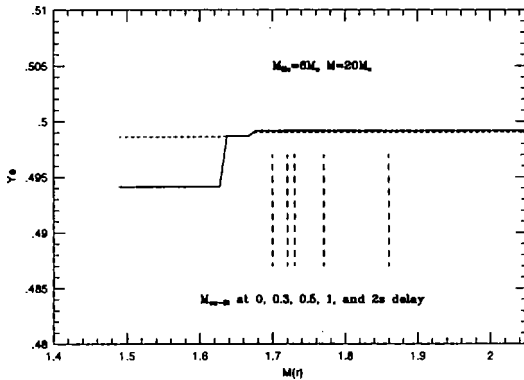
Figure 2: The Y_e-distributions in a 20M$_\odot$ star and the position of the outer boundary of complete Si-burning, as a function of the delay/accretion period t_{de}. A required amount of Ni-ejecta and the delay time t_{de} determine Y_e and the composition in the ejected material. The steep drop in Y_e corresponds to the edge of core O-burning.

and supernova remnants (e.g. Cas A, G292.0+1.8, N132D) give constraints on element abundances (like C, O, Si, Cl, Ar, Co, and Ni) and isotopic abundances (like ^{56}Ni, ^{57}Ni, ^{44}Ti, and ^{26}Al) from optical, UV, and X-ray spectra, supernova lightcurves, as well as gamma-ray lines following nuclear decay [40, 7], which constrain the products of hydrostatic burning stages like C, O, Ne and Mg and the composition close to the mass cut between the central neutron star and the supernova ejecta (^{56}Co, ^{57}Co, ^{44}Ti). They give a consistent picture for neutrino heating delay times of 0.3-0.5s, explosion energies of the order 10^{51}erg, and a mass cut close to or outside the O-burning shell with minute permitted admixtures of deeper layers so that only matter with $Y_e \geq 0.497$-0.498 is ejected. These constraints have to be met by self-consistent hydro calculations.

4 Type Ia Supernovae

There are strong observational and theoretical indications that SNe Ia are thermonuclear explosions of accreting white dwarfs [43, 13, 30]. Theoretically, both Chandrasekhar mass white dwarf models and sub-Chandrasekhar mass models have been considered [32, 9, 14]. These corresponds to a single degenerate scenario, i.e., accretion of H or He via mass transfer from a binary

companion at a relatively high rate. In the case of He accretion at low rates, He detonates at the base of the accreted layer before the system reaches the Chandrasekhar mass [45, 24, 2]. A double degenerate scenario, i.e., the merging of two C+O white dwarfs in a binary system with a combined mass exceeding the Chandrasekhar mass limit [15] exists as well.

The Chandrasekhar vs. sub-Chandrasekhar mass issue has recently experienced some progress. Observational features of SNe Ia in early phases clearly indicate that Chandrasekhar models give a more consistent picture than the sub-Chandrasekhar models of helium detonations [13, 33]. On the other hand, late time spectra challenge the traditional model W7 [32] due to a too large ^{58}Ni content and too high central densities [23]. Thus, this model requires improvements (i) in terms of the Fe-group composition and (ii) the central ignition densities. The recent findings of supersoft X-ray sources, potential progenitors of SN Ia events with high accretion rates and low ignition densities [31, 22], leave hope also for late time spectra.

4.1 Ignition and Burning Front Propagation

For Chandrasekhar mass models carbon ignition in the central region leads to a thermonuclear runway. High accretion rates cause a higher central temperature and pressure, favoring lower ignition densities. A flame front then propagates at a subsonic speed as a *deflagration wave* due to heat transport across the front [32]. Here the most uncertain quantity is the flame speed which depends on the development of instabilities of various scales at the flame front. Multidimensional hydro simulations of the flame propagation have been attempted by several groups, though the results are still preliminary [21, 27, 28]. These simulations have suggested that a carbon deflagration wave might propagate at a speed v_{def} as slow as a few percent of the sound speed v_s in the central region of the white dwarf. Though the calculated flame speed is still very preliminary, due to the lack of a proper treatment of turbulence, it is useful to examine nucleosynthesis consequences of such a slow flame speed. After an initial deflagration in the central layers, the deflagration is assumed to turn into a detonation at lower densities [20, 45].

In the deflagration wave, electron captures enhance the neutron excess. The amount of electron capture depends on both v_{def} (influencing the time duration of matter at high temperatures, and with it the availability of free protons) and the central density of the white dwarf (increasing the electron chemical potential). The resultant nucleosynthesis in slow deflagrations [20] has some distinct features compared with faster deflagrations like W7 [32],
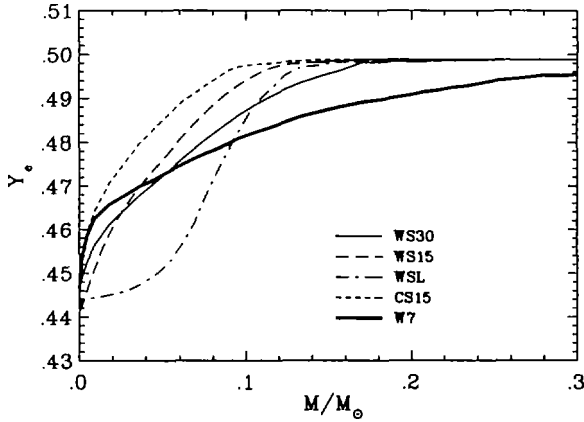
Figure 3: Y_e after freeze-out of nuclear reactions measures the electron captures on free protons and nuclei. Small burning front velocities lead to steep Y_e-gradients which flatten with increasing velocities (see the series of models WS15, WS30, and W7). Lower central ignition densities shift the curves up (CS15), but the gradient is the same for the same propagation speed. Only when the Y_e from electron captures is smaller than for stable Fe-group nuclei, subsequent β^--decays will reverse this effect(WSL).

thus providing important constraints on these two parameters. Initially slower deflagrations cause an earlier expansion of the outer layers with respect to the arrival of the burning front (as information of the central ignition propagates with sound speed and lead to lower densities for the outer deflagration and detonation layers. Here we want to concentrate on the main aim, which is to find the "average" SN Ia conditions responsible for their nucleosynthesis contribution to galactic evolution, i.e. especially the Fe-group composition.

4.2 The Fe-Group Composition in Slow Deflagrations

We adopt two models with central densities of ρ=1.37 (C) and 2.12×10^9 g cm^{-3} (W) at the onset of thermonuclear runaway and assume that a slow (S) deflagration propagates with speeds $v_{\text{def}}/v_s = 0.015$ (WS15, CS15) and 0.03 (WS30) and consider also the extreme case of an initially laminar flame front (WSL). The central region undergoes electron captures on free protons and iron peak nuclei.

Fig. 3 summarizes the major options to change Y_e values in the central part of SNe Ia explosions are: (i) the burning front speed, determininig the Y_e gradient and (ii) the central ignition densities, being inversely proportional to

Y_e. These features hold true as long as Y_e values in explosive burning do not drop below 0.44, when competing β^--decays have also to be taken into account (case WSL). Such parameter studies can give important clues to v_{def} and $\rho_{c,ign}$. Y_e values of 0.47-0.485 lead to dominant abundances of ^{54}Fe and ^{58}Ni, values between 0.46 and 0.47 produce dominantly ^{56}Fe, values in the range of 0.45 and below are responsible for ^{58}Fe, ^{54}Cr, ^{50}Ti, ^{64}Ni, and values below 0.43-0.42 are responsible for ^{48}Ca.

For all cases discussed here (WSL, WS15, WS30, CS15) ^{58}Ni can be produced within the permitted uncertainty limits. ^{54}Cr is produced within these limits in CS15, but overproduced in WSL, WS15 and WS30, due to the too low central Y_e's. ^{50}Ti is produced close to solar values for CS15, well produced for WS30, and clearly overproduced in WSL and WS15 (for full details see [16]). From this exercise we see that this would make CS15 a better model than WS15, WS30 or WSL, in terms of avoiding overproduction of these elements, and would permit solar abundances in total. This interpretation is also in agreement with identifying the recently discovered supersoft X-ray sources as SN Ia progenitor systems. Their high accretion rates (close to $\dot{M}=10^{-7}M_\odot$) would be in agreement with such low ignition densities.

References

[1] Arnett, W.D. 1995, Ann. Rev. Astron. Astrophys. 33, 115

[2] Arnett, W.D. 1996, *Nucleosynthesis and Supernovae*, Princeton Univ. Press

[3] Baraffe, I. et al. 1997, *NuPECC Report on Nuclear and Particle Astrophysics*, http://quasar.physik.unibas.ch/nupecc

[4] Brown, G.E., Bethe, H.A. 1994, Ap. J. 423, 659

[5] Burrows, A. 1990, Ann. Rev. Nucl. Part. Sci. 40, 181

[6] Burrows, A., 1996, Nucl. Phys. A606, 151

[7] *Supernova Explosions: Their Causes and Consequences*, eds. A. Burrows, K. Nomoto, F.-K. Thielemann, http://www.itp.ucsb.edu/online/supernova/snovaetrans.html

[8] Burrows, A., Sawyer, R.F. 1998, Phys. Rev. D, submitted

[9] Canal, R., 1997, in *Thermonuclear Supernovae*, eds. P. Ruiz-Lapuente, R. Canal, J. Isern, Kluwer Academic Publishers, p. 257

[10] Freiburghaus, C. et al. 1997, Nucl. Phys. A621, 405c; 1998, Ap. J., in press

[11] Hashimoto, M., Iwamoto, K., Nomoto, K., 1993, Ap.J. 414, L105

[12] Herant, M. et al. 1994, Ap. J. 435, 339

[13] Höflich, P., Khokhlov, A. 1996, Ap. J., 457, 500

[14] Höflich, P., Wheeler, J.C., Thielemann, F.-K. 1998, Ap.J., in press

[15] Iben, I.Jr., Tutukov, A.V. 1984, Ap. J. Suppl. 54, 335

[16] Iwamoto, K. et al. 1998, Ap. J., submitted

[17] Janka, H.-T., Müller, E. 1996, Astron. Astrophys. 306, 167

[18] Käppeler, F., Wiescher, M., Thielemann, F.-K. 1998, Ann. Rev. Nucl. Part. Sci., in press

[19] Keil, W., Janka, H.-T. 1995, Astron. Astrophys. 296, 145

[20] Khokhlov, A.M. 1991, A&A 245, 114; 245, L25

[21] Khokhlov, A.M. 1995, Ap. J. 449, 695

[22] Li, X.D., van den Heuvel, E.P.J. 1997, Astron. Astrophys. 322, L9

[23] Liu, W.H., Jeffery, D.J., Schultz, D.R. 1997, Ap. J. 483, L107

[24] Livne, E., Arnett, W.D. 1995, Ap. J. 452, 62

[25] Mezzacappa, A., Bruenn, S.W. 1993, Ap. J. 405, 637

[26] Mezzacappa, A. et al. 1997, Ap. J., in press

[27] Niemeyer J.C., Hillebrandt W. 1995, Ap. J., 452, 769

[28] Niemeyer, J.C., Woosley, S.E. 1997, Ap. J. 475, 740

[29] Nomoto, K. et al. 1997, Nucl. Phys., A616, 79c

[30] Nomoto, K., Iwamoto, K., Kishimoto, N. 1997, Science 276, 1378

[31] Nomoto, K., Kondo, Y. 1991, Ap. J. 367, L19

[32] Nomoto, K., Thielemann, F.-K., Yokoi, K. 1984, Ap. J. 286, 644

[33] Nugent, P. et al. 1997, Ap. J. 485, 812

[34] Prakash, M. et al. 1997, Phys. Rep. 280, 1

[35] Rauscher, T., Thielemann, F.-K., Kratz, K.-L. 1997, Phys. Rev. C56, 1613

[36] Reddy, S., Prakash, M., Lattimer, J.M. 1997, Nucl. Phys. A, in press

[37] Schinder, P.J. 1990, Ap. J. Suppl. 74, 249

[38] Takahashi, K., Witti, J., Janka, H.-T. 1994, Astron. Astrophys. 286, 857

[39] Thielemann, F.-K., Arnett, W.D. 1985, Ap. J. 295, 604

[40] Thielemann, F.-K., Nomoto, K., Hashimoto, M. 1996, Ap. J. 460, 408

[41] Thielemann, F.-K. et al. 1997, in *Nuclear and Particle Astrophysics*, ed. J. Hirsch, Cambridge Univ. Press, in press (astro-ph/9802077)

[42] Weaver, T.A., Woosley, S.E. 1993, Phys. Rep. 227, 65

[43] Wheeler, J.C. et al. 1995, Phys. Rep., 53, 221

[44] Woosley, S.E. et al. 1997, Nucl. Phys. A621, 445c

[45] Woosley, S.E., Weaver, T.A. 1994, Ap. J., 423, 371

[46] Woosley, S.E., Weaver, T.A. 1995, Ap. J. Suppl. 101, 181

[47] Woosley, S. E. et al. 1994, Ap. J. 433, 229

NUCLEAR INPUT IN SUPERNOVA PHYSICS

K. LANGANKE

Institute for Physics and Astronomy and Center for Theoretical Astrophysics,
University of Aarhus, DK-8000 Aarhus,Denmark

Abstract

The recently developed Shell Model Monte Carlo (SMMC) approach allows the calculation of nuclear properties at finite temperature and in much larger and hence more realistic model spaces than previous methods. The manuscript discusses two applications of the SMMC to nuclear problems of relevance in supernova physics: the calculation of a) electron capture rates on nuclei in the iron mass region and of b) level densities.

1 Introduction

The impact of nuclear structure on astrophysics has become increasingly important, particularly in the fascinating and presently unsolved problem of type-II supernova. In this context I will discuss two rather distinct nuclear problems: i) electron capture rates and ii) nuclear level densities. As their common feature, significant progress has been achieved in both areas being made possible by the development and applicability of a novel solution to the nuclear shell model. This novel method, the Shell Model Monte Carlo (SMMC) approach [1, 2], describes the nucleus by a canonical ensemble at finite temperature $T = \beta^{-1}$ and employs a Hubbard-Stratonovich linearization of the imaginary-time many-body propagator, $\exp\{-\beta H\}$, to express observables as path integrals of one-body propagators in fluctuating auxiliary fields. The SMMC approach overcomes the severe mass limitations faced by standard diagonalization techniques. As a shortcoming, the SMMC method does not provide detailed spectroscopic informations. However, it naturally allows the study of thermal properties of nuclei as they are often required in astrophysics. A review of the SMMC method and its applications can be found in Ref. [3]. As a highlight SMMC calculations in the complete pf-shell have been able to consistently reproduce the experimentally observed Gamow-Teller strength distributions [4] (if the universal renormalization of the spin-operator is employed [5, 6]). This property as well as its ability to study nuclei at finite temperature is the basis for the progress achieved recently in the calcu-

lation of electron capture rates for the presupernova collapse and of nuclear level densities. These two topics will be discussed in turn in the following two sections.

2   Electron capture in presupernova collape

Key inputs for the precollapse scenario are the electron capture cross sections and rates for iron group nuclei [7, 8]. The core of a massive star at the end of hydrostatic burning is stabilized by electron degeneracy pressure as long as its mass does not exceed the appropriate Chandrasekhar mass M_{CH}. If the core mass exceeds M_{CH}, electrons are captured by nuclei [7]. Thus, the depletion of the electron population due to capture by nuclei is a crucial factor determining the initial collapse phase.

The presupernova electron capture rate λ_{ec} is given by folding the total electron capture cross section with the flux of a degenerate relativistic electron gas:

$$\lambda_{ec} = \frac{\ln 2}{6163\sec} \int_0^\infty d\xi S_{GT}(\xi, T) \frac{c^3}{(m_e c^2)^5} \int_{\mathcal{L}}^\infty dp p^2 (-\xi + E_e)^2 \frac{F(Z, E_e)}{1 + \exp\left[\beta_e(E_e - \mu_e)\right]} ,$$
(1)

where $1/\beta_e$, p, and μ_e are the electron temperature, momentum, and chemical potential, and $\mathcal{L} = (Q_{if}^2 - m_e^2 c^4)^{1/2}$ for $Q_{if} \leq -m_e c^2$, and 0 otherwise, and $Q_{if} = -E = E_i - E_f$ is the energy difference between the nuclear states i and f, respectively. Here we have additionally accounted for the distortion of the electron's wave function due to the Coulomb field of the nucleus by introducing the Fermi function $F(Z, E_e) = 2\pi\eta / [\exp(2\pi\eta) - 1]$ where $\eta = Z\alpha/\hat{\beta}$, α is the fine-structure constant, $\hat{\beta} = |\vec{\beta}|$ is the magnitude of the velocity of the incoming electron, and Z is the charge of the parent nucleus. In writing down Eq. (1) we have also considered that, under presupernova conditions ($T \approx 0.5$ MeV, $\mu \approx 1.5$ MeV), the electron capture rate is dominated by Gamow-Teller (GT) transitions. The appropriate GT strength distribution at temperature T, $S_{GT}(E, T)$, is related to the dynamical GT response function (with $\mathcal{A} = \sum_{i=1}^A \tau_+(i)\sigma_{eff}(i)$ where $\sigma_{eff} = 0.8\sigma$ is the renormalized spin operator)

$$R_{\mathcal{A}}(\tau) = \frac{\text{Tr}_A[e^{-(\beta-\tau)\hat{H}}\hat{\mathcal{A}}^\dagger e^{-\tau\hat{H}}\hat{\mathcal{A}}]}{\text{Tr}_A[e^{-\beta\hat{H}}]} = \frac{\sum_{if}(2J_i+1)e^{-\beta E_i}e^{-\tau(E_f - E_i)}|\langle f|\hat{\mathcal{A}}|i\rangle|^2}{\sum_i(2J_i+1)e^{-\beta E_i}}.$$
(2)

by an inverse Laplace transform

$$R_{\mathcal{A}}(\tau) = \int_{-\infty}^\infty S_{\mathcal{A}}(E, T)e^{-\tau E}dE.$$
(3)

Note that here E is the energy transfer within the parent nucleus, and that the strength distribution $S_{GT}(E,T)$ has units of MeV^{-1}. The response function can be directly calculated within the SMMC and the desired strength distribution is then obtained by using maximum entropy techniques to numerically perform the inverse Laplace transformation.

In Ref. [9] we have presented SMMC Gamow-Teller distributions for those pf-shell nuclei in the iron mass region for which experimental data are available ($^{54,56}Fe$, $^{58,60,62,64}Ni$, ^{51}V, ^{55}Mn and ^{59}Co). The agreement between theory and data was very satisfying in all cases and it has been concluded that the SMMC approach has the predictive power to estimate the Gamow-Teller strength distribution for nuclei for which no data exist. In the meantime we have extended the SMMC calculation to other pf-shell nuclei [10] which are of interest for the presupernova collapse: $^{55,57}Co$, ^{56}Ni, $^{50,52}Cr$, $^{55,58}Fe$, ^{56}Ni and ^{50}Ti.

In Table 1 we compare the SMMC results for the Gamow-Teller peak in the daughter nucleus with the parametrization given by Fuller, Fowler and Newman [11] and subsequently used in the update of the presupernova electron capture rates by Aufderheide *et al.* [8]. We observe that Ref. [11] generally places the Gamow-Teller strength for even-even parent nuclei at too high an excitation energy in the daughter, while it is the opposite for odd-A parent nuclei. The same trend as in the SMMC distributions is found in the data. ¿From the SMMC calculations and the data we can conclude that for an even-even parent, the Gamow-Teller strength, at low temperatures, is at low daughter excitation energies (~ 2 MeV), while it is at significantly higher excitation energies (~ 5 MeV) for an odd-A nucleus. This different behavior is related to the pairing energy difference between the even-even parent and odd-odd daughter. As the Gamow-Teller distributions usually have widths of order 1-2 MeV, our SMMC calculations for odd-A nuclei might miss weak Gamow-Teller transitions at low excitation energies which could potentially increase the electron capture rates. It appears therefore reasonable to follow the prescription of [11] and add some strength at low energies to the rates obtained from the SMMC Gamow-Teller distributions for odd-A nuclei. Such a procedure seems to be unnecessary for even-even parent nuclei.

Do the present electron capture rates indicate potential implications for the pre-collapse evolution of a type II supernova? To make a judgement on this important question, we compare in Table I the SMMC rates for selected nuclei with those currently used in collapse calculations [8] assuming typical physical conditions [8]. Furthermore the table lists the partial electron capture rate which has been attributed to Gamow-Teller transitions in Ref. [8]. For even parent nuclei, Table I shows significant differences between the present

rate and the one attributed to the Gamow-Teller transition in [8]. As discussed above, the origin of this discrepancy is due to the fact that Ref. [11] places the Gamow-Teller resonance for even-even nuclei systemetically at too high an excitation energy. Of course, this shortcoming has been corrected for in Refs. [11, 8] by adding low-lying strength on top of the one attributed to Gamow-Teller transitions. However, the overall good agreement between the SMMC results for even-even nuclei and the recommended rates indicates that our SMMC approach also accounts correctly for this low-lying strength. We conclude therefore that, for even-even nuclei, the SMMC approach is able to predict the *total* electron capture rate rather reliably, even if no experimental data are available. We note that our SMMC rate is somewhat larger than the recommended rate for ^{56}Fe and ^{60}Ni. In both cases the experimental Gamow-Teller distribution is known and agrees well with the SMMC results [9]. While the proposed increase of the rate for ^{60}Ni is not expected to have noticeable influence on the pre-collapse evolution, the increased rate for ^{56}Fe makes this nucleus to an important contributor in the change of Y_e during the collapse.

Turning now to electron capture on odd-A nuclei. Here we observe that the SMMC electron capture rate, derived from the Gamow-Teller distributions, is significantly smaller than the recommended total rate. As already stressed above, this is simply due to the fact that for odd-A nuclei the Gamow-Teller transition peaks at rather high excitation energies in the daughter nucleus. The electron capture rate on odd-A nuclei is therefore carried by weak transitions at low excitation energies. Comparing our rates to those attributed to Gamow-Teller transitions in Refs. [11, 8] reveals that the latter have been in general significantly overestimated which is simply caused by the fact that the position of the Gamow-Teller resonance is usually put at too low excitation energies in the daughter. For example, Ref. [8] attributes 87% of the total capture rate on ^{55}Co to Gamow-Teller transitions (Table I), while our calculation predicts the contribution of the Gamow-Teller strength distribution to be negligible. Thus, we recommend that the capture rate on ^{55}Co is significantly smaller (only 13% of the rate given in Table 4 of Ref. [8]). Our SMMC calculation implies that the Gamow-Teller transitions should not contribute noticeably to the electron capture rates on odd-A nuclei at the low temperatures studied in Tables 14–16 in [8]. Thus, the rates for odd-A nuclei given in these tables should generally be replaced by the non-Gamow-Teller fraction.

Table 1: Comparisons of the present SMMC electron capture rates with the total (λ_{ec}) and partial Gamow-Teller (λ_{ec}^{GT}) rates as given in Ref. [8]. The last two columns compare the position of the Gamow-Teller strength as calculated in the SMMC (E_{GT}) and parametrized in Ref. [11]. The calculation has been performed for a density $\rho = 5.9 \cdot 10^7$ g/cm^3, temperature $T = 3.4 \cdot 10^9$ K and electron-to-baryon ratio $Y_e = 0.47$.

nucleus	λ_{ec} (sec^{-1}) (SMMC)	λ_{ec} (sec^{-1}) (Ref. [8])	λ_{ec}^{GT} (sec^{-1}) (Ref. [8])	E_{GT} (MeV)	E_{FFN} (MeV)
^{55}Co	2.25E-04	1.41E-01	1.23E-01	6.9	3.78
^{57}Co	1.97E-06	3.50E-03	1.31E-04	4.8	3.77
^{54}Fe	4.64E-05	3.11E-04	9.54E-07	2.8	3.8
^{55}Fe	7.22E-09	1.61E-03	1.16E-07	6.1	5.4
^{56}Ni	1.96E-02	1.60E-02	6.34E-03	2.6	3.78
^{58}Ni	6.02E-04	6.36E-04	4.04E-06	2.0	3.76
^{60}Ni	1.34E-05	1.49E-06	4.86E-07	1.0	2.0

3 Nuclear level densities

Nuclear level densities play an essential role for theoretical estimates of nuclear reaction rates needed in various astrophysical nucleosynthesis processes like the s-, r- and rp-process [12]. Nuclear level densities have been described in these astrophysical studies by the backshifted Fermi gas model of Gilbert and Cameron [13]. This model extends the non-interacting Fermi gas model of Bethe [14] by considering pairing among like nucleons via a backshift of the excitation energy E. Thus one has [12]

$$\rho(U) = \frac{\sqrt{\pi}}{12a^{1/4}} \frac{\exp 2\sqrt{aU}}{U^{5/4}} \; ; \; U = E - \Delta \tag{4}$$

where Δ, a are the backshift and level density parameter [12]

$$a \approx A/8 \text{ MeV}^{-1} \tag{5}$$

$$\Delta \approx \pm\frac{12}{\sqrt{A}} - \frac{10}{A} \text{ MeV} \tag{6}$$

with the positive (negative) sign for even-even (odd-odd) nuclei and $\Delta = 0$ for odd-A nuclei.

First attempts to determine level densities within the SMMC method have been reported by Ormand [15] and by Narada and Alhassid [16]. Both ap-

proaches are based on the fact that the excitation energy

$$E(\beta) = \frac{Tr\left[He^{-\beta H}\right]}{Tr\left[e^{-\beta H}\right]} = \frac{\int dE e^{-\beta E} E \rho(E)}{Z} \tag{7}$$

can be evaluated within the SMMC [3]. Here, Z is the partition function with

$$ln\left[\frac{Z(\beta)}{Z(0)}\right] = -\int_0^\infty d\beta' E(\beta'), \tag{8}$$

$Z(0)$ is the total number of states in the model space. Using a saddle-point approximation to perform the inverse Laplace transform leads to [16]

$$\rho(E) = \frac{e^{\beta E + lnZ(\beta)}}{\sqrt{-2\pi\frac{dE(\beta)}{d\beta}}} \tag{9}$$

where $\beta = \beta(E)$ is obtained by inverting $E = E(\beta)$.

We have calculated nuclear level densities for the nuclei $^{48-50}$Cr and ^{50,51}Mn in the complete pf shell [17]. They contain only positive (negative) parity states for even-A (odd-A) nuclei which should be a reasonable approximation for the low-excitation spectrum considering that the splitting between major shells is $\hbar\omega \approx 10$ MeV. For the residual interaction in the Hamiltonian the form pairing+multipole-multipole has been assumed. A missing isospin repulsion has been corrected for by adding $\alpha\hat{T}^2$ to the Hamiltonian ($\hat{T}$ is the isospin operator) and by treating this extra term in perturbation theory. At intermediate energies ($E \approx 3-8$ MeV) the SMMC level densities agree nicely with the backshifted Fermi gas model if the level density parameter $a = A/7.6$ MeV^{-1} is chosen. For the backshift we obtain $\Delta \approx 1$ MeV for even-even nuclei, which is slightly smaller than the phenomenological value, and $\Delta = 0$ for odd-A nuclei in agreement with expectation. The SMMC calculation also shows that in the odd-odd $N = Z$ nucleus ^{50}Mn (which has ground state isospin $\hat{T} = 1$) the number of isoscalar ($\hat{T} = 0$) levels is significantly larger than the number of isovector ($\hat{T} = 1$) levels at moderate excitation energies. It is suggested to parametrize the level density of odd-odd $N = Z$ nuclei in terms of $\hat{T} = 0$ and $\hat{T} = 1$ components (the latter being identical to the analog even-even nucleus, in which one proton has been changed into a neutron) to account for the fact that these nuclei at low excitation energies are dominated by proton-neutron correlations rather than like-nucleon pairing [18, 19] which is the basis of the backshift in the level density formula (4).

4 Summary

In summary, the SMMC has been established in recent years as a very use-
ful tool for nuclear structure calculations, including nuclear properties at fi-
nite temperature. This is of particular interest for astrophysics as this new
method allows improved and more realistic investigations of nuclear properties
that are of importance in various astrophysical scenarios (see e.g. [3]). This
manuscript has highlighted some of the very recent applications and gives a
flavor of the kind of studies that can be performed with the shell model Monte
Carlo method.
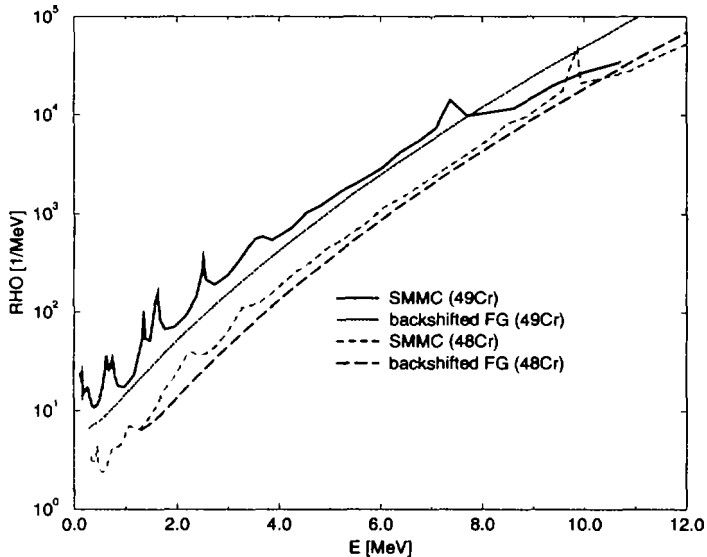
Fig. 1. Comparison of the level density in ^{48}Cr and ^{49}Cr as calculated within
the SMMC and the backshifted Fermi gas (FG) model.

References

[1] C. W. Johnson, S. E. Koonin, G. H. Lang, and W. E. Ormand, Phys. Rev.. Lett. **69**, 3157 (1992).

[2] G. H. Lang, C. W. Johnson, S. E. Koonin, and W. E. Ormand, Phys. Rev. C **48**, 1518 (1993).

[3] S.E. Koonin, D.J. Dean and K. Langanke, Physics Repor **278** (1997) 1

[4] K. Langanke, D. J. Dean, P. B. Radha, Y. Alhassid, and S. E. Koonin, Phys. Rev. C **52**, 718 (1995).

[5] B. Brown and B. Wildenthal, Ann. Rev. Nucl. Part. Sci. **38**, 29 (1988).

[6] E. Caurier, A. Zuker, A. Poves, and G. Martinez-Pinedo, Phys. Rev. C **50**, 225 (1994).

[7] H.A. Bethe, Rev. Mod. Phys. **62** (1990) 801

[8] M. B. Aufderheide, I. Fushiki, S. E. Woosley, and D. H. Hartmann, Astrophys. J. Suppl. 91 (1994) 389

[9] P.B. Radha, D.J. Dean, S.E. Koonin, K. Langanke, and P. Vogel, Phys. Rev. **C56** (1997) 3097.

[10] D.J. Dean, K. Langanke, L. Chatterjee, P.B. Radha and M.R. Strayer, submitted to Phys. Rev. C

[11] G.M. Fuller, W.A. Fowler and M.J. Newman, ApJS **42** (1980) 447; **48** (1982) 279; ApJ **252** (1982) 715; **293** (1985) 1

[12] J.J. Cowan, F.-K. Thielemann and J.W. Truran, Phys. Rep. **208** (1991) 267

[13] A. Gilbert and A.G.W. Cameron, Can. J. Phys. **43** (1965) 1446

[14] H.A. Bethe, Phys. Rev. **50** (1936) 332

[15] W.E. Ormand, Phys. Rev. **C56** (1997) R1678

[16] H. Nakada and Y. Alhassid, Phys. Rev. Lett. **79** (1997) 2939

[17] K. Langanke, submitted to Physics Letters

[18] J. Engel, K. Langanke and P. Vogel, Phys. Lett. **B389** (1996) 211

[19] K. Langanke, D.J. Dean, P.B. Radha and S.E. Koonin, Nucl. Phys. **A613** (1997) 253

LIFETIME OF ^{44}Ti AS PROBE
FOR SUPERNOVA MODELS

J. GÖRRES [1], J. MEISSNER, H. SCHATZ, E. STECH, P. TISCHHAUSER,
M. WIESCHER

University of Notre Dame, Notre Dame, IN 46556

D. BAZIN, R. HARKEWICZ, M. HELLSTRÖM, B. SHERRILL, M.
STEINER

Michigan State University, East Lansing, MI 48824

R.N. BOYD

Ohio State University, Columbus, OH 43210

L. BUCHMANN

TRIUMF, Vancouver, BC V6T 2A3

D.H., Hartmann

Clemson University, Clemson, SC 29634

J.D. Hinnefeld

Indiana University South Bend, South Bend, IN 46634

Abstract

The recent observation of ^{44}Ti radioactivity in the supernova remnant
Cassiopeia A with the Compton Gamma Ray Observatory allows the
determination of the absolute amount of ^{44}Ti. This provides a test for
current supernova models. The main uncertainty is the lifetime of ^{44}Ti.
We report a new measurement of the lifetime of ^{44}Ti applying a novel
technique. A mixed radioactive beam containing ^{44}Ti as well as ^{22}Na
was implanted and the resulting γ-activity was measured. This allowed
the determination of the lifetime of ^{44}Ti relative to the lifetime of ^{22}Na,
$\tau = (87.0 \pm 1.9)$ y. With this lifetime, the ^{44}Ti abundance agrees with
theoretical predictions within the remaining observational uncertainties.

---

[1] presently on leave at Forschungszentrum Karlsruhe, IK III

1 Introduction

Supernovae are one of the main sources of galactic radioactivity. The light
curve of supernovae are powered by the energy released by the decay of un-
stable nuclei, first by ^{56}Ni and its long-lived daughter ^{56}Co, then by ^{57}Co and
^{44}Ti. These nuclei are created in the α-rich freeze-out during the supernova
explosion [1, 2, 3, 4]. Here, material cools in nuclear statistical equilibrium
at low densities and the build-up of heavy elements is handicapped by the
slow triple-α-process. In particular the production of ^{44}Ti depends critically
on entropy and density conditions in the α-rich freeze-out [4, 5]. Of special
interest is therefore the observation of the 1157 keV γ-line from the decay
of ^{44}Ti. So far, the only source for this line is the supernova remnant Cas-
siopeia A [6]. From the observed γ-flux the total ^{44}Ti mass ejected by Cass A
can be determined, which provides a sensitive test for the various supernova
models. However, a meaningful determination of this mass is hampered by
the uncertainty of the ^{44}Ti lifetime. The reported lifetime values (67 - 96 y)
[7, 8, 9, 10, 11] lead to an uncertainty in the ^{44}Ti mass of a factor of three. For
this reason we measured the lifetime of ^{44}Ti using a novel technique. A mixed
radioactive beam containing ^{44}Ti and ^{22}Na was implanted into a stack of foils
and the resulting activity was measured using a high-resolution Ge detector.
This method allowed the determination of the ^{44}Ti lifetime relative to the well-
known lifetime of ^{22}Na reducing the systematic uncertainties. The lifetime of
^{44}Ti depends only on two ratios, the relative amount of ^{44}Ti and ^{22}Na in the
beam, $N_{^{44}Ti}/N_{^{22}Na}$, and the resulting relative activities, $A_{^{44}Ti}/A_{^{22}Na}$:

$$\tau_{^{44}Ti} = \left(\frac{A_{^{44}Ti}}{A_{^{22}Na}} \right)^{-1} \cdot \left(\frac{N_{^{44}Ti}}{N_{^{22}Na}} \right) \cdot \tau_{^{22}Na}. \tag{1}$$

In the following we describe the experimental setup and analysis of the
data followed by a discussion of the results.

2 Experimental Setup

A secondary ion beam was produced at the National Superconducting Cy-
clotron Laboratory at Michigan State University. A primary beam of ^{46}Ti
with an energy of E/A = 70.6 MeV/u with an intensity of about 4 p-nA was
directed onto a ^{9}Be target with a thickness of 202 mg/cm^2, which was lo-
cated at the target position of the A1200 projectile fragment separator [12].
The A1200 was operated in the medium acceptance mode and optimized for
maximum ^{44}Ti intensity at the focal plane. With this setting all other N=Z

fragments (e.g. ^{22}Na) are also transmitted to the focal plane. The experiment was run in two modes. In the first, all fragments were implanted into a stack of Al foils located at the focal plane. The stack consisted of seven Al foils each with a thickness of 457 μm except for the fifth foil which had a thickness of 50 μm. The ^{44}Ti ions were implanted into the center of the third foil and the ^{22}Na ions into the center of the sixth foil. The second mode provided for particle identification of the implanted species. In this mode, the primary beam current was reduced and a set of detectors replaced the implantation foils. The set of detectors consisted of a 300 μm Si detector, a position-sensitive Parallel Plate Avalanche Counter and a plastic detector. This identified the different particle groups at the implantation spot by means of their energy loss, total energy, and their time-of-flight through the separator, and also provided a determination of the fragment intensity across the implantation spot.

Fragments were implanted for an accumulated time of 29 hours. About every three hours the relative intensities of the fragments were measured switching to the second mode. The mean ratio $N_{^{44}Ti}/N_{^{22}Na}$ of all runs is 76.78 with 1σ errors of ±0.73 (internal error) and ±0.78 (external error). The absolute ^{44}Ti intensity was $\approx 5\cdot10^5$/s or about 5% of the total intensity and a total of $\approx 5\cdot10^{10}$ ^{44}Ti ion were implanted. The position spectra gated on the ^{44}Ti and ^{22}Na groups showed the same distribution of the implanted particles for both fragments.

The specific activities of the implanted foils were measured by detecting the characteristic γ-decay line of the radio-isotopes using a Ge detector which was completely shielded with 10 cm of Pb to reduce the room background. A sample holder allowed the placement of the foils at distances of 13.9mm, 23.9mm, 44.0mm, and 83.9mm from the surface of the Ge-crystal. Short-lived activities were allowed to decay during a 3-month period between the end of the implantation and the beginning of the activity measurement. The activities were measured in four cycles and during each cycle the foils were placed in each of the four position. The γ-activity following the decay of ^{44}Ti and ^{22}Na is very similar [13] and only small corrections to the ratio of the γ-activities are necessary to obtain the ratio of their activities. In 99.87 % of the ^{44}Ti decays a γ-ray with an energy of 1157 keV is emitted and in 99.94 % of the ^{22}Na decays a γ-ray with an energy of 1274 keV. Figure 1 shows the relevant part of the γ-spectra with a ^{22}Na foil in place (top panel) and with a ^{44}Ti foil in place (bottom panel). From the observed relative intensities of these γ-lines the ratio of the ^{44}Ti and ^{22}Na activities was determined to $A_{^{44}Ti}/A_{^{22}Na}$ = 3.322 $\pm$ 0.054. This final value includes a small correction (1%) of the ^{22}Na activity to account for secondary ^{22}Na production in the implantation foils.
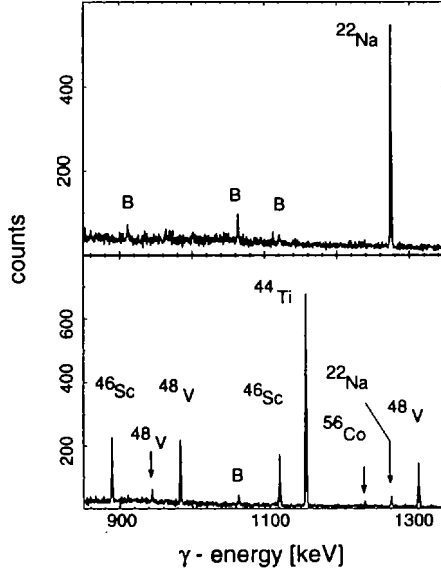
Fig. 1. Relevant part of the γ-spectra obtained with the ^{22}Na foil (top) and with the ^{44}Ti foil (bottom).

This correction has been estimated from the ^{22}Na activity of the neighboring foils and a systematic error of 1% was included in the error of the relative activities.

3 Results and Discussion

With these results for the ratios of the fragment intensities and the activities of ^{44}Ti and ^{22}Na the lifetime of ^{44}Ti is given by equation 1: $\tau_{^{44}Ti} = (87.0 \pm 1.9)$ y. The error is the linear sum of the 1σ-statistical error of 1.0 y and the systematic error of 0.9 y. The present lifetime is in good agreement with two recently reported values of (85.1 ± 0.9) y [14] and (89.4 ± 2.9) y [15]. With the present lifetime, the observed γ-flux from Cass A [6], a date of 1680 AD for the explosion and a distance of 3.4 kpc [16], supernova Cass A ejected a ^{44}T mass of $(1.72\,^{+0.56}_{-0.48}) \cdot 10^{-4}\ M_\odot$. The lifetime of ^{44}Ti contributes now only little (6%) to the uncertainty which is now dominated by the experimental errors of the γ-flux and the distance measurements. The amount of ^{44}Ti is in agreement with supernova model predictions (see e.g. [4, 5]), but an improvement in the

accuracy of the astrophysical input parameters is necessary before the observed ^{44}Ti mass can be used to test and calibrate supernova models.

References

[1] S.E. Woosley, W.D. Arnett, D.D. Clayton, Ap.J. Suppl. **26** (1973) 231;

[2] F.-K. Thielemann, M.A. Hashimoto, K. Nomoto, Ap.J. **349** (1990) 222;

[3] S.E. Woosley and R.D. Hoffman, Ap.J. **368** (1991) L31;

[4] F.X. Timmes et al., Ap.J. **464** (1996) 332;

[5] F.-K. Thielemann, K. Nomoto, M. Hashimoto, Ap.J. **460** (1996) 408;

[6] C. Dupraz et al., Astron. Astrophys. **324** (1997) 683;

[7] J. Wing et al., J. Inorg. Nucl. Chemistry **27** (1965) 487;

[8] P.E. Moreland and D. Heymann, J. Inorg. Nucl. Chem. **27** (1965) 493;

[9] D. Frekers et al., Phys. Rev. **C28** (1983) 1756;

[10] D.E. Alburger and G. Harbottle, Phys. Rev. **C41** 1990) 2320;

[11] E.B. Norman et al., Nucl. Phys. **A621** (1996) 92c;

[12] B.M. Sherrill et al. , Nucl. Instrum. Methods **B56/57** (1991) 1106;

[13] P.M. Endt, Nucl. Phys. **A521** (1990) 1

[14] I. Ahmad et al., submitted to Phys. Rev. Lett.

[15] E.B. Norman et al., submitted to Phys. Rev. C

[16] J.E. Reed et al., Ap. J. **440** (1995) 706

THE EOS AND NEUTRINO INTERACTIONS IN DENSE MATTER

M. PRAKASH and S. REDDY

Department of Physics & Astronomy
SUNY at Stony Brook, Stony Brook, NY 11794-3800, USA

Abstract

The deleptonization and cooling times of a newly born neutron star depend on the equation of state (EOS) and neutrino opacities in dense matter. Through model calculations we show that effects of Pauli blocking and many-body correlations due to strong interactions reduce both the neutral and charged current neutrino cross sections by large factors compared to the case in which these effects are ignored.

1 The Fate of a Newborn Neutron Star

After a supernova explosion, the gravitational mass of the remnant is ~ 1 $M_\odot$. It is lepton rich and has an entropy per baryon of $S \simeq 1$ (in units of Boltzmann's constant k_B). The leptons include both electrons and neutrinos, the latter being trapped in the star because their mean free paths in the dense matter are of order 1 cm, whereas the stellar radius is about 15 km. Accretion onto the neutron star increases its mass to the 1.3–1.5 $M_\odot$ range, and should mostly cease after a second. It then takes about a few tens of seconds [1] for the trapped neutrinos to diffuse out, and in the diffusion process they leave behind most of their energy, heating the protoneutron star to fairly uniform entropy values of about $S = 2$. Cooling continues as thermally-produced neutrinos diffuse out and are emitted. After several tens of seconds, the star becomes transparent to neutrinos, and the neutrino luminosity drops precipitously [2].

Denoting the maximum mass of a cold, catalyzed neutron star by M_{max} and the maximum mass of the protoneutron star with abundant trapped leptons by M_{max}^L, there are two possible ways that a black hole could form after a supernova explosion. First, accretion of sufficient material could increase the remnant's mass to a value greater than either M_{max} or M_{max}^L and produce a black hole, which then appears on the accretion time scale [3]. Second, if exotic matter plays a role and if accretion is insignificant after a few seconds, then for $M_{max}^L > M > M_{max}$, where M is the final remnant mass, a black hole will form as the neutrinos diffuse out [4-8] on the deleptonization time scale.

The existence of metastable neutron stars has some interesting implications [4, 11]. First, it could explain why no neutron star is readily apparent in the remnant of SN1987A despite our knowledge that one existed until at least 12 s after the supernova's explosion. Second, it would suggest that a significant population of relatively low mass black holes exists [9], one of which could be the compact object in the X-ray binary 4U1700-37 [10].

2   Neutrino-Poor versus Neutrino-Rich Stars

A detailed discussion of the composition and structure of protoneutron stars may be found in Refs. [4, 11]. The main findings were that the structure depends more sensitively on the composition of the star than its entropy and that the trapped neutrinos play an important role in determining the composition. Since the structure is chiefly determined by the pressure of the strongly interacting constituents and the nature of the strong interactions is poorly understood at high density, several models, including matter with strangeness-rich hyperons, a kaon condensate and quark matter were studied there.

Evolutionary calculations [1, 7] without accretion show that it takes a few tens of seconds for the trapped neutrino fraction to vanish for a nucleons-only EOS. To see qualitatively what might transpire during the early evolution, we show in Fig. 1 the dependence of the maximum stellar mass upon the trapped neutrino fraction Y_{ν_e}, which decreases during the evolution. When the only hadrons are nucleons (np), the maximum mass increases with decreasing Y_{ν_e}, whereas when hyperons (npH) or kaons (npK) are also present, it decreases. Further, the rate of decrease accelerates for rather small values of Y_{ν_e}. Coupled with this is the fact that the central density of stars will tend to increase during deleptonization. The implication is clear. *If* hyperons, kaons, or other negatively-charged hadronic species are present, an initially stable star can change into a black hole after most of the trapped neutrinos have left, and this takes a few tens of seconds. *This happens only if the remnant mass M satisfies* $M_{max}^L > M > M_{max}$.

On February 23 of 1987, neutrinos were observed [12] from the supernova SN1987A, indicating that a neutron star, not a black hole, was initially present. (The appearance of a black hole would have caused an abrupt cessation of any neutrino signal [2].) The neutrino signal was observed for a period of at least 12 s, after which counting statistics fell below measurable limits. From the handful of events observed, only the average neutrino energy, ~ 10 MeV, and the total binding energy release of $\sim (0.1 - 0.2) M_\odot$ could be estimated.

These estimates, however, do not shed much light on the composition of
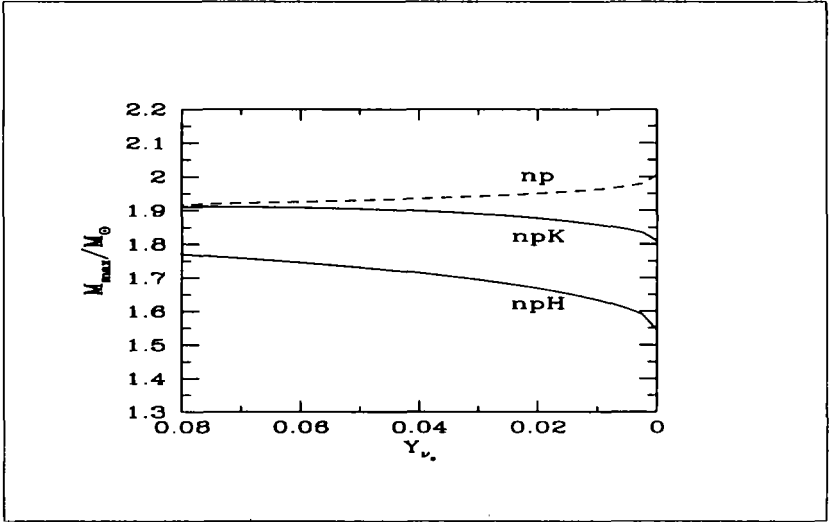
Figure 1: Maximum neutron star mass as a function of Y_{ν_e} for hadronic matter with only nucleons (np) or with nucleons and hyperons (npH) or kaons (npK).

the neutron star. This is because, to lowest order, the average neutrino energy is fixed by the neutrino mean free path in the outer regions of the protoneutron star. Further, the binding energy exhibits a universal relationship [4] for a wide class of EOSs, including those with strangeness bearing components, namely

$$B.E. = (0.065 \pm 0.01)(M_B/M_\odot)^2 M_\odot, \tag{1}$$

where M_B is the baryonic mass. This allows us only to determine a remnant gravitational mass of $(1.14 - 1.55)M_\odot$, but not the composition.

It must be emphasized that the maximum mass of the cold catalyzed star still remains uncertain due to the uncertainty in strong interactions at high density. At present, all nuclear models can only be effectively constrained at nuclear density and by the condition of causality at high density. The resulting uncertainty is evident from the range of possible maximum masses predicted by the different models. Notwithstanding this uncertainty, our findings concerning the effects of neutrino trapping offer intriguing possibilities for distinguishing between the different physical states of matter. These possibilities include both black hole formation in supernovae and the signature of neutrinos to

be expected from supernovae. In an optimistic scenario, several thousand neutrinos from a typical galactic supernova might be seen in upgraded neutrino detectors (for rough characteristics of present and future neutrino detectors, see Ref. [13].) Among the interesting features that could be sought are:

• possible cessation of a neutrino signal, due to black hole formation;

• possible burst or light curve feature associated with the onset of negatively-charged, strongly interacting matter near the end of deleptonization, whether or not a black hole is formed;

• identification of the deleptonization/cooling epochs by changes in luminosity evolution or neutrino flavor distribution;

• determination of a radius-mean free path correlation from the luminosity decay time or the onset of neutrino transparency; and

• determination of the neutron star mass from the universal binding energy-mass relation.

3   Neutrino Opacities in Dense Matter

To date, calculations of neutrino opacities in dense matter have received relatively little attention [14-17] compared to other physical inputs such as the EOS. The neutrino cross sections and the EOS are intimately related. This relationship is most transparent in the long-wavelength or static limit, in which the response of a system to an external probe is completely determined by the ground state thermodynamics (EOS). Thus, in this limit, neutrino opacities consistent with the EOS can be calculated [14]. However, when the energy and momentum transferred by the neutrinos are large, full consistency is often difficult to achieve in practice. Despite this, many salient features of an underlying dense matter model may be incorporated in the calculation of the neutrino opacities. In §4, we describe how this is accomplished for a potential model. The effects of nucleon-nucleon correlations are calculated using the random phase approximation (RPA) in §5, where we show that the magnitudes of these many-body effects on both the scattering and absorption reactions are large. The scattering cross section in a multi-component system including the effects of correlation due to both strong and electromagnetic interactions are presented in §6 using a relativistic formalism. The implications of these results for neutrino transport in a protoneutron star are in §7.

4 Model Calculations

In the non-relativistic limit for the baryons, the cross-section per unit volume for the two body reaction $\nu + B_2 \to l + B_4$ is given by [17]

$$\frac{\sigma(E_1)}{V} = \frac{G_F^2}{4\pi^2}(\mathcal{V}^2 + 3\mathcal{A}^2) \int_{-\infty}^{E_1} dq_0 \; \frac{E_3}{E_1}(1 - f_3(E_3)) \int_{|q_0|}^{2E_1-q_0} dq \; qS(q_0, q) \, . \quad (2)$$

The particle labels are: 1:=incoming neutrino, 2:=incoming baryon, 3:=outgoing lepton (electron or neutrino), and 4:=outgoing baryon. The energy transfer to the baryons is denoted by $q_0 = E_1 - E_3$ and the momentum transfer $q = |\vec{k_1} - \vec{k_2}|$. Eq. (2) describes both the charged and neutral current reactions with the appropriate substitution of vector and axial vector coupling constants, $\mathcal{V}$ and $\mathcal{A}$, respectively [17]. The factor $(1 - f_3)$ accounts for Pauli blocking of the final state lepton. The response of the system is characterized by $S(q_0, q)$, often called the dynamic form factor. In §5, we consider the modifications required in the presence of spin and isospin dependent forces.

At the mean field level, the function $S(q_0, q)$ may be evaluated exactly if the single particle dispersion relation is known [17]. We illustrate this using a potential model. In this case, if we retain only a quadratic momentum dependence, the single particle spectrum closely resembles that of a free gas and is given by

$$E_i(p_i) = \frac{p_i^2}{2M_i^*} + U_i \, , \quad i = n, p \, . \quad (3)$$

The single particle potentials U_i and the effective masses M_i^* are density dependent. Because the functional dependence of the spectra on the momenta is similar to that of the noninteracting case, it is possible to obtain an analytic expression for the dynamic form factor $S(q_0, q)$ [17]. Explicitly,

$$S(q_0, q) = \frac{M_2^* M_4^* T}{\pi q} \frac{\xi_- - \xi_+}{1 - \exp(-z)} \quad (4)$$

where

$$\xi_\pm = \ln\left[\frac{1 + \exp((e_\pm - \mu_2 + U_2)/T)}{1 + \exp((e_\pm + q_0 - \mu_4 + U_2)/T)}\right]$$

$$e_\pm = \frac{2q^2}{2M^*\chi^2}\left[\left(1 + \frac{\chi M_4^* c}{q^2}\right) \pm \sqrt{1 + \frac{2\chi M_4^* c}{q^2}}\right] \, ,$$

with $\chi = 1 - (M_4^*/M_2^*)$ and $c = q_0 + U_2 - U_4 - (q^2/2M_4^*)$. The factor $U_2 - U_4$ is the potential energy gained in converting a particle of species "2" to a
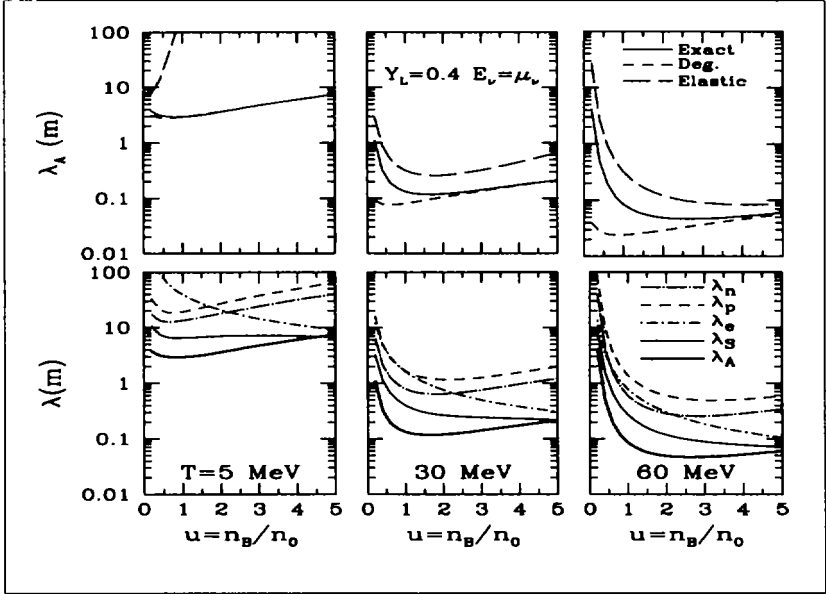
Figure 2: Absorption (top panels) and scattering (bottom panels) mean free paths in β-equilibrated stellar matter.

particle of species "4". In neutral current reactions, the initial and final state particles are the same; hence, the strong interaction corrections are due only to M_2^*. For the charged current reactions, modifications due to interactions are twofold. First, the difference in the neutron and proton single particle potentials appears in the response function and also in $\hat{\mu} = \mu_n - \mu_p$. Second, the response depends upon the nucleon effective masses.

Results obtained using Eq. (4) are shown in Fig. 2, where electron neutrino absorption (top panels) and scattering (bottom panels) mean free paths are shown in matter containing nucleons and leptons. Various limiting forms are also shown for comparison. The charged current mean free paths are shown as thick solid lines in the bottom panel. These results demonstrate that effects due to kinematics, Pauli blocking, mass, and energy shifts are quantitatively important [17].

5 Effects of Correlations

The random phase approximation (RPA) is particularly suited to investigate the role of particle-hole interactions on the collective response of matter. In this approximation, ring diagrams are summed to all orders. In terms of this more general response, the differential cross-sections are given by

$$\frac{1}{V}\frac{d^3\sigma}{d^2\Omega\, dE_3} = \frac{G_F^2}{\pi}(1 - f_3(E_3))\ R(q_0, q),\tag{5}$$

where $R(q_0, q)$ describes the system's response. For the neutral current reactions [15]

$$R_S(q_0, q) = \left[c_V^2\ (1 + \cos\theta)S_{00}(q_0, q) + c_A^2\ (3 - \cos\theta)S_{10}(q_0, q)\right].\tag{6}$$

S_{00} and S_{10} are the density-density and spin-density response functions. Similarly, the charged current response may be written in terms of the isospin-density and the spin-isospin density response functions as

$$R_A(q_0, q) = \left[g_V^2\ (1 + \cos\theta)S_{01}(q_0, q) + g_A^2\ (3 - \cos\theta)S_{11}(q_0, q)\right].\tag{7}$$

5.1 Neutral Currents

Neutrino scattering on neutrons is the dominant source of scattering opacity. We therefore begin by considering the response in pure neutron matter. For a one component system, the RPA response functions are given by

$$
\begin{aligned}
S_{ij}(q_0, q) &= \left[\frac{1}{1 - \exp(q_0/T)}\right]\frac{Im\ \Pi^0(q_0, q)}{\epsilon_{ij}}\\
\epsilon_{ij} &= [1 - V_{ij}Re\ \Pi^0(q_0, q)]^2 + [V_{ij}Im\ \Pi^0(q_0, q)]^2.
\end{aligned}\tag{8}
$$

The dielectric screening function ϵ_{ij} is the modification introduced by the RPA to Eq. (2). The zeros of ϵ_{ij} correspond to collective excitations, such as zero-sound and spin zero-sound. The potential V_{ij}, which measures the strength of the particle-hole interaction in the medium, is a function of density, temperature, q_0, and q. Both the energy and momentum transferred in the particle-hole channel are of order T. Since the particle-hole interaction is short ranged ($\sim$1/meson mass), explicitly density dependent interactions play a major role in determining the magnitude of V_{ij}. Momentum dependent interactions introduce additional structure to V_{ij}, which in turn alters the structure of S_{ij}. We will consider these latter effects separately.
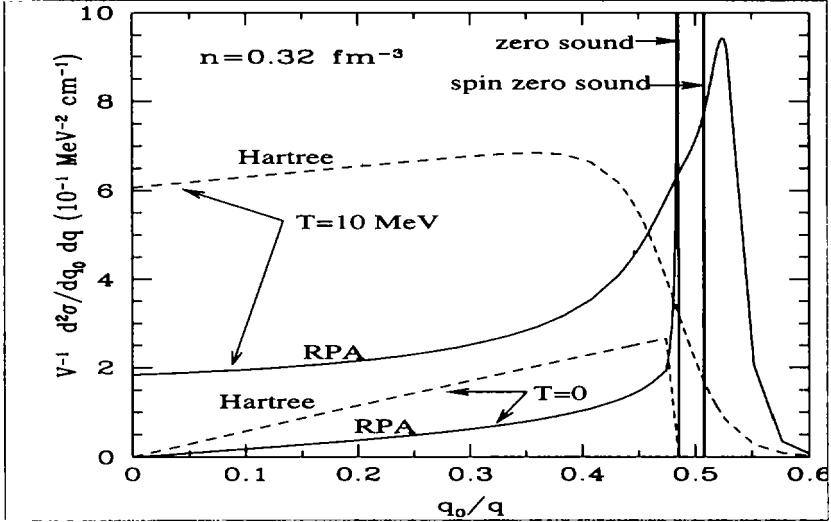
Figure 3: Neutrino scattering cross sections versus q_0/q in pure neutron matter for $q=10$ MeV and a neutrino energy of $E_\nu = 50$ MeV.

For situations in which $q/k_{F_i} \ll 1$ and $T/\mu_i \ll 1$, the quasi-particle interaction may be obtained using Fermi-liquid theory. Here, the quasi-particle interaction is given by $V_{ij} = (\delta^2 E/\delta n_i \delta n_j)$, and is usually expressed in terms of the Fermi-liquid parameters. For pure neutron matter, the force in the spin independent channel is given by F_0, while the force in the spin dependent channel is given by G_0. Thus, $V_{00} = F_0/N_0$ and $V_{10} = G_0/N_0$, where N_0 is the density of states at the Fermi surface [18]. We employ the results of Bäckmann et al., [19] who have calculated F_0 and G_0 in pure neutron matter for the densities of interest here.

In Fig. 3, the differential cross sections for $\nu + n \rightarrow \nu + n$ are shown. The effects due to correlations lead to significant reductions at small q_0, since the interaction is repulsive and the excitation of collective modes enhances the response at large q_0. The well defined zero-sound and spin zero-sound seen at $T = 0$ are damped at finite temperatures. The contribution from the low q_0 region dominates the total cross-section due to final state blocking. The presence of a repulsive particle-hole force acts to reduce the neutrino cross sections for neutrino energies of order T.
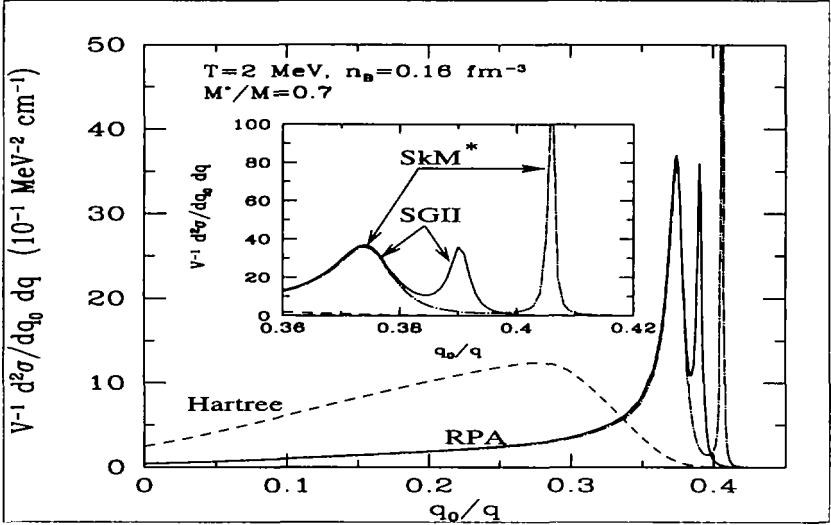
Figure 4: Charged current reaction cross sections in symmetric nuclear matter.

The composition of charge neutral, β-equilibrated stellar matter depends on the EOS of dense matter, which contains an admixture of protons and electrons. The correlations due to interactions between the different particle species and electromagnetic correlations also play an important role. In §6, we discuss a relativistic framework to describe the RPA response of a mixture of neutrons, protons, and electrons.

5.2 Charged Currents

The charged current reaction is kinematically different from the neutral current reaction, since the energy and momentums transfers are not limited only by the matter temperature. The energy transfer is typically of order $\hat{\mu} = \mu_n - \mu_p$. The charged current probes smaller distances; hence, the q_0 and q dependencies of the particle-hole force are likely to play an important role. In symmetric nuclear matter $\hat{\mu} = 0$, and therefore, the situation is very similar to the neutral current case. Since the collective response of laboratory nuclei is well established in nuclear physics, we begin by considering the response of symmetric nuclear matter to a charged current weak probe. Here the strength parameters
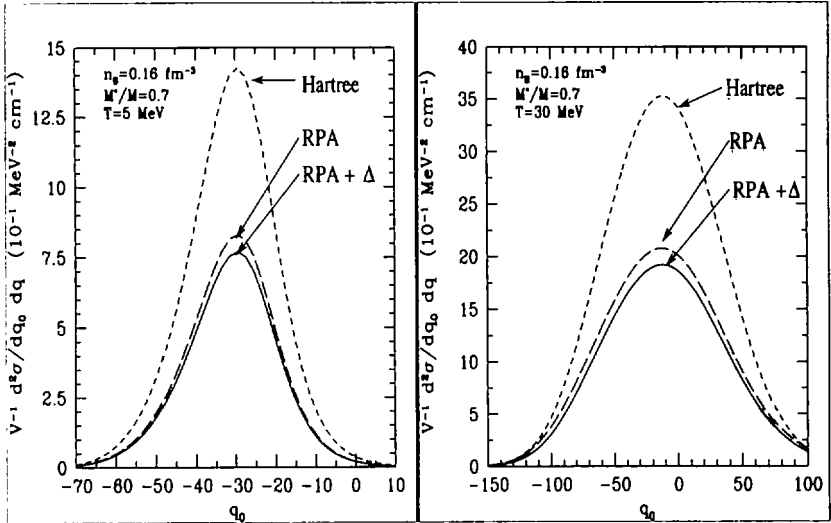
Figure 5: Neutrino absorption cross sections in asymmetric matter.

V_{01} for the spin independent iso-spin channel and the V_{11} for the spin dependent iso-spin channel are required. In nuclear matter, the particle-hole force (retaining only the $l = 0$ terms) is given by [18]

$$\mathrm{F}(k_1, k_2) = N_0^{-1}[F_0 + G_0\sigma_1\sigma_2 + \tau_1\tau_2(F_0' + G_0'(\sigma_1\sigma_2)]. \qquad (9)$$

For the charged current reaction, isospin and charge are transferred along the particle-hole channel; hence, only the last two terms in Eq. (9) contribute. The potentials required to calculate the RPA response in Eq. (8) are given by $V_{10} = 2F_0'/N_0$ and $V_{11} = 2G_0'/N_0$, where the factor two arises due to isospin considerations. The Fermi-liquid parameters may be calculated from an underlying dense matter model, as for example, a Skyrme model, which successfully describes the low-lying excitations of nuclei [20]. In Fig. 4, the response of symmetric nuclear matter to the charged current probe is shown. Results are for two different parameterizations of the Skyrme force, SGII and SkM*. The excitation of giant-dipole and Gamow-Teller resonances shifts the strength to large q_0, and as in the case of scattering, the low q_0 response is significantly suppressed.

In asymmetric matter, the energy and momentum transfers are large. There-

fore, the momentum dependence of the particle-hole force becomes important. At high momentum transfer, the conservation of the vector current implies that the response function S_{10} is not strongly modified. Further, since its contribution to the differential cross section is roughly three times smaller than the spin-dependent response function S_{11}, we focus on the Gamow-Teller part and assume that the Fermi matrix elements are not screened. The iso-vector interaction in the longitudinal channel arises due to π exchange, and in the transverse channel due to ρ meson exchange. In addition, to account for the large repulsion observed, Migdal [18] introduced screening in this channel through the parameter g'. This form for the particle-hole interaction has been successful in describing a variety of nuclear phenomena. The longitudinal and transverse potentials in the $\pi + \rho + g'$ model are given by [21]

$$
\begin{aligned}
V_L(q_0, q) &= \frac{f_\pi^2}{m_\pi^2} \left(\frac{\mathbf{q}^2}{q_0^2 - \mathbf{q}^2 - \mathbf{m}_\pi^2} F_\pi^2(q) + g' \right) \\
V_T(q_0, q) &= \frac{f_\pi^2}{m_\pi^2} \left(\frac{\mathbf{q}^2 \ \mathbf{C}_\rho}{q_0^2 - \mathbf{q}^2 - \mathbf{m}_\rho^2} F_\rho^2(q) + g' \right) ,
\end{aligned}
\tag{10}
$$

where $F_\pi = (\Lambda^2 - m_\pi^2)/(\Lambda^2 - q^2)$ and $F_\rho = (\Lambda_\rho^2 - m_\rho^2)/(\Lambda_\rho^2 - q^2)$ are the πNN and ρNN form factors. Numerical values used are $C_\rho = 2, g' = 0.7, \Lambda = 1.4$ GeV, and $\Lambda_\rho = 2$ GeV. The RPA response function then takes the form

$$
\begin{aligned}
S_{11}(q_0, q) &= \left[\frac{1}{1 - \exp(q_0/T)} \right] \ Im \ \Pi^0(q_0, q) \left(\frac{1}{3\epsilon_L} + \frac{2}{3\epsilon_T} \right) \\
\epsilon_{L,T} &= [1 - 2V_{L,T} Re \ \Pi^0(q_0, q)]^2 + [2V_{L,T} Im \ \Pi^0(q_0, q)]^2
\end{aligned}
\tag{11}
$$

The cross sections in charge neutral stellar matter with a fixed lepton fraction $Y_L = 0.4$ are shown in Fig. 5. The RPA screening reduces the cross sections by about a factor of two. The inclusion of virtual Δ-hole excitations reduces the cross sections further. Unlike in the case of ordinary β decay, where the Δ-hole contribution is important, the role of these excitations is marginal here due to the large energy and momentum transfers.

6   Relativistic Treatment

At high density the baryons become increasingly relativistic and thus a rela-tivistic description may be more appropriate. Such a description also allows us to treat the baryons and the electrons on an equal footing. The basic formalism and some illustrative results may be found in [16, 17]. Here we present results
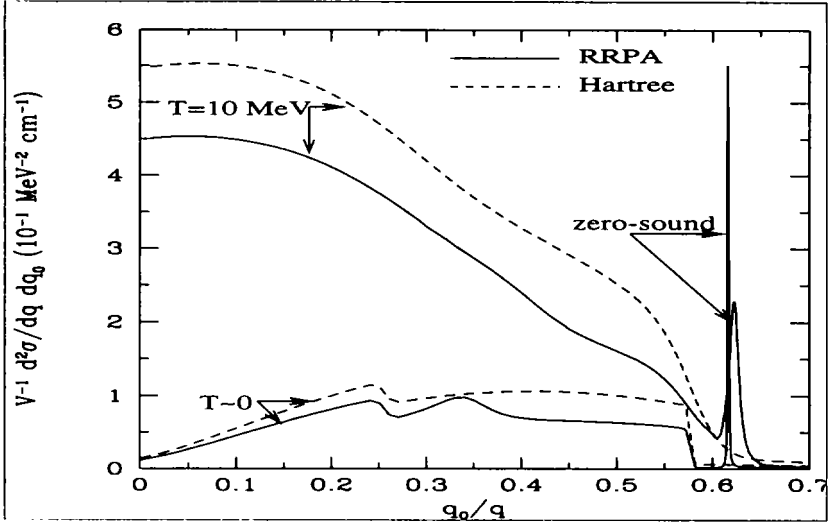
Figure 6: Neutrino scattering cross sections in a relativistic approach.

for a system of neutrons, protons, and electrons at finite temperature. The ground state is described by a field-theoretical model at the mean field level, in which isoscalar σ, ω and isovector ρ meson exchanges modify the in-medium baryon propagators. We calculate the Hartree response by accounting for these modifications. Correlations are incorporated through the relativistic random phase approximation (RRPA), where the particle-hole interaction is mediated by the σ and ω mesons between the baryons, and electromagnetic interactions between protons and electrons are mediated by photons. Fig. 6 shows the results (baryon density of 0.32 fm^{-3}). Compared to the non-relativistic models, the screening effects are small, the dominant suppression arising mainly due to density dependent nucleon effective masses.

7 Discussion

We have highlighted the influence of correlations and collective phenomena on the neutrino opacities in dense matter. Our findings here indicate that the neutrino cross sections are significantly reduced, and the average energy transfer in neutrino-nucleon interactions is increased due to the presence correlations

in the medium. Several improvements are necessary before we can assess the influence of these results on the macrophysical evolution of a protoneutron star. Among the most important of these are calculations that provide (1) the dynamic form factor, (2) the particle-hole and particle-particle interactions, (3) the renormalization of the axial charge, and, (4) the means to assess the role of multi-pair excitations, in charge neutral, beta-equilibrated dense matter at finite temperature. While investigations along these directions are in progress (see also [22]), some general trends may be anticipated. The many-body effects studied here, including the improvements listed above, suggest considerable reductions in the opacities compared to the free gas estimates often employed in many applications. In the particular instance of the early evolution of a protoneutron star, the suggested modifications imply shorter time scales over which the deleptonization and cooling occur. Since mean free paths λ are much less than the stellar radius R, evolution is via diffusion. To order of magnitude, therefore, the timescale $\tau \propto 1/\lambda$. However, there are important feedbacks between these evolutionary consequences and the underlying EOS, in particular the specific heat of multicomponent matter, which have to be studied before firm conclusions may be drawn.

Acknowledgement

References

[1] A. Burrows and J.M. Lattimer, Astrophys. J. **307** (1986) 178; A. Burrows, Ann. Rev. Nucl. Sci. **40** (1990) 181.

[2] A. Burrows, Astrophys. J. **334** (1988) 891.

[3] G.E. Brown et al., *Comments Astrophys.* **16** (1992) 153.

[4] M. Prakash *et al.*, Phys. Rep. **280** (1997) 1.

[5] M. Prakash et al., Phys. Rev. **D52** (1994) 661.

[6] V. Thorsson et al., Nucl. Phys. **A572** (1994) 693.

[7] W. Keil and H.T. Janka, Astron. & Astrophys. **296** (1994) 145.

[8] N.K. Glendenning, Astrophys. J. **448** (1995) 797.

[9] G.E. Brown and H.A. Bethe, Astrophys. J. **423** (1994) 659. G.E. Brown et al., Astrophys. J. **463** (1996) 297.

[10] G.E. Brown et al., Astrophys. J. **463** (1996) 297.

[11] P.J. Ellis et al., *Comments on Nucl. and Part. Phys.* **22** (1996) 63.

[12] K. Hirata *et al.*, Phys. Rev. Lett. **58** (1987) 1490; R.M. Bionta *et al.*, Phys. Rev. Lett. **58** (1987) 1494.

[13] A. Burrows et al., Phys. Rev. **D45** (1992) 3361.

[14] R. F. Sawyer, Phys. Rev. **D11** (1975) 2740; Phys. Rev. **C40** (1989) 865.

[15] N. Iwamoto and C. J. Pethick, Phys. Rev. **D25** (1982) 313.

[16] C. J. Horowitz and K. Wehrberger, Nucl. Phys. **A531** (1991) 665; Phys. Rev. Lett. **66** (1991) 272; Phys. Lett. **B226** (1992) 236.

[17] S. Reddy, M. Prakash, and J. M. Lattimer, 1997 Phys. Rev. **D** submitted.

[18] A. B. Migdal, 1962, *Theory of Finite Fermi Systems and Applications to Atomic Nuclei* (New York: Interscience).

[19] S. O. Bäckmann and C.-G. Källman, Phys. Lett. **B43** (1973) 263.

[20] G. Bertsch and S. F. Tsai, Phys. Rep. **18** (1975) 125.

[21] E. Oset, H. Toki, and W. Weise, Phys. Rep. **83** (1982) 280.

[22] A. Burrows A and R. F. Sawyer, Phys. Rev. **D** (1989) submitted.

NEUTRINOS FROM PROTONEUTRON STARS

S. REDDY[a], J. PONS[a,b], M. PRAKASH[a] AND J. M. LATTIMER[a]

[a]*Department of Physics & Astronomy,*
SUNY at Stony Brook, Stony Brook, NY 11794.

[b]*Departament d'Astronomia, Universitat de València*
E-46100 Burjassot, València, Spain.

Abstract

We study the diffusive transport of neutrinos in a newly born neutron star to explore its sensitivity to dense matter properties. Energy and lepton number which are trapped during the catastrophic implosion diffuse out on the time scale of a few tens of seconds. Results for different dense matter models are presented.

1 Introduction

The core of a massive star implodes when its mass exceeds the Chandrashekar mass. The hot and dense remnant formed subsequent to the implosion is a protoneutron star. Numerical simulations of the implosion (and the subsequent formation of a shock wave at core bounce) indicate that, due to the high densities and temperatures, most of the star's gravitational binding energy and lepton number released remains trapped in the star as neutrinos. The general features of the early evolution have been discussed in prior work [1, 2]. The object of this work is to elucidate the role played by the microphysical inputs (equation of state (EOS) and neutrino opacities) on the macrophysical evolution of the protoneutron star.

2 The Basic Equations

The structure of the star is assumed to be in quasi-static equilibrium, and is described by the general relativistic equation for hydrostatic equilibrium. The loss of lepton number and energy due to neutrino flows is treated in the diffusion approximation. The equations governing the early evolution may be found in [1, 2]. To solve the structure equations we need to specify the finite temperature EOS discussed in §3. Other microphysical inputs required to solve the transport equations are the neutrino mean free paths and bulk properties such as the specific heat and the nuclear symmetry energy.

2.1 Deleptonization

To illustrate how microphysical inputs influence lepton number transport, we examine the Newtonian diffusion equation [3]

$$n\frac{\partial Y_L}{\partial t} \simeq \frac{1}{r^2}\frac{\partial}{\partial r}\left[r^2\left((D_2 + D_{\bar{2}})\frac{\partial(\mu_\nu/T)}{\partial r} - (D_3 - D_{\bar{3}})\frac{\partial(1/T)}{\partial r}\right)\right]. \qquad (1)$$

Here $Y_L = Y_e + Y_\nu$ is the total lepton fraction and μ_ν is the local neutrino chemical potential. The neutrino mean free path $\lambda(E_\nu)$ enters Eq. (1) via the unnormalized diffusion coefficients D_n (and $D_{\bar{n}}$ for anti-neutrinos) defined by $D_n = \int_0^\infty dE_\nu\, E_\nu^n\, \lambda_\nu(E_\nu)\, f_\nu(E_\nu)(1 - f_\nu(E_\nu))$. The time scales crucially depend on the magnitude of $\lambda(E_\nu)$ and its energy dependence. For electron neutrinos, the dominant contributions to $\lambda(E_\nu)$ arise from the charged current reaction $\nu + n \rightarrow e^- + p$. The rate of this reaction is sensitive to both temperature and the composition of the ambient matter [3-6]. Under degenerate conditions, the phase space for this reaction is proportional to $\mu_n T^2(\hat{\mu} + E_\nu)$, where μ_n is the neutron chemical potential and $\hat{\mu} = \mu_n - \mu_p$. The left hand side of Eq. (1) illustrates one way the EOS directly influences the lepton number flows. Note that $\frac{\partial Y_L}{\partial t} = \frac{\partial Y_L}{\partial Y_\nu}\frac{\partial Y_\nu}{\partial t}$, and that $\frac{\partial Y_L}{\partial Y_\nu}$ is directly related to the nuclear symmetry energy $S(n_B)$. Since $\hat{\mu} = 4S(n_b)(1 - 2Y_P)$, where Y_p is the proton fraction, the nuclear symmetry energy will play a crucial role in the deleptonization phase. Further, the possible presence of hyperons at high density affects both $\frac{\partial Y_L}{\partial Y_\nu}$ and the neutrino mean free path λ will be altered [3, 4].

2.2 Cooling

At early times, the flow of electron neutrinos due to chemical potential gradients results in net heating rather than cooling. This Joule heating and negative temperature gradients warm the central regions until the center reaches the maximum temperature. At this stage, the center begins to cool as the thermal gradients force all six neutrino species radially outwards. Due to the high densities and temperatures present, the pair production processes are sufficiently rapid to ensure that μ and τ neutrinos are in thermal equilibrium. Energy transport is governed by

$$nT\frac{\partial s}{\partial t} = \frac{c}{6\pi(\hbar c)^3}\frac{1}{r^2}\frac{\partial}{\partial r}\left[r^2\sum_\ell \frac{D_{4,\ell}}{T^2}\frac{\partial T}{\partial r}\right]. \qquad (2)$$

All general relativistic corrections and terms arising due to lepton number gradients have been dropped to highlight the essential role of the microphysics. The dominant opacity for μ and τ pairs is that due to scaterring on baryons and

electrons, as the charged current reactions are kinematically inaccessible. The charged current reactions are still the dominant source of opacity for electron neutrinos; thus, relative to the μ and τ pairs their contribution to energy transport is significantly suppressed. Under partially degenerate conditions, the phase space for scattering reactions is roughly proportional to $M^{*2}T^3$ (note that the ambient temperature determines the average E_ν); M^* arises since it determines the density of states at the Fermi surface. The left hand side of Eq. (2) is directly related to the specific heat since $Tds = C_v dT$, and is strongly dependent on the effective baryon mass M^*. Neutrino mean free paths depend on the same physics, since they are proportional to the number of target particles which do not suffer significant Pauli blocking.

3 Microphysics

3.1 The Equation of State (EOS)

The dense matter EOS is an important ingredient in protoneutron star simulations. For a detailed discussion of a variety of dense matter models see [7]. In this work, we have explored four different models (see Table) to study the early evolution. We broadly classify them as soft (GM3) and stiff (GM1) models [8], and models can contain (GM1-H, GM3-H) or not contain (GM1-N, GM3-N) hyperons. Hyperons begin to appear only towards the late stages of the deleptonization [7]. This results in these models having significantly lower maximum masses for $Y_{\nu=0}$ (4th column) and the existence of a range (3rd & 4th columns) of initial masses that become unstable upon deleptonization.

Model	Composition	$M_{Y_L=0.4}^{MAX}(T=0)$	$M_{Y_\nu=0}^{MAX}(T=0)$
GM1-N	n,p + leptons	2.52	2.76
GM1-H	n,p,H + leptons	2.25	1.96
GM3-N	n,p + leptons	2.16	2.35
GM3-H	n,p,H + leptons	1.95	1.74

3.2 Neutrino Interactions

Neutrino interactions are significantly modified in a hot and dense medium. The effects of Pauli blocking and strong interactions on the weak interaction rates have been investigated in Refs. [3-6] which showed that density and temperature dependence of the neutrino mean free path are significantly different from those employed in earlier proto-neutron star simulations [1, 2]. Strong interaction effects may be incorporated by employing appropriate dispersion relations and effects of Pauli blocking may be incorporated exactly. In addition, Ref. [3] shows that the neutrino mean free path also depends on the composition of the ambient matter. In particular, the appearance of hyperons leads to significant reduction in λ_ν during the cooling phase.

4 Results
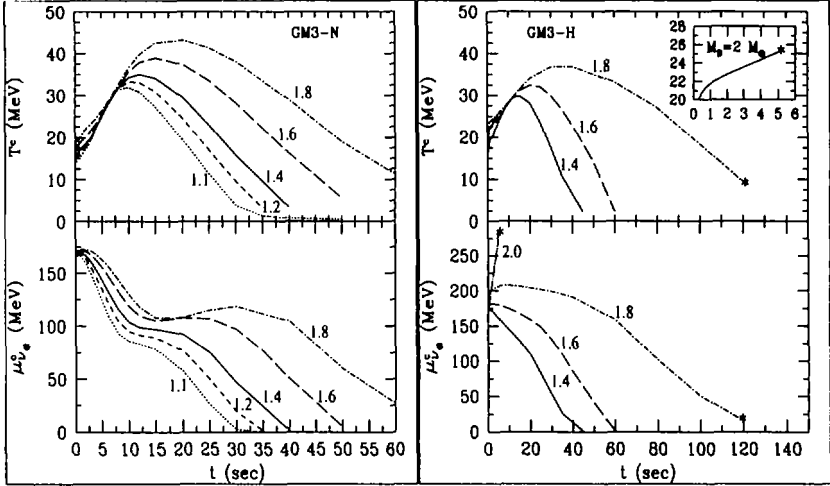
Figure 1: Central temperature and neutrino chemical potential vs time (model GM3). Right (left) panels: matter with (without) hyperons. Curves are labelled by the initial baryon masses. Models $M_B \geq M_{Y_\nu=0}^{MAX} = 1.74 M_\odot$ are unstable and collapse as they deleptonize (denoted by an asterix). Note, however, that if the baryon mass does not significantly exceed this value the meta-stable state lasts for a very long time.

We turn now to results of simulations which include the full effects of general relativity. In Fig. 1, the time evolution of the central temperatures are shown for models with (right top) and without (left top) hyperons for different initial masses. The deleptonization times are related to the time evolution of the neutrino chemical potential, which are shown for models with (right bottom) and without (left bottom) hyperons. The identification of time scales associated with deleptonization and cooling depend on their precise definition. Here, we opt to define the deleptonization time τ_D as the time it takes for the central value of μ_{ν_e} to drop below 10 MeV, and the cooling time τ_C as the time it takes for the central temperature T^c to drop below 5 MeV. Fig. 2 clearly shows the generic trends; (1) Softening leads to higher central densities, and thus higher temperatures, both of which act to decrease λ_ν, (2) Hyperons decrease the baryon degeneracy in the central regions, and since the neutrinos couple quite strongly to the hyperons [4], λ_ν is reduced; and (3) Hyperonization is accompanied by compressional heating and neutrino production, both of which delay the cooling and deleptonization times. Hyperons thus always act to

increase the deleptonization and cooling times. Fig. 2 also shows that a softer
EOS favors longer diffusion times due to higher temperatures and densities
in the inner regions of the star. To discriminate observationally between these
different dense matter scenarios, the neutrino luminosities must be folded with
the response of terrestrial detectors.
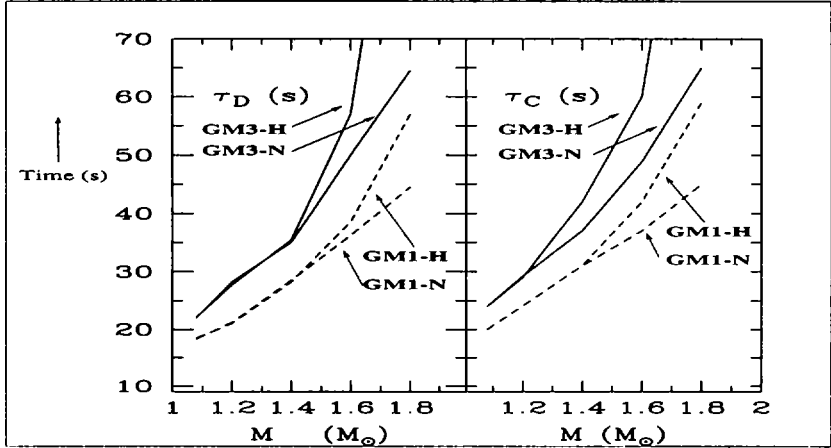
Figure 2: Deleptonization and cooling times. Left panel: τ_D for various models as a
function of the initial baryon mass. Right Panel: τ_C for the different models.

References

[1] A. Burrows and J.M. Lattimer, ApJ. **307** (1986) 178;

[2] W. Keil and H.T. Janka, Astron. & Astrophys. **296** (1995) 145;

[3] S. Reddy, M. Prakash and J. M. Lattimer, Phys. Rev. **D** (1997) submitted.

[4] S. Reddy and M. Prakash, Astrophys. Jl. **423** (1997) 689

[5] R. F. Sawyer, Phys. Rev. **D11** (1975) 2740; Phys. Rev. **C40** (1989) 865.

[6] N. Iwamoto and C. J. Pethick, Phys. Rev. **D25** (1982) 313.

[7] M. Prakash, et. al, Phys. Rep **280** (1997) 1.

[8] N. K. Glendenning and S. A. Moszkowski, Phys. Rev. Lett. **67** (1991)
2414.
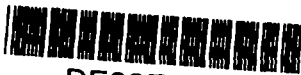
THE $(\nu, \nu' N \gamma)$ REACTION ON ^{16}O AND THE STRANGENESS CONTENT OF THE NUCLEON

E. KOLBE

Departement für Physik und Astronomie der Universität Basel,
CH-4056 Basel, Switzerland

Abstract

Recently we have pointed out that photons with energies between 5 and 10 MeV, generated by the $(\nu, \nu' p \gamma)$ and $(\nu, \nu' n \gamma)$ reactions on ^{16}O, constitute a signal which allows a unique identification of supernova ν_μ and ν_τ neutrinos in water Čerenkov detectors. It was also shown that the cross sections for neutrino-induced knockout of a nucleon via a neutral current reaction on nuclei are affected by the strange quark content of the nucleon. Hence strangeness in the nucleon could have an influence on the energy spectrum of the photons emitted in these processes, which is investigated in the following.

1 Motivation

Astrophysics offers an application sphere for many branches of physics, i.e., in order to describe an astrophysical event, often detailed input from various other fields in physics is needed. Vice versa, sometimes observations in Astrophysics allow to go back and draw conclusions concerning parameters or assumptions contained in the input. From the outcome of Big Bang Nucleosynthesis, e.g., the restriction $N_\nu \leq 3.5$ [1] for the number of existing neutrino generations can be inferred, that is, a question originally from elementary particle physics is (also[1]) answered by Nuclear Astrophysics.

It is the aim of this paper to investigate another connection of this type. Our question from elementary particle physics is: "What is the strangeness content of the nucleon? That is, to what extent do pairs of $s\bar{s}$-quarks in the nucleon contribute to its properties? A positive answer to this question has been indicated by experiments [2]." And we are going to point out that a $s\bar{s}$-quark sea in the nucleon will affect the following astrophysical events: i) The outcome of the so-called "ν"-nucleosynthesis, which is the possibly substantial production of some rare isotopes that is caused by neutrino-induced reactions

---

[1]The precise, but to some extent complementary LEP-result is $N_\nu = 2.991 \pm 0.016$ [1].

on nuclei in explosive supernova burning [3]. ii) The outcome of the r-process. iii) The energy spectrum of the photons emitted in $(\nu, \nu'p\gamma)$ and $(\nu, \nu'n\gamma)$ reactions on ^{16}O. These photons have been shown to constitute a signal for supernova ν_μ and ν_τ neutrinos in water Čerenkov detectors [4].

2 Theory

The link between the $s\bar{s}$-sea in the nucleon and Astrophysics is provided by inelastic neutrino scattering on nuclei. In calculating the corresponding cross sections we assume a two-step process. The ^{16}O$(\nu, \nu'p)$- and ^{16}O$(\nu, \nu'n)$- reactions were described within the continuum random phase approximation (RPA) [5], while the branching ratios in the various decay channels of the daughter nuclei were determined with the statistical model code SMOKER [6].

Due to the smallness of the Fermi coupling constant the neutrino scattering cross sections are accurately obtained within first order Born approximation. For low neutrino energies and small momentum transfer the weak Hamiltonian can be written, according to the Standard Model, in current-current form. Thereby leptonic and hadronic currents have the well-known (V-A)-structure:

$$j_\lambda^{(0)} = \overline{\psi}_\nu \gamma_\lambda (1 - \gamma_5)\psi_\nu \quad , \quad J_\lambda^{(0)} = \overline{\psi}_N \left\{ F_1^Z \gamma_\lambda + F_2^Z \frac{i\sigma_{\lambda\nu}q^\nu}{2M_N} + G_A \gamma_\lambda \gamma_5 \right\} \psi_N.$$

The neutral weak form factors in the hadronic current account for the fact that protons and neutrons are extended objects. They are constructed from the underlying quark-currents and are given by ($\tau_3 = \pm 1$ for protons, neutrons):

$$F_{1,2}^Z = (\frac{1}{2} - \sin^2\theta_W) \left[\frac{F_{1,2}^p - F_{1,2}^n}{2} \right] \tau_3 - \sin^2\theta_W \left[\frac{F_{1,2}^p + F_{1,2}^n}{2} \right] - \frac{1}{2}F_{1,2}^s,$$

$$G_A = -\frac{1}{2}G_A^3 \tau_3 + \frac{1}{2}G_A^s .$$

Arising from the $s\bar{s}$-sea $F_{1,2}^s$ and G_A^s are purely isoscalar and therefore do not contribute to charged current reactions like ν_e-capture or β-decay. Neglecting final state interactions and assuming that the axial-vector current gives the dominant contribution to the cross section a thumb-rule for the ratio of the proton-to-neutron neutrino-induced yield R_ν can be applied:

$$R_\nu := \frac{(\nu, \nu'p)}{(\nu, \nu'n)} = \frac{(G_A^p)^2}{(G_A^n)^2} = \frac{\left(-\frac{1}{2}G_A^3 + \frac{1}{2}G_A^s\right)^2}{\left(+\frac{1}{2}G_A^3 + \frac{1}{2}G_A^s\right)^2} \approx 1 - \frac{16}{5}G_A^s + ... \tag{1}$$

This approximately linear dependence of R_ν on G_A^s is confirmed within a more sophisticated continuum RPA calculation and was proposed as a sensitive way to measure G_A^s at LAMPF [2].
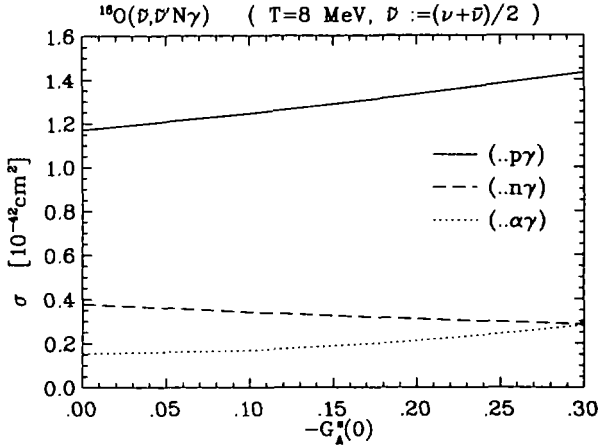
Figure 1: Cross sections for the for neutrino induced $(..p\gamma)$-, $(..n\gamma)$-, and $(..\alpha\gamma)$-reactions on ^{16}O as a function of $G_A^s(q^2 = 0)$.

3 Results

As we have already discussed the effects of a $s\bar{s}$-quark sea in the nucleon on ν-nucleosynthesis in an earlier paper [7], we shall just summarize these results here: (i) Like indicated by the thumb-rule (see Eq. (1)), the number of neutrino-released neutrons will be decreased in favor of the number of released protons. We found, e.g., for scattering on ^{16}O, that R_ν can rise due to strangeness by up to 56%, (ii) Combining the selection rules for transitions with the fact that the contribution from the $s\bar{s}$-sea is purely isoscalar, we showed that there are (discrete) states in nuclei that can only be excited by (ν, ν')-scattering, if G_A^s does not vanish (so-called "strangeness allowed transitions"), (iii) Neutrino scattering off an isoscalar nucleus (T=0) dominantly leads to excitations of T=1 states. As $(\nu, \nu'\alpha)$-reactions are isospin-forbidden, their cross sections are very small. But with increasing G_A^s also T=0 states are populated and therefore the probability for neutrino-induced α-knockout from an isoscalar nucleus strongly rises with the strangeness content of the nucleon.

For the r-process it has been recently shown that an intense neutrino flux could affect its outcome by spallation of neutron-rich nuclei after the freeze-out [8]. In a first investigation [9] we have pointed out, that for neutron-rich nuclei the $A(\nu, \nu')X$-cross section is reduced with increasing strangeness in the
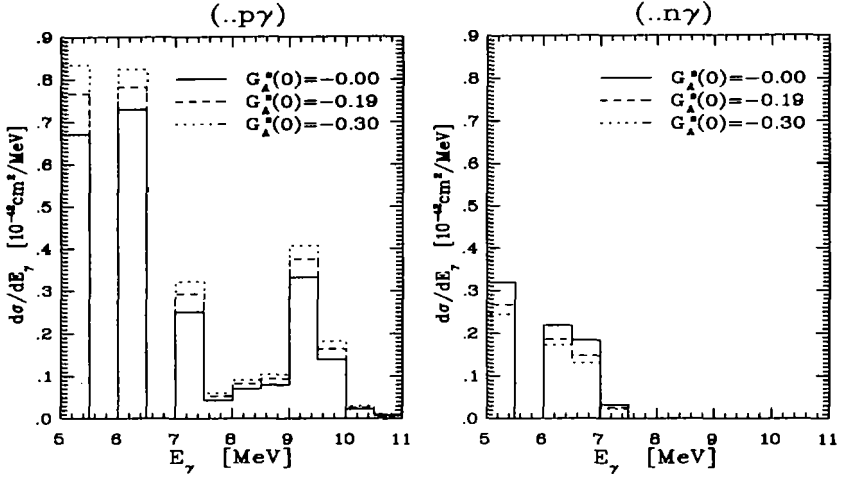
Figure 2: Differential cross sections for the $^{16}O(\nu, \nu'p\gamma)$- (left) and $^{16}O(\nu, \nu'n\gamma)$-reactions (right) plotted versus the energy of the emitted photon with a binning of 0.5 MeV. The solid, dashed and dotted curve show the dependence on G_A^s.

nucleon by up to 40%. Therefore, to describe the effects of neutrino-induced spallation on the r-process quantitatively, strangeness in the nucleon cannot be neglected.

Let us now examine, to what extent the **energy spectrum of photons** emitted in $(\nu, \nu'p\gamma)$ and $(\nu, \nu'n\gamma)$ reactions on ^{16}O depend on G_A^s. For this purpose we calculated the $^{16}O(\nu, \nu'x\gamma)$-reaction cross sections for $x = p, n, \alpha$ as a function of the strangeness content of the nucleon. The energy spectrum of the incoming neutrinos was assumed to follow a Fermi-Dirac distribution with a temperature of 8 MeV and a chemical potential zero, which is typical for ν_μ and ν_τ neutrinos coming from a type II supernova. In Fig.1 these cross sections, averaged over neutrinos and antineutrinos, are plotted. We read from this plot that for a variation of G_A^s within the experimental range, the cross sections for the $(\nu, \nu'p\gamma)$-, $(\nu, \nu'n\gamma)$- and $(\nu, \nu'\alpha\gamma)$-reactions on ^{16}O change by +22%, -25% and a factor of roughly 2, respectively. Especially the ratio of the $(\nu, \nu'p\gamma)$- and $(\nu, \nu'n\gamma)$-cross sections rises by more than 60%. Note, that the systematic error within our calculations can be estimated by comparing the $(\nu, \nu'p)$- and $(\nu, \nu'n)$-branching ratios obtained within continuum RPA and statistical model and was found to be $\approx 10\%$.

The Superkamiokande-detector (SK) has a lower threshold for γs of approximately 5 MeV. As the first excited states in ^{15}N ($E^* = 5.27$ MeV) and ^{15}O ($E^* = 5.18$ MeV) lie at energies larger than this threshold, all photons from the $(\nu,\nu'p\gamma)$- and $(\nu,\nu'n\gamma)$-reactions on ^{16}O can be observed in SK. However, the γs from $(\nu,\nu'\alpha\gamma)$-reactions dominantly come from the $J^\pi = 2^+$ excited state in ^{12}C at 4.44 MeV and therefore are below the SK threshold. The spectrum of the photons measurable at SK is depicted in Fig.2 for a vanishing, medium and strong strangeness content of the nucleon, the latter causes changes in the spectra by $\approx \pm 20\%$. A measurement of this effect will be very difficult and will probably require to discriminate $(\nu,\nu'p\gamma)$- and $(\nu,\nu'n\gamma)$-reactions.

From Fig.2 it can also be seen that the sum of the photons from $(\nu,\nu'p\gamma)$- and $(\nu,\nu'n\gamma)$-reactions is not very sensitive to G_A^s, therefore the sum still constitutes a good signal for supernova ν_μ and ν_τ in water Čerenkov detectors.

4   Summary

We have shown that a strong strangeness content of the nucleon will considerably affect ν-nucleosynthesis, the outcome of the r-process and the energy spectrum of photons emitted in ^{16}O$(\nu,\nu'p\gamma)$- and ^{16}O$(\nu,\nu'n\gamma)$-reactions. However, considering the astrophysical uncertainties and experimental conditions for these processes at present time, it is certainly impossible to go back and draw conclusions from their outcome about the strangeness in the nucleon.

References

[1] Particle Data Group, Phys. Rev. **D54** (1996) 1.

[2] G.T. Garvey, E. Kolbe, K. Langanke, S. Krewald, Phys. Rev. **C48**, 1919 (1993); and references therein.

[3] S.E. Woosley et al., Astrophys. J. **356** (1990) 272.

[4] K. Langanke, P. Vogel, and E. Kolbe, Phys. Rev. Lett. **76** (1996) 2629.

[5] M.Buballa, S.Drożdż, S.Krewald, J.Speth, Ann. of Phys. **208** (1991) 346; E.Kolbe, K.Langanke, S.Krewald, F.K.Thielemann, **NPA540** (1992) 599.

[6] J.J. Cowan, F.-K. Thielemann, J.W. Truran, Phys. Rep. **208**, 267 (1991).

[7] E.Kolbe et al., APJ Lett. **401** (1992) L89.

[8] Y.Z.Qian,W.C.Haxton,K.Langanke,P.Vogel, Phys.Rev. **C55** (1997) 1532.

[9] E. Kolbe, F.K. Thielemann, in *Proceedings of the 2nd Oak Ridge Symposium on Atomic & Nuclear Astrophysics*, 1997, (IOP, 1998).

COSMIC RAY INTERACTIONS
IN THE GALAXY

PETER L. BIERMANN

Max Planck Institut für Radioastronomie (MPIfR)
Postfach 2024, D-53010 Bonn, Germany

Abstract

Cosmic rays are particles, which have been accelerated in the Galaxy or in extragalactic space. Cosmic rays come as electrons, protons, heavier nuclei, and their antiparticles. The interactions of cosmic rays produce high energy photons, secondary electrons and positrons, neutrinos, and as spallation products, other nuclei. Up to energies of some tens of TeV of particle energy it is possible to derive chemical abundances of cosmic rays. It has been proposed that cosmic ray particles can be attributed to three main sites of origin and acceleration, a) supernova shocks in the interstellar medium, b) supernova shocks in a stellar wind of the predecessor star, and c) powerful radio galaxies. This proposal leads to quantitative tests, which are encouraging sofar. Li, Be, B are secondary in cosmic rays, as are many of the odd-Z elements, as well as the sub-Fe elements. Some of the spallation products are radioactive, therefore decay and allow quantitative tests of any propagation model for cosmic rays. At very low energies, cosmic ray particles are subject to ionization losses, which produce a steep low energy cutoff; all particles below the cutoff are moved into the thermal material population, and the particles above it remain as cosmic rays. This then changes the chemical abundances in the interstellar medium, and is a dominant process of origin for many isotopes of Li, Be, B. The gamma-ray emission from our Galaxy observed by the instruments EGRET, COMPTEL and OSSE on board the Compton observatory satellite suggest that the interactions of cosmic rays with matter and the photon fields are powerful indicators of the origin of these energetic particles. In the lecture a brief outline will be given of the origin of cosmic rays, their interactions, and the tests with abundances, and the gamma ray spectrum.

1   Introduction

Cosmic Rays are energetic particles, which come to us from outer space, and are measured either through satellites, balloons, or Earth based experiments.

These energetic particles interact, and the result of these interactions are the spallation products as well as gamma rays. Gamma rays arise either from collisionally excited nuclei or nuclear fragments, or as a continuum from π-decay. In this review we limit ourselves to protons and heavier nuclei, ignoring the electrons, which produce ubiquitous radio, Inverse Compton or Bremsstrahlung emission.

The origin of cosmic rays is still a question [32, 37, 18, 19, 26, 30, 5] which is not finally settled. The debate has reached a consensus, that most are produced in the shockwaves of supernova explosions [2, 59, 24, 25, 42, 15, 13, 4, 35, 27, 28], be it into the interstellar medium, or into a stellar wind [63, 60, 6]. Many of the relevant issues here have been dealt with in the excellent review by Hillas [33] and in the books by Hayakawa [30], Berezinsky *et al.* [5] and Gaisser [20].

Here we are concerned with the interactions of cosmic rays in the Galaxy, and so we will adopt the picture that indeed the cosmic ray particles originate in the shocks of supernova explosions, and thus limit ourselves to lower energies.

The structure of this review is as follows: First we briefly summarize a recent proposal to account for the origin of cosmic rays; then we go through the arguments for interaction with the material close to the progenitor star; then we briefly address the issue where the interaction happens which produces the observed gamma ray emission from the Galaxy. Finally we draw some conclusions and stress the importance of better cross sections.

2   A quantitative proposal for the origin of galactic cosmic rays

Cosmic rays arrive at earth with energies from several hundred MeV/particle to $3 \cdot 10^{20}$ eV; their spectrum for protons is at GeV energies close to $E^{-2.75}$, and for He and higher elements close to $E^{-2.65}$ below a *knee* at $\approx 5 \cdot 10^{15}$ eV, where the spectrum turns down to about $E^{-3.1}$, to flatten out again near $3 \cdot 10^{18}$ eV, called the *ankle* (*e.g.* [43, 47, 65]). The chemical composition is roughly similar to that of the interstellar medium, with reduced hydrogen and helium relative to silicon.

A proposal (see, *e.g.*, [6, 11]) is that three sites of origin account for the cosmic rays observed, i) supernova explosions into the interstellar medium, ISM-SN, ii) supernova explosions into the stellar wind of the predecessor star, wind-SN, and iii) radio galaxy hot spots. Here, in this concept, the cosmic rays attributed to supernova-shocks in stellar winds, wind-SN, produce an

important contribution at all energies up to $3 \cdot 10^9$ GeV.

Particle energies go up to 100 Z TeV for ISM-SN, and to 100 Z PeV with a bend at 600 Z TeV for wind-SN, where Z is the charge of the nucleus considered. Radiogalaxy hot spots contribute up to about 100 EeV at the source, with some sources up to $4 \cdot 10^{21}$ eV [12]. These numerical values are estimates with uncertainties of surely larger than a factor of 2, since they derive from an estimated strength of the magnetic field, and estimated values of the effective shock velocity.

The spectra are predicted to be $E^{-2.75\pm0.04}$ for ISM-SN, and $E^{-2.67-0.02\pm0.02}$ for wind-SN below the knee, and $E^{-3.07-0.07\pm0.07}$ for wind-SM above the knee, and $E^{-2.0}$ at injection for radiogalaxy hot spots.

These predictions can be compared at some detail with data, and we have given comparisons in previous work (e.g. [8, 6, 64, 10, 12]).

3 Spallation of cosmic ray nuclei

Cosmic ray nuclei can be broken up in collisions with thermal matter; this process is called spallation. Obviously, there is a corresponding interaction between energetic protons, and thermal material comprising heavier nuclei such as Carbon. In such collisions the remaining nuclei can also be excited, and then emit γ-ray lines.

Spallation is relevant in various sites (see, e.g., the recent work in this area [22, 16, 23, 17, 58] and the classical reviews by Reeves [54, 55]). The site normally explored is interstellar clouds [61]; cosmic rays travel through the interstellar medium, and interact. Good evidence for this interaction is the excellent correlation of the observed gamma ray continuum emission (arising from π^0 decay following p-p interaction) with the observed column density of interstellar material [34].

3.1 Source related spallation

Massive stars are believed to be the sources of energetic particles; massive stars also have powerful winds, which sweep up interstellar matter. Massive stars have so much mass loss, that they shed their outer layers, expose the processed material and thus late in life show a highly enriched wind. The wind, on the other hand, plows into the environmental gas, and sweeps it up; gas left over from the formation of the star may still be around as well, so as to increase the target for the expanding wind and form a shell. It is through this enriched wind and associated shell, that the supernova shock races, and

causes particle acceleration and spallation by these particles directly. We note that the supernova shock compresses the wind itself into a shocked shell, which then smashes into the shell produced by the progenitor stellar wind. As the previous wind was also already enriched, spallation necessarily occurs in an enriched environment: This is actually required by the light element data as shown by Ramaty *et al.* [53]; Ramaty, Kozlovsky and Lingenfelter have contributed significantly in this area of research over many years.

Stars along the main sequence need to be considered in four separate zero age mass ranges:

- Stars below about 8 $M_\odot$ do not explode as supernovae.

- Stars from about 8 to about 15 $M_\odot$ explode as supernovae, but do not have a strong stellar wind, and so explode into the interstellar medium.

- Stars from about 15 to 30 $M_\odot$ have a substantial wind [9]; the wind is enriched only in Helium. The chemical composition of the wind at the time of explosion is approximately 0.5 in He and 0.5 in H. The mass in the shell of wind-swept material is moderate.

- Stars from about 30 $M_\odot$ have a strong wind; the wind is enriched in heavy elements and has little Hydrogen left. The mass in the shell of wind-swept material is large.

Therefore we can ask the following question: What happens when the supernova shock smashes into the wind-driven shell? The supernova shock shell is loaded with cosmic ray particles. In the enriched shock shell and wind shell the energetic particles may reside for some time, and then leak out into the normal interstellar medium. What is the wavefield that governs this leakage in the limit that the leakage is diffusive?

Therefore, we need to consider the diffusive loss from a shell, which is traversed by a shock filled with a cosmic ray population. So we first derive the wavefield in magnetic fields excited by the cosmic rays. Then, in a second step we consider the diffusive leakage from the shell under the influence of this wave field.

Turbulence is an ubiquitous phenomenon, and also is a key ingredient in the interstellar medium (see reviews [56, 29]). Key concepts to turbulence theory have been introduced by Prandtl and von Karman & Howarth [51, 36], Kolmogorov [38, 39, 40], Obukhov, Heisenberg, and Kraichnan [48, 31, 41], and have been reviewed by Sagdeev [57]. One key argument which we wish to use,

is the concept of the turbulent cascade. There the energy of the turbulence is injected into the gas at some large wavelength, and cascades down through wavenumber space, to the small wavelengths where the energy is dissipated; in many examples this leads in a three-dimensional isotropic model to the Kolmogorov cascade [45], which can be described in a local approximation by the following diffusion equation in wavenumber space [44, 1]:

$$\frac{d}{dt}\frac{I(k)}{4\pi k^2} - \frac{1}{k^2}\frac{\partial}{\partial k}\left(\frac{k^4}{3\tau_k}\frac{\partial}{\partial k}\left(\frac{I(k)}{4\pi k^2}\right)\right) = A\,\delta(k - k_o) \tag{1}$$

Here $I(k)$ is the energy density of the turbulence per wavenumber k, and per volume element, and τ_k is the time scale of diffusion, which can be written as

$$\tau_k = \frac{1}{k(\gamma_{eff}I(k)k/\rho)^{1/2}}. \tag{2}$$

Here ρ is the matter density, and γ_{eff} is an effective adiabatic constant for the turbulent energy. The turbulence has a source-term, here limited to a single wavenumber k_o. Below we will consider an entire range of excitation wave numbers. The turbulence diffusion equation basically says that the turbulence moves through wavenumber space with no additional source or sink, as a constant energy current in wavenumber phase space [38, 39, 40]. The solutions to this diffusion equation can be written as $I(k) \sim k^2$ for $k \leq k_o$ and $I(k) \sim k^{-5/3}$ for $k \geq k_o$. This latter behaviour is commonly referred to as the Kolmogorov cascade, and is found ubiquitously in nature.

The basic equation for the excitation of wavefields can be written as follows [3, 15]:

$$\frac{d}{dt}\frac{I(k)}{4\pi k^2} = (\sigma_{excit} - \Gamma_{damp})\frac{I(k)}{4\pi k^2} \tag{3}$$

with σ_{excit} the excitation term and Γ_{damp} the damping term. Here we will concentrate on the excitation of waves, and ignore any damping. The excitation term can be written as

$$\sigma_{excit} = \frac{4\pi}{3}\frac{v_A}{I(k)k}p^4 v\frac{\partial f}{\partial x} \tag{4}$$

where v is the particle velocity, f the particle distribution function in phase space (assumed to be isotropic), and x the local coordinate perpendicular to the shock plane. We need to emphasize that only the difference of the particle spectrum across a shock wave or any other spatial gradient can excite waves;

therefore, the first shock wave loaded with cosmic ray particles sweeping across the molecular gas shell around exploding stars and their winds is an excitation mechanism. Now the particle spectrum in energy space (in the relativistic domain of particle speeds) is $N(E) = E^{-7/3}$ from the arguments of shocks in winds [6, 7]. Of course, this step in the argument depends on the proposal for the origin of cosmic rays summarized earlier to be correct.

We therefore need to determine which wave spectrum can balance the cascading with the excitation from the freshly injected cosmic rays. Equating the two expressions above for the cascading (eq. 1) and the excitation (eq. 3) in their k-dependence using an arbitrary powerlaw for $I(k) \sim k^{-\beta}$ then yields the condition $-\frac{1}{2} - \frac{3}{2}\beta = \frac{7}{3} - 5$ which means $\beta = \frac{13}{9}$. We omit here for lack of space a thorough discussion of the errors in this line of argument, as in e.g. [7, 11, 64]. From [15] we obtain the diffusion coefficient based on the wavefield, and then the diffusive time scale of loss from the diffusion coefficient in turn. This entails an energy dependence of the leakage time from the zone of interaction

$$\tau_L \sim E^{-5/9} \tag{5}$$

This then means that the local spectrum of primary cosmic rays is steeper by this much, and so all secondaries are produced with a spectrum which is steeper by this much from the start.

Therefore secondaries are produced with a spectrum of

$$N_{sec}(E) \sim E^{-26/9}. \tag{6}$$

After transport through the Galaxy and insignificant further spallation this means that the ratio of secondaries to primaries remains at

$$N_{sec}/N_{prim} \sim E^{-5/9} \tag{7}$$

which is rather close to the observed dependence from the Boron to Carbon ratio of $E^{-0.6}$ [17].

Clearly, this treatment breaks down at two ends, both on the low energy side, and on the high energy side. On the high energy side, it is obvious that from some energy the diffusive approximation breaks down, and from the low energy end it is clear that convective losses and the full break up of the shell will be faster than diffusion below some energy.

This is in contrast to the usual finding that a *stationary* leaky box gives a ratio of secondary to primaries $\sim E^{-1/3}$, if we use a Kolmogorov spectrum for

turbulence; this latter result is obtained, when the interaction happens evenly throughout the residence period in the Galaxy.

This is also in contrast to the concept of clouds capturing and then releasing cosmic ray particles derived in [10].

Therefore, considering the history of the travel of cosmic rays through the normal interstellar medium (see also, *e.g.* [10, 49]), we can readily explain the ratio of secondaries to primaries, and at the same time use a spectrum of turbulence which is consistent with all other observational evidence. Translating this result into the language common in the literature, this means that escape length as measured in gm/cm^2 and escape time can not be used synonymously. The escape time is given by $\tau_{L,gal}$, and is proportional to $E^{-1/3}$ in the relativistic range of particle energies. The escape length as a means to describe interaction is here $\sim E^{-5/9}$.

4 The gamma ray spectrum of the Galaxy

It has been argued for decades that the Galaxy should emit gamma rays from the decay of π^0 particles resulting from collisions of cosmic ray protons, and interstellar medium protons, with a probably small contribution from nuclear collisions of higher element nuclei such as helium (much of the early work was done by Floyd Stecker [62]). The data originally collected appeared to confirm this hypothesis very nicely. One could even fit in detail the bumps and wiggles of the column density of the interstellar medium with the gamma ray emission, confirming rather well and quantitatively the expectations of the model. There has been a worry for a long time, that in such a fit, the radial variation of the cosmic rays deduced appeared to be small, while we believe to know from other galaxies, that at least the electron component has a clear radial drop off, and so one might think the proton component ought to show such a gradient as well.

Recently the gamma ray spectrum of the Galaxy has been measured with great precision using the EGRET satellite [34]. It turned out, that once again, the spatial variation of the gamma ray emission can be fit rather well, while the spectrum can not be fitted. The observed spectrum is much too flat to match the expectation based on the average cosmic ray spectrum - as deduced from either direct measurements or from radio data, once again connecting electrons and protons in this argument. This has caused quite a stir, but sofar no obvious solution appears to be convincing [46, 50].

The gamma ray emission can be fitted very well with a proton spectrum which is quite a bit flatter than the observed proton spectrum [21, 52], perhaps

suggesting that we see the sources of cosmic rays. The picture raised here would suggest the following:

As one goes up the main sequence from about 15 $M_\odot$, the mass in the shell produced by the stellar wind increases slowly, to become quite substantial for very high mass stars at the end of their lifetimes, just before the stars explode. Therefore, one might expect that the leakage of cosmic ray particles may not be diffusive for lower stellar masses. One the other hand, the enrichment also increases with higher stellar mass, and therefore, the spallation of carbon, oxygen and other nuclei will play an important role as a source for boron and other light elements only for the high mass stars. Thirdly, there are many more lower mass stars, and so the π^0-producing collisions are dominated by the interaction in the shells of the lower mass stars, where the leakage is probably convective, and not diffusive. Then the interaction is with the primary spectrum, and so the gamma ray spectrum would be expected to match a proton energy spectrum of $E^{-7/3}$ approximately. This does appear to be consistent with the data.

5 Outlook

Given that a quantitative theory is beginning to show the promise of an explanation for the origin of cosmic rays, it may be worthwhile to obtain much better cross sections for the cosmic ray interactions, especially near the critical threshold for any reaction. This would then, not only, provide a quantitative explanation of the various abundances, but also allow to actually use them to study both cosmic rays and the interstellar medium. A test would be a calculation with the model proposed here using all the element abundance data in cosmic rays, basically reinterpreting the results already obtained by, *e.g.*, Garcia-Munoz *et al.* [23]. An important next step would be an interpretation of the isotopic data (*e.g.* [14]). The future in cosmic ray research promises to be rich for astrophysicists, particle physicists, and nuclear physicists.

maty, Wolfgang Rhode, Eun-Suk Seo, Todor Stanev, Alan Watson, and Barbara Wiebel-Sooth. The new element, the concept of wave excitation in the stellar wind-shell interaction, was developed during a visit to the University of Chicago in November 1997 after intense discussions with Jim Connell and Dietrich Müller, who were my generous hosts. Furthermore, I would like to thank Torsten Enßlin, Stan Hunter, Norbert Langer, Hinrich Meyer, Wolfgang Rhode and Barbara Wiebel-Sooth for helpful comments on the manuscript. I thank all my discussion partners and apologize for any errors and omissions which surely remain in this short manuscript.

References

[1] Achterberg, A. 1979 A&A 76, 276 - 286

[2] Baade, W., Zwicky, F.: 1934 *Proc. Nat. Acad. Science*, **20**, no. 5, 259 - 263.

[3] Bell, A.R.: 1978a, *Monthly Not. Roy. Astron. Soc.* **182**, 147 - 156

[4] Berezhko, E.G., Krymskii, G.F.: 1988 *Sov. Phys. Usp.* **31**, 27 - 51.

[5] Berezinskii, V.S., *et al.*: 1990 *Astrophysics of Cosmic Rays*, North-Holland, Amsterdam

[6] Biermann, P.L.: 1993 *Astron. & Astrophys.* **271**, 649 - 661 (paper CR I), astro-ph/9301008.

[7] Biermann, P.L., and Cassinelli, J.P.: 1993 *Astron. & Astrophys.* **277**, 691 - 706 (paper CR II), astro-ph/9305003.

[8] Biermann, P.L.: 1993 in *Currents in Astrophysics and Cosmology*, (Conf. 1990) Eds. G.G. Fazio & R. Silberberg, Cambridge Univ. Press, Cambridge, UK, p. 12 - 19.

[9] Biermann, P.L., Gaisser, T.K., Stanev, T.: 1995 *Physical Review* **D 51**, 3450 - 3454, astro-ph/9501001.

[10] Biermann, P.L.: 1996 in Proc. Nuclear Physics meeting MESON96 (Cracow), Eds. E. Grosse et al., Jagiellonian University, Acta Physics Polonica, **B27**, 3399 - 3415, 1996, sissa: astro-ph/9609110

[11] Biermann, P.L.: 1997 in *Cosmic Winds and the Heliosphere*, ed. J.R. Jokipii *et al.* (University of Arizona Press, Tucson), (in press), astro-ph/9501030.

[12] Biermann, P.L. 1997 *J. of Physics G* **23**, 1 - 27

[13] Blandford, R.D., Eichler, R.D.: 1987 *Phys. Rep.* **154**, 1 - 75.

[14] Connell, J.J., Simpson, J.A.: 1997 *Astrophys. J.* **475**, L61 - L64

[15] Drury, L.O'C: 1983 *Rep. Prog. Phys.* **46**, 973 - 1027.

[16] Engelmann, J.J., *et al.*: 1985 *Astron. & Astroph.* **148**, 12 - 20.

[17] Engelmann, J.J., *et al.*: 1990 *Astron. & Astroph.* **233**, 96 - 111.

[18] Fermi, E.: 1949 *Phys. Rev.* 2nd ser., **75**, no. 8, 1169 - 1174.

[19] Fermi, E.: 1954 *Astrophys.J.* **119**, 1 - 6.

[20] Gaisser, T.K.: 1990 *Cosmic Rays and Particle Physics*, Cambridge Univ. Press

[21] Gaisser, T.K., Protheroe, R.J., Stanev, T.: 1998 *Astrophys. J.* **492**, 219, also in astro-ph

[22] Garcia-Munoz, M., Mason, G.M., Simpson, J.A.: 1977 *Astrophys.J.* **217**, 859 - 877

[23] Garcia-Munoz, M., Simpson, J.A., Guzik, T.G., Wefel, J.P., Margolis, S.H.: 1987 *Astrophys.J. Suppl.* **64**, 269 - 304

[24] Ginzburg, V.L.: 1953 *Usp. Fiz. Nauk* **51**, 343 - . See also 1956 *Nuovo Cimento* **3**, 38 - .

[25] Ginzburg, V.L.: 1953 *Dokl. Akad. Nauk SSSR* **92**, 1133 - 1136 (NSF-Transl. 230).

[26] Ginzburg, V.L., Syrovatskij, S.I.: 1969 *The Origin of Cosmic Rays*, Gordon and Breach, New York

[27] Ginzburg, V.L.: 1993 *Phys. Usp.* **36**, 587 - 591.

[28] Ginzburg, V.L. 1996 *Uspekhi Fizicheskikh Nauk* **166**, 169 - 183

[29] Goldstein, M.L., Roberts, D.A., Matthaeus, W.H.: 1995 *Ann. Rev. Astron. & Astroph.* **33**, 283 - 325

[30] Hayakawa, S.: 1969 *Cosmic Ray Physics*, Wiley-Interscience, New York

[31] Heisenberg, W. 1948 Z. Physik 124, 628

[32] Hess, V.F.: 1912 *Phys. Z.* **13**, 1084.

[33] Hillas, A.M.: 1984 *Ann. Rev. Astron. Astrophys.* **22**, 425 - 444.

[34] Hunter, S.D. *et al.*: 1997 *Astrophys. J.* **481**, 205 - 240

[35] Jones, F.C., Ellison, D.C. : 1991 *Space Science Rev.* **58**, 259 - 346.

[36] Karman, Th. de, Howarth, L.: 1938 *Proc. of the Royal Soc. of London* **164**, 192 - 214.

[37] Kohlhörster, W.: 1913 *Phys. Z.* **14**, 1153.

[38] Kolmogorov, A.N. 1941a Dokl. Akad. Nauk SSSR 30, 299 - 303

[39] Kolmogorov, A.N. 1941b Dokl. Akad. Nauk SSSR 31, 538 - 541

[40] Kolmogorov, A.N. 1941c Dokl. Akad. Nauk SSSR 32, 19 - 21

[41] Kraichnan, R.H.: 1965 *Phys. Fl.* **8**, 1385.

[42] Lagage, P.O., Cesarsky, C.J.: 1983 *Astron. & Astroph.* **118**, 223 - 228.

[43] Lawrence, M.A., *et al.*: 1991 *J. Phys. G* **17**, 733 - 757

[44] MacIvor, I. 1977 MNRAS 178, 85 - 99

[45] Matthaeus, W.H., Zhou, Y.: 1989 *Phys. Fluids* **B1**, 1929 - 1931

[46] Mori, M.: 1997 *Astrophys. J.* **478**, 225 - 232

[47] Nagano, M. *et al.*: 1992 *J. Phys. G* **18**, 423 - 442

[48] Obukhov, A.M. 1941 Dokl. Akad. Nauk SSSR 32, 22 - 24

[49] Pohl, M. *et al.*: 1997 *Astrophys. J.* (in press)

[50] Pohl, M. *et al.*: 1997 *Astrophys. J.* **491**, 159 - 164

[51] Prandtl, L.: 1925 *Zeitschrift angew. Math. und Mech.* **5**, 136 - 139.

[52] Protheroe, R.J., Stanev, T.: 1997 at the ICRC meeting in Durban, South Africa, OG 3.4.3

[53] Ramaty, R., Kozlovsky, B., Lingenfelter, R.E., Reeves, H.: 1997 *Astrophys. J.* **488**, 730 - 748

[54] Reeves, H.: 1974 *Ann. Rev. Astron., & Astroph.* **12**, 437 - 469.

[55] Reeves, H.: 1994 *Rev. of Modern Physics* **66**, 193 - 216

[56] Rickett, B.J.: 1990 *Ann. Rev. Astron. & Astroph.* **28**, 561 - 605.

[57] Sagdeev, R.Z. 1979 Rev. Mod. Phys. 51, 1 - 20

[58] Shibata, T.: 1996 *24th Internat. Cosmic Ray Conf.*, rapporteur talk, Nuovo Cimento **19C**, 713 - 736

[59] Shklovskii, I.S.: 1953 *Dokl. Akad. Nauk, SSSR* **91**, no. 3, 475 - 478 (Lib. of Congress Transl. RT-1495).

[60] Silberberg, R., *et al.*: 1990 *Astrophys.J.* **363**, 265 - 269.

[61] Spitzer. L. Jr.: 1968 *Diffuse Matter in Space*, Interscience Publishers, Wiley, New York

[62] Stecker, F.W.: 1971 *Cosmic Gamma Rays*, NASA SP-249

[63] Völk, H.J., & Biermann, P.L.: 1988 *Astrophys.J. Letters* **333**, L65 - L68.

[64] Wiebel-Sooth, B., Biermann, P.L., Meyer, H.: 1998 *Astron. & Astroph.* **330**, 389 - 398 (paper CRVII), astro-ph/9709253

[65] Zatsepin, V.I.: 1995 *J. of Phys. G* **21**, L31 - L34

SELECTED RESULTS FROM
GROUND-BASED COSMIC RAY AND
GAMMA-RAY EXPERIMENTS

N. MAGNUSSEN

Bergische Universität Wuppertal
Gaußstr. 20, D-42097 Wuppertal, Germany

Abstract

Selected results from the HEGRA experiment on charged Cosmic Rays and on very high energy gamma-rays are discussed. The MAGIC Telescope is presented as an outlook to the future of gamma-ray astronomy.

1 Introduction to Ground-Based Cosmic Ray Data

As a general rule the dynamic range of precision detectors is limited to roughly 2 to 3 orders of magnitude in energy. In case of the charged Cosmic Rays (CR) with an energy spectrum extending over more than 13 orders of magnitude, this neccesitates a large number of different experimental setups in order to cover the full spectrum. Space-borne, i.e., direct experiments, cover the spectrum from $\approx 10^7$ eV to $\approx 10^{15}$ eV/nucleon, and ground-based experiments operate above total energies of a few 10^{12} eV up to more than 10^{20} eV.

In the following we will concentrate on the ground-based measurements. Here various experiments which are sensitive in the energy region around 10^{15} eV consistently show a significant steepening of the all-particle spectrum around this energy. When studying the data more closely, however, the agreement between the experiments turns out to be not so good, i.e., well above the fluctuation given by the individual errors. This is shown in fig. 1 where the data on the 'knee' in the all-particle spectrum are collected [1]. From these data one must conclude that the absolute position, the 'sharpness' of the knee, and also the absolute flux in this energy region are more uncertain than expected from the individual errors. Ground-based experiments use a detector, i.e., the atmosphere as absorber with some added readout elements, like scintillators, Cherenkov detectors, etc., which can only be calibrated in the laboratory to a very limited degree. The calibration therefore has to rely very heavily on MC simulations of the development of the extensive air showers and of the performance of the detectors. One possible reason for the deviations in
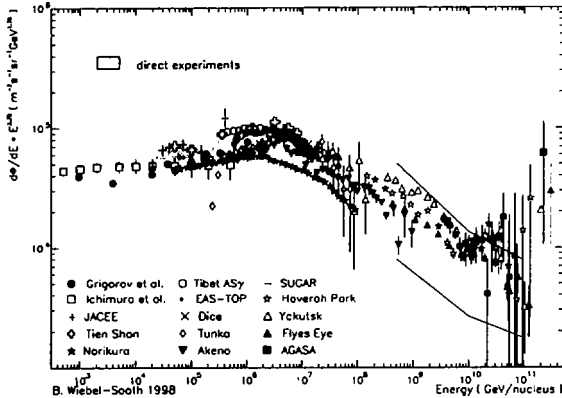
Figure 1: The charged Cosmic Rays all-particle spectrum around the 'knee' as measured by a number of ground-based experiments (taken from [1]).

the measured spectra might thus be the use of different Monte Carlo (MC) generators in the data analyses. This will be briefly discussed below for the most recent data.

2 The Energy Spectrum and the Chemical Composition

Currently the two experiments, HEGRA [3], located within the Observatorio del Roque de los Muchachos on the Canary island La Palma, and KASKADE [4], located near Karlsruhe, Germany, are analysing their airshower data with respect to the all-particle spectrum and the chemical composition of the CR near the 'knee'. In the following we shall discuss some of the preliminary HEGRA results and compare to KASKADE where appropriate.

The HEGRA setup for the detection of CR with energies above $\approx$ 15 TeV has 3 components: (i) 243 scintillator stations of 1 m^2 each distributed over 40,000 m^2, (ii) 77 AIROBICC Cherenkov detectors spread out over the same area, and (iii) 17 Geiger towers within the central 15,000 m^2.

2.1 The Reconstruction of Energy and Mass

The measured distribution of particle densities in the scintillator array is used to fit the shower size N_e at the detector level and the correlated shower size at the maximum (X_{max}) of the shower development. The lateral Cherenkov

light density $\rho_C(r)$ as measured by AIROBICC is analysed in the intervall 7.5 m $< r <$ 100 m and can be described by an exponential

$$\rho_C(r) = a \cdot exp(r/R_{light}), \tag{1}$$

where the shape parameter, R_{light}, is inversely proportional to the *absolute* penetration depth, X_{max}, of the analysed shower. As MC investigations show, this proportionality is essentially independent of the mass A of the incident primary particle. The achieved resolution for X_{max} varies between 1.0 and $\approx$ 0.5 radiation lenghts ($X_0 = 36$ g/cm^2) for energies between 100 TeV and a few PeV. The reconstruction of the energy in two independent analyses relies either on a combination of N_e and R_{light}, or on a combination of N_e, N_μ (the corresponding muon shower size), and R_{light}. In both cases an energy resolution of $\approx$ 30% is achieved. Using the CORSIKA simulation program [5] different hadronic interaction generators (i.e., VENUS, QGSJET, HDPM, DPMJET, SIBYLL) can be used. MC investigations have shown that the qualitative sensitivity for physics parameters and e.g. the energy resolution is independent of the hadronic interaction generator. The absolute energy scale, however, turns out to be dependent on the MC generator and the chemical composition.

2.2 The Energy Spectrum

Using the VENUS model within CORSIKA, HEGRA performed a regularized unfolding of the measured N_e distributions on a run-by-run basis (see [1] for details). The result of the unfolding is shown in fig. 2.

The spectral index of the all-particle spectrum *below* the 'knee' is found to be

$$\gamma = 2.63 \pm 0.02(\text{stat.}) \pm 0.05(\text{syst.}) \pm 0.05(\text{model}), \tag{2}$$

where the last error is an estimation of the dependence on the hadronic interaction generator in the MC.

2.3 The Chemical Composition around the 'Knee'

In order to get a first indication of the behaviour of the chemical composition around the 'knee' and in order to check the MC generators, HEGRA made in one analysis the simple ansatz of using parametrized MC distributions for the energy determination [6]. A more involved unfolding procedure based on the full MC and detector information is used in a second analysis decribed in detail in [1]. In both analyses the composition around the 'knee' is observed to be
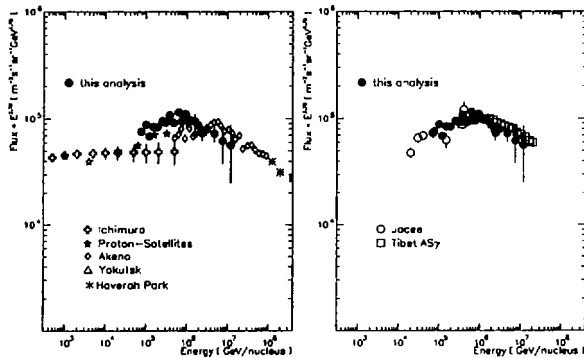
Figure 2: The charged Cosmic Ray all-particle spectrum around the 'knee' as measured by HEGRA (denoted 'this analysis') compared to older and recent (Tibet) data of other experiments. The unfolding of the detector smearing was done by a regularized unfolding procedure based on Monte Carlo events simulated with the VENUS interaction generator. (for details see [1]).

consistent with an unchanged or slightly heavier composition. For illustrating the results and the observed MC dependence the first approach is discussed in the following.

In the energy range from 300 TeV to 3 PeV the height of individual shower maxima can be reconstructed with an accuracy comparable to the RMS spread for iron showers ($\mathrm{rms}(X_{max,iron}) = 33 \pm 2$ g/cm^2) and thus much better than the RMS spread for proton showers ($\mathrm{rms}(X_{max,proton}) = 84 \pm 6$ g/cm^2). Since the mean X_{max} values of protons and iron showers differ by about 140 g/cm^2, the fractions of light (hydrogen and helium) and heavy elements (oxygen and iron) contributing to the measured distribution can thus be obtained from fitting model X_{max} distributions to the data for different energy bins. The details of this analysis can be found in [2]. Under the assumption that the chemical composition is the same for the different energy bins, the mean fraction of light elements is fitted to be 0.52 ± 0.10 (total error), which within errors, is compatible with direct measurements below 100 TeV.

Besides the shape of the X_{max} distribution the mean value may serve to determine the elemental composition. The measured mean values, however, turn out to be systematically smaller by 45 ± 24 g/cm^2 than expected from MC for the composition compatible with the fitted fractions which are based

on the *detailed shape* of the X_{max} distribution. This apparant discrepancy between data and MC can be due to detector, atmospheric, or MC generator effects. After careful investigations HEGRA now suspects the longitudinal shower development in the MC to yield too large X_{max} values due to a non-perfect simulation of the longitudinal shower development. The investigations, however, are not yet completed. Note that the AIROBICC-type detectors as employed e.g. by HEGRA are the only airshower detectors which are sensitive to the *absolute* position of the shower maximum due to the translation of the longitudinal development into the radial Cherenkov photon density. This is the consequence of the varying refractive index and height of emission along the shower.

Like HEGRA, the KASKADE collaboration also finds little change in the chemical composition around the 'knee' [7]. The absolute determination which relies on the MC is, however, still biased by large discrepancies between some of the hadronic interaction generators. Here still considerable effort is needed in order to achive reliable results in the future.

3   Gamma-Ray Astronomy

Since the detection of the Crab nebula as a source of gamma-rays (γ-rays) with energies above 500 GeV in 1989 [9], about 10 galactic and extragalactic sources of very high energetic photons ($E > 300$ GeV) have been detected by about as many experiments. The status of the field is indicated in fig. 3 which shows the skymap of the very high energy (VHE), i.e., $E > 300$ GeV, γ-ray sources as of August 1997. Note that contrary to former beliefs also *extragalactic* sources of VHE γ-rays were discovered during the last 5 years. The fast progress of the field will be illustrated below by the most recent HEGRA results concerning the brightest source on the γ-ray sky in 1997, the active galactic nucleus (AGN) Mkn 501 at a distance of $z = 0.034$ (≈ 600 million light years, for $H_0 = 50$ km sec^{-1} Mpc^{-1}).

3.1   The HEGRA Cherenkov Telescopes

In 1996 the HEGRA experiment completed the installation of six Imaging Air Cherenkov Telescopes (IACTs). Four identical IACTs are operated in coincident mode, i.e., for each airshower up to four different views are recorded. Hereby the energy threshold can be lowered and the γ/hadron separation efficiency can be improved. This is an advantage for the study of weak and especially for extended sources but is less than optimal for strong point-like

VHE Gamma Sources (E > 300 GeV)
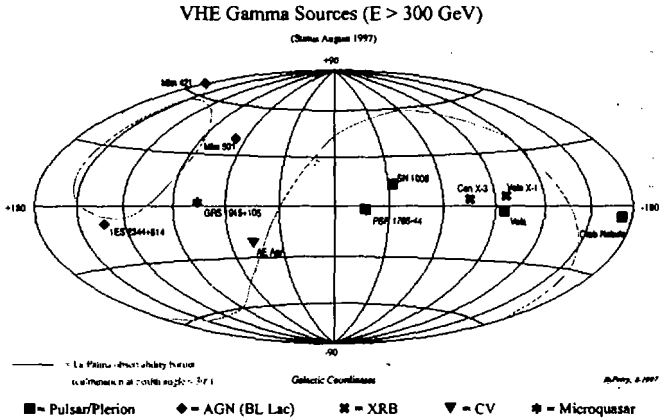
Figure 3: The galactic coordinates of point sources of Gamma-radiation of energy $E > 300\,\mathrm{GeV}$ as observed by the various Cherenkov telescope observatories around the world [8].

sources due to the restricted effective collection area. For the current energy range of IACTs, i.e., above 300 GeV, and the current stage of γ-ray astronomy, i.e., the discovery age in which we learn how to optimize the detectors, this setup, however, has its merits due to the redundancy of the information. For energies below 100 GeV where air showers only produce very little Cherenkov light, however, the redundancy will be lost to a large degree due to the very limited number of particles above the Cherenkov threshold, i.e., different telescopes will view *different tracks* in the shower. In this energy regime therefore very sensitive telescopes like the MAGIC Telescope discussed below will be needed which will not compromise on the effective photon collection area.

3.2 The Extragalactic TeV photon source Mkn 501

Mkn 501 belongs to the blazar class of AGN, i.e., it is an AGN with a large plasma jet which is pointing along the line-of-sight, and it has been observed at TeV energies since 1995 [10] when its activity level corresponded to about 8% of the flux of the strongest galactic source, the Crab nebula. Due to its steady emission level the Crab nebula has become the Standard Candle for γ-ray astronomy. The activity level of Mkn 501 in 1996 rose to about
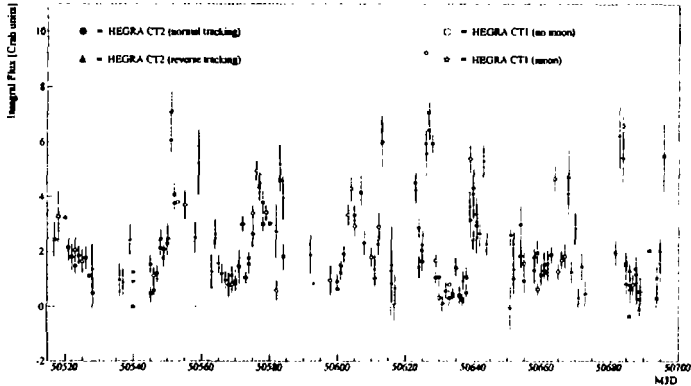
Figure 4: The light curve of the blazar Mkn 501 as measured by the HEGRA telescopes CT1 and CT2 during the 1997 observation campaign. MJD (Modifieds Julian Date) 50700 corresponds to the 8th of September 1997.

30% of the Crab flux [11] and in 1997 HEGRA recorded on average a flux corresponding to about 200% of the Crab flux, and, in addition to this much higher average activity level, huge flares, i.e., up to 10 times the Crab flux, on time-scales as short as a day or less were recorded. As summarized in [12] a great number of Cherenkov telescopes (Whipple, CAT, TACTIC, Telescope Array, HEGRA) were able to detect this signal and record a light curve. The most complete light curve was obtained by the stand-alone telescopes CT1 and CT2 of the HEGRA collaboration, because CT1 was also operational during moonshine. The light curve extending from March until September 1997 is shown in fig. 4. The short-term flares point towards very compact sources, i.e., regions in the vicinity of the supermassive ($\mathcal{O}(10^8)$M$_\odot$) black hole thought to be in the centre of the galaxy and powering the very strong non-thermal emission of the AGN. These large fluxes, which for the first time were recorded from an extragalactic source, allowed the determination of the energy spectrum extending beyond 5 TeV. The energy spectrum as measured by the HEGRA IACT system telescopes in 1997 is shown in fig. 5 [13]. As the analysis of systematic effects at higher energies is not yet completed, the spectrum is only shown up to 10 TeV.

But already the unabsorbed spectrum extending up to 10 TeV allows to extract a fundamentally important upper limit on the density of infrared (IR)
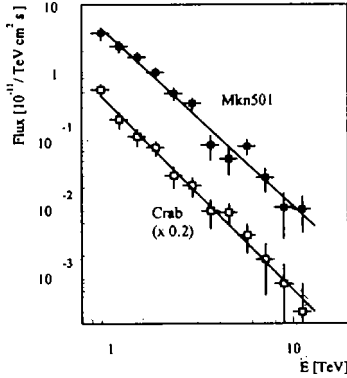
Figure 5: The energy spectrum of the blazar Mkn 501 as measured by HEGRA system telecopes during the 1997 observation campaign. Measured points beyond 10 TeV are not shown.
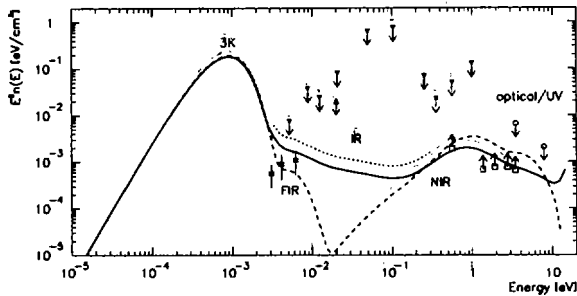
Figure 6: Energy density of the extragalactic diffuse background radiation. For detailed references see [14]. Symbols stand for: *stars:* tentative detection of the FIR background without CMBR, *full downward triangles:* upper limits from the DIRBE experiment, *squares:* lower limit from faint blue galaxies, *circles:* upper limit of possible detection, *open triangle:* IRAS upper limit, *full upward triangles:* evolution mode dependent lower limits from number counts of infrared-bright galaxies, *solid line:* average model from MacMinn & Primack including the CMBR [15], *dashed line:* average model from Fall, Charlot & Pei added to the CMBR [16], *dotted line:* upper limit derived in [14].
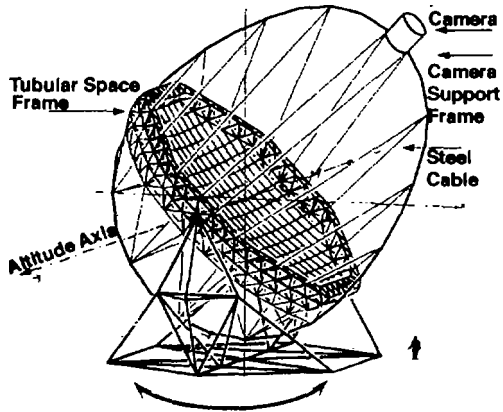
Figure 7: Sketch of the planned 17 m diameter MAGIC Telescope [17].

relic photons in intergalactic space. This density is dependent on the era of galaxy formation and thus on the nature of the Dark Matter.

One extraction of an upper limit on the IR photon density was performed in [14] where it is assumed that the IR background is uniformly distributed in the Universe. The result, together with existing upper limits, lower limits, and an average model for galaxy evolution based on a mixed Dark Matter ansatz is shown in fig. 6. The resulting low density of photons limits the parameter space for Dark Matter models and at the same time opens up the deeper regions of the Universe (i.e., $z = \mathcal{O}(0.1)$) for TeV astronomy.

3.3 The Future of Gamma-Ray Astronomy

Currently space-borne γ-astronomy is limited to energies *below* 10 GeV and ground-based γ-astronomy to energies *above* 300 GeV. In both cases the reasons are limitations of sensitivity and/or effective collection areas. The result is an observation gap between 10 GeV and 300 GeV where the Universe has not been observed in, and where we expect to find hints or answers to important physics questions in astrophysics, cosmology, and particle physics.

In order to bridge this gap the ground-based 17 m diameter MAGIC Telescope (see fig. 7) has been designed during the last 2 years [17]. Using innovative elements it will be possible to close the last observation gap for about 1% (!) of the cost of a satellite experiment, which until now was believed to be necessary in order to do measurements in this energy domain. At the same

time the sensitivity in the energy region of current Cherenkov telescopes will be improved by up to an order of magnitude.

References

[1] B. Wiebel-Sooth, Ph D Thesis, University of Wuppertal, 1998, in preparation.

[2] J. Cortina et al. (HEGRA coll.), to be published.

[3] A. Lindner et al. (HEGRA coll.), Proc. 25th ICRC Durban, South Africa, **5** (1997) 113.

[4] J. Weber et al. (KASKADE coll.), Proc. 25th ICRC Durban, South Africa, **6** (1997) 153.

[5] D. Heck et al. (KASKADE coll.), Proc. 25th ICRC Durban, South Africa, **6** (1997) 245.

[6] A. Lindner, Proc. 25th ICRC Durban, South Africa, **4** (1997) 57; astro-ph/9801147, to appear in Astropart. Phys.

[7] J. Knapp, Rappateur talk at the 25th ICRC Durban, South Africa, 1997.

[8] D. Petry, Ph D thesis, Max-Planck-Institut für Physik, München, MPI-PhE/97-27 (1997).

[9] T. Weekes, M.F. Cawley, and D.J. Fegan, ApJ **342** (1989) 379.

[10] J. Quinn et al. (Whipple coll.), ApJL **456**, (1996) L83.

[11] S.M. Bradbury et al. (HEGRA coll.), A&A **320** (1997) L5.

[12] R.J. Protheroe et al., Highlight Session at the 25th ICRC Durban, South Africa, 1997, astro-ph/9710118.

[13] F. Aharonian et al. (HEGRA coll.), A&A to appear.

[14] B. Funk et al., submitted to Astropart. Phys..

[15] D. Macminn and J.R. Primack, Spac. Sci. Rev. **75** no.1-2 (1996) 413.

[16] S.M. Fall, S. Charlot and Y.C. Pei, ApJ **464** (1996) L43.

[17] 'The MAGIC Telescope' Design Report, to appear.

GAMMA RAYS FROM COSMIC RAYS, NUCLEAR INTERACTIONS, AND NUCLEOSYNTHESIS

H. BLOEMEN

SRON-Utrecht
Sorbonnelaan 2, NL-3584 CA Utrecht, The Netherlands

Gamma-ray astronomy has become a rich field of research and matured significantly since the launch of NASA's Compton Gamma Ray Observatory (CGRO) in 1991. The gamma-ray sky in the 1 MeV to 10 GeV regime is seen to be dominated by a diffuse glow from the Milky Way which can largely be attributed to cosmic-ray electrons and protons interacting with the interstellar gas and photon fields. Embedded in this diffuse emission, a wide variety of sources can be expected and is already seen. This presentation will focus on the new progress that is being made in the 1 to 30 MeV regime, which was largely unexplored until recently but which is now well covered (imaging and spectroscopy) by the COMPTEL instrument aboard CGRO. At these MeV energies, gamma-ray lines provide a unique tool to trace radioactive and energetic ($\sim$ 2–100 MeV/nucleon) nuclei in the Galaxy. All astrophysical (non-solar) gamma-ray lines that are firmly detected so far originate from the decay of long lived radionuclei produced in nucleosynthesis processes (^{26}Al, ^{44}Ti, and $^{56/57}$Co) (in addition to the 511 keV line). The second category of gamma-ray lines, i.e. nuclear deexcitation lines from energetic particle interactions, is well known from solar flares and COMPTEL provides now the possibility to study the presence of such lines in the emission from astrophysical sources. First evidence has been seen, but conclusive line identifications are still lacking.

ASTRONOMICAL RADIOACTIVITY MEASUREMENTS

R. DIEHL with the COMPTEL Collaboration

Max Planck Institut für extraterrestrische Physik (MPE)
D-85740 Garching, Germany
rod@mpe-garching.mpg.de

Abstract

The telescopes aboard the NASA Compton Observatory have recorded gamma-ray line signals from several radioactive species: ^{57}Co, ^{44}Ti, ^{26}Al, and possibly ^{56}Co. Radioactivities in the universe provide a direct measure of current nucleosynthesis processes through the gamma-ray lines emitted in the radioactive decay. Different isotope lifetimes address specific astrophysical questions, from integrated current nucleosynthesis event frequencies in the Galaxy to nucleosynthesis yields of specific stars or supernova events. We discuss the status of those results from the on-going mission, and address issues for nuclear astrophysics.

1 Introduction

The discovery by HEAO-C (Mahoney et al. 1982) of γ-ray emission from radioactive ^{26}Al has provided a boost for experiments targetting radioactivity astronomical measurements (see review by Prantzos & Diehl 1996). Even more than the numerous ^{26}Al measurements, the detection of decay gamma-rays from supernova 1987A originating from shortlived (and therefore sufficiently intense) ^{56}Co and ^{57}Co gamma-rays (see review by Diehl & Timmes 1998) was a convincing proof of supernovae being prime sources of new element formation. Even though the list of isotopes that can serve as such nucleosynthesis tracers is short, the absence of a chain of corrections makes such gamma-ray measurements a valuable complement in the study of cosmic nucleosynthesis: e.g., atomic lines observations require a precise account of their excitation function, putting high demands on stellar atmosphere models and atomic data; meteoritic abundance measurements require models of the nucleation and the fragmentation processes in the 4.6 Gy history of the material samples. Instrumental capabilities still are in their infancy, compared to other astronomical fields: Spatial resolutions of most instruments is in the 10-100 degree regime, with the exeption of the COMPTEL telescope ($\simeq$4 degrees FWHM); spec-

tral resolutions of the scintillation-detector based instruments are $\simeq$ 6-10% (FWHM), while a few short experiments with Ge detector instruments (0.1% resolution) give an outlook for the next-generation missions in preparation. The astrophysical value of the measurements depends manily on the ability to locate the source of emission on the sky, for identification with a specific astronomical object. Imaging resolution of $\simeq$ arcmin or below can be achieved, yet spectral resolution can help indirectly, utilizing Doppler shifts of the lines (e.g., Gehrels & Chen 1995). We summarize the current understanding of the ^{26}Al measurements from the Galaxy, and of the supernova diagnostics using shortlived ^{44}Ti and Co isotopes.

2 ^{26}Al Measurements from the Galaxy

With its one-million year decay time, ^{26}Al accumulates in the interstellar medium from many source events. Therefore astronomical studies in the 1.809 MeV gamma-ray line from ^{26}Al decay to ^{26}Mg address the issue of the current average nucleosynthesis activity in the Galaxy and solar vicinity. Maximum entropy deconvolution images derived from the Compton Telescope (COMP-TEL) measurements aboard the *Compton Gamma Ray Observatory* (CGRO) show the spatial structure of the emission (Fig. 1; Oberlack et al. 1998). The ridge of the Galactic plane dominates, but there is asymmetry in the emission profile along the disk, and there are several prominent regions of emission such as Vela and Cygnus.

Spiral-arm emission is indicated from the image and from model fits, including between 1.1 $M_\odot$ and all of the ^{26}Al (Diehl et al. 1997). All measurements of the integrated flux from the inner region of the Galaxy ($\pm$ 30°in Galactic longitude) in the 1.809 MeV line with different instruments are consistent with values $\sim 4 \times 10^{-4}$ ph cm^{-2} s^{-1} rad^{-1}.

If massive stars are the candidate sources, they were thought to follow an irregular spatial distribution such as the one from the molecular gas (Dame et al. 1987), rather than a smooth exponential disk profile. Although both models are generally compatible with the ^{26}Al map, other tracers were found to provide a better fit. In a recent multi-frequency image comparison it was demonstrated that a map of the ionization power from massive stars as derived from the COBE DMR map with its intrinsic resolution of $\simeq$ 7 °by correction for the synchrotron contribution) is proportional to the 1.809 MeV map in all significant detail over the entire plane of the Galaxy(Knödlseder 1997). Assuming a standard initial mass function, this calculation reproduces the expected massive star population and the supernova rate from both maps

consistently, if Wolf-Rayet stars from high-metallicity regimes in the inner Galaxy provide the bulk of ^{26}Al (Knödlseder 1997). Therefore it seems most plausible that the ^{26}Al distribution in the Galaxy follows the distribution of massive stars, and thus the dominating source type has been identified. Open issues still are the relative contributions from explosive and wind release of ^{26}Al into the interstellar medium; and, of course the limits on contribution from the other candidate source types, novae and AGB stars. From ^{26}Al contributions from classical novae, a smooth distribution of the emission with a pronounced peak in the central bulge region would be expected. The upper limit for such contribution is probably 1 $M_\odot$ of ^{26}Al. On the other hand, Ne-rich novae in our Galaxy may occur more frequently in the disk, hence be less clearly dscriminated against massive stars in general. For the AGB contribution a similar problem is expected, since massive AGB stars $M \geq 3M_\odot$) are most likely candidate sources of ^{26}Al.
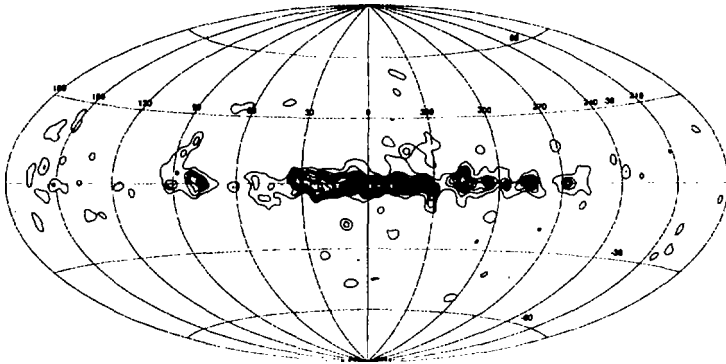
Fig. 1: COMPTEL all-sky image of current nucleosynthesis in the Galaxy, as measured through 1.8 MeV γ-rays over 5 years (Oberlack et al. 1998)

Physically, ^{60}Fe should be a good discriminant of different source types generating ^{26}Al, because massive stars produce ^{26}Al and ^{60}Fe in the same regions and in roughly comparable amounts (Timmes et al. 1996). These core collapse nucleosynthesis models suggest that the majority of both ^{26}Al and ^{60}Fe are produced, mainly during the presupernova evolution, between 3-6 $M_\odot$. These two isotopes should have similar spatial distributions after the explosion of these

stars, and thus may help to disentangle explosive from hydrostatic nucleosynthesis contributions.

The ^{60}Fe flux map is then expected to follow the ^{26}Al distribution, and the ^{60}Fe/^{26}Al line flux ratio should be 16 ± 10%. A few recent ^{60}Fe studies are known (), yet do not have sufficient sensitivity to detect the ^{60}Fe component.

A direct calibration of core-collapse supernova nucleosynthesis with the Vela SNR, which was a tantalizing prospect two years ago (Diehl et al. 1995), now appears less constraining due to superimposed other sources (a newly discovered young supernova remnant, and/or by OB associations and shell-like features at larger distances). The other prominent candidate source in the Vela region is the binary system γ^2 Velorum, representing the Wolf Rayet star "WR11" closest to the sun with an O star companion (van der Hucht et al. 1988). Recent Hipparcos parallax measurements suggest that this binary system is at a distance of 250-310 pc, which is closer than previous estimates of 300-450 pc (van der Hucht et al. 1997; Schaerer, Schmutz & Grenon 1997). At this closer distance the absence of a signal from γ^2 Velorum in the COMPTEL 1.8 MeV data is unexpected, particularly since recent models have increased the expected ^{26}Al yields for this object (Meynet et al. 1997). Modification of the ^{26}Al ejected from WR11 due to the O star companion seems inadequate to account for the discrepancy (Braun and Langer 1995; Langer et al. 1997).

About 80% of the prominent 1.809 MeV emission associated with the Cygnus region can be understood in terms of the expected ^{26}Al signal from known sources (del Rio et al. 1996). One may be concerned with this high fraction, since ^{26}Al decays on a timescale longer than the observable features of supernova remnants and Wolf-Rayet winds prevail. It has been suggested that the ^{26}Al from this region attributed to "seen" sources should be multiplied by a factor 1-10 to account for "unseen" sources. The latest COMPTEL images show structures which suggestively align with the Cygnus superbubble and Cyg OB1. Further analysis may be able to spatially separate source regions, and in particular assess the significance of emission from the prominent group of Wolf-Rayet stars in this region.

Supernova Constraints from ^{44}Ti and $^{56/57}$Co

Only in the inner regions of supernovae, temperatures and densities are considered adequate for formation of the surprisingly abundant ^{44}Ca isotope, produced as radioactive ^{44}Ti in the "α-rich freeze-out". (e.g., Hix & Thielemann 1996). Models predict ^{44}Ti yields of typically $\sim 3 \times 10^{-5}$ M$_\odot$ for the Type II models, or twice that value for the Type Ib models. Type Ia supernovae of

could also be important sources of ^{44}Ti if the sub–Chandrasekhar model turns out to be viable. Depending upon how frequently these sub-Chandrasekhar mass white dwarfs explode, the large production factors (up to 10^3 times the solar isotope ratio) suggest that these types of thermonuclear events might be the principal origin of ^{44}Ca, rather than the typical core-collapse event.

The measurement of radioactive decay of ^{44}Ti is possible through 3 gamma-ray lines, the 1.157 MeV deexcitation of ^{44}Ca following ^{44}Sc decay, or the 68 and 79 keV hard X-rays from deexcitation of ^{44}Sc following ^{44}Ti decay, in this ^{44}Ti ^{44}Sc ^{44}Ca decay chain. The shortlived ^{44}Sc stage ($T_{1/2} \simeq 3.8$ hrs) equilibrizes quickly since ^{44}Ti has a much longer decay time ($T_{1/2} \simeq 60\pm1$ y). The ^{44}Ti decay time had been controversial until very recently (see Görres et al. these proceedings), incurring large uncertainties in ^{44}Ti mass estimates from astronomical gamma-ray results. The discovery of 1157 keV gamma-rays from the ~ 300 year-old Cas A supernova remnant (Iyudin et al. 1994) was unexpected, model predicted γ-ray intensity generally below instrument flux sensitivities. The Cas A supernova remnant is relatively close (3.4 kpc) and young (explosion in 1668−1680), and probably a Type Ib explosion with indications of asymmetries, making it prime candidate among historic supernovae for ^{44}Ti discovery. Further analysis of recent COMPTEL data supports a 5σ detection of Cas A at $4.2 \pm 0.9 \times 10^{-5}$ ph cm^{-2} s^{-1} in the 1.157 MeV line (Iyudin et al. 1997), implying 2.4×10^{-4} $M_\odot$ of ^{44}Ti. The COMPTEL flux value appears to be consistent with the marginal measurements of OSSE (The et al. 1996) and RXTE (Rothschild et al. 1997) within their respective uncertainties.

Current core collapse nucleosynthesis models (Timmes et al. 1996) suggest that any ^{44}Ti ejection depends critically on the exact position of the mass cut, and that if ^{44}Ti is ejected, so is a relatively large mass of at least 0.05 $M_\odot$ of ^{56}Ni. This much shortlived radioactivity implies a bright supernova. Cas A was not widely reported as such; some 10 magnitudes of visual extinction is required to make the γ-ray ^{44}Ti measurements consistent with these historical records (or rather their absence). There may indeed have been such a large visual extinction to Cas A at the time of the explosion. ROSAT studies of the X-ray scattering halo of supernova remnants indicate that Cas A could have been embedded in a dusty region at the time of the supernova, making its optical display unobservable from Earth (Hartmann et al. 1997).

SN 1987A is an epoch where the dominant energy source should be from the decay of ^{44}Ti. Bolometric light curves of SN 1987A can be fit to light curve evolution models, and suggest $\sim 10^{-4}$ $M_\odot$ of ^{44}Ti (Fransson & Kozma 1997). The order of magnitude of $\sim 10^{-4}$ $M_\odot$ of ^{44}Ti inferred to have been ejected in SN 1987A and in Cas A is surprisingly similar. If this ^{44}Ti ejection should

be typical, core collapse supernovae could be revealed even from embedded and hence occulted sites through their ^{44}Ti decay gamma-ray lines. The first COMPTEL search for additional ^{44}Ti sources in the Galaxy from 1991-1993 data have been evaluated, and show no additional sources (Dupraz et al. 1997). This may be constraining the Galactic supernova rate; statistical fluctuations of this rate could conspire with light propagation differences from the supernova sites to the observer, and easily produce a supernova record gap of 300 years, however.

A long-standing goal of γ-ray astronomy has been detection of radioactive ^{56}Ni and ^{56}Co from supernovae, mainly from type Ia events (Clayton, Colgate & Fishman 1969). Only one such event has been seen in γ-rays, SN 1991T in NGC 4527 by the COMPTEL telescope (Morris et al. 1995, 1997). The host galaxy is $\sim$ 17 Mpc distant and in the direction of the Virgo cluster. This supernova is considered a prototype of a peculiar subclass, it was unusually bright at maximum and the light curve evolved unusually slow. Its spectra did become more typical of Type Ia events at later epochs when the expanding debris became more transparent. Detection of high velocity ($\sim$13000 km s^{-1}) iron and nickel in the outer layers of SN 1991T favors models with delayed detonation. However, sub-Chandrasekhar mass models of Type Ia supernova are discussed as well, and may be favorable for ejecting a larger than average ^{56}Ni mass. COMPTEL data from two relatively (for ^{56}Co) early epochs (66 and 176 days after the explosion) reveal a clear hint of a signal as expected from ^{56}Co decay (at $> 3\sigma$ significance). This is surprising for a supernova in general, as one would assume the ^{56}Co still burried inside. But in the case of SN1991T mixing of ^{56}Ni into the outer layers has been inferred already from early light curve and spectra. The COMPTEL detection indicates that this isotope was present in the outer envelope, and thus supports extensive mixing scenarios. The COMPTEL measurement converts into a surprisingly large ^{56}Ni mass, however, between 1.3 $M_\odot$(for a distance of 13 Mpc, Morris et al. 1995 and Lichti et al. 1995) and 2.3 $M_\odot$for the 17 Mpc favoured currently (Ruiz-Lapuente, priv. comm.). This requires that almost all of the Chandrasekhar mass white dwarf must be turned into radioactive ^{56}Ni. OSSE upper limits (Leising et al. 1995) may indicate that the ^{56}Co line flux derived by Morris et al. (1995) is too high, although the detection itself is confirmed at the same 3-4σ significance in more rigorous analysis employing different and independent analysis alternatives (Morris et al. 1997).

3   Summary

COMPTEL measurements of radioactivity set constraints on nucleosynthesis in astrophysical objects. The ^{26}Al results from gamma-ray line imaging of the full sky in the 1.809 MeV gamma-ray line settle the massive-star origin of most of the ^{26}Al in the Galaxy, although some contributions from novae or from special local regions cannot be excluded. The prominent deviations from a smooth distribution along the plane of the Galaxy can be understood as globally reflecting recent formation patterns of massive stars. In the Vela region, two known candidate source objects, the Vela SNR and the $\gamma^2 Velorum$ system with its Wolf Rayet star, are not seen as localized sources. This is compatible with expectations from models in the case of the Vela SNR, but inconsistent with current Wolf Rayet nucleosynthesis predictions. The discovery of ^{44}Ti from Cas A by COMPTEL presents a puzzle for core collapse supernova models, but also for the consistency of the Cas A observational database. The absence of a bright optical supernova may be reconciled with the hypothesis of a local dust concentration at Cas A at the time of the supernova, consistent with X-ray observed anomalies of Cas A SNR. No other prominent ^{44}Ti sources have been found yet, and even the prospect of detecting SN1987A could be dim. Current searches for other ^{44}Ti sources can help to assess how atypical Cas A might have been. The peculiar thermonuclear supernova SN1991T resulted in a ^{56}Co signal in the COMPTEL data. The derived ^{56}Ni mass appears too high, yet the detection itself favours delayed detonation scenarios or merger scenarios, consistent with anomalies detected in SN1991T's spectra and light curve evolution. In view of these results, gamma-ray line astronomy of cosmic radioactivities appears as a newly opened discipline with tantalizing perspectives. The INTEGRAL mission, to be launched in 2001, is the next major experiment addressing this field.

References

[1] Braun, H., & Langer, N., 1995, A&A, 297, 483

[2] Clayton, D. D., Colgate, S. A., & Fishman, G. 1969, ApJ, 220, 353

[3] Clayton, D. D. et al. 1992, ApJL, 399, L141

[4] Dame, T. M., et al., 1987, ApJ, 322, 706

[5] Diehl, R., & Timmes F.X., 1998, PASP, in press

[6] Dupraz, C., et al., 1997, A&A, in press

[7] Fransson, C., & Kozma, C., 1997, in SN 1987A: Ten Years After, The Fifth CTIO/ESO/LCO Workshop, eds M. M. Phillips & N. B. Suntzeff, ASP in press

[8] Gehrels, N., & Chen, W., 1996, A&A Supp., 120, 331

[9] Hartmann, D. H., et al., 1997, in Nuclei in the Cosmos IV, eds. M. Wiescher, Nuc. Phys. A, in press

[10] Hix, W. R., & Thielemann, F. K., 1996, ApJ, 460, 869

[11] Iyudin, A. F., et al., 1994, A&A, 284, L1

[12] Iyudin, A. F., et al., 1997, in Proc. 2nd INTEGRAL Workshop, eds. C. Winkler, T. J. -L. Courvoisier, P. Durouchoux, ESA SP-382, 37

[13] Kurfess, J. D., et al. 1992, ApJL, 399, L137

[14] Lichti, G. G., et al., 1994, A&A, 292, 569

[15] Mahoney, W. A., et al., 1982, ApJ, 262, 742

[16] Meynet, G., et al., 1997, A&A, 320, 460

[17] Morris, D. J., et al., 1995, 17th Texas Symposium, N.Y. Acad. Sci., 759, 397

[18] Morris, D. J., et al., 1997, in 4th Compton Symposium, eds. C. Dermer, J. Kurfess, & M. Strickland, AIP, New York in press

[19] Oberlack, U., et al, 1998, in preparation

[20] Prantzos, N. & Diehl, R., 1996, Phys. Rep., 267, 1

[21] Predehl, P., & Schmitt, J. H. M. M., 1995, A&A, 293, 889

[22] Rothschild, R. E., et al., 1997, in 4th Compton Symposium, eds. C. Dermer, J. Kurfess, & M. Strickland, AIP, New York in press

[23] Schaerer, D., Schmutz, W., & Grenon, M., 1997, ApJ, 484, L153

[24] The, L. S., et al., 1996, A&A Supp., 120, 357

[25] Thielemann, F. -K., Nomoto, K., & Hashimoto, M. A. 1996, ApJ, 460, 408

[26] Timmes, F. X., Woosley, S. E., Hoffman, R. D., & Hartmann, D. H., 1996, ApJ, 464, 332

[27] van der Hucht, K. A., Hidayat, B., Admiranto, A.G., Supelli, K.R., Doom, C., 1988, A&A, 199, 217

SOURCE COMPOSITION OF ULTRA HEAVY COSMIC RAYS DERIVED FROM UHCRE MEASUREMENTS USING A LEAKY BOX MODEL

J. FONT and C. DOMINGO

Grup de Física de les Radiacions. Departament de Física. Edifici Cc. Universitat Autònoma de Barcelona. E-08193 Bellaterra (Barcelona) Spain.

Abstract

The histogram of Ultra Heavy (UH) elemental abundances for $Z > 65$ in the Earth's neighbourhood is determined from the UHCRE results obtained by our group. The UH cosmic ray source abundances may be deduced by means of an appropiate propagation model. A Leaky Box model has been used for cosmic ray propagation studies. In this work, two different Solar System source abundances and an r-type source abundance have been assumed as starting point of the propagation calculation. It has been found that the UHCRE experimental results are better reproduced when an r-type source abundances is taken.

1 Introduction

The Ultra Heavy Cosmic Ray Experiment (UHCRE) has collected over 2500 ions with $Z > 65$ with a charge resolution that allows the separation of the Lead and Platinum abundance peaks [1, 2, 3]. These abundances provide information about the relative contribution of the r and s processes to nucleosynthesis as well as about the astrophysical conditions of the sites where this nucleosynthesis takes place. Because propagation models connect the source abundances of cosmic ray elements with the abundances of these elements measured in the Earth's neighborhood, it is possible to determine the abundances of cosmic ray UH ions at their sources from the UHCRE results and, in particular, to study how the Platinum and Lead peaks vary with propagation from the Earth to the cosmic ray sources.

In this work the influence on cosmic ray transport calculation of source composition is studied, assuming a Leaky Box propagation model to describe the travel of UH ions through the interstellar medium. The propagation model is described in next section, whereas in the results section the abundances determined in the UHCRE are presented and compared to those obtained from our propagation model when three different source abundances are used

2 The Propagation Model

We have developed a simple propagation model based on the well known Leaky Box (LB) model, firstly proposed by Cowsik *et al.*[4]. In order to obtain the transport equations corresponding to our model, only production and breaking up processes of the ions involved on the propagation have been considered. In addition, several assumptions have been taken into account in order to simplify our propagation model calculation: (1) neglecting energy loss by ionization and energy gain by re-acceleration; (2) neglecting particle injection processes after initial acceleration; (3) neglecting particle diffusion processes; (4) ISM atom density, n, taken constant along trajectory of particles; and (5) ISM composed only by Hydrogen atoms.

Taking into account the above assumptions for our model, the resulting transport equation for the i-th element may be written as:

$$\frac{dN_i(x)}{dx} = \sum_{j<i} \left(\frac{1}{\lambda_{dec}^{j\rightarrow i}} + \frac{1}{\lambda_{spall}^{j\rightarrow i}} \right) N_j(x) - \left(\frac{1}{\lambda_{esc}} + \frac{1}{\lambda_{dec}^{i}} + \frac{1}{\lambda_{int}^{i}} \right) N_i(x)$$

which coincides with the transport equation used by Waddington [5]. In the above equation: x is the matter traversed by the UH cosmic ray ions from their sources, so that $x = 0$ g/cm^2 characterizes these sources; λ_{dec}^{i} and λ_{dec}^{i} are respectively the mean free paths for decay of nuclides of type i, and radioactive decay of nuclides of type j to lighter nuclides of type i; λ_{esc} is the escape mean free path of cosmic rays before leaking from the propagation region; and $\lambda_{spall}^{j\rightarrow i}$ and λ_{int}^{i} are the spallation and nuclear interaction mean free paths, which can be obtained from the appropiate partial and total inelastic cross sections [6, 7].

The Weighted Slab Technique [8] has been utilized in the present work for solving the LB transport equation, in spite of solving the equations analiticaly as in former works of our group [3, 9]. This technique involves the resolution of the transport equations for N_i as a function of the matter traversed x *(in g/cm^2)*, $N_i(x)$, and the subsequent application of a Path Length Distribution (PLD) in order to obtain the propagated abundances.

We have utilized our LB model to propagate UH cosmic ray ions with charge comprised between 65 and 83 from the source to near the Earth. We have taken three different source abundances which, mathematically, play the role of initial conditions for transport calculations. The assumed source abundances are: the Cameron Solar System abundances [10], the Anders and Ebihara Solar System abundances [11] and an r-source type source abundances previously used by Binns *et al.* [12]. The First Ionization Potential (FIP) correction given by Letaw *et al.* [13], which accounts for initial acceleration, has been

applied to all these assumed source abundances. Only the most stable and most abundant isotope of each element is considered for propagation as a first approximation, thus disintegration terms in the transport equations vanish. A galactic volume with a value of $\lambda_{esc} = 6.0$ g/cm^2 is taken as the propagation region and, in consequence, only UH ions of Galactic origin are considered. An exponential PLD truncated at $T = 1.0$ g/cm^2 has been used in order to obtain the abundances in the Earth's neighbourhood of each UH element from the corresponding solution $N_i(x)$ of the above transport equation.

3   Results and discussion

The abundances relative to Lead obtained using our propagation model, under the conditions and with the parameters described above, are illustrated in figure 1. In this figure, the UH ion abundances for charges between 65 and 83 propagated to the Earth's neighbourhood with our LB model, using the three different source compositions, are shown. An overabundance of r-synthesized ions (Platinum peak) after performing propagation is observed for all of the assumed source compositions.
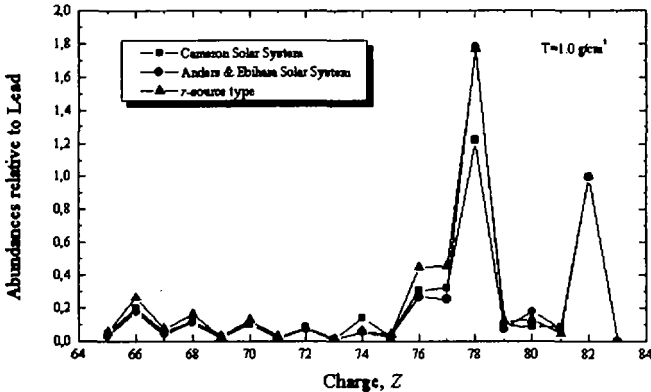
Fig. 1. Abundances relative to Lead of UH cosmic ray ions in the Earth's neighbourhood, obtained using three different source compositions and propagating at an energy of 5 GeV/n with the Silberberg & Tsao expressions for cross sections.

The experimental abundances of UH cosmic ray ions with charge comprised between 65 and 92, obtained from UHCRE [2, 3] are plotted in figure 2, together with a gaussian fit of the two abundance peaks (Lead and Platinum group peaks). In order to distinguish which of the assumed source abundance better agrees with the UHCRE experimental results, the following abundance ratio is defined,

$$R = \frac{Lead\ peak\ abundance}{Platinum\ peak\ abundance} = \frac{\sum N_i\ (81 \leq Z \leq 86)}{\sum N_i\ (74 \leq Z \leq 80)}$$
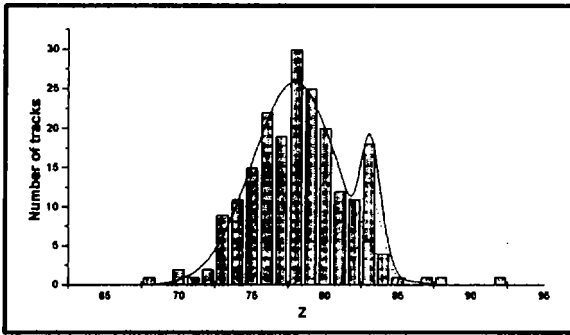
Fig. 2. Experimental abundances of UH cosmic ray ions in the Earth's neighbourhood, as measured in UHCRE.

The calculated values for this ratio are 0.496 if the Cameron SS abundances are used, 0.407 when the Anders & Ebihara SS abundances are considered, and 0.349 when an r-type source is taken. The UHCRE experimental value is 0.32 These values may suggest that UH cosmic ray sources are better explained by an r-type source abundances. This conclusion is in agreement with previous works [12], although the study of the influence of other transport parameters, such as cross sections involved, may lead to different conclusions [14].

Acknowledgements

References

[1] D. O'Sullivan, A. Thompson, J. Bosch, R. Keegan, K.P. Wenzel, F. Jansen, C. Domingo, Adv. Space Res. **15** (1995) 15.

[2] C. Domingo, J. Font, C. Baixeras, F. Fernandez, Proc. 24th ICRC (Rome). **2** (1995) 572.

[3] C. Domingo, J. Font, C. Baixeras, F. Fernandez, Radiation Meas. **26** (1996) 825.

[4] R. Cowsik, Y. Pal, S.N. Tandon, R.P. Verma, Phys. Rev. **158** (1967) 1238.

[5] C.J. Waddington, Astrophys. J. **470** (1996) 1218.

[6] J.R. Letaw, R. Silberberg, C.H. Tsao, Astrophys. J. Suppl. **51** (1983) 271.

[7] R. Silberberg and C.H. Tsao, Astrophys. J. Suppl. **25** (1973) 315, Astrophys. J. Suppl. **25** (1973) 335, Phys. Rep. **191** (1990) 351.

[8] R.J. Protheroe, J.F. Ormes, C.M. Comstock, Astrophys. J. **247** (1981) 362.

[9] J. Font, C. Domingo, M. Mendjeli, C. Baixeras, F. Fernandez, Proc. 24th ICRC (Rome). **3** (1995) 144.

[10] A.G.W. Cameron, Essays in nuclear astrophysics. Cambridge University Press 1982, p. 23.

[11] E. Anders and M. Ebihara, Geochim. et Cosmichim. **46** (1982) 2263.

[12] W.R. Binns, N.R. Brewster, D.J. Fixsen, T.L. Garrard, M.H. Israel, J. Klarmann, B.J. Newport, E.C. Stone, C.J. Waddington, Astrophys. J. **297** (1985) 111.

[13] J.R. Letaw, R. Silberberg, C.H. Tsao, Astrophys. J. **279** (1984) 144.

[14] J. Font, C. Domingo, C. Baixeras, F. Fernández, Proc. Advances in Nuclear Physics and Related Areas (Thessaloniki). (1997).

Interaction of Cosmic Ray Nuclei with the Sun

Janusz Kempa
Department of Experimental Physics, University of Lodz
90-236 Lodz, ul.Pomorska 149/153, Poland

Adam Michalec
Astronomical Observatory of Jagiellonian University
30-244 Cracow, ul.Orla 171, Poland

Abstract
Nuclear interactions of high energy particles of cosmic radiation with nuclei present in the solar corona generate secondary particles which can reach outer regions of the terrestrial atmosphere causing small atmospheric showers which can be registered at the surface of the Earth. In this paper an attempt is made at interpreting measurements of coincidences between detectors situated at large distance in the framework of such a scheme.

1. Introduction

The existence of groups of genetically connected particles, generated in the Earth atmosphere by particles of the primary cosmic radiation and propagating at large distances in the direction of the primordial particle, was confirmed many years ago (Auger and Maze, 1938). Coincidences were observed between the Geiger-Miller counters put away over a distance ranging from 2 m to 20 m causing diminishing in the number of observed coincidences from 1.7 to 0.9 per hour, respectively. Thus the ten-fold increase of the distance lowered the number of counts by the factor of nearly 2. This experimental result in the pioneering measurements by Auger and Maze is widely considered as the discovery of great atmospheric showers in the cosmic radiation (so-called EAS – Earth Atmospheric Showers).

Today we know, on the basis of many measurements performed by numerous groups both in the mountains and at the sea level, that the particles in the showers propagate in the direction perpendicular with respect to the shower axis at a distances ranging from hundreds of meters to about 10-15 kilometres for the largest showers.

The measurement of coincidences between detectors situated in Geneva and Basel, and thus separated by the distance of about 180 km, should be considered as a real sensation (Carrel and Martin, 1994). The situation resembles closely that in the year 1938 since the separation of counters exceeded nearly two orders of magnitude the distances achieved earlier in the coincidence measurements.

We estimate that in order to explain this phenomenon – as caused by a single shower – the energy of the primary nuclei should be very high, i. e, equal approximately to 10^{19} eV. Shower produced by nuclei having such high (or even higher) energies were – and still are – measured in several experiments in the world (e. g. Akeno, Jakuck, Haverah-Park, Fly's-Eye). However, it is absolutely evident that charged particles in the showers of these values of primary energies don not propagate at such enormous distances. How to explain the coincidences measured in Switzerland then?

In the present work (see also Kempa and Michalec, 1998, for more details) we are trying to show that probably the only way to explain the observational data is to adopt the assumption that these showers are multi-core ones. As such they are produced by several γ quanta rather then by just one, arriving simultaneously at the top of the Earth atmosphere. In our opinion such γ quanta are produced in interactions of the primary cosmic radiation nuclei with the nuclei present in the solar corona. From the ring-like solar „boundary", where the gas density is relatively small (in particular it depends on the current phase of the solar cycle), such particles can escape and reach the upper layers of the terrestrial atmosphere. Their mutual separation on the distance Sun-Earth (1 astronomical unit) may be as high as 100 km. Showers created by them, both „individual" and small, yield on the surface of the Earth multi-core picture, capable of producing coincidences between detectors distances of which may be hundreds of kilometres.

2. Experimental data.

Recently, for the first time, coincidences caused by the particles of the cosmic radiation between distant detectors have been measured. The distances were at least several tens of kilometres (cf. Carrel and Martin, 1994). There were four detectors, each of the area $3 \times 0.7 \times 0.4 \text{ m}^2 = 0.84 \text{ m}^2$, located in Geneva, Basel, Bern and Le Locle in the form similar to the „Southern Cross". This so-called „Northern

Cross" may be circumscribed on an ellipse with the area equal to 5000 km^2. Having adopted that each detector – in order to act – requires at least one particle, and that the density of particles inside the above mentioned ellipse is constant, one can estimate the entire number of charged particles in the shower which causes such a coincidence as $N = 5 \times 10^9$.

Assuming further that each charged particle in the shower (before its maximal phase) has its energy between 1 and 2 GeV we may roughly estimate the energy of the primary nuclei, which caused such a gigantic shower, as $E = 10^{19}$ eV taking also into account the fact that in the EAS distribution of charged particles is not uniform.

On the background of random coincidences an excess on the level of 4.8 σ was measured. It was clearly visible during 180 hours between December 15th and December 22nd 1991. In this period 548 events above the background were detected.

It is very important that the detected signal was *not* uniformly distributed in time. During each 24-hour period it was visible only twice – during two hours: between 4 and 6 universal time and between 16 and 18 universal time. Thus the 12-hour separation is evident. Average frequency of registered signal per each 24-hour period was 73 showers which gives 18.3 showers per hour.

We may thus estimate that the unknown source, emitting nuclei responsible for the creation of such showers, radiates in our direction flow of energy of at least $L = n \times E_0 = 10^{-2}$ W detected by the device distributed on the area 5000 km^2. Unfortunately, as to the directions, from which the showers arrive, we know nothing since an attempt of their estimation failed (cf. Carell and Martin, 1994). Having analysed various parameters they concluded that the probability of accidental detection of such coincidences is smaller then 10^{-4}.

3. Sun as a target

The undoubtful fact that the showers were detected by the „Northern Cross" every 12 hours, i. e. shortly before sunrise and shortly after sunset, strongly suggest their close connection with the Sun.

Our hypothesis presented in this note states the following: measured in Switzerland coincidences were produced by particles from

great atmospheric showers, created in the terrestrial atmosphere by a group of coherent particles generated during collisions of nuclei from cosmic radiation with light nuclei (mainly protons) in the solar corona. Among the created particles there are both particles produced in nuclear reactions and nucleons from the nuclei coming to the Sun which did not participated directly in the non-elastic interactions. We further suggest (see Kempa and Michalec, 1998) that the source itself may be located somewhere behind the Sun, on the line source-Sun-Earth, continuously emitting energetic nuclei. Let us now have a look at some features which may be essential for accepting or rejecting our hypothesis.

a). We know very little about sub-horizontal propagation of large showers in the terrestrial atmosphere. Regarding the horizontal showers we know that they create an ellipse on the Earth surface with its semiaxes ratio equal 1:10 (Billoir 1996). This effect may be caused by the bending of charged particles trajectories in the Earth magnetic field. It is possible that, in the case sub-horizontal showers, the structure of magnetic field in the solar wind may be absolutely crucial.

b). The very design of the Swiss device favours registering of showers in the direction Basel-Geneva. If the azimuthal angle Θ increases then the relative distances decrease which in turn increases the probability of coincidence. In the period 15-22 of December 1991 the Sun was rising in Geneva along a small circle inclined to the horizon at 20°. This value seems to favour the above mentioned hypothesis.

The sensitivity of the device (with respect to changes in number of registered coincidences when the Θ-angle changes) may be estimated from the shape of their registered temporal distribution during 24-hour period. Figure 5 in the work of Carrel and Martin reveals that the number of events during 2 hours period decreases twice whereas during the next 2 hours reaches effectively the background level.

c). It is relatively difficult to explain why the described effect was observed during 180 hours, i.e. during 7.5 days and nights. Our reasoning here is purely intuitive. We refer to the following dependence: number of events versus Θ-angle. During 180 hours the change in the Earth position (in the Earth-Sun frame of reference) is equal to 7°.4. That means that the Earth leaves the preferred direction: source-Sun-Earth. Since the sensitivity of the „Northern Cross" in the directional dipole distribution is very high, it seems that this should be the simplest possible explanation of the observed effect.

4. Possible candidates for the source.

In the period 15-22 of December 1991 the Sun, as observed from the Earth, had its co-ordinates on the sky sphere:
Right Ascension ranging from $17^h 30^m$ to $18^h 02^m$
Declination ranging from $-23° 15'$ to $-23° 26'$.

In this area, or very close to it, we find (cf. Zombeck, 1980) the following objects:

- M6 – 1736-321 or NGC 6405;
- M8 – HII region in Sagittarius constellation or GC 6523;
- Kepler's supernova: $17^h 30^m.4$, $-21° 29'$ or radio source 3C358;
- QSO 1748 –25.3;
- NGC 6440 or X-ray source MX1746-20;
- Variable star of the type δ Cep - X Sgr 1747-2750, with magnitude 4.2-4.8 and the period 7 days;
- Galactic microquasars: 1E 1740.7-2942; (Ziolkowski, 1997).
- γ-emitting sources: GRS 1758-258, and a new source in the Galactic centre discovered by SIGMA, X-ray nova: GRS 1739-278;
- Radio sources: Sgr A 1743-2856, Galactic Centre.

Concluding: Taking into account the fairly good agreement of the position of the Sun and the possible source (in right ascension) it seems reasonable to assume that the source, ejecting nuclei with high energy which subsequently generate showers measured by the „Northern Cross", is located near the galactic centre.

5. Conclusion

In this paper an attempt has been made to prove that the observed coincidences between the detectors located in Basel, Geneva, Bern and Le Locle may be entirely explained by adopting hypothesis that they are caused by multi-core showers (see Kempa & Michalec, 1998, for more details). These in turn require the initial bundle of particles which would arrive at the top of the atmosphere some 200 km apart from each other. Of course, these particles must also be coherent. In normal showers there are no such particles.

The hypothesis we tried to prove intuitively asserts that such groups of particles may be produced in the solar corona as a result of interaction of primary nuclei from the cosmic radiation with those already

present in the corona. The energies required for these nuclei are fairly reasonable. In the case of multi-core showers the required energies may be much lower then 10^{19} eV. In principle, four particles having energies 10^{15} eV may produce showers which could give coincidences observed in the Swiss device. This would even make possible to consider much lower initial energies, say $- 10^{16}$ eV. Having assumed so low energies of the primary nuclei we can easily explain the above mentioned 100 km separation of the shower, both for iron nuclei and protons. Lower energies enable also to understand, at least qualitatively, the problem of anisotropy. If the results presented here required energies as high as 10^{19} eV then their source in the centre of our Galaxy would undoubtedly be discovered in earlier measurements. Also, the position of the source in the centre of Galaxy is a crucial evidence which strongly supports our hypothesis. For its experimental verification it would be necessary to build a special device dedicated, from the very beginning, to measuring of multi-core showers with large separation of their sub-cores (of order of tens of kilometres). Before that one should prove that we indeed observe multi-core showers from the Sun.

We strongly believe that an attempt of such measurements could be performed using KASCADE (Klages *et al.*, 1997) which is at present the largest European device and very suitable for investigating multi-core showers having asymmetry in the distribution of particles on the detection plane, and for distances not exceeding 200 metres. If the measuring capabilities of this device could be increased by the factor of 10 – which is already possible at low costs – then it would be indeed a perfect device aimed at measuring the sub-cores generated in the solar corona during interactions of iron nuclei with protons.

On the other hand, in the larger scale, say 60 kilometres, multi-core showers can be analysed in PAO (Pierre Auger Observatory). It seems that such an investigating program could be successfully realised with only minor changes in the location of the detectors.

In conclusion we would like to remark that in order to verify our hypothesis one should, unfortunately, wait till December 1998 when the same configuration as that of 1991 will be repeated. However, possible negative result of the future observation does not exclude our hypothesis since the source of primary particles may be only periodical or it may have exhausted its power and terminated its activity.

References

P. Auger, R. Maze 1938, Comptes Rendus, Vol.207, p.228.

P. Billoir, 1996, http//www-td-auger.fnal.gov:82.

O. Carell, M. Martin 1994, Physics Letters **B** 325, pp.526-530.

J. Kempa and A. Michalec, 1998, Acta Astronomica, submitted for publication.

H. Klages *et al.*1997, XXV ICRC, Durban, Highlight Talk.

J. Ziolkowski, Galactic Microquasars, pp.38-48, in: *Relativistic Jets in AGNs*, Cracow, 1997.

M. V. Zombeck, *High Energy Astrophysics Handbook*, SAO, Cambridge, 1980.

SOLAR MODELS:
ACHIEVEMENTS AND FAILURES

A. WEISS

Max-Planck-Institut für Astrophysik,
Postfach 1523, D-85740 Garching, Germany

Abstract

In this talk the present status of solar models is reviewed. After an introduction to solar modelling, the results of helioseismology are discussed, which show that modern standard solar models agree with the Sun at a level of better than 1%. While this rules out all non-standard solar models, the deviation is significant due to the high accuracy of observations. Nevertheless, it suffices to prove that the solar neutrino problem will find its solution in new particle physics, the most popular explanation now being the MSW neutrino oscillation effect.

1 The concept of a solar model

Since the first solar neutrino experiment has proven that the Sun shines due to nuclear reactions converting hydrogen to helium, the deficit of more than a factor 2 in the measured neutrino events compared to theoretical predictions has cast doubt on the quality of solar models (SM) and therefore stellar evolution theory in general. Only recently, due to the results of several neutrino experiments and of helioseismology the high quality of modern SM has become evident. The solution of the solar neutrino problem will therefore be found by extending the standard model of particle physics.

A *solar model*[1] is actually the final product of a whole sequence of models, in which the evolution of a star with the mass of the Sun (1 $M_\odot$) is followed until the solar age $t_\odot$ is reached. The initial model at $t = 0$ is a star with pristine homogeneous composition, getting its energy either completely out of nuclear (main sequence) or thermal (pre main sequence) energy. In the calculations of classical standard solar models (SM), two free parameters exist: the initial helium content and a parameter needed for the description of convective energy transport. They must be chosen in such a way that the solar radius and luminosity are matched at $t_\odot$. The calculation of a solar model is therefore an

---

[1]For an introduction, see [12].

interative process with the final parameter values depending on the details of the model assumptions.
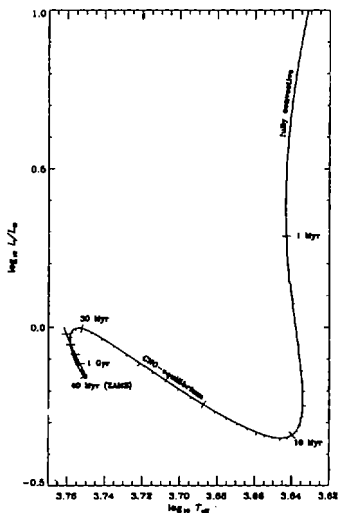

Fig. 1. Evolutionary track of the Sun from the pre-main-sequence until its present state (courtesy of H. Schlattl)

quantity	value	ref.
$M_\odot$	$(1.9891 \pm 0.0012) \cdot 10^{33}$ g	
$L_\odot$	$(3.844 \pm 0.01) \cdot 10^{33}$ erg/s	
$R_\odot$	$(6.959 \pm 0.001) \cdot 10^{10}$ cm	
$T_{\text{eff},\odot}$	5777 ± 2.5 K	
$(Z/X)_\odot$	0.0245 ± 0.001	[7]
$Y_\odot$	0.246	[3]
	$0.238 - 0.259\ (0.246)$	[6]
R_{cz}	$0.713 \pm 0.003\, R_\odot$	[5]
$t_\odot$	$(4.57 \pm 0.02) \cdot 10^9$ yrs	

Table 1: Solar quantities: mass, luminosity, radius and effective temperature $M_\odot$, $L_\odot$, $R_\odot$, $T_{\text{eff},\odot}$. $Y_\odot$: present surface helium content; R_{cz}: radius of the convective envelope's lower boundary; errors are 1σ errors as given in the original papers.

The model ingredients are fairly simple: we assume spherical symmetry (ignoring magnetic fields and rotation) and hydrostatic equilibrium. Energy sources are thermal and nuclear ones; energy transport is either via radiation (diffusive) or convection. For the former the opacity of the material is important. Here, great progress has taken place in the last years (e.g [9]) as well as in the EOS (e.g [10]). Lacking a rigid theory for convection, simplified mixing-length approaches are still in use, although there are some improvements ([11]).

The most important additional physical aspect of modern SMs is the inclusion of the diffusion of H, He, CNO and other metals. Although applied already in early models to check its influence on the neutrino fluxes (which is minor), only recently ([2]) it has become evident that it is a necessary ingredient for accurate models. In particular, only these modern SM can reproduce the depth of the convective envelope (R_{cz}) and the helium content ($Y_\odot$) in it,

as deduced from helioseismology. For example, $Y_{\odot} \approx 0.245$ (Table 1), while models without diffusion predict it to be the initial value, which is close to 0.28. Note that the consideration of metal diffusion adds another parameter to the models, the initial metal content, because only the present value relative to hydrogen, $(Z/X)_{\odot}$, is known.

2 Helioseismology − confirming the standard model

Leighton in 1960 observed that the solar surface oscillates with a period of about 5 minutes and Ulrich ten years later showed that these oscillations are the superposition of many non-radial modes of very small amplitude. This was the beginning of *helioseismology*.[2] Since 1975, starting with the work of Deubner, several thousands of eigenmodes have been identified by 2d-power spectra analysis. These non-radial eigenmodes are characterized by their radial order n, the degree l and m (fine-splitting due to breaking of spherical symmetry). Typical frequencies are between 3000 and 4000 μHz. Observations usually make use of the Doppler-effect. Incredible accuracy is achieved: the velocity amplitude is only $10-20$ cm/s, which must be compared to the width of the Fraunhofer-lines, which is equivalent to 10 km/s!

Whether the eigenmodes are of oscillatory or damped nature depends on two critical frequencies, the buoyancy or *Brunt-Väisälä frequency* N

$$N^2 = g \left(\frac{1}{\Gamma_1} \frac{d\ln p}{dr} - \frac{d\ln \rho}{dr} \right)$$

where $\Gamma_1 = \left(\frac{d\ln p}{d\ln \rho} \right)_S$, and the *acoustic frequency* S_l

$$S_l = \frac{l(l+1)c^2}{r^2}$$

(c being sound speed). Oscillatory solutions to the linear perturbation equations of solar structure exist if

$$|w| > |N| \ \wedge \ |w| > |S_l| \quad \text{or} \quad |w| < |N| \ \wedge \ |w| < |S_l|$$

The first conidition is fulfilled for modes, where the restoring force is pressure (*p-modes*; high ν), the second if it is gravity (*g-modes*; low ν). The modes are exponentially damped for $|N| < |w| < |S_l|$ or $|S_l| < |w| < |N|$.

---

[2]An excellent introduction is provided by the lecture notes of Christensen-Dalsgaard, available from http://www.obs.aau.dk/ jcd/oscilnotes

Fig. 2 shows ν as a function of l for solar oscillations obtained from a SM and observational results. Their incredibly accuracy is evident from the fact that the errorbars correspond to 1000-σ errors!
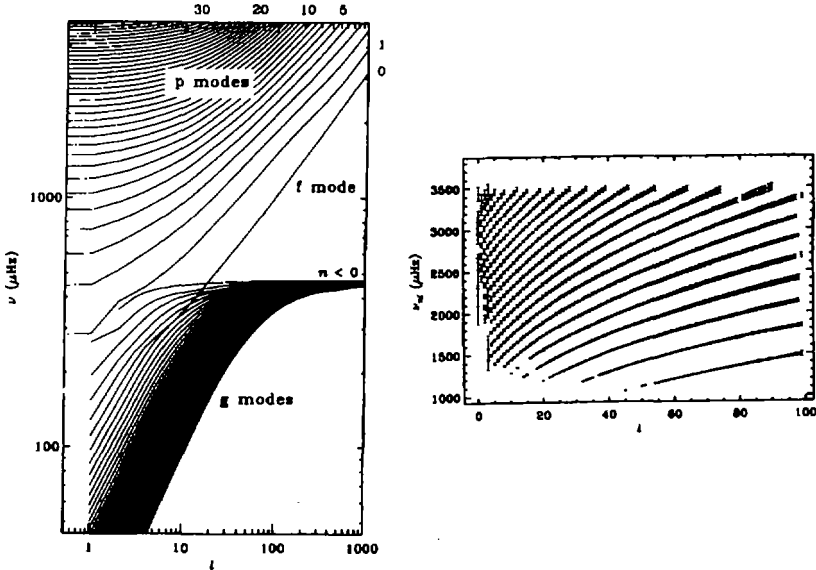

Fig. 2: left: p- and g-mode model frequencies. Lines connect modes of the same radial mode number n. The f-mode is a surface gravity mode; right: observed frequencies of p-modes. Errorbars correspond to 1000-σ errors(!) (from [4])

Mode frequencies depend on the equilibrium state of the fluid, in particular on ρ, p, Γ_1 and g (gravitational acceleration). However, since the equilibrium must fulfill the stellar structure equations, this can be reduced to two variables (as function of radius r), usually ρ and Γ_1, from which the two others can be derived. Note that Γ_1 is a thermodynamical function depending on ρ, p and composition. With the first two quantities known, one can derive the latter one from helioseismology! In particular, this is possible in the deep convective envelope (modes with $l > 40$ are trapped here), where convection is adiabatic (minimum uncertainty in convection theory; no influence of opacities) and composition homogeneous. Based on these facts the surface helium content $Y_\odot$ has been derived (the result, of course, depends on the EOS used, but seems to be fairly accurate).

In general, since p-modes are standing acoustic waves, sound speed c and ρ

are derived from the observations and can be compared with the models. This is called the *inverse* method. From the properly scaled squared sound speed the bottom of the convective zone can easily be identified, as seen from Fig. 3.
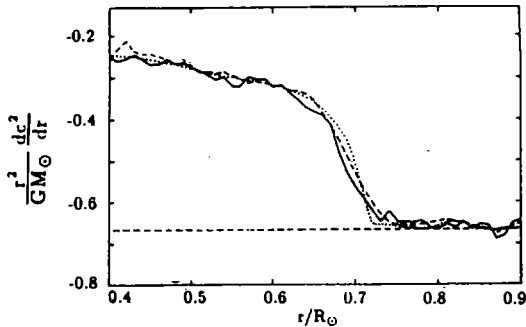

Fig. 3: Scaled squared sound speed in the solar interior. Within the convective envelope, this quantity is constant, below it rises sharply. Solid line: observations; others: two different models (from [12])

Another quantity of interest is the angular velocity of the rotating Sun, which is obtained from the fine-splitting (m) of frequencies. The result is that within a factor 2 the Sun appears to have the same angular velocity throughout. Variations within this range are: on the surface, higher latitudes are rotating faster than those closer to the equator, but at half radius the Sun appears to rotate like a rigid body. There is no evidence for a faster spinning core. These results justify the neglect of rotation in the models for the present level of accuracy.

The alternative *forward* method of comparison is the calculation of theoretical p-mode frequencies from a SM. Relative deviations from observations are of order 10 μHz.

Recently, we have turned around the solar model problem ([13]): we treated the solar age as a free parameter in addition to the usual ones and determined them from the best-fitting models of the Sun. Without diffusion considered in the models, the so-determined age can deviate by up to 100% from the true one, but even applying the best physics of the SM we could not determine the solar age with an accuracy better than +10%. This demonstrates that there are still systematic uncertainties in the models.

3 Solar neutrinos – solar models leading the way to new particle physics

It is well known that all four existing solar neutrino experiments (Homestake (^{37}Cl; (Super-)Kamiokande (H_2O); GALLEX and SAGE (^{71}Ga)) agree in the fact that they measure a too low event rate compared with the prediction of the SM.[3] The discrepancy is of the order of a factor of 2, well above the experimental errors ($\approx 10\%$). There are the following arguments against the *astrophysical solution*, i.e. a model substantially different from the SM:

1. The SM is confirmed by helioseismology to a high degree (better than 1%; rms error in $c < 0.004$). For the central temperature, relative deviations of only 0.002 are still possible. To account for, e.g., the Be-ν flux, which is $\sim T^{24}$ this implies a maximum error of only 5% in the prediction.

2. The experiments are inconsistent with each other. The argument goes as follows: Kamiokande can measure only ^{8}B-ν due to its high threshold; take the event rate as measured and predict from this the ^{8}B-ν rate in the Homestake experiment (result: 3.2 SNU = $3.2 \cdot 10^{-36}$ captures per target atom and second). The Homestake rate is 2.55 ± 0.25 SNU, such that there is no room for the additional ^{7}Be-ν which should also be measured here! Similarly, the GALLEX-experiment measures ≈ 70 SNU, which can be accounted for by the solar luminosity and the argument that at least 1 pp-ν must be emitted per 4 H-atoms converted to He. With the additional SNU from Kamiokande (7) this again leaves no room for any ^{7}Be (predicted 34 from Homestake results) and/or CNO-cycle ν!

3. The relative number of neutrinos would be different if one assumes that the various nuclear cross sections in the pp-cycle were wrong. Forgetting for the moment that they are believed to be known to better than 10%, even this cannot solve the neutrino problem. For example, to get rid of the ^{7}Be-ν as seems to be indicated by argument 2, one had to increase the p-capture rate on ^{7}Be by a factor of 100 to prefer the ^{8}B branch over the competing e^- capture. However, this would in turn raise the expected Kamiokande-rate accordingly, such that this experiment would deviate from prediction even more.

4. Finally, there is a beautiful *"no solar model"* argument: the measured flux of any experiment is the sum of the individual fluxes from all neutrino sources. If one, in addition, assumes that the solar luminosity must also be a linear combination of the same fluxes, it can be shown that at 99.5% confidence level there is no solution to account for all experimental results ([8]). (Even without the $L_\odot$-constraint it is 95% excluded, and with additional constraints

---

[3] For a recent review of the matter contained in this section, see [1]

about relative branching ratios the argument gets even stronger.)

The conclusion, in particular due to arguments 2 and 4 is that something happens to the neutrino numbers and energy spectra on their way from source to detector. The favourite model for this "something" are neutrino flavour oscillations converting ν_e into ν_μ and ν_τ which cannot be measured in present-day experiments (but SNO will, due to neutral current reactions on deuterium). Without going into a deeper discussion of these oscillations, in particular of the MSW-effect, it suffices to say that the density structure of SM *does* allow solutions of the neutrino problem: one for a small mixing angle $\sin^2(2\theta) \approx 0.008$ and a squared mass difference between ν_e and ν_μ of $\approx 6 \cdot 10^{-6}$ (SMA) and one for a large mixing angle $\sin^2(2\theta) \approx 0.7$ and $\triangle m^2 \approx 10^{-5}$ (LMA). In the future, Super-Kamiokande and/or SNO might be able to discriminate between these two due to the so-called *earth regeneration effect*. This effect is based on the fact that at night the neutrinos pass through the earth interior and therefore further matter-induced oscillations take place, which lead to a higher number of ν_e. Seasonal effects due to the excentricity of earth's orbit might be detectable by BOREXINO (for this and other questions concerning neutrino experiments see the contribution by L. Oberauer in this volume).

4 Summary of successes and failures of the SM

It appears that the field of solar models has reached a critical point, from which on the questions about the internal structure of the SUN and about the results of the solar neutrino experiments will separate. From all we know from helioseismology, there is presently no doubt that modern standard solar models describe the real Sun with high accuracy (rms error < 0.004). There is no room left, even for arbitrary changes in the models, to explain the neutrino experiments and we have no reason to distrust the predicted neutrino emission rates, which do not depend significantly on the remaining uncertainties any longer. While this is a great success for stellar structure theory, helioseismology also has resulted in the biggest failure of the SM: given the high accuracy of the observations, the SM clearly fail to reproduce them, as was demonstrated by our attempt to determine the solar age from solar models. In spite of all recent improvements in the model physics (in particular in opacities, EOS and diffusion), the models show a significant deviation from reality. However, the same improvements also have greatly inhanced our faith in stellar evolution theory which is one of the basics of astrophysics!

Solar models also have demonstrated that there is a need for an extension of the standard model of particle physics. This I consider another great achieve-

ment. (There are other particle-related questions which can also be addressed or even solved by stellar evolution results.) SM currently allow MSW solutions to the neutrino problem, but alternative solutions still have to be tested and predictions for further experiments have to be made.

In summary, thanks to the big efforts in the neutrino experiments and in helioseismology, the theory of solar models has become a success story with place for further improvements. In the future, we will have to include hydro-dynamical effects, rotation, magnetic fields and super-photospheric effects for even better models.

References

[1] J.N. Bahcall, An introduction to solar neutrino research, XXV SLAC Summer Institute on Particle Physics (1997) preprint hep-ph/9711358;

[2] J.N. Bahcall and M.H. Pinsonneault, Rev. Mod. Phys. **64** (1992) 885;

[3] S. Basu, J. Christensen-Dalsgaard, J. Schou, M.J. Thompson and S. Tomczyk, Astrophys. J. **460** (1996) 1064;

[4] J. Christensen-Dalsgaard, Lecture Notes on Stellar Oscillations, Univ. of Aarhus (1997);

[5] J. Christensen-Dalsgaard, D.O. Gough and M.J. Thompson, Astrophys. J. **378** (1991) 413;

[6] S. Degl'Innocenti, W.A. Dziembowski, G. Fiorentini and B. Ricci, Astroparticle Physics **7** (1997) 77;

[7] N. Grevesse and A. Noels, Phys. Scripta **T47** (1993) 133;

[8] K.H. Heeger and R.G.H. Robertson, Phys. Rev. Lett. **77** (1996) 3720;

[9] F.J. Rogers and C.A. Iglesias, Astrophys. J. Suppl. **79** (1992) 50;

[10] F.J. Rogers, F.J. Swenson and C.A. Iglesias, Astrophys. J. **456** (1996) 902;

[11] H. Schlattl, A. Weiss and H.-G. Ludwig, Astron. Astrophys. **322** (1997) 646;

[12] S. Turck-Chiéze, W. Däppen, E. Fossat, J. Provost, E. Schatzman and D. Vignaud, Phys. Rep. **230** (1993) 57;

[13] A. Weiss and H. Schlattl, Astron. Astrophys. (1998) in press.

Status of Astrophysical Neutrino Experiments and Prospects

L. OBERAUER

Technische Universität München, Physik-Dpt. E-15
Sonderforschungsbereich Astro- Teilchenphysik SFB 375
James-Franck Str., D-85747 Garching, Germany

Abstract

The status of experiments searching for neutrinos of astrophysical sources is reported. This includes solar neutrino experiments, searches for atmospheric neutrinos, Supernova neutrinos, and neutrinos in high energy cosmic rays. Recent results in some of this fields may hint to physics beyond the standard model. Future experiments can find the clue for the solution of this puzzle.

1 Solar Neutrino Experiments

The solar neutrino problem comes from the discrepancy between the ν_e expectations of the solar neutrino flux, as calculated by the Solar Standard Model [1], and the experimental results. In Table 1 the experimental results are compared with the expected values of the standard model.

Table 1:

Experiment	Measured flux S.M. expectation	Threshold (MeV)
Homestake	0.27±0.06	0.814
Kamiokande	0.44±0.06	7.5
Superkamiokande	0.358±0.009±0.014	6.5
Gallium (Gallex, Sage)	0.6 ± 0.06	0.235

All solar neutrino experiments are located in deep underground laboratories in order to shield the detector against cosmic rays. Pioneer work has been performed 1970 by R. Davis and coworkers by detetcing solar neutrinos in a radiochemical experiment by means of the reaction $^{37}Cl + \nu_e \rightarrow ^{37} Ar + e$ at a

threshold of 0.814 MeV [2]. Due to this threshold high energetic ^8B neutrinos dominate the signal. Since the flux of this branch is sensitive to small changes of the solar model, astrophysical solutions were discussed at this time as most prominent possibilities.

The radiochemical gallium detectors, GALLEX (Gran Sasso, Italy) [3] and SAGE (Baksan, Russia) [4], have been measuring the integral solar neutrino flux exploiting the capture reaction $^{71}Ga + \nu_e \rightarrow\ ^{71}Ge + e^-$. As the energy threshold is only 233 keV, this reaction allows to detect the pp-neutrinos from the initial solar fusion step which contribute about 90 % to the total solar neutrino flux.

In a typical run the target, consisting of 30 tons of gallium in the form of 101 t $GaCl_3$ solution for GALLEX and 55 t of metallic gallium for SAGE, is exposed to the solar neutrino flux for 3-4 weeks. Both experiments use the signature provided by the Auger electrons and X-rays associated with the decay $^{71}Ge + e^- \rightarrow\ ^{71}Ga + \nu_e$ for identification of ^{71}Ge during a several months counting time.

The combined result of all 65 GALLEX solar runs is $76.4 \pm 6.3\ ^{+4.5}_{-4.9}$ SNU[1]. The present result from SAGE, $74\ ^{+11}_{-10}\ ^{+5}_{-7}$ SNU [4], is in agreement with GALLEX. The overall results from both experiments are only about 60% of the predictions from solar model calculations.

Up to now only the Kamiokande experiment [5] in Japan records solar neutrinos in real time with energy information. In a large water Cherenkov detector elastic neutrino electron scattering is used as detection mechanism. Background rejection is realized mainly by measuring the direction of the scattered electron. It is peak in forward position. Since April 1996 an even larger water Cherenkov detector, Superkamiokande with 22.5kt fiducial target mass, is running. Superkamiokande confirms the data measured before with improved statistics (see Table 1) [6]. The systematic error has been reduced by calibration with a linear electron accelerator.

Information from helioseismology confirm the solar standard model. In addition, experimental results from the LUNA experiment (see M. Junker, this proc.) low energy measurements in the $^3He +^4 He$-channel seem to exclude explanations based on discrepancies in nuclear cross sections. At last, the overall performance of both gallium experiments has been tested by terrestial neutrino sources, and no discrepancy from the expected values has been found [3].

Data analysis of the existing experiments leads to the assumption of se-

---

[1] 1 SNU = 1 neutrino interaction per second in 10^{36} atoms.

vere supression of the solar ^7Be-branch (e. g. [7]), which probably cannot be explained by modifications of the standard astrophysical model of the sun.

If neutrinos have non-zero masses and if they mix in analogy to the quark sector, neutrino oscillations arise. It can be shown (e. g. [3]) that certain parameter on neutrino masses and mixing angles provide an excellent solution to all observed results. Future experiments may give the clue to the final solution of the solar neutrino puzzle (Table 2).

Table 2:

Experiment	Reaction	Experimental method	Threshold (MeV)	Expected start-up	Statistics [full SSM]
SuperK	$\nu_x e^- \rightarrow \nu_x e^-$	Č events	5.	already running	65/d
GNO	$\nu_e^{71}Ga \rightarrow e +^{71}Ge$	Ge	0.235	1998	1/d
Iodine	$\nu_e^{127}I \rightarrow e +^{127}Xe$	I	0.789	-	-
SNO	$\nu_e d \rightarrow ppe^-$	Č events	5.	1997	20/d
	$\nu_x d \rightarrow \nu pn$			1999?	7/d
Borexino	$\nu_x e^- \rightarrow \nu_x e^-$	liquid scint.	0.25	2000	55/d

Superkamiokande (SK) is as reported above already running and has confirmed the discrepancy in the solar neutrino flux as obtained in the Kamiokande experiment. Due to the enhanced statistics SK gets information of the solar ^8B-spectrum by unfolding the experimental data with the theoretical spectrum of neutrino electron scattering. As the phase of neutrino oscillations is energy dependent detected detoriations in the spectral shape could prove the oscillation hypothesis. How pronounced this effect shows up depends on the actual oscillation parameter. For certain parameter day/night effects must show up which are detectable in high statistic experiments as SK.

GNO (Gallium Neutrino Observatory) is a prolongation of Gallex with increased volume and an upgrading of the analysis devices. In this way the Gallex collaboration planes to depress both the statistical and the systematical uncertainties.

SNO is sensitive to ^8B-neutrinos only. Since it will measure both neutral and charged current interaction direct information on neutrino flavour oscillations can be obtained. Here the measured neutral current flux can be considered as a monitor of the total solar neutrino flux independent of flavour

oscillations. In addition the neutrino energy spectrum is measured directly. No unfolding is necessary and the same argument for proving neutrino oscillations as for SK holds also for SNO.

The aim of Borexino is to measure in real time the solar neutrino flux with low energy threshold at high statistics, and energy resolving via pure leptonic neutrino electron scattering $\nu + e \rightarrow \nu + e$. Here liquid scintillator (300t fiducial mass) will be target and detector material. The monoenergetic ^7Be-neutrinos give rise to a compton like recoil spectrum in Borexino with a edge at 660 keV. Assuming validity of the standard model a counting rate for ^7Be-neutrinos, which would consist in this case purely as ν_e, of roughly 55/day in Borexino is expected.

In scenarios of total neutrino flavour conversion (i.e. for neutrino mass differences $\Delta m^2 \approx 10^{-6} \rightarrow 10^{-5}\ eV^2$) a reduced flux of approximately 12/day would be measured due to the lower cross section of $\nu_{\mu,\tau}$ scattering, which occurs only via neutral current interaction.

In case of vacuum oscillations (i.e. for neutrino mass differences $\Delta m^2 \approx 10^{-10}\ eV^2$) Borexino would see a distinct time dependent periodical neutrino signal due to the seasonal eccentricity of the earths orbit around the sun.

For neutrino mass differences in the range of $\Delta m^2 \approx 10^{-7}\ eV^2$ and for large mixing Borexino should see a 'day/night' effect due to electron neutrino recovery during the path through the earth.

Borexino also can serve for additional projects in neutrino physics. Via the inverse beta-decay $\bar{\nu}_e + p \rightarrow e^+ + n$ Borexino can look for signals from geo-physical neutrinos as well as for neutrinos emitted by european nuclear power plants. The latter would serve as a long baseline neutrino oscillation experiment probing the so-called large mixing angle solution for the solar neutrino problem.

A new radiochemical experiment is under way at Homestake with ^{127}I as target material. At the treshold of 789 keV a quite large fraction of ^7Be-neutrinos contribute to the signal. Two new experiments, still in R&D phase, are Supermunu and Hellaz. Both are based on gas TPC's. Hellaz planes to use a 2000 m^3 TPC filled with He-CH_4 at 5-10 bars, cooled at 77 K. The energy threshold should be ~ 100 KeV. Supermunu is similar to Hellaz, but it should employ CF_4 as target.

We can conclude that there is a good chance that the solar neutrino problem should be solved in the first years of the 21st century. Experiments on ^7Be neutrinos, on neutral current events and on time variations could be decisive in this field.

2 Atmospheric neutrinos

Atmospheric neutrinos are produced in the cascade originated in the atmosphere by a primary cosmic ray. Pion and muon decays are the main sources, disintegration of kaons plays a role only at high energies. From these decay channels one expects at low energies about twice muon neutrinos with respect to electron neutrinos. This ratio is not very sensitive to detailed calculations.

The water Cherenkov experiments, IMB in the United States and Kamiokande in Japan, discovered that this ratio between events with a muon and those with an electron was lower than expected. A possible interpretation of this anomaly is the oscillation of the neutrino species in the path length between the production point and the detector (in the range 10 -13000 km). Recently this discrepancy was confirmed by the iron calrorimetric experiment Soudan in Canada. However, the anomaly was not confirmed by the proton decay iron fine-grained experiments at Frejus and by NUSEX. The latter experiment suffered under small statistics.

By separating into a low energy region with $E < 1 \, GeV$ and into a high energy region different event topologies in a detector can be defined. The low energy region generally corresponds to events fully contained inside the fiducial volume. High energy events can be defined by the topology of the interaction vertex inside and not fully contained tracks, or with the interaction vertex in the rock outside the detector. In the latter case background considerations imply, that only upgoing muons can be interpreted as neutrino signals.

The absolute neutrino fluxes are predicted with uncertainties of 20%. However the ratio of $\nu_\mu + \overline{\nu_\mu}$ to $\nu_e + \overline{\nu_e}$ fluxes is known to better than 5% and therefore experiments measure the double ratio $R \equiv (\mu/e)_{DATA}/(\mu/e)_{MC}$, where μ/e denote the ratio of μ-like to e-like neutrino interactions.

Due to the huge target mass Superkamiokande (SK) now has the best statistics. Particle identification in SK is based on the pattern of Cherenkov rings. Electrons create diffuse patterns and are separated from sharper Cherenkov rings caused by muons. The misidentification probability for single-ring events is estimated by the collaboration to be $0.8 \pm 0.1\%$. At the end of 1997 at about 20.1 kton-years of SK has been sampled. From these data one obtains: $R = 0.63 \pm 0.03(stat) \pm 0.05(sys)$ [8].

We can conclude, that the deficit of muon neutrinos reported from earlier experiments has been confirmed during the first year of data collection in Super-Kamiokande. In addition the angular distribution of reconstructed tracks has been studied [8] and an asymmetry has been observed for both energy regions. Those results may suggest the neutrino oscillation interpretation.

However, the collaboration concludes, that more data are needed to exclude any possibility of detector related biases.

The atmospheric neutrino discrepancy can be explained either by muon-electron neutrino oscillation, or by the muon- tau neutrino mode. Very recently results from a long baseline reactor experiment at Chooz [9] (France) has been published, which excludes the possibility of relevant muon- electron mixing, as it was necessary for onterpreting the Kamiokande result in terms of oscillations, completely.

The possibilty of muon- tau oscillation can be verified (or falsified) by long baseline accelerator experiments in which muon neutrino beams are created. In Japan a muon neutrino beam from KEK will be directed to Superkamiokande. Data taking there is expected to start in 1999. Projects of long baseline experiments are considered also at CERN to Gran Sasso, and from Fermilab to the underground laboratory at Soudan.

3 Collapsing Stars and Neutrino Observations

At the initial stage of a collapsing star with $M \geq 1.5\ M_{sun}$ the ν_e- flux of the neutronization process $e^- + p \rightarrow n + \nu_e$ dominates. However, during the very early cooling phase neutrinos of any flavour will be created by thermal processes $(e^+ + e^- \rightarrow \nu + \bar{\nu})$. One can estimate that in total $\simeq 10^{53}$ erg in neutrinos will be emitted. Calculations yield comparable, but not equal, fluxes of ν_e, ν_μ and ν_τ.

Approximately $5 \cdot 10^{52}$ erg can be expected in form of $\bar{\nu}_e$, with typical average energies of about 10 MeV. Water Cherenkov detectors such as Kamiokande or IMB are mainly sensitive to $\bar{\nu}_e$, because this neutrinos can be detected via charged current weak interaction $(namely\ \bar{\nu}_e + p \rightarrow n + e^+)$, which has a much higher cross section as neutrino electron scattering. IN february 1987 a neutrino pulse was detected prior to the optical outburst of SN1987a. Kamiokande measured 12 pulses within $\Delta t \simeq 13\ sec$ [10] and IMB detected 8 neutrinos with $\Delta t \simeq 6\ sec$ [11].

This coincidental (within 1 minute precision) neutrino observation in two independent detectors confirms the general princips of supernova mechanism. Calculations yielded 6 ± 4 counts in 2000 t of water for a collapse like SN 1987a (distance $\simeq 50$ kpc), in fair agreement with the number of events seen in both Cherenkov detectors.

Since 1987 several new experiments looking for future supernova neutrinos are under way. The 50kton water Cherenkov detector Superkamiokande in Japan is already under operation, the segmented liquid scintillation detector

LVD (Large Volume Detector) at Gran Sasso is going to be build up.

The Galactic SN rate is estimated to be about 20 ± 8 per millennium [12]. There are only 6 historical supernovae on record which would imply, that roughly 2/3 of all Galactic supernovae have been hidden. Supernovae in the Local Group have been observed in M31 (S And: SN 1885A) and in the Large Magellanic Cloud (SN 1987A). The prediction for the Local Group is slightly above 2 (excluding the Galaxy), which appears consistent. The small observational baseline, however, excludes any firm conclusion from such a comparison.

Therefore supernovae which can be observed in the light of neutrinos are very rarely. In spite of this the development of new detectors looking for supernova neutrinos is considered seriously, because its observation not only would yield important information about processes in stellar collapses, but also could reveil unknown neutrino properties. Superkamiokande would receive about 4000 events from the inverse beta reaction if a supernova at 10 kpc happens[2]. This would be enough statistics to determine a significant neutrino lightcurve. From the prompt ν_e burst one expects about 15 events in a few ms. Its detection would set interesting constraints on neutrino oscillation parameter. Due to neutrino dispersion a direct mass limit of about 1 eV could be set. In addition one would expect to see about 40 events for each $\nu_\mu + \bar{\nu}_\mu$ and $\nu_\tau + \bar{\nu}_\tau$ from elastic neutrino electron scattering. Since the scattered electrons are peaked in forward direction one can separate them from non-directional $\bar{\nu}_e$ reactions. Hence, massive ν_μ or ν_τ would imply delayed forward signals, leading to sensitivities of about 100 eV [13], orders of magnitude more sensitive than existing laboratory limits.

4 High energy neutrino telescopes

Experimental search for high energy cosmic neutrinos is motivated by several items. Without claiming completeness a few are listed here:

- Search for neutrino point sources, like the galactic center and active galactic nuclei (AGN).

- Search for an isotropic high energy neutrino background due to AGN.

- Search for neutrino signals coincident with gamma ray bursts.

- Search for very high energy neutrinos from cosmological origin like strings.

---

[2]Recall that the solar system is at a distance of about 8 kpc from the galactic center.

- Neutrino emission in the 10 GeV region due to solar WIMP annihilation. Here WIMP stands for Weak Interacting Massive Particles: they are candidates for cold dark matter.

This physical program sets certain requirements on the experimental setup. The detector should be located deep underground in order to shield against background, the target mass must be large (about $1km^3$), and the possibility for measuring the direction of the interacting neutrino must be given.

Two projects are described here, Amanda and Antares. Both rely on Cherenkov detection. Amanda is located at the south pole. Strings with photomultipliers were brought inside the ice. At the end of 1997 two modules have been realized: Amanda A at a depth from 810m to 1000m and Amanda B which is ranges between 1520m and 1950m. Amanda B consists of 4 strings with 20 tubes each which was realized in 1996. In addition there are now installed 6 strings with 36 tubes each.

Crucial for the proper operation are absorption and scatter lenghts of the Cherenkov photons in the ice. In the wavelength band between 340nm and 460nm absorption lengths of about 100m has been measured, whereas the effective scatter length is shorter and was determined to be at 24m for Amanda B. Muon track reconstruction is realized by the timing information of the individual tubes. With this method upgoing muons which result from neutrino interaction can be separated by background muons produced in the atmosphere by cosmic rays.

Antares is aiming towards a deep-sea high energy neutrino telescope. It is planned to set up a "demonstrator", consisting of three strings 100m apart which is scheduled for 1999. Site for the demostrator should be at 2410m depth in the mediterranean sea, close to the city of Toulon, France. Aim is to realize finally a detector with $1km^3$ target volume. The detection concept is very similar to Amanda. Since it is located on the northern hemisphere Antares is sensitive to neutrinos emitted in the southern sky, whereas Amanda is a neutrino telescope for the opposite direction.

References

[1] J. N. Bahcall, M. Pinsonneault, Rev. Mod. Phys. 67, (1995) 781.

[2] R. Davis, "Second International Workshop on Neutrino Telescopes", ed. by Milla Baldo Ceolin, Venezia, Italy (1990).

[3] Gallex collaboration, Phys. Lett. B 388, (1996) 384.

[4] SAGE Collaboration, Phys. Rev. Lett. **77** (1996) 4708. K. S. Hirata et al., Phys. Lett B **205**, (1988).

[5] Y. Fukuda et al., Phys. Rev. Lett. **77**, (1996) 1683.

[6] Y. Fukuda, SuperKamiokande, Proc. of the Int. workshop on Neutrino-Astrophysics, Ringberg, Germany, October (1997).

[7] F. von Feilitzsch, Proc. of the IV Int. Symposium on Weak and Electromagnetic Interactions in Nuclei, Osaka Japan, Ed. H. Ejiri, T. Kishimoto, T. sato, World Scientific, June 12-16, (1995)

[8] D. Kielczewska, Proc. of the Int. workshop on Neutrino- Astrophysics, Ringberg, Germany, October (1997).

[9] Y. Declais, talk at the Techn. University Munich, SFB 375 Seminar, December 11, (1997)

[10] K. Hirata et al., Phys. Rev. Lett. **58**, (1987) 1490.

[11] R. M. Bionta et al., Phys. Rev. Lett. **58**, (1987) 1494.

[12] B. Leibundgut, J. Spyromilio, The Early Universe with the VLT, ed. B. Bergeron, Heidelberg: Springer, (1997), 95.

[13] G. Raffelt, Stars as Laboratories for Fundamental Physics, Chikago Press, (1996) 445-450.

PRESENT STATUS AND FUTURE PROSPECTS OF UNDERGROUND NUCLEAR ASTROPHYSICS

M. JUNKER (LUNA–COLLABORATION [1])

Laboratori Nazionali del Gran Sasso (LNGS)
I-67010 Assergi(AQ), Italy

Abstract

A 50 kV accelerator has been installed by the LUNA–Collaboration in the underground laboratories of the Laboratori Nazionali del Gran Sasso (LNGS) in Italy making it possible for the first time to determine the cross section of the reaction ^{3}He(^{3}He,2p)^{4}He in the thermal energy region of the sun.

As a next step the LUNA–Collaboration will build a new facility at the LNGS. It will consist of a 400/200 kV accelerator with gas and solid target stations and a low background detector set up for gamma-spectroscopy. The system will offer the possibility to study the other key reactions of the pp-chain at very low energies. In addition the reactions of the other hydrogen burning phases such as the NeNa and the MgAl cycles can be investigated.

1 Introduction

Due to the Coulomb Barrier involved in the nuclear fusion reactions, the cross section of a nuclear reaction drops nearly exponentially at energies which are lower than the Coulomb Barrier, leading to a low-energy limit of the feasible cross section measurements in a laboratory at the earth surface. Since this energy limit has up to now always been far above the thermal energy region of the sun, the high energy data have been extrapolated down to the energy region of interest transforming the exponentially dropping cross section $\sigma(E)$ to the astrophysical S–factor

$$S(E) = \sigma(E) \, E \, \exp(2\,\pi\,\eta),$$

with the Sommerfeld parameter given by $2\,\pi\,\eta = 31.29\,Z_1\,Z_2(\mu/E)^{1/2}$ [1]. The quantities Z_1 and Z_2 are the nuclear charges of the interacting particles in the

---

[1] for full collaboration list see [11]

entrance channel, μ is the reduced mass (in units of amu), and E is the center-of-mass energy (in units of keV). In case of a non resonant reaction $S(E)$ may then be parameterized by the polynom

$$S(E) = S(0) + S'(0)E + 0.5\,S''(0)E^2.$$

As usual in physics, extrapolation of data into the "unknown" can lead onto "icy ground". Although experimental techniques have improved over the years to extend cross section measurements to lower energies, it has not yet been possible for the most reactions to perform measurements within the thermal energy region in stars.

For nuclear reactions studied in the laboratory, the target nuclei and the projectiles are usually in the form of neutral atoms/molecules and ions, respectively. The electron clouds surrounding the interacting nuclides act as a screening potential: the projectile effectively sees a reduced Coulomb barrier. This leads to a higher cross section, $\sigma_s(E)$, than would be the case for bare nuclei, $\sigma_b(E)$, with an exponential enhancement factor [2, 3]

$$f_{\mathrm{lab}}(E) = \sigma_s(E)/\sigma_b(E) \simeq \exp(\pi\eta\,U_e/E),$$

where U_e is the electron-screening potential energy (e.g. $U_e \simeq Z_1 \cdot Z_2 \cdot e^2/R_a$ approximately, with R_a an atomic radius). For a stellar plasma the value of $\sigma_b(E)$ must be known because the screening in the plasma can be quite different from that in laboratory studies [4], and $\sigma_b(E)$ must be explicitly included in each situation. Thus, a good understanding of electron-screening effects is needed to arrive at reliable $\sigma_b(E)$ data at low energies. Low-energy studies of several fusion reactions involving light nuclides showed [5, 6, 7] indeed the exponential enhancement of the cross section at low energies. The observed enhancement (i.e. the value of U_e) was in all cases close to or higher than the adiabatic limit derived from atomic-physics models. An exception are the $^3\mathrm{He}+^3\mathrm{He}$ data of Krauss et al [8], which show apparently no electron screening down to $E=25$ keV, although the effects of electron screening should have enhanced the data at 25 keV by about a factor 1.2 for the adiabatic limit $U_e=240$ eV. Thus, improved low-energy data are particularly desirable for this reaction.

2 Measurements of ^{3}He(^{3}He,2p)^{4}He at the LNGS

The low-energy studies of thermonuclear reactions in a laboratory at the earth's surface are hampered predominantly by the effects of cosmic rays in the detectors. Passive shielding around the detectors provides a reduction of gammas and neutrons from the environment, but it produces at the same time an increase of gammas and neutrons due to the cosmic-ray interactions in the shielding itself. A 4π active shielding can only partially reduce the problem of cosmic-ray activation. The best solution is to install an accelerator facility in a laboratory deep underground [9]. The worldwide first underground accelerator facility has been installed at the Laboratori Nazionali del Gran Sasso (LNGS) in Italy, based on a 50 kV accelerator [10]. This pilot project is called LUNA and has been supported since 1992 by INFN, BMBF, DAAD-VIGONI and NSF/NATO.

The major aim of the LUNA project is to measure the cross section of ^{3}He(^{3}He,2p)^{4}He which is one of the major sources of uncertainties for the calculation of the neutrino source power of the sun. It has been studied previously [8] down to about E_{cm}=25 keV, but there remains the possibility of a narrow resonance at lower energies that could enhance the rate of path I of the pp-chain at the expense of the alternative paths that produce the high-energies neutrinos ($E_\nu > 0.8$ MeV). The LUNA–facility allows to study this important reaction over the full range of the solar Gamow Peak, where the cross section is as low as 8 pbarn at E_{cm}=25 keV and about 20 fbarn at E_{cm}=17 keV.

Figure 1 shows the results obtained in the energy region between E_{cm}=25 keV and E_{cm}=20.7 keV. The lowest counting rate was of 3 events per day at E_{cm}=20.7 keV. At this energy about 1000 Cb of ^{3}He$^+$ have been accumulated on the target. The data obtained at higher energies (450 kV accelerator in Bochum) with the LUNA setup [10] are included for completeness. Previous data obtained [8] at E_{cm}=25 are also shown in figure 1. The LUNA data have been obtained at energies within the solar Gamow Peak, i.e. below the 21 keV center of this peak, and represent the first measurement of an important fusion cross section in the thermal energy region. The astrophysical S-factor has been extrapolated to zero energy [11]:

$$S(0) = 5.40 \pm 0.05(\text{stat}) \pm 0.30(\text{sys}) \pm 0.30(\text{screen}).$$

The first error contains the statistical error (one standard deviation) including counting statistics and apparative variations of pressure, beam power and temperature measurement. The second error is the systematical error (one standard deviation) including uncertainties in pressure, beam energy and power,
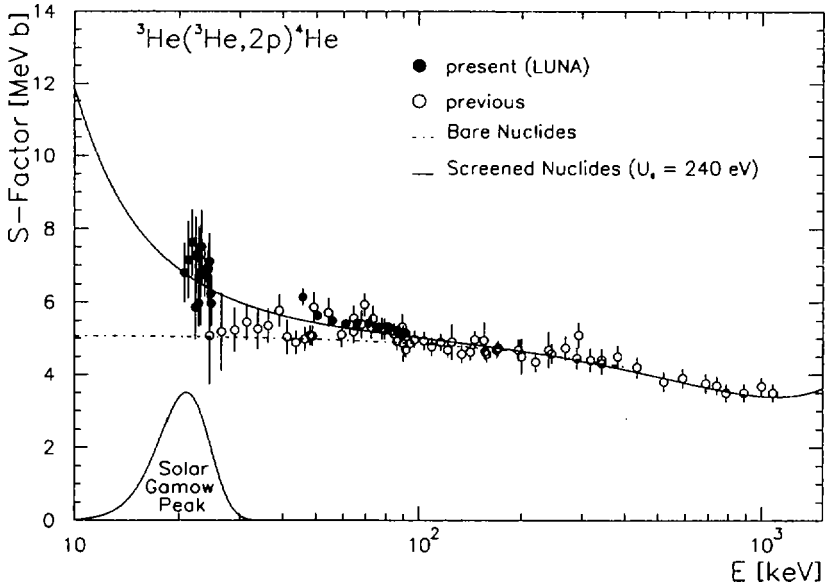
Figure 1: The $S(E)$ factor of ^{3}He^{3}He from [8] and the present work. The dashed and solid curves represent $S_b(E)$ and $S_s(E)$, respectively. The solar Gamow Peak is shown in arbitrary units.

efficiency and energy loss data. The 10% error of the energy loss data transforms to an uncertainty of 0.1 to 0.2 keV in the effective energy. This in turn leads to an error of 1 to 3.5 % for the astrophysical S-factor. This is due to the exponential decrease of the cross section at low energies. The third component of the error results from the lack of understanding of electron screening: Fitting all existing data sets with $S(0)$, $S'(0)$, $S''(0)$ and U_e as free parameter gives an Electron Screening Potential U_e of 323 eV with $S(0) = 5.30$ MeVb. Fixing $S(0)$, $S'(0)$ and $S''(0)$ at energies higher than 100 keV (where the electron screening effect is neglectible) gives $S(0) = 5.1$ MeVb. In turn fitting U_e in a second step including also the low energy data gives $U_e = 432$ eV. A fit to the data assuming no electron screening gives $S(0) = 5.7$ MeVb. The adiabatic limit for U_e based on theoretical atomic physics is 240 eV. The first two methods give U_e values higher than the adiabatic limit (240 eV), consistent with observations in other fusion reactions. The difference between observed

and predicted U_e values is not understood at present giving a considerable uncertainty on $S(0)$.

The excess of the screening potential could also be explained as a tail of a narrow resonance lying in the not measured low-energy region. Upper limits for the strength of such a resonance have been calculated assuming the adiabatic limit for the screening potential. Our data seem to exclude the existence of a resonance with a strength high enough to give a sizeable contribution to the ^{3}He(^{3}He,2p)^{4}He reaction rate in the sun in the energy region below 9 keV and between 9 and 20 keV, if the resonance width is $\geq$ 2 keV. Once again, it must be remembered that these calculations are dependent on the description of the screening potential and only measured upper limits can definitively confirm this conclusion. For energies higher than 20 keV such a resonance is excluded by the exsisting data. In the near future the LUNA collaboration will extend the measurements down to $E = 17$ keV: the foreseen running time here is one year. Definite conclusions with respect to the expected solar neutrino fluxes have to await the results of these experiments. For this next phase a new detection setup, designed to reduce the background induced by deuterium contamination in the beam and in the gas target, has been developed. The data taking with this new setup started recently.

3 Future Prospects

Also the other key reactions of the pp–chain like ^{3}He(α,γ)^{7}Be and ^{7}Be(p,γ)^{8}B and the key reaction of the CNO–cycles, ^{14}N(p,γ)^{15}O, have never been studied in or even near their solar Gamow peaks. All these reactions are critical to the solar neutrino puzzle. The reaction rate of ^{14}N(p,γ)^{15}O is also one of the ingredients needed to determine the theoretical scenario used to constrain both the age and the distance of the oldest stellar system in our galaxy, namely the Globular Clusters.

Due to the higher Coulomb barrier of the actual 50 kV LUNA accelerator is not suited to investigate these reactions but a 200 kV machine is needed to get an overlap with the previous measurements. In addition, a new 200 kV accelerator will give the possibility to study many (p,γ) reactions of the NeNa and MgAl cycles below an incident proton energy E_p=200 keV. Experimental data about these channels, very important for the understanding of nucleosynthesis processes in Red Giant stars, are up today still missing or very uncertain [12]. The NeNa cycle may play a role in understanding the almost pure ^{22}Ne abundance found in meteorites samples, while the MgAl cycle may provide the mechanisms for production of ^{26}Al, the decay of which gives rise

to the ^{26}Al/^{27}Al anomaly found in some meteorites. All the involved (p,γ) cross sections of these cycles are scarcely known at low energies. For example the strength of the low lying resonances in the reaction ^{25}Mg(p,γ)^{26}Al, which is crucial for the production of ^{26}Al, could be experimentally determined for the first time. Also other reactions of these cycles like ^{26}Mg(p,γ)^{27}Al and ^{27}Al(p,γ)^{28}Si can be investigated using accelerator and detector systems of the LUNA experiment.

While studying the reaction ^{3}He(^{3}He,2p)^{4}He in the low energy region of the solar Gamow Peak an enlarged LUNA II collaboration will install a new accelerator facility at Gran Sasso. The maximum proton energy reachable with this machine will be 400 keV. The acceleration and beam transport system however will be optimized for optimal transmission in the energy region from 200 to 50 keV. In this energy range a proton current of 500 μA will be available on the target with a long term energy stability of better than $1 \cdot 10^{-4}$. The maximum energy of 400 keV has been chosen to get a sufficient overlap with literature data. In addition it allows to check the energy calibration of the accelerator using standard resonances and to perform tests on the stoichiometry of the solid targets used. A new windowless gas target as well as solid target stations will be developed. In order to achieve high beam currents on the target the development of accelerator and target stations will be linked together closely.

Special care has to be taken for the choice of the detectors for the new underground accelerator. As the measured cross sections are of the order of a some 100 fbarn or lower high efficiency detection systems are required. In addition the background counting rate of the detectors must be reduced as much as possible. The aim of the development is to detect count rates as low as a few events per day in the region of interest. While cosmic ray background is suppressed efficiently due to the massive shielding provided by the Gran Sasso rock, background events from environmental and intrinsic radioactivity must be eliminated as well as events caused by electronic noise [13].

In the setup used for the measurements on ^{3}He(^{3}He,2p)^{4}He reaction presented above the problem of intrinsic activity has been solved by asking for coincidences between two detectors of one telescope, while the suppression of electronic noise has been realised using an anticoincidence condition with all the other detectors mounted in the target chamber. This procedure is not possible for the study of the (p,γ) reactions of interest. In order to investigate these reactions, two detector setups could be used:

1. A high purity germanium detector, giving detailed information on the different gamma-transitions of the reaction. The knowledge on the construction of germanium detector systems with a low background counting rate has been accumulated over the years by running HPGe detectors in neutrinoless double beta decay experiments (see [13] for a review). In addition due to there good resolution HPGe-detectors would allow for an efficient suppression of beam induced background. On the other hand germanium detectors have a quite low intrinsic efficiency specially at photon energies of a few MeV and normally cover only small solid angles. This makes it difficult to identify all the different lines and the corresponding branching ratios induced by the nuclear reaction studied and may thus lead to considerable uncertainties in the deduced solar rates.

2. A summing crystal made from BGO or NaI(Tl). These detectors can cover solid angles of nearly 4π, adding up all the photons of one cascade in the "sum-peak". While some spectroscopic information will be lost, the stellar reaction rate could be extracted from measurements with this kind of detector without any additional assumptions. First experiments with a 12"x 12" NaI(Tl) detector showed that due to the incomplete absorbtion of the gammas an energy region must be studied which reaches from the "sum-peak" down to about 3 MeV, in order to get the nuclear cross section independently from the Q-value, the branching ratios of the gamma cascades and the energy of the different gammas involved in the specific reaction. This in turn imposes an effective reduction in beam induced and intrinsic background in the energy region of interest. Due to its high mass number BGO detectors have a better "sum-peak" efficiency than NaI(Tl) detectors. However there worse energy resolution may lead to a worse signal to peak to background ratio for the signature of the reaction studied as well as for beam induced background.

The LUNA II collaboration is currently investigating the different aspects of the detection setup in order to have it available on completion of the new 400/200kV LUNA Accelerator at LNGS.

References

[1] C. Rolfs and W.S. Rodney, Cauldrons in the Cosmos (University of Chicago press, 1988)

[2] H.J. Assenbaum et al., Z. Phys. **A327** (1987) 461;

[3] L. Bracci et al., Nucl. Phys. **A513** (1990) 316;

[4] B. Ricci et al., Phys. Rev. **C52** (1995) 1095;

[5] U. Greife et al., Z.Phys. **A351** (1995) 107;

[6] P. Prati et al., Z.Phys. **A350** (1994) 171;

[7] K. Langanke et al., Phys.Lett. **B369** (1996) 211;

[8] A. Krauss et al., Nucl.Phys. **A467** (1987) 273;

[9] G. Fiorentini, R. W. Kavanagh, and C. Rolfs, Zeitsch. Phys. **A350** (1995) 289;

[10] U. Greife et al., Nucl.Instr.Meth. **A350** (1994) 327;

[11] The LUNA-Collab., LANL-Preprint Nucl-Ex/9707003, sub. to Phys. Rev.;

[12] Nuclear and Particle Astrophysics, Report for the NUPECC Committee, conven. F.K.Thielemann, available at HTTP://quasar.unibas.ch/ fkt/nupecc;

[13] G. Heuser, Ann. Rev. Part. Sci. **45** (1995), 543;

THE p-PROCESS IN TYPE II SUPERNOVAE

M. ARNOULD, S. GORIELY and M. RAYET

Institut d'Astronomie et d'Astrophysique
Université Libre de Bruxelles, Campus Plaine, CP 226
B-1050 Bruxelles, Belgium

Abstract

The p-nuclidic yields from the Type II supernova explosion of massive stars are reviewed. The nucleosynthetic predictions rely on detailed stellar models, on quantitative p-process seed abundances, as well as on extended nuclear reaction networks. Our predictions are confronted with the bulk solar system composition with the help of a simplified galactic evolution model. The production of ^{146}Sm is also briefly discussed on grounds of new nuclear data. This radionuclide is inferred to have been present in the early solar system, and could help developing a p-process chronometry.

1   Introduction

The stable neutron-deficient isotopes of the elements with charge number $Z \geq$ 34 are classically referred to as the p-nuclei. Those nuclides are observed only in the solar system, where they represent no more than 1% to 0.1% (with increasing Z) of the bulk $Z \geq$ 34 elemental abundances, made predominantly of the more neutron rich s- and r-nuclei. Isotopic anomalies involving p-nuclei are also found in some primitive meteorites.

It seems now astrophysically plausible that the p-nuclides originate from oxygen/neon layers of highly evolved massive stars during their pre-supernova phase [1], or during their explosion either as Type II supernovae (SNII) [20], or even as pair-creation supernovae [3]. At the temperatures of about 2 to 3 billion degrees that can be reached in those layers, the p-nuclei may be synthesized by the (γ, n) photodisintegrations of pre-existing more neutron-rich species (especially s-nuclei), possibly followed by cascades of (γ, p) and/or (γ, α) reactions. It has also been proposed that those nuclear transformations could take place in the C-rich zone of Type Ia supernovae (SNIa) as well [10].

This review summarizes in Sect. 2 some of the p-process calculations that have been conducted recently on grounds of a variety of detailed SNII models. These extended calculations represent the first step towards a quantitative

build-up of a model for the evolution of the galactic p-nuclidic content, which allows a comparison to be made with the bulk solar system composition. Section 3 deals briefly with the p-process anomalies, and in particular with the one attributed to the decay of the long-lived p-nuclide ^{146}Sm. Some conclusions are drawn in Sect. 4.

2 The p-process in SNII

The p-process can develop in the SNII O/Ne layers that are heated to peak temperatures in the approximate $1.8\,10^9 \lesssim T_m \lesssim 3.3\,10^9$ K range [20]. These zones are referred to in the following as the p-process layers (PPL's), the precise characteristics of which are derived from pre-SN and SN models of $Z = Z_\odot$ stars with masses M ranging from 13 to 25 M$_\odot$ (see [20] for detailed references to the adopted stellar models). Specific calculations have also been conducted for the supernova SN1987A [16]. In all cases, the PPL's are far enough from the SNII mass cut for its precise location not to affect the predicted p-process yields in any significant way. In contrast, the precise extent and mass of the PPL's, and consequently the predicted p-process abundances, may be sensitive to the still somewhat uncertain ^{12}C$(\alpha,\gamma)^{16}$O reaction rate, as well as to the assumed final kinetic energy of the ejecta. The nominal values adopted for these quantities are the reaction rate proposed by [6] (see [20] for a justification of this choice), and a kinetic energy of 10^{51} erg. The impact of a change of the values of these two quantities on the SNII p-process yield predictions has been evaluated by [20].

The adopted nuclear reaction network is thoroughly described in [19]. It includes approximately 1050 nuclei and 11000 reactions induced by neutrons, protons, and α-particles, as well as photodisintegrations. As for the reaction rates, the Hauser-Feshbach model of [22] is used for targets heavier than Si. For lighter nuclei, the compilations of [7] for charged particle reactions [except for the nominal ^{12}C$(\alpha,\gamma)^{16}$O rate] and of [5] for neutron captures are adopted.

The selected p-process seed abundances are discussed in detail by [20]. In the $A > 40$ range, they derive mainly from the s-process that develops during hydrostatic core He burning. The concentrations of the lighter species are assumed to be equal to the presupernova values.

The nuclear flows leading to the production of the p-nuclides are discussed in detail by [20]. We limit ourselves here to a brief presentation of the predicted yields. For this purpose, let us define the mean overproduction factor $\langle F_i \rangle(M)$ of the p-nuclide i in a star of mass M as the total mass of this p-nuclide produced in the PPL's divided by the corresponding mass if the PPL's

Figure 1: Normalized p-nuclei overproductions obtained in SN1987A. Solid lines join different p-isotopes of the same element. Fig. 1a: self-consistent seed abundances; Fig. 1b: artificial, solar-like, abundances

had a solar composition. We then introduce the normalized overproduction as the ratio $\langle F_i \rangle(M)/F_0(M)$, where $F_0(M)$ is the mean overproduction factor averaged over the 35 p-nuclei. With such definitions, all the normalized over-productions would be equal to unity if the derived abundance pattern were solar. Figure 1a displays the normalized overproductions derived for SN1987A from the nominal model ingredients defined above.

The normalized overproductions predicted on the same grounds for the $Z = Z_\odot$ $13 \leq M \leq 25$ $M_\odot$ stars lie in the ranges indicated in Fig. 2 by the vertical bars associated with each p-nucleus. Roughly speaking, these overproduction factors are seen to depend only relatively weakly on the star masses, this being less true, however, for the lightest p-nuclei ^{74}Se, ^{78}Kr and ^{84}Sr. This result is discussed in [20].

Following test calculations performed for the $Z = Z_\odot$ 25 $M_\odot$ star [20], it appears that the impact on the p-process yields of a change in the ^{12}C$(\alpha, \gamma)^{16}$O rate or in the explosion energy is roughly of the same magnitude as the changes implied by the consideration of models of different masses calculated with the same input physics (see Fig. 2). The abundances of ^{74}Se, ^{78}Kr and ^{84}Sr are again the most sensitive to variations in the input physics (see [20] for a discussion of this feature).

The SNII yields for individual stars have been used by [20] in order to evaluate for the first time the evolution of the galactic content of the p-nuclides. As a zeroth-order approximation to the build-up of a full galactic chemical

Figure 2: Ranges of variations of the normalized p-nuclei overproductions predicted for the individual SNII explosions of $Z = Z_\odot$ stars with masses in the range from 13 to 25 $M_\odot$. For the sake of simplicity, these ranges are just schematized by vertical bars, the results for individual model stars not being represented (Precise data for each of the considered stars can be found in Table 2 of [20]). Open squares indicate the values of the normalized overproductions obtained by integration over the IMF proposed by [11]. Solid lines join different p-isotopes of the same element

evolution model, the p-process yields have been averaged over an Initial Mass Function (IMF), leading to the IMF-averaged normalized overproduction factors displayed in Fig. 2. ·Of course, the build-up of a model for the temporal evolution of the galactic content of the p-nuclides not only requires the knowledge of the stellar mass dependence of their yields, but also their variations with the metallicity. This question has been first addressed qualitatively by [20], who have just evaluated the role of metallicity from a comparison between the results obtained for the 20 $M_\odot$ star with $Z = Z_\odot$ and the predictions by [16] for the 20 $M_\odot$ SN1987A progenitor with the LMC metallicity $Z \approx 0.3$ $Z_\odot$. It appears that the p-process is about twice less efficient in SN1987A than in its solar metallicity counterpart. This conclusion is likely to be safely extrapolated to the other considered model stars.

From the IMF-averaged overproduction factors displayed in Fig. 2, it is concluded that about 60% of the produced p-nuclei fit the solar system composition within a factor of 3. Let us note in particular that $^{180}Ta^m$ can emerge in large quantities from the PPL's in all the considered SNII models. The s-process could also produce this nuclide [14]. The relative contribution of these

various mechanisms to this interesting nuclide remains to be unravelled.

Some discrepancies are also apparent. We just limit ourselves here to a brief discussion of the underproduction of the Mo and Ru p-isotopes. The origin of this problem is not fully identified yet. As discussed in some detail by [20], it cannot be cured by a mere change in photodisintegration rates. On the other hand, the necessary level of transformation of $A < 90$ seeds by proton captures appears to be unlikely in view of the very low PPL proton concentrations obtained in our calculations, except of course if the predicted proton capture rates are grossly underestimated.

In order to examine the Mo–Ru question further, test calculations have been performed by enhancing artificially the abundances of the $A \gtrsim 90$ seed nuclei above the predicted core He burning s-process values. This indeed alleviates to a large extent the SNII underproduction of the Mo and Ru p-isotopes [2], as shown in Fig. 1b, based on a solar-like seed distribution used by [10] for their p-process calculations in SNIa explosions. At this point, it is not possible, however, to provide any realistic justification for such increased PPL seed abundances. However, one notes that the s-process calculations fall short to account for the Ba observed in SN1987A by a factor of about 10 [15]. Could it be that the puzzle of the Mo and Ru p-isotopes lies in our inability to model the s-process in massive stars correctly ? Alternatively, other sources of these isotopes have been proposed, but no truly plausible candidate has been identified yet.

As stressed by [20], another embarassment might come from a global SNII underproduction (compared to solar) of the p-nuclides with respect to oxygen by a factor of about 4 ± 2 in the $Z = Z_\odot$ 25 $M_\odot$ star. This problem of the oxygen overproduction may be eased in lower mass SNII explosions, while it is worsened with decreasing metallicity [20]. It may thus be that the p-process enrichment of the Galaxy has been slower than the oxygen enrichment. There is at present no observational test of this prediction. At this point, it must also be kept in mind that uncertainties on stellar convection introduce also a large uncertainty (a factor of 2–3) in the oxygen yield of massive stars [23].

3   The p-process isotopic anomalies and chronometry

There is now observational evidence for the existence of isotopic anomalies due to the p-isotopes of Kr, Sr, Xe, Ba and Sm in various meteoritic materials, including different classes of grains of possible circumstellar origin (e.g. [20] for references). In particular, there is now strong evidence for the existence in the early solar system of the two p-process radionuclides $^{92}Nb^g$ ($t_{1/2} = 3.6 \, 10^7$

y) and ^{146}Sm $(t_{1/2} = 1.03\,10^8$ y) ([9], and references therein). The case of ^{92}Nb^{g} has been discussed by [20], and will not be repeated here. It is concluded that various uncertainties in the level of production of this radionuclide by SNII explosions make rather unreliable at this time the development of a ^{92}Nb-based p-process chronometry.

The situation concerning samarium has improved, in particular as a result of new experimental data that have helped putting on firmer grounds the evaluation of the rate of ^{148}Gd $(\gamma, \alpha)\,^{144}$Sm. This reaction, along with ^{148}Gd $(\gamma, n)\,^{147}$Gd, is known to influence the SNII ^{146}Sm/^{144}Sm production ratio entering the development of a Sm-based p-process chronometry (e.g. [18]). More specifically, a direct measurement of the ^{144}Sm $(\alpha, \gamma)\,^{148}$Gd cross section down to energies very close to the Gamow window of relevance to the ^{144}Sm production has been conducted [21]. These data, complemented with an (α, α) elastic scattering experiment [13], have helped constraining the parameters of the α–^{144}Sm optical potential, the poor knowledge of which has been identified as the main source of uncertainty in the evaluation of the rate of ^{144}Sm $(\alpha, \gamma)\,^{148}$Gd and, consequently (through the detailed balance theorem), of its reverse. In fact, it has been possible to construct an energy-dependent α-nucleus optical potential with a Woods-Saxon shape which satisfies several physical constraints, and which accounts remarkably well for the experimental cross section data, including the lowest energy data points, as demonstrated by Fig. 3 [21]. This potential leads to an astrophysical rate that is about 5 to 10 times lower than the latest predictions of [17] and [13] in the temperature range of relevance for the production of the Sm p-isotopes. By application of the detailed balance theorem, the rate of the reverse ^{148}Gd $(\gamma, \alpha)\,^{144}$Sm of direct astrophysical interest is reduced accordingly.

This revised rate is used to re-evaluate the production ratio $P \equiv {}^{146}$Sm/^{144}Sm in the SNII models considered in Sect. 2. Its values are shown in Fig. 4 for stars with masses $M = 13$, 15, 20 and 25 $M_\odot$ and compared with the values obtained by using the old estimate for the ^{148}Gd $(\gamma, \alpha)\,^{144}$Sm rate calculated with the global α-nucleus optical potentials of [12] (see Fig. 3). The revision to lower values of the ^{148}Gd $(\gamma, \alpha)\,^{144}$Sm rate lowers the production of ^{144}Sm, and favours concomitantly the ^{146}Sm synthesis through the main production channel ^{148}Gd$(\gamma,n)^{147}$Gd$(\gamma,n)^{146}$Gd $(\beta^+)^{146}$Sm. As a net result, the P values are increased.

Other nuclear problems add to the uncertainty in the evaluation of P. As noted above, this concerns in particular the ^{148}Gd $(\gamma, n)\,^{147}$Gd reaction, for which no experimental information can be foreseen in a very near future in view of the unstable nature of ^{147}Gd $(t_{1/2} \approx 38$ h). A more complete discussion
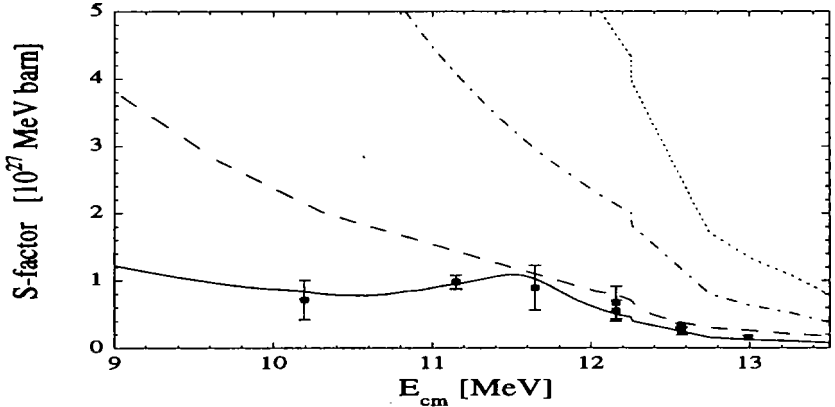
Figure 3: The astrophysical S–factor for ^{144}Sm$(\alpha,\gamma)^{148}$Gd. The dot-dashed and dotted lines are estimates obtained with the Hauser-Feshbach code MOST [8] and the global α-nucleus optical potentials of [12] (as used in the code SMOKER [22]) and [4], respectively. The solid line is obtained with the code MOST and the energy-dependent optical potential developed in this work. The dashed line is from [13].
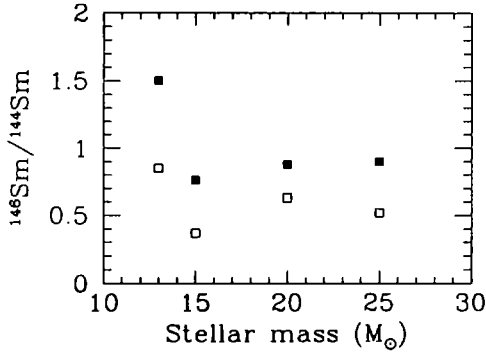

Figure 4: The production ratio $P \equiv {}^{146}$Sm$/^{144}$Sm in the explosion of stars with masses $M = 13$, 15, 20 and 25 $M_\odot$, calculated with 2 different rates for ^{148}Gd$(\gamma,\alpha)^{144}$Sm. Open squares: using the global α-nucleus optical potentials of [12]. Full squares: using the energy-dependent optical potential developed in this work (see Fig. 3).

of the effect of the present nuclear uncertainties on P is presented in [21]. In addition, astrophysical uncertainties concur to the difficulty of predicting P reliably. The consequences of these various uncertainties on the possibility of a ^{146}Sm based s-process chronometry are briefly discussed in [21].

4 Conclusions

This contribution reviews the unprecedented effort to model the p-process developing during SNII of massive stars. The variety of considered stellar cases makes possible for the first time the calculation of IMF-averaged abundances of the p-nuclides, and a meaningful comparison with the bulk solar system p-nuclidic content. It appears that about 60 % of the p-nuclides are nicely co-produced (with respect to solar). Some problems are also identified, and a speculative remedy to the relative underproduction of the Mo and Ru p-isotopes is briefly discussed.

Some anomalies found in various meteoritic materials are attributed to p-isotopes . This concerns in particular ^{142}Nd excesses attributed to the in-situ decay of ^{146}Sm that can be synthesized in the SNII p-process. New rates for the key reaction ^{148}Gd (γ, α) ^{144}Sm based on recent experimental data for ^{144}Sm (α, γ) ^{148}Gd are proposed, and the corresponding ^{146}Sm/^{144}Sm production ratios are presented. In spite of this advance made in the nuclear physics involved in the synthesis of ^{146}Sm, some uncertainties of nuclear and astrophysics nature remain in the predicted level of production of this radionuclide. These uncertainties of course hamper the development of a truly reliable p-process chronometry based on the ^{146}SM-^{144}Sm pair.

References

[1] M. Arnould, 1976, A&A **46** (1976) 117;

[2] M. Arnould, M. Rayet and M. Hashimoto M., in: Kubuno S., Kajino T. (eds.) Unstable Nuclei in Astrophysics. World Scientific, Singapore (1992) p. 23;

[3] M. Arnould, M. Rayet and M. Hashimoto, in: Tours Symposium on Nuclear Physics III (1997), in press;

[4] V. Avrigeanu, P.E. Hodgson and M. Avrigeanu, Phys. Rev. **C49** (1994) 2136;

[5] Z. Y. Bao and F. Käppeler, ADNDT **36** (1987) 411;

- 287 -

[6] G. R. Caughlan, W. A. Fowler, M. J. Harris and B. A. Zimmerman, AD-NDT **32** (1985) 197;

[7] G. R. Caughlan and W. A. Fowler, ADNDT **40** (1988) 283;

[8] S. Goriely, in: Proceedings of Nuclear Data for Science and Technology, Trieste (Italy), 1997, in press;

[9] C. L. Harper, ApJ. **466** (1996) 437;

[10] W. M. Howard and B. S. Meyer, in: Käppeler F., Wisshak K. (eds.) Nuclei in the Cosmos. Institute of Physics Publishing, Bristol (1993) p. 575;

[11] P. Kroupa, C. A. Tout and G. Gilmore, MNRAS **262** (1993) 545;

[12] F.M. Mann, Hauser 5, A Computer Code to Calculate Nuclear Cross Sections, Hanford Engineering HEDL-TME (1978) p. 78;

[13] P. Mohr et al., Phys. Rev. **C55** (1997) 1523;

[14] Zs. Németh, F. Käppeler and G. Reffo, ApJ **392** (1992) 277;

[15] N. Prantzos, M. Arnould and M. Cassé, ApJ **331** (1988) L15;

[16] N. Prantzos, M. Hashimoto, M. Rayet and M. Arnould, A&A **238** (1990) 455;

[17] T. Raucher, F.K. Thielemann and H. Oberhummer, ApJ Lett. **451** (1995) 37;

[18] M. Rayet and M. Arnould, in: Delbar Th. (ed.) Radioactive Nuclear Beams 1991. Adam Hilger, Bristol (1992) p. 347;

[19] M. Rayet, N. Prantzos and M. Arnould, A&A **227** (1990) 271;

[20] M. Rayet, M. Arnould, M. Hashimoto, N. Prantzos and K. Nomoto, A&A **298** (1995) 517;

[21] E. Somorjai et al., A&A (1998), to be published;

[22] F.-K. Thielemann, M. Arnould and J. W. Truran, in: Vangioni-Flam E., Audouze J., Cassé M., Chièze J.-P., Tran Thanh Van J. (eds.) Advances in Nuclear Astrophysics, Editions Frontières, Gif-sur-Yvette (1986) p. 525;

[23] T. A. Weaver and S. E. Woosley, Phys. Rep. **227** (1993) 65;

DE98F8397

DE011451396

GLOBAL TRANSMISSION COEFFICIENTS IN HAUSER–FESHBACH CALCULATIONS FOR ASTROPHYSICS

T. RAUSCHER[1]

Institut für Physik, Universität Basel
Klingelbergstr. 82, CH-4056 Basel

Abstract

The current status of optical potentials employed in the prediction of thermonuclear reaction rates for astrophysics in the Hauser–Feshbach formalism is discussed. Special emphasis is put on α+nucleus potentials. Further experimental efforts are motivated.

1 Introduction

The investigation of explosive nuclear burning in astrophysical environments is a challenge for both theoretical and experimental nuclear physicists. Highly unstable nuclei are produced in such processes which again can be targets for subsequent reactions. Cross sections and astrophysical reaction rates for a large number of nuclei are required to perform complete network calculations which take into account all possible reaction links and do not postulate a priori simplifications.

The majority of reactions can be described in the framework of the statistical model (compound nucleus mechanism, Hauser–Feshbach approach, HF) [1], provided that the level density of the compound nucleus is sufficiently large in the contributing energy window [2]. In astrophysical applications usually different aspects are emphasized than in pure nuclear physics investigations. Many of the latter in this long and well established field were focused on specific reactions, where all or most "ingredients", like optical potentials for particle transmission coefficients, level densities, resonance energies and widths of giant resonances to be implemented in predicting E1 and M1 γ-transitions, were deduced from experiments. As long as the statistical model prerequisites are met, this will produce highly accurate cross sections. For the majority of nuclei in astrophysical applications such information is not available. The real challenge is thus not the well–established statistical model, but rather to provide

---

[1]APART fellow of the Austrian Academy of Sciences

all these necessary ingredients in as reliable a way as possible, also for nuclei where none of such information is available.

2 Transmission Coefficients

The final quantities entering the expression for the cross section in the statistical model [1] are the averaged transmission coefficients. They do not reflect a resonance behavior but rather describe absorption via an imaginary part in the (optical) nucleon–nucleus potential [3]. In astrophysics, usually reactions induced by light projectiles (neutrons, protons, α particles) are most important. Global optical potentials are quite well defined for neutrons and protons. It was shown [4, 5] that the best fit of s–wave neutron strength functions is obtained with the optical potential by [6], based on microscopic infinite nuclear matter calculations for a given density, applied with a local density approximation. It includes corrections of the imaginary part [7, 8]. A similar description is used for protons. Deformed nuclei are treated by an effective spherical potential of equal volume [5]. For a detailed description of the formalism used to calculate E1 and M1 γ–transmission coefficients and how to include width fluctuation corrections, see [2, 5] and references therein.

2.1 α+Nucleus Potentials

Currently, there are only few global parametrizations for optical α+nucleus potentials at astrophysical energies. Most global potentials are of the Saxon–Woods form, parametrized at energies above about 70 MeV, e.g. [9, 10]. The high Coloumb barrier makes a direct experimental approach very difficult at low energies. More recently, there were attempts to extend those parametrizations to energies below 70 MeV [11].

Early astrophysical statistical model calculations [12, 13] made use of simplified equivalent square well potentials and the black nucleus approximation. Improved calculations [14] employed a phenomenological Saxon–Woods potential [15], based on extensive data [16]. This potential is an energy– and mass–independent mean potential. However, especially at low energies the imaginary part of the potential should be highly energy–dependent.

Most recent experimental investigations [17, 18] found a systematic mass– and energy–dependence and were very successful in describing experimental scattering data, as well as bound and quasi–bound states and B(E2) values, with folding potentials [19]. Motivated by that description (a global parametrization is not given in [18]), the following global α+nucleus potential is

proposed. The real part $V = \lambda V_f$ of the optical potential is calculated by a double–folding procedure:

$$V_f(r) = \int \int \rho_P(r_P)\,\rho_T(r_T)\,v_{\text{eff}}\big(E, \rho_N = \rho_P + \rho_T, s = |\vec{r} + \vec{r_P} - \vec{r_T}|\big)\,d^3r_P\,d^3r_T \quad , \tag{1}$$

where ρ_P, ρ_T are the nuclear densities of projectile and target, respectively, and v_{eff} is the effective nucleon–nucleon interaction taken in the well–established DDM3Y parametrization [20]. The remaining strength parameter λ can be determined from the systematics [17] of the volume integral per interacting particle pair

$$J_R = \frac{1}{A_P A_T} \int V(r)\,d^3r \quad . \tag{2}$$

Introducing a mass–dependence in addition to the energy–dependence, one can reproduce the behavior derived from the imaginary part by applying the dispersion relation [18], by the relation

$$J_R = \begin{cases} f(A) + 0.67 E_{\text{c.m.}} & (E_{\text{c.m.}} \leq 26) \\ [0.011 f(A) - 2.847]\, E_{\text{c.m.}} - 1.277 f(A) + 626.591 & (26 < E_{\text{c.m.}} < 120), \end{cases} \tag{3}$$

with $f(A) = 311.0132 \exp\left(A_T^{-2/3}\right)$ and $E_{\text{c.m.}}$ given in MeV. Using Eqs. 2 and 3, the value of λ can be set.

The mass– and energy–dependence of the imaginary part is more crucial for the calculation of transmission coefficients. The volume integral of the imaginary part can be parametrized according to [21]:

$$J_I(E_{\text{c.m.}}) = \begin{cases} 0 & \text{for } E_{\text{c.m.}} \leq E_0 \\ J_0 \cdot \frac{(E_{\text{c.m.}} - E_0)^2}{(E_{\text{c.m.}} - E_0)^2 + \Delta^2} & \text{for } E_{\text{c.m.}} > E_0 \quad , \end{cases} \tag{4}$$

where E_0 is the threshold energy for inelastic channels, J_0 is a saturation parameter and Δ the rise parameter.

As can be seen [18], the resulting volume integrals are quite diverse for different nuclei and a straight–forward mass–dependent parametrization is not possible. In Ref. [18], J_0 and Δ were fitted to experimental data. For a global parametrization, one has to include nuclear structure and deformation information into the fit. Having chosen the (probably energy–dependent) geometry parameters [11] (and appropriately modified them for deformed nuclei), the depth W of an imaginary Saxon–Woods potential can be determined with Eq. 4. At energies $E_{\text{c.m.}} > 100$ MeV, the value of W should reach the saturation value [10]. This determines the parameter J_0. The threshold $E_0 = E_0(\rho)$

is given by the energy of the first excited state. The increase in the number of inelastic (competing) channels is described by Δ. As a first estimate, this can be related to the increase in the total number $n = n(\rho)$ of levels: $\Delta = f\,(dn/dE) = \alpha E_0 + \beta A^{2/3} + \gamma \ln\,(dn/dE)$. The functional dependence is found by comparison with experimental values for Δ [18]. Thus, microscopic and deformation effects are implicitly included via the level density $\rho = \rho(E)$.

With nuclear level densities $\rho(E)$ taken from [2], a good fit is obtained to the values given in [18], as well as for various (α,γ) and (n,α) data [22]. However, it has to be emphasized that the aim is to obtain a reasonable *global* potential, i.e. with a low *average* deviation from experiment. For specific reactions, such a potential might be improved by fine–tuning to a particular nucleus (e.g. [23, 24]) but will lose predictive power by that.

3 Conclusion

With the recent improvements of the level density treatment [2] and the α+nucleus potential, the two major remaining uncertainties in the existing global astrophysical reaction rate calculations have been attacked. The new descriptions will provide more reliable predictions of the low–energy cross sections of unstable nuclei.

Nevertheless, to check and further improve current parametrizations, not only of α+nucleus potentials but of all involved quantities, experimental data is needed. Especially investigations over a large mass range would prove useful to fill in gaps in the knowledge of the nuclear structure of many isotopes and to construct more powerful parameter systematics. Such investigations should include neutron– and proton–strength functions, as well as radiative widths, and charged particle scattering and reaction cross sections for *stable* and unstable isotopes. This information can be used to make future large–scale statistical model calculations even more accurate.

References

[1] W. Hauser and H. Feshbach, Phys. Rev. **87** (1952) 366

[2] T. Rauscher, F.-K. Thielemann, and K.-L. Kratz, Phys. Rev. C **56** (1997) 1613

[3] C. Mahaux, H.A. Weidenmüller, Ann. Rev. Part. Nucl. Sci. **29** (1979) 1

[4] F.-K. Thielemann, J. Metzinger, and H.V. Klapdor, Z. Phys. A **309** (1983) 301

[5] J.J. Cowan, F.-K. Thielemann, J.W. Truran, Phys. Rep. **208** (1991) 267

[6] J.P. Jeukenne, A. Lejeune and C. Mahaux, Phys. Rev. C **16** (1977) 80

[7] S. Fantoni, B.L. Friman and V.R. Pandharipande, Phys. Rev. Lett. **48** (1981) 1089

[8] C. Mahaux, Phys. Rev. C **82** (1982) 1848

[9] P.P. Singh and P. Schwandt, Nukleonika **21** (1976) 451

[10] M. Nolte, H. Machner and J. Bojowald, Phys. Rev. C **36** (1987) 1312

[11] V. Avrigeanu, P.E. Hodgson, M. Avrigeanu, Phys. Rev. C **49** (1994) 2136

[12] M. Arnould, A&A **19** (1972) 92

[13] S.E. Woosley, W.A. Fowler, J.A. Holmes, and B.A. Zimmerman, At. Data Nucl. Data Tables **22** (1978) 371

[14] F.-K. Thielemann, M. Arnould and J.W. Truran, in *Advances in Nuclear Astrophysics*, ed. E. Vangioni–Flam, Gif sur Yvette 1987, Editions Frontière, p. 525

[15] F.M. Mann, 1978, Hanford Engineering, report HEDL-TME 78–83

[16] L. McFadden and G.R. Satchler, Nucl. Phys. **84** (1966) 177

[17] P. Mohr, H. Abele, U. Atzrott, G. Staudt, R. Bieber, K. Grün, H. Oberhummer, T. Rauscher, and E. Somorjai, in *Proc. Europ. Workshop on Heavy Element Nucleosynthesis*, eds. E. Somorjai and Zs. Fülöp, Institute of Nuclear Research, Debrecen 1994, p. 176

[18] U. Atzrott, P. Mohr, H. Abele, C. Hillenmayer, and G. Staudt, Phys. Rev. C **53** (1996) 1336

[19] G.R. Satchler and W.G. Love, Phys. Rep. **55** (1979) 183

[20] A.M. Kobos, B.A. Brown, R. Lindsay, and R. Satchler, Nucl. Phys. **A425** (1984) 205

[21] G.E. Brown and M. Rho, Nucl. Phys. **A372** (1981) 397

[22] V. Hansper, private communication

[23] P. Mohr, T. Rauscher, H. Oberhummer, Z. Máté, Zs. Fülöp, E. Somorjai, M. Jaeger, and G. Staudt, Phys. Rev. C **55** (1997) 1523

[24] E. Somorjai, Zs. Fülöp, Á.Z. Kiss, C.E. Rolfs, H.P. Trautvetter, U. Greife, M. Junker, S. Goriely, M. Arnould, M. Rayet, T. Rauscher, and H. Oberhummer, A&A, in press

LARGE-SCALE CALCULATIONS OF THE BETA–DECAY RATES AND R–PROCESS NUCLEOSYNTHESIS

I.N. BORZOV[1], S. GORIELY, J.M. PEARSON[2]

Institut d'Astronomie et d'Astrophysique
Université Libre de Bruxelles, Campus Plaine, CP 226
B-1050 Bruxelles, Belgium

Abstract

An approximation to a self-consistent model of the ground state and β–decay properties of neutron-rich nuclei is outlined. The structure of the β–strength functions in stable and short-lived nuclei is discussed. The results of large-scale calculations of the β–decay rates for spherical and slightly deformed nuclides of relevance to the r-process are analysed and compared with the results of existing global calculations and recent experimental data.

1.Introduction

The modeling of explosive astrophysical events is bound to a knowledge of a large body of nuclear data. The β–decay rates of short-lived nuclides are at the present time among the most uncertain nuclear quantities in the calculations of the r-process nucleosynthesis. For some neutron-rich nuclides the β–decay rates have been measured with RIB facilities and high-flux reactors. However, given the lack of experimental data for the vast majority of the neutron-rich nuclei produced by the r-process, theoretical predictions of nuclear properties far from stability are of fundamental importance. Since most of the nuclear models are fitted to experimental data along the valley of β-stability, sometimes only crude extrapolations to remote regions of the nuclear chart are available. Thus, among the different nuclear models used for practical purposes, those having the most reliable predictive power far from stability are to be preferred for the r-process modeling. In addition, for a reliable calculation of the r-process nucleosynthesis, the different nuclear quantities, such as masses, deformations, β-decay rates, ... have to be estimated within the same model.

---

[1]On leave from Institute of Physics & Power Engineering, 249020 Obninsk, Russia

[2]Laboratoire de Physique Nucléaire, Université de Montréal, Montréal, H3C 3J7 Canada

The main characteristic of the nuclear β-decay process is the β-strength function, i.e the spectral distribution of the β-decay transition probability which defines the β-decay half-life. For the short-lived nuclides produced by the r-process ($T_{1/2} < 1s$), the approximation of allowed Gamow-Teller (GT) transitions ($\Delta L=0$, $\Delta S=1$, $\Delta \pi =no$) is usually accurate enough. Experimental measurements of β-strength functions show a typical resonance structure which is quite pronounced in spherical nuclides and more spread-out in deformed ones. The resonance shape is essentially due to single-particle transition effects. This gives grounds to the "gross theory" [1] (a statistical approach corrected for single-particle and pairing effects). The latest version of the "gross theory" (GT2) is widely used for astrophysical applications.

At the same time, realistic microscopic models like the proton-neutron quasi-particle random phase approximation (QRPA) show that the single-particle properties as well as the pairing and spin-isospin components of the effective NN-interactions play an important role. Various microscopic predictions of the β-decay properties [2, 3] have been performed. In particular, the recent work [3] contains the ground state and β-decay characteristics obtained within the Finite-Range Droplet Model (FRDM) and simplified QRPA approach based on an empirical one body single-particle potential, a simple pairing interaction and a separable A-dependent effective NN-interaction.

Despite this important effort, the lack of consistent theoretical models still makes the predictions of the β-decay properties quite unreliable. The half-lives calculated with empirical models [1, 2, 3] show deviations among each other, but also with new experimental data near neutron-rich closed-shell nuclei (see NUBASE [4]). A common problem to all the non-self-consistent models is related to the empirical choice of a suitable mean field, for which the extrapolation to exotic nuclei has to be questioned.

A fully self-consistent Hartree-Fock-Bogoliubov (HFB) plus QRPA approach applicable to large-scale calculation of the ground state and β-decay properties far from stability is not feasible so far. However, as a practical step in this direction, it is possible to develop the QRPA on the ground state description given by self-consistent mean-field models[5] and especially by those used for large-scale calculations of nuclear masses [6, 7]. The predictive power of the latter approaches can be significantly improved if the form and parameters of the corresponding density functional or effective force are fitted not only to the nuclear ground state properties near the line of stability, but also to the ones away from stability.

For astrophysical applications, the simultaneous evaluation of many different nuclear properties for a great number of nuclides is required, hence we are

forced to consider microscopically founded approximations to self-consistent methods. Much effort has been devoted to build up such a unified microscopic model based on the Extended Thomas-Fermi plus Strutinsky Integral (ETFSI) approximation to the HF method [6]. The present work is devoted to ETFSI based approximation to the description of the spin-isospin excitations in very neutron-rich nuclei.

2.The ETFSI+cQRPA model of β-decay properties

For large-scale calculations of β-decay rates, existing fully self-consistent HF + RPA schemes based on the Skyrme effective interaction [8, 9, 10] are of limited practical use. For this reason, we consider here the continuum QRPA (cQRPA) based on the ETFSI ground state description [6]. The main features of the resulting ETFSI+cQRPA method are:

1. The nuclear mean field is obtained by folding the Skyrme force over the smooth (fourth order) ETF nuclear density. The density-dependent two-body option of the Skyrme force with an effective mass $m^*/M=1$ [6] is used.

2. The quasi-particle basis is constructed by including a staggered δ-pairing [12] on top of the HF solution (in practice, the pairing strength is taken to be 2% stronger for an odd neutron number than for an even one).

3. In order to control the description of the spin properties of the Skyrme force, its parameters can be constrained by the values of the dimensionless Landau–Migdal spin-isospin constant g_0' or spin-spin constant g_0 [11].

4. Based on 1-3, the Skyrme force parameters are determined by optimizing the fit to known nuclear masses. The resulting force corresponds to $g_0'=0.21$, $g_0=-0.04$ (normalized to $N_0^{-1} = 150.5 \text{MeV fm}^3$). Note that $g_0'=0.45$ is the highest value of the spin-isospin constant that can be used to constrain the Skyrme parameters without violating the spin stability condition of the nuclear matter ($g_0 > -1$). Increasing further the value of g_0' also makes the mass fit worse. At the same time, the nuclear-matter symmetry energy of the Skyrme force is chosen to be equal to J=28 MeV in order to avoid the unphysical collapse of neutron matter at lower J values. The resulting force (SkSC17) predicts nuclear masses with a root mean square deviation of 732 keV from the 1722 $A > 35$ masses of the 1995 Audi-Wapstra compilation.

5. The strength function of the charge-exchange excitations and the resulting β-decay rate is calculated within the spherical cQRPA with the exact account for the single-particle continuum in the particle-hole (ph) channel.

7. Only allowed transitions are included in the global calculation of the β-decay half-live of short-lived nuclides.

8. The effective spin-isospin NN-interaction strength used in the cQRPA calculations corresponds to a renormalized Landau–Migdal constant g'_0 with respect to the one constraining the ETFSI Skyrme parameters. We adopt for the spin-isospin interaction in the ph channel a renormalized one-pion exchange term F_π plus a contact δ-term with a Landau-Migdal constant $g'_0 = 1.94$ obtained by a fit to the experimental position of the GT resonance in ^{208}Pb. In the present approach with the constraint on $m^*/M = 1$, it is impossible simultaneously to describe a spin-stable nuclear matter and to keep a good quality fit to the masses using the empirical value of the $g' = 1.6$-1.8 ($F_\pi = 0$) [11].

In the pp channel, a form of the effective NN-interaction similar to that of the pairing is used with the strength constant derived from the β^+-decay data in [13, 5].

3. GT strength in stable nuclei

Making use of the SkSC17 force to describe the ground state properties, we perform continuum QRPA calculations of some experimentally known energies of the giant GT resonances in order to check the derived value of g'_0. First, let us discuss the single-particle energies which are the basic ingredients in the calculation of the GT strength function.

Experimental [18] singe-particle energies in ^{132}Sn are compared in Table 1 with ETFSI predictions obtained with force SkSC4 ($g'_0 = 0.21$, J=27 MeV) [6], and SkSC17 ($g'_0 = 0.21$, J=28 MeV). Non-negligible deviations are observed between SkSC4 and SkSC17 predictions reflecting their different behaviours at increasing neutron excesses due to different adopted values of J. Only insignificant changes are produced by the change of g'_0 and g_0, as the ground state properties are basically insensitive to the spin-dependent component of the density functional. However, for the specific application to the calculation of the GT decay, the main contributing single-particle transition energies turn out to be quite similar for both forces. The energies of the main GT resonance component $\nu 1g_{9/2}\pi 1g_{7/2}$ are -6.73 and -5.91 for SkSC4 and SkSC17, respectively. The same conclusion is found for the GT component $\nu 1g_{7/2}\pi 1g_{9/2}$. Note that no special adjustment to the experimental single-particle spectra has been performed.

The GT resonance energies calculated for the chain of tin isotopes are compared with available experimental data obtained from (^{3}He,t) reactions [14] in Table 2. The overall good agreement with experiment confirms the estimated value of $g'_0 = 1.9$. However, a possible underestimate of about 5%

Table 1: Single-particle levels (in MeV) in ^{132}Sn calculated for Skyrme forces SkSC4 and SkSC17. Experimental data are taken from [18]

Level	ϵ_{exp}	ϵ_{SkSC4}	ϵ_{SkSC17}	Level	ϵ_{exp}	ϵ_{SkSC4}	ϵ_{SkSC17}
$\nu1g_{9/2}$		-15.67	-15.19	$\pi2p_{3/2}$	.	-16.82	-17.32
$\nu2d_{5/2}$	-9.041(38)	-11.21	-10.64	$\pi2p_{1/2}$	-16.131(52)	-15.39	-15.91
$\nu1g_{7/2}$	-9.820(38)	-9.96	-9.63	$\pi1g_{9/2}$	-15.778(44)	-14.39	-14.81
$\nu3s_{1/2}$	-7.718(38)	-9.29	-8.80		***		
$\nu1h_{11/2}$	-7.628(38)	-7.87	-7.43	$\pi1g_{7/2}$	-9.653(43)	-8.94	-9.28
$\nu2d_{3/2}$	-7.386(38)	-8.52	-8.42	$\pi2d_{5/2}$	-8.691(43)	-9.66	
	***			$\pi1h_{11/2}$	-6.860(43)	-6.85	-7.24
$\nu2f_{7/2}$	-2.445(49)	-3.32	-2.88	$\pi2d_{3/2}$	-6.945(43)	-6.80	-7.34
$\nu3p_{3/2}$	-1.5913	-1.56	-1.24	$\pi3s_{1/2}$		-6.87	-7.38
$\nu1h_{9/2}$	-0.8841	0.11	-0.21	$\pi2f_{7/2}$		-1.02	-1.48
$\nu3p_{1/2}$	(-0.75)	-0.87	-0.56				
$\nu2f_{5/2}$	-0.4404	-0.27	0.08				

on the value of g'_0 cannot be ruled out. The RPA approaches are known to overestimate the experimental energy of the giant resonances by about 1 MeV. Only the extended RPA approach including higher order (damping) effects predicts a spread of the GT resonance and the shift of its maximum by about 1 MeV downwards [17]. Thus, deriving the strength parameter g'_0 from the direct reproduction of the experimental position of the giant GT resonance within the 1st order QRPA might lead to some underestimate of its value.

Another test for the adopted value of g'_0 can be found in the description of the low-energy GT strength. As seen in Table 3, the maxima for several GT pygmy resonances in ^{118}Sn calculated with force SkSC17 are in satisfactory agreement with the averaged excitation energies derived from the experimental triton energy spectrum of ^{118}Sn(^{3}He,t)^{118}Sb [14]. This also increases our confidence in the adopted value of g'_0.

4. β–decay rates for spherical nuclides near closed shells

The major relative uncertainties in the QRPA prediction of β–decay half-lives arise for nuclides characterized by a low Q_β-value and/or a low β-decay transition energy ω. In the first case, the uncertainty is essentially related to the typical errors (0.5-1 MeV) in the prediction of the Q_β- and ω-values,

Table 2: Experimental and calculated Q_β–values and GT resonance excitation energies in the chain of tin isotopes and in the ^{208}Pb.

Nucleus	$-Q_{\beta-}$, MeV		E_x, MeV	
	SkSC17	exp.	SkSC17	exp.
^{112}Sn	7.30	7.06	8.6	8.94(25)[a]
^{114}Sn	6.07	5.88	9.3	9.39(25)[a]
^{116}Sn	4.55	4.71	10.2	10.04(25)[a]
^{117}Sn	1.77	1.76	12.6	12.87(25)[a]
^{118}Sn	3.52	3.66	10.5	10.61(25)[a]
^{119}Sn	0.71	0.59	13.2	13.71(25)[a]
^{120}Sn	2.50	2.68	11.0	11.45(25)[a]
^{122}Sn	1.53	1.62	12.1	12.25(25)[a]
^{124}Sn	1.00	0.62	13.0	13.25(25)[a]
^{208}Pb	3.08	2.88	15.8	15.6(3)[b]

[a] ref. [14], [b] ref. [15]

Table 3: Calculated and experimental [14] mean excitation energies of the low-lying GT pygmy resonances in ^{118}Sn (Given in the first line are the energy intervals from [14] in which the averaging has been performed) .

ΔE	0.8 – 2.0 MeV	2.0 – 3.8 MeV	3.8–5.6 MeV
E_{calc}	1.5	3.0	5.2
E_{exp}	1.47 ±0.20	3.17 $\pm$ 0.20	5.38 ±0.25

as well as to the contribution of the first forbidden transitions. In the case of a low-energy GT β-decay, high-order effects beyond the QRPA cannot be neglected.

For spherical and slightly deformed nuclides ($\beta_2 \lesssim 0.1$) with a high-energy GT β–decay, the ETFSI+cQRPA calculation [19, 20] shows a reasonable agreement with experimental β-decay half-lives. This is illustrated in Figs.1,2 which compares different half-live predictions in the Ni, Cu, Ag, Cd and Sn isotopic chains with available experimental data [4]. The half-lives calculated with self-consistent single-particle potentials [5, 20] reveals a quite regular A-dependence which can be understood in terms of the monotonic A-dependence of the energies of those single-particle levels responsible for the GT-transitions. The calculations also show some systematical overestimate (by a factor of 2 to 8) of the experimental half-lives which can be attributed to the possible existence

of an additional transition strength within the Q_β–window. It may originate from the contribution of forbidden transitions or effects beyond the QRPA (such as the spreading of the 1p1h strength over more dense neighbouring np-nh configurations or/and the appearance of an additional GT strength due to np-nh correlations in the ground state). The impact of this additional strength on the half-lives depends on the β–decay transition energy. In the vicinity of the Z=28 closed shell, calculations predict the existence of a high-energy GT β-decay transition both for isotopes below and above the proton shell closure. On the contrary, for the Z$\geq$50 nuclides in the region of the double magic ^{132}Sn a switch to low-energy GT β–decay regime is found by all QRPA models. This naturally results in a large overestimate of the experimental half-lives as seen in Fig.1c. In the case of low-energy GT β–decay, even a weak additional strength located at high transition energies has a strong impact on the total half-life (because of the strong energy dependence in the phase space factor).

To account for the spreading width $(\Gamma^\downarrow)$, a semi-microscopic scheme [16] can be used including the Green functions averaging procedure and some elements of the optical model. The energy dependent quasi-particle damping is described in terms of a complex self-energy $\Sigma_{ph}(E_x)$ depending on the excitation energy E_x, spin S and isospin T transfered by the (ph) pair [17]. We have used a parametrization for the spreading width which is numericaly close to [17]. The line shape of the individual GT excitation has been described by a Lorentz function with $\Gamma^\downarrow = \alpha(Q_\beta - \omega)^2$, where $\alpha \approx$0.02 roughly corresponds to the experimental width of the GT resonance in medium and heavy nuclei. Such a simple recipe allows us to improve the half-lives description significantly, especially for the nuclides with a low-energy GT β–decay in the Z=50-54 region near ^{132}Sn.

Large-scale calculations of the β–decay rates of spherical and slightly deformed ($\beta_2 <$0.1, $\beta_4 <$0.02) short-lived nuclides ranging from Fe to U have been performed within ETFSI+cQRPA [20]. The comparison of our predictions with the phenomenological "gross-theory" (GT2) [1] and empirical FRDM+QRPA [3] show that although the different models give quite similar predictions of the very high-energy β–decay rates around N=184, large deviations between them can be observed near the other neutron shell closures (N=28, 50 and 126), especially between the ETFSI+cQRPA and FRDM+QRPA models. These deviations are partially due to differences in the ground state description. In particular, Fig. 3 compares theoretical predictions of the β–decay rates for the N=82 and 126 neutron shells. Since the production of the heavy elements by the r-process is very sensitive to the predicted β–decay rates of the nuclides along the various neutron closed shells, the differences shown
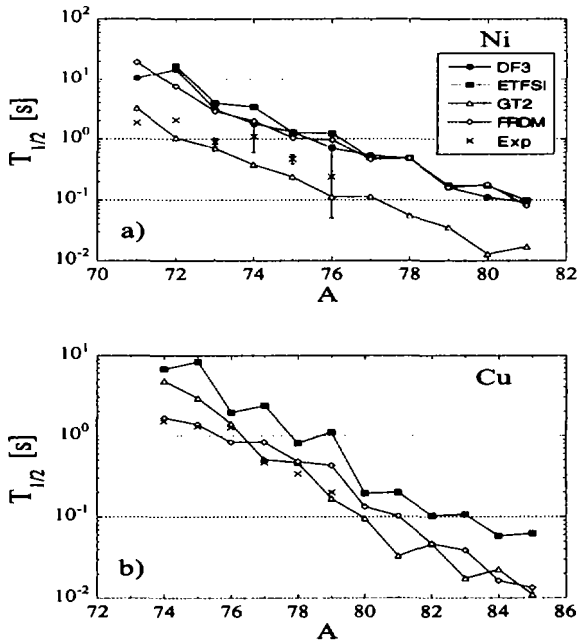
Figure 1: Comparison for Ni and Cu isotopic chains of the experimental half-lives with the ETFSI+cQRPA, GT2 [1], FRDM+QRPA [3] and DF3 [5] predictions.

in Fig. 3 are expected to affect the predicted r-abundance distribution.

5. Conclusions

The model outlined in the present work for the calculation of the β–decay properties of spherical neutron-rich nuclides is based on a self-consistent description of the ground state properties which not only reproduces masses and radii of experimentally known nuclei remarkably well, but also predicts single-particle energies of relevance to high-energy GT decay in fair agreement with available experimental data. The calculated set of β-decay half-lives of spherical neutron-rich nuclei near exotic shell closures can be regarded as more coherent and reliable than the one derived by previous large-scale calculations
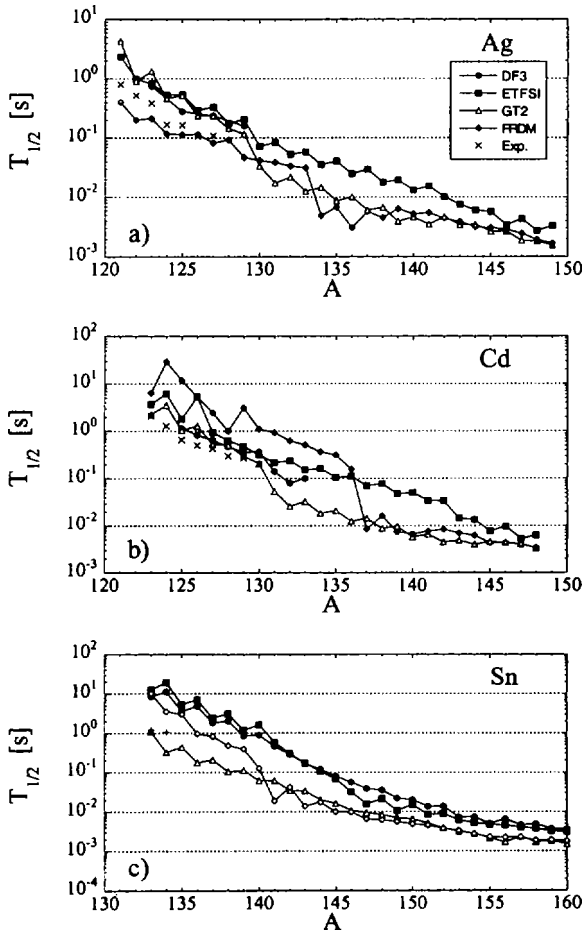
Figure 2: Same as Fig.1 for Ag, Cd and Sn isotopic chains

[1, 2, 3]. It remains of high interest to elucidate the influence of high-order effects on the β–strength function on a more microscopic level. A consistent account for deformation effects will allow us to complete a fully coherent table of β-decay half-lives, which would help to improve our understanding of the
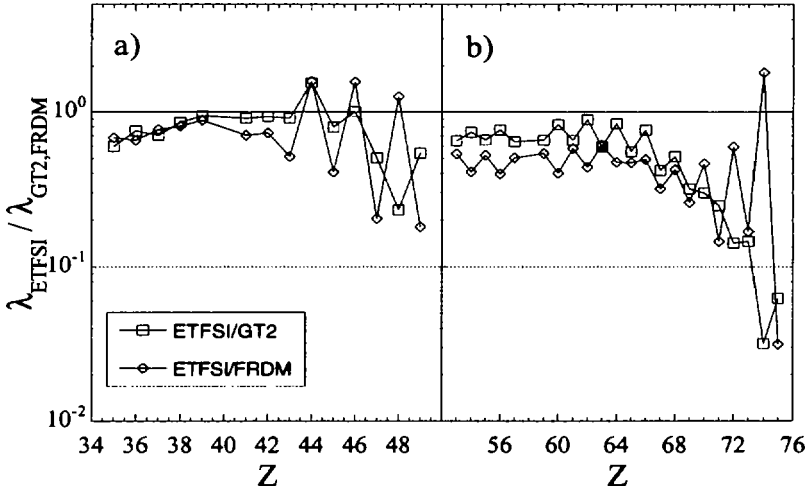
Figure 3: a) Ratios of the ETFSI(SkSC17)+cQRPA to GT2 and to FRDM+QRPA β-rates for the neutron-rich N=82 isotones. b) same as a) for the N=126 isotones.

explosive nucleosynthesis.

References

[1] K.Takahashi, M.Yamada, T.Kondoh ADNDT. **12** (1975) 101
T.Tachibana,M.Yamada,N.Yoshida, Prog. Theor. Phys. **84** (1990) 641.

[2] M. Hirsch, A. Staudt, H-V. Klapdor-Kleingrothaus., ADNDT **51** (1992) 244.

[3] P.Möller, J.R.Nix, K.-L.Kratz. ADNDT **66** (1997) 131.

[4] Audi G., Wapstra A.H., Nucl. Phys. **A624** (1997) 1.

[5] I.N.Borzov, S.A.Fayans, E.Kromer, D.Zawischa, Zeit.Phys. **A335** (1996) 127.

[6] Y.Aboussir, J.M.Pearson, A.K.Dutta, F.Tondeur., ADNDT **61** (1995) 127.

[7] J.Dobaczewski, W.Nazarewicz, T.R.Werner, Phys. Scripta **T56** (1995) 15.

[8] S.Krewald, V.Klempt, J.Speth, A.Faessler, Nucl.Phys. **A281** (1977) 166.

[9] N.Van Giai, H.Sagawa, Phys.Lett. **106B** (1981) 379.

[10] K-F.Liu, H-D.Luo, Z.Ma, M.Feng, Nucl.Phys. **A534** (1991) 48.

[11] A.B.Migdal. "Theory of finite Fermi systems and atomic nuclei properties" Interscience, N.-Y.,1983 [Russ.original 2nd ed., Nauka, Moscow, 1983]

[12] R.C.Nayak, J.M. Pearson, Phys. Rev. **C52** (1995) 2254.

[13] I.N.Borzov, S.A.Fayans, E.L.Trykov., Nucl.Phys.**A584** 335 (1995).

[14] K.Pham, J.Janeke, D.Roberts et.al., Phys.Rev. **C51** (1995) 526.

[15] P.J.Horen, C.D.Goodman, C.C.Foster et al., Phys.Rev.Lett. **B95** (1980) 27.

[16] S.Adachi, N.Auerbach., Phys.Lett. **131B** (1983) 11.

[17] S.Drozd, S.Nishizaki, S.Speth, J.Wambach., Phys.Rep. **197** (1990) 1.

[18] K.A. Mezilev, Y.N. Novikov, V.A. Popov, B. Fogelberg, L. Spanier., Phys. Scripta **T56** (1995) 227; ISOLDE COLLABORATION (1996) in press.

[19] I.N.Borzov, S.Goriely, J.M.Pearson., Nucl.Phys. **A621** (1997) 307c.

[20] I.N.Borzov, S.Goriely, J.M.Pearson, M.Arnould., to appear in Proc. Int.Conf."Nucl.Data in Science and Technology", (1997) Trieste, Italy.

NEW EXPERIMENTS ON r-PROCESS NUCLEI IN THE ^{132}S$_{82}$ REGION

K.-L. KRATZ

for the Mainz – Maryland – Troitzk – Leuven – Basel –CERN-ISOLDE
Collaboration

Institut für Kernchemie
Johannes-Gutenberg-Universität Mainz
Fritz-Strassmann-Weg 2, D-55128 Mainz, Germany

The structure and decay of very neutron-rich isotopes in the vicinity of the doubly magic, unstable nucleus ^{132}Sn play a crucial role in the description of the astrophysical r-process in this mass region. Stable nuclides produced by this nucleosynthesis process show a pronounced solar-system r-abundance peak at A$\simeq$130, that has been attributed to the specific nuclear-structure properties of their isobaric progenitors lying on or near the closed neutron shell N=82.

In this context, experimental investigations of the classical "waiting-point" isotopes below ^{132}Sn are of particular interest; however, they were severely complicated in the past by (i) very low production yields and (ii) chemically non-selective plasma ionization modes at conventional isotope separators. Therefore, in recent years element-selective laser ion-source systems based on resonance ionization of atoms in a hot cavity have been developed – e.g. for $_{47}$Ag, $_{48}$Cd and $_{50}$Sn – at the CERN-ISOLDE facility.

We will report here on our recent studies of very neutron-rich Ag-isotopes at the GPS of CERN-ISOLDE. Gamma-rays and β-delayed neutrons following the decays of $^{122-128}$Ag have been investigated. Excited structures beyond the first 2^+ level have been studied in the even-even Cd-daughters. Using a high-efficiency neutron long-counter, the long searched-for N=82 r-process waiting-point isotope ^{129}Ag was unambiguously identified. So far, only the half-life of its $\pi g_{9/2}$ ground-state decay could be determined to 46^{+5}_{-9} ms. The existence of the $\pi p_{1/2}$ ^{129}Ag-isomer, predicted to lie roughly 300 keV above the ground state and to decay with a half-life of about 350 ms, could not yet been verified due to the still too high isobaric background from unavoidable surface-ionization of ^{129}In. For these investigations, the use of the high-resolution ISOLDE separator is foreseen.

NUCLEAR- AND ASTROPHYSICAL INTERPRETATION OF THE CA-TI-CR ISOTOPIC ANOMALIES IN THE INCLUSION EK 1-4-1 OF THE ALLENDE-METEORITE

W. BÖHMER[1], K.-L. KRATZ[1], B. PFEIFFER[1]
C. FREIBURGHAUS[2], T. RAUSCHER[2], F.-K. THIELEMANN[2]

[1]*Institut für Kernchemie, University Mainz, Fritz-Straßmann-Weg 2*
D-55128 Mainz, Germany

[2]*Universität Basel, Department für Physik und Astronomie, Klingelbergstraße 82,*
CH-4056 Basel, Switzerland

Abstract

In the framework of our investigation to explain the nucleosynthetic ori-
gin of the correlated Ca-Ti-Cr Isotopic Anomalies in the refractory in-
clusion EK 1-4-1 of the Allende Meteorite, β-decay properties and defor-
mation of the nuclear shape as well as neutron capture cross sections of
neutron-rich isotopes in the N=28 region have been determined. These
nuclear data are important input parameters for dynamic astrophysical
calculations in a complete reaction network. As astrophysical scenario
a high entropy bubble at the outer core of a type II supernova was as-
sumed. It will be outlined that at certain entropies between 1 and 200
k_B/Baryon the observed Ca-Ti-Cr Anomalies can be reproduced simul-
taneously.

1 Introduction

The progress in understanding nucleosynthesis is closely combined with the
knowledge of physical properties of nuclei. In this context, both, the extrac-
tion of nuclear data, observable in experiments and by the use of self-consistent
models is aspired. In particular, if energy levels, spin and parity as well as de-
formation are known, reaction-rates and β-decay properties can be determined.
For r-process like scenarios neutron separation energies (S_n), half-lives $(T_{1/2})$
and the probability of β-delayed neutron emission (P_n) of nuclei far from sta-
bility are of intereset mainly for three reasons. (i) By investigation of these
nuclear structure properties the behaviour of nuclei with increasing neutron
number can be studied. With the $T_{1/2}$- and P_n-values, the nuclear shape can be
determined at least for light nuclei due to the fact that only a few energy levels

have a significant influence on the global β-decay properties. These parameters can be considered in the theoretical description and improve the predictive power of the models. (ii) Approximately half of the stable isotopes above the iron group elements are created in the r-process. During this neutron capture process the vicinity of the closed neutron shells $N=28$, 50, 82 and 126 will be reached quickly. In order to reproduce the observed solar r-process abundances the investigation of β-decays after and during neutron-capture as well as the discovery of the branching-points and the so called *turning-points* are important. Branching appears at nuclei where the number of further neutron captures is of the same order as the number of β-decays ($T_{1/2}(n) \simeq T_{1/2}(\beta)$). Whether a nucleus has such branching-points depends i. a. on the neutron-separation energy (S_n). With the measurement of the global nuclear physics parameters the models can be improved as mentioned above. That leads to reliable predictions concerning deformation and S_n-values. Turning-points appear at nuclei with a relativly small neutron capture cross section so that β-decays dominate further neutron-captures ($T_{1/2}(n) > T_{1/2}(\beta)$). If the branching- and turning-points are known, the nucleosynthetic-path can be determined more exactly. This admits the conclusions of temperature (T_9) and neutron-density (n_n) of mass-rich stars where the r-process takes place. Thus the number of possible astrophysical scenarios can be limited. (iii) The understanding of nucleosynthesis in our solar-system is closely combined with the clarification of the origin of isotopic composition in meteorites. In the context of this investigation, isotopic compositions which differ from those of the remaining solar system, the so called isotopic anomalies, were found in Ca-Al rich inclusions of primitive meteorites. In such high temperature condensates of the stardust, inhomogenities can be covered which derive probably from one single nucleosynthetic event. These condensates are the best source of information of protosolar element- and isotopic-compositions [1]. The explanation of these anomalies can also be received if the nuclear properties of its instable progenitors are understood. It could be shown already in earlier investigations that the β-delayed neutron emission of neutron rich progenitor isotopes influence directly the isotopic abundance of $^{48}Ca/^{46}Ca$ in the refractory inclusion EK 1-4-1 of the Allende-Meteorite [2].

2   The Experiment

In order to delimit the uncertainties in nuclear-structure properties, already mentioned above, we performed an experiment at the Grand Accelerateur National d'Ion Lourds (GANIL) in Cean, France. In this experiment the gross

nuclear properties $T_{1/2}$ and P_n of the neutron-rich isotopes ^{43}P, ^{42}S, ^{44}S, ^{45}S, ^{44}Cl, ^{45}Cl, ^{46}Cl and ^{47}Ar could be measured. The isotopes were produced by the methode of projectile fragmentation. The separation of the fragments was done by the use of LISE3 spectrometer. Our detector-system was a β-telescope consisting of three silicon detectors with a thickness of 300 μm for the first and the second detector and 5500 μm for the third one. This β-telescope was placed at the end of the beam tube. It was surrounded by the neutron detector consisting of a polyethylen moderator where 60 ^{3}He-tubes were placed in three concentrical rings. The β-telescope delivered the ΔE1, ΔE2 and the E3 signal. With the complete detector system single β- and neutron events, and β-neutron coincidences could be observed. The experimental setup and the identification of the isotopes are described in detail in [3].

In this experiment half-lives and P_n-values of the isotopes ^{43}P, ^{42}S, ^{44}S, ^{45}S, ^{44}Cl, ^{45}Cl, ^{46}Cl and ^{47}Ar were measured. The half-lives of ^{44}S, ^{45}Cl and ^{46}Cl which were already obtained in an earlier experiment could be confirmed. The experimental results are outlined in Tab. 1.

3   Deformations from a QRPA Parameter Study

One of the motivating questions for the parameter study was to get at least a

Tab. 1 QRPA-calculation of $T_{1/2}$ and P_n with an optimized quadrupole deformation ε_2 of the investigated nuclei. In column 2 the quadrupole deformation is given which leads to the best agreement between the calculated $T_{1/2}$- and P_n-values (columns 3 and 4) and the experimentaly observed values (columns 5 and 6).

Isotop	ε_2	optimized adjustment		experimental values	
		$T_{1/2}$[ms]	P_n[%]	$T_{1/2}$[ms]	P_n[%]
^{43}P	$-0,175$	70	100,0	36 ± 4	100 ± 10
^{42}S	$-0,300$	1300	0,9	579 ± 46	<4
	$+0,300$	1570	0,1		
^{44}S	$+0,325$	133	15,3	123 ± 10	18 ± 3
^{45}S	$-0,200$	83	39,8	72 ± 5	54 ± 6
	$+0,125$	90	36,7		
^{44}Cl	$-0,250$	434	1,8	438 ± 19	<8
^{45}Cl	$-0,200$	392	10,4	412 ± 39	38 ± 5
^{46}Cl	$+0,100$	204	57,9	223 ± 37	60 ± 9
^{47}Ar	$-0,180$	705	0,1	613 ± 197	<1
	$+0,125$	709	0,1		

first idea of the nuclear shape of the investigated nuclei. The nuclei examined in this work, contain 15 to 18 protons and 26 to 29 neutrons. In this low mass region the single-particle levels do not have a high density in the Nilsson-diagram. The energy distance is about 1-5 MeV. This leads to the fact that there are only a few Gamow-Teller transitions possible. $T_{1/2}$ and P_n are dominated by one or two strong transitions in the corresponding energy interval. Thus the investigated correlation between the gross β-decay properties and the nuclear shape of the corresponding nuclei is unambiguous at least in the fundamental decision whether the nucleus is spherical or deformed. If heavier nuclei are examined this is certainly not the case due to the high level-density (approx. 10 levels per MeV).

In the detailed parameter study $T_{1/2}$ and P_n were calculated as a function of the quadrupole deformation ε_2. The ε_2-values were varied from -0.35 to 0.35. Starting from the FRDM-model prediction ^{44}S should be spherical. This would lead to the gross β-decay properties $T_{1/2} = 1.12$ s and $P_n = 100\%$. However, since the first GANIL experiment in 1991 we know: $T_{1/2} = (123\pm10)$ ms, $P_n = (18\pm3)\%$ [4]. The discrepancy concerning the half-live is a factor of 10, the P_n-value is a factor of 5 less than in the prediction. A spherical shape of the nucleus ^{44}S can be excluded. Good agreement with the experimentally observed values is reached if a prolate deformation of $\varepsilon_2 = 0.325$ is assumed: $T_{1/2} = 133$ ms, $P_n = 15.3\%$. Similar results are obtained for other investigated nuclei. Tab. 1 summarizes the quadrupole deformation which leads to the best agreement with the experimentally observed values. For ^{42}S, ^{45}S and ^{47}Ar it can not be determined whether the shape is prolate or oblate deformed. For ^{42}S the absolute value is the same for both possible deformations, $|\varepsilon_2| = 0.300$. Meanwhile an experiment at Michigan State University (MSU) was performed where the B(E2)-values of $^{36-44}$S were measured via Coulomb-exitation [7]. The absolute value of the quadrupole deformation can be determined directly from the B(E2)-values. The deformation values obtained from the parameter study for ^{42}S and ^{44}S are in excellent agreement with the experimentally observed ones. Although in the experiment no information of the sign is given. For the calculation of the neutron-capture cross sections only the absolute deformation value is needed due to the equally increasing level-density.

For ^{45}S we get a prolate and an oblate value which both reproduces the experimental results. The values differ a bit. The prolate value is in agreement with the RMF-prediction [5]. The QRPA-calculation of ^{47}Ar reaches good agreement with the experimental values for ε_2=-0.180 and +0.125.

4 Network calculations

Important input data in the calculation of nucleosynthesis are neutron-capture cross section (σ_n). Typical astrophysical neutron energies favor two reaction mechanisms [6]: (i) capture reactions where a *compound nucleus, CN* is created. Cross sections will be calculated by the use of the statistical model of Hauser-Feshbach; and (ii) reactions where a neutron is directly captured into bound states (*direct capture, DC*). The DC-mechanism can dominate the neutron-capture for nuclei with low lying level density in the vicinity of the neutron separation energy. This is especially the case for even-even nuclei because here the level density is lower compared to in nuclei with one or two unpaired nucleons. Thus in addition to the CN-cross sections the DC-contribution of the even-even nuclei from ^{40}S to ^{74}Fe were calculated [6].

Nucleosynthesis in the late phase of a massiv star is dominated by neutron capture reactions. The process paths as well as the development of the star can be calculated by computers nowadays. The reliability of such calculations depends on nuclear properties of the involved isotopes. Thus, in our calculations of nucleosynthesis all nuclear input data such as energy-levels, neutron-separation energies, spin and parity, nuclear shape, neutron-capture cross sections and decay-properties were taken into account. If available experimental data were used; if not, the input data were calculated by the use of *internally consistent* models. In this work we tried to find a process which synthesises much ^{48}Ca, ^{50}Ti and ^{54}Cr. The deduced stellar parameters, especially neutron density (ρ_n), radiation-entropy $(S \propto T_9^3/\rho)$ and time scale of the process (τ), point out the possible astrophysical scenarios.

In the late phase of massiv stars rapid neutron capture can occur. But first of all, due to the high temperatures $T_9 \geq 3$, reactions with charged particles such as (p,γ), (p,n), (α,n) and (α,γ), the reverse reactions, β^+-decay and electron capture take place. Due to that the computer-code is organized in two steps. The network which calculates the reactions with charged particles in the so called α-*process* is developed by F.-K. Thielemann and extends from H to Pd (Z=46). On the neutron-rich side all nuclei up to the neutron-drip line are included. On the proton-rich side the first three isotopes beginning from β-stability are taken into account. After the calculations in the α-process, further calculations will be performed with the r-process code from C. Freiburghaus. This makes sense if there exits one or more free neutrons per seed-nuclei $(Y_n/Y_{seed} \leq 1)$. A detailed description of the physical processes and the requested system of equations is given in [8]. The r-process calculations are fully dynamical and do not make use of the (n,γ)-(γ,n) equilibrium

as former calculations did.

4.1 Reproduction of the Isotopic-Ratios

In this work the network-calculations were applied to find out if the observed isotopic anomalies can be reproduced. During the process the stellar temperature varies from $T_9 \simeq 9$ to 2.6. As electron abundances $Y_e = < Z/A >$ in the astrophysical scenario the values 0.42, 0.45 and 0.48 were choosen. In Fig. 1 the abundance ratios for ^{48}Ca/^{46}Ca, ^{48}Ca/^{50}Ti and ^{48}Ca/^{54}Cr at $Y_e = 0.42$ are displayed. The entropy is varied from $S = 3$ to 300 k$_B$/Baryon. The dashed lines represent the values observed in EK 1-4-1.
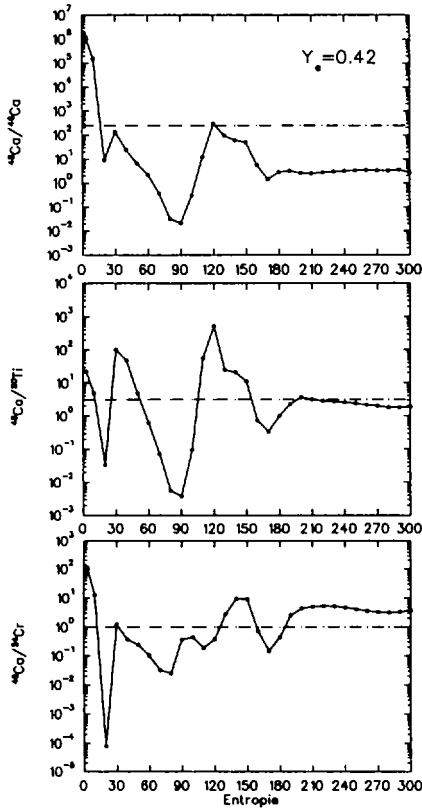
Fig. 1 Calculated isotopic-ratios dependent on entropy. The Y_e-value equals 0.42.
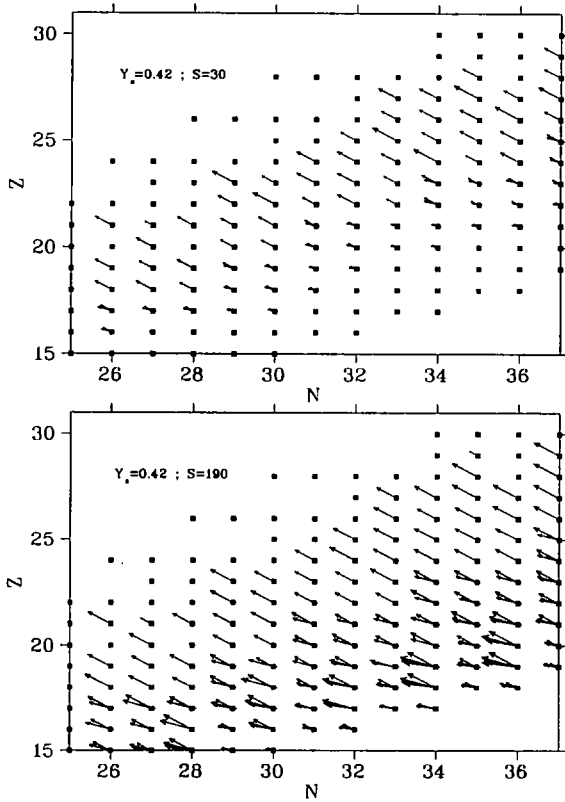
Fig. 2 Flow-charts obtained from the r-process calculations. Shown is the status after neutron-capture just before the different decay-modes start.

The isotopes ^{48}Ca, ^{50}Ti and ^{54}Cr are the most neutron-rich ones observed in the corresponding isotopic chain. Plotted are the ratios ^{48}Ca/^{46}Ca, ^{48}Ca/^{50}Ti and ^{48}Ca/^{54}Cr, because they represent the most sensitive test for the reproduction of the anomalies. In solar matter normaly less neutron-rich isotopes of each isotopic chain were mostly produced due to the homogenization. A simultaneous reproduction of the observed abundance ratios is obtained at the entropies $S = 30$, 130 and 190 k_B/Baryon.

In Fig. 2 the flow charts with the electron abundance $Y_e = 0.42$ and two different entropies $S = 30$ (upper part) and $S = 190$ (lower part) are shown. The figures are a snapshot where the most neutron-rich isotopes in each chain are

- 312 -

reached just before the different decay-modes start (β-decay, β-delate emission of one, two or more neutrons). In the plots this is marked with the corresponding arrows. Fig. 2 shows that a higher entropy leads to more neutron-rich isotopes. This makes sense, because at high entropies the alpha-rich freeze-out leaves more neutrons, which can be captured.

4.2 Possible Astrophysical Scenario

As astrophysical scenario for this type of nucleosynthesis a type II supernova can be considered. At the entropy $S \simeq 30$ k_B/Baryon the isotopes are synthesized in a process of α-rich freeze-out. ^{48}Ca is built directly without significant neutron captures. The observed anomalies are also obtained with entropies of $S \simeq 150$ and 190 k_B/Baryon. In this case ^{48}Ca is generated by β-decay of ^{48}Ar. The astrophysical location in these cases is presumably the outer core of a type II supernova. Typical values for the produced masses with $S = 150$ k_B/Baryon are 1×10^{-10} $M_{\odot}$ for ^{46}Ca, 4×10^{-8} $M_{\odot}$ for ^{48}Ca, 2×10^{-9} $M_{\odot}$ for ^{50}Ti and 3×10^{-8} $M_{\odot}$ for ^{54}Cr. This is about 2 to 3 orders of magnitude less than in a type Ia supernova. In addition type II supernovae events are approximately 10 times more seldom than type Ia supernovae. All together the contribution of produced and ejected matter on type II supernovae is a factor 10^3 till 10^4 less than via type Ia supernova scenarios and therefore not sufficient to generate the solar ^{48}Ca, ^{50}Ti and ^{54}Cr. The majority of the solar matter is built in SN Ia. This is in agreement with [9]. However, the amount of matter ejected by type II supernovae is enough to explain the observations in EK 1-4-1. First evidence that the outer core of a type II supernova can be considered as astrophysical scenario, is already mentioned in [10].

5 Summary

The parameter study showed clearly that the experimentally observed $T_{1/2}$- and P_n-values can only be reproduced when significant quadrupole-deformation is assumed. The nuclear shape and therefore ist locations of the single-particle levels are crucial nuclear physics input-parameters for r-process calculations. Due to this, it is a challenge to observe quadrupole deformation via Coulomb excitation. First experiments showed already that this is nowadays possible. Further the flow chart of each nucleosynthesis calculation gives information about the isotopes involved. The comparison with the observed abundance pattern leads to isotopes whose decay properties are especially worth to be investigated by experimentalists. The better the process paths can be deter-

mined owing to the nuclear physics parameters the more exact statements of stellar temperature, neutron density and entropy can be made. A detailed investigation of these correlations and therefore of the chemical evolution in SN Ia and SN II is of interest.

6 Acknowledgement

References

[1] U. Ott, Nature **364** (1993) 25

[2] W. Ziegert, PhD-Thesis, University of Mainz, 1985

[3] W. Böhmer, PhD-Thesis, University of Mainz, 1996

[4] O. Sorlin et al., Phys. Rev. C47 (1993) 2941

[5] T. R. Werner et al., Phys. Lett. B333 (1994) 303

[6] T. Rauscher et al., Proceedings ENAM, Arles (1995)

[7] T. Glasmacher et al., Phys. Lett. B 395 (1997) 163

[8] C. Freiburghaus, Diploma-Thesis, University Basel, 1995

[9] B. S. Meyer et al., Ap. J. 462 (1995) 825

[10] K.-L. Kratz et al., Physikalische Blätter 51 (1995) 183

ESTIMATED PRODUCTION OF ISOTOPES APPROACHING THE R-PROCESS PATH

J. BENLLIURE, F. FARGET, A. GREWE, M. DE JONG,
K. -H. SCHMIDT and S. ZHDANOV

Gesellschaft für Schwerionenforschung (GSI)
Postfach 110552, D-64220 Darmstadt, Germany

Abstract

The production and study of the nuclei involved in the r-process is fundamental for the full understanding of the heavy-element synthesis. In this work we describe the results of a model calculation on the possibility to extend the limits of the chart of the nuclides towards the neutron-rich side. In particular, we make quantitative predictions for the production rates which will be reached after the intensity upgrade of the GSI accelerator complex.

1 Introduction

The absence of experimental information on the nuclei involved in the r-process is one of the main limitations for the understanding of the solar-system r-abundance distribution. The first difficulty of this experimental study is the production of such neutron-rich isotopes. Experiments performed at GSI [1, 2] have shown that it is possible to produce isotopes approaching the r-process path in the region of light fission fragments by means of inverse kinematic heavy-ion collisions at relativistic energies.

Two reaction mechanisms are responsible for the production of very neutron-rich isotopes, namely projectile fragmentation and fission which populate different regions in the chart of the nuclides. On one hand, fission populates the neutron-rich side of the β-stability valley, while the maximum of the fragmentation process is situated at the neutron-deficient side. On the other hand, the width of the mass distribution of isotopes produced by fragmentation is much larger than that produced by fission. Thus, the full understanding of both processes is needed to conclude about the production of isotopes approaching the r-process path.

Using a modern version of the abrasion-ablation model [3] which includes a detailed description of the fission process [4] we discuss the production of these neutron-rich isotopes and the expected yields for both, fragmentation and

fission, taken into account the present limitations and future developments on beam intensities.

2   The model

Heavy-ion reactions at relativistic energies can be described as a two-steps process consisting of a fast interaction between the projectile and the target and the subsequent deexcitation of the reaction products. The initial stage can be described by a Glauber-type model where only the nucleons in the overlapping region between the projectile and the target, the "participant" interact strongly, while nucleons in the non-overlapping zone, the "spectator", continue to move almost undisturbed. The mass of the spectators is a function of the impact parameter [3]. Their mean excitation energy of about 27 MeV per abraded nucleon is given by hole excitations and interactions with the hot participant zone [5]. At larger impact parameters without nuclear contact, electromagnetic excitations are considered.

The second stage of the reaction is treated in the framework of the statistical model. The emission probability of a particle is calculated using the Weisskopf formalism.

We use a simplified approach, similar to the one proposed in ref. [6], to estimate the production yields of very neutron-rich nuclei. Excited nuclei with large neutron excess almost exclusively deexcitate by evaporating neutrons; they have a negligible probability to emit protons or other charged particles. Therefore, in the deexcitation phase leading to the production of very neutron-rich projectile fragments, only neutron evaporation is considered. In this way, the computing time could be reduced many orders of magnitude, allowing to estimate very low production cross sections.

The fission decay width in the statistical deexcitation has been included according to the transition-state method of Bohr and Wheeler [7].

We introduced also a semiempirical description of the fission-fragment properties taking into account the influence of nuclear structure on the fission process. The model is supposed to be able to predict the magnitudes and widths of the different fission channels (symmetric and asymmetric), the even-odd fluctuations and the neutron-to-proton ratio of the fission-fragment distributions as a function of nuclear charge, mass and excitation energy of the fissioning nucleus in a global way. A more detailed description of the model can be found in ref. [4].
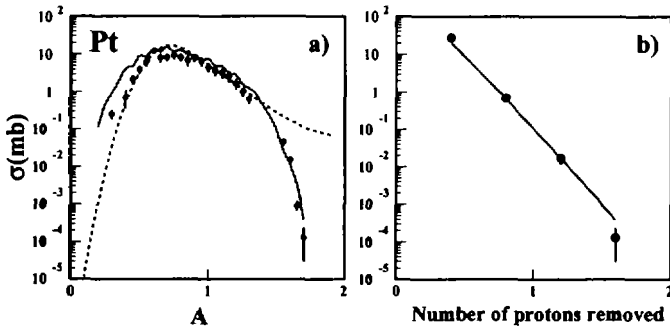
Figure 1: *Isotopic production cross sections obtained in the reaction Pb(1 A.GeV)+Cu (circles) from ref.[8]. a) Cross sections for Pt isotopes compared with the result of the abrasion-ablation model (solid line) and the EPAX formula (dashed line). b) Cross sections of the proton removal channel for the same reaction.*

3   Results on production rates by fission and fragmentation reactions.

A complete calculation with this model allows us to predict the complex nuclide distribution resulting from peripheral relativistic heavy-ion collisions. In order to illustrate the different reaction mechanisms contributing to these distributions we have compared existing experimental data with our calculations.

In figure 1 we report the production cross sections of Pt isotopes (a) and the proton-removal cross sections (b) obtained in the reaction Pb(1 A.GeV)+Cu [8]. These data are compared with our model calculations and the EPAX formula [9]. The discrepancy for very neutron-rich isotopes between the data and the EPAX calculation shows that this formula does not correctly reproduce the cold fragmentation. In contrast, the abrasion-ablation model shows a fair agreement with the data even for the most neutron-rich isotopes. The predictions of the present model closely compare also with the cross sections of the proton-removal channels(b), indicating a realistic description of the cold fragmentation process which is dominant in the production of very neutron-rich isotopes.

Fig. 2 shows the variation of the mass distribution and the N/Z ratio, of Zr isotopes, for fission of ^{238}U at different excitation energies. When increasing
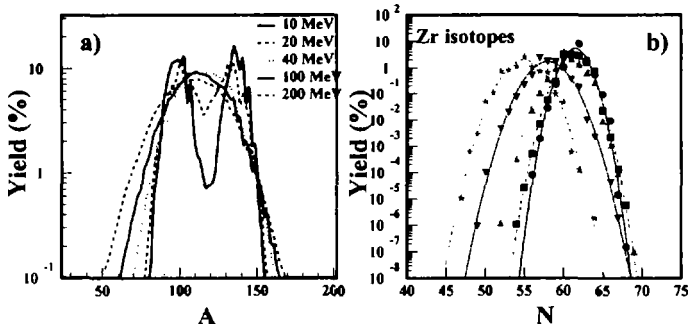
Figure 2: *Mass distribution of fission fragments (a) and N/Z ratio of Zr iso-topes (b) produced from ^{238}U fission at different excitation energies. The steps in excitation energy are the same in both cases.*

the temperature, the mass distribution broadens considerably, leading to dras-tically increased production rates of very light and heavy fission fragments. The width of the isotopic distribution grows also when increasing the exci-tation energy. However, due to neutron evaporation, the neutron-rich side is almost independent of energy up to about 100 MeV.

In order to compare the isotopic distributions produced by fission and frag-mentation, in figure 3 we report the calculated Zr isotopic distribution in the induced fission of ^{238}U in a beryllium target (triangles and solid line) and in the projectile fragmentation of ^{136}Xe in an aluminium target. In this picture, the open squares represent experimental production cross sections of Zr fission fragments measured in the reaction ^{238}U+Be [2]. The fair agreement between the measured and calculated production cross sections of fission residues in-dicates that the proposed model gives a good description of the N/Z ratio of fission residues. As we have already seen, this ratio together with the width of the fission-fragment mass distribution determines the population of neutron-rich isotopes by fission. From this picture, we can conclude that the fission mechanism allows to produce high intensities of moderately neutron-rich iso-topes. However, the fragmentation process dominates the production of very neutron-rich isotopes, in particular those involved in the r-process path, as indicated in the picture.
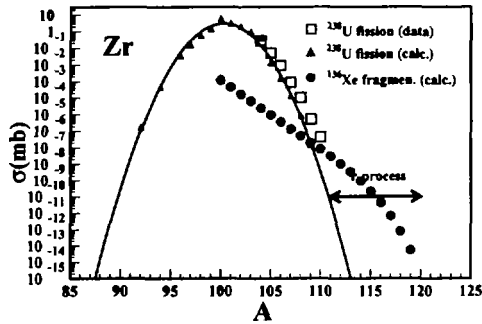
Figure 3: *Production cross sections of Zr isotopes produced by fission of ^{238}U (solid line) and fragmentation(full circles) in the reaction $^{136}Xe(1\ A.GeV)+Al$. The fission production cross sections are compared with experimental data obtained in the reaction $^{238}U(750\ A.MeV)+Be$ [2] (open squares).*

4 Future perspectives on the production of neutron-rich secondary beams at GSI.

Inverse-kinematic reactions at relativistic energies seem to be a very promising tool for the production of very neutron-rich isotopes. The choice of different projectiles allows to profit from the advantages of fission and fragmentation reaction mechanisms.

We have estimated the expected production rates of neutron-rich isotopes taking into account the final primary-beam intensities delivered by the SIS synchrotron at GSI after the intensity upgrade. The results of these calculations are shown in figure 4. In this picture, the different hatched areas represent different production rates of neutron-rich isotopes ranging from 200 ions/s till 10 ions/day, as indicated in the scale. Calculations were performed assuming a primary-beam intensity of $2\ 10^9$ ions/s and a 1.5 g/cm^2 thickness Al target for fragmentation and a Be target for fission, respectively.

The predictions of the proposed model show that the r-process path can be reached for a large number of nuclear species with production rates about 100 ions/week by using different projectiles. ^{238}U fragmentation seems to be the only chance to approach the r-process at the waiting point around A=195, while ^{176}Yb and ^{136}Xe fragmentation can compete with ^{238}U fission to approach the r-process at the waiting point around A=130.

Perspectives on the production of neutron-rich nuclei at GSI
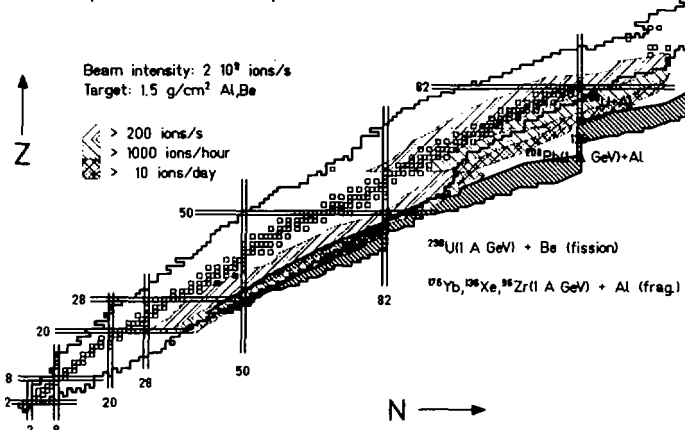
Figure 4: *Calculated production rates of neutron-rich isotopes obtained with primary beam intensities available after the intensity upgrade of GSI. The predictions are given in three different regions with different projectile-target combinations. The neutron-deficient limit in the calculations is determined by the maximum of the production rate.*

5   Conclusion.

We conclude that fission is an efficient reaction type to produce high-intensities of moderately neutron-rich isotopes in the mass region of fission products. Projectile fragmentation reaches further to the neutron-rich side, however, with very low production cross sections. Nontheless, projectile fragmentation seems to be the most promising tool for extending our knowledge on nuclear properties when approaching the neutron drip line. The primary-beam intensities are decisive for the limits to be in reach.

References

[1] M. Bernas et al., Phys. Lett. B 331 (1994) 19
[2] M. Bernas et al., to be published in Phys. Lett. B
[3] J.-J. Gaimard, K.-H. Schmidt, Nucl. Phys. A 531 (1991) 709
[4] J. Benlliure et al.,to be published in Nucl. Phys. A
[5] K.-H. Schmidt et al., Phys. Lett. B 300 (1993) 313
[6] K.-H. Schmidt et al., Nucl. Phys. A 542 (1992) 699
[7] N. Bohr, J.A. Wheeler, Phys. Rev. 56 (1939) 426
[8] M. de Jong et al, to be published in Nucl. Phys. A
[9] K. Sümmerer et al., Phys. Rev. C42 (1990) 2546

UNCERTAINTIES IN THE SOLAR SYSTEM r-ABUNDANCE DISTRIBUTION

S. GORIELY

Institut d'Astronomie et d'Astrophysique
Université Libre de Bruxelles, Campus Plaine, CP 226
B-1050 Bruxelles, Belgium

Abstract

The solar system r-abundance distribution is commonly derived from the observed solar values by subtracting the possible nucleosynthetic contribution of the s-process. A new model of the s-process called the canonical multi-event model is used to derive the s-component of the solar abundance distribution and to study the impact of nuclear and observational uncertainties on the solar r-abundance distribution.

1 Introduction

The slow neutron-capture process (or s-process) and the rapid neutron-capture process (or r-process) are known to be the 2 major nucleosynthetic mechanisms responsible for the production of the elements heavier than iron observed in nature. Though both processes invoked neutron captures on light seed nuclei to produce the heavy elements, they take place in completely different astrophysical environments and on very different timescales. About 30 nuclei, called s-only isotopes, are exclusively synthesized during the low-neutron-densities ($N_n \simeq 10^8 \mathrm{cm}^{-3}$) events characteristic of the s-process. Most of the neutron-rich stable isotopes cannot be produced by the s-process and the high neutron densities ($N_n \gtrsim 10^{20} \mathrm{cm}^{-3}$) found in the r-process are called for to explain their origin. In addition to these s-only and r-only nuclei, a large number of stable isotopes (called sr-isotopes) are potentially produced by both processes. In order to understand these 2 very different nucleosynthetic mechanisms, it is of first importance to decompose the observed solar system abundance distribution into its s- and r-components. To do so, the s-contribution is obtained by fitting parametric s-process models to the abundance of the s-only isotopes. Such a fit defines the s-component of the sr-nuclei, and consequently the solar r-abundance distribution by a simple subtraction of the s-contribution from the observed solar values.

For this specific purpose, fully parametric s-process models, free of all astrophysical constraints, have been introduced. The most popular of these parametric models, well-known as the classical s-process model, is based on the original canonical model of [1] which assumes that some stellar material composed of iron nuclei only is subjected to neutron densities and temperatures that remain constant over the whole time scale of the neutron irradiation. In addition, the classical model assumes that the solar s-element composition results from a superposition of exponentially decreasing neutron exposures (for a review, see [2]).

However, when dealing with the separation of the s- and r-components of the solar abundances, the reliability of the classical model naturally comes to mind. Obviously, the solar s- and r-abundance distributions are affected by uncertainties related to observational data, but also with theoretical shortcomings inherent to the classical s-process model. In particular, the fundamental assumptions made in the classical model regarding the exponential form of the exposure distribution can be questioned. In order to test the influence of this assumption, a new s-process model has been developed[3]. This so-called multi-event s-process is reviewed in Sect.2 and compared with the classical model predictions. In Sect.3, the uncertainties related to imprecise observed abundance data and inaccurate experimental or theoretical (n, γ) rates of relevance in the s-process nucleosynthesis are discussed. Their impact on the solar r-abundance distribution is analysed.

2   The multi-event s-process model

The canonical multi-event s-process is defined as a superposition of a given number of canonical events taking place in different thermodynamic conditions. Each canonical event is characterized by a given neutron irradiation on the ^{56}Fe seed nuclei during a time t at a constant temperature T and a constant neutron density N_n. The combination of s-process events that provides the best fit to the solar abundances is derived with the aid of an iterative inversion procedure described in [3]. In contrast to the classical model which assumes a superposition of exponentially decreasing exposures, the multi-event model makes no hypothesis concerning any particular predefined exposure distribution. By considering a set of astrophysically plausible events, an optimized s-abundance curve is derived by the iterative inversion method, along with the corresponding exposure distribution. For each event, a full network calculation including 640 nuclei between Cr and Po is solved to derive the abundances. The latest experimental neutron capture cross sections are used.
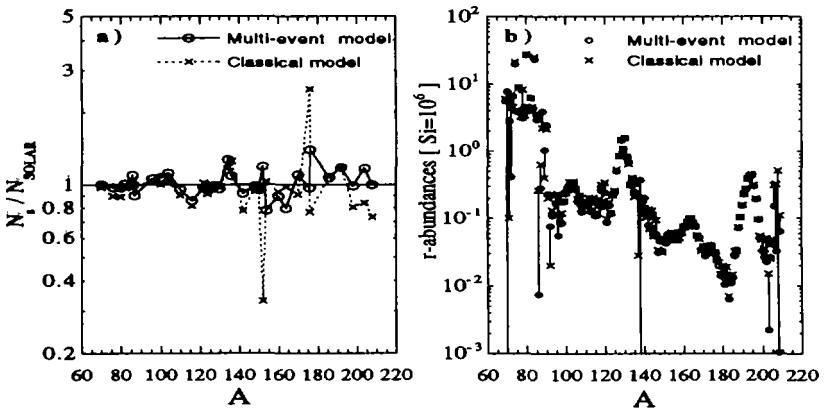
Figure 1:   a) Ratio of the calculated s-abundances to the solar value for the s-only isotopes. Circles corresponds to the multi-event model predictions and crosses to the classical fit [7]. b) Comparison of the solar r-abundances deduced from the multi-event (circles) and classical (crosses) models.

When not available, the cross sections are calculated within an updated statistical Hauser-Feshbach model called MOST[4].

For a given set of nuclear physics data, two degrees of freedom appear in the multi-event approach, namely the range of allowed thermodynamic conditions and the set of nuclei the inversion method is supposed to fit (or equivalently the set of nuclei the s-process is expected to produce). With respect to the set of nuclei the s-process should produce in solar abundances, it seems clear to consider the s-only nuclei which cannot be produced by any other known nucleosynthetic process. The solar abundances are taken from [6], and for comparative purposes we consider the classical model prediction of [7]. As regards the astrophysical conditions in which the s-process events are allowed to take place, we consider temperatures in the $1.5 \leq T[10^8\text{K}] \leq 4$ range and neutron densities in the $7.5 \leq \log N_n[\text{cm}^{-3}] \leq 10$ range. Each of the 121 (T_8, N_n) events evenly distributed in grid steps of 0.25 in $T[10^8\text{K}]$ and $\log N_n[\text{cm}^{-3}]$ are assumed to take place at 40 different irradiation times.

Figure 1a shows that an excellent fit to the solar system abundances of the s-only nuclei can be obtained with the multi-event model. The multi-event predictions are also in good agreement with the classical model [7]. The residual r-abundances calculated within the multi-event model are compared with

the classical model predictions in Fig.1b. Non-negligible deviations can be seen for $A \lesssim 90$ and $A \gtrsim 204$ nuclei. This result is to be expected, because of the difficulty for the classical model reliably to determine the characteristic neutron exposures of the weak and strong components. As regards the solar r-abundances in the $90 \lesssim A \lesssim 204$ range, both models globally predict the same abundance distribution, although some small differences are observed for the $A \simeq 120, 140, 180$ nuclei. These so-called s-dominant nuclei are significantly synthesized by the s-process, and their resulting residual abundances are consequently affected by small modifications in the s-process modelling. More generally, the r-abundance of all the s-dominant nuclei is expected to be very sensitive to uncertainties in the nuclear physics and astrophysical modelling of the s-process, as well as in the observational data. The multi-event s-process model is particularly well suited to an analysis of the impact of such uncertainties on the solar r-abundance distribution. As a matter of fact, it offers the advantage of determining, for a given input, the best fit to the abundances of the s-only isotopes. Through the iterative inversion procedure, a modification of the input parameters automatically leads to a renormalization of the thermodynamic conditions required to fit the s-only abundances.

3   Uncertainties in the solar r-abundance distribution

Different types of uncertainties affect the determination of the solar r-abundance distribution. First, the quality of the observational data is inevitably influenced by the spectroscopic or physico-chemical peculiarities of each species [6]. In particular, three specific elements still raise severe problems. These are the non-observable Kr, Xe and the ill-detectable Hg. To calculate the impact of such uncertainties on the solar r-abundances, we consider the multi-event calculations described in the previous sections when a random selection is made among the upper and lower limits of each solar value [6]. Such a procedure is performed 10 times in order to pick out a representative sampling. The resulting uncertainties in the calculated r-abundance distribution are illustrated in Fig.2a as error bars around the standard calculation of Sect.2.

Second, nuclear uncertainties in the s-process model could also influence the r-abundance distribution. These concern mainly the estimate of the neutron capture and β-decay rates. Although all the β-decay rates of relevance in the s-process modelling are known in terrestrial conditions, the contribution of thermally populated excited states, as well as atomic effects in the strongly ionised stellar plasma can drastically modify the laboratory value [5]. The calculated β-rates in stellar environments are subject to nuclear uncertainties
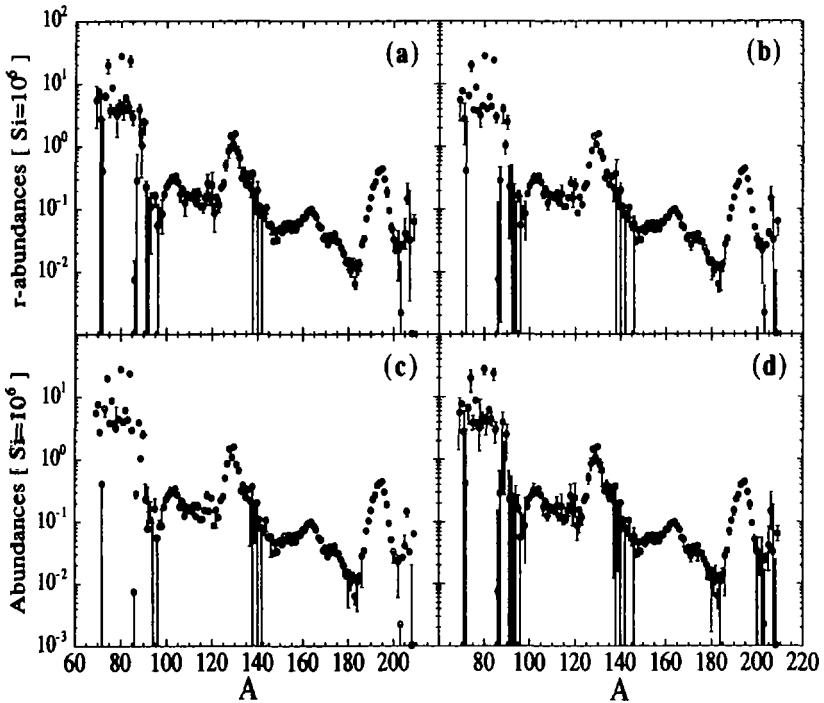
Figure 2: Uncertainties in the solar r-abundance distribution due to uncertain a) observational data, b) experimental (n,γ) rates, c) theoretical (n,γ) rates. (d) corresponds to the cumulative effects of uncertainties a), b) and c).

which remain difficult to estimate systematically. For this reason, the study of β-decay uncertainties are postponed to a future work. As regards the neutron capture rates, effects due to experimental and theoretical imprecision were studied separately. First, multi-event calculations were reiterated allowing for various random changes of the experimental (n,γ) rates within the prescribed error bars (note that the thermalization effects were systematically included, but not added to the experimental uncertainties at this stage). The resulting effects on the solar r-abundances are illustrated in Fig.2b. Similarly, tests were conducted with the recommended experimental data, but when not available, with (n,γ) rates predicted by an older version of the Hauser-Feshbach code (called SMOKER [8]) and based on a different descriptions of the nuclear struc-

ture input. The impact of the remaining uncertainities in the experimentally unknown (n, γ) rates on the r-abundances is shown in Fig.2c.

Finally, observational and nuclear uncertainties in the s-process calculations are studied simultaneously. Their impact on the r-abundances is shown in Fig.2d. As summarized by Fig.2d, the solar r-abundances can be considered as relatively well determined around the r-only isotopes corresponding to the $A \simeq 130$ and $A \simeq 195$ peaks and the $A \simeq 160$ hill. Unfortunately, the uncertainties in observational data and nuclear input of the s-process modelling still affect our predictions of the r-contribution to the abundance of the s-dominant nuclei, i.e. the $A \simeq 90, 120, 140, 180$ and 200 regions. Moreover, it should be recalled that other uncertain factors in the s-modelling have not been considered here and could also exert influence on the separation of the solar s- and r-components. These mainly concern nuclear uncertainties in the β-decay rates and most of the assumptions inherent to the canonical s-process model, i.e. the seed abundance distribution, the range of thermodynamic conditions to be considered and the time-independent thermodynamic profiles.

References

[1] E.M. Burbidge, G.R. Burbidge, W.A. Fowler, F. Hoyle, Rev. Mod. Phys. **29** (1957) 547;

[2] F. Käppeler, H. Beer, K. Wisshak, Rep. Prog. Phys. **52** (1989) 945;

[3] S. Goriely, A&A **327** (1997) 845;

[4] S. Goriely, in: Proceedings of the International Conference on Nuclear Data for Science and Technology, Trieste (Italy), 1997, in press;

[5] K. Takahashi, K. Yokoi, ADNDT **36** (1987) 375;

[6] E. Anders,N. Grevesse, Geochim. Cosmochim. Acta **53** (1989) 197;

[7] H. Palme, H. Beer, in: Landolt Börnstein, New Series, Group VI, Astronomy and Astrophysics, Subvolume 3a, Springer, Berlin, (1993), 196;

[8] F.-K. Thielemann, M. Arnould and J.W. Truran, in: E. Vangioni-Flam et al. (eds.) Advances in Nuclear Astrophysics, Editions Frontières, Gif-sur-Yvette (1986) p. 525.

(n,γ) AND (p,γ) RATES FOR
s- AND p-PROCESS NUCLEOSYNTHESIS

F. KÄPPELER

Forschungszentrum Karlsruhe, IK-III,
Postfach 3640, D-76021 Karlsruhe, Germany

Abstract

The late stages of stellar evolution are characterized by a series of nu-
cleosynthesis events. With respect to the heavy elements, these are
the s process associated with the helium burning layers in Red Giant
stars as well as the r and p processes which occur in supernova explo-
sions. In contrast to the explosive scenarios, the nuclear physics data
for s-process studies can be determined in laboratory experiments as
illustrated at few recent examples. The application of these techniques
to measurements of relevance for the p process are also discussed.

1   Nucleosynthesis between Fe and the Actinides

In realistic astrophysical scenarios charged particle reactions are not contri-
buting to the formation of the elements in the mass range A>60 due to the
increasing Coulomb barriers and the decreasing binding energies. Therefore,
the origin of the heavy elements must be ascribed to neutron capture reactions.
The characteristic features of the observed abundance distribution between
iron and the actinides [1] require essentially three processes: The dominating
mechanisms are the slow and the rapid neutron capture processes (s and r
process), each accounting for approximately 50% of the heavy element abun-
dances, while the p process adds the rare proton rich nuclei.

The s process is associated with stellar helium burning where relatively low
neutron densities imply neutron capture times of the order of several months,
much longer than typical β–decay half–lives. Therefore, the s–process path
follows the stability valley, and the resulting s abundances are inversely pro-
portional to the respective (n,γ) cross sections. In contrast, the r and p proces-
ses are related to explosive scenarios, presumably to supernovae (SN). In these
cases, the reaction paths are driven off the stability valley where experimental
data are extremely difficult to obtain. Correspondingly, the synthesized mate-
rial consists of short–lived nuclei, which decay back to the stability valley after
the explosion.
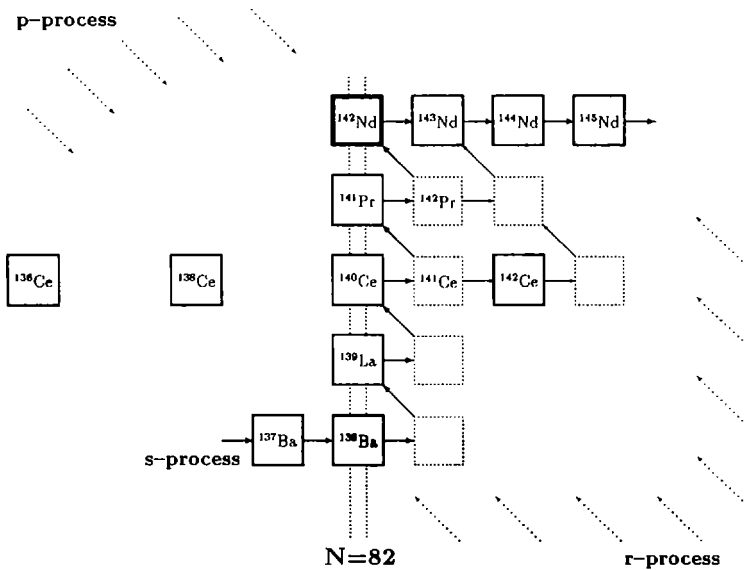
Fig. 1. Reaction flows and abundance contributions in the mass region between Ba and Nd.

The various reaction paths are sketched in Fig. 1. The s–process flow is shown by the solid line connecting the nuclei in the stability valley whereas the r and p contributions are schematically indicated by dotted arrows. Obviously most isotopes received abundance contributions from both main mechanisms, the s and the r process. But there are pure s isotopes – e.g. ^{142}Nd in Fig. 1 – which are shielded by stable isobars against the r–process β–decays. On the other hand, there is also an ensemble of r–only nuclei that are not reached by the s process because of their short–lived neighbors. The abundances of these two subsets represent the most crucial test for the various nucleosynthesis models.

Compared to the clear signatures from the two main processes, the p abundances represent only a few % of the s and r components. Therefore, the p-abundance features are much less pronounced.

The following discussion in Section 2 deals with the s process, which is more easily accessible to laboratory experiments and which can be studied by stellar models and astronomical observations as well [2]. Contrary to the s process, the experimental basis for the p process is extremely limited. First attempts for measurements in this context are addressed in Section 3.

2 Neutron Data for the s Process and Astrophysical Implications

2.1 The Karlsruhe 4π BaF$_2$ Detector

The Karlsruhe 4π BaF$_2$ detector is sketched in Fig. 2, showing the setup at the accelerator. The detector consists of 42 individual BaF$_2$ crystals, forming a spherical BaF$_2$ shell of 15 cm thickness and 20 cm inner diameter. The essential features of this detector are a resolution in γ–ray energy ranging from 14% at 662 keV to 6% at 6.13 MeV, a time resolution of 500 ps, and an overall efficiency for capture events of better than 98% (for a detailed description and typical measurements see Refs. [3, 4]).
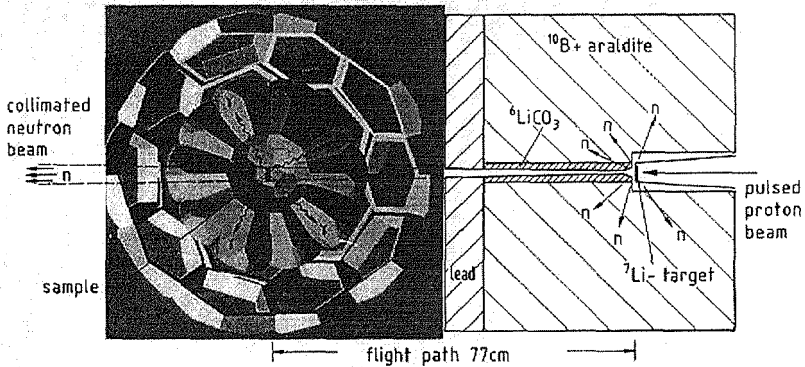
Fig. 2. The Karlsruhe 4πBaF$_2$ detector.

Neutrons are produced by means of a pulsed Van de Graaff accelerator (repetition rate 250 kHz, average beam current 2 μA, pulse width 0.7 ns) via the ^{7}Li(p,n)^{7}Be reaction. The collimated neutron beam hits the sample in the center of the detector at a flight path of 77 cm. Up to 9 samples can be mounted on a vertical ladder. One of these positions holds a gold sample for determining the neutron flux, and two others are used for background determination.

With this detector, differential (n,γ) cross sections are measured by the time-of-flight technique, usually in the neutron energy range from 3 to 225 keV. The stellar cross sections are obtained by folding these differential data, $\sigma(E_n)$, with the stellar neutron spectra for various temperatures. In a recent study of the stable Nd isotopes [5, 6], the Maxwellian averages for the "standard"

thermal energy of $kT=30$ keV could be determined with uncertainties of 1.5% to 2%. These uncertainties are slightly larger than for other REE isotopes [7] due to the unfavorable capture/scattering ratio in the vicinity of the magic neutron number N=82. Among the investigated nuclei, the s-only isotope ^{142}Nd is an important normalization point for the overall s-process abundance pattern.

2.2 The Activation Technique

The activation technique represents an interesting alternative for the determination of stellar (n,γ) rates. Compared to the techniques based on the detection of prompt capture γ-rays, it offers far superior sensitivity (which means that much smaller samples can be measured reliably – an important aspect for the investigation of radioactive isotopes on the s-process path), it is selective via the specific signatures of different reaction products (which means that more than one cross section may be determined using a natural sample), and it is comparably simple. However, this technique is restricted to reactions leading to unstable nuclei, and is also affected by uncertainties of typically 3 to 5%.
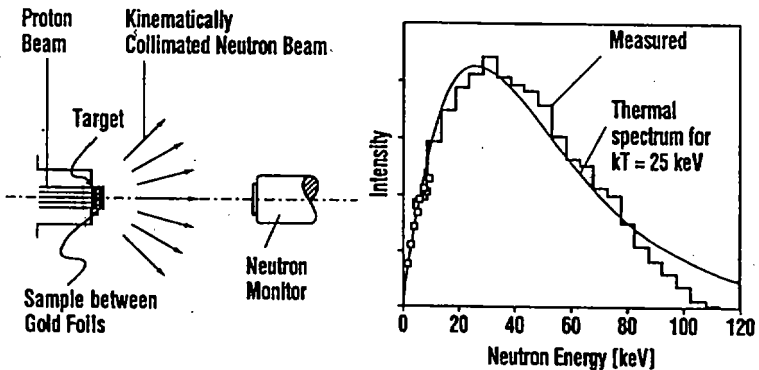
Fig. 3. The activation technique: irradiation of a sample sandwich at the accelerator (left) and the angle-integrated neutron spectrum (right).

The setup for such a measurement is shown in the left part of Fig. 3. The sample is sandwiched between thin gold foils which serve for neutron flux determination, and is directly attached to the neutron target. The neutron yield is continuously monitored during the irradiations by means of a ^{6}Li glass

detector, an option that allows to consider the decay of the induced activity during the irradiation properly.

For this technique it is essential that stellar neutron spectra can be simulated in the laboratory. With the ^{7}Li(p,n)^{7}Be reaction, a continuous energy spectrum with a high–energy cutoff at $E_n = 106$ keV and a maximum emission angle of 60° can be obtained that corresponds closely to a Maxwell–Boltzmann distribution for kT=25 keV [8, 9] as shown in the right part of Fig. 3. Hence, the reaction rate measured in such a spectrum yields immediately the proper stellar cross section.

The activation technique was also successfully used to determine the stellar cross sections of radioactive branch point nuclei, e.g. for ^{155}Eu [10] and ^{163}Ho [11]. Thanks to the excellent sensitivity of this method, the sample mass could be reduced in these experiments to less than 1 μg, resulting in a manageable sample activity.

2.3   The s Process Yields of the Rare Earth Elements

Together with the here reported results, stellar (n,γ) cross sections have been remeasured for 32 of the 55 stable isotopes in the REE region over the last 4 years, 23 with the 4πBaF$_2$ detector. These investigations included the s-only nuclei ^{142}Nd, ^{150}Sm, and ^{160}Dy which are important normalization points of the s process abundance distribution. The general shape of this distribution versus mass number yields information on the required seed nuclei as well as on the corresponding neutron exposure [2].

Fig. 4 shows the product of stellar cross section times abundance, $[\langle\sigma\rangle N_s]_A$, that is characteristic of the classical approach, an often used phenomenological s-process model [2]. In this mass region the empirical products for the s–only isotopes carry uncertainties smaller than the size of the symbols. Obviously, the differences between the classical approach (solid line) and the empirical values for the expected normalization points ^{142}Nd and ^{160}Dy exceed the uncertainties considerably. The value of ^{142}Nd lying *below* the calculated curve means that this isotope is *over*produced by the model, even if a possible p contribution is neglected. This discrepancy is inherent to the assumption of an exponential distribution of neutron exposures, on which the classical approach is based. Correspondingly, this result reveals a severe deficiency of that model, which should, therefore, be used with some reservation in the future.

In contrast to ^{142}Nd, the value for ^{160}Dy is 11% higher than the curve. Principally, such a difference could be explained by a small p-process contribution to the observed abundance. In this case, however, current p-process
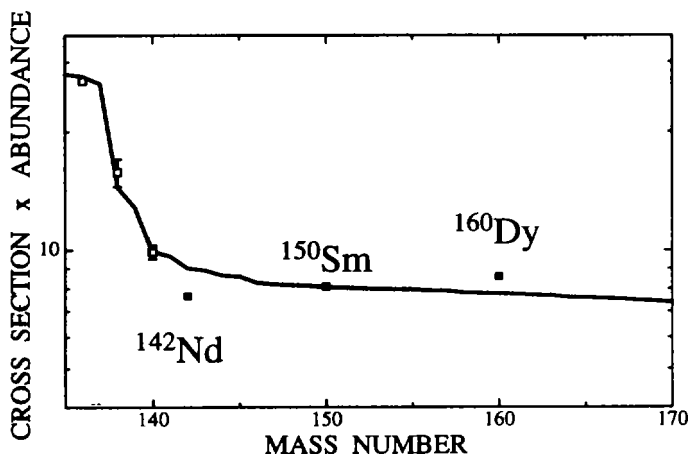
Fig. 4. The $\langle\sigma\rangle N_s(A)$–curve in the mass region of the REE. The differences between the classical s–process approach (solid line) and the empirical values for the expected normalization points ^{142}Nd and ^{160}Dy (black squares) are discussed in the text. Note that in some cases the uncertainties have already been reduced to the symbol size.

models [12, 13, 14] predict this component to be comparable to that of p-only ^{158}Dy, which would explain only 30% of that difference. Very likely, this apparent excess of ^{160}Dy is the first experimental evidence for a thermal effect: At s-process temperatures the excited state in ^{160}Dy at 87 keV becomes significantly populated. Though this state may have a larger cross section than the ground state due to its larger spin, the total (n,γ) cross section is reduced by the competing reaction channel for inelastic scattering from the excited state down to the ground state. This process is sometimes denoted as *superelastic* scattering. In contrast to this experimental result, previous statistical model calculations predicted a 10% enhancement for the stellar ^{160}Dy cross section [15, 16].

3 Measurements for the p Process

The presently favored site of the p process is the explosively burning O/Ne layer in SN of type II where temperatures of 2 to 3 GK are reached for about 1 s at densities of $\approx 10^6$ g cm^{-3}. Under these conditions, proton-rich nuclei are produced by a sequence of (γ,n) and subsequent (γ,p) and (γ,α) reactions. In total, this scenario involves about 1000 nuclei and 10000 reactions.

In view of this huge number of reactions it is surprising that experimental data are almost completely missing. Therefore, the (p,γ) cross sections for a set of Mo isotopes was measured via the activation technique by proton irradiation of thin, natural molybdenum layers. In this way, the (p,γ) cross sections of ^{92}Mo, ^{94}Mo, ^{95}Mo, and ^{98}Mo could be determined simultaneously in the same experiment (for details see [17]).

The metallic Mo layers were prepared by sputtering with thicknesses between 1200 to 5000 Å corresponding to proton energy losses of 10 to 40 keV in the investigated range between 1.5 and 3.0 MeV. The experiment was carried out in energy steps of 50 keV using a proton beam of typically 45 μA. Each of the 31 activations lasted for 3 to 4 h. The resulting γ spectrum was measured off-line with a HPGe detector, the intensities of the γ lines from the various reaction products being a measure for the respective cross sections. On average, typical uncertainties of 4 % could be achieved.
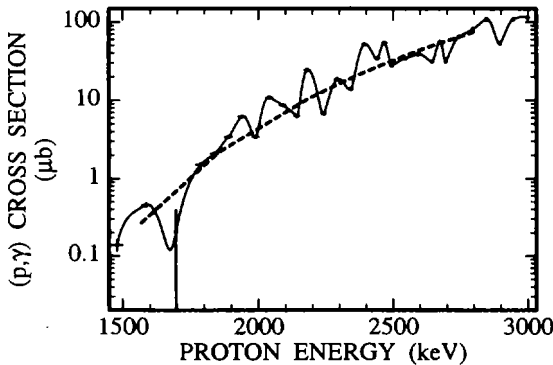
Fig. 5. The (p,γ) cross section of ^{92}Mo compared to a statistical model calculation (dashed line).

In Fig. 5, the final cross section of ^{92}Mo is shown as an example. The fluctuations in the cross section reflect the small level density of the neutron magic nucleus ^{92}Mo. For comparison, the result of a statistical model calculation with the Hauser-Feshbach code SMOKER [18] is also included. While in excellent agreement with the experimental data for ^{92}Mo, the calculated cross sections for ^{94}Mo and ^{95}Mo differ from the respective experimental results by factors of 1.5 and 2. Hence, a more complete set of experimental data will be useful for improving the parameter systematics for such calculations, which are indispensible for most unstable isotopes in the p-process network.

References

[1] E. Anders and N. Grevesse, Geochim. Cosmochim. Acta **53**, 197 (1989).

[2] F. Käppeler, H. Beer, and K. Wisshak, Rep. Prog. Phys. **52**, 945 (1989).

[3] K. Wisshak *et al.*, Nucl. Instr. Meth. A **292**, 595 (1990).

[4] K. Wisshak *et al.*, Phys. Rev. C **52**, 2762 (1995).

[5] K. Wisshak *et al.*, report FZKA-5967, Forschungszentrum Karlsruhe (1997), and Phys. Rev. C (in print).

[6] K. Wisshak, F. Voss, and F. Käppeler, report FZKA-5968, Forschungszentrum Karlsruhe (1997).

[7] K. Wisshak *et al.*, Phys. Rev. C **48**, 1401 (1993).

[8] H. Beer and F. Käppeler, Phys. Rev. C **21**, 534 (1980).

[9] W. Ratynski and F. Käppeler, Phys. Rev. C **37**, 595 (1988).

[10] S. Jaag and F. Käppeler, Phys. Rev. C **51**, 3465 (1995).

[11] S. Jaag and F. Käppeler, Ap. J. **464**, 874 (1996).

[12] M. Rayet, N. Prantzos, and M. Arnould, Astron. Astrophys. **227**, 271 (1990).

[13] W. Howard, B. Meyer, and S. Woosley, Ap. J. **373**, L5 (1991).

[14] M. Rayet *et al.*, Astron. Astrophys. **298**, 517 (1995).

[15] J. Holmes, S. Woosley, W. Fowler, and B. Zimmerman, Atomic Data and Nucl. Data Tables **18**, 305 (1976).

[16] M. Harris, Ap. Space Sci. **77**, 357 (1981).

[17] T. Sauter and F. Käppeler, Phys. Rev. C **55**, 3127 (1997).

[18] H. Schatz, private communication (unpublished).

CHARACTERISTICS OF THE rp-PROCESS IN X-RAY BURSTS

M. WIESCHER

University of Notre Dame
Department of Physics, Notre Dame, IN 46556, USA

Abstract

The rp-process was first suggested by Wallace and Woosley (1981) as the dominant nucleosynthesis process in explosive hydrogen burning at high temperature and density conditions. The process is characterized by a sequence of fast proton capture reactions and subsequent The time structure of the energy release is discussed within the frame work of a self consistent one-zone model for the thermonuclear runaway. Within a sufficiently long time scale for the thermonuclear runaway mainly N=Z even-even nuclei are produced in the associated nucleosynthesis.

1 Introduction

X-ray bursts have been suggested as possible sites for hot temperature hydrogen burning via the rp- and αp-process [1, 2, 3]. While x-ray bursts are frequently observed phenomena [4], the nucleosynthesis and the correlated nuclear energy generation, are not completely understood yet. The standard models for type-I x-ray bursts are based on accretion processes onto the surface of a neutron star. Typical predictions for the accretion rate vary from 10^{-10} to 10^{-9} $M_\odot$ y^{-1}. The accreted matter is continuously compressed by the freshly accreted material until it reaches sufficiently high pressure and temperature conditions which allow the thermonuclear ignition.

Nuclear burning is ignited at high density, $\rho \geq 10^6$ g/cm^3, in the accreted envelope, via the pp-chains, the hot CNO-cycles and the triple-α-process. The released energy triggers a thermonuclear runaway at the electron degenerate conditions at the bottom of the accreted layer near the surface of the neutron star. Peak temperatures up to $2 \cdot 10^9$ K can be reached before the degeneracy is completely lifted [5]. These temperatures are sufficiently high to trigger the rp- and the αp-process which cause rapid nucleosynthesis towards heavier mass regions. The time-scale for the thermal runaway and the subsequent cooling phase varies between 10 s up to 100 s [2]. Within this time-scale, the rp-process can proceed well up to ^{56}Ni [1] or even further up to ^{96}Cd [6].

The fast proton capture reactions drive the path out towards the proton drip-line until a waiting point nucleus is reached where a (p,γ)-(γ,p) and/or a (p,γ)-(p)-equilibrium is achieved. This causes an enrichment in these isotopes until β-decay or, for nuclei with low Z, (α,p) reactions occur. Waiting point nuclei are typically even-even nuclei which are characterized by low or negative Q-values for subsequent proton capture. Typical waiting points are the even-even Z=N nuclei ^{56}Ni, ^{64}Ge, ^{68}Se up to ^{92}Ru, ^{96}Pd, and ^{100}Sn.
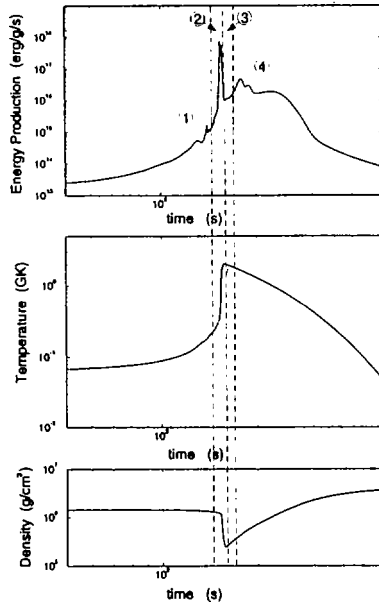
Figure 1: Shown is the energy production (luminosity), the temperature, and the density as a function of time for the thermonuclear runaway in a simplified x-ray-burst model. Indicated are different phases in the thermonuclear runaway.

2   The rp-process in the thermal runaway of the x-ray burst

The following section will focus on the rp-process characteristics calculated for temperature conditions during the thermonuclear runaway in a one mass zone x-ray burst model. The hydrostatic evolution during the process in terms of

pressure p and temperature T is determined by the radiative flux F which changes with the depth y of the accreted layer, the nuclear energy production ϵ, and the mass accretion rate $\dot{m}$,

$$\frac{\partial F}{\partial y} + \epsilon = C_p \left(\frac{\partial T}{\partial t} + \dot{m}\frac{\partial T}{\partial y} \right) - \frac{C_p T \dot{m}}{y} \nabla_{ad} \tag{1}$$

C_p is the specific heat at constant pressure and ∇_{ad} is the adiabatic change in the neutron star atmosphere. The pressure P in the burning zone is determined by the ion pressure P_{ion}, the pressure of the degenerate electron gas P_e, and the radiation pressure P_{rad}.
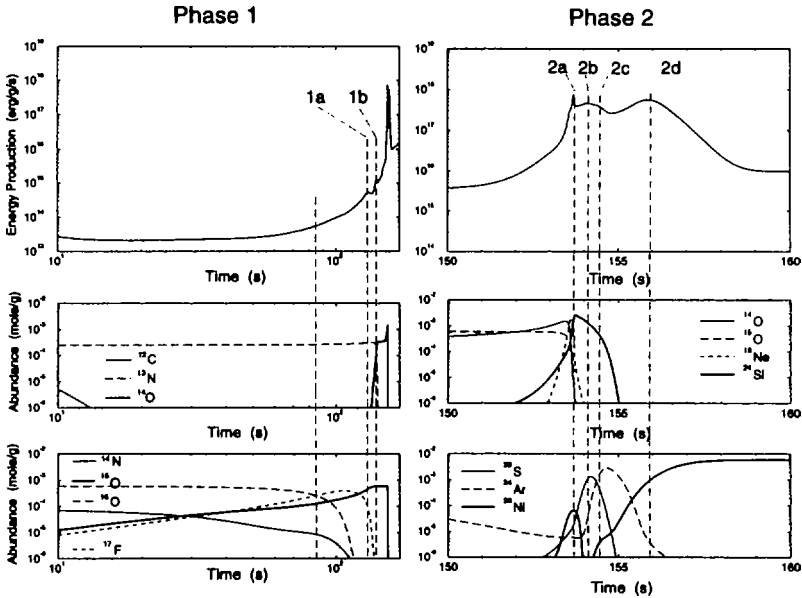

Figure 2: Energy production (luminosity) and nucleosynthesis in the early phase (1) of an x-ray burst. Peak 1a and 1b correspond to the burning of ^{17}F and ^{13}N. The second part of the figure shows phase 2 of the x-ray burst. The structure of the energy generation curve is determined by the waiting point characteristics of the rp-process.

The total pressure P is kept constant [5]. The timescale for thermonuclear runaway is faster than for convective processes, the temperature conditions are

therefore only determined by the energy release from the thermonuclear reactions in the runaway, ϵ, and by the various cooling processes [5, 7]. When the cooling rate becomes equal to the nuclear energy generation, further temperature increase is prevented and the peak temperature of the burst is reached.

Figure 1 shows the energy production, the temperature and the density in the accreted envelope (burning-zone), and the hydrogen and helium abundances calculated as a function of time over the duration of the x-ray burst. The structure of the energy production curve is directly correlated with the waiting point concept of the rp-process [6]. A series of fast proton captures and β-decay processes causes a peak in the energy production. The energy production drops when the material is stored in waiting point nuclei with slow β-decay. Initially the temperature
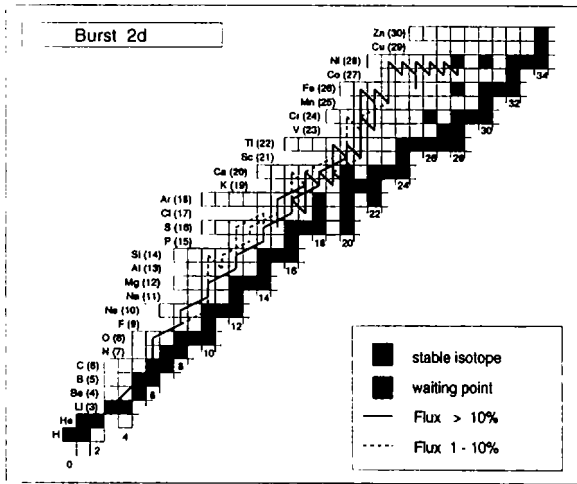
Figure 3: The αp- and rp-process reaction path in the thermonuclear runaway phase (2) of the x-ray burst.

increases dramatically due to the energy generation in the thermonuclear runaway and the density remains constant as long as the pressure is dominated by the pressure of the degenerate electron gas. When the cooling rate becomes equal to the energy production rate of $\epsilon_{nucl} \approx 10^{18}$ erg/g·s the temperature reaches its peak value of $T \approx 2 \cdot 10^9$ K. At this point the pressure has dropped by approximately one order of magnitude to $\rho \approx 2.5 \cdot 10^5$ g/cm^3. With the

decrease in temperature the density increases due to the condition of constant pressure.

The energy production in the burst is characterized by four periods, the ignition phase of the burst (1), the peak of the burst (2), the dormant phase of the burst (3), and the phase of the after-burst (4). Phase (1) is characterized by the hot CNO cycles. The energy production and the nucleosynthesis are shown in figure 2. The two peaks in the energy production are caused by the conversion of the initial abundance of ^{12}C into ^{14}O and of ^{16}O into ^{15}O by two subsequent proton capture reactions.
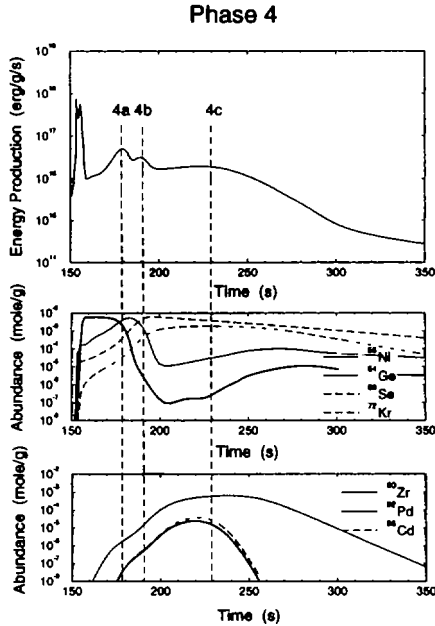
Phase 4

Figure 4: Energy production (luminosity) and nucleosynthesis in the late phase (4) of an x-ray burst. The peaks in the luminosity correspond to the destruction of waiting point nuclei.

Phase (2) is initiated at a temperature of $T \approx 2.4 \cdot 10^8$ K via the triple α-process. Parallel to that the ^{14}O and ^{15}O waiting point nuclei are rapidly depleted by α-capture processes. The fine structure of the energy burst is characterized by the different waiting points along the process path and is shown

in figure 2 together with the abundances of the most important waiting point nuclei along the process path. During the first burst (2a) the waiting point isotopes ^{14}O, ^{15}O, and ^{18}Ne are rapidly converted by the αp-process to ^{24}Si. Because the process has to wait for its β-decay, the energy production drops until it is reinitiated by proton and α capture reactions leading to the next waiting point isotopes ^{29}S (2b) and ^{34}Ar (2c). The rapid increase in temperature allows subsequent α-capture to bridge these waiting points forming ^{56}Ni. The reaction flow, integrated over the duration of the last phase (2d) of the
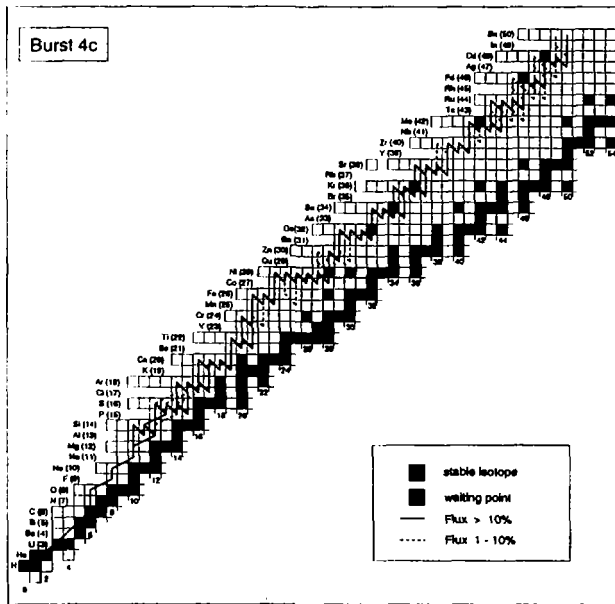
Figure 5: The reaction flux in the late phase (4d) of the x-ray burst. The overall flux is dominated by the rp-process. Indicated are the light p-nuclei which are possibly produced in the x-ray burst.

burst is shown in figure 3. Because most of the reaction path is characterized by (α,p) reactions considerably more helium is burned than hydrogen. At this point, peak temperatures of $T \approx 1.5 \cdot 10^9$ K have been reached and further processing is halted by the ^{56}Ni(p,γ)-(γ,p) equilibrium [6]. The energy production drops rapidly while most of the initial heavy isotope abundances as well as a large fraction of the initial helium remains stored in the waiting point nucleus

^{56}Ni.

At peak temperature conditions the ^{56}Ni has an equilibrium lifetime of approximately 100 s. However, with the decrease in temperature and the parallel increase in density, the ^{56}Ni(p,γ)-(γ,p) falls out of equilibrium and the effective lifetime of ^{56}Ni decreases to fractions of a second at temperatures $T \approx 1.5 \cdot 10^9$ - $1 \cdot 10^9$ K. At these temperatures, phase (4) of the energy burst is initiated by the rp-process beyond ^{56}Ni. Figure 4 shows the details of the burst structure in the cooling phase. The energy production is due to the depletion of ^{56}Ni and the further processing towards the waiting points ^{64}Ge and ^{68}Se. In the final phase the waiting point ^{68}Se is converted to heavier isotopes up to the mass 100 region. Figure 5 shows the reaction flow integrated over the duration of (4c). Most of the initial helium as well as most of the other isotopes has been converted to heavy isotopes with masses A$\geq$72.
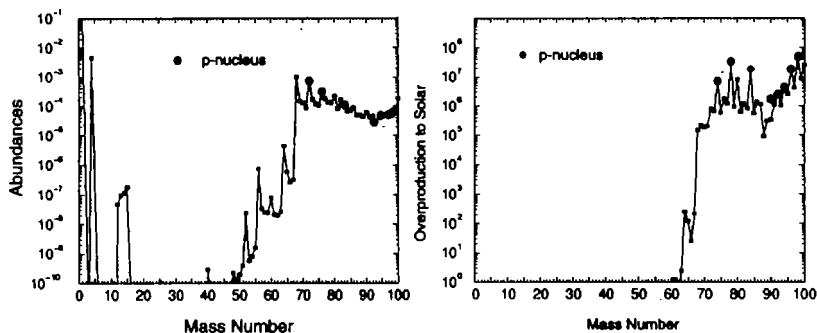
Figure 6: The abundance distribution and the ratio of the produced abundances and the initial solar abundances after the thermonuclear runaway. The light p-nuclei are marked as black dots, their overabundance is about one order of magnitude larger than the of other isotopes.

3   x-ray burst nucleosynthesis of the light p-nuclei?

Figure 6 shows the abundance distribution in the material after the freeze out of the thermonuclear runaway. This means that the β-unstable isotopes along the process path have decayed back to the line of stability. While there is still an appreciable amount of hydrogen, the bulk of the material has been converted to nuclei with masses A$\geq$70. Figure 6 shows also the comparison

with the solar abundances. All isotopes above mass A=68 are enriched by more than four orders of magnitude compared to the solar abundances. Clearly peaking are the abundances of the light p-nuclei ^{74}Se, ^{78}Kr, ^{84}Sr, ^{92}Mo, ^{94}Mo, ^{96}Ru, ^{98}Ru [8]. They are overproduced by up to seven orders of magnitudes compared to the solar abundances of these particular isotopes. This is in particular noticable because the relatively high observed abundances for these isotopes have not been explained yet in classical p-process scenarios [9, 10] or in alternative neutrino-induced processes in type II supernovae [11]. If a suffiently high mass loss out of the gravitational potential of the neutron star can be achieved by photon or neutrino driven winds or by jet-ejection, x-ray bursts may be a potential source for these isotopes [6].

Acknowledgments

References

[1] R. Wallace and S.E. Woosley, Astrophys. J. Suppl. **45** (1981) 389;

[2] R. Taam, Ann. Rev. Nucl. Sci. **35** (1985) 1;

[3] R. Taam, S. Woosley, T. Weaver, and D. Lamb, Astrophys. J. **413** (1993) 324;

[4] W. Lewin, J. van Paradijs, and R. Taam, Space Sci. Rev. **62** (1993) 233;

[5] L. Bildsten, in The many Faces of Neutron Stars, eds. A. Alpar, L. Buccheri, J. van Paradijs (Dordrecht, 1997)

[6] H. Schatz *et al*, Phys. Rep. **294** (1998) 167;

[7] M.Y. Fujimoto, T. Hanawa, S. Miyaji, Astrophys. J. **247** (1981) 267;

[8] D.L. Lambert, Astr. Astrophys. Rev. **3** (1992) 201;

[9] S.E. Woosley, E.M. Howard, Astrophys. J. **354** (1990) L21;

[10] M. Rayet *et al*, Astr.& Astrophys. **298** (1995) 517;

[11] R.D. Hoffman, S.E. Woosley, G.M. Fuller, B.S. Meyer, Astrophys. J. **460** (1996) 478.

RP PROCESS STUDIES WITH RADIOACTIVE
BEAMS AT ATLAS

K. E. REHM

Argonne National Laboratory
Physics Division
9700 South Cass Av.
Argonne, IL 60439, USA

Abstract

Reactions of interest to nuclear astrophysics have been studied with radioactive beams at the ATLAS accelerator. Using a modified ISOL technique, beams of ^{18}F($T_{1/2}$=110min) and ^{56}Ni($T_{1/2}$=6.1d) have been produced. The reactions ^{18}F(p,α)^{15}O, ^{18}F(p,γ)^{19}Ne, and ^{56}Ni(d,p)^{57}Ni have been investigated. The results indicate that the ^{18}F(p,γ) route is a small contributor to the breakout from the hot CNO cycle into the rp process, while the ^{56}Ni(p,γ)^{57}Cu rate is about ten times larger than previously assumed.

1   Introduction

The development of radioactive ion beams[1] during the last ten years has opened many new research opportunities in the area of nuclear astrophysics. While in quiescent hydrogen burning the nuclear reactions inside a star involve mainly stable isotopes, the cataclysmic events at the end of a star's life happen on such a rapid time scale that reactions with short-lived isotopes play the dominant role. These conditions occur in various stellar explosions, such as novae, supernovae and X-ray bursts[2]. The network of nuclear reactions that transforms lighter CNO material to heavier elements involves hundreds of reaction rates. These processes have been simulated in network calculations[3] using reaction rates which were obtained from theoretical estimates, e.g by using Hauser-Feshbach calculations. If the excitation energy in the compound system is high enough these estimates are usually quite reliable. For reactions involving nuclei in the vicinity of closed shells, however, in the proton capture reactions mainly states at low excitation energies are populated and, thus, properties of the individual levels become important. In this contribution we discuss two examples of reactions in the vicinity of ^{18}F and ^{56}Ni, where nuclear structure effects play a dominant role.

2 Beam production techniques

Since the half-life of ^{18}F ($T_{1/2}$=110 min) and ^{56}Ni ($T_{1/2}$=6.1d) are relatively long, a modified version of the ISOL technique[4] was used for generating the radioactive ion beams. The ^{18}F material was produced by bombarding enriched $H_2^{18}O$ water with a 11 MeV proton beam from the medical cyclotron at the University of Wisconsin. After a chemical separation the ^{18}F material was mounted in a copper insert for a negative ion sputter source (SNICS) which is installed at the tandem injector of the superconducting ATLAS accelerator at Argonne National Laboratory. Details of the source preparation technique and the beam intensities obtained in actual experiments are given in Ref.[5].

The ^{56}Ni source material was produced via the ^{58}Ni(p,p2n)^{56}Ni reaction by bombarding a small (125 mg) ^{58}Ni pellet with a 50 MeV proton beam from the injector of the Intense Pulsed Neutron Source at Argonne National Laboratory. Taking into account the cross section of the (p,p2n) reaction, and the size of the beam spot of the proton beam, a fraction of $\sim 5 \times 10^{-6}$ of the ^{58}Ni nuclei was converted into ^{56}Ni. Because of the larger cross section of the ^{58}Ni(p,2pn)^{56}Co reaction, the source material contained about 10 times more ^{56}Co, which due to the small mass difference $\Delta m(^{56}Ni - {}^{56}Co)/m = 3.5 \times 10^{-5}$ is difficult to suppress, even using a high resolution mass separator. The ^{56}Ni pellet was also mounted in a copper insert for the negative ion sputter source. Further details can be found in Ref. [6].

3 The Breakout from the hot CNO cycle to the rp-process via the ^{18}F(p,γ)^{19}Ne reaction

The rapid proton (rp) capture process is a series of (p,γ) and (p,α) reactions followed by β^+ decays, where nuclei up to ^{56}Ni and beyond are produced. The border line between the hot CNO cycle and the rp process passes through ^{19}Ne since the reaction Q values in this mass region are such that, once nuclei beyond ^{19}Ne are formed, no recycling into lighter CNO material is possible. The ^{18}F(p,γ)^{19}Ne reaction is, together with the ^{15}O(α,γ)^{19}Ne and the ^{18}Ne(α,p)^{21}Na reactions, one of the pathways leading from the hot CNO cycle into the rp process. However, due to the positive Q value of the ^{18}F(p,α)^{15}O reaction, the contribution of the ^{18}F(p,γ) route to the breakout from the hot CNO cycle depends strongly on the cross section ratio $\sigma[^{18}F(p,\gamma)]/\sigma[^{18}F(p,\alpha)]$.

The cross section of the ^{18}F(p,α)^{15}O reaction has been measured recently

in the energy range $E_{c.m.}$ = 265 - 740 keV[7, 8, 9]. It is dominated by the contribution of a new $3/2^+$ (s-wave) resonance at E_x= 7.064 MeV in ^{19}Ne and, at lower temperatures, by the $3/2^-$ state at 6.741 MeV[9]. The maximum angle-integrated cross section for the higher of the two resonances is $\sim$ 250 mb, while for the proton capture reaction ^{18}F(p,γ)^{19}Ne only an upper limit of 42 μb has been determined[10] so far.

With these cross sections the astrophysical reaction rates and, thus, the mean lifetimes of ^{18}F in a star can be calculated. The results for a star with a density ρ=5000 g/cm^3 and a mass fraction X_H=0.77 are given in Fig. 1 as function of the temperature T_9, where T_9 is the temperature in 10^9 K. Also included are the mean lifetimes for the ^{19}Ne(p,γ)^{20}Na and ^{15}O(α,γ)^{19}Ne reactions[11] using a mass fraction X_{He}=0.2.
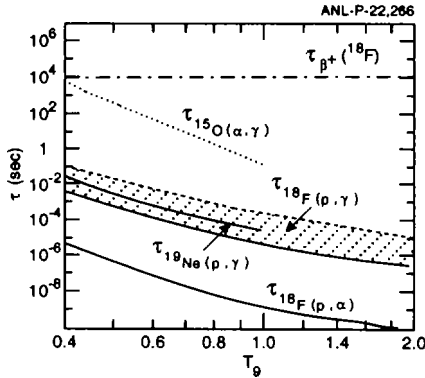
Figure 1: Mean lifetimes of ^{18}F, ^{19}Ne and ^{15}O in a star with a density ρ=5000 g/cm^2 as function of the temperature T_9.

As can be seen, the lifetime of ^{18}F in hydrogen is dominated by the (p,α) reaction which destroys ^{18}F within less than 10^{-5} sec. The lifetime for converting ^{18}F via the (p,γ) reaction is typically 3 orders of magnitude larger and comparable with the lifetime of the ^{19}Ne(p,γ)^{20}Na reaction. Although the lifetime for producing ^{19}Ne via the ^{15}O(α,γ) reaction is still 4-5 orders of magnitude higher, the amount of ^{15}O available in the stellar environment makes the ^{15}O(α,γ) reaction the main route for generating ^{19}Ne. This was shown in a simplified network calculation involving the ^{18}F(p,α), ^{18}F(p,γ) and ^{15}O(α,γ) reactions. From the time dependence of the relative contributions for ^{18}F, ^{15}O

and ^{19}Ne, respectively, it can be seen that due to the large ^{18}F(p,α) reaction rate the ^{18}F material is immediately converted into ^{15}O, indicating that the ^{18}F(p,γ)^{19}Ne route is only a small branch for the production of ^{19}Ne, which is more efficiently produced via the ^{15}O(α,γ) reaction.

4 The ^{56}Ni waiting point

The doubly closed shell nucleus ^{56}Ni is of considerable interest to astrophysics. ^{56}Ni is produced via helium burning in the core of massive stars, in supernova explosions and in the rp process[2]. The small Q-value (Q=0.695 MeV) for the (p,γ) proton capture reaction on ^{56}Ni makes this nucleus a 'waiting point' for the reaction flow towards heavier nuclei. For a realistic determination of the astrophysical reaction rate, detailed information on the structure (excitation energy and spectroscopic factors) of nuclei around A=56 is required.

We have therefore measured spectroscopic factors for low-lying states in ^{57}Ni, populated via the inverse d(^{56}Ni,p)^{57}Ni reaction using the 250 MeV ^{56}Ni beam described above. The ^{56}Ni beam bombarded a 500 μg/cm^2 CD$_2$ target located in the scattering chamber of the Fragment Mass Analyzer (FMA)[12]. The protons emitted at backward angles from the d(^{56}Ni,p)^{57}Ni reaction were detected in a large Si detector array consisting of a position sensitive annular detector and six 5×5 cm^2 Si strip detectors (strip width 1 mm), covering a total solid angle of 2.8 sr. To separate the (d,p) reactions on ^{56}Ni from those induced by the ^{56}Co and ^{56}Fe beam impurities, the reaction products were identified by their mass and nuclear charge at the focal plane of the FMA in coincidence with protons. For the Z identification of the reaction products it was necessary to use a passive absorber[13] consisting of a stack of ten Au foils with a total thickness of 7 mg/cm^2 that slowed down the Fe, Co and Ni particles differently.

A Q-value spectrum for protons from the d(^{56}Ni,p) reaction, as measured with the annular Si detector that covers the angular range $\theta = 147°$ - $162°$ in coincidence with ^{57}Ni ions detected in the FMA is shown in Fig. 2a. In the center-of-mass system this range corresponds to forward angles for a (d,p) reaction, where transitions to low-spin states (ℓ=0,1) should be strongly populated. Indeed, the spectrum is dominated by the transitions to the 3/2$^-$ (E$_x$=0 MeV) and the 1/2$^-$ (E$_x$=1.113 MeV) states in ^{57}Ni while the yields for states at E$_x$=2.5 and E$_x$=3.8 MeV are considerably smaller indicating little single-particle strength for low-spin states in ^{57}Ni at higher excitation energy. The spectrum is quite different from the one obtained for the d(^{28}Si,p)^{29}Si re-
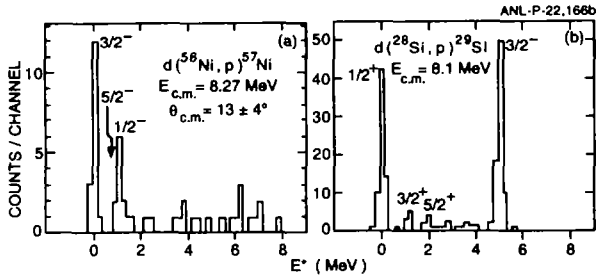
Figure 2: (a) Q-value spectrum measured at forward c.m. angles for the d(^{56}Ni,p)^{57}Ni reaction at E(^{56}Ni)=250 MeV. (b) Q-value spectrum for the d(^{28}Si,p)^{29}Si reaction. In this angle range, only l= 0,1 states are strongly populated

action, where a strong population of the high-lying $2p_{3/2}$ single-particle state at E_x=4.9 MeV is observed (see Fig. 2b).

The angular distributions for the first three states in ^{57}Ni are presented in Fig. 3. The uncertainties in the measured differential cross sections include the statistical errors as well as uncertainties associated with beam current determination and detection efficiency. The solid lines in Fig. 3 are the result of DWBA calculations for the reaction mechanism with spectroscopic factors from shell-model calculations. The code PTOLEMY[14] was used with optical model parameters taken from the literature. A shell-model calculation was performed within a space containing the $f_{7/2}$, $f_{5/2}$, $p_{3/2}$ and $p_{1/2}$ orbitals with a Hamiltonian described in Ref.[15]. The configurations included 0, 1 and 2 particles excited out of the $f_{7/2}$ orbital. This calculations yielded spectroscopic factors of S=0.91 ($2p_{3/2}$), S=0.91($1f_{5/2}$) and S=0.90($2p_{1/2}$), respectively. With these spectroscopic factors good agreement between the experimental and the calculated angular distributions is obtained, indicating that these states in ^{57}Ni are indeed well characterized as the $2p_{3/2}$, $2p_{1/2}$ and $1f_{5/2}$ single-particle states. These angular distributions together with the low yields observed in the excitation energy region between 2-4 MeV, where higher lying $1/2^-$, $3/2^-$, and $5/2^-$ states are expected, support the fact that the main single particle strength for these low-spin states is concentrated in the first three excited states.

The observation of the single-particle structure of ^{57}Ni allows us to make
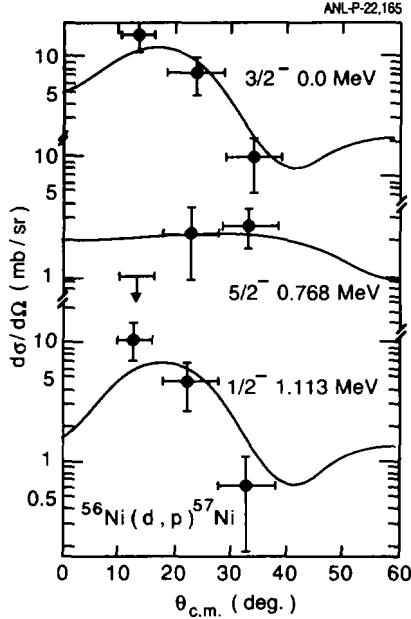
Figure 3: Differential cross sections as function of the center-of-mass angle θ_{cm} for the three lowest states populated in the d(^{56}Ni,p)^{57}Ni reaction. The solid lines are the result of DWBA calculations.

predictions for the strength of the ^{56}Ni(p,γ) reaction leading to the mirror nucleus ^{57}Cu, which is crucial for the production of heavier proton-rich nuclei in explosive nucleosynthesis[16]. Because of the small Q-value, the yield of the radiative capture reaction depends on the excitation energies and the spectroscopic strengths of specific low-lying states in ^{57}Cu. The excitation energies of these states were determined recently[17]. At the temperatures occurring in typical nova and supernova explosions and in X-ray bursts ($T_9 \sim 0.5$ - 1), the main contribution comes from the low-lying ($E_x \leq 3$ MeV) 5/2$^-$ and 1/2$^-$ states. Assuming charge symmetry and using the same spectroscopic factors C^2S as measured for the mirror nucleus ^{57}Ni, we estimate the proton widths Γ_p for proton-unbound mirror states in ^{57}Cu from the expression:

$$\Gamma_p(E, \ell) = C^2 S \cdot \Gamma_p^{s.p.}(E, \ell) \tag{1}$$

The single particle widths $\Gamma_p^{s.p.}(E, \ell)$ were calculated in a Woods-Saxon potential with a radius parameter of $r_o = 1.25$ fm and a diffuseness of a= 0.65 fm or from R-matrix theory using a radius of 5.36 fm (see Ref.[6] for details).

The calculated astrophysical reaction rates are shown in Fig. 4 as a function of the temperature T_9 . In the critical temperature region $T_9 < 1$ the $1/2^-$ state completely dominates. Higher-lying states in ^{57}Cu with $E_x > 2.5$ MeV contribute only at temperatures $T_9 > 1$.

ANL-P-22,267
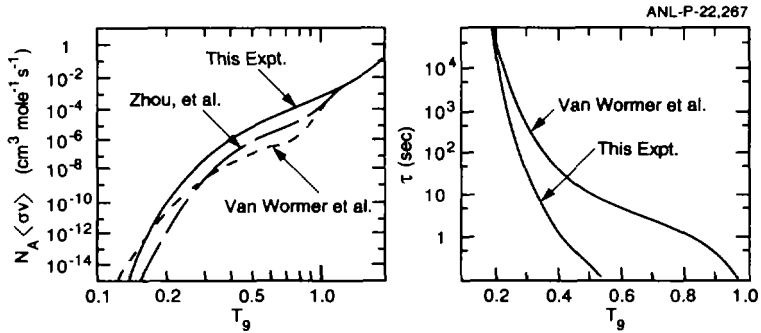
Figure 4: (a) Astrophysical reaction rates $N_A < \sigma v >$ for the ^{56}Ni(p,γ)^{57}Cu reaction. Also shown are the results from Refs. 3 and 17, respectively. (b) Lifetimes of ^{56}Ni calculated using the results from the present experiment and Ref. 3 , respectively.

The dashed lines in Fig. 4a represents the result for the astrophysical reaction rate obtained in Refs. [17] and [3], respectively. Since these authors used a smaller proton width for the $1/2^-$ state [17] or a higher (p,γ) threshold [3] their estimates of the reaction rate for the ^{56}Ni(p,γ)^{57}Cu reaction are lower by more than an order of magnitude at temperatures below $T_9 = 1$.

The mean life of ^{56}Ni with respect to the (p,γ) reaction as function of the temperature T_9 is shown in Fig. 4b in comparison with the results of Ref.[3] As can be seen, a considerable decrease in the lifetime of ^{56}Ni is observed in the critical temperature region between $T_9=0.3 - 1$. This shorter lifetime will result in an increased production rate of elements and isotopes on the proton-rich side of the mass valley above ^{56}Ni.

References

[1] Proceed. of the Fourth Intern. Conf. on Radioactive Nuclear Beams, Omiya, Japan 1996; Nucl. Phys.**A616**, 1(1997)

[2] A. E. Champagne and M. Wiescher, Annu. Rev. Nucl. Part. Sci **42**, 39(1992)

[3] L. van Wormer et al., Astrophys. J. **432**, 326(1994)

[4] A. C. Mueller and B. M. Sherill, Annu. Rev. Nucl. Part. Sci **43**, 529(1993)

[5] A. Roberts et al., Nucl. Instrum. Methods Phys. Res. **B103**, 523(1995)

[6] K. E. Rehm et al., Phys. Rev. Lett. **80**, 676(1998)

[7] K. E. Rehm et al., Phys. Rev. **C52**, R460(1995)

[8] R. Coszach et al., Phys. Lett. **B353**, 184(1995)

[9] J. S. Graulich et al., Nucl. Phys. **A626**, 751(1997)

[10] K. E. Rehm et al., Phys. Rev. **C55**, R566(1997)

[11] M. S. Smith, PhD thesis, Yale University 1990 (unpublished)

[12] C. N. Davids et al., Nucl. Instrum. Methods Phys. Res. **B70**, 358(1992)

[13] W. Henning et al., Nucl. Instrum. Methods **184**, 247(1981)

[14] M.H. MacFarlane and S. C. Pieper, Argonne National Laboratory Report No. ANL-76-11(Rev.1) (1978)

[15] G. Kraus et al., Phys. Rev. Lett. **73**, 1773(1994)

[16] M. Wiescher, H. Schatz and A. E. Champagne, Phil. Trans. R. Soc. London A (in print)

[17] X. G. Zhou et al., Phys. Rev. **C53**, 982(1996)

STRUCTURE OF PROTON–RICH NUCLEI
OF ASTROPHYSICAL INTEREST

E. ROECKL

Gesellschaft für Schwerionenforschung (GSI)
Postfach 110552, D-64220 Darmstadt, Germany

Abstract

Recent experimental data concerning proton–rich nuclei between A=20 and A=100 are presented and discussed with respect to their relevance to the astrophysical rp process and to the calibration of solar neutrino detectors.

1 Introduction

During the past few years, improvements in experimental techniques have opened the possibility to study very proton–rich nuclei close to and even beyond the proton drip line. Such nuclei are characterized by exotic ground–state decay properties, in particular by direct emission of charged–particles such as protons, α–particles and clusters, and β–decay with high energy release. Due to the latter fact, the Gamow–Teller (GT) strength in β–decay can be measured for a large range of excitation energies in the daughter nucleus, and the quality of theoretical predictions can thus be stringently tested by comparing them to experimental GT data. In this way, unusually interesting insights are gained into phenomena relevant to nuclear physics as well as to astrophysics.

This motivation holds in particular for proton–rich nuclei near double shell closures, as will be exemplified by presenting recent experimental data for ^{20}Mg, ^{36}Ca, ^{45}Cr, ^{49}Ni, ^{56}Cu, and for nuclei near ^{100}Sn. The results were obtained by means of the LISE3 spectrometer at GANIL, the Projectile Fragment Separator FRS or the On–line Mass Separator at GSI. Similar experiments have also been performed at MSU and RIKEN. With a focus on the astrophysical rp process, the identification of new nuclei near the proton drip line and the measurement of their β–decay properties will be discussed (Sect. 2). Furthermore, the relevance of β–decay experiments on ^{37}Ca and ^{40}Ti for the calibrating of the ^{37}Cl and ^{40}Ar solar–neutrino detectors, respectively, will be presented (Sect. 3). Sect. 4 contains the summary and an outlook.

2   Astrophysical rp Process

As can be seen, e.g., from recent network calculations [1, 2, 3], the rp process path involves nuclei with N~Z and takes a course near the proton drip line. Input data for such calculations concern (i) masses, Q–values for β^+/EC–decay and proton or alpha capture reactions, delineation of the proton drip line; (ii) (p,γ) and (α,γ) rates, (iii) half–lives for β^+/EC and direct proton decay; and (iv) clarification of the structure of selected "threshold states", e.g. by using β^+/EC–data. In this section, I shall present data related to the topics (i) and (iv).

As far as identification of new isotopes and mapping of the proton drip line are concerned, the following experiments are of interest, which use fragmention reactions of proton–rich stable isotopes and analyse the radioactive reaction products by a magnetic spectrometer combined with of energy loss and time–of–flight measurements:

- The first T_Z=-3 nucleus ^{22}Si was identified [4], whereas ^{19}Na (T_Z=-3/2) and ^{21}Al (T_Z=-5/2) were *not* observed. Experiments of this kind only yield half-life limits with reference to the time–of–flight between target and detector, but do not give any quantitative information on mass etc.. It is previous reaction work [5] that has shown that ^{19}Na and ^{21}Al are unbound, the proton separation energies S_p being –333(12) and –1260(300) keV, respectively.

- Since the first identification of the T_Z=-7/2 nuclei ^{45}Fe and ^{49}Ni [6] it seems possible to reach the double shell closure at ^{48}Ni. There would then be three double shell closures for one and the same element becoming available to experiment. This speculation does not have any immediate relevance to the rp process. However, this exceptionally long chain of nickel isotopes from A=48 to A=78 would definitely be interesting for testing mass and radius predictions in the spirit of P.–G. Reinhards talk [7].

- There is some experimental evidence that ^{69}Br, ^{73}Rb may lie beyond the proton drip line [8, 9], which would mean that the rp process had to proceed by means of a double proton capture [2, 3].

As far as β^+/EC decay studies are concerned, one should note that the quenching of the GT strength is of great astrophysics interest [10], that considerable experimental and theoretical progress has been made in the nuclear physics interpretation of the quenching of the GT strength in β decay near ^{40}Ca [11], ^{56}Ni [12] and ^{100}Sn [13], and that further progress is expected from

the high–resolution and low–resolution measurements being performed near ^{100}Sn [14]. Furthermore, β–decay data of proton–rich nuclei may help to clarify the structure of threshold states that are important in some of the (p,γ) reactions in the rp process. In this context I would like to mention the following examples which are meant to show the perspectives *and limits* of such investigations:

- From the β–decay results obtained for ^{20}Mg, a tentative 1^+ assignment can be deduced [15] for the 2645 keV state in ^{20}Na. This level lies 450 keV above the proton threshold of the ^{19}Ne$(p,\gamma)^{20}$Na reaction $(S_p(^{20}$Na$)=2195(7)$ keV [5]) and is thus relevant to the "break out" from the hot Ne–Na cycle to the rp process. It is interesting to note that a recent measurement of interaction cross–sections at relativistic energies yielded information on the matter (and charge) radii of A=20 nuclei from ^{20}N to ^{20}Mg [16]. Even though the experimental indications for a neutron or proton skin, respectively, are weak, they may be relevant for the calculation of (p,γ) rates.

- On the basis of experimental data for the β–decay of ^{36}Ca, a 1^+ assignment can be excluded [11] for the 1670 and 1890 keV states in ^{36}K, which lie close to the threshold $(S_p(^{36}$K$)=1666(8)$ keV [5]) of the ^{35}Ar$(p,\gamma)^{36}$K reaction.

- In a recent experiment, the β–decay of ^{56}Cu decay to the doubly–magic nucleus ^{56}Ni was measured for the first time [12], and the β–strength, deduced for four transitions, was compared to shell–model predictions. As in the case of light nickel isotopes mentioned above, there is no immediate connection to astrophysics except in the general sense of testing nuclear models in a region of nuclei relevant to the rp process. I would like to mention, in particular, the new data on the ^{56}Ni$(p,\gamma)^{57}$Cu reaction [3, 17], and shall return to the question of further related experiments in Sect. 4.

- If the rp process indeed extends to the ^{100}Sn region, the synthesis of "p nuclei" such as ^{92}Mo and ^{96}Ru will critically depend upon β–delayed proton branching ratios. However, the latter quantities were found [18] to be small for the A=96 and A=98 chains, which is not surprising in view of the known systematics of GT decay properties near ^{100}Sn. Correspondingly, β–delayed proton emission does not seem to have a major influence on the (puzzle of the) production of p nuclei.
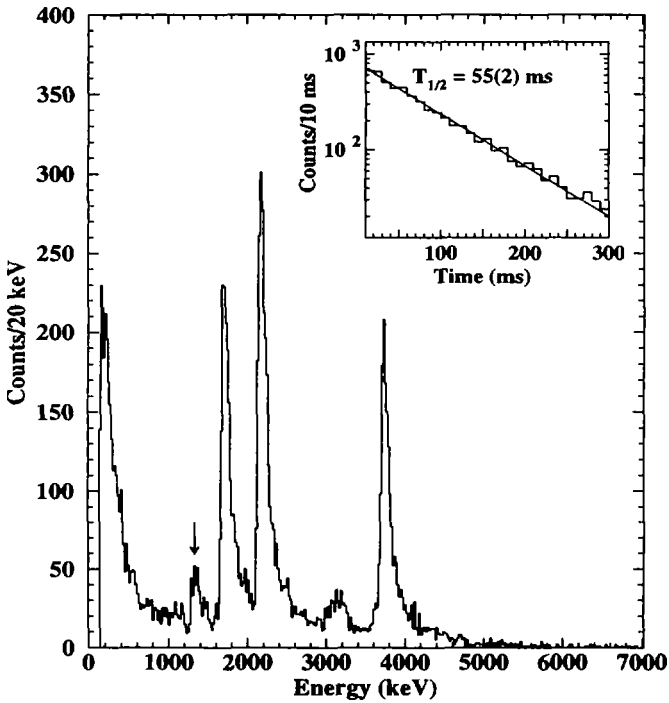
Fig. 1. Energy spectrum of β–delayed protons from the decay of ^{40}Ti. The proton peak, characterized by coincidences with 2.5 MeV γ-rays, is marked by an arrow. This peak as well as that at 3.8 MeV are interpreted as being due to Fermi decay, whereas the remaining strength is attributed to GT transitions. The insert shows the time distribution of proton events with energies above 1.5 MeV, which was used to determine the half–life of 55(2) ms [19]

3 Calibration of the ^{37}Cl and ^{40}Ar Solar–Neutrino Detectors

The β–decay data obtained for ^{37}Ca [11] and ^{40}Ti [19] (see Fig. 1) can be used to determine, under the assumption of isospin symmetry, the neutrino absorption cross-section for ^{37}Cl and ^{40}Ar, respectively. In the former case,

the result of $1.09(3) \cdot 10^{-42}$ cm^{-2} agrees very well with that used for the evaluation of data from the Homestake Mine detector. In the latter case, the result of $1.38(6) \cdot 10^{-42}$ cm^{-2} for the neutrino absorption cross–section in ^{40}Ar represents the first experimental information on the calibration of the liquid–argon detector ICARUS. It is interesting to note that the experimental value is approximately 3 times larger than a previous estimate [20] which only took Fermi transitions into account.

4 Summary and Outlook

In this paper, experimental results on proton–rich nuclei were discussed in their relation to the astrophysical rp process and to solar neutrino detection. According to my opinion, the influence of the β–decay data on our understanding of the rp process has been rather modest so far. In an attempt to improve this situation, the following questions were discussed at the workshop:

- Would it be interesting to measure β–delayed γ–rays of ^{57}Zn in order to clarify the structure of ^{56}Ni(p,γ)^{57}Cu threshold states? This idea does not seem to be promising as the allowed β–decay of ^{57}Zn ($7/2^-$) will not strongly populate the dominant 1106 keV ($1/2^-$) threshold level in ^{57}Cu.

- Are Coulomb breakup reactions of relativistic beams of ^{40}Ti [21] or ^{57}Cu a suitable tool for clarifying the ^{38}Ca(2p,γ)^{40}Ti or ^{56}Ni(p,γ)^{57}Cu rates, respectively? At preseent, such experiments do not seem to be possible in view of the low beam intensities. In the case of ^{40}Ti, a value of about one atom per minute has been reached so far [19]. Improvements by one to two orders of magnitude can be expected by choosing ^{50}Cr instead of ^{58}Ni as a primary beam and by taking advantage of intensity upgrade program underway at GSI. However, the ^{40}Ti intensity will still be many orders of magnitudes lower than that used, e.g., in the ^{8}B Coulomb breakup measurement [22].

All in all, in planning experiments on proton–rich nuclei *far from stability* that are of *astrophysical interest*, one may end up making experiments *far from astrophysical interest.....*

References

[1] L. Van Wormer et al., Astrophys. J. **432** (1994) 326;

[2] H. Schatz et al., Phys. Rep. (1998), in press;

[3] M. Wiescher, contribution to this workshop;

[4] M. G. Saint Laurent et al., Phys. Rev. Lett. **59** (1987) 33;

[5] G. Audi et al., Nucl Phys. **A624** (1997) 1;

[6] B. Blank et al., Phys. Rev. Lett. **77** (1996) 2893;

[7] P.-G. Reinhard, contribution to this workshop;

[8] B. Blank et al., Phys. Rev. Lett. **74** (1995) 4611;

[9] Pfaff et al., Phys. Rev. **C53** (1996) 1753;

[10] K. Langanke, contribution to this workshop;

[11] W. Trinder et al., Phys. Lett. **B348** (1995) 331; Phys. Lett. **B349** (1995) 267; Nucl. Phys. **A620** (1997) 191;

[12] M. Ramdhane et al., submitted to Phys. Lett. **B**;

[13] B. A. Brown and K. Rykaczewski, Phys. Rev. **C50** (1994) R2270;

[14] Darmstadt–St. Petersburg–Valencia–Warsaw Collaboration, unpublished results;

[15] A. Piechaczek et al., Nucl. Phys. **A584** (1995) 509;

[16] L. V. Chulkov et al., Nucl. Phys. **A603** (1996) 219, O. V. Bochkarev et al., Eur. Phys. J. **A1** (1998) 15;

[17] K. E. Rehm et al., Phys. Rev. Lett. **80** (1998) 676, and contribution to this workshop;

[18] M. Hellström et al., Z. Phys. **A356** (1997) 229;

[19] W. Liu et al., Z. Phys. **A359** (1997) 1, and to be published;

[20] J. N. Bahcall, Phys. Lett. **B178** (1986) 324;

[21] W. Baur, contribution to this workshop;

[22] T. Motobayashi, contribution to this workshop.

MEASUREMENT OF PROTON CAPTURE REACTIONS IN THE HOT CYCLES : AN EVALUATION OF EXPERIMENTAL METHODS

Pierre LELEUX

Institut de Physique Nucléaire, Université Catholique de Louvain, B-1348 Louvain-la-Neuve, Belgium

Abstract

In the hot cycles, most of the proton capture reactions involve radioactive nuclei in the entrance and exit channels. This paper evaluates the specific methods that were designed to measure such reactions.

1 Introduction

The Hot CNO cycles and the rp-process are characteristic of explosive stellar environments. Hydrogen burning happens in cycles starting from a seed even-even nucleus (^{12}C, ^{16}O, ^{20}Ne, ...), continuing through two proton captures, a β^+ decay, another capture, a β^+ decay and finally a (p,α) reaction : the chain ^{12}C(p,γ) ^{13}N(p,γ)^{14}O(β^+)^{14}N(p, γ)^{15}O(β^+)^{15}N(p,α)^{12}C is a well-known example ; another one is the ^{20}Ne(p,γ)^{21}Na(p,γ)^{22}Mg(β^+)^{22}Na(p, γ) ^{23}Mg(β^+)^{23}Na(p,α)^{20}Ne. Moreover, cycles can be extended and/or possibly escaped through additional capture reactions, like ^{15}O (α, γ) in the first example and ^{23}Mg(p,γ) in the second one. A thorough discussion of these processes and of their evolution versus temperature can be found in ref.[1]. Proton capture reactions occur thus frequently and some of them involve radioactive isotopes. In the last decade, the advent of radioactive beams has allowed to measure several capture reactions. The purpose of the present contribution is to evaluate critically the methods used in experiments performed in Louvain-la-Neuve [2, 3], and to extrapolate to other cases.

In order to measure the cross section of a A(p,γ)B reaction, three possibilities exist, i.e. to detect γ-rays, B nuclei or both in coincidence ; I will consider successively each of them. However, as the detection problems are deeply dependent on earlier characteristics of the set-up, i.e. the beam and the target, these points will be examined first.

2   Prior to the detection : the beam and target

As is well known, radioactive beams have to be preferred to radioactive targets for lifetimes shorter than a few hours. This means that most of the (p,γ) reactions will have to be measured in inverse kinematics (proton target). In Louvain-la-Neuve, radioactive beams are accelerated up to an energy typical of explosive processes, i.e. 1 MeV/amu, by a cyclotron, implying that beams are : i) broad in energy (typical $\Delta E/E$ is about 1 %) and ii) affected with a large emittance of the order of 60 mm mrad. Keeping in mind that proton capture reactions are most of the time dominated by resonances in the B compound nucleus, it becomes obvious that the conjunction of a broad beam and a thin gas target would cause difficult deconvolution problems if a broad resonance has to be measured. A CH_2 polyethylene foil of typical thickness 100-300 $\mu g/cm^2$ appears as a good choice [4]. While traversing the target, the beam will scan an extended range of excitation energy in the B compound nucleus. Moreover, the CH_2 target is favored by the fact that : i) recoil protons and ions scattered from C can be detected and used for normalization purposes (this point will be discussed further on) and ii) charge equilibrium of beam and final nuclei is certainly reached in the target, which is not the case in a thin windowless gas target [5]. However, some drawbacks should be mentioned as well : i) a CH_2 target contains 0.015 % of Deuterium which, though the (d,n) reaction, leads to the same final B nuclei with a much larger cross section (mb instead of μb for the (p,γ)) ; ii) the presence of C causes a loss of efficiency (typically a factor of 3) with respect to a pure H target of the same thickness.

3   Detection methods

3.1   Prompt γ-rays

This method is mostly dependent on the Q-value of the reaction and the decay scheme of the B-nuclei. Due to the large ambient activity of 511 keV γ-rays brought in by the β^+ decay of the proton-rich beam, the best cases are characterized by a large Q-value and a small number of excited levels in B below the (p,γ) threshold. The $^{13}N(p,\gamma)^{14}O$ reaction appears as such a very good case, with a Q-value of 4.62 MeV and a first excited level at 5.15 MeV in ^{14}O. On the contrary, the $^{21}Na(p,\gamma)^{22}Mg$ reaction is a very bad case with a large Q-value (5.50 MeV), but a final nucleus having 4 excited levels within 1 MeV above threshold and 8 excited levels below threshold ; problems of summation effects in large volume γ-ray detectors would render difficult a measurement in a radioactive beam.

The energy resolution of the detectors is an important parameter. In a case like ^{21}Na(p,γ), it is mandatory to use detectors with the best possible resolution, e.g. Ge crystals. In a case like ^{13}N(p,γ), fast detectors, e.g. NaI scintillators, packed closely around the target, could be used [6].

The importance of an additional signature has to be stressed : a bunched accelerator offers the possiblity to record the time-of-flight of the γ-rays with respect to a RF signal or a signal indicating the passage of a beam burst through the target (the second method is more precise). In the ^{13}N(p,γ) measurement [2] the signal-over-background ratio was increased by a factor 5 after the correlation with the t.o.f. peak was taken into account.

In this method, another factor to control is the cosmic ray background : big γ-ray detectors are very efficient also to cosmic rays. In particular cylindrical detectors disposed horizontally will produce a continuous spectrum of amplitudes from cosmic rays. Vetoing on the latter is indeed very useful : the gain in signal-to-background was a factor 2 in the ^{13}N(p,γ) measurement. Large surface plastic scintillators are the most effective detectors for vetoing ; however, in order to veto efficiently, they have to be close to the γ-ray detectors, and thus close to the beam, which implies that they are also susceptible to record a large number of background 511 keV γ-rays. An alternative solution is plastic Cerenkov detectors which have a detection threshold large enough to suppress most of the interactions of 511 keV γ-rays [7].

3.2   Radioactivity of B-nuclei : detection of positrons

Both the B and A nuclei are positron emitters. Being further away from the stability line, B will have a larger β^+ endpoint and a shorter lifetime : these are the two signatures that can be used to separate B from A. B and A being implanted in a catcher foil perpendicular to the beam direction beyond the target, a brute force method using a set of plastic scintillators would appear sufficient to select positrons from A (stopping the first part of the stack), from positrons from B (continuing further on in the stack). A more elaborate solution is a positron magnetic spectrometer along the beam axis in which low energy positrons spiral in the axial field and are stopped in an obstacle a few cm beyond the catcher, while high energy positrons are able to escape the obstacle and they are guided to a stack of scintillators. Alternating beam ON-OFF time with a period determined by the lifetime of B, and recording the stack counting rate versus time inside a period allowed to get the lifetime signature, in addition to the (rough) energy signature of the positrons in the stack. This method was used successfully in the ^{19}Ne(p,γ)^{20}Na case ; the

endpoint energy and lifetime of ^{19}Ne are 2.2 MeV and 17.2 s, respectively, which are very different indeed from the same quantities in ^{20}Na, i.e. 11.2 MeV and 0.44 s. Other favourable cases are : ^{7}Be(p,γ)^{8}B, ^{11}C(p,γ)^{12}N, ^{27}Si(p,γ)^{28}P, ^{35}Ar(p,γ)^{36}K.

In such a magnetic spectrometer, cosmic rays were found to be an important source of background. Although the spectrometer was surrounded by plastic scintillators it appeared that the neutral cosmic component could interact in the iron and the coils of the solenoid and create particles reaching the detectors. A solution to this problem was to separate the first scintillator of the stack from the rest (40 cm in front of the rest), and to record the time-of-flight between this first scintillator and the other ones. A remaining background of about 2 events/hour survived after all the cuts were applied [8].

It should be realised that, contrary to the γ-ray detection (3.1), this method suffers from a less precise signature. As a consequence, the contribution of Carbon in the target can be a problem as soon as direct reactions with beam particles are energetically possible and they lead to final nuclei having a lifetime and a β^+ endpoint close to the ones of the B nuclei. This problem was experienced in the ^{19}Ne(p,γ)^{20}Na measurement, where the ^{19}Ne (^{12}C,t)^{28}P was possibly occuring.

3.3   Delayed activity of B-nuclei : detection of hadrons

In a limited number of cases, the positron decay of B nuclei is followed by subsequent emission of hadrons (α-particles or protons). The branching ratio of such decays varies from 100 % (in ^{7}Be(p,γ)^{8}B) to 0.05 % (in ^{35}Ar(p,γ)^{36}K). The ^{19}Ne(p,γ)^{20}Na is intermediate with a branching ratio of 20 %.

In order to detect with a decent efficiency the delayed particles, one has thus to place solid state detectors close to the implantation of the B-nuclei, which is also the source of the positrons from the beam nuclei : thin segmented detectors have to be used to limit the sensitivity to positrons. These detectors should really be as thin as possible : double sided strip silicon detectors of 34 μm-thickness detected delayed α-particles from the ^{19}Ne(p,γ)^{20}Na reaction [9], in which the maximal α-energy is 4.4 MeV, with a range of about 20 μm in Si ; a clear signal was obtained from the energy spectrum only. Due to their larger range, the detection of delayed protons appears more problematic ; two solutions are i) identification in ΔE/E thin strip detectors and ii) recording of the time-of-flight information in addition to the energy.

The delayed α-particles can be detected as well in passive nuclear track detectors, which reveal the presence of α-particles when they are subsequently

etched. The difficulty is to treat properly the foils in order to decrease as much as possible the background tracks before the irradiation ; a number as small as $1.6/cm^2$ was obtained [9]. This background problem is particularly serious here as the only signature is the lifetime of the B-nuclei, which is obtained after the activity was moved successively in front of different track detectors (the information is thus strongly discretized).

3.4 Direct detection of B-nuclei in a recoil mass spectrometer

As far as the collection efficiency si concerned, this method is by far superior to the previous ones : typically a gain of one order of magnitude can be expected, from a few percent to a few tens of percent. A spectrometer is well adapted to capture reactions performed in inverse kinematics. Beyond the target, beam and final nuclei are contained in a narrow cone of which the opening angle is determined by three factors : the kinematics of the reaction, the multiple scattering in the target, the emittance of the accelerator. Both species come out of the target in a superposition of different charge states, of which the most abundant can represent about 40 % of the total [10]. Moreover, momentum conservation implies that beam and final nuclei have nearly the same momentum, which means that their velocity is slightly different. In Louvain-la-Neuve, these characteristics were used to design a recoil mass spectrometer (RMS) presently under construction : a dipole magnet will first select the most abundant charge state of B (and of A as well), then a velocity filter will transmit the B nuclei and deflect the A nuclei, and finally a ΔE-E detector will record the B-nuclei. This last item will be of particular importance to achieve the desired global rejection of 10^{10} to 10^{11} (which is the usual ratio of beam to final nuclei) ; not only the ΔE-E identification but also the ΔE-t.o.f. two dimensional spectrum will be utilized. Each selection element - dipole, filter, detector - is preceded by a quadrupole magnet. The total length of the spectrometer is 9 m.

3.5 Detection of B-nuclei and γ-rays in coincidence

In principle, combining a recoil mass separator with a set of γ-ray detectors around the target would provide with a reduced background. However, this reduction in background will be obtained at the expense of a decrease in detection efficiency when compared with the efficiency of method 3.1 or 3.4, and of a large increase in cost. In addition, γ-ray detectors will furnish a timing signal, which is useful only near non-bunched accelerators, and they will also give some spectroscopic information on the B-nuclei, which can probably be

obtained more easily through nuclear reactions other than proton capture. In case a RMS set-up would suffer from a background problem, a first action should be to surround the B-nuclei detector with a large solid angle positron detector.

4 The recoil protons

Detecting the recoil protons from the target appeared mandatory in measurements with radioactive beams [11], for several reasons : i) the number of recoil protons is proportional to the product of the beam intensity and the hydrogen density in the target, whereas the ratio of recoil protons to scattered beam nuclei is a measurement of the stability of the hydrogen content in the target ; ii) the upper and lower boundaries in a recoil proton spectrum measure the CH_2 target thickness, versus time ; iii) the proton spectra at different angles contain important spectroscopic informations on the levels of the B nuclei which are scanned by the beam across the target, provided these levels have a total width larger than about 1 keV ; iv) proton spectra can be self-normalized through a fit to a squared amplitude which is the sum of a Coulomb and resonant contributions, and thus recoil protons provide with an absolute normalization to the (p,γ) measurement ; v) proton spectra monitor continuously that the resonant states of interest are effectively scanned completely by the beam through the target.

5 The (d,n) reaction : poison or help ?

As mentioned earlier, the deuterium content in the CH_2 target induces the $A(d,n)B$ reaction leading to the same final B nuclei. Although it is in principle possible to make CH_2 foils which are deuterium free, the procedure is so complicated that it was not tried (in particular, not only the initial hydrogen has to be deuterium-free, but also in the further steps, any organic catalyst has to be such as well). In practice, an additional measurement with a CD_2 target has thus to be performed, in order to subtract the deuterium contribution in the CH_2 target, which in fact can be as large as the (p,γ) signal and leads thus to a significant increase of the error affecting the (p,γ) measurement. More positively, the CH_2 measurement allows to calibrate the (p,γ) experimental set-up very quickly and efficiently. Positive also is the fact that the (d,n) cross section is needed to extract spectroscopic factors of levels in B that are used to calculate the direct (non-resonant) component of the (p,γ)-cross section [12].

Among the methods described above, the positron spectrometer (3.2) can

easily be modified to decrease the deuterium contribution : the CH_2 target is replaced with a static gas cell containing protium, i.e. hydrogen in which the natural deuterium content was depleted by a few orders of magnitude. Beam and final nuclei are then stopped in the back face of the cell, wherefrom positrons are emitted into the spectrometer. Beam nuclei backscattered from the thin entrance window of the cell are used for normalization.

Finally, one can notice that the recoil mass spectrometer (3.4) is nearly insensitive to the presence of deuterium in the CH_2 target ; the kinematics of the (d,n) reaction is very different from the (p,γ) reaction : not only the emission cone but also the momenta of the B-nuclei will strongly differ.

6 Conclusion

This contribution has summarized some experimental methods which were used to measure proton capture reactions induced by radioactive beams. These methods had existed long before radioactive beams became available, but they had to be adapted to this new situation. In fact,two obvious factors to take into account were the radioactivity of the beam, and its low intensity with respect to stable beams used formerly to study capture reactions. Moreover, other problems deserved some reflection, like the choice of the target, the absolute normalization of the cross section, the optimization of the detector efficiency and of the signal-to-background ratio.

References

[1] F. Rembges et al., Ap. J. **484** (1997) 412.

[2] Th. Delbar et al., Phys. Rev. **48** (1993) 3088.

[3] G. Vancraeynest et al., submitted to Phys. Rev. C.

[4] W. Galster et al., Phys. Rev. **C44** (1991) 2776.

[5] L. Gialanella et al., Nucl. Instr. Meth. Phys. Res. **A376** (1996) 174.

[6] L. Bonnet et al., Nucl. Instr. Meth. Phys. Res. **A292** (1990) 343.

[7] P. Leleux et al., Nucl. Instr. Meth. Phys. Res. **A329** (1993) 518.

[8] C. Michotte et al., Nucl. Instr. Meth. Phys. Res. **A366** (1995) 155.

[9] R.D. Page et al., Phys. Rev. Lett. **73** (1994) 3066.

[10] K. Shima et al., At. Data Nucl. Data Tables **51** (1992) 173.

[11] R. Coszach et al., Phys. Rev. **C50** (1994) 1695.

[12] P. Decrock et al., Phys. Rev. **C48** (1993) 2057.

Breakout from the Hot CNO Cycle: the ^{15}O(α,γ) and ^{18}Ne(α,p) Reactions

W. Bradfield-Smith[1], A.M. Laird[1], T. Davinson[1], A. Di Pietro[1],
A.N. Ostrowski[1], A.C. Shotter[1], P.J. Woods[1], S. Cherubini[2], W. Galster[2],
J.S. Graulich[2], P. Leleux[2], L. Michel[2], A. Ninane[2], J Vervier[2], M. Aliotta[3],
D. Cali[3], F. Cappuzzello[3], A. Cunsolo[3], C. Spitaleri[3], J. Gorres[4],
M. Wiescher[4], J. Rahighi[5], J. Hinnefeld[6]

1: Department of Physics and Astronomy, University of Edinburgh, UK
2: Institute de Physique Nucléaire, UCL, Louvain-la-Neuve, Belgium
3: INFN, Catania, Italy   4: University of Notre Dame, USA
5: Van de Graaf Laboratory, Tehran, Iran   6: University of Indiana South Bend,
USA

Abstract

One of the most important reactions which determines the rate of breakout from the hot CNO cycle is the ^{15}O$(\alpha,\gamma)^{19}$Ne. The reaction ^{18}Ne$(\alpha,p)^{21}$Na may also provide an alternative breakout route. Experiments are being undertaken at Louvain-La-Neuve using the radioactive ^{18}Ne beam to study these reactions by measurement of $\alpha(^{18}$Ne,p$)^{21}$Na and d$(^{18}$Ne,p$)^{19}$Ne$^{*} \rightarrow ^{15}$O $+ \alpha$

1   Introduction.

During explosive hydrogen burning, the seed nuclei C, N and O may leak out of the CNO cycle to produce heavier elements and isotopes. The main reaction which determines the leak rate is ^{15}O$(\alpha,\gamma)^{19}$Ne[1]. However in high temperature situations it may be that other reactions in addition provide alternative leakout routes. In particular the reactions ^{18}Ne(α,p) and ^{18}Ne$(2p,\gamma)$ have been suggested as possible candidates, although for the 2p reaction abnormally high densities would be required[2].

There is some information concerning the ^{15}O(α,γ) reaction deduced from direct experimental measurements of the α branching ratios for higher lying resonance states in the compound nucleus ^{19}Ne*, but there is no direct information for the 4.033 MeV resonance state in the ^{19}Ne* corresponding to the first resonance at an energy of 504 keV in the ^{15}O $+ \alpha$ system[3]. However, some information on this resonance has been deduced from reactions on the mirror system[4].

For the reaction ^{18}Ne$(\alpha,p)^{21}$Na no information is known about the reactions strength. Indeed there is limited information concerning even the position of states in the compound system ^{22}Mg at and above the α particle threshold energy of 8.14 MeV.

The paper here describes progress on two experiments carried out at Louvain-La-Neuve using the ^{18}Ne radioactive beam, to study the ^{18}Ne(α,p) reaction, and the

$^{15}O(\alpha,\gamma)$ reaction via the $^{18}Ne(d,p)^{19}Ne^* \rightarrow^{15}O + \alpha$ reaction.

2   Beam production.

The ^{18}Ne used in these experiments was created via a (p,2n) reaction, using a 30 MeV proton beam from the CYCLONE 30 cyclotron on a lithium flouride target. The ^{18}Ne produced was extracted from the target and passed to an ECR source. The ejected ions in the 3^+ charge state were then mass separated by a 90° analysing magnet before being passed to a second cyclotron, which accelerated the ions, giving a beam of ^{18}Ne with an intensity of of up to 10^6 particles per second.

3   The $^{18}Ne(\alpha,p)$ experiment.

3.1   Experimental method.

The helium gas target was contained inside a large chamber at a pressure of 500 mb, separated from the beam line vacuum by a nickel window of 2 mg/cm^2. Charged particles produced during the experiment were studied using a three detector telescope composed of double sided silicon strip detectors, DSSSD's, in an arrangement as shown in Figure 1. The thickness's used were 60μ, 300μ and 500μ. The use of such a thin ΔE detector allowed protons to be identified down to an energy of 3.3 MeV, above a background of coincidences of elastically scattered protons or helium nuclei with β particles. The 'quasi pixellisation' of the DSSSD's allowed the trajectory of a proton event to be reconstructed in the analysis.
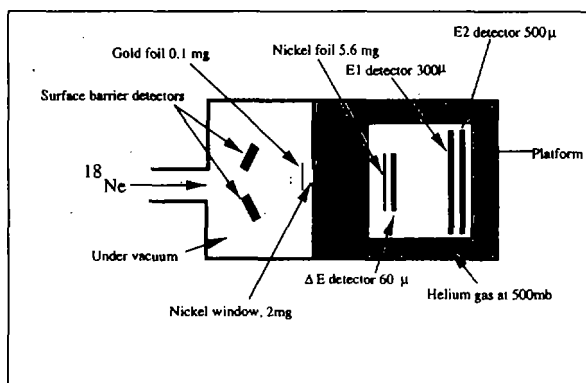
Figure 1: A schematic diagram of the experimental setup for $^{18}Ne(\alpha,p)$.

The telescope system was protected from the beam particles by a nickel foil of 5.6 mg/cm^2 directly in front of the first detector, as shown in figure 1. The telescope system, together with this nickel foil, was mounted upon a movable platform which allowed the distance that the beam particles could travel through the gas to be varied, and so different energy ranges to be scanned in the compound nucleus.

The 30 MeV ^{18}Ne beam entered the gas volume at an energy of 17 MeV and degraded to an energy of 9 MeV before being stopped in the nickel foil. Resonant reactions between ^{18}Ne and α could therefore be detected between 3 and 1.8 MeV in the CoM of the ^{18}Ne $+ \alpha$ system.

The data was normalised using the Rutherford scattering of beam particles from the gold foil into the surface barrier detectors in the backward angle.

3.2 Results.

Proton energy spectra are shown in figure 2 for two different cases, with and without a gas target. Various groups of protons are seen which may be interpreted either as being due to the reaction ^{18}Ne(α,p) or as being due to the elastic scattering of proton contamination present in either the nickel and gold foils or in the gas.

The peaks labeled #4 and #6, present when the gas was evacuated from the target chamber, are due to the elastic scattering of protons from water contamination from the beam line side and the target chamber side of the nickel window respectively. Peaks #1, #2, #3 and #5 are due to reactions with the gas and correspond to two different levels being excited in the compound state.

3.3 Discussion.

These results indicate that there are at least two resonance states in the energy range between 2.5 and 3.0 MeV. The peaks shown in figure 2 indicate that the upper level resonance decays to the 3.544 Mev excited state and the 0.331 MeV excited state of ^{21}Na. The lower resonance decays to the ground state and the 1.716 MeV excited state of ^{21}Na.

Preliminary analysis indicates that the $\omega\gamma$ values of the two resonances are of order of keV. If this analysis is confirmed then these resonances will have a significant contribution in the reaction rate for temperatures $> 10^9$K. Further work is in progress to investigate the systematic errors in order to specify the most appropriate final values of $\omega\gamma$ in each case.

4 ^{15}O(α,γ)^{19}Ne

4.1 Background.

The first scattering resonance for the ^{15}O $+ \alpha$ system occurs at an energy of 504 keV, corresponding to a compound state at 4.033 MeV in ^{19}Ne. Since the α branching
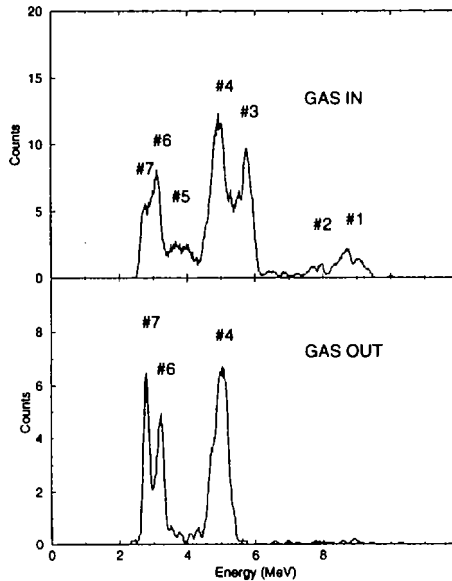
Figure 2: The proton energy spectra for the gas target in and the gas target out. A smoothing of the raw data over a width of 150 keV was performed in both cases.

ratio for this state is expected to be very small ($\sim 10^{-4}$), then $\omega\gamma \simeq \omega\Gamma_\alpha$. Excitation of states in ^{19}Ne above the $\alpha + {}^{15}$O threshold of 3.529 MeV and investigating their α decay can give information concerning $\omega\gamma$ for such states, and therefore the reaction rate for helium burning of ^{15}O.

An excellent experiment using the reaction ^{19}F(^{3}He,t)^{19}Ne* to excite ^{19}Ne states gave information concerning the α decay for states down to 4.379 MeV[3]. With the production of radioactive beams other reactions become available for study. This paper reports first results for the reaction d(^{18}Ne,p)^{19}Ne* $\rightarrow \alpha + {}^{15}$O. The advantage of this reaction is that in general (d,p) reactions tend to have significantly higher cross sections than charge exchange reactions, however the beam intensities of radioactive beams are at present lower than for stable beams.

4.2 Experimental methods.

A beam of ^{18}Ne at 42 MeV, with an intensity of 10^5 pps, was allowed to interact with a CD$_2$ target of thickness 0.5 mg/cm^2 in a chamber with various silicon detector

$$d(^{18}Ne, ^{19}Ne^*)p$$
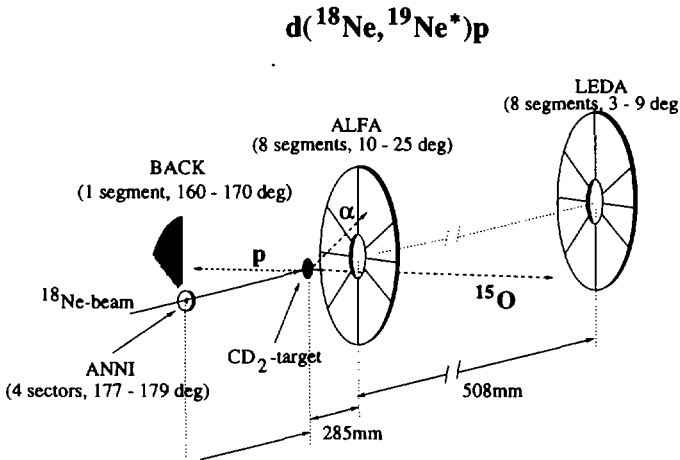
Figure 3: The $d(^{18}Ne,p)^{19}Ne^* \rightarrow \alpha + {}^{15}O$ detector arrangement.

arrays to detect the reaction particles. In total, the arrays composed 276 individual detectors. The arrangement of the scattering chamber is shown in figure 3. Since the reaction is inverse, the maximum yield of protons will be in the backward direction. Forward silicon (LEDA) arrays were used to detect the recoiling ^{15}O and α particles. TDC's were used on all detector channels for measurement of time of flight spectra for particle identification purposes.

4.3 Results.

Preliminary results of a proton spectrum recorded in the back proton detectors under the conditions that the event caused 3 detectors to fire in coincidence in separate arrays:(BACK,ALFA,LEDA), is shown in figure 4. Such a multiplicity 3 condition would be consistent with an event of the type $d(^{18}Ne,p)^{19}Ne^* \rightarrow \alpha + {}^{15}O$. However due to intense β^+ background caused by the radioactive beam, events of the type $d(^{18}Ne,p)^{19}Ne^* \rightarrow {}^{19}Ne + \gamma$ are also present in the spectrum of figure 4, of multiplicity 3 and type: (p, ^{19}Ne, β^+). The spectrum shows many states that can be identified as belonging to ^{19}Ne. For the events shown in figure 4, when a total energy requirement is placed on the three energy signals so that $\sum_i E_i > 35$ MeV, nearly all the events above 2.5 MeV in the spectrum vanish. This is exactly as expected since such a gate will reject the (p,^{19}Ne,β^+) events, and the α branching ratio becomes small for the ^{19}Ne states below 4.5 MeV.
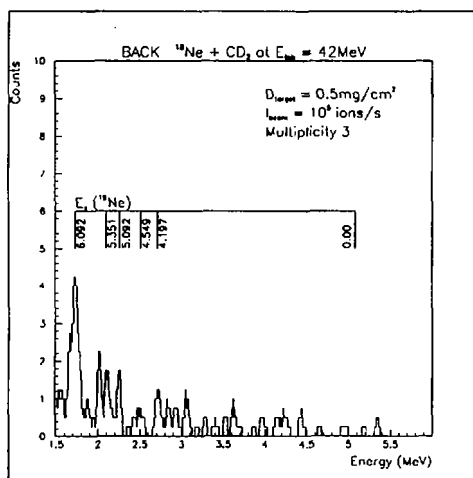
Figure 4: The proton multiplicity 3 spectrum.

4.4 Discussion.

This preliminary experiment shows the yield that can be expected from such a reaction. With straightforward improvements in beam intensity to 10^6 pps and detector arrangements (giving an increase by a factor of ten in the solid angle) the information that is obtainable would be similar to that of the earlier (^{3}He,t) experiment[3]. To have a reasonable chance of obtaining useful information concerning the α branching of the 4.033 MeV state would require an intensity $> 10^7$ pps of ^{18}Ne. It is hoped that such an intensity will be possible in the future.

References.

1. A.E. Champagne and Wiescher, Ann.Rev.Nucl.Part.Sci. 42(1992)39.

2. J. Görres et al. Phys.Rev.C51(1995)392.

3. P.V. Magnus et.al. Nucl.Phys.A506(1990)332

4. Z.Q. Mao et.al. Phys.Rev.Lett 74(1995)3760.

INVESTIGATIONS OF ASTROPHYSICALLY INTERESTING NUCLEAR REACTIONS BY THE USE OF GAS TARGET TECHNIQUES ♣

J. W. HAMMER

*Institut für Strahlenphysik (IfS), Universität Stuttgart,
Allmandring 3, D-70550 Stuttgart, Germany*

Abstract

A brief review of the common properties of windowless and recirculating gas targets is presented. As example the Stuttgart gas target facility RHINOCEROS in the extended and in the supersonic jet mode with its properties and techniques is explained, also with respect to gas purification techniques. Furthermore several typical experiments from the field of nuclear astrophysics with characteristic results are described ($D(\alpha,\gamma)^6$Li, $^{15}N(\alpha,\gamma)^{19}$F, $^{16}O(p,\gamma)^{17}$F, $^{16}O(\alpha,\gamma)^{20}$Ne, ^{20}Ne$(\alpha,\gamma)^{24}$Mg, ^{21}Ne$(\alpha,n)^{24}$Mg, $^{18}O(\alpha,n)^{21}$Ne, $^{17}O(\alpha,n)^{20}$Ne). In several cases the experimental sensitivity could be raised by up to a factor of 10^6.

1   Introduction

Windowless gas targets are a unique tool for physics experiments in nuclear, astro-, atomic, molecular and plasma physics. They are required to bring an intense particle beam from the high vacuum side of an accelerator into a gas which is under a pressure in the range of mbars up to bars[1].

These targets have proven to be undestructible under high beam power. Gas recirculation makes experiments with very expensive isotopic enriched gas possible. The gas can be recovered after each run to about 98 % in the storage bottle. Using pure gases avoids stoichiometric problems. The target thickness can easily be controlled by the target pressure and the target is changed by changing the gas without breaking the vacuum. Mixtures of gases make calibration runs simple. In contrast to the work performed with solid state targets on backings experiments with gas targets don't suffer from high background, especially when worked in transmission geometry when the beam is dumped far away from the reaction chamber in a Faraday cup. Using properly passivated reaction chambers and gas purification elements allows clean working

with no build up of deposits. In the cases where high enrichment of a gas or isotop is not available, differential measurements allow to distinguish the yield contribution of each component.

Windowless gas targets are constructed as extended e.g. merely differential pumped systems and as supersonic jet systems, where the target zone is a gas jet behind a Laval nozzle.

A gas target can be used in regular kinematics with the gases H_2, D_2, ^{3}He, ^{4}He, $^{14}N_2$, $^{15}N_2$, $^{16}O_2$, $^{17}O_2$, $^{18}O_2$, ^{20}Ne, ^{21}Ne, ^{22}Ne, and all heavier rare gases. Furthermore the use of compounds like CO, CO_2, CF_4 gives access to carbon and fluor as a target. Working with inverse kinematics nearly all nuclei are accessible as a projectile and the target consists of H_2, D_2, ^{3}He, ^{4}He and heavier species. This method is especially of interest for the work with radioactive beams.
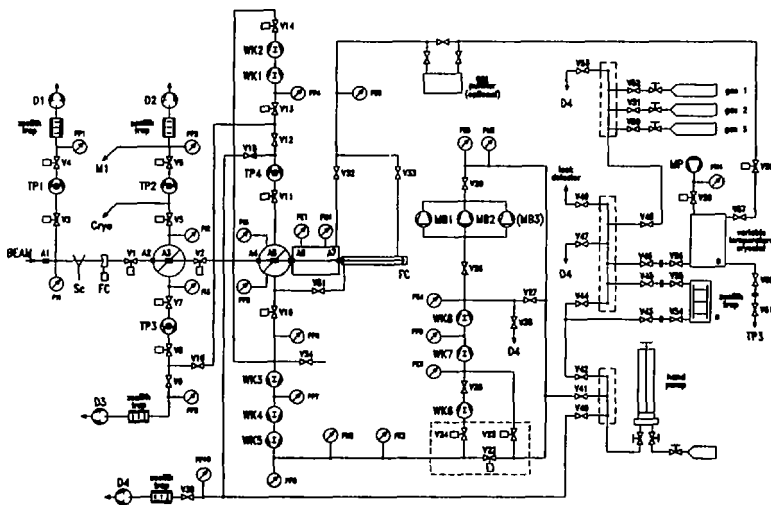
Fig. 1: *Scheme of the differentially pumped ("static" or "extended") version of* RHINOCEROS *with all essential elements. The beam enters the recipients from the left and is controlled by a diaphragm (A 1), a beam profile monitor (Sc) and a Faraday cup (FC). It is transferred to the target chamber through six apertures, (A 1–A 6) which are mounted in two spheres, each consisting of two semispheres. Each semisphere is connected to a pumping stage, in total four stages. On the right side of the scheme one finds three purifier elements.*

2 The Stuttgart gas target facility RHINOCEROS

The Stuttgart gas target facility RHINOCEROS has been designed for experiments with high intensity beams in the kW range from a DYNAMITRON accelerator where one is searching for rare events of very different subjects of physics f.i. extreme low cross sections. The advantage of the RHINOCEROS facility is its versatility and its technical design which opened new experimental fields. The facility (block scheme see Fig. 1) has the following criteria: both configurations can be set easily using the same set of pumps: the extended set-up for thick target applications and the jet configuration for cases where a pointlike target is needed. Because of the use of isotopic enriched target gases the recirculation mode and the purification of the gas is mandatory. To achieve a maximum of versatility the target pressure can be chosen between 10^{-4} and about 2000 mbar in the extended mode and a target thickness of up to 25 mg/cm^2 can be obtained. In the jet mode a maximum target thickness of $10\,\mu$g/cm^2 is achievable. Fig. 2 shows the cross section of the jet configuration. With 4 to 6 differential pumping stages and 20 mechanical pumps and compressors a pressure reduction of up to $1 : 10^{11}$ can be reached. Using enriched isotopes a gas investment of 0.5 - 1 l is sufficient to run an experiment at a mbar–level in the extended mode.
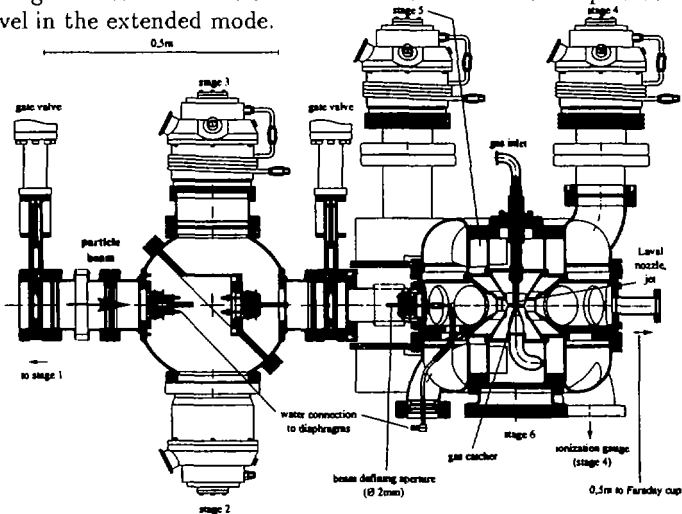
Fig. 2: *Sectional drawings of the recipients of the supersonic jet set-up. On the right side one finds the jet surrounded by a scattering chamber. On the left side the beam enters through a differential pumping section (stage 1 and 2), the same which is used in the extended setup.*

Attention was directed to avoid leakage and contamination of the facility as far as possible by the use of metal sealed connections, proper lubrication of the pumps, grease for the turbo pumps and oil with low vapour pressure for the roots blowers. The leakage of the whole RHINOCEROS facility is in the range of 10^{-7} mbar·l·sec^{-1}. The purification of the target gas is performed by the use of three elements: absorber, cryotrap and getter. The purification works up to a level of 10^{-7} for rare gases. For critical applications as the use of chemical active or aggressive gases the reaction chambers have been gold plated and some of the pumps have been passivated. By this also experiments with metal vapours or with fluorine rare gas mixtures could be undertaken to a certain extent. All parts which guide the beam are directly watercooled in an efficient way.

3 Characteristic experiments and their results obtained with the RHINOCEROS facility

3.1 Investigation of D$(\alpha,\gamma)^6$Li as example for big bang nucleosynthesis

The reaction D$(\alpha,\gamma)^6$Li is producing ^{6}Li according to the big bang model, but the amount of ^{6}Li produced depends on the reaction rate at the appropriate temperature.

Fig. 3: *Excitation function of D($\alpha,\gamma)^6$Li around the 3^+ resonance at $711\,keV$ (CM) together with a DC model description. The extrapolation towards lower energies is not shown, but leads to a S-factor of $2.7 \cdot 10^{-9}\,MeV \cdot b$ at $E_{CM} = 53\,keV$*
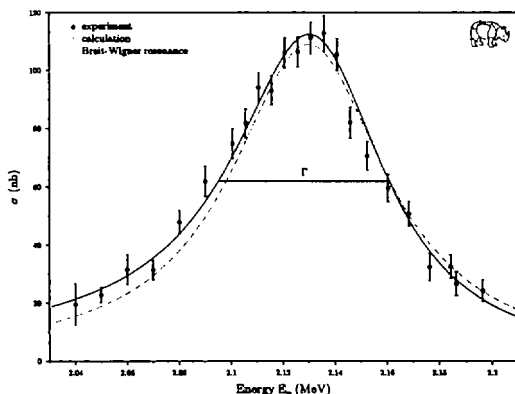
To improve the situation concerning the experimental data of this reaction a direct measurement has been undertaken to obtain the excitation function around the dominating 3^+ resonance at $711\,keV$ (CM) and to describe the

experimental data within the framework of a DC model. From the model description the cross section at low energies is deduced. The result of the gas target experiment on $D(\alpha,\gamma)^6Li$ is shown in Fig. 3 together with the result of the calculation [2]. The conclusion concerning the reaction rate was, that the big bang synthesis of ^6Li cannot explain the ^6Li abundance.

3.2 Search for a mirror state in ^{19}Ne concerning the breakout from the HotCNO cycle by observing $^{15}N(\alpha,\gamma)^{19}F$

The reaction $^{15}N(\alpha,\gamma)^{19}F$ gets involved because ^{19}F is the mirror nucleus of the unstable ^{19}Ne nucleus which is responsible for the breakout or recycling from the HotCNO cycle. The question was to find a $3/2^+$ state at $E_x \approx 7.1$ MeV which might lead to a considerable reaction rate at $T_9 = 0.5 - 1$ MeV. Therefore a direct search for a resonance of $^{15}N(\alpha,\gamma)^{19}F$ at $E_\alpha \approx 4$ MeV should give clarity and show a clear and unique signature in the γ decay scheme for a $3/2^+$ state in contrast to an already known $7/2^+$ state. The experiment at the maximum voltage of the Stuttgart DYNAMITRON yielded the result of Fig. 4. There was observed a clear evidence for a $3/2^+$ resonance at $E_x = 7100.7 \pm 0.8$ keV with $\Gamma_\alpha = 27.9 \pm 1.1$ keV and a strength of $\omega\gamma = 0.77 \pm 0.11$ eV. Since the γ-width is only $\Gamma_\gamma = 0.38 \pm 0.06$ eV the $^{18}F(p,\alpha)^{15}O$ reaction is the dominating branch which recycles material back to the HotCNO cycles [3]. On the other hand the reaction $^{15}N(\alpha,\gamma)^{19}F$ is also of interest for the production of ^{19}F and it has been investigated by [4].

Fig. 4 : *Exci-tation function of $^{15}N(\alpha,\gamma)^{19}F$ around the $3/2^+$ resonance at $E_\alpha \approx 4$ MeV. The signature for the $3/2^+$ state was obtained clear by the γ-decay scheme.*
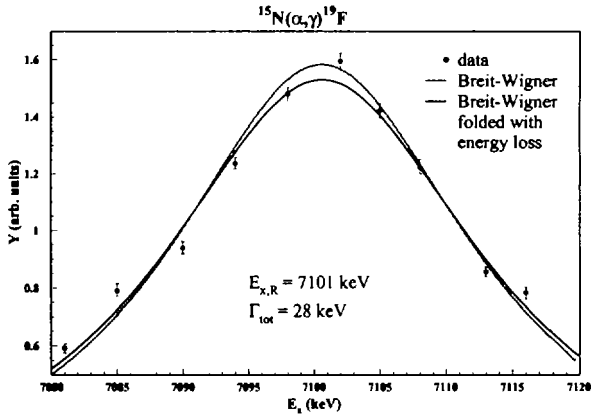
3.3 The reaction $^{16}O(p,\gamma)^{17}F$ in the CNO cycle

The reaction $^{16}O(p,\gamma)^{17}F$ occurs in the regular CNO cycle II and the β^+-decay of ^{17}F leads to a ν emission which gives information on the original oxygen abundance. The $^{16}O(p,\gamma)^{17}F$-reaction proceeds in the energy range below 2.6 MeV by two branches of nonresonant direct capture. The excitation function for both branches has been obtained in a gas target experiment in the energy range $E_{CM} = 200 - 3600$ keV. The astrophysical S-factor shows a quite different behaviour for the DC → 1 and the DC → 0 branch which can be explained in the framework of a Direct Capture model [5]. For the DC → 1 branch the overlap integral of the interaction has its maximum at a radius of about 42 fm in contrast to the DC → 0 branch ($r \approx 18$ fm) and therefore one characterizes the properties of the $1/2^+$ state as halo [6].

Fig. 5 : *S-factor curves of $^{16}O(p,\gamma)^{17}F$ for the DC → 1 and the DC → 0 branch together with a model fit [5]. The S-factor for the capture to the first excited $1/2^+$ state of ^{17}F is enhanced towards low energies because of the halo properties of this state.*
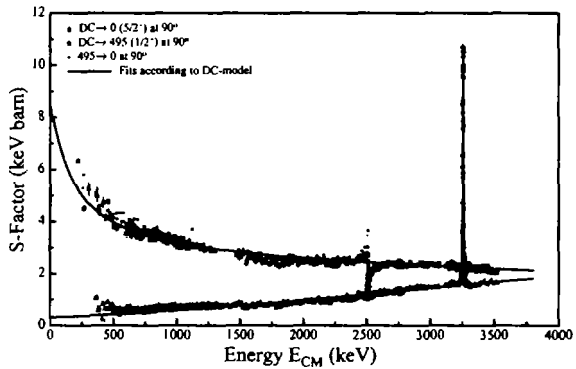

3.4 The helium capture reactions $^{16}O(\alpha,\gamma)^{20}Ne$ and $^{20}Ne(\alpha,\gamma)^{24}Mg$

In the helium burning the reaction $^{16}O(\alpha,\gamma)^{20}Ne$ proceeds with a rather slow reaction rate because in the relevant temperature range ($T_9 \approx 0.2$) no resonance is present and only the nonresonant direct capture will contribute [7]. To extrapolate this nonresonant capture into the energy range of interest the whole excitation function has to be explored to extract this nonresonant part in a proper manner by an R-matrix analysis. The data points at the lowest yield correspond to a cross section of about 10 pikobarn. Because of the extended geometry the yield cannot be transfered to a cross section point by point. The experimental result is shown in Fig. 6. The $^{16}O(\alpha,\gamma)^{20}Ne$ reaction is also of interest in hotter scenarios where the back reaction (photodisintegration) can occur. For the same reason the $^{20}Ne(\alpha,\gamma)^{24}Mg$ reaction has been investigated

improving the dynamic sensitivity by a factor of about 1000. This was due either to the advanced target technique but also to the improved detectors (100 % Ge with BGO active shielding) [8].


Fig. 6 : *Excitation function of $^{16}O(\alpha,\gamma)^{20}Ne$ obtained in a direct gas target experiment. The lowest data points correspond to a cross section of about 10 pikobarn. The curves represent different calculations.*
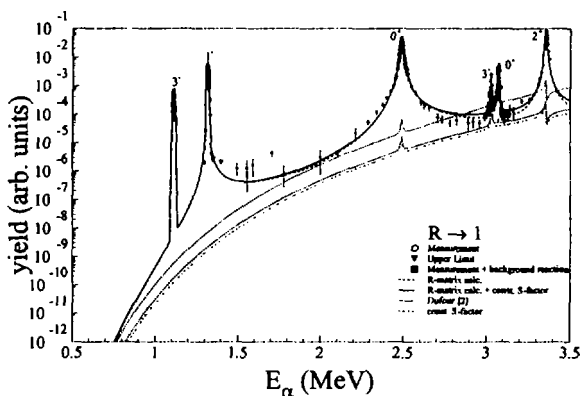
3.5 Some (α,n)-reactions of interest for neutron production in stars

All (α,n)-reactions for the elements up to Mg have been investigated in our lab [9], some of them using the gas target RHINOCEROS. The neutrons escaping the tubular reaction chamber have been detected in a 4π neutron detector with up to 40 % absolute efficiency. Using the gas target the range of the excitation function for $^{21}Ne(\alpha,n)^{24}Mg$ (see Fig 7) could be extended towards lower energies in a dynamic range of $1:10^6$ compared to measurements with a drive-in target. The reaction $^{18}O(\alpha,n)^{21}Ne$ could be measured directly from threshold at 860 keV up to about 2 MeV. Similar the excitation function for $^{17}O(\alpha,n)^{20}Ne$ could be determined, however because ^{17}O was only available with 50 % enrichment, the yield due to $^{18}O(\alpha,n)^{21}Ne$ (29 %) had to be subtracted very carefully, a typical advantage of the gas target technique [10]. ^{16}O (21 %) has no (α,n)-reaction in this energy range. In the same manner the reaction rate of the prominent $^{22}Ne(\alpha,n)^{25}Mg$ reaction has been determined [11] using a differential measurement against ^{20}Ne as target gas to get rid of some neutron background from the walls of the reaction chamber. By this the sensitivity limit was at a level of $4 \cdot 10^{-10}$ b and it comes mainly from neutrons induced by cosmic rays.

Fig. 7 : *Excitation function of $^{21}Ne(\alpha,n)^{24}Mg$. The arrow indicates the dynamic range which has been gained by the use of the windowless gas target and of the 4π-detector.*
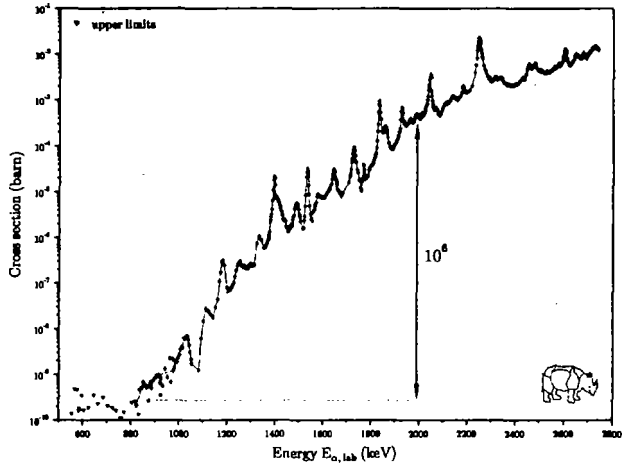
References

[1] J.W. Hammer, IfS-report 03–98, Stuttgart 1998

[2] P. Mohr et al., Phys. Rev. C48 (1993) 1420.

[3] Y. Butt et al., submitted to Phys. Rev. C

[4] S. Wilmes et al., Phys. Rev. C52 (1995) R 2823

[5] R. Morlock, R. Kunz, A. Mayer, M. Jaeger, A. Müller, J.W. Hammer, P. Mohr, H. Oberhummer, G. Staudt, V. Kölle, Phys.Rev.Let. 79 (1997) 3837.

[6] K. Riisager et al., Nucl. Phys. A548 (1992) 393

[7] H. Knee, Dissertation, Stuttgart, Verlag Shaker, Aachen, 1994, ISBN 3–8265-0528-X.

[8] V. Kölle, Dissertation, Tübingen 1997.

[9] R. Kunz et al., Proc. of the 4th Int. Conf. of Appl. of Nucl. Techn. "Neutrons and their Applications", Crete, Greece, Eds. G. Vourvopoulos, Th. Paradellis, Bellingham 1995, 2339, 33-55

[10] A. Denker, Dissertation, Stuttgart, Verlag Shaker, Aachen 1994, ISBN 3–8265-0191-8.

[11] H.W. Drotleff, A. Denker, H. Knee, M. Soiné, G. Wolf, U. Greife, C. Rolfs, H.P. Trautvetter and J.W. Hammer, Ap.J. 414 (1993) 735.

MEASUREMENT OF REACTION RATES OF INTEREST IN STELLAR STRUCTURE AND EVOLUTION

F. TERRASI[1], L. CAMPAJOLA[2], A. D' ONOFRIO[1], L. GIALANELLA[2,3], U. GREIFE[3], G. IMBRIANI[2], V. ROCA[2], C. ROLFS[3], M. ROMANO[2], O. STRANIERO[4], F. STRIEDER[3] and H.P. TRAUTVETTER[3]

[1] *Dipartimento di Scienze Ambientali, Seconda Università di Napoli, I-81100 Caserta and INFN, Napoli, Italy*

[2] *Dipartimento di Scienze Fisiche, Università Federico II, I-80125 Napoli and INFN, Napoli, Italy*

[3] *Institut für Experimentalphysik III, Ruhr-Universität Bochum, D-44780 Bochum, Germany*

[4] *Osservatorio Astronomico di Collurania, I-64100 Teramo, Italy*

Abstract

Accurate determinations of reaction rates at astrophysical energies are very important in stellar structure and evolution studies. The cases of two key reactions, namely $^7Be(p,\gamma)^8B$ and $^{12}C(\alpha,\gamma)^{16}O$ are discussed, both from the point of view of their astrophysical interest and of the experimental difficulties in the measurement of their cross section.

1 Introduction

The study of both the quiescent and explosive phases of stellar evolution requires an accurate knowledge of the rate of several reactions taking place in astrophysical environments. These nuclear inputs in stellar models are fundamental quantities needed to perform reliable predictions of the structural evolution of the star and the energy production, as well as of the nucleosynthesis of elements [1,2].

The cross sections of a large fraction of the reactions of interest at the relevant energies are still poorly known to date, due to the extremely small rates with which laboratory investigations are confronted. This may be ascribed either to the very small cross sections, in the case of very low energy reactions involved in quiescent burning, or to the difficulties of producing adequate targets or beams, in the case of reactions at Coulomb energies in which one of the partners is a short-lived radioactive nucleus.

New efficient experimental approaches which allow high selectivity are then needed to put stellar model predictions on more solid bases. In this paper we present some

preliminary results on the study of (p,γ) and (α,γ) capture reactions, which play a key role in the above scenarios. This study is based on the use of inverse kinematics to obtain cross section measurements in singles by a Recoil Mass Separator (RMS), identifying and counting with high efficiency the heavy residues of the reaction.

Attention is devoted to the cross sections of the ^{1}H(^{7}Be,γ)^{8}B reaction, which plays a key role in the solar neutrino problem and is to date affected by large uncertainties, and of the ^{4}He(^{12}C,γ)^{16}O reaction. The latter is known to be crucial in establishing the stellar lifetime during the He burning phases as well as in determining the late evolution of massive stars. Some key quantities, like the cosmological He abundance as derived from the oldest galactic stellar population or the remnant mass of a type II supernova explosion, might be affected by a change in the current rate of ^{12}C(α,γ)^{16}O. We report some preliminary calculations of stellar models showing the influence of this reaction rate on the current stellar evolutionary scenario.

First results obtained with the Naples RMS for the ^{1}H(^{7}Be,γ)^{8}B reaction at 1 MeV center of mass energy, using a radioactive ^{7}Be beam and a windowless H$_2$ gas target, are reported in section 2. Modifications to the RMS lay-out which have lead to the improved momentum- and angle-acceptance ERNA recoil separator, under construction at the Bochum accelerator for the study of the ^{4}He(^{12}C,γ)^{16}O reaction, are discussed in section 3.

2   The ^{7}Be(p,γ) reaction

The astrophysical S-factor S(E) = σ(E)·E·exp(2πη) of the ^{7}Be(p,γ) reaction at solar energies is a fundamental parameter for the predictions of the Standard Solar model (SSM) [3] concerning the expected flux of high energy neutrinos, and therefore plays a key-role in the solar neutrino problem.

2.1   Astrophysical motivation

Apart from the overall discrepancy between the experimental data obtained from the operating solar neutrino experiments (GALLEX, SAGE, HOMESTAKE and KAMIOKANDE) and the SSM predictions, the so-called Be/B anomaly, i.e. the incompatibility of Chlorine and ν-scattering experiments, is closely related to the above nuclear input. The predicted rates in the high energy neutrino flux measurements (both for the operating one and for those planned for the future), as well as the dominant contribution in SSM predictions of the rate of the Cl experiment, are proportional to the low-energy rate of the ^{7}Be(p,γ) reaction. Whatever the right solution to the Be/B anomaly will be found to be (i.e. a nuclear solution or the need of a new neutrino physics, in contrast with the standard

electroweak model), an accurate determination of the cross section of the $^7Be(p,\gamma)$ reaction at the Gamow energy (~18 keV) is perhaps "the most important experiment to be performed in nuclear astrophysics" [4]. This cross section has been to date measured down to 140 keV using ^7Be targets and, in most cases, detecting the α particles coming from the β-delayed decay of ^8B. The target stoichiometry can be the source of systematic errors, which have produced the big discrepancies in the absolute values measured in different experiments [5].

Direct access to the astrophysical energy is extremely difficult, due to background problems [6], so that extrapolations from higher energy measurements have to be performed. In next section we briefly report on preliminary results of an experiment aiming to solve the problem of possible systematic errors, due to the use of radioactive targets, by means of an inverse kinematic approach. The result is expected to be a reliable normalization point at 1 MeV center-of-mass energy, which can be used for a more accurate extrapolation.

2.2 Measurements in inverse kinematics

For the purpose of the inverse kinematic measurement of the cross section of the $^1H(^7Be,\gamma)$ reaction, a pure ^7Be beam has to be guided on a windowless H_2 gas target. A radioactive ^7Be beam at $E_{lab}=8MeV$ from the 3 MV tandem TTT-3 accelerator of the University of Naples was produced [7] using a proton-activated Li_2O cathode in the sputtering source of the accelerator, injecting the BeO^- molecules into the accelerator at 2.614 MV, accelerating the $^7Be^{3+}$ ions in the high energy stage, post-stripping them to the 4^+ charge state in a thin carbon foil and finally separating the radioactive beam from the $^7Li^{3+}$ ions by the analyzing magnet. Charge state ambiguities were eliminated by use of a "purification" Wien filter between the accelerator and the analyzing magnet. With a low activity cathode a 30 pA beam, lasting about 12 hours, was obtained and focused onto a differentially pumped gas target system filled with H_2 gas at a pressure of 5 mbar [8]. The interaction region was surrounded by Si detectors used for normalization of the cross section to the Rutherford backscattering of heavy projectiles, measured through the detection of recoiling protons.

The ^8B recoil nuclei are separated from the beam – with equal linear momentum – by a Recoil Mass Separator featuring a 30° magnet and a crossed field velocity filter [9]. The angular and momentum acceptance, as well as the beam suppression factor and the charge state probability, have been accurately measured, using also as a test case the $^1H(^{12}C,\gamma)$ reaction at $E_{cm}=0.841MeV$ [9].

The first run for the $^1H(^7Be,\gamma)$ reaction yielded in the final detector the matrix shown in fig. 1. The five ^8B events give a cross section of 0.5 µb, with a 50% statistical error due to the low statistics. It is presently planned to continue this experiment using high activity cathodes produced via hot chemistry to achieve

higher beam intensity and therefore better statistics. In any case, our results show that the present RMS is able to accurately measure radiative capture cross sections when the angular and momentum spread of recoil products are not larger than 7 mrad and 1.9%, respectively.
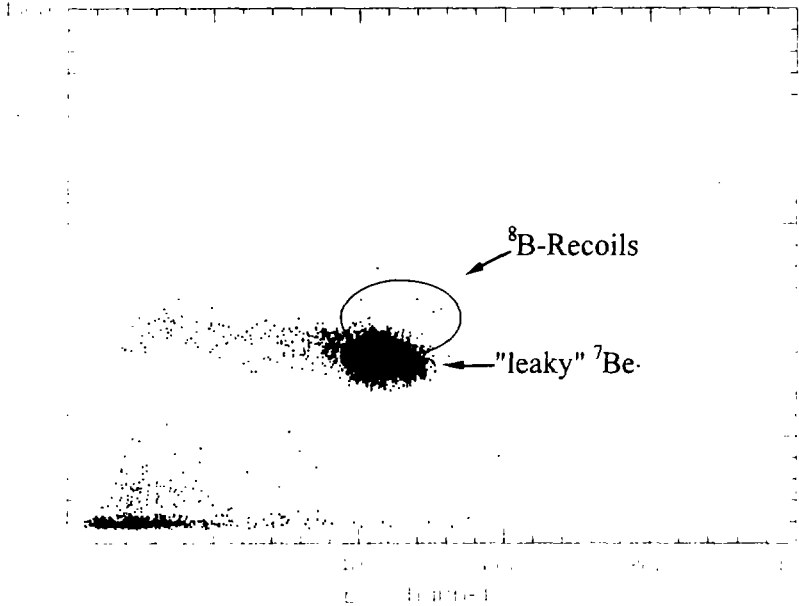

Fig. 1. Identification matrix obtained in the $^1H(^7Be,\gamma)^8B$ experiment.

3   The $^{12}C(\alpha,\gamma)$ reaction

The $^{12}C(\alpha,\gamma)^{16}O$ reaction is since several decades at the same time the dream and the nightmare of nuclear astrophysicists. Despite the enormous experimental efforts devoted to the measurement of its cross section, the corresponding rate at astrophysical energies is far from being well established. On the other hand, its accurate knowledge would be a milestone in all stellar structure and evolution studies.

3.1   Astrophysical motivation

All the stars with mass larger than $0.5M_o$ will experience a central He burning. These stars are quite bright, so that they are easily identified in the Color-Magnitude diagrams (CMD) of very different stellar systems, from the oldest galactic globular clusters up to the very young supergiant population of the galactic disk and of the Magellanic Clouds. For this reason the study of the He burning phase of stellar evolution is a fundamental step for the comprehension of the galactic history, from its very early stage up to the present one. In addition, the measurement of the overall properties of these stars can be used to test the reliability of stellar models with very different masses.

M (M_o)	t_{He} (yr) $\times 10^6$			X_{12C}			t_C (yr) $\times 10^4$		
	(a)	(b)	(c)	(a)	(b)	(c)	(a)	(b)	(c)
11	2.04	2.42	2.36	0.61	0.21	0.21	3.08	0.98	0.87
13	2.44	1.62	1.67	0.59	0.24	0.19	2.79	0.64	0.49
15	1.08	1.29	1.25	0.58	0.20	0.19	2.01	0.36	0.36
18	0.85	0.92	0.96	0.54	0.22	0.15	0.78	0.27	0.19
20	0.80	0.80	0.81	0.54	0.20	0.16	0.61	0.23	0.13
22	0.61	0.72	0.73	0.53	0.18	0.13	0.48	0.19	0.11
23	0.66	0.67	0.70	0.53	0.18	0.13	0.48	0.30	0.10
24	0.56	0.65	0.65	0.52	0.17	0.14	0.42	0.09	0.08
25	0.53	0.61	0.62	0.52	0.19	0.14	0.40	0.15	0.05

Table 1. Dependence of He-burning life-time, central ^{12}C mass fraction at the end of He-burning, C-burning life-time on stellar mass with three assumptions for the S-factor of $^{12}C(\alpha,\gamma)$ reaction: (a) lower limit (62 keVb) suggested in [10]; (b) compilation in [14]; (c) upper limit (270 keVb) suggested in [10].

In this context, a precise theoretical evaluation of the He burning lifetime might be immediately compared with the observed distribution of stars in the CMDs: the larger the lifetime, the larger the expected number of these stars. It is probably unnecessary to emphasize that such a precise evaluation of the stellar lifetime is strictly connected with the accuracy of the measurement of the relevant thermonuclear reaction rates which are at work during the He burning.

When the central temperature is a few 10^8 $^\circ$K, the burning of He into C occurs by means of the 3α reaction. As the stellar core becomes richer in ^{12}C, the $^{12}C(\alpha,\gamma)^{16}O$ reaction takes place. As it is well known, the cross section of this reaction is dominated by three resonances (two of which below the particle threshold) and the direct capture process, with interference terms between some of them, so that its rate is presently very poorly known [10].
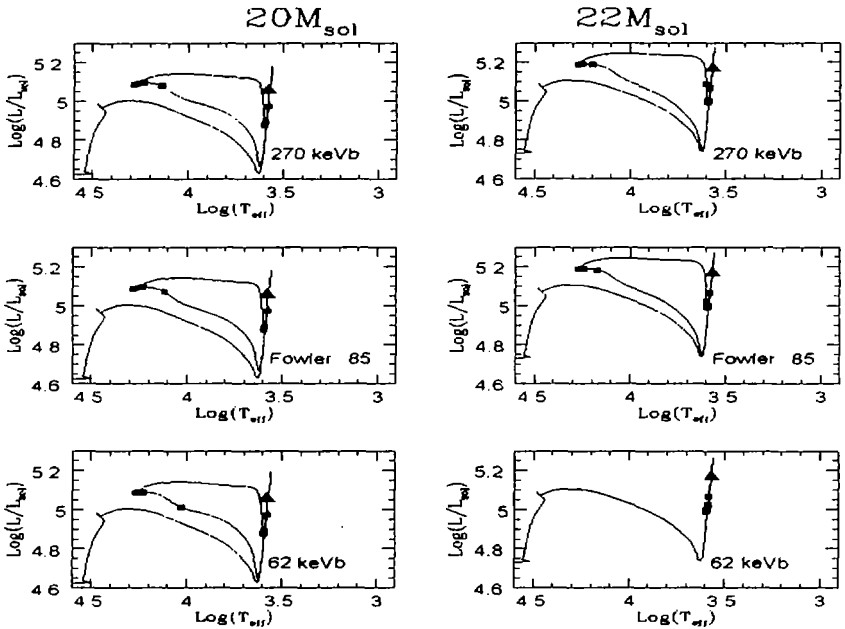
Fig. 2. Theoretical paths followed in the CMD of two stars of 20 and 22M_o, obtained under different assumptions about the reaction rate of the $^{12}C(\alpha,\gamma)^{16}O$ reaction. The squares indicate time intervals of 100 kyr.

This uncertainty sets a lasting limit to our knowledge of the properties of stellar interior. In fact, although the energy released by the $^{12}C(\alpha,\gamma)^{16}O$ reaction is comparable to that of the 3α process, the He consumption is just 1/3. Thus, owing to the competition between the two reactions, the He-burning lifetime is strongly affected by a change of the $^{12}C(\alpha,\gamma)^{16}O$ reaction rate: the larger the reaction rate, the larger the lifetime. Direct evidences of the corresponding structural changes can be found in the different theoretical paths followed in the CMD of a star of 20-25 M_o, obtained under different assumptions about this reaction rate (fig. 2). A larger He-burning lifetime favors the production of more compact (blue) giants, while a

shorter lifetime implies the formation of a red supergiant. In addition the central amount of ^{12}C left after the He burning is also strongly influenced by the quoted uncertainty. Such an occurrence has dramatic consequences on our understanding of the final evolution of massive stars. The related hydrostatic nucleosynthesis and even the modality of the supernova explosion are affected by the central C abundance in the He exhausted core of the star. More quantitatively in Table 1 we report the results of our stellar model computations as obtained under different assumptions for the critical reaction rate. Note, in particular, that for the greatest values of the astrophysical factor, which are still compatible with the presently available experimental determinations, very little Carbon is left by the He- burning, so that the C-burning phase is drastically reduced.

Let us finally mention another important astrophysical consequence of an eventual revision of the ^{12}C$(\alpha,\gamma)^{16}$O reaction rate. As firstly noted by Iben [11], the number ratio of the horizontal branch (HB) stars (which corresponds to the central He-burning phase) and red giant (RGB) stars (which corresponds to the shell H-burning phase) is a linear function of the original amount of He. Such an occurrence provides us the opportunity to put a stringent upper limit to the cosmological He, which is - in the framework of the standard big bang model – the main product of the primordial nucleosynthesis. The calibration of Buzzoni et al. [12] is widely accepted. By analyzing a sample of the old galactic globular clusters, they found Y $= 0.23 \pm 0.02$. Such a calibration was obtained by using theoretical HB models based on the tabulation of thermonuclear reaction rates of Fowler [13]. Obviously, a revision of the ^{12}C$(\alpha,\gamma)^{16}$O reaction rate would imply a change in the estimated HB lifetime and in turn a modification of the theoretical calibration of the primordial He. We recall that the evaluation of the big bang nucleosynthesis products is commonly used to constrain the total amount of barionic matter (visible and dark) which is one of the main goals of modern cosmology.

3.2   Measurements in inverse kinematics

A Montecarlo simulation of the measurement of ^{16}O recoils emitted in the ^{4}He$(^{12}$C$,\gamma)^{16}$O reaction by an RMS shows that the angular and momentum spreads of recoils are very large compared with the ^{1}H$(^{7}$Be$,\gamma)$ case, essentially owing to the very different Q-values, and therefore the present RMS has not a wide enough acceptance to collect them. In addition, the ^{4}He$(^{12}$C$,\gamma)^{16}$O recoil is a stable and very abundant isotope; charge exchange processes on O ions not originated from the reaction can give rise to a background undistinguishable from reaction products.

A test experiment [15] was performed to investigate the last point, exploiting the fact that the E_{cm}=3.2 MeV 4^{+} resonance decays strongly to the 2^{+} 6.92 MeV state

ΔE–E
TELESCOPE

WIEN
FILTER

FC

MAGNETIC
QUADRUPOLE
SINGLET

MAGNETIC
QUADRUPOLE
TRIPLET

FC

$60°$
DIPOLE
MAGNET

$^{12}C(\alpha,\gamma_0)^{16}O$

$E_{cm} = 0.7$ MeV

$\Delta p/p = 7.2\%$

$\vartheta = 35$ mrad

FC

MAGNETIC
QUADRUPOLE
SINGLET

C FOIL

POSITION
SENSITIVE
FARADAY CUP

WIEN
FILTER

MAGNETIC
QUADRUPOLE
TRIPLET

$L_{tot} = 10$ m

Beam suppression factor $= 10^{-15}$

Momentum acceptance $= 10.0\%$

Angular acceptance $= 40$ mrad

JET
GAS
TARGET
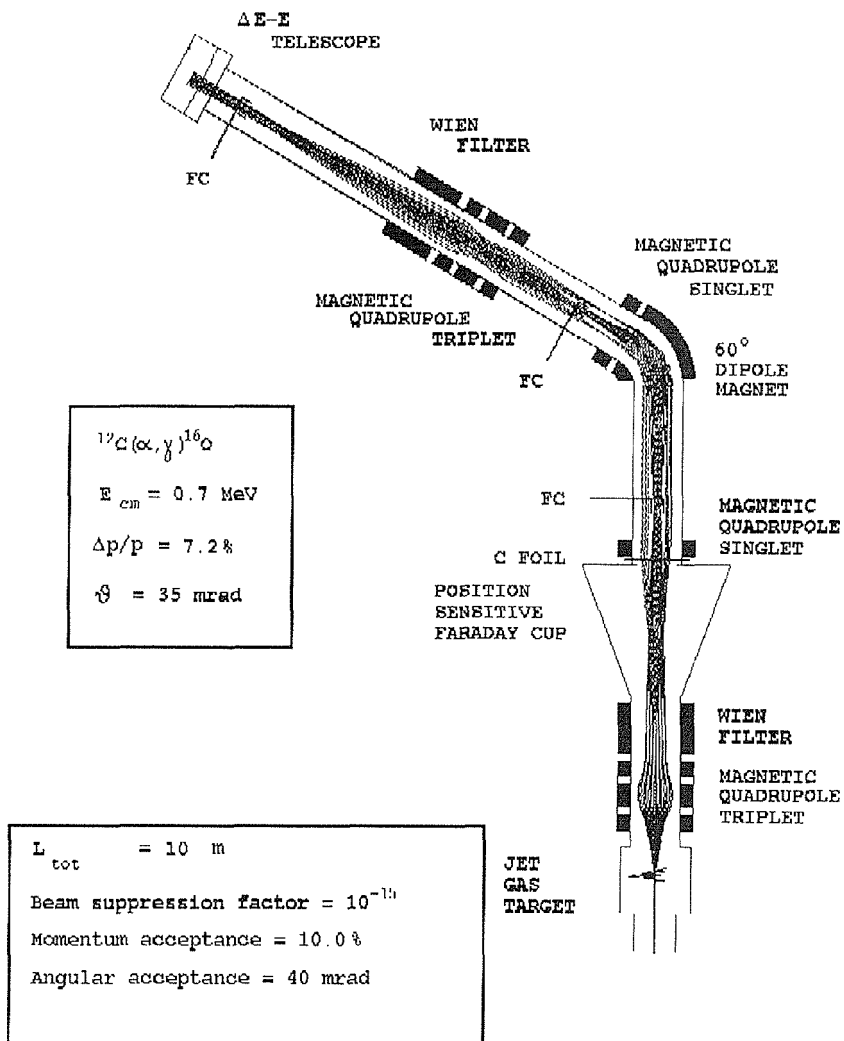
Fig. 3. Scheme of the ERNA recoil separator.

[16], giving rise - with its reduced γ-recoil effect - to ^{16}O ions falling within the acceptance of the RMS. Using the "purification" Wien filter, placed before the analysing magnet, on and off it was possible to show that the background can be strongly reduced and subtracted, obtaining at the same time an estimate of the cross section on top of the resonance consistent with the value quoted in [16]. These encouraging results show, for the first time, that it is possible to detect ^{16}O recoils from $^4He(^{12}C,\gamma)^{16}O$ without any coincidence condition with γ-rays, as it was done before [17]. It is also clear in which direction the major efforts have to be done to setup an optimised RMS able to measure $^4He(^{12}C,\gamma)^{16}O$ over an energy range from =.7 to 5.0 MeV, that would allow to gain astrophysically significant information. Namely the desired specifications of such a system should be a momentum acceptance up to 7.2%, an angular acceptance up to 35 mrad, a very good beam purification (suppression of ^{16}O contaminant better than 10^{-8}) and a beam suppression factor in the separator of about 10^{-15}, with a free choice of the recoil charge state to allow good detection efficiency.

Having this in mind, a new RMS was designed to be installed at the Dynamitron Tandem of the Ruhr University in Bochum. The beam purification system consists of two Wien filters and a dipole magnet between the accelerator and the analyzing magnet which will provide an adequate contaminant beam suppression. A jet gas target, with much smaller length, will replace the extended one, so that the maximum angle defined by the apertures contains the angular spread of recoils and, in addition, a focusing quadrupole triplet with larger gap can be placed closer to the interaction region. The new RMS has been designed increasing the gap of all transport elements to 4" and inserting a first Wien filter to eliminate as soon as possible the bulk of the incident beam. The 30° magnet will be replaced by a 60° one and again will be followed by a velocity filter. The system is arranged to have an horizontal and vertical achromatic waist at the entrance of a ΔE-E telescope with very thin entrance window for low threshold detection. Fig. 3 shows a scheme of the RMS starting from the jet gas target and the results of optics calculations for the trajectories of a 2.8 MeV $^{12}C^{3+}$ beam incident on the gas target and three $^{16}O^{3+}$ recoils with $\Delta P/P = 0\%$, +3.6% and –3.6% with respect to the paraxial beam with an emittance of $2\pi \cdot 2 \cdot 40$ mm mrad at the gas target emplacement. The design specifications of the recoil separator are an angular acceptance of ±40 mrad, a beam spot of ±2 mm, an image size of ±10 mm, a momentum acceptance of ±4%. The estimated beam suppression factor of the primary beam is of the order of 10^{-15}.

4 Conclusions

A big effort has been devoted to the measurement of the cross section of the $^7Be(p,\gamma)$ reaction, fundamental for the understanding of the H burning phase in the

Sun. The role of the inverse kinematics approach and of the use of a performant and selective RMS has been underlined. The experience gained in this study has been exploited for the design of a new tool for the measurement of another key reaction, namely $^{12}C(\alpha,\gamma)^{16}O$. Its importance in the context of the evolution of massive stars has been recalled and the predictions of an evolutionary code, showing the criticality of the corresponding reaction rate, have been presented. The results of first observations of ^{16}O recoil nuclei produced in an inverse kinematics study of the reaction show the potentialities of the experimental method.

References

1 I. Baraffe et al., *Nuclear and Particle Astrophysics*, NUPECC Report, 1997
2 C. Rolfs and W.S. Rodney, *Cauldrons in the Cosmos*, Univ. of Chicago Press (1988)
3 J.N. Bachall and M.H. Pinsonneault, Rev. Mod. Phys. **67** (1995) 781
4 J.N. Bachall and J.P. Ostriker, *Unsolved Problems in Astrophysics*, Princeton University Press, 1997
5 C.W. Johnson et al., Astrophys. J. **392** (1992) 320
6 M. Junker et al., Proceedings of this Workshop
7 L. Campajola et al., Z. Phys. **A356** (1996) 107
8 F. Strieder et al., Z. Phys. **A355** (1996) 209
9 L. Gialanella et al., Nucl. Instr. Meth. in Phys. Res. **A376** (1996) 174
10 L. Buchmann et al., Phys. Rev. **C54** (1996) 393
11 I. Iben Jr., Nature **220** (1968) 143
12 A. Buzzoni et al., Astron. And Astrophys. **128** (1983) 94
13 W.A. Fowler et al., A.R.A. & A. **5** (1967) 525
14 G.R. Caughlan at al., At. Data Nucl. Data Tables **32** (1985) 197
15 L. Gialanella et al., 8th Int. Conf. on Nucl. Mech., Varenna (Italy) 1997
16 K.U. Kettner et al., Z. Phys. **A308** (1982) 73
17 R.M. Kremer at al., Phys. Rev. Lett. **60** (1988) 1475
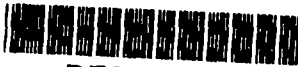
STATUS OF THE WORK
WITH RADIOACTIVE NUCLEI

U. GREIFE

Institut für Experimentalphysik III
Fakultät für Physik und Astronomie, Ruhr-Universität Bochum
D-44780 Bochum, Germany

This talk shall mainly present the status of the ^{7}Be target work undertaken at the Dynamitron Tandem Laboratory in Bochum. First beamtimes are scheduled for November 1997, so first spectra might be available. Depending on the results and the granted time, this contribution will also deal with the preparations for radioactive ion beam measurements at Oak Ridge National Laboratory and at TRIUMPF, where several experiments have been proposed with the participation of the Ruhr-Universität Bochum.

APPLICATION OF COULOMB DISSOCIATION
TO NUCLEAR ASTROPHYSICS*

G. BAUR,

Institut für Kernphysik, Forschungszentrum Jülich
D-52425 Jülich, Germany

S. TYPEL and H. H. WOLTER

Sektion Physik, Universität München
Am Coulombwall 1, D-85748 Garching, Germany

Abstract

We give an overview of new applications of Coulomb dissociation for
nuclear astrophysics.

1   Theory of Electromagnetic Dissociation

It is interesting to study nuclear collisions where the colliding nuclei interact
only electromagnetically. This can be achieved by using bombarding energies
below the Coulomb barrier or by choosing very forward scattering angles in
high energy collisions. With increasing beam energy states at higher excita-
tion energies can be excited; this may lead, in addition to Coulomb excitation,
also to Coulomb dissociation [1]. Such experiments are also feasible with se-
condary (radioactive) beams. Because Coulomb dissociation is generally well
understood theoretically, a clean interpretation of the experimental data is
possible. This is of interest for nuclear structure and nuclear astrophysics
[2, 3, 4].

We first discuss some questions that have to be considered in the theore-
tical treatment of Coulomb dissociation. Multiple electromagnetic excitation
may be important. We mention two aspects: it is a means to excite new
nuclear states, like the double phonon giant dipole resonance [4]; but it also
appears as a correction to the one-photon excitation [5, 6, 7]. In the equiva-
lent photon approximation the cross section for an electromagnetic process is
written as $\sigma = \int \frac{d\omega}{\omega} n(\omega) \sigma_\gamma(\omega)$ where $\sigma_\gamma(\omega)$ denotes the corresponding cross
section for the photo-induced process and $n(\omega)$ is called the equivalent pho-
ton number. For high enough beam energies the latter is well approximated

by $n(\omega) = \frac{2}{\pi}Z^2\alpha \ln \frac{\gamma v}{\omega R}$ where R denotes some cut-off radius. More refined expressions, which take the dependence on multipolarity, beam velocity or Coulomb-deflection into account, are available in the literature [1, 6, 8]. The theory of electromagnetic excitation is well developed, for nonrelativistic as well as relativistic projectile velocities. In the latter case, an analytical result for all multipolarities was obtained in ref. [8]. The projectile motion was treated classically in a straight-line approximation. Using Glauber theory, the projectile motion can be treated quantally [1, 7, 9, 10, 11]. This gives rise to characteristic diffraction effects. The main effect is due to the strong absorption at impact parameters less than the sum of the two nuclear radii. Effects due to nuclear excitation have also to be taken into account [10, 12]. They are generally small and show a characteristic angular dependence, which can be used to separate such effects from electromagnetic excitation.

Higher order effects can be considered in a coupled channels approach, or using higher order perturbation theory. This involves a sum over all intermediate states considered to be important. Another approach is to integrate the time-dependent Schrödinger equation directly for a given model Hamiltonian [13].

For a sudden collision the time ordering in the usual perturbation approach can be neglected and the interaction can be summed up to infinite order. In this case one only has to calculate the matrix-element of the excitation operator between the initial and final states (i.e. the intermediate states do not appear explicitly). A related approach was developed for small values of ξ in Refs. [5, 6, 7].

2   New applications of Coulomb dissociation for nuclear astrophysics

In nuclear astrophysics radiative capture reactions of the type $b + c \rightarrow a + \gamma$ play a very important role. They can also be studied in the time-reversed reaction $\gamma + a \rightarrow b + c$, at least for those cases where the nucleus a is in the ground state. As a photon beam we use the equivalent photon spectrum which is provided in the fast peripheral collision. Recent reviews, both from an experimental and a theoretical point of view have been given [2], thus we concentrate here on a few points.

Nucleosynthesis beyond the iron peak proceeds mainly by the r- and s-processes (rapid and slow neutron capture) [14, 15]. To establish the quantitative details of these processes, accurate energy-averaged neutron-capture cross sections are needed. Such data provide information on the mechanism and

time scales of the process, as well as on temperatures involved in the process. The data should also shed light on neutron sources, required neutron fluxes and possible sites of the processes (see Ref. [14]).

With the new radioactive beam facilities (either fragment separator or ISOL-type facilities) some of the nuclei far off the valley of stability can be produced, which are relevant for the r-process. In order to assess the r-process path, it is important to know the nuclear properties like β-decay half-lifes and neutron binding energies. Sometimes the waiting point approximation [14, 15] is introduced, which assumes an (n,γ)- and (γ,n)-equilibrium in an isotopic chain. It is generally believed that the waiting point approximation should be replaced by dynamic r-process flow calculations, taking into account (n,γ), (γ,n) and β-decay rates as well as time-varying temperature and neutron density. In slow freeze-out scenarios, the knowledge of (n,γ) cross sections is important.

In such a situation, the Coulomb dissociation can be a very useful tool to obtain information on (n,γ)-reaction cross sections on unstable nuclei, where direct measurements cannot be done. Of course, one cannot and need not study the capture cross section on all the nuclei involved; there will be some key reactions of nuclei close to magic numbers. Quite recently, it was proposed [16] to obtain information about (n,γ) reaction cross sections, using nuclei like ^{124}Mo, ^{126}Ru, ^{128}Pd and ^{130}Cd as projectiles. The optimum choice of beam energy will depend on the actual neutron binding energy. Since the flux of equivalent photons has essentially an $\frac{1}{\omega}$ dependence, low neutron thresholds are favourable for the Coulomb dissociation method. Note that only information about the (n,γ) capture reaction to the ground state is possible with the Coulomb dissociation method. The situation is reminiscent of the loosely bound neutron-rich light nuclei, like ^{11}Be and ^{11}Li. In this context the recent Coulomb dissociation experiment of 28.53 MeV/nucleon ^{9}Li is worth mentioning [17]. It is relevant for the ^{8}Li(n,γ) reaction which is of interest for inhomogeneous big bang nucleosynthesis.

For future radioactive beam facilities, like ISOL od SPIRAL, the maximum useful beam energy is an important issue. We propose to use the handy formalism of Ref. [5] to assess, how far one can go down in beam energy. In Ref. [5] the 1st and 2nd order Coulomb excitation amplitudes are given analytically in a zero range model for the neutron-core interaction. Meaningful results with the Coulomb dissociation method are obtianed when the 1st order amplitude is not too much disturbed by corrections due to higher orders. For Coulomb dissociation with two charged particles in the final state, like in the ^{8}B $\rightarrow$ ^{7}B + p experiment with a 26 MeV ^{8}B beam [18] such simple formulae seem to

be unavailable and one should resort to more involved approaches mentioned above.

A new field of application of the Coulomb dissociation method could be two particle capture reactions. Evidently, they cannot be studied in a direct way in the laboratory. However, sometimes the relevant information about resonances involved can also be obtained by other means (transfer reactions, etc.), like in the triple α-process. Two-neutron capture reactions in supernovae neutrino bubbles are studied in [19]. In the case of a high neutron abundance, a sequence of two-neutron capture reactions, $^4\text{He}(2n,\gamma)^6\text{He}(2n,\gamma)^8\text{He}$ can bridge the $A = 5$ and $A = 8$ gaps. The ^6He and ^8He nuclei may be formed preferentially by two-step resonant processes through their broad 2^+ first excited states [19]. Dedicated Coulomb dissociation experiments can be useful. Another key reaction can be the $^4\text{He}(\alpha n,\gamma)$ reaction [19]. The $^9\text{Be}(\gamma,n)$ reaction has been studied directly (see Ref. [20]) and the low energy $s_{\frac{1}{2}}$ resonance is clearly established. Despite this, a ^9Be Coulomb dissociation experiment could be worthwhile (cf. also Ref. [21]). Other useful information is obtained from (e,e') and (p,p') reactions on ^9Be [22].

Also in the rp-process, two-proton capture reactions can bridge the waiting points [23, 24, 25]. From the $^{15}\text{O}(2p,\gamma)^{17}\text{Ne}$, $^{18}\text{Ne}(2p,\gamma)^{20}\text{Mg}$ and $^{38}\text{Ca}(2p,\gamma)$ ^{40}Ti reactions considered in Ref. [24], the latter can act as an efficient reaction link at conditions typical for X-ray bursts on neutron stars. A $^{40}\text{Ti} \rightarrow p + p + {}^{38}\text{Ca}$ Coulomb dissociation experiment should be feasible. The decay with two protons is expected to be sequential rather than correlated ("^2He"-emission). The relevant resonances are listed in Table XII of Ref. [24]. In Ref. [25] it is found that in X-ray bursts 2p-capture reactions accelerate the reaction flow into the $Z \geq 36$ region considerably. In Table 1 of Ref. [25] nuclei are listed on which 2p-capture reactions may occur; the final nuclei are ^{68}Se, ^{72}Kr, ^{76}Sr, ^{80}Zr, ^{84}Mo, ^{88}Ru, ^{92}Pd and ^{96}Cd (see also Fig. 8 of Ref. [23]). It is proposed to study the Coulomb dissociation of these nuclei in order to obtain more direct insight into the 2p-capture process.

In summary peripheral collision of medium and high energy nuclei (stable or radioactive) passing each other at distances beyond nuclear contact and thus dominated by electromagnetic interactions are important tools of nuclear physics research. The intense source of quasi-real (or equivalent) photons has opened a wide horizon of new experimental possibilities (also for the GSI) to investigate efficiently photo-interactions. i.e. single- and multiphoton excitations and electromagnetic dissociation, in nuclei.

- 393 -

References

[1] C. A. Bertulani and G. Baur, Phys. Rep. **163** (1988) 299

[2] G. Baur and H. Rebel, J. Phys. G: Nucl. Part. Phys. **20** (1994) 1, and Ann. Rev. Nucl. Part. Sci. **46** (1996) 321

[3] J. Vervier, Prog. Part. Nucl. Phys. **37** (1996) 435

[4] G. Baur and C. A. Bertulani, Phys. Lett. **B174** (1986) 23

[5] S. Typel and G. Baur, Nucl. Phys. **A573** (1994) 486

[6] S. Typel and G. Baur, Phys. Rev. **C50** (1994) 2104

[7] S. Typel, H. H. Wolter and G. Baur, Nucl. Phys. **A613** (1997) 147

[8] A. Winther and K. Alder, Nucl. Phys. **A319** (1979) 518

[9] C. A. Bertulani and A. M. Nathan, Nucl. Phys. **A554** (1993) 158

[10] A. Muendel and G. Baur, Nucl. Phys. **A609** (1996) 254

[11] G. Baur and C. A. Bertulani, Phys. Rev. **C56** (1997) 581

[12] K. Hencken, G. Bertsch and H. Esbensen, Phys. Rev. **C54** (1996) 3043

[13] H. Esbensen et al., Nucl. Phys. **A581** (1995) 107

[14] C. E. Rolfs and W. S. Rodney, Cauldrons in the Cosmos, The University of Chicago Press, 1988

[15] J. J. Cowan, F.-K. Thielemann and J. W. Truran, Phys. Rep. **208** (1991) 267

[16] M. Gai, ISOL workshop, Columbus/Ohio, July 30 — August 1, 1997

[17] P. Zecher et al., preprint, August 1997, MSUCL-1080

[18] J. von Schwarzenberg et al., Phys. Rev. **C53** (1996) R2598

[19] J. Görres et al., Phys. Rev. **C52** (1995) 2231

[20] F. Ajzenberg-Selove, Nucl. Phys. **A490** (1988) 1

[21] D. M. Kalasse and G. Baur, J. Phys. G: Nucl. Part. Phys. **22** (1996) 115

[22] G. Kuechler, A. Richter and W. von Witsch, Z. Phys. **A326** (1987) 447

[23] NuPECC Report, Nuclear and Particle Astrophysics, July 16, 1997, I. Baraffe et al., F.-K. Thielemann (convener)

[24] J. Görres, M. Wiescher and F.-K. Thielemann, Phys. Rev. **C51** (1995) 392

[25] H. Schatz et al., Phys. Rep. (1997), in press

COULOMB DISSOCIATION STUDIES FOR ASTROPHYSICAL THERMONUCLEAR REACTIONS

T. MOTOBAYASHI

Department of Physics, Rikkyo University
3 Nishi-Ikebukuro, Toshima, Tokyo 171, Japan

Abstract

The Coulomb dissociation method was applied to several radiative capture processes of astrophysical interest.. The method has an advantage of high experimental efficiency, which allow measurements with radioactive nuclear beams. The reactions $^{13}N(p,\gamma)^{14}O$ and $^7Be(p,\gamma)^8B$ are mainly discussed. They are the key reaction in the hot CNO cycle in massive stars and the one closely related to the solar neutrino problem, respectively.

1 Introduction

In thermonuclear burning processes in stars or in early universe, nuclear reactions at low energies play important roles. In so called explosive burning situation, where both temperature and matter density are high, nuclear reactions on unstable nuclei can be faster than their competing β decays. To study directly the reactions in such explosive nuclear burning scenarios, radioactive targets should be used. Therefore measurements are very difficult or sometimes not possible when short-lived isotopes are involved.

Recent development on radioactive (or RI) beam production allows for new approaches to those difficult-to-measure reactions. One possibility is to realize the reaction system with the unstable nucleus as the beam at a low energy. This approach becomes possible only if a strong RI beam at several hundreds keV/u is available. The first example is the $^{13}N(p,\gamma)^{14}O$ reaction studied at Louvain-la-Neuve [1] using a ^{13}N beam of 3×10^8 s^{-1} intensity at 630 keV/u incident energy.

Another possibility is to use intermediate-energy RI beams, which are now available at many laboratories with variety of ions. Low-energy cross sections can be extracted indirectly from the data of Coulomb dissociation, for example, at several hundred MeV/u. An advantage is availability of thick targets.

Targets with several tens or several hundred mg/cm² thickness are commonly used in actual experiments. This is larger by an order of 3 or 4 than the typical thickness of targets in low-energy direct measurements, where the thickness is limited by the energy loss of the incident beam. This makes experiments with weak radioactive nuclear beams realistic.

2   Coulomb Dissociation Experiments

In the Coulomb dissociation method, the residual nucleus B of the capture reaction A(x,γ)B bombards a high-Z target and is Coulomb excited to an unbound state that decays to the A+x channel. Since the process is regarded as absorption of a virtual photon, $i.e.$ B(γ,x)A, the radiative capture (the inverse of the photoabsorption) cross section can be extracted from the dissociation yield. This idea was first proposed by Baur [2] based on the virtual photon theory. Topical reviews were given by Baur and Rebel [3]. In addition to the advantage discussed before, the Coulomb dissociation method enhances the original capture cross section by a large factor. This is due to the large virtual-photon number and the phase space factor. The two factors can be in the order of 100 or 1000 in some actual cases like the ^{14}O and ^{8}B dissociation, which will be discussed later in this report.

   Pioneering studies of the Coulomb dissociation were made for the stable Li isotopes, ^{6}Li→ α+d and ^{7}Li→ α+t, at around E_{in}=10 MeV/u [4, 5, 6, 7]. The asymmetry observed in the ^{6}Li dissociation at 10 MeV/u [6] vanishes at a higher incident-energy of 26 MeV/u [8]. This suggests the dominance of the Coulomb dissociation mechanism at high incident energies. However, Hirabayashi and Sakuragi [9] argue possible strong contribution of nuclear breakup based on a microscopic cluster model applied to the wave function of ^{6}Li-d+α.

   The first Coulomb dissociation experiments with radioactive beams were made for the ^{208}Pb(^{14}O,^{13}N p)^{208}Pb reaction at yet higher incident energies of 87.5 MeV/u [10] and 70 MeV/u [11]. The results demonstrates the usefulness of the method, and stimulated further studies of the Coulomb dissociation such as ^{12}N→^{11}C+p [12] and ^{8}B→^{7}Be+p [13, 15, 16, 17].

3 ^{14}O Breakup and Hot CNO Cycle

In the core of super massive stars, novae or at the surface of neutron stars, the ^{13}N(p,γ)^{14}O reaction becomes faster than the β^{+} decay of ^{13}N, and the hot CNO cycle starts instead of the regular CNO cycle. This key reaction

^{13}N$(p,\gamma)^{14}$O was difficult to be studied because the radioactive nucleus ^{13}N
(10 min. half life) is involved. The experimental goal is to determine the
E1 electromagnetic-width Γ_γ of the first 1$^-$ state in ^{14}O, because this resonant
state dominates in the hot CNO burning. The experimental accuracy obtained
in the indirect measurements, where a small branching ratio ($\approx 10^{-4}$) of the
γ decay was measured, was rather poor. We performed an experiment of
Coulomb dissociation [10] hoping that the experimental accuracy for Γ_γ might
be improved.

An ^{14}O beam was obtained by the projectile-fragmentation scheme with
the RIPS separator at RIKEN [18]. It bombarded a thick (350 mg/cm^2)
^{208}Pb target. Outgoing particles were detected in coincidence. The detec-
tion system consisted of a mosaic of 24 ΔE(Si)-E(CsI(Tl)) counter telescopes
"EMRIC" [19] and two (x and y) planes of plastic scintillator hodoscopes.

By comparing the result with the predicted cross section, the radiative
width Γ_γ was deduced to be 3.1±0.6 eV, which agrees with the width obtained
by the direct measurement of the ^{13}N$(p,\gamma)^{14}$O reaction performed at Louvain
la Neuve [20] almost at the same time as our Coulomb dissociation experiment.
Another Coulomb dissociation experiment at 70 MeV/u [11] at GANIL also
yields a value consistent with above value within errors.
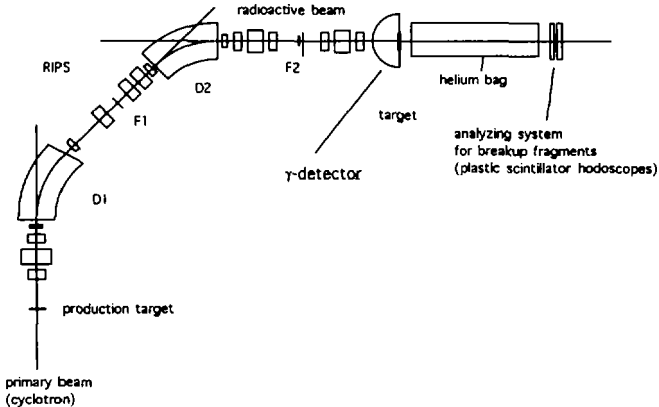
Figure 1: Experimental setup for the ^{8}B Coulomb dissociation experiment.

4 ^{8}B Breakup and Solar Neutrino Problem

The ^{7}Be(p,γ)^{8}B reaction at low energies is relevant to the high energy neutrino production in the sun through the β decay of ^{8}B. A series of experiments has been and is being performed for the Coulomb dissociation of ^{8}B at RIKEN. They are intended to simulate this important reaction cross section. It should be noted that the astrophysical process is dominated by the E1 transition to the unbound continuum state of ^{8}B. Therefore the Coulomb dissociation to continuum states should be studied.

The first measurement is described in two articles [13, 14], and a part of the second result is reported in Ref. [15]. The data obtained in the third experiment is now being analyzed. A schematic view of the experimental setup is shown in Fig. 1. Beams of ^{8}B were produced by the ^{12}C+^{9}Be interaction at 92 MeV/u for the first two experiments and 135 MeV for the third one. The ^{8}B energies in the center of the target, 50 mg/cm^2 ^{208}Pb, were approximately 50 MeV/u. We employed the time-of-flight (TOF) technique to determine the energies of fragments. A plastic scintillator hodoscope was set 3-5 m from the target. The outgoing particles of the Coulomb dissociation, ^{7}Be and p, are identified by the ΔE-E method. Their scattering angles are determined by the positions in the 10×16 segments formed by the ΔE and E scintillators. A p-^{7}Be relative energy spectrum could be constructed from the measurement and it was converted to the ^{7}Be(p,γ)^{8}B cross section with the help of a Monte-Carlo simulation calculation on detection efficiency and theoretical calculation for the Coulomb dissociation mechanism.

In the second and third experiments, the DALI setup [21] was also used to measure the deexcitation γ rays from the first excited state of ^{7}Be at 429 keV populated in the dissociation process. The contribution from this process was measured to be about 5% of the Coulomb dissociation yield.

In Fig. 2 the astrophysical S-factors obtained in the first and second experiments are shown together with the ones determined in direct (p,γ) measurements. Our Coulomb dissociation data are consistent within errors with the results by Filippone et al. [22] and Vaughn et al. [23].

Figure 3 shows the angular distributions for the scattering angle θ_8, the angle of the center-of-mass for the p-^{7}Be system. They are well fitted by the DWBA type calculation assuming pure E1 transition. This suggests that possible mixture of the E2 amplitude is small enough to be neglected. Small E2 mixture is also supported by the low energy measurement performed at Notre Dame University [17] using 3.25 MeV/u ^{8}B beams. An inclusive ^{7}Be spectrum was measured with a ^{58}Ni target.
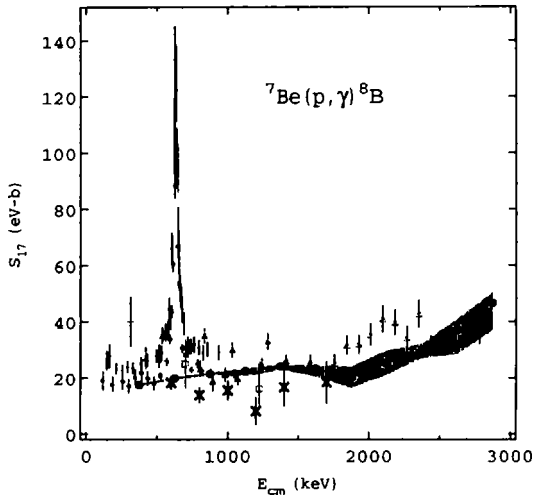
Figure 2: Astrophysical S_{17}-factors for the ^{7}Be(p,γ)^{8}B reaction extracted from the first (thick crosses) and second (large solid dots) experiments. Existing direct (p,γ) data are also shown.

The post Coulomb-acceleration effect is expected to be small owing to the special situation for ^{8}B where the proton binding energy is only 137 keV. Trajectories very far from the target are enough to excite the continuum state of ^{8}B, because a low energy virtual photon is responsible for the excitation. Recent theoretical calculations supports this picture [24, 25]

In general, higher order processes including the post acceleration is less important at higher incident energy. We also performed a Coulomb dissociation experiment at GSI using ^{8}B beams of 254 MeV/u and a ^{208}Pb target [16]. Outgoing fragments were measured in coincidence by a magnetic spectrograph called KaoS [26], which has a momentum acceptance large enough to allow for detecting protons and ^{7}Be that have quite different magnetic rigidities. Our analysis in a preliminary stage suggests that S_{17} factors are quite similar to the Coulomb dissociation results obtained in the second RIKEN experiment, and therefore to the direct (p,γ) results by Filippone *et al.* [22] and Vaughn *et al.* [23]. The agreement between the two results obtained at the different energies (50 MeV/u at RIKEN and 250 MeV/u at GSI) might indicate smallness of the higher-order contribution.
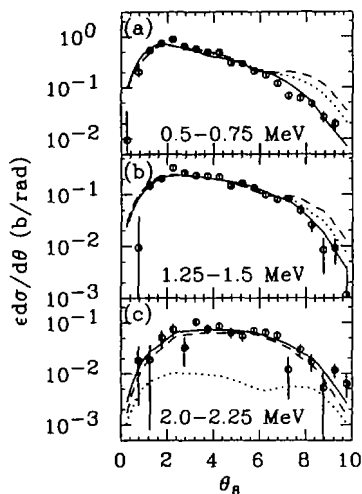
Figure 3: Angular distribution of the ^{8}B Coulomb dissociation reaction.

5 Further Applications of Coulomb Dissociation

We plan to extend the Coulomb dissociation method to several cases where the capture cross sections are not known. An example is the ^{8}B$(p,\gamma)^9$B reaction. In very high temperature and high pressure situation, this reaction becomes faster than the β^+ decay of ^{8}B, and the regular pp-chain nuclear burning is switched to the hot pp mode [27]. No experimental information is available so far for this ^{8}B$(p,\gamma)^9$B reaction, and its cross sections are only estimated by theoretical calculations [28, 29]. Recently, a Coulomb dissociation measurement of ^{9}C+^{208}Pb→^{8}B+p+^{208}Pb has been performed with almost the same technique as for the ^{8}B dissociation experiments. Preliminary analyses yield S_{18} factors which are consistent with those prediction by Descouvemont [29], but are smaller by a factor of four than the evaluation of Wiescher et al. [28].

6 Summary

Since the idea of laboratory experiments for astrophysical thermo-nuclear reactions was proposed in 1950s, much progress has been achieved. Recent development of producing radioactive nuclear beams allows now for access to unstable nuclei important in explosive nuclear burning. So called indirect method using

projectiles of unstable nuclei at intermediate-energies can also be applied to "hard-to-access" cases. Especially the Coulomb dissociation method has been studied for several important reactions. The ^{14}O and ^{8}B dissociation provide typical examples of resonant and non-resonant breakups. Their experimental results encourage new measurements of astrophysical reactions. Further experimental investigation to control the possible ambiguities as well as theoretical works are desirable.

The works present in this report were performed in collaboration with T. Kikuchi, T. Takei, N. Iwasa, Y. Ando, K. Ieki, M. Kurokawa, S. Moriya, H. Murakami, T. Nishio, J. Ruan (Gen), S. Shirato, S. Shimoura, T. Uchibori, Y. Yanagisawa (*Rikkyo University*), A. Goto, T. Ichihara, N. Inabe, T. Kubo, H. Sakurai, T. Teranishi, Y. Watanabe, M. Ishihara (*RIKEN*), M. Hirai, T. Nakamura (*University of Tokyo*), S. Kubono (*INS*), Y. Furutaka(*TIT*), Y. Futami(*Tsukuba University*), S. Kox, C. Perrin, F. Merchez, D. Rebreyend (*ISN Grenoble*), M. Gai, R. France III, K.I. Hahn, Z. Zhao (*Yale University*), Th. Delbar, P. Lipnik and C. Michotte (*Louvain la Neuve*).

References

[1] P. Decrock *et al.*, Phys. Rev. Lett. **67** (1991) 808; Th. Delbar *et al.*, Phys. Rev. **C48** (1993) 3088.

[2] G. Baur, C.A. Bertulani, and H. Rebel, Nucl. Phys. **A458** (1986) 188.

[3] G. Baur and H. Rebel, J. Phys. **G20** (1994) 1; Ann. Rev. Nucl. and Part. Sci. **46** (1996) 321.

[4] A.C. Shotter, V. Rapp, T. Davinson, D. Brandord, N.E. Sanderson and N.A. Nagarajan, Phys. Rev. Lett. **53** (1984) 1539; A.C. Shotter, V. Rapp, T. Davinson and D. Brandord, J. Phys. G: Nucl. Phys. **14** (1988) L169

[5] H. Utsunomiya *et al.*, Phys. Lett. **B211** (1988) 24; Nucl. Phys. **A511** (1990) 379; Phys. Rev. Lett **65** (1990) 847.

[6] J. Hesselbarth, S. Khan, Th. Kim and K.T. Knöpfle, Z. Phys. **A331** (1988) 365; J. Hesselbarth and K.T. Knöpfle, Phys. Rev. Lett. **67** (1991) 2773.

[7] S.B. Gazes, J.E. Mason, R.B. Roberts and S.G. Teichmann, Phys. Rev. Lett. **68** (1992) 150; J.E. Mason, S.B. Gazes, R.B. Roberts and S.G. Teichmann, Phys. Rev. **C45** (1992) 2870.

[8] J. Kiener, H.J. Gils, H. Rebel and G. Baur, Z. Phys. **A332** (1989) 359; J. Kiener et al., Phys. Rev. **C44** (1991) 2195.

[9] Y. Hirabayashi and Y. Sakuragi, Phys. Rev. Lett. **69** (1992) 1892.

[10] T. Motobayashi et al., Phys. Lett. **B264** (1991) 259.

[11] J. Kiener et al., Nucl. Phys. **A552** (1993) 66.

[12] A. Lefebvre et al., Nucl. Phys. **A592** (1995) 69.

[13] T. Motobayashi et al., Phys. Rev. Lett. **73** (1994) 2680.

[14] N. Iwasa et al., J. Phys. Soc. Jpn. **65** (1996) 1256.

[15] T. Kikuchi et al., Phys. Lett. **B391** (1997) 261.

[16] N. Iwasa et al., Proc. Tours Symp. Nucl. Phys. III, to be published; K. Sümmere et al., Contribution to this Workshop.

[17] J. Schwarzenberg et al., Phys. Rev. **C53** (1996) R2598.

[18] T. Kubo et al., Nucl. Instr. Meth. **B70** (1992) 309.

[19] F. Merchez et al.: Nucl. Instr. Meth., **A275** (1989) 133.

[20] P. Decrock et al., Phys. Rev. Lett. **67** (1991) 808.

[21] T. Nishio et al., RIKEN Accel. Prog. Rep. **29** (1996) 184.

[22] B. Filippone, S.J. Elwyn, C.N. Davids, and D.D. Koetke, Phys. Rev. Lett. **50** (1983) 412; Phys. Rev. **C28** (1983) 2222.

[23] F.J. Vaughn, R.A. Chalmers, D. Kohler, and L.F. Chase, Jr., Phys. Rev. **C2** (1970) 1657.

[24] C.A. Bertulani, Phys. Rev. **C49** (1994) 2688.

[25] S. Typel and G. Baur, Phys. Rev. **C50** (1994) 2104.

[26] P. Senger et al., Nucl. Instr. Meth. **A327** (1993) 393.

[27] G.M. Fuller, S.E. Woosley and T.A. Weaver, Astrophys. J. 307 (1986) 675; A. Jorrisen and M. Arnould, Astron. Astrophys. **221** (1989) 161.

[28] M. Wiescher, J. Görres, S. Graff, L. Buchmann, F.K. Thielemann, Astrophys. J. **343** (1989) 352.

[29] P. Descouvemont, Astrophys. J. **405** (1993) 518.

COULOMB DISSOCIATION OF ^{8}B AT 254 A MeV

K. SÜMMERER^a, N. IWASA^{a,b}, F. BOUE^a, G. SUROWKA^{a,h},
T. BAUMANN^a, B. BLANK^c, S. CZAJKOWSKI^c, A. FÖRSTER^d, M. GAI^e,
H. GEISSEL^a, E. GROSSE^f, M. HELLSTRÖM^a, P. KOCZON^a,
B. KOHLMEYER^g, R. KULESSA^h, F. LAUE^d, C. MARCHAND^c,
T. MOTOBAYASHI^i, H. OESCHLER^d, A. OZAWA^{a,b}, M.S. PRAVIKOFF^c,
E. SCHWAB^a, W. SCHWAB^a, P. SENGER^a, J. SPEER^d, A. SUROWIECZ^a,
C. STURM^d, T. TERANISHI^b, F. UHLIG^d, A. WAGNER^d, W. WALUS^h,

^{a} Gesellschaft für Schwerionenforschung (GSI), Postfach 110552, D-64220
Darmstadt, Germany; ^{b} RIKEN (Institute of Physical and Chemical Research),
Hirosawa, Wako, Saitama 351-01, Japan; ^{c} Centre d'Etudes Nucléaires de
Bordeaux-Gradignan, F-33175 Gradignan Cedex, France; ^{d} Technische Universität
Darmstadt, Karolinenplatz 5, D-64289 Darmstadt, Germany; ^{e} Department of
Physics, University of Connecticut, Storrs, CT 06269-3046, U.S.A.; ^{f} Institut für
Kern- und Hadronenphysik, Forschungszentrum Rossendorf, Postfach 510119,
D-01314 Dresden, Germany; ^{g} Fachbereich Physik, Philipps Universität, D-3550
Marburg, Germany; ^{h} Institute of Physics, Jagiellonian University, PL-30-059
Krakow, Poland; ^{i} Department of Physics, Rikkyo University, Toshima, Tokyo 171,
Japan.

Abstract

As an alternative method for determining the astrophysical S-factor for
the ^{7}Be(p,γ)^{8}B reaction we have measured the Coulomb dissociation
of ^{8}B at 254 A MeV. From our preliminary results, we obtain good
agreement with both the accepted direct-reaction measurements and
the low-energy Coulomb dissociation study of Iwasa et al. performed at
about 50 A MeV .

1   Introduction

The Coulomb dissociation of ^{8}B into ^{7}Be + p is an alternative method for de-
termining the astrophysical S-factor for the ^{7}Be(p,γ)^{8}B reaction which is a key
quantity in solar neutrino physics [1]. Experiments with a ^{8}B beam of about
50 A MeV were performed at RIKEN [2]. In their first experiment, Iwasa et
al. [3] determined the ^{7}Be(p,γ)^{8}B S-factor for center-of-mass energies 0.6 MeV
$\leq E_{cm} \leq$ 1.7 MeV. In a subsequent study, Kikuchi et al. [4] studied the an-
gular distribution of the breakup products and found it compatible with pure

E1 multipolarity. Even at their energy around 50 A MeV the E2 contribution to the cross section was found practically negligible.

At GSI, we have measured the Coulomb dissociation of ^{8}B at 254 A MeV. The aim of this study was to check the results of the RIKEN experiment at a higher bombarding energy (which should yield a lower E2 contribution and a higher M1 contribution to the Coulomb-dissociation cross section). In addition, the strong forward focussing allows to use the large-acceptance spectrometer KaoS at GSI [5] for a simultaneous detection of the breakup products, proton and ^{7}Be. Moreover, angular and energy straggling effects should in principle allow to obtain cleaner results at the higher incident energy.

2 Experimental procedure

A ^{208}Pb target with a thickness of 200 mg/cm^2 located at the entrance of the large-acceptance spectrometer KaoS [5] was bombarded with a secondary ^{8}B beam produced by the fragment separator FRS at GSI [6] through projectile fragmentation of a 350 A MeV ^{12}C beam. The ^{8}B secondary-beam intensity was of the order of 10^4 ions/spill, with a purity of about 80%. The ^{8}B projectiles were identified event by event with the help of an energy-loss time-of-flight measurement.

Fig. 1 shows a schematic view of the experimental setup at KaoS. The scattering angles of the reaction products, ^{7}Be and proton, behind the ^{208}Pb breakup target were measured with an accuracy of about 2 mrad by two pairs of silicon micro-strip detectors (100 μm pitch) placed a distances of 15 and 30 cm, respectively, downstream from the target. Each of the detectors of the pairs was position sensitive only in one direction orthogonal to the incident beam (x or y). While the ^{7}Be breakup particles could be identified unambiguously from their energy loss in the four Si strip detectors and from the hit multiplicity, the low energy loss of the breakup protons ($\Delta E \approx 200$ keV) does not allow an unambiguous discrimination from noise. Therefore, only those hits were attributed to breakup protons that had their vertex at the target position. The breakup position at the target in beam direction (z) could be reconstructed with an accuracy of about $\sigma_z = 3$ cm. In this way also the large background from nuclear breakup in the micro-strip detectors or other layers of matter downstream from the target could be identified event by event.

The momenta of p and ^{7}Be were obtained from measuring both the positions and angles of the particles in front of KaoS as described above and from a position measurement behind KaoS with two large-area multi-wire proportional counters (MWPC). From the momenta and angles measured, the invari-
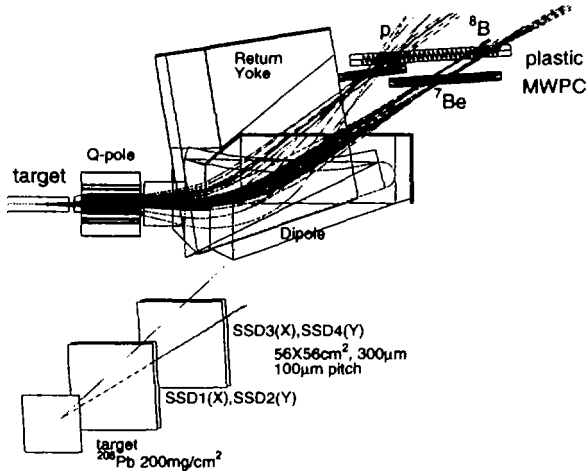
Fig. 1. Schematic view of the experimental setup used to detect the ^{8}B breakup products, ^{7}Be and proton, in coincidence at the KaoS spectrometer at GSI. The secondary ^{8}B beam from FRS enters from the left. The insert in the lower part of the figure shows the arrangement of the ^{208}Pb breakup target and the two pairs of Si strip detectors at the entrance of KaoS.

ant mass of the p-^{7}Be system and thus the relative energy between the proton and the ^{7}Be ion in the c.m. system, E_{rel}, could be reconstructed. Corrections necessary to account for the finite acceptance and the finite E_{rel}-resolution of the setup were estimated with the help of extended GEANT simulations.

3   Preliminary results

We could determine the ^{8}B$(\gamma,p)^7$Be cross section in the energy interval 0.15 MeV $\leq$ E_{rel} ≤ 2.95 MeV. Preliminary results are shown in Fig. 2. As indicated by the full histogram, our E_{rel}-distribution is in good agreement with the results of the direct (p,γ) measurement [7]. The full histogram was
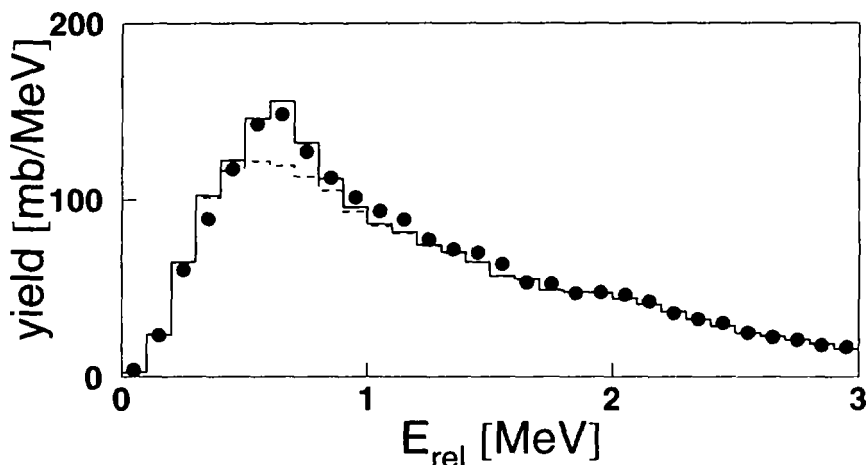
Fig. 2. Preliminary differential cross section distribution, $d\sigma/dE_{rel}$. The solid curve has been obtained by a Monte-Carlo simulation using the results from the direct (p,γ) measurements of Filippone *et al.* and Vaughn *et al.* [7]. The dashed curve has been obtained in the same way but using only the nonresonant (E1-) component of the direct measurement.

obtained by converting properly the (p,γ)- into Coulomb-dissociation cross sections and by running a complete GEANT simulation of our experiment to take into account our finite angular and momentum resolution. The dashed histogram has been obtained in the same way but without the (M1) resonance at $E_{rel} = 632$ keV, i.e. it should represent the nonresonant (E1-) contribution. We have tacitly assumed that the E2 contribution is negligible in accordance with the results of Kikuchi *et al.* [4] obtained at ≈ 50 *A* MeV; at our energy, the E2 contribution should be even smaller [8]. Unfortunately our experiment does not allow to extract the angular distribution of the combined (^{7}Be+p)-system relative to the incoming ^{8}B beam since the PPAC detectors designed to track the ^{8}B beam in front of the target could not be used during the production run. The angular distribution that we measure is determined entirely by the emittance of the ^{8}B beam.

It is clear that the E_{rel}-resolution of the present experiment is much poorer than that of the direct reaction studies, which is mainly due to our rather thick Pb breakup target necessitated by the relatively low secondary-beam

intensities. This is particular obvious from the broadening of the M1 peak which is hardly visible as an isolated peak in Fig. 2. On the other hand, the lowest E_{rel} bin measured is (150 ± 50) keV, where the direct (p,γ)-reaction has a cross section of the order of only 10 nb and which is below the range covered by the most recent (p,γ)-measurement [9]. We hope to extract an astrophysical S-factor from our cross sections in the near future when the remaining problems of the efficiency determination have been solved.

References

[1] J.N. Bahcall, Ap. J. **467** (1996) 475, and references therein.

[2] T. Motobayashi *et al.*, invited talk at this conference.

[3] N. Iwasa *et al.*, J. Phys. Soc. Japan **65** (1996) 1256; T. Motobayashi *et al.*, Phys. Rev. Lett. **70** (1994) 2680.

[4] T. Kikuchi *et al.*, Phys. Lett. **B 391** (1997) 261.

[5] P. Senger *et al.*, Nucl. Instr. Meth. **A 327** (1993) 393.

[6] H. Geissel *et al.*, Nucl. Instr. Meth. **B 70** (1992) 286.

[7] B.W. Filippone *et al.*, Phys. Rev. C **28** (1983) 2222; F.J. Vaughn *et al.*, Phys. Rev. C **2** (1970) 1657.

[8] S. Typel *et al.*, Nucl. Phys. **A 613** (1997) 147.

[9] F. Hammache *et al.*, Phys. Rev. Lett., in print.

RADIATIVE CAPTURE REACTION $^7Be(p,\gamma)^8B$ IN THE CONTINUUM SHELL MODEL

K. BENNACEUR†, F. NOWACKI†‡, J. OKOLOWICZ‡§ and
M. PLOSZAJCZAK†

† *Grand Accélérateur National d'Ions Lourds (GANIL), CEA/DSM –
CNRS/IN2P3, BP 5027, F-14076 Caen Cedex 05, France*
‡ *Laboratoire de Physique Théorique Strasbourg (EP 106), 3-5 rue de l'Universite,
F-67084 Strasbourg Cedex, France*
§ *Institute of Nuclear Physics, Radzikowskiego 152, PL - 31342 Krakow, Poland*

Abstract

We present here the first application of realistic shell model (SM) in-
cluding coupling between many-particle (quasi-)bound states and the
continuum of one-particle scattering states to the calculation of the to-
tal capture cross section and the astrophysical factor in the reaction
$^7Be(p,\gamma)^8B$.

The theoretical description of weakly bound exotic nuclei is one of the
most exciting challenges today. What makes this subject both particularly
interesting and difficult, is the proximity of the particle continuum implying
strong modification of the effective $N - N$ interaction and causing unusual
spatial properties of the nucleon density distribution, such as halo or large
diffusivity. Many of those nuclei are involved in the chain of thermonuclear
reactions and, in the absence of data at relevant energies, the models of stars
rely to certain extent on calculated astrophysical factors[1] . The number of
excited bound states or narrow resonances in weakly bound exotic systems
is small, and they couple strongly to the particle continuum. Hence, these
systems should be described in the quantum open system formalism which
does not artificially separate the subspaces of (quasi-)bound (the Q-subspace)
and scattering (the P-subspace) states. Coupling between Q and P subspaces
modifies both the scattering solutions as well as the spectroscopic quantities
for interior bound states.

The influence of scattering continuum on the SM properties has not been
addressed before. A possible starting point could be the Continuum Shell
Model (CSM) approach [2], which in the restricted space of configurations
generated using the finite-depth potential, has been applied to giant resonances
and radiative capture reactions[3, 4] . This is insufficient for nuclei close to

- 408 -

drip lines, where it is essential to have a realistic description of bound state subspace. For that reason, the corner-stone of our approach, which we call the Shell Model Embedded in the Continuum (SMEC), is the *realistic SM* itself. The SM is used to generate the many-particle wavefunctions for (quasi-)bound configurations. In descibing the particle continuum we restrict ourselves to a subset of one-nucleon decay channels, which apart from few rare cases of two-nucleon halo, should be a good approximation in weakly bound systems. The coupling between SM states and the one-particle scattering continuum is given by the residual interaction : $V = -V_0(a + bP_{12}^\sigma)\delta(\mathbf{r}_1 - \mathbf{r}_2)$, with $a + b = 1$ and $a = 0.73$. The key element of both SMEC and CSM is the treatment of single-particle resonances; the part of resonance inside a nucleus is included in Q subspace, whereas the remaining part is left in the P subspace[3] . The wavefunctions of both subspaces are then renormalized in order to ensure the mutual orthogonality of wavefunctions in both subspaces.

In the SMEC, we solve identical equations as in the CSM [3] but, due to specific features of exotic nuclei, ingredients of both models are different. For the (quasi-)bound states we solve the realistic SM problem using the code ANTOINE [5] . The quasi-bound resonances in the continuum are included as well. For the continuum part, we solve the coupled channel equations : $(E^{(+)} - H_{PP})\xi_E^{c(+)} = 0$, where index c denotes different channels and $H_{PP} \equiv PHP$. The sign $\pm$ characterizes the boundary conditions, i.e., wheather we consider incoming '−' or outgoing '+' scattering waves. The channel states are defined by coupling one nucleon in the continuum to a 'hole state' of $(A-1)$ -nucleus, described by the SM. To generate both single-particle (s.p.) resonances and the radial formfactors in the coupling matrix elements between states in Q and P , we use in the first iteration the finite-depth average potential of Saxon-Woods (SW) type with the spin-orbit part included. The parameters of the average potential are fitted to reproduce experimental s.p. states. The microscopic coupling of bound and scattering states generates important correction to the mean-field, modifying the s.p. wavefunctions for each J^π of the quasi-bound state. This correction deepens the average potential, increases slightly its diffusivity and produceses a maximum at the center. It is this corrected potential which is then used to calculate the radial formfactors of coupling matrix elements, the s.p. wavefunctions and the new correction term to the mean-field. We iterate this procedure until convergence is reached. The third system of equations are the coupled channel equations with the source term : $(E^+ - H_{PP})\omega_i^{(+)} = H_{PQ}\Phi_i$. These equations define functions $\omega_i^{(+)}$, which describe the decay of quasi-bound state Φ_i in the continuum. The source term couples the wavefunction of A - nucleon localized
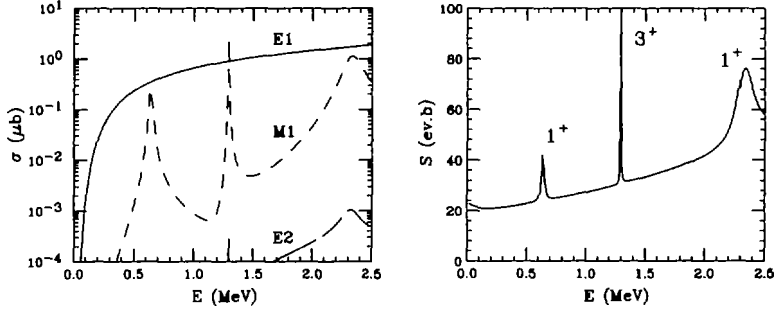
Figure 1: Multipole contributions to the total capture cross section (left hand side) and the astrophysical S factor (right hand side) of $^7Be(p,\gamma)^8B$ as a function of the center of mass energy. The SMEC calculations has been done with the residual interaction strength $V_0 = 1200$ MeVfm^3.

states with $(A - 1)$ - nucleon localized states + one nucleon in the continuum. The complete solution of SMEC can be expressed by means of the three functions : Φ_i , ξ_E^c and ω_i[3, 7] .

As an example of SMEC calculations, let us consider the proton-rich nucleus ^8B which is produced in the solar interior via the reaction $^7Be(p,\gamma)^8B$ at the center of mass (c.m.) energy of about 20 keV. This nucleus is the main source of high energy neutrinos observed in many solar-neutrino experiments[6] . The observed deficit of ^8B neutrinos as compared to the prediction of standard solar model[1] , can be partly related to the value of the $^7Be(p,\gamma)^8B$ cross section. We have calculated the spectrum of ^8B in p - shell, both in the SM and in the SMEC, using the CK interaction[8] . Calculations in SMEC have been done for different strength V_0 of the residual interaction. The SW average potential with parameters : $U_0 = -31.924$ MeV, $U_{so} = 6.84$ MeV, $R_0 = R_{so} = 2.95$ fm and $a = a_{so} = 0.52$ was used as a starting guess. The agreement with the data is largely improved by taking into account the microscopic coupling between (quasi-)bound and scattering states in SMEC. For example, the energy difference between the 1_1^+ resonance and the 2_1^+ ground state is 843 keV for $V_0 = 1200$ MeVfm^3, whereas the SM yields 1083 keV and the experimental value is 637±6 keV. The calculated width of 1_1^+ state is 27keV for $V_0 = 1200$ MeVfm^3 , whereas the experimental value is 37 ± 5keV. In the SMEC, the

initial wavefunction $\Psi_i([^7Be + p]_{J_i^\pi})$ is :

$$\Psi_i(r) = \sum_{l_a j_a} i^{l_a} \frac{\psi_{l_a j_a}^{J_i}(r)}{r} \Big[[Y^{l_a} \times \chi^s]^{j_a} \times \chi^{I_t} \Big]_{m_i}^{(J_i)} \tag{1}$$

and the final wavefunction $\Psi_f([^8B]_{J_f^\pi = 2^+})$ is :

$$\Psi_f(r) = \sum_{l_b j_b} A_{l_b s j_b}^{j_b l_b J_f} \frac{u_{l_b j_b}^{J_f}(r)}{r} \Big[[Y^{l_b} \times \chi^s]^{j_b} \times \chi^{I_t} \Big]_{m_f}^{(J_f)} . \tag{2}$$

I_t and s denote the spin of target nucleus and incoming proton, respectively. $A_{l_b s j_b}^{j_b l_b J_f}$ is the coefficient of fractional parentage and $u_{l_b j_b}^{J_f}$ is the s.p. wavefunction in the many-particle state J_f . With those wavefunctions we calculate the transition amplitudes :

$$T^{E\mathcal{L}} = C(E\mathcal{L}) i^{l_a} \hat{J}_f \hat{l}_b \hat{j}_b \hat{j}_a < \mathcal{L}\delta J_f m_f \mid J_i m_i >< l_b 0 \mathcal{L} 0 \mid l_a 0 > \\ \times W(j_b I_t \mathcal{L} J_i; J_f j_a) W(l_b s \mathcal{L} j_a; j_b l_a) I_{l_a j_a, l_b j_b}^{\mathcal{L}, J_i} \tag{3}$$

for $E1$ and $E2$ and :

$$T^{M1} = i^{l_a} \mu_N \hat{J}_f < 1\delta J_f m_f \mid J_i m_i > \\ \times \Bigg\{ W(j_b I_t 1 J_i; J_f j_a) \hat{j}_a \hat{j}_b \\ \left[\mu \Big(\frac{z_t}{m_t^2} + \frac{z_a}{m_a^2} \Big) \hat{l}_a \tilde{l}_a W(l_b s 1 j_a; j_b l_a) + (-1)^{j_b - j_a} 2\mu_a \hat{s}\tilde{s} W(s l_b 1 j_a; j_b s) \right] \\ + \mu_t (-1)^{J_f - J_i} \hat{I}_t \tilde{I}_t W(I_t j_b 1 J_i; J_f I_t) \delta_{j_a j_b} \Bigg\} \delta_{l_a l_b} I_{l_a j_a, l_b j_b}^{0, J_i} \tag{4}$$

for $M1$ transitions, respectively. In the above formula, $\delta = m_i - m_f$, $\hat{a} \equiv \sqrt{2a+1}$, $\tilde{a} \equiv \sqrt{a(a+1)}$ and $I_{l_a j_a, l_b j_b}^{\mathcal{L}, J_i} = \int u_{l_b j_b} r^{\mathcal{L}} \psi_{l_a j_a}^{J_i} dr$. The radiative capture cross section can then be expressed in terms of those amplitudes as :

$$\sigma^{E1, M1} = \frac{16\pi}{9} \Big(\frac{k_\gamma}{k_p} \Big)^3 \Big(\frac{\mu}{\hbar c} \Big) \Big(\frac{e^2}{\hbar c} \Big) \frac{1}{2s+1} \frac{1}{2I_t + 1} \sum \mid T^{E1, M1} \mid^2 \tag{5}$$

$$\sigma^{E2} = \frac{4\pi}{75} \Big(\frac{k_\gamma^5}{k_p^3} \Big) \Big(\frac{\mu}{\hbar c} \Big) \Big(\frac{e^2}{\hbar c} \Big) \frac{1}{2s+1} \frac{1}{2I_t + 1} \sum \mid T^{E2} \mid^2 \tag{6}$$

μ stands for the reduced mass of the system. Fig. 1 shows the calculated multipole contributions to the total capture cross section and the astrophysical S factor as a function of the c.m. energy. The proton threshold energy in SMEC is adjusted to yield the energy of calculated 1_1^+ state

at the experimentally observed value. This corresponds to a trivial read-justement of the energy scale. The photon energy is given by the difference of c.m. energy of $[^7Be + p]_{J_i}$ system and the experimental energy of the 2^+_1 ground state of ^8B . The calculated value of the S factor at c.m. energy of 20 keV is $S = 22.70$ eV·b , and disagrees with the most recent experimental value[9] . One should stress however, that different experiments show significant fluctuations in the extrapolated values of S . The ratios of S factors at different c.m. energies are : $S(20)/S(100) = 1.07$ and $S(20)/S(500) = 0.997$. The resonant part of $M1$ transitions , which yields the contribution of $S^{M1} = 18.23$ eV·b at the 1^+_1 resonance energy, decreases fast and becomes $S^{M1} = 1.3 \cdot 10^{-1}, 6.95 \cdot 10^{-3}, 1.03 \cdot 10^{-3}$ eV·b at c.m. energies of 500, 100, 20 keV , respectively. This value is sensible to the spectroscopic factor of p-states, i.e. to the SM force. At the position of 1^+ resonance, the predicted by SMEC calculations value of S - factor $(S = 41.97\text{eV·b})$ is somewhat smaller than seen in the experiments, but part of this discrepancy could be related to the absence of quenching factor in our calculations.

In conclusion, we have shown results of SMEC calculations which couple the realistic SM solutions for (quasi-)bound states with the scattering solutions of one-particle continuum. The application to $^7Be(p, \gamma)^8B$ reaction yields satisfactory description of different components of the radiative capture cross section, including the resonant components. At present, we are applying the SMEC to many other reactions of astrophysical interest such as $^{14}C(n, \gamma)^{15}C$, $^{16}O(p, \gamma)^{17}F$, $^{18}O(n, \gamma)^{19}O$.

References

[1] J.N. Bahcall, *Neutrino Astrophysics* (Cambridge University Press, 1989).

[2] C. Mahaux and H. Weidenmüller, *Shell-Model Approach to Nuclear Reactions* (Amsterdam: North-Holland, 1969).

[3] H.W. Bartz *et al*, Nucl. Phys. **A 275** (1977) 111; *idem* **A 307** (1977) 285.

[4] B. Fladt *et al*, Annals of Physics (NY) **184** (1988) 254, 300.

[5] E. Caurier, (1989), unpublished.

[6] J.N. Bahcall, in *Solar modeling*, (World Scientific, Singapore, 1994) p.1.

[7] K. Bennaceur *et al*, J. Phys. G (1998), to be published.

[8] S. Cohen and D. Kurath, Nucl. Phys. **A 73** (1965) 1.

[9] F. Hammache *et al*, Phys. Rev. Lett. (1998), in print.

PHYSICS OF THE CONTINUUM
OF BORROMEAN NUCLEI

J. S. VAAGEN

Department of Physics, University of Bergen, Norway

with the RNBT collaboration

B. V. DANILIN[1], S. N. ERSHOV[2], T. ROGDE[3], I. J. THOMPSON[4] and
M. V. ZHUKOV[5]

Abstract

The continuum states of two-neutron halo nuclei are calculated in the
method of hyperspherical harmonics. Using DWIA theory appropriate
for dilute halo matter we have probed the structure of the low-lying ^{6}He
continuum via calculations of charge-exchange and inelastic scattering.

1   Introduction

At Hirschegg'96 [1] we reported the first exploratory calculations for the con-
tinuum of Borromean halo nuclei, using ^{6}He as a benchmark system. We
emphasized that (i) a few-body approach employing expansion on hyperspher-
ical harmonic (HH) functions seemed technically feasible, and (ii) that the
calculated continuum response exhibited interesting new structures.

Since then we [2, 3] (and also [4]) have extended and improved the calcu-
lations technically to allow for sufficiently large expansions, and we have tried
to assess the physical nature of the continuum. The eigenproperties of the
continuum as would appear in 3-3 scattering cannot be easily probed in the
laboratory, but possibly in dense astrophysical scenarios. What is accessible to
experiment are various responses (transition properties) for observables of long
and short range, associated symmetries and multipolarities. Genuine 3-body
resonances, which are very complex in shell-model language, have simple char-
acteristics in few-body HH representation. This is also evidenced by various
correlation plots connecting Jacobi coordinates in momentum space as well

[1]RRC The Kurchatov Institute, Kurchatov Sq. 1, 123182, Moscow, Russia
[2]JINR - Dubna, 141980 Dubna, Moscow region, Russia
[3]Department of Physics, University of Bergen, Norway
[4]Department of Physics, University of Surrey, Guildford GU2 5XH, U.K.
[5]Chalmers University of Technology and Göteborg University, S-41296 Göteborg, Sweden
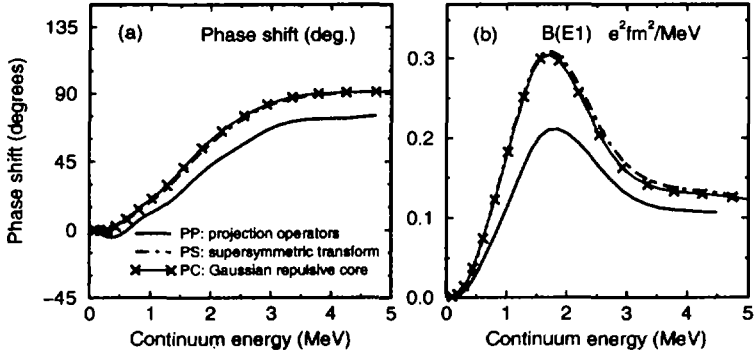
Figure 1: Diagonal phase shifts (a) and $dB(\mathcal{E}1)/dE$ distributions (b) in the 1^- continuum, for the $K = L = 1$, $S = l_{nn} = 0$, $l_{(nn)\alpha} = 1$ channel, for different Pauli treatments PP, PS and PC (see text). All curves used $K_{max} = 10$ and a three-body potential adjusted to reproduce the ground state energy.

as in ordinary space. Such plots are also used to explore more complicated accumulation of low-lying strength such as that with 1^-.

The calculation of $\mathcal{E}1$ dipole breakup of two-neutron halo nuclei requires the calculation of the continuum states of the three-body $n+n+$core system. Because of the large size of the ground state, the wavefunctions in the continuum interval $0 < E < 3$ MeV must be accurately calculated, and it is precisely in this region that the question of any soft-dipole mode must be answered.

2   Continuum Structure of ^{6}He

In a three-body model, we find three-body scattering states in a basis of hyperspherical harmonics up to some K_{max}, and find a 'continuum phase shift' for each harmonic K. In doing so, we must take into account that there are $0s$ occupied states in the ^{4}He core. This can be done by (PC) a repulsive Gaussian potential [4, 2], (PS) a supersymmetric transform of the n-core potential, (PA) by removing the lowest adiabatic energy surface [5], or (PP) by using projection operators and solving the Schrödinger equation within the allowed space [3]. The PP method removes that part of the total wavefunction which would disappear under full antisymmetrisation, while the other methods do this only approximately. The methods differ, for example, in the number of interior nodes in the bound state and scattering wave functions.

	HH		CS1[7]		CS2[8]		Exp.[6]	
J^π	E	Γ	E	Γ	E	Γ	E	Γ
0_1^+	−0.98		−0.6		−0.78		−0.97	
2_1^+	0.8	0.60	0.74	0.06	0.8	0.26	0.822	0.113
2_2^+	2.7	1.2	-	-	2.5	4.7	-	-
1^-	not	found	not	found	not	found	-	-
1^+	3.2	1.8	-	-	3.0	6.4	-	-
0_2^+	5.4	6.0	-	-	3.9	9.4	-	-

Table 1: Comparison of resonance positions and widths of ^{6}He continuum states. Results from the present method (HH) and the Complex Scaling method (CS) [7, 8] are shown, with experimental data. In the HH case, a three-body potential was fitted to the the 0_1^+ and 2_1^+ positions. The existence of the 0_2^+ state is least certain.

The ground state energies are slightly different in the 4 methods, but after renormalising an effective three-body potential, the bound state properties are not very different. In [5] it was shown that the PC and PA methods give similar bound state wave functions, but the three-body scattering phase shifts were not examined. This similarity does not hold, however, for the PP continuum properties: we see in fig. 1 that the PP continuum phase shifts differ noticeably from the others, while the non-PP methods give 50% more $dB(\mathcal{E}1)/dE$ strength at the low-energy peak. This indicates that the three-body continuum probes the off-shell structure of the two-body interactions, and therefore that phase-equivalence is not a sufficient physical specification for those interactions.

We have made predictions [2, 3] for the strengths of the isoscalar monopole, electric dipole and quadrupole excitations, as well as for nuclear inelastic and charge-exchange response functions. The known 2^+ resonance in ^{6}He is reproduced. Strength concentrations at lower energies are found and in table 1 we list the new 0^+, 1^+ and 2^+ resonances expected [2, 3].

Using DWIA theory appropriate for dilute halo matter we have probed the structure of the low-lying ^{6}He continuum (below two-body threshold) via calculations of charge-exchange (Fig. 2) and inelastic scattering [2].

Here we will only comment on the new 2_2^+ resonance and the so-called "soft dipole mode". To this end, as in binary systems, we look for pockets in the diagonal potentials $V_{K\gamma, K\gamma}(\rho)$, and we study the energy dependence of three-body phase shifts (extracted from diagonal elements of the S-matrix) and of eigenphases. To discriminate between genuine 3-body resonant behaviour and
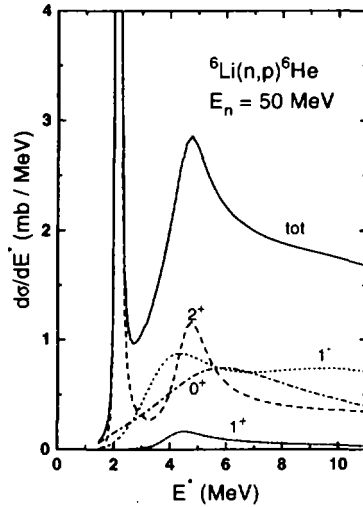
Figure 2: Predicted charge-exchange cross section for the ^{6}He continuum. The total magnitude and multipole decomposition are given.

response in particular binary partitions, we study how energy correlation plots vary with choice of Jacobi coordinates. As for the much narrower 2_1^+, the 2_2^+ behaviour shown in Fig. 3 for 'di-neutron' $\{r_{nn}, r_{\alpha(nn)}\}$ coordinates stays the same when we change to the $\{r_{\alpha n}, r_{n(\alpha n)}\}$ system. Potential pockets and phase shifts also support a classification of these responses as due to a genuine 3-body resonance.

This is not the case for the dipole response peak which shows preference for the di-neutron partition. It is easier to say what it is not than what it is: it is not a simple di-neutron oscillation either. Nature does not seem to quite favor an idea that created a lot of enthusiasm, at least not in ^{6}He.

The question is then: May soft-dipole resonances be realized in other halo systems? The natural candidate would be the halo nucleus par excellence, ^{11}Li. A problem for theory has been the rudimentary information on the binary n-^{9}Li channel, with implications for the question about the relative proportion of $p_{1/2}^2$- and $s_{1/2}^2$-motion in the ground state of ^{11}Li. The only calculations that agree with the available data (MSU and RIKEN) for the electric dipole response in ^{11}Li, have a large component of s^2-motion [9]. They produce again a strength accumulation at low energies, but no genuine dipole resonance. The
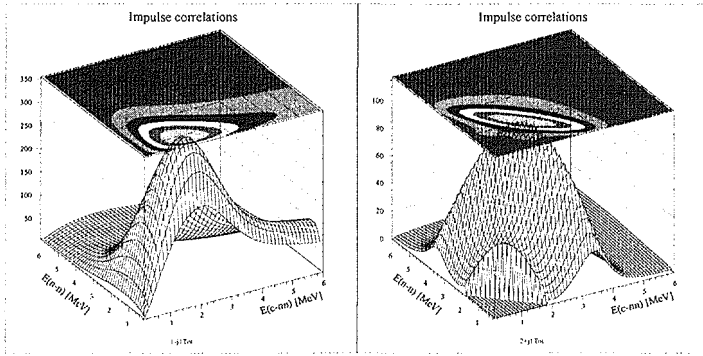
Figure 3: Correlated response for 1^- 'soft dipole' (left), and 2_2^+ resonance (right).

exploration of the ^{11}Li continuum is not a closed chapter.

References

[1] J.S. Vaagen et al., Proceedings of the International Workshop X XIV on Gross Properties of Nuclei and Nuclear Excitations, Hirschegg (1996) 338.

[2] B.V. Danilin, T. Rogde, S.N. Ershov, H. Heiberg-Andersen, J.S. Vaagen, I.J. Thompson, and M.V. Zhukov, Phys. Rev. **C55** (1997) R577; S.N. Ershov, T. Rogde, B.V. Danilin, J.S. Vaagen, I.J. Thompson and F.A. Gareev, Phys. Rev. **C56** (1997) 1483, and references therein.

[3] B.V. Danilin, I.J. Thompson, M.V. Zhukov and J.S. Vaagen, Nucl. Phys. **A**, in press.

[4] A. Cobis, D.V. Fedorov and A.S. Jensen, Phys. Rev. Lett. **79** (1997) 2411.

[5] E. Garrido, D.V. Fedorov and A.S. Jensen, Phys. Rev. **C53** (1996) 3159.

[6] F. Ajzenberg-Selove, Nucl. Phys. **A490** (1988) 1.

[7] A. Csótó, Phys. Lett. **B315** (1993) 24; Phys. Rev. C **48** (1993) 165; ibid C **49** (1994) 3035, 2244.

[8] S. Aoyama et al., Progr. Theor. Phys. **93** (1995) 99; **94** (1995) 343.

[9] B.V. Danilin et al., Phys. Lett. **B333** (1994) 299.

Re/Os COSMOCHRONOMETRY

T. FAESTERMANN[a] , K. TAKAHASHI[a,b] , P. KIENLE[a]
and F. BOSCH[c]

[a] *TU München, James-Franck-Str., D-85748 Garching, Germany*
[b] *MPI für Astrophysik, Karl-Schwarzschild-Str. 1, D-85740 Garching, Germany*
[c] *GSI, Postfach 110552, D-64220 Darmstadt, Germany*

Abstract

The use of the ^{187}Re/^{187}Os solar abundance ratio to determine the age of our galaxy has been improved by : I. A survey for the most reliable data on meteoritic abundances. II. A measurement of the decay of completely ionized ^{187}Re nuclei in the Experimental Storage Ring of the GSI. This is dominated by bound-state β decay with a halflife of (32.9 ± 2.0) yr. III. A detailed analysis of the fate of ^{187}Re and ^{187}Os after being processed in stars of the relevant range of masses. IV. Constraining a model of the galactic chemical evolution by astrophysical observations. The analysis leads to an age of the Galactic disk of (15 ± 3) Gyr.

1 Introduction

Apart from astronomical observations on globular clusters, the age of our galaxy can be estimated from abundancies of longlived radionuclides and their daughters. The pair ^{187}Re and ^{187}Os has been proposed as such a chronometer by Clayton [1] a long time ago. ^{187}Re has a half-life of 42 Gyr, which exceeds by far the age of the universe. It is produced by the r-process but not its β decay daughter ^{187}Os. This is a great advantage compared with other chronometers like ^{232}Th/^{238}U, where the relative r-process production ratios are required.

From today's abundances in meteorites we can easily calculate the ^{187}Re and ^{187}Os abundance 4.56 Gyr ago, when the meteorites (and the solar system) formed and were closed off from the admixture of newly synthesized heavy nuclei. But in the commonly used compilation [2] the abundance ratio is only given with 11% uncertainty. To get a more precise ratio we have extensively searched the literature for recent data. The results will be discussed in section 2. ^{187}Os is not only populated by β decay, but also in the s-process by n-capture on ^{186}Os. Assuming equilibrium this contribution can be estimated from the abundance of ^{186}Os, a pure s-process nuclide (apart from a possible tiny contribution from the p-process [3]), and the two (n,γ) cross sections. The

latter have to be averaged over thermal neutron energies, and the n-capture by the thermally excited 9.75 keV first excited state in ^{187}Os has to be taken into account [4].

A major obstacle in using the ^{187}Re/^{187}Os chronometer has been the fact that the decay rate of ^{187}Re can change dramatically if embodied from the interstellar medium into a new star. Then it becomes highly ionized and bound-state β decay, even to the first excited state in ^{187}Os becomes possible. This can enhance the decay rate, as estimated by Takahashi et al. [5], by more than 9 orders of magnitude. The recent experimental determination of that decay rate [6] will be described in section 3. This result can be used to calculate the half-life of ^{187}Re in any charge state.

To take the astration effects into account, stellar evolution models [7] have been adopted to calculate fractions of ^{187}Re and ^{187}Os embedded in a newly born star that are ejected. Using this information the chemical evolution of the galaxy can be modelled [8] with its age as a parameter, to reproduce in addition to observational constraints the relative abundances of ^{187}Re, ^{187}Os and ^{186}Os.

2 Meteoritic abundances

The solar system abundance ratio of ^{187}Re and ^{187}Os, taken from the compilation of Anders and Grevesse [2] , is only known with 11% uncertainty. This would restrict in any case the precision of the galactic age. Therefore we have searched the literature for new data. The best representatives of the solar system composition are the most primitive meteorites, the carbonaceous chondrites, where measurements are apparently difficult. But already from iron meteorites we can deduce important information.

Very precise and reproducible measurements on iron meteorites have been reported recently by two groups [9, 10] . In these the Re/Os ratio varies over a large range, but the ^{187}Os/^{188}Os ratio plotted versus the ^{187}Re/^{188}Os ratio defines perfectly a linear relationship, as it should, if all the samples have the same age and the same fraction of ^{187}Re has decayed. The individual measurements are so precise that even slightly different slopes and initials can be deduced for different classes of meteorites. The slope equals $(exp(\lambda T) - 1)$ with the ^{187}Re decay constant λ and the age T of the meteorites, the initial gives the ^{187}Os/^{188}Os ratio at the time of its formation. Smoliar et al. [9] use the isochrone for the iron meteorites of class IIIA, whose age is assumed as (4558 ± 5) Myr to determine the decay constant $\lambda = (1.666\pm 0.017)\times10^{-11}$yr^{-1}. This is in agreement with values derived from differently dated meteorites

[10, 11, 12], corresponds to a half-life of 41.6 Gyr and is considerably more precise than the only direct determination by Lindner et al. [13]. The initial $^{187}Os/^{188}Os$ ratio decreases also correctly with increasing age and amounts to 0.0952(2) for the oldest meteorites, like the carbonaceous chondrites, which formed 4.56(1) Gyr ago.

For chondrites even the recent data are not as consistent. Meisel et al. [14] published 5 measurements on CM2 and CV3 chondrites with an average $^{187}Re/^{188}Os$ ratio of 0.389, significantly lower than the average for ordinary chondrites of about 0.44. These do not nicely determine an isochrone and Meisel et al. report that the $^{187}Re/^{188}Os$ in different samples of the same meteorite are not reproducible within the quoted uncertainties, but that the $^{187}Os/^{188}Os$ ratios are. Therefore they suggest that the latter ratio reflects the original composition, and that the former has been altered in a late stage. If this were the case, we could determine the original ^{187}Re from the ^{187}Os content using the initial value derived from the iron meteorites and arrive at a $^{187}Re/^{188}Os$ ratio of 0.390(5). But for the time being we use their directly measured values (neglect older measurements by the same group [15]) and combine them with four recent measurements of CI to CK4 carbonaceous chondrites by Jochum [16] yielding a present day solar abundance ratio and rms deviation of $^{187}Re/^{188}Os = 0.392 \pm 0.010$. Thus the $^{187}Re/^{187}Os$ abundance ratio is determined with a precision better than 3%.

3   Half-life of bare ^{187}Re

The β decay of neutral ^{187}Re atoms has a Q value of 2.66 keV. Because the total electronic binding energy is higher in Os than in Re, β decay of bare $^{187}Re^{75+}$ nuclei to continuum states is energetically forbidden. Instead bare $^{187}Os^{76+}$ nuclei can decay to $^{187}Re^{75+}$ by capturing an electron from the continuum. But $^{187}Re^{75+}$ can β decay when the decay electron is bound in the atomic K-shell of $^{187}Os^{75+}$. This bound-state decay is even possible to the nuclear first excited state with a Q value of 63.22 keV. Whereas the ground-state transition is unique first forbidden, that to the excited state is of non-unique first forbidden character and thus its nuclear matrix element expected to be larger by orders of magnitude. To determine this matrix element was the main purpose of the experiment [6] to measure the half-life of bare $^{187}Re^{75+}$, which was estimated earlier [5] to be 14 yr. At the GSI Darmstadt ^{187}Re ions were accelerated to 70% of the speed of light, completely stripped of electrons and injected into the experimental storage ring (ESR). In the ring the ions were cooled with the electron cooler and for about 30 minutes ion bunches were accumulated until

some 10^8 ions were coasting in the ring, which has a circumference of 106 m.
After a waiting time of up to 5 hours the number of $^{187}Os^{75+}$ ions produced by
bound-state β decay were counted with two independent methods. Since the
hydrogen-like $^{187}Os^{75+}$ ions differ from the $^{187}Re^{75+}$ mother nuclei not in charge
but only by a miniscule mass difference, they are indistinguishable. Only after
turning on a gas stripper the $^{187}Os^{75+}$ can loose their electron and proceed on
a different trajectory. In the first method of identification, this trajectory was
intercepted by a particle detector which yielded information on position and
the nuclear charge. The second, very elegant method measured the revolution
frequency of the coasting ions with high precision and thus could identify and
count the $^{187}Os^{76+}$ ions. A dozen measurements with either method yielded
consistent results for the half-life and an average value of $T_{1/2} = 32.9 \pm 2.0$ yr.
This is indeed 10^9 times shorter than for the neutral atoms and yields the
desired nuclear matrix element between the $5/2^+$ ground state in ^{187}Re and
the $3/2^-$ first excited state in ^{187}Os.

4   Astration effects

With the necessary nuclear matrix element now determined one can calculate
the decay rates of ^{187}Re ions for β^- decay and of ^{187}Os ions for capture of
a continuum electron in a hot environment as a function of temperature and
electron density. Takahashi et al. [7] have used realistic models of stellar evo-
lution to calculate the fate of small quantities of these two isotopes embedded
in a newly born star. The result is shown in fig. 1 as a function of the stars
mass M for masses between 1 and 50 $M_\odot$. The fraction below the solid line is
lost, because it stays in the white dwarf (WD) or neutron star (NS) remnant
or is destroyed by (n, γ) reactions in heavy stars. In light stars a considerable
fraction of the original ^{187}Os is transformed into ^{187}Re (between solid and up-
per dashed line), whereas in massive stars (M $\geq 10 \cdot M_\odot$) more of the ^{187}Re has
decayed by bound-state β^- decay to ^{187}Os (between the long dashed and the
solid line).

5   Chemical evolution and age of our galaxy

Taking into account these astration effects, Takahasi [8] uses essentially a sim-
ilar model of the galactic chemical evolution as earlier [17] to estimate the age
of the galactic disk. This model is constrained by observations of present-day
quantities, like the mass function and the relative stellar birth rate, the total
mass and the gas mass in the galactic disk, the infall rate from the halo onto
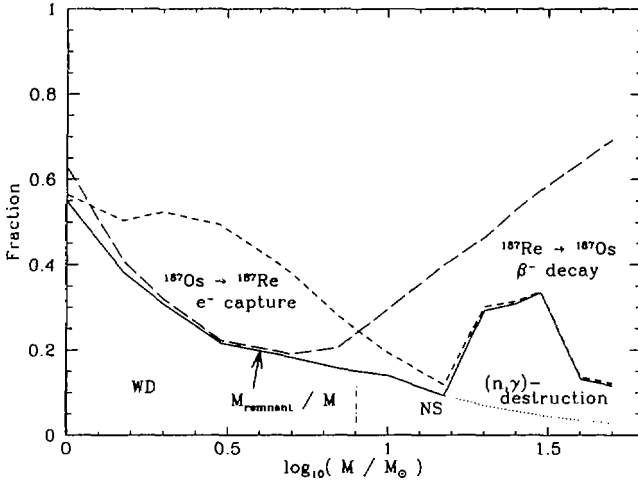
Figure 1: Fractions of ^{187}Re and ^{187}Os which are ejected by a dying star of mass M. For details see text.

the disk and metallicity data. One variable parameter is the total mass (in form of gas) at the beginning of stellar nucleosynthesis in the galaxy. Another parameter describes the time dependence of the infall rate and one the time dependence of the star formation rate, which is assumed as a step function. With this model the solar abundancies of ^{186}Os, ^{187}Os and ^{187}Re have to be reproduced. The adjustment yields an age of the galactic disk of (15 ± 3) Gyr. The somewhat pessimistic error is meant as a 1σ uncertainty and accounts for uncertainties in the chemical evolution model and errors in cross sections and abundancies. This age is in agreement with values derived from globular clusters, although in the last couple of years these ages tend to get shorter with an average of about 12 Gyr (see the contribution of A. Weiss to this workshop). An age of the universe in excess of 15 Gyr would imply a rather low Hubble parameter, e.g. $h_o \leq 0.5$ for a density $\Omega_o \geq 0.4$ and $\lambda = 0$.

6 Acknowledgement

References

[1] D. D. Clayton, Astrophys. Journal **139** (1964) 637

[2] E. Anders, N. Grevesse, Geochim. Cosmochim. Acta **53** (1989) 197

[3] F. Käppeler et el., Astrophys. Journal **366** (1991) 605

[4] R. R. Winters et al., Phys. Rev. **C34** (1986) 840

[5] K. Takahashi et al., Phys. Rev. **C36** (1987) 1522

[6] F. Bosch et al., Phys. Rev. Lett. **26** (1996) 5190

[7] K. Takahashi, N. Langer, J. Wagenhuber, to be published

[8] K. Takahashi et al., to be published, and K. Takahashi, Proc. Tours Nucl. Symp. III, Tours, France, Sept. 2-5 1997

[9] M.I. Smoliar, R.J. Walker, J.W. Morgan, Science **271** (1996) 1099

[10] J.J. Shen, D.A. Papanastassiou, G.J. Wasserburg, Geochim. Cosmochim. Acta **60** (1996) 2887

[11] M.I. Smoliar, R.J. Walker, J.W. Morgan, Proc. 60th Meteoritical Society Meeting, Hawai, (1997)

[12] A. Shukolyukov, G. W. Lugmair, Proc. 28th Lunar and Planetary Science Conf., (1997)

[13] M. Lindner et al., Geochim. Cosmochim. Acta **53** (1989) 1597

[14] T. Meisel, R.J. Walker, J.W. Morgan, Nature **383** (1996) 517

[15] R.J. Walker, J.W. Morgan, Science **243** (1989) 519

[16] K.P. Jochum, Geochim. Cosmochim. Acta **60** (1996) 3353

[17] K. Yokoi, K. Takahashi, M. Arnould, Astron. & Astrophys. **117** (1983) 65

NUCLEAR ASTROPHYSICS

PROGRAM

.

MONDAY, JANUARY 12, 1998

.

Morning Session 9:00 - 12:00 h   chair: GERD RÖPKE

VIJAY R. PANDHARIPANDE (Urbana)
Many-body theory of neutron star structure

NORMAN K. GLENDENNING (Berkeley)
Deconfinement signal in pulsar timing

HENNING HEISELBERG (Nordita Copenhagen)
Phase transitions in rotating neutron stars

HANS-JOSEF SCHULZE (INFN Catania)
Hyperonic nuclear matter in Brueckner theory

- 424 -

Afternoon Session 17:00 - 19:00 h   chair: FRIEDRICH-K. THIELEMANN

MADAPPA PRAKASH (Stony Brook)
Neutrinos from newly born neutron stars: The EOS and neutrino interactions
in dense matter

SANJAY REDDY (Stony Brook)
Neutrinos from protoneutron stars

ARMEN SEDRAKIAN (Cornell)
Neutron-phonon interactions in neutron star crusts

FREDERICK K. LAMB (Urbana)
Constraints on neutron star masses and radii and the equation of state of dense
matter from observations of kilohertz QPOs

Evening Session 20:30 - 21:50 h   chair: JÖRN KNOLL

INGO SICK (Basel)
Nuclear matter at short internucleon distances

KLAUS SCHERTLER (Gießen)
Medium effects and the structure of neutron stars in the effective mass bag
model

STEFAN TYPEL (LMU München)
Relativistic mean field theory with density dependent coupling constants for
nuclear matter and finite nuclei with large charge asymmetry

JÜRGEN SCHAFFNER-BIELICH (Berkeley)
Strange condensates in neutron stars

Tuesday, January 13, 1998

Morning Session 9:00 - 12:10 h   chair: Wolfgang Nörenberg

Ewald Müller (MPA Garching)
Core collapse supernovae

Friedrich-K. Thielemann (Basel)
Explosive burning and nucleosynthesis in supernovae

Karlheinz Langanke (Århus)
Nuclear physics input in supernova physics

Joachim Görres (Notre Dame)
Lifetime of ^{44}Ti as probe for supernova models

Thomas Faestermann (TU München)
Re/Os cosmochronometry

Afternoon Session 17:00 - 19:00 h   ·   chair: Freder Beck

Peter L. Biermann (MPIfR Bonn)
Cosmics ray interactions in the Galaxy

Norbert Magnussen (Wuppertal)
Experimental results from ground-based gamma-ray and cosmic ray experiments

Hans Bloemen (SRON Utrecht)
Gamma rays from nuclear interactions and nucleosynthesis

Evening Session 20:30 - 21:30 h   chair: Jan S. Vaagen

Roland Diehl (MPE Garching, COMPTEL Team)
Results from astronomical radioactivity measurements

Carles Domingo (Barcelona)
Source composition of ultra heavy cosmic rays derived from UHCRE measurements using a leaky box model

Chang-Hwan Lee (Stony Brook)
Neutron star observables and the high density equation of state

WEDNESDAY, JANUARY 14, 1998

Morning Session 9:00 - 12:00 h   chair: GERHARD BAUR

CHRIS PETHICK (Nordita Copenhagen)
Phases of dense matter with non-spherical nuclei

PAUL-GERHARD REINHARD (Erlangen)
Nuclear structure models and nuclei far from stability

THOMAS RAUSCHER (Basel)
Predicting nuclear reaction rates far from stability

ERNST ROECKL (GSI Darmstadt)
Structure of proton-rich nuclei of astrophysical interest

Afternoon Session 17:00 - 19:20 h   chair: GOTTFRIED MÜNZENBERG

KARL-LUDWIG KRATZ (Mainz)
New experiments on r-process nuclei in the $^{132}Sn_{82}$ region

IVAN BORZOV (IPPE Obninsk)
Large-scale calculations of the beta-decay rates and the r-process nucleosyn-
thesis

FRANZ KÄPPELER (FZ Karlsruhe)
(n,γ) and (p,γ) rates for s-and p-process nucleosynthesis

KARIM BENNACEUR (GANIL)
A study of nuclei of astrophysical interest within the continuum shell model

THURSDAY, JANUARY 15, 1998

Morning Session 9:00 - 12:00 h   chair: HANS FELDMEIER

MICHAEL WIESCHER (Notre Dame)
The characteristics of the rp-process at x-ray burst conditions

K. ERNST REHM (Argonne)
rp-process studies with radioactive beams at ATLAS

MARCEL ARNOULD (Bruxelles)
The p-process in exploding massive stars

ALAN C. SHOTTER (Edinburgh)
Breakout from the hot CNO cycle: the $^{15}O(\alpha,\gamma)$ and $^{18}Ne(\alpha,p)$ reactions

Afternoon Session 17:00 - 19:00 h   chair: LASZLO CSERNAI

PIERRE LELEUX (Louvain-la-Neuve)
Explosive nucleosynthesis and the hot-CNO cycle: a laboratory approach

JOSE BENLLIURE (GSI Darmstadt)
Estimated production of isotopes approaching the r-process path

GERHARD BAUR (FZ Jülich)
Coulomb dissociation as a tool of nuclear astrophysics

TOHRU MOTOBAYASHI (Rikkyo)
Coulomb dissociation studies for astrophysical thermonuclear reactions

FRIDAY, JANUARY 16, 1998

Morning Session 9:00 - 12:00 h   chair: JOCHEN WAMBACH

ACHIM WEISS (MPA Garching)
Solar models: achievements and failures

MATTHIAS JUNKER (Gran Sasso)
Present status and future prospects of underground nuclear astrophysics

LOTHAR OBERAUER (TU München)
Status of astrophysical neutrino experiments and prospects

EDWIN KOLBE (Basel)
The $(\nu, \nu'N\gamma)$ reaction on ^{16}O and the strangeness content of the nucleon

Afternoon Session 17:00 - 19:00 h   chair: INGO SICK

J. WOLFGANG HAMMER (Stuttgart)
Investigation of astrophysically interesting nuclear reactions by the use of gas target techniques

FILIPPO TERRASI (Napoli)
Measurement of reaction rates of interest in stellar structure and evolution

UWE GREIFE (Bochum)
Status of the work with radioactive nuclei

SEBASTIAN KUBIS (Kraków)
Nuclear matter with isovector-scalar mesons

LIST OF PARTICIPANTS

DIETER ACKERMANN
ackermann@lnl.infn.it
phone: +39-49 8068 436
fax: +39-49 641925

LNL - INFN
Laboratori Nazionali di Legnaro - INFN
via Romea 4
I-35020 LAEGNARO (PD)
ITALY

MARCEL ARNOULD
marnould@astro.ulb.ac.be
phone: +32-2 650 2864
fax: +32-2 650 4226

Institut d'Astrophysique et d'Astrophysique
Université Libre de Bruxelles
Campus Plaine, CP-226, Bvd du Triomphe
B-1050 BRUXELLES
BELGIUM

GERHARD BAUR
g.baur@fz-juelich.de
phone: +49-2461-61-4457 or 4401
fax: +49-2461-61-3930

Institut für Kernphysik
Postfach 1913
Forschungszentrum Jülich
D-52425 JÜLICH
GERMANY

FRIEDRICH BECK
freder.beck@physik.tu-darmstadt.de
phone: +49-6151-16-2672
fax: +49-6151-16-6076

Institut für Kernphysik
Technische Universität Darmstadt
Schloßgartenstraße 9
D-64289 DARMSTADT
GERMANY

JOSE BENLLIURE
j.benlliure@gsi.de
phone: +49-6159-71-2727
fax: +49-6159-71-2902

Gesellschaft für Schwerionenforschung (GSI)
Postfach 110552
D-64220 DARMSTADT
GERMANY

KARIM BENNACEUR
bennaceur@ganil.fr
phone: +33-02 31 45 46 44
fax: +33-02 31 45 46 65

GANIL
Bd Henri Becquerel
BP 5027
F-14076 CAEN CEDEX 5
FRANCE

PETER L. BIERMANN
plbiermann@mpifr-bonn.mpg.de
phone: +49-228-525-279
fax: +49-228-525-229

Max-Planck-Institut für Radioastronomie
Auf dem Hügel 69
D-53121 BONN
GERMANY

DAVID BLASCHKE
david@darss.mpg.uni-rostock.de
phone: +49-381-498-2853
fax: +49-381-498-2857

Universität Rostock
Universitätsplatz 1
D-18051 ROSTOCK
GERMANY

- 430 -

HANS BLOEMEN
h.bloemen@sron.ruu.nl
phone: +31-30-2538572 / 2535600
fax: +31-30-2540860

SRON-Utrecht
Sorbonnelaan 2
NL-3584 CA UTRECHT
THE NETHERLANDS

WIGBERT BÖHMER
boehmer@vkcmzd.chemie.uni-mainz.de
phone: +49-6131-39-5315
fax: +49-6131-39-5253

Institut für Kernchemie
Johannes-Gutenberg-Universität Mainz
Fritz-Strassmann-Weg 2
D-55128 MAINZ
GERMANY

IVAN N. BORZOV
iborzov@astro.ulb.ac.be
phone: +32-2-650 28 63
fax: +32-2-650 42 26

Institut d'Astronomie et d'Astrophysique
Université Libre de Bruxelles
Campus Plaine, CP 226, Bvd du Triomphe
B-1050 BRUSSELS
BELGIUM

MICHAEL BUBALLA
michael.buballa@physik.tu-darmstadt.de
phone: +49-6151-16-3272
fax: +49-6151-16-6076

Institut für Kernphysik
Technische Universität Darmstadt
Schloßgartenstraße 9
D-64289 DARMSTADT
GERMANY

LASZLO P. CSERNAI
csernai@fi.uib.no
phone: +47-55 58 28 01
fax: +47-55 58 94 40

Fysisk Institutt
University of Bergen
Allégaten 55
N-5007 BERGEN
NORWAY

ROLAND DIEHL
rod@mpe.mpg.de
phone: +49-89-3299-3850
fax: +49-89-3299-3235

MPE Garching
Postfach 1603
D-85740 GARCHING
GERMANY

CARLES DOMINGO
c.domingo@cc.uab.es
phone: +34-3-5811530
fax: +34-3-5812155

Grup de Física de les Radiacions
Departament de Física, Edifici Cc
Universitat Autònoma de Barcelona
E-08193 BELLATERRA (BARCELONA)
SPAIN

ANTONIO DONOFRIO
donofrio@na.infn.it
phone: +39-823 275215
fax: +39-823 275210

Dipartimento di Scienze Ambientali
Seconda Universitá di Napoli and INFN
Centro Dir. S. Benedetto, Via Arena 22
I-81100 CASERTA
ITALY

THOMAS FAESTERMANN
thomas.faestermann@physik.tu-muenchen.de
phone: +49-89-28912438
fax: +49-89-28912297

TU München
Fakultät für Physik E12
James-Franck-Str.
D-85748 GARCHING
GERMANY

HANS FELDMEIER
h.feldmeier@gsi.de
phone: +49-6159-71-2744
fax: +49-6159-71-2990

Gesellschaft für Schwerionenforschung (GSI)
Postfach 110552
D-64220 DARMSTADT
GERMANY

JOAN FONT
j.font@cc.uab.es
phone: +34-3-5812935
fax: +34-3-5812155

Grup de Física de les Radiacions
Departament de Física, Edifici Cc
Universitat Autònoma de Barcelona
E-08193 BELLATERRA
SPAIN

NORMAN K. GLENDENNING
nkg@lbl.gov
phone: +1-510 486 5420
fax: +1-510 486 4794

Nuclear Science Division &
Institute for Nuclear & Particle Astrophysics
Lawrence Berkeley Nat. Lab., MS 70A-3307
BERKELEY, CA 92740
USA

JOACHIM GÖRRES
jgoerres@nd.edu
phone: +1-219-631-7716
fax: +1-219-631-5952

Department of Physics
University of Notre Dame
NOTRE DAME, IN 46556
USA

UWE GREIFE
greife@ep3.ruhr-uni-bochum.de
phone: +49- 234 - 700 35 97
fax: +49 -234 - 709 41 72

Ruhr-Universität Bochum
Fakultät für Physik u. Astronomie
Institut für Experimentalphysik III
D-44780 BOCHUM
GERMANY

J.WOLFGANG HAMMER
hammer@ifs.physik.uni-stuttgart.de
phone: +49-711-685 3891 / 3888
fax: +49-711-685 3866

Institut für Strahlenphysik (IfS)
Universität Stuttgart
Allmandring 3
D-70550 STUTTGART
GERMANY

HENNING HEISELBERG
hh@nordita.dk
phone: +45-35 32 52 04
fax: +45-35 38 91 57

NORDITA
Blegdamsvej 17
DK-2100 COPENHAGEN Ø
DENMARK

CHANG-HO HYUN
hch@zoo.snu.ac.kr
phone: +82-2-880-8164
fax: +82-2-884-7167

Department of Physics
Seoul National University
Shillim-Dong San 56-1, Kwan-Ak-Gu
SEOUL 151-742
KOREA

MATTHIAS JUNKER
matthias.junker@lngs.infn.it
phone: +39-862 437 547/358
fax: +39-862 437 570

Instituto Nazionale Fisica Nucleare
Lab. Naz. del Gran Sasso (LNGS)
S.S. 17bis, km 18+910
I-67010 ASSERGI (AQ)
ITALY

FRANZ KÄPPELER
kaepp@ik3.fzk.de
phone: +49-7247-82 3991
fax: +49-7247-82 4075

Forschungszentrum Karlsruhe
IK-III
Postfach 3640
D-76021 KARLSRUHE
GERMANY

JÖRN KNOLL
j.knoll@gsi.de
phone: +49-6159-71-2749
fax: +49-6159-71-2990

Gesellschaft für Schwerionenforschung (GSI)
Postfach 110552
D-64220 DARMSTADT
GERMANY

EDWIN KOLBE
kolbe@quasar.physik.unibas.ch
phone: +41-61-267-3754
fax: +41-61-267-3784

Departement für Physik und Astronomie
Universität Basel
Klingelbergstrasse 82
CH-4056 BASEL
SWITZERLAND

KARL-LUDWIG KRATZ
klkratz@vkcmzd.chemie.uni-mainz.de
phone: +49-6131-39-5892 / 5883
fax: +49-6131-39-5253

Institut für Kernchemie
Johannes-Gutenberg-Universität Mainz
Fritz-Strassmann-Weg 2
D-55128 MAINZ
GERMANY

SEBASTIAN KUBIS
kubis@solaris.ifj.edu.pl
phone: +48-12-6370222

H.Niewodniczanski Institute
of Nuclear Physics in Cracow
ul.Radzikowskiego 152
31-342 KRAKOW
POLAND

FREDERICK K. LAMB
flamb@sirius.astro.uiuc.edu
phone: +1-217-333-6363
fax: +1-217-333-8919

Dep. of Physics, 337 Loomis Lab.
University of Illinois at
Urbana-Champaign
URBANA, IL 61801
USA

KARLHEINZ LANGANKE
langanke@dfi.aau.dk
phone: +45-89 42 3671
fax: +45-86 12 0740

Institut for Fysik og Astronomi
University of Aarhus
Ny Munkegade Bld. 520
DK-8000 AARHUS C
DENMARK

CHANG-HWAN LEE
chlee@nuclear.physics.sunysb.edu
phone: +1-516-632-8128
fax: +1-516-632-9718

Dept. of Physics and Astronomy
State University of New York at
Stony Brook
STONY BROOK, NY 11794-3800
USA

PIERRE LELEUX
leleux@fynu.ucl.ac.be
phone: +32-10473229
fax: +32-10452183

Institut de Physique nucleaire
University of Louvain
Chemin du Cyclotron, 2
B-1348 LOUVAIN-LA-NEUVE
BELGIUM

NORBERT MAGNUSSEN
magnus@wpos1.physik.uni-wuppertal.de
phone: +49-202-439 2626
fax: +49-202-439 2662

Fachbereich Physik
Bergische Universität Wuppertal
Gauß Str. 20
D-42097 WUPPERTAL
GERMANY

TOHRU MOTOBAYASHI
motobaya@rikkyo.ac.jp
phone: +81-3 3985 2379
fax: +81-3 5992 3434

Department of Physics
Rikkyo University
3-Nishi-Ikebukuro, Toshima
TOKYO 171
JAPAN

EWALD MÜLLER
emueller@mpa-garching.mpg.de
phone: +49-89-3299-3209
fax: +49-89-3299-3235

Max-Planck-Institut für Astrophysik
Karl-Schwarzschild-Str. 1
D-85748 GARCHING
GERMANY

GOTTFRIED MÜNZENBERG
g.muenzenberg@gsi.de
phone: +49-6159-71-2733
fax: +49-6159-71-2902

Gesellschaft für Schwerionenforschung (GSI)
Postfach 110552
D-64220 DARMSTADT
GERMANY

WOLFGANG NÖRENBERG
w.nrnbrg@gsi.de
phone: +49-6159-71-2747
fax: +49-6159-71-2990

Gesellschaft für Schwerionenforschung (GSI)
Postfach 110552
D-64220 DARMSTADT
GERMANY

LOTHAR OBERAUER
oberauer@e15.physik.tu-muenchen.de
phone: +49-89-28912509
fax: +49-89-28912680

Fakultät für Physik E-15
Technische Universität München
James Franck Str.
D-85748 GARCHING
GERMANY

MICAELA OERTEL
micaela.oertel@physik.tu-darmstadt.de
phone: +49-6151-16-3272
fax: +49-6151-16-6076

Institut für Kernphysik
Technische Universität Darmstadt
Schloßgartenstraße 9
D-64289 DARMSTADT
GERMANY

VIJAY R. PANDHARIPANDE
vijay@rsm1.physics.uiuc.edu
phone: +1-217-333-8079
fax: +1-217-333-8919

Dep. of Physics, 337 Loomis Lab.
University of Illinois
1110 West Green Street
URBANA, IL 61801-3080
USA

CHRIS J. PETHICK
pethick@nordita.dk
phone: +45-35 32 52 26
fax: +45-35 38 91 57

NORDITA
Blegdamsvej 17
DK-2100 COPENHAGEN Ø
DENMARK

JOSE PONS
pons@scry.daa.uv.es
phone: +34-63983081
fax: +34-63983084

Universitat de Valencia
Dpt. Astronomia i Astrofisica
BURJASSOT 46100 (VALENCIA)
SPAIN

MADAPPA PRAKASH
prakash@nuclear.physics.sunysb.edu
phone: +1-516-632-8162
fax: +1-516-632-9718

Department of Physics and Astronomy
SUNY at Stony Brook
STONY BROOK, NY 11794-3800
USA

THOMAS RAUSCHER
tommy@quasar.physik.unibas.ch
phone: +41-61-267-3757
fax: +41-61-267-3784

Institut für Physik
Universität Basel
Klingelbergstr. 82
CH-4056 BASEL
SWITZERLAND

SANJAY REDDY
reddy@crankme.physics.sunysb.edu
phone: +1-516-632-9843
fax: +1-516-632-9718

Department of Physics and Astronomy
SUNY at Stony Brook
STONY BROOK, NY 11794-3800
USA

K. ERNST REHM
rehm@anph12.phy.anl.gov
phone: +1-630-252-4073
fax: +1-630-252-6210

Argonne National Lab.
9700 South Cass Av.
ARGONNE, IL 60439
USA

PAUL-GERHARD REINHARD
mpt218@theorie2.physik.uni-erlangen.de
phone: +49-9131-85-8458
fax: +49-9131-85-8444

Institut für Theoretische Physik
Staudtstr. 7
D-91058 ERLANGEN
GERMANY

ERNST ROECKL
e.roeckl@gsi.de
phone: +49-6159-71-2433
fax: +49-6159-71-2902

Gesellschaft für Schwerionenforschung (GSI)
Postfach 110552
D-64220 DARMSTADT
GERMANY

GERD RÖPKE
gerd@darss.mpg.uni-rostock.de
phone: +49-381-498-2855
fax: +49-381-498-2857

FB Physik
Universität Rostock
Universitätsplatz 3
D-18051 ROSTOCK
GERMANY

PRADIP KUMAR SAHU
pradip@theorie.physik.uni-giessen.de
phone: +49-641-99-33314
fax: +49-641-99-33309

Institut für Theoretische Physik
Universität Giessen
Heinrich-Buff-Ring 16
D-35392 GIESSEN
GERMANY

JÜRGEN SCHAFFNER-BIELICH
schaffne@nsdssd.lbl.gov
phone: +1-510-486-4464
fax: +1-510-486-4794

Nuclear Science Division
Laurence Berkeley National Laboratory
1 Cyclotron Road
BERKELEY, CA 94720
USA

KLAUS SCHERTLER
klaus.schertler@theo.physik.uni-giessen.de
phone: +49-641-99-33324
fax: +49-641-99-33309

Institut für Theoretische Physik
Universität Giessen
Heinrich-Buff-Ring 16
D-35392 GIESSEN
GERMANY

HANS-JOSEF SCHULZE
schulze@alp1ct.ct.infn.it
phone: +39-95-7195440
fax: +39-95-383023

INFN
Sezione di Catania
Corso Italia 57
I-95129 CATANIA
ITALY

ARMEN SEDRAKIAN
sedrakia@spacenet.tn.cornell.edu
phone: +1-607-255-52 85
fax: +1-607-255-88 03

CRSR
Cornell University
Space Sciences Building Rm 526
ITHACA, NY 14853
USA

ALAN C. SHOTTER
alan.c.shotter@ed.ac.uk
phone: +44-13 16 50 52 86
fax: +44-13 16 50 71 65

University of Edinburgh
JCMB, The King's Buil.
Mayfield Road
EDINBURGH EH9 3JZ
UNITED KINGDOM

INGO SICK
sick@ubaclu.unibas.ch
phone: +41-61-267-3741
fax: +41-61-267-3784

Dept. für Physik und Astronomie
Universität Basel
Klingelbergstr. 82
CH-4056 BASEL
SWITZERLAND

KLAUS SÜMMERER
k.suemmerer@gsi.de
phone: +49-6159-71-2737
fax: +49-6159-71-2902

Gesellschaft für Schwerionenforschung (GSI)
Postfach 110552
D-64220 DARMSTADT
GERMANY

FILIPPO TERRASI
terrasi@na.infn.it
phone: +39-823 275215
fax: +39-823 275210

Dipartimento di Scienze Ambientali
Seconda Universitá di Napoli and INFN
Centro Dir. S. Benedetto, Via Arena 22
I-81100 CASERTA
ITALY

FRIEDRICH-K. THIELEMANN
fkt@quasar.physik.unibas.ch
phone: +41-61-267-3748
fax: +41-61-267-3784

Dept. für Physik und Astronomie
Universität Basel
Klingelbergstr. 82
CH-4056 BASEL
SWITZERLAND

STEFAN TYPEL
stypel@laser.physik.uni-muenchen.de
phone: +49-89-28914118
fax: +49-89-28914008

Sektion Physik
Universität München
Am Coulombwall 1
D-85748 GARCHING
GERMANY

JAN S. VAAGEN
jans.vaagen@fi.uib.no
phone: +47-55 58 2724
fax: +47-55 58 94 40

Department of Physics
University of Bergen
Allégaten 55
N-5007 BERGEN
NORWAY

MIRKO WACHS
wachs@landau.ikp.physik.tu-darmstadt.de
phone: +49-6151-16-2416
fax: +49-6151-16-6076

Institut für Kernphysik
Technische Universität Darmstadt
Schloßgartenstraße 9
D-64289 DARMSTADT
GERMANY

THOMAS WAINDZOCH
thomas.waindzoch@uni-tuebingen.de
phone: +49-7071-29-76374
fax: +49-7071-29-5850

Universität Tübingen
Institut für Theoretische Physik
Auf der Morgestelle 14
D-72076 TÜBINGEN
GERMANY

JOCHEN WAMBACH
jochen.wambach@physik.tu-darmstadt.de
phone: +49-6151-16-2872
fax: +49-6151-16-6076

Institut für Kernphysik
Technische Universität Darmstadt
Schloßgartenstraße 9
D-64289 DARMSTADT
GERMANY

ACHIM WEISS
weiss@mpa-garching.mpg.de
phone: +49-89-3299-3236
fax: +49-89-3299-3235

Max-Planck-Institut für Astrophysik
Karl-Schwarzschild-Str. 1
D-85748 GARCHING
GERMANY

MICHAEL WIESCHER
wiescher.1@nd.edu
phone: +1-219-631-6788
fax: +1-219-631-5952

Department of Physics
University of Notre Dame
NOTRE DAME, IN 46556
USA

ANDREAS WIRZBA
andreas.wirzba@physik.tu-darmstadt.de
phone: +49-6151-16-3274
fax: +49-6151-16-6076

Institut für Kernphysik
Technische Universität Darmstadt
Schloßgartenstraße 9
D-64289 DARMSTADT
GERMANY

.

AUTHOR INDEX